UNIVERSITAT DE BARCELONA

Processes and catalysts for the electrochemical removal of persistent organic micropollutants from urban wastewater at mild Ph

Zhihong Ye

Programa de Doctorat en

Electroquímica. Ciència i Tecnologia

Universitat de Barcelona

Departament de Ciència de Materials i Química Física

Processes and catalysts for the electrochemical removal of persistent organic micropollutants from urban wastewater at mild pH

Memória presentada per **Zhihong Ye** per optar al títol de Doctor per la Universitat de Barcelona

Director

Ignacio Sirés Sadornil

Professor Agregat del Departament de Ciència de Materials i Química Física de la Universitat de Barcelona

Tutor

Enrique Brillas Coso

Professor Catedràtic del Departament de Ciència de Materials i Química Física de la Universitat de Barcelona

Barcelona, Octubre 2019

Universitat de Barcelona

Facultat de Química

Departament de Ciència de Materials i Química Física

Processes and catalysts for the electrochemical removal of persistent organic micropollutants from urban wastewater at mild pH

Zhihong Ye

PhD Thesis

To my beloved family

Acknowledgements

I would like to express my sincere gratitude to my advisor, Prof. Ignacio Sirés Sadornil, as well as to my tutor, Prof. Enrique Brillas Coso, for their continuous support during my PhD and with related research. Thanks for their patience, motivation, and immense knowledge. I am very grateful for their scientific advices and many insightful discussions on my PhD work. Their guidance helped me throughout the period of research and writing of this Thesis. They have been my primary resource for getting my scientific questions answered and were instrumental in helping me carry out this demanding task. I wish that I could become as lively, enthusiastic, and energetic as them to someday be able to conduct research in the same rigorous manner. I also thank the members of LEMMA, Prof. Pere L. Cabot Julià and Prof. Francesc Centellas Masuet, for their helpful suggestions in general, and Prof. Elvira Gómez Valentín for her helpful career advice.

I would especially like to thank Prof. Camille Petit for giving me the opportunity to carry out a short stay at the Imperial College London, where she was my advisor. She has provided many valuable comments and encouragement related to my research. Her careful guidance greatly broadened my research scope, allowing me to acquire a lot of knowledge on materials science. I also thank to the colleagues there for their kind help in research and life.

I am also indebted to my Master supervisor, Prof. Hui Zhang from Wuhan University. He has been helpful in providing advice during my Master study. And, more important, he was the reason why I decided to pursue a career in research. Prof. Zhang was and remains my best role model for a scientist and teacher.

I would like to thank my Thesis committee members for their precise comments and suggestions, which widened my research from various perspectives.

My very sincere thanks also goes to the colleagues at LEMMA group: Roger, Julia, Anlin Xu, Gengbo Ren, Yanyu Zhang, Heng Lin, Alex, Juliana, Diego, Ömür, Gabriela, and some others, who provided me a lot of help during my PhD. A good support system is fundamental to survive and stay sane. Without their precious support it would have not been possible to conduct this research so successfully.

A special thanks to my family. Words cannot express my gratitude to my mother and father for all the sacrifices that you have made on my behalf. Thank you for supporting me for everything in my life!

Last, I would like to thank the China Scholarship Council for awarding the scholarship to support my PhD study for 3 years.

书痴者文必工，艺痴者技必良.

——蒲松龄

TABLE OF CONTENTS

Abstract

Global water scarcity is driving the need of identifying new water resources. Wastewater could become a potential candidate if appropriate and reliable treatment technologies were established. One of the most solid barriers for the obtention of high quality water from wastewater arises from the presence of organic micropollutants, which are defined as anthropogenic organic chemicals occurring in the aquatic environment well above their natural background level due to human activities, but with concentrations remaining at trace levels. Organic micropollutants originate from a great variety of sources including massive pharmaceutical and personal care product consumption, pesticide application to crops, use of plasticizers and stabilizers in industrial manufacture, or dyeing processes for clothes, food and objects in general. Most of them are polar, persistent and non-biodegradable compounds, which means that they may become persistent because their elimination by the current conventional methods in wastewater treatment plants (WWTPs) is negligible. The continuous discharge of organic micropollutants into water resources is an ever-expanding environmental problem, leading to the accumulation of highly hazardous chemicals.

Over the last decades, the electrochemical technologies, especially the electrochemical advanced oxidation processes (EAOPs), have been proven to behave as clean and effective alternatives to eliminate the organic micropollutants from wastewater effluents due to the direct or indirect generation of strong oxidizing agents such as the hydroxyl radical (E^0 ($^{\bullet}OH/H_2O$) = 2.8 V/SHE). However, the utilization of conventional electro-Fenton (EF) and photoelectro-Fenton (PEF) is limited by several drawbacks: (i) long time needed to destroy large contents of organics; (ii) requirement of pH adjustment to 2.5-3.5; (iii) poor electroreduction and photoreduction of Fe(III); (iv) high amount of iron catalyst required; (v) deactivation of iron species; and (vi) production of iron sludge. Aiming to overcome these disadvantages, several processes and catalysts are proposed in this Thesis to modify the conventional EF and PEF.

In the first part, electrocoagulation (EC) was envisaged as a valid pre-treatment before the application of the EAOPs, thus addressing the abovementioned limitation (*i*). This involved the in situ generation of coagulants from dissolution of a sacrificial anode, forming flocs that precipitated and adsorbed part of the organics rapidly. Additionally, when an Fe/Fe cell was employed, the residual dissolved iron species after precipitation acted as the required catalyst for subsequent treatment. The removal of butylated hydroxyanisole (BHA) and benzophenone-3 (BP-3) from urban wastewater was tested by means of either single or sequential EC/EAOPs treatment. Overall mineralization of BP-3-loaded wastewater was attained by PEF after EC pre-treatment, being superior to the single EAOPs and requiring a shorter time.

The second part investigated, for the first time, the feasibility of employing a soluble Fe(III)–EDDS complex as homogeneous EF or PEF catalyst to destroy micropollutants. The systems allowed working at near-neutral pH, exhibiting a high quantum yield for Fe^{2+} generation from Fe(III)–EDDS photoreduction. The performance of Fe(III)–EDDS-assisted EF and PEF processes was thoroughly evaluated from the degradation of BHA and fluoxetine (FLX) in sulfate medium, as well as in urban wastewater.

Heterogeneous EF and PEF processes using solid catalysts have been developed in the third part as promising alternatives to overcome the drawbacks (*ii*)-(*vi*). The development of new types of catalysts with high activity, stability and recyclability is still a great challenge in the field. Metal-organic frameworks (MOFs) have attracted substantial attention in recent years as ordered porous materials with many potential applications. In this Thesis, Fe-MOFs or their derivatives were introduced as efficient and innovative heterogeneous EF or PEF catalysts to treat micropollutants in urban wastewater. FeS_2/C nanoparticles were fabricated by sulfidation and carbonization of an Fe-MOF precursor; nano-ZVI@C-N was derived from NH_2-MIL(Fe)-88B; and a 2D MOF was developed using bpydc as linker. Their unique properties conferred an unprecedented degradation ability to EF and PEF at mild pH.

Nomenclature and symbols

AA	Annual average
AOP	Advanced oxidation process
BDC	Benzene-1,4-dicarboxylic acid (i.e., terephthalic acid)
BDD	Boron-doped diamond
BHA	Butylated hydroxyanisole
BP-3	Benzophenone-3
BPA	Bisphenol A
BP-S	Bipolar electrodes in serial connection
Bpydc	2,2′-Bipyridine-4,4′-dicarboxylic acid
BQ	*p*-Benzoquinone
BZF	Bezafibrate
CEC	Contaminant of emerging concern
CF	Carbon felt
COD	Chemical oxygen demand
DBP	Disinfection byproduct
DMF	*N*,*N*-Dimethylformamide
DOC	Dissolved organic carbon
DSA®	Dimensionally stable anode
EAOP	Electrochemical advanced oxidation process
EC	Electrocoagulation
EC_{50}	Sample dilution causing a 50% reduction in bacterial luminescence
ECs	Emerging contaminants
EDC	Endocrine disrupting chemical
EDDS	Ethylenediamine-*N*,*N*'-disuccinic acid
EEM	Excitation-emission matrix
EF	Electro-Fenton
EO	Electro-oxidation
ESR	Electron spin resonance (i.e., EPR)

EQS	Environmental quality standard
FDA	Food and Drug Administration
FLX	Fluoxetine
FO	Forward osmosis
GC-MS	Gas chromatography coupled to mass spectrometry
GDE	Gas-diffusion electrode
GDP	Global gross domestic product
GEM	Gemfibrozil
HPLC	High-performance liquid chromatography
IC	Ion chromatography
ICP-OES	Inductively-coupled plasma with optical emission spectrometry
$k_{\bullet OH}$	Rate constant of hydroxyl radical reaction with a compound
$k_{O_2^{\bullet -}}$	Rate constant of superoxide reaction with a compound
LC-QToF-MS	Liquid chromatography coupled to hybrid quadrupole time-of-flight mass spectrometry
MAC	Maximum allowable concentration
MF	Microfiltration
MIL	Materials Institute Lavoisier
MMO	Mixed metal oxide
MOF	Metal-organic framework
MP-P	Monopolar electrodes in parallel connection
MP-S	Monopolar electrodes in serial connection
NF	Nanofiltration
NPOC	Non-purgeable organic carbon
NPX	Naproxen
NTA	Nitrilotriacetic acid
$^{\bullet}OH$	Hydroxyl radical
OCP	Organochlorine pesticide
OER	Oxygen evolution reaction
OPP	Organophosphorus pesticide

PAC	Polyaluminum chloride
PAH	Polycyclic aromatic hydrocarbon
PARAFAC	Parallel factor analysis
PAS	Polyaluminum sulfate
PBDE	Polybrominated diphenyl ether
PCB	Polychlorinated biphenyl
PCP	Personal care product
PEC	Photoelectrocatalysis
PEF	Photoelectro-Fenton
PHS	Priority hazardous substance
pK_a	The decimal logarithm of the acid dissociation constant
POP	Persistent organic pollutant
PS	Priority substance
PTFE	Polytetrafluoroethylene
RO	Reverse osmosis
SEM	Scanning electron microscopy
$SO_4^{\bullet-}$	Sulfate radical
SPEF	Solar photoelectro-Fenton
TBA	*tert*-Butanol
TC	Total carbon
TN	Total nitrogen
TOC	Total organic carbon
UF	Ultrafiltration
UV	Ultraviolet light
WHO	World Health Organization
WFD	Water Framework Directive
WRRF	Water resource recovery facility
WTP	Water treatment plant
WWTP	Wastewater treatment plant

CHAPTER 1
INTRODUCTION

1. Introduction

1.1. Water contamination

1.1.1. Water resources

Water is widely considered as the most prominent element for the life of all beings that inhabit our planet. In our case, an evidence of this is given by the fact that human settlements have been historically established around areas with enough water to support socio-economic activities and fulfill daily personal needs. However, driven by a significant increase in water catchments, water scarcity has been a critical environmental issue worldwide during the last century. Faced with the prospect of an unprecedented population growth, a decline of the natural environment and upcoming climate change, water scarcity is projected to be further exacerbated within the near future [1]. By 2025, 1800 million people are expected to be living in countries or regions with "absolute" water scarcity (< 500 m^3 $year^{-1}$ per capita), and two-thirds of world population could be under "stress" conditions (between 500 and 1000 m^3 $year^{-1}$ per capita) [2].

Water resources can be divided into renewable and non-renewable ones. The former account for the total volume of surface water and groundwater that appear through the hydrological cycle, whereas deep aquifers, without a significant replenishment rate on the human time scale, are classified as non-renewable water resources [3,4]. Nearly 97% of water is present in the oceans, which are saline in nature; the remaining 3% of water is freshwater [5]. Freshwater is very unevenly distributed in the world as large differences exist between continents, regions and countries. In 2015, the total renewable freshwater resources per capita in the world were estimated to be 5829 m^3 (Table 1) [3]. The American continent has the largest share of the world's total freshwater resources, with 19725 m^3 $year^{-1}$ per capita, followed by Europe with 8895 m^3 $year^{-1}$ per capita,

Africa with 3319 m^3 $year^{-1}$ per capita and Asia with the lowest volume per capita (2697 m^3 $year^{-1}$). Worth noting, in the Northern Africa and the Arabian Peninsula regions, renewable freshwater resources were only 256 and 77 m^3 $year^{-1}$ per capita, respectively.

Table 1. Long-term average annual internal renewable water resources [3].

Continent Regions ***Subregions***	**Volume per year (km^3 or 10^9 m^3)**	**% of the world freshwater resources**	**Per capita in year 2015 (m^3)**
World	**42810**	**100.0**	**5829**
Africa	**3931**	**9.2**	**3319**
Northern Africa	47	0.1	256
Sub-Saharan Africa	3884	9.1	3879
Sudano Sahelian	160	0.4	992
Gulf of Guinea	952	2.2	3450
Central Africa	1876	4.4	13604
Eastern Africa	285	0.7	1094
Southern Africa	270	0.6	1934
Indian Ocean Islands	341	0.8	12918
Americas	**19536**	**45.6**	**19725**
Northern America	6077	14.2	12537
Northern America	5668	13.2	15845
Mexico	409	1.0	3220
Central America and Caribbean	735	1.7	8397
Central America	637	1.5	13922
Caribbean-Greater Antilles	93	0.2	2367
Caribbean-Lesser Antilles and Bahamas	5	0.0	2071
Southern America	12724	29.7	30428
Guyana	340	0.8	259542
Andean	5337	12.5	38790
Brazil	5661	13.2	27236
Southern America	1386	3.2	19405
Asia	**11865**	**27.7**	**2697**
Middle East	484	1.1	1444
Arabian Peninsula	6	0.0	77
Caucasus	73	0.2	4359
Islamic Republic of Iran	129	0.3	1624
Near East	276	0.6	1730
Central Asia	242	0.6	2420
Southern and Eastern Asia	11139	26.0	2809
South Asia	1935	4.5	1131
East Asia	3410	8.0	2115

Mainland Southeast Asia	1898	4.4	7985
Maritime Southeast Asia	3896	9.1	9658
Europe	**6576**	**15.4**	**8895**
Western and Central Europe	2129	5.0	4006
Northern Europe	836	2.0	31500
Western Europe	621	1.4	2385
Central Europe	249	0.6	2250
Mediterranean Europe	423	1.0	3159
Eastern Europe	4448	10.4	21383
Eastern Europe	136	0.3	2104
Russian Federation	4312	10.1	30058
Oceania	**902**	**2.1**	**29225**
Australia and New Zealand	819	1.9	28739
Other Pacific Islands	83	0.2	35053

Since the 1980s, water use has been increasing worldwide by about 1% per year. This steady rise has principally been led by surging demand in developing countries and emerging economies [6]. Global water demand is expected to continue increasing at a similar rate until 2050, accounting for an increase from 20% to 30% above the current level of water user rent. Current analyses suggest that much of this growth will be attributed to the increase in demand by the industrial and domestic sectors [7,8].

Fig. 1 shows the global water demand by different sectors in 2040 [6]. Generally, water consumption for all sectors grows up to 9% of total freshwater resources [9], with agriculture being the largest user, accounting for 69% of annual water withdrawals globally. The agricultural sector is responsible for up to two-thirds of the total water withdrawals and accounts for almost 90% of the total water consumption in the world. Meanwhile, industry accounts for 19% and households for 12%. Agriculture's share of total water use is estimated likely to fall in comparison with other sectors, but it will still remain the largest user over the coming decades in terms of both, water withdrawal and water consumption[1].

[1] **Water withdrawal**: The volume of water removed from a source and, by definition, withdrawals are always greater than or equal to consumption.
Water consumption: The volume withdrawn that is not returned to the source and, by definition, it is no longer available for other uses locally.

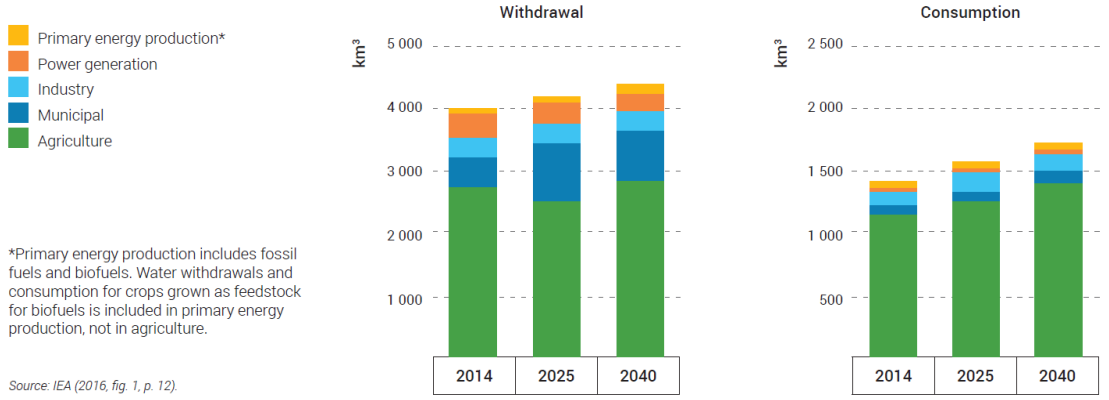

Figure 1. Global water demand by sector in 2040 [6].

The growth of water demand driven by population growth and socio-economic development, the misuse of water resources, the lack of infrastructures to supply water, and climate change result in the increase of water scarcity, which is becoming a great threat to sustainable development of human societies. Fig. 2 provides a global overview of countries experiencing different levels of water stress [6]. Over 2 billion people live in countries experiencing high water stress. Although the global average water stress is only 11%, there are 31 countries experiencing water stress between 25% and 70%, and 22 countries are above 70%, therefore under serious water stress [10].

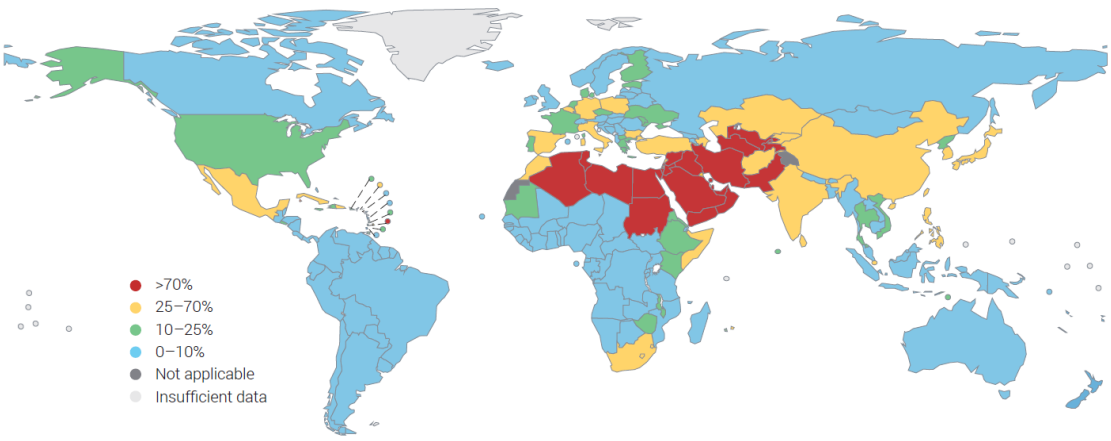

Figure 2. Level of physical water stress[2] [6].

[2] **Physical water stress**: The ratio of total freshwater withdrawn annually by all major sectors to the total amount of renewable freshwater resources, expressed as a percentage.

Increasing water scarcity shows serious impacts on food safety, human health, society and environmental sustainability [11]. Estimates suggest that if the unsustainable pressures on global water resources continue, 45% of the global gross domestic product (GDP), 52% of the world's population and 40% of the global grain production will be at great risk in 2050 [10]. Thus, finding sustainable solutions to overcome future water scarcity will be a great challenge in the following decades. One of the feasible solutions is to improve water reuse by the treatment of contaminated water.

The surface water and groundwater constitute the major water resources for both urban and rural water supply system, whereas imported water is abstracted from external regions. As shown in Fig. 3, the whole system includes water abstraction, transportation, distribution through the network and wastewater treatment and reclamation [12]. Among them, wastewater treatment and reclamation plays an important role on the water ecosystem since wastewater reclamation can generate environmental benefits by decreasing wastewater discharges, preventing pollutions and even recovering useful resources.

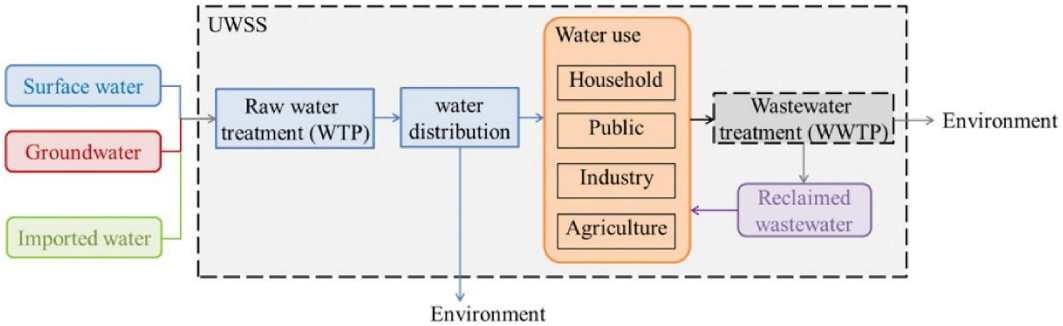

Figure 3. Schematic diagram of a generic water supply system [12].

Apart from the development of industry, increase in human population and environmental catastrophes, the quality of surface water and groundwater around the world is getting rapidly degraded due to massive discharge of industrial wastes, domestic sewage, mine drainage and extensive use of agro-chemicals [13]. Nowadays, water pollution has become a global problem leading to the continuous reduction of the available drinking water, threatening the entire biosphere and affecting the life of

millions of people. According to recent estimates, more than 1.2 billion people do not have access to clean drinking water, and everyday approximately 2 million tons of industrial, sewage and agriculture waste are discharged into water, causing serious health problems and the death of around 14000 people per day [14,15]. Facing such severe situation, the world leaders agreed to 17 Global Goals for Sustainable Development in 2015. One of them is so-called "clean water", wishing to improve water quality by reducing pollution, eliminating dumping and minimizing release of hazardous chemicals and materials, halving the proportion of untreated wastewater and substantially increasing recycling and safe reuse globally.

The different types of water pollutants can be categorized as: inorganic, organic, biological and macroscopic contaminants. The most common inorganic water pollutants are heavy metals, like arsenic, mercury, chromium and barium, which are highly toxic and carcinogenic. Also nitrates, phosphates, sulfates, fluorides, chlorides can cause serious hazardous effects [16].

The toxic organic pollutants mainly consist of proteins, carbohydrates, fats and nucleic acids. A fraction of these organic compounds, called persistent organic pollutants (POPs), are anthropogenic chemicals that have been a major concern because of their toxicity, persistence, bioaccumulation tendency and long-range transport. Generally, POPs such as polychlorinated biphenyls (PCBs), organochlorine pesticides (OCPs), polybrominated diphenyl ethers (PBDEs) and polycyclic aromatic hydrocarbons (PAHs) have drawn great attention in the past decades [17].

The biological pollutants, including bacteria, fungi algae, viruses, protozoa and other worms, can lead to serious diseases affecting animals and humans [18]. The macroscopic pollutants are large, visible items in water, such as macro/microplastics. Some chemicals used as additives in plastic have high toxicity, and plastics have the capacity to adsorb persistent organic pollutants as well as trace metals. In water bodies, the macro/microplastics can be ingested by fish and other organisms, clogging their

digestive system and also release adsorbed hazardous chemicals that could harm the biota [19].

In the past several decades, research has revealed the occurrence of hundreds of organic contaminants in wastewater, such as pharmaceuticals, pesticides and personal care products (PCPs), that significantly affect the water quality, and whose concentrations typically range from ng L^{-1} to μg L^{-1}. This group of contaminants, so-called emerging contaminants (ECs), are chemicals that are commonly present in water but only recently being recognized as significant water pollutants [20]. However, given the qualification of "emerging" as an important water contamination several decades ago, they might no longer be qualified as ECs. Within a broader context, the focus on emerging contaminants (contaminants appeared recently) can be extended to contaminants of emerging concern (CECs, contaminants that have been in the environment for a while but the concerns of which have been raised recently) [21]. Thus, the challenges for the study of CECs are not only the detection and quantification of their concentration, but also the investigation of their behavior, persistence and environmental impact.

1.1.2. Occurrence of organic micropollutants in water

Over the last few decades, the occurrence of CECs, also called persistent organic micropollutants, has become a worldwide issue of increasing environmental concern. Organic micropollutants consist of a vast and expanding array of anthropogenic as well as natural substances. Their concentrations are usually at trace level, but have been detectable by the advances in analytical chemistry theory and instruments, and their massive presence in the environment raised great awareness in the fields of environmental protection, legislation and public health. In general, organic micropollutants are categorized as pharmaceuticals, personal care products (PCPs), pesticides, endocrine disrupting chemicals (EDCs), industrial chemicals, food additives and many other emerging compounds [22-24]. The dominant four kinds of components are described in more detail hereby.

Pharmaceuticals

The pharmaceutical residues are of considerable interest due to their relatively high stability. Approximately, > 3000 substances are used as pharmaceutical ingredients, including impotence drugs, antibiotics, antidiabetics, painkillers, beta-blockers, lipids regulators, X-ray contrast media, antidepressant and contraceptives [25]. These pharmaceuticals are challenging to digest completely, being excreted through feces and urine, thereby providing connectivity of sources to receptors. According to research, 90% of pharmaceutically active compounds enter into domestic water through excretion and can enter into the environment through wastewater treatment plants due to their ineffectiveness [26]. Recent studies showed that pharmaceuticals are widely detected in tap water, surface water and groundwater in different countries. It has been an alarming situation that > 100 pharmaceuticals are detected above their detection limit in developed countries such as United States and European countries, and > 30 pharmaceuticals were detected in Asia-Pacific, Western European and Latin America countries. Many of these are reported as acutely toxic to the ocean life [27].

Personal care products (PCPs)

PCPs are organic chemicals included in many products widely used in daily human life, such as lotions, gels, cosmetics and even food. Unlike pharmaceuticals, which are intended for internal use, PCPs are products intended for external use on the human body and thus, they are not subjected to metabolic alterations; therefore, large quantities of PCPs enter into the environment unaltered through regular usage [28]. Consequently, significant amounts of these products and their metabolites go down the drain and reach wastewater treatment plants, finally appearing in surface water and groundwater due to the inefficient treatment. PCPs mainly include organic ultraviolet (UV) filters, preservatives, antimicrobials, musk fragrances, insect repellents and siloxanes [29]. Many of these compounds are environmentally persistent, bioactive and have the potential for bioaccumulation.

Pesticides

Pesticides are classified as either organic or inorganic depending on their structure. Organic pesticides, based on the functional groups, can be classified into three main categories: organochlorine pesticides (OCPs), organophosphorus pesticides (OPPs) and carbamates. Pesticides encompass a wide range of organic compounds used to control weeds, fungi and moulds, insects and pests. Widespread use and disposal of pesticides by farmers, general public, research and educational institutions serve as probable sources of pesticides in the environment. Traces of these compounds may enter into rivers and surface water as run-off from agricultural land or via non-agricultural use [30].

Endocrine disrupting chemicals (EDCs)

EDCs remain an active topic in contemporary ecotoxicology due to their proven environmental impacts. They are defined as exogenous compounds that affect hormone synthesis, secretion, metabolism, and/or actions [31]. EDCs can act either as agonists or as antagonists of receptors of multiple hormones such as glucocorticoids, estrogens, progesterone, androgens, mineralocorticoids, thyroid hormones, peroxisome proliferator-activated receptor, and others. EDCs can also alter the availability of active hormones by affecting their synthesis and metabolic enzymes [32]. EDCs are widely used in a variety of products including food packaging and processing materials, medical products, consumer goods and personal care products [33].

The potential sources and routes of micropollutants are shown in Fig. 4 [34]. These contaminants can be generated from industrial wastewater, animal and livestock, agriculture, landfill and wastewater treatment plants. The release of effluents from municipal wastewater treatment plants is the main source of micropollutants due to their incomplete removal. Similarly, landfill sites are major source because micropollutants may leach and reach the groundwater and surface water [35]. Actually, the transport pathways of micropollutants are highly affected by their physicochemical properties

and their interaction with the environmental matrix, making it difficult to be characterized owing to the scarcity of information on the fate and behavior in the environment of most of these compounds. Thus, the receptors of micropollutants, including animals, human beings, plants and also the water bodies usually suffer from many potential risks.

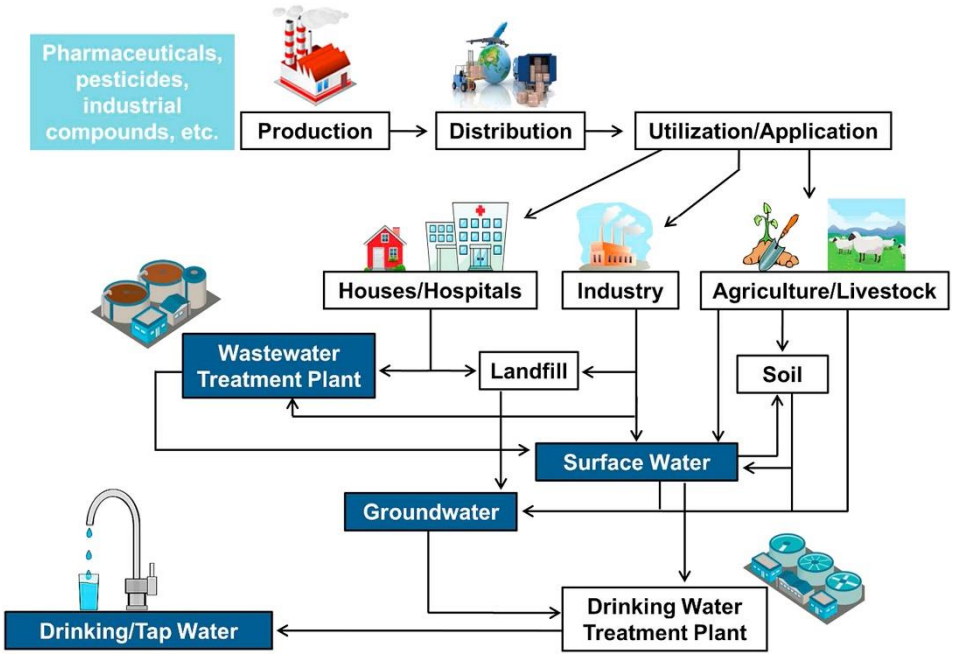

Figure 4. Potential sources and routes of organic micropollutants in the environment [34].

The concentrations obtained from literature surveys of 48 organic micropollutants occurring in surface water and effluents from wastewater treatment plants (WWTPs) are summarized in Table 2 [36-42]. As can be seen, organic micropollutants are frequently detected in both, surface water and treated effluents of WWTPs at concentrations ranging from ng L^{-1} to µg L^{-1}. They can also be detected in soil, sludge, sediments, drinking water and groundwater due to their persistence in the environment. The types and concentrations of organic pollutants in water highly depend on regions and seasons, as well as on the consumption of these substances and treatment technologies in WWTPs in different countries. The presence of organic micropollutants in aquatic environment has been known to potentially affect organisms and result in changes that threaten the sustainability of ecosystems. Their determination in environment is no longer a challenge due to the advances in analytical chemistry theory

and instruments. However, their ultimate fate (i.e., bioaccumulation and spatial distribution) in the environment is still relatively unclear. Consequently, not only the systematical summary of the occurrence of organic micropollutants in the environment needs to be investigated, but also their transportation, metabolites and environmental impacts should be carefully evaluated.

Table 2. Concentration ranges of 48 commonly detected organic micropollutants in surface water and the effluent from full-scale WWTPs [36-42].

Contaminant Class	**Micropollutant**	**Range in concentration (ng L^{-1})**	
		Surface water	**Effluent from WWTPs**
Pharmaceuticals			
Analgesic			
	Naproxen	< 1-81	< MQL-33900
	Ibuprofen	1-2370	< MQL-24600
	Ketoprofen	0.3-75.3	< MQL-1620
	Diclofenac	< 0.5-253	< MQL-5164
	Paracetamol	110-10000	-
	Salicylic acid	0.3-302	< MQL-10100
	Mefenamic acid	0.3-31	-
	Acetaminophen	527	< MQL-24525
Antibiotic			
	Trimethoprim	1-2	< MQL-3052
	Ciprofloxacin	0-28.2	< MQL-5692
	Sulfamethoxazole	1-46	< MQL-544
	Azithromycin	29.6	38-784
	Erythromycin-H_2O	0.5-195	15-2841
	Ofloxacin	< MQL-20.7	71-8637
Antiepileptic			
	Carbamazepine	24.9-214	< MQL-4596
	Gabapentin	4.5	7651-56810
	Sulpride	-	110-294
Beta-blocker			
	Propranolol	10.4	< MQL-615
	Atenolol	1-487	< MQL-7602
	Metoprolol	0.5-10	< MQL-5762
Blood lipid regulator			
	Clofibric acid	< 0.05	< MQL-91
	Gemfibrozil	48-790	< MQL-5233
	Bezafibrate	10-60	< MQL-4800

Antidepressant			
	Fluoxetine	2.0-19.5	18.3-128
	Diazepam	0-305	-
PCPs			
Preservative			
	Ethylparaben EPB	0.2-23.1	-
	Methylparaben	3.4-22.8	< MQL-155000
	Propylparaben	38.6-57.0	-
Bactericide/Disinfectant			
	Methyltriclosan MTCS	< 0.2	-
	Triclocarbon TCC	4-13	-
	Triclosan TCS	1-157	< MQL-82000
Fragrance			
	Galaxolide HHCB	3.1-2184	< MQL-108000
	Toxalide	13-283	-
Sunscreen UV filter			
	Octocrylene OC	-	< MQL-300
	Oxybenzone	-	< MQL-700
	Benzophenone-4	< 1-600	-
	Benzophenone-3	<12-79	< MQL-2196000
Antioxidant			
	Butylated hydroxyanisole	2000	-
Pesticides			
	Terbuthylazine	-	10.3-75
	Atrazine	-	7.4-732
	Chlortoluron	-	98-178
	Metolachlor	23.7	-
	Isoproturon	-	13-26
	Linuron	-	-
	Simazine	300	12.5-1990
EDCs			
	Nonyphenol	< 0.5-1589	-
	Bisphenol A	<1.0-145	-
	4-*tert*-Octylphenol	8-226	-

* Data was mainly collected from European countries.

-: not available in the literature.

MQL: method quantification limit.

1.1.3. Environmental concerns and regulations related to organic micropollutants

Due to the absence of relevant data on the impacts, fate and concentration levels of organic micropollutants, it is a great challenge for governments to control their utilization and also manage the level that they have already reached in the environment. Once these micropollutants are discharged into water bodies, their concentrations can exceed the acceptable levels of the ecosystems. The widespread occurrence of organic micropollutants in water has high probability of their incorporation in crops irrigated with contaminated water and possesses risk to animal and human health upon consumption [43]. Organic micropollutants can cause harmful impacts on aquatic and terrestrial wildlife and human communities. Table 3 summarizes the adverse effects of organic micropollutants in the environment [44]. These contaminants include a list of daily life compounds such as pharmaceuticals, UV filters, water disinfection byproducts, perfluorinated compounds, food additives and so on, as discussed in the subsection 1.1.2. Their rapid and extensive use in urban areas, industry, transportation and agriculture render them readily available in environments up to hazardous levels [35]. For instance, EDCs cause a number of reproductive and sexual abnormalities in wildlife and humans, whereas propranolol and fluoxetine have strong acute toxicity towards benthos and zooplankton [44,45]. Indeed, the existence of many organic pollutants in small quantity are not effectively hazardous to the environment and human health, but long-term exposure to these low dose micropollutants can cause chronic toxic effects [46]. Similarly, animal guts can absorb a large number of veterinary antibiotics, whereas 30-90% of these antibiotics are excreted through waste, mixed with freshwater sources and act as contaminants. Recently, it has been demonstrated that an excessive use of veterinary antibiotics causes an accelerating growth and emergence of new resistant strains of bacteria [35].

Over the past few years, a great deal of research has been focused on investigating the concentration, evolution and environmental impacts of organic micropollutants, but it

is still insufficient for most of them. There are no laws or mandates illustrating the upper limits of concentrations of micropollutants in wastewater discharge, drinking water or the environment. Since the aquatic compartments are crucial for the survival and maintenance of all ecosystems, surface water should be protected by monitoring programs, risk assessment and mitigation measures upstream of the release of micropollutants, such as the source of their production, use and disposal [47]. In the United States, an archive was set up illustrating the preparatory way to deal with EDCs and to decrease its intrusion in people and wildlife [48].

Table 3. Environmental effects of organic micropollutants [44].

Chemicals	**Adverse effects**
Penicillin, sulfonamides, tetracylines (*Antibiotics*)	Cause resistance among bacterial pathogens that leads to altered microbial community structure in the nature and affects higher food chain
Roxithromycin, clarithromycin, tylosin *(Antibiotics*)	Growth inhibition of algae
Caffeine (*Stimulant drug*)	Endocrine disruption in goldfish
Diclofenac (*Nonsteroidal anti-inflammatory drug*)	Renal lesions and gill alterations of rainbow trout
Carbamazepine (*Antiepileptic drug*)	Oxidation stress of rainbow trout
Gemfibrozil (*Blood lipid regulator*)	Growth inhibition of algae
Propranolol (*β-blocker*)	Reduction of viable eggs of Japanese medaka
HHCB (*Synthetic musk*)	Oxidative stress in goldfish
Fragrances (*Musk*)	Carcinogenic to rodents, easily absorbed by human skin and may damage the nervous system
Triclosan and triclocarban (*Antimicrobial agents*)	Growth inhibition of algae

Bisphenol A (*Endocrine disrupting chemical*)	Proven to have estrogenic effects in rats and hormonal effects which increase breast cancer risk in humans
Estrone and 17-β estradiol (*steroidal estrogens*) and 17-α ethynylestradiol (*synthetic contraceptive*)	Feminization of male fishes, mimic as estrogen hormone to non-target species
Preservatives, i.e., parabens *(alkyl-phdroxybenzoate*)	Shows weak estrogenic activity
Disinfectants/antiseptics, i.e., triclosan	Act as toxic or biocide agents and cause microbial resistance

Besides, the U.S. Food and Drug Administration (FDA) published guidelines for the evaluation of human drugs. Switzerland proposed environmental quality criteria for several organic micropollutants such as hormones and pesticides. Many disinfection byproducts that are transformation products of organic micropollutants are regulated by the EU, United States and the World Health Organization (WHO) [44].

The Water Framework Directive (WFD) was adopted by the EU in 2000 (Directive 2000/60/EC) in order to set the bases for the regulation of water resources with the objective to preserve, protect and improve their quality and sustainable use [49]. In 2001, Decision 2001/2455/EC set the first list of 33 priority substances or groups of priority substances (PSs) which entail a significant risk to the aquatic environment because of their toxicity and persistence [50]. In 2008, Directive 2008/105/EC amended the WFD and defined PS environmental quality standards (EQS), including annual average (AA) and maximum allowable concentrations (MAC) in surface water, publishing the EQS value for the 33 PSs and 8 additional pollutants [51]. In 2013, Directives 2000/60/EC and 2008/105/EC were developed and established again, and the new Directive 2013/39/EU recommended the monitoring of 45 PSs (41 organic compounds and 4 metals) (Table 4), set more restrictive EQS and highlighted the demand to develop new water treatment solutions. Furthermore, the Directive 2013/39/EU proposed a first Watch List for Union-wide monitoring [52].

Table 4. List of priority substances (PSs) in the field of water policy (Directive 2013/39/EU) [52].

Number	Substance	Class	CAS number
1	Alachlor	Pesticides	15972-60-8
2	Anthracene †	-	120-12-7
3	Atrazine	Pesticides	1912-24-9
4	Benzene	Industrial compounds	71-43-2
5	Brominated diphenylethers †‡	Industrial compounds	-
6	Cadmium and its compounds †	-	7440-43-9
7	Chloroalkanes, $C1_{0-13}$ †	Industrial compounds	85535-84-8
8	Chlorfenvinphos	Pesticides	470-90-6
9	Chlorpyrifos (Chlorpyrifos-ethyl)	Pesticides	2921-88-2
10	1,2-dichloroethane	Industrial compounds	107-06-2
11	Dichloromethane	Industrial compounds	75-09-2
12	Di(2-ethylhexyl)phthalate (DEHP) †	Industrial compounds	117-81-7
13	Diuron	Pesticides	330-54-1
14	Endosulfan †	Pesticides	115-29-7
15	Fluoranthene	-	206-44-0
16	Hexachlorobenzene †	Pesticides	118-74-1
17	Hexachlorobutadiene †	Pesticides	87-68-3
18	Hexachlorocyclohexane †	Pesticides	608-73-1
19	Isoproturon	Pesticides	34123-59-6
20	Lead and its compounds	-	7439-92-1
21	Mercury and its compounds †	-	7439-97-6
22	Naphthalene	-	91-20-3
23	Nickel and its compounds	-	7440-02-0
24	Nonylphenols †‡	Industrial compounds	-
25	Octylphenols	Industrial compounds	
26	Pentachlorobenzene †	Industrial compounds	608-93-5
27	Pentachlorophenol	Pesticides	87-86-5

28	Polyaromatic hydrocarbons (PAH) †	-	-
29	Simazine	Pesticides	122-34-9
30	Tributyltin compounds †‡	Pesticides	-
31	Trichlorobenzenes	Industrial compounds	12002-48-1
32	Trichloromethane (chloroform)	Industrial compounds	67-66-3
33	Trifluralin †	Pesticides	1582-09-8
34	Dicofol †	Pesticides	115-32-2
35	Perfluorooctane sulfonic acid and its derivatives (PFOS) †	Industrial compounds	1763-23-1
36	Quinoxyfen †	Pesticides	124495-18-7
37	Dioxins and dioxin-like compounds †‡	-	-
38	Aclonifen	Pesticides	74070-46-5
39	Bifenox	Pesticides	42576-02-3
40	Cybutryne	Pesticides	28159-98-0
41	Cypermethrin	Pesticides	52315-07-8
42	Dichlorvos	Pesticides	62-73-7
43	Hexabromocyclododecanes (HBCDD) †‡	Industrial compounds	-
44	Heptachlor and heptachlor epoxide †	Pesticides	76-44-8 / 1024-57-3
45	Terbutryn	Pesticides	886-50-0

† Substances identified as priority hazardous substances (PHSs).
‡ Some of their compounds identified as PHSs.

In 2015, the Decision 2015/495/EU published an updated Watch List including 17 substances or groups that must be monitored and considered in the future revisions of the concern list [53]. This Watch List must be revised periodically in order to gather relevant information to support decisions. The newest Watch List, Decision 2018/840/EU, published in 5 June 2018 updated the previous list of substances according to the monitoring and ecotoxicological data during 2015-2017, the referred Watch List encompasses 15 organic micropollutants which is presented in Table 5 [54].

Table 5. Watch List of substances for Union-wide monitoring, their class, CAS number and pK_a (Decision 2018/840/EU) [54].

Class	Substance	CAS number
Estrogens		
	17-Alpha-ethinylestradiol (EE2)	57-63-6
	17-Beta-estradiol (E2)	50-28-2
	Estrone (E1)	53-16-7
Macrolide antibiotics		
	Erythromycin	114-07-8
	Clarithromycin	81103-11-9
	Azithromycin	83905-01-5
Carbamate pesticides		
	Methiocarb	2032-65-7
Neonicotinoid pesticides		
	Imidacloprid	105827-78-9 /13861-41-3
	Thiacloprid	111988-49-9
	Thiamethoxam	153719-23-4
	Clothianidin	210880-92-5
	Acetamiprid	135410-20-7
Semicarbazones		
	Metaflumizone	139967-49-3
Penicillin antibiotics		
	Amoxicillin	26787-78-0
Fluoroquinolone antibiotics		
	Ciprofloxacin	85721-33-1

These organic micropollutants included in the Watch List are still under assessment and considered as the candidate substances for prioritization, since the EQS values are still unclear and the European countries should monitor these unregulated pollutants in order to support future prioritization exercise.

The frequent occurrence of organic micropollutants in aquatic environment and their inefficient removal by conventional WWTPs promoted the amendment of the framework to cover a larger set of hazardous pollutants, as well as recommendations for wastewater treatment steps or even new treatment technologies [34].

1.1.4. Technologies for the treatment of micropollutants in urban wastewater

The ecological issues raised by organic micropollutants have become a major public concern all around the world. The increasing worldwide consumption of chemical products has greatly promoted the discharge of wastewater containing organic micropollutants into WWTPs. However, the current conventional WWTPs are designed to remove the solid waste, suspended solids, easily biodegradable dissolved organic matter and nutrients (phosphorus and nitrogen) from wastewater. The organic micropollutants are usually at very low concentration and with high resistance to biodegradation, leading to inefficient removal during the treatment, then directly entering into the aquatic systems. Similarly, the conventional water treatment plants (WTPs) are also unprepared to manage the complex and refractory organic micropollutants. The parent micropollutants and their metabolites can eventually end up in finished drinking water and distribution systems when the water source used has been impacted by WWTPs effluents. Fig. 5 illustrates the potential fate and transport of CECs in typical WWTPs and WTPs [55]. Generally, the influent wastewater will undergo preliminary treatment firstly by some mechanical technologies, such as sieving and sand filtration, to separate the solid waste substances like plastics, oils and grit. The primary treatment technologies, such as coagulation and flocculation, are commonly used to remove the suspended solid and turbidity, and also some inorganic and organic pollutants. The most common secondary treatment in WWTPs is biological degradation, which is usually followed by a tertiary advanced technology like disinfection or membrane filtration. The removal mechanisms and the fate of micropollutants in different systems are described below.

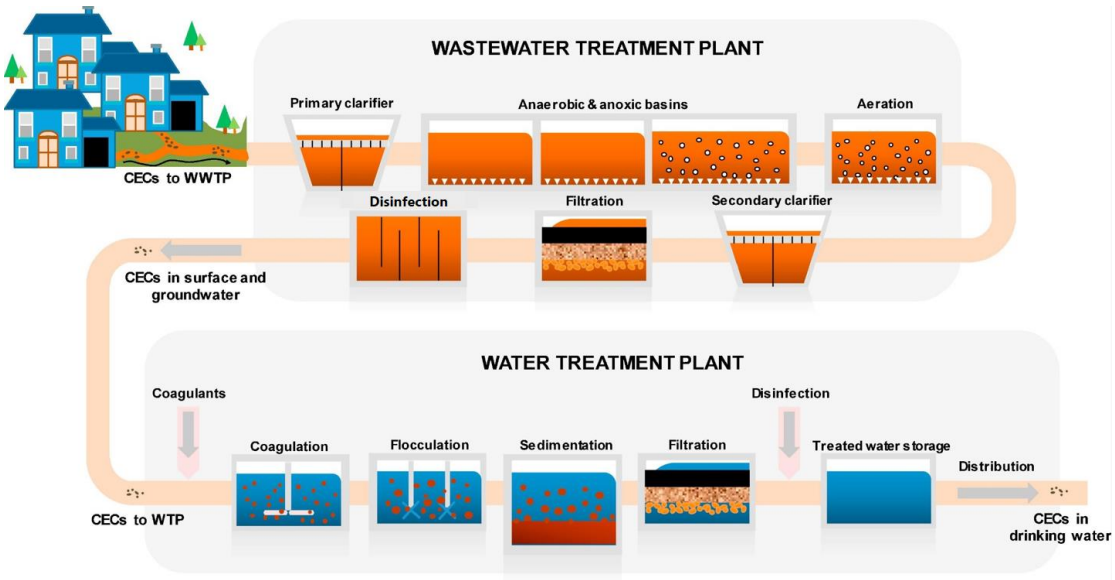

Figure 5. Possible fate and transport of CECs in conventional WWTPs and WTPs [55].

Coagulation-flocculation

The coagulation-flocculation process is one of the most widely used technologies for purification of urban and industrial wastewater, aiming at reducing turbidity, natural organic matter, inorganic pollutants as well as colloidal organic substances. This process consist of two distinct stages (Fig. 6): (a) rapid mixing of dispersed coagulant into water/wastewater via vigorous stirring and (b) flocculation for agglomeration of small particles into well-defined flocs via gentle stirring; finally, the flocs are allowed to settle and then removed as sludge [56].

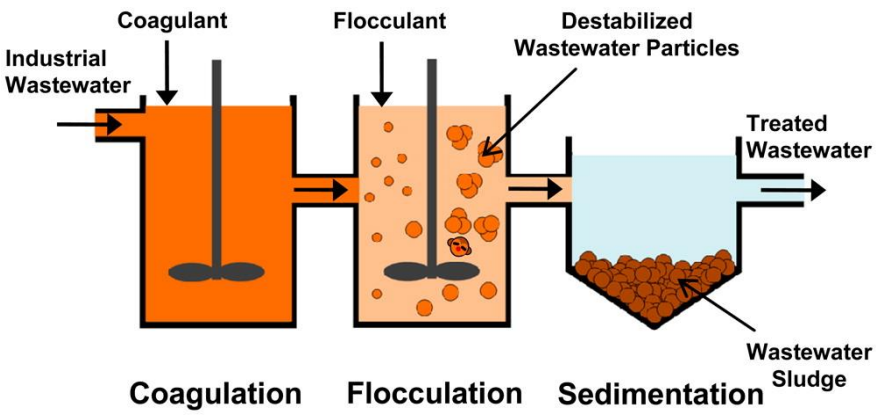

Figure 6. Typical coagulation-flocculation process for wastewater treatment [56].

The crucial step of this process is the agglomeration of colloidal microparticles, which

includes various mechanisms such as charge neutralization, entrapment, adsorption and complexation with the coagulant's metal ions into insoluble aggregates [57]. The most commonly used coagulants are aluminum and iron, whereas prepolymerized coagulants such as polyaluminum chloride (PAC) and polyaluminum sulfate (PAS) have also been widely studied during the last two decades [56,58]. The main factors affecting the coagulation-flocculation process are pH, coagulant type and dosage and temperature [44]. The removal of organic micropollutants by coagulation-flocculation process has been reported in the literature. For instance, some pharmaceuticals such as betaxolol, warfarin and hydrochlorothiazide are effectively removed (80% removal) using aluminum sulfate coagulant combined with sand filtration [59]. Musk compounds, like celestolide and galaxolide, and tonalide from hospital wastewater were observed to be removed with notable rate (83%, 79% and 78%, respectively) [60].

Chemical coagulation-flocculation is an additive based water treatment process in which the addition of coagulants is required. The additive results in high amount of sludge and residual chemicals in the treated wastewater [61]. In contrast to chemical coagulation, electrocoagulation (EC), one of the most eco-friendly water treatment technologies, can in situ generate coagulant species triggered by applying electric current through metal electrodes. This method has received growing attention due to its operation advantages over the conventional chemical coagulation technique [62].

Biological treatment

Biological treatment technologies have been the most widely used systems in WWTPs around the world to remove organic pollutants predominantly by the mechanism of biodegradation. They can be divided into aerobic and anaerobic processes. Aerobic methods include activated sludge, membrane bioreactor and sequence batch reactor. Anaerobic methods include anaerobic sludge reactors and anaerobic film reactors [63]. The main mechanisms for organic micropollutants in biological treatment systems are shown in Fig. 7, including: (a) sorption onto sludge particles, (b) biological

transformation, (c) volatilization and (d) abiotic degradation [64]. Sorption onto sludge or particulate matter can be an important removal mechanism for hydrophobic or positively charged micropollutants, especially if they are poorly biodegradable. For many hydrophilic organic micropollutants, biological transformation is the dominant removal mechanism (metabolic and co-metabolic). However, for most micropollutants, the concentrations are too low to support the growth of microorganisms, generally other carbon and energy sources are required during the biological transformation of organic micropollutants [65]. The surface volatilization and abiotic degradation of micropollutants can potentially occur during the treatment, but it is not expected significant impact in biological systems [64].

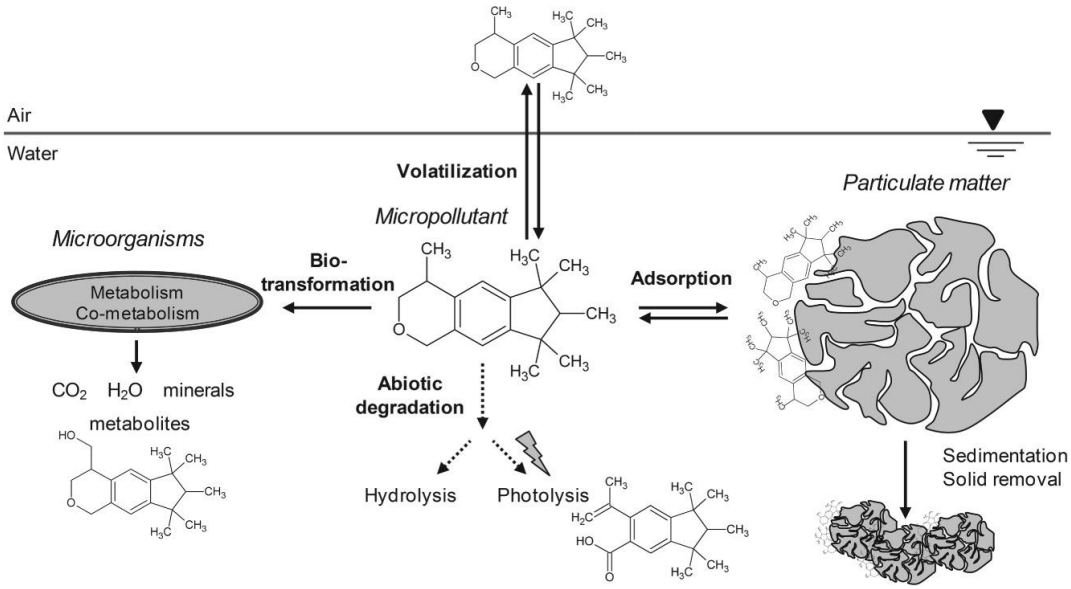

Figure 7. Main removal mechanisms of micropollutants in biological treatment systems [64].

The removal of organic micropollutants by biological treatment depends on various factors including the physicochemical properties of micropollutants, sludge retention times, hydraulic retention time, in-situ carbon loading and microbial community composition, which make the removal efficiency vary to a large extent [66]. The conventional biological methods are usually efficient to remove nutrients and oxidize biodegradable carbonaceous organic matter, whereas a significant number of organic micropollutants experience very little or no removal. Furthermore, the metabolites and transformation products during biological degradation can be more toxic than the parent

compounds, leading to greater threat to the ecosystems [20]. Therefore, alternative advanced treatment systems are explored to be combined with biological methods in order to improve the removal efficiency of organic micropollutants.

Disinfection

Disinfection technologies are still the most widespread conventional methods for the secondary wastewater effluent and drinking water treatment. Currently, they are widely implemented at large and medium scale and have successfully protected public health against waterborne disease throughout the world for decades. Conventional disinfection technologies include chlorination, chloramination, the use of chlorine dioxide, ozonation and radiation, which can inactivate or destroy the pathogenic microorganisms and degrade the refractory organics [67].

Among them, chlorination is the most popular process for disinfecting the effluent from biological treatment and produce drinking water. It consists in the addition of chlorine to water, where chlorine reacts to form hypochlorous acid (HClO) and hypochlorite ion (ClO^-), usually known as "free chlorine", from reactions (1) and (2) [68]:

$$Cl_2 + H_2O \rightarrow HClO + Cl^- + H^+ \quad (1)$$

$$HClO \leftrightarrow ClO^- + H^+ \quad (2)$$

The acid-base equilibrium (2) presents a dissociation constant $K_{HClO} = 2.9 \times 10^{-8}$ ($pK_a = 7.54$ at 25 °C). In the pH range 6-9 (typical of water treatment conditions), HClO and ClO^- are the predominant chlorine species produced [69]. The generated active chlorine is a strong oxidizing disinfectant and can readily react with numerous inorganic and organic micropollutants present in water. The main advantages of chlorination are the low cost and that chlorine persists in water after dosing, so its disinfectant activity continues within the distribution and storage systems [67]. However, the main disadvantage is the formation of possible harmful disinfection byproducts (DBPs), like halogenated compounds, which may be more toxic than the parent substances [70].

Ozone (O_3) is another very powerful oxidant that can react selectively with double bonds and aromatic rings of organic micropollutants with a high electron density [71]. Ozonation has been implemented as the principal treatment technology or to enhance the biodegradability and efficiency of subsequent treatment, which is more effective than chlorine and chlorine dioxide, requiring less contact time and lower concentrations to achieve disinfection [67]. However, ozone production is an energy-intensive process, and its concentration in water decays more rapidly than other disinfectants, making it costly to implement. An ozonation system may increase the energy demand over a conventional WWTPs by 45-50% [63]. Furthermore, ozone is known to react with natural organic matter and Br^- ion to produce a range of byproducts, including bromate, quinones, ketones and aldehydes [72].

UV disinfection of water is normally achieved by passing the water through tubes lined with UV lamps with a wavelength around 254 nm [67]. It can directly act on the DNA of microorganisms to disable them from growing, but it is usually inefficient to degrade most organic micropollutants because of their high persistence in water. Recently, the green and promising photocatalytic disinfection using visible or solar light is advocated and developed by employing various visible-light active photocatalysts, such as zinc oxide (ZnO) and titanium oxide (TiO_2), to tackle wastewater contamination. This procedure can greatly reduce the energy consumption and increase the removal efficiency of organic micropollutants [73].

Membrane technology

Membrane processes, including reverse osmosis (RO), nanofiltration (NF), forward osmosis (FO), microfiltration (MF) and ultrafiltration (UF), are phase-transfer processes with a variety of applications in WWTPs and WTPs [55]. Membrane processes are based on the use of hydrostatic pressure to remove suspended solids, microorganisms and high molecular weight substances, and allow water and low molecular weight solutes to pass through. The material properties of different

membranes give rise to their specific filtration features, such as surface charge, pore size and hydrophobicity, and determine the pollutants that can be retained [20]. Fig. 8 presents the different membrane types and their pore size ranges, as well as the contaminants that can be removed [74].

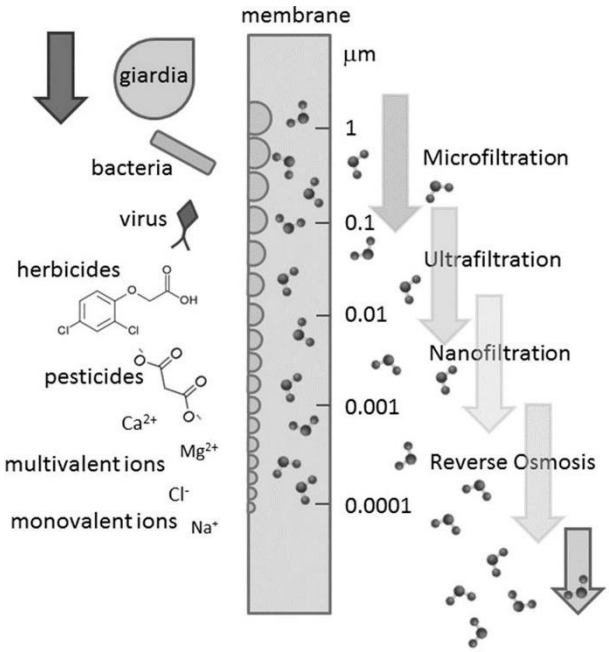

Figure 8. Types of membranes, pore size ranges and contaminants removed for every pore size range [74].

The molecular weight of organic micropollutants lies typically in the range of 100-400 Da (molecular radii < 1 nm) with some exceptions such as macrolidic antibiotics that can be substantially larger. Thus, they are scarcely retained by MF and UF, since their pore sizes commonly vary from 0.1-1 μm and 0.01-0.1 μm [75]. NF can be used to remove organic micropollutants because of its smaller pore size (10-100 Å). This process can be operated at a low feed water pressure, which allows a reasonable operational cost. The removal of organic micropollutants by NF has been demonstrated with quite high efficiency, such as 46-84% removal for caffeine [76]. For RO and FO, a semi-permeable membrane is employed to separate water from soluble solutes. They have a greater efficiency for organic micropollutants removal because particles as small as 10 Å can be retained [20]. The mechanisms for the rejection of organic substances by NF, RO and FO membranes have been identified as: (a) size exclusion, (b) Donan

exclusion and (c) adsorption [77]. These processes are not only governed by the solute and membrane properties but also by the operational conditions, feed water quality and module and system design [75]. Membrane technologies can be effective to remove some organic micropollutants. However, the pollutants are usually accumulated in a concentrate stream and an additional step is required to treat it. Urtiaga et al. [78,79] proposed the combination of electrochemical technologies with membrane processes to eliminate the concentrated pollutants and also reduce the energy consumption of the electrochemical step. The final disposal of the contaminated membranes is a great challenge for this technology.

Adsorption

Adsorption is another phase-transfer technology that has been widely reported in the removal of inorganic ions, organic pollutants, microorganisms and heavy metals, as well as the persistent organic micropollutants. The materials used as adsorbents can take a broad range of chemical forms and different geometrical surface structures, which can be usually classified as: (a) natural materials such as wood and sawdust, (b) treated natural materials such as activated carbon and (c) manufactured materials such as polymeric resins [80]. The conventional and frequently used materials include commercial activated carbon, zeolites, ion-exchange resins and silica gel. These materials usually possess a well-developed structure, superior porosity and large surface area, which allows high sorption capacities for many contaminant species [81]. For instance, activated carbon is the most commonly used material because of its high specific surface area and low cost. Its application to the removal of organic micropollutants has been intensively studied and more than 90% removal can be achieved for a wide variety of compounds, selectively removing some organic micropollutants such as ciprofloxacin [20]. The adsorption process predominantly consists of the subsequent steps: (a) film diffusion, adsorbate transport across the liquid film surrounding the adsorbent particles, (b) porous diffusion, adsorbate diffusion in the liquid contained within the pores and along the pore walls to the active sites, and (c)

the interaction between the active sites and the adsorbate [82]. The efficiency of the adsorption process is affected by both, the physicochemical properties of the target pollutants and the adsorbent surface characteristics. Moreover, external factors such as pH and temperature of wastewater also affect the removal of organic micropollutants [75]. Instead of degradation methods, adsorption processes are still separation technologies, which usually should be coupled with other treatment methods to achieve the destruction of organic micropollutants.

Advanced oxidation processes (AOPs)

Intensive studies on the application of AOPs for water and wastewater treatment have been conducted in the past three decades, and their potential application to the removal of organic micropollutants has increased dramatically. Compared with conventional treatment technologies, AOPs can achieve higher removal rates for organic pollutants, especially for the refractory substances, owing to the formation of reactive secondary species such as hydroxyl radicals ($^{\bullet}OH$) (standard reduction potential of 2.8 V) [83]. AOPs involve different methods of activation as well as oxidant generation and can potentially utilize a number of different mechanisms for the destruction of organics and hence, the classification of AOPs should not be viewed as strict since several processes could be assigned to various categories. In general, AOPs can be classified as: (a) O_3-based processes such as O_3/UV, O_3/H_2O_2 and O_3/catalyst, (b) Fenton-based processes such as classical Fenton (H_2O_2/Fe^{2+}), Fenton-like (H_2O_2/Fe^{3+}), photo-Fenton (UV, visible or solar/H_2O_2/Fe^{2+}) and sono-Fenton (ultrasound/H_2O_2/Fe^{2+}) and (c) other AOPs such as wet oxidation, sulfate radical ($SO_4^{\bullet-}$)-based AOPs (persulfate(PS)/Fe^{2+}, peroxymonosulfate(PMS)/Fe^{2+}), and chlorine radical ($Cl^{\bullet}$)-based AOPs (UV/chlorine, HClO/Fe^{2+}) [83-85]. Conventional AOPs can be also classified as homogeneous or heterogeneous processes depending on whether they can use of a homogeneous catalyst or a heterogeneous one like metal supported catalysts, carbon materials or semiconductors [84]. All AOPs comprise two steps, i.e., the in situ generation of reactive oxygen species and the reaction of oxidants with target contaminants. Many

parameters, including reaction conditions such as pH and chemical dosage, system design and water quality can affect the removal efficiency of organic pollutants. AOPs have been proven to be very efficient to destroy organic micropollutants due to the generation of highly reactive radicals like $^{\bullet}OH$, which can non-selectively react with most micropollutants with rate constants up to 10^9 M^{-1} s^{-1}, yielding CO_2, H_2O and, eventually, inorganic ions as final products [86]. Table 6 summarizes the degradation of organic micropollutants by different types of AOPs in water/wastewater [20,24].

Table 6. Treatment of organic micropollutants by different AOPs [20,24].

System	Pollutant	Treatment conditions	% Removal efficiency
UV/H_2O_2	Doxycycline	pH 3.0, $[Dox]_0$ = 10 mg L^{-1}, $[H_2O_2]_0$ = 100 µmol L^{-1}, 20 min	100
UV/O_3	Caffeine	$[C]_0$ = 40 mg L^{-1}, pH 7.0, UV 32W, 22.5 min	> 95
O_3/H_2O_2	Ketoprofen	$[O_3]$ = 2 or 4 mg L^{-1}, H_2O_2/O_3 ratio = 0.5 or 1, 2 min, $[C]_0$ = 1 mg L^{-1}	90-96
	Naproxen		96-98
	Piroxicam		96-98
$O_3/H_2O_2/UV$	Estrone	$[C]_0$ = 5 mg L^{-1}, pH 6.5, 30 min	> 99
Fenton	Doxycycline	$[C]_0$ = 100 mg L^{-1}, $[Fe^{+2}]_0$ = 25 mg L^{-1}, $[H_2O_2]_0$ = 611 mg L^{-1}	100
Photo-Fenton	26 drugs	pH 7.4, $[Fe^{+2}]_0$ = 5 mg L^{-1}, $[H_2O_2]_0$ = 50 mg L^{-1}, 30 min	> 97
UV/Chlorine	E2	$[Cl_2]_0$ = 1 mg L^{-1}, $[ClO_2]_0$ = 0.4 mg L^{-1}	100
	Benzotriazole		> 85
	Tolytriazole		> 85
	Iopamidole		> 85

The use of AOPs for organic micropollutants removal also faces several challenges, including: (a) the small concentration of these compounds in water, (b) the production of toxic intermediates when complete mineralization is not achieved, and (c) relatively

high cost of processes for large-scale application [85]. In order to overcome those drawbacks, many modified and developed AOPs have been proposed in the last decades, being the electrochemical advanced oxidation processes (EAOPs) one of the most popular groups.

Electrochemical technologies

Apart from the conventional treatment technologies mentioned above, the electrochemical processes have achieved a rapid development for the treatment of organic micropollutants due to the significant improvement of the electrode materials and the coupling with low-cost renewable energy sources [87]. The electrochemical technologies offer an alternative solution to many environmental problems in the industry, because the electron provides a versatile, efficient, cost effective, easily automatable and clean reagent [88]. Moreover, decentralized wastewater treatment is widely regarded as the future of WWTPs, especially for rural communities and peri-urban areas, due to the numerous advantages over the conventional centralized systems, such as cost efficiency, easy operation and eco-friendliness. The modular design and small footprint of electrochemical systems make them particularly suitable for decentralized water treatment [89]. The use of electricity for water treatment was first proposed in 1889 [90]. Since then, many electrochemical technologies have been developed for wastewater remediation. They can be classified into two main categories: (a) electrochemical separation technologies such as electrodialysis, which isolate the xenobiotics from the aqueous medium without altering their chemical structure, and (b) electrochemical transformation technologies, which cause the bond cleavage inducing the conversion of initial pollutant into by-products [88]. The transformation technologies can be further subdivided into electrochemical reduction and oxidation processes. Among the electrochemical oxidation processes, EAOPs, including electro-oxidation (EO), Fenton-based EAOPs and photoelectrocatalysis (PEC), have attracted great attention for the treatment of organic micropollutants in the past years. More specific advantages and disadvantages are discussed in Section 1.2, 1.3 and 1.4.

The WWTPs are indeed designed to remove various pollutants in wastewater, accompanying inevitable energy consumption. However, the WWTPs in the future are expected to be energy neutral or even energy positive service providers, namely water resource recovery facilities (WRRFs) [91]. Unfortunately, the current technologies are insufficient to capture the intrinsic value in wastewater and then, it is urgent to develop potentially new technologies to realize the true WRRFs concept.

1.1.5. Micropollutants of interest in this Thesis: Occurrence and treatment

Butylated hydroxyanisole

Butylated hydroxyanisole (BHA) is a synthetic phenolic antioxidant widely used to preserve and stabilize the freshness, nutritional value, flavour and colour of food and animal feed products. It is also used in food packaging, cosmetics, pharmaceuticals and rubber and petroleum products [92]. BHA is available in the form of two liposoluble isomers, 2-*tert*-butyl-4-hydroxyanisole and 3-*tert*-butyl-4-hydroxyanisole [93], which can cause harmful effects on animals and human health because of the potential formation of complexes with nucleic acids leading to DNA damage [94]. Sufficient evidence has been found for carcinogenicity in experimental animals, but no data are available for humans. The carcinogenic potential in humans is still controversial, with some researchers classifying it as carcinogenic and other as non-carcinogenic [92]. BHA is recognized as an environmental endocrine disrupting chemical by many countries in the world. The Joint FAO/WHO Expert Committee on Food Additives (JECFA) limits the acceptable daily intake to 0.5 mg kg^{-1} [94,95]. In Europe, BHA is limited to 200 mg kg^{-1} on the fat content of products such as dehydrated soups and meat, gravies and bouillons [94]. Due to its frequent usage, it has been detected in rivers, groundwater and wastewater from various European and American countries, reaching up to 2 μg L^{-1} [95]. However, the removal of BHA from water has only been reported in few works, focusing on UVC photolysis [96], and its combination with ozone [96], or $S_2O_8^{2+}$ [97], ozonation [96,98] and chlorination [99]. They yield stable by-products

like 3-*tert*-butyl-4,5-dihydroxyanisole, *tert*-butyl-1,4-hydroquinone and hydroquinone [96,99], which should be completely destroyed because they are highly toxic.

Benzophenone-3

Benzophenone-3 (BP-3), also called oxybenzone, is widely employed as sunscreen agent due to its large ability to absorb UV light, limited photodecomposition and high lipophilicity [100]. It is an active ingredient in lotions and personal care products including bath oils, soaps, mascaras and anti-aging creams [101]. A release of 14000 ton y^{-1} of BP-3 into the aquatic environment is estimated via wash-off from skin and clothes or indirectly via solid waste landfill leachate and wastewater treatment facilities, thereby being detected in natural water bodies, soil, fish and even in human milk [101] [102]. It has reached up to 7800 ng L^{-1} in untreated municipal wastewater, being reduced to 700 ng L^{-1} upon treatment [103]. It has also been detected within the 10-20 ng g^{-1} range in sewage sludge and 3-21 ng g^{-1} in fish [103]. Its potential toxicity arises from endocrine disruption, genotoxicant actuation, pro-carcinogenic activity, mutagenic ability of its derivatives and skin penetration in humans [101]. The water solubility of BP-3 (pK_a = 9.65 [104,105]) is very high at pH > 10, where its anionic form predominates, whereas its neutral form prevailing at pH ≤ 9 has very low solubility (< 5 mg L^{-1}). Effective removal of BP-3 from synthetic aqueous matrices at pH 3-9 has been attained by biodegradation [103], ultrasounds [106], ozonation and peroxone oxidation [102], membrane catalytic ozonation [107], photo-Fenton [108], TiO_2/photocatalysis [109] and UV/H_2O_2 [110]. Most of these works only determined the decay kinetics of BP-3 at concentrations ≤ 1 mg L^{-1}, but they did not assess the formation of hydroxylated and/or chlorinated derivatives, potentially more toxic [105].

Fluoxetine

Fluoxetine (FLX) is a selective serotonin reuptake inhibitor, being one of the most frequently prescribed drugs to treat depressive disorder, obsessive-compulsive disorder, bulimia nervosa, panic disorder and premenstrual dysphoric disorder. It is cited within

the World Health Organization's List of Essential Medicines and considered as an important medication for a basic health system [111]. FLX is only partially metabolized (less than 10%) after oral administration, the residual is excreted in the urine and enter into the wastewater treatment plants [112]. Because of its extensive production and prescription in the entire world, recalcitrance to hydrolysis and microbial degradation, FLX might finally enter into surface water and groundwater unintentionally. It has been detected in surface water with concentrations up to 0.5 μg L^{-1}, and in sludge from WWTPs up to 4.7 mg (kg of organic carbon)$^{-1}$ [111,113]. Furthermore, it has been detected in drinking water at very low concentrations [114]. Despite the low concentration of FLX in the aquatic environment, several studies have demonstrated its bioaccumulation in fish tissues (from 0.14 to 1.02 μg kg^{-1}) [111]. Consequently, their existence in aqueous systems and in the environment has raised concerns as ecotoxicological effects on humans and living microorganisms. The median effective concentration value (EC_{50}) of FLX on *Pseudokirchneriella* was reported to be 90.0 μg L^{-1} [115]. Chronic exposure to FLX can alter the biological activity of aquatic organisms, leading to reproduction reduction, abnormalities in embryo development, dysfunction in endocrine systems and sexual maturation [113]. Therefore, appropriate methods should be adapted to impede the spread of FLX in the environment after the secondary treatment. Recently, different methods such as ozonation [116], O_3/H_2O_2 [117], H_2O_2/UV [118], adsorption [119] and electrochemical technologies [113] have been reported to eliminate FLX. It is still crucial to develop other promising and efficient technologies for the treatment of FLX in the effluent of WWTPs.

Gemfibrozil

Gemfibrozil (GEM) is a drug for regulating blood lipid content, which decreases serum triglycerides and increases high-density lipoproteins. It is among the most highly consumed drugs and used daily for long periods throughout the world [120]. GEM is a fibric acid derivative, the peak plasma levels of which are reached in 1-2 h after it is absorbed by the gastrointestinal tract. Its metabolites mainly include four substances

and approximately 70% is excreted in the urine [121]. After application, GEM enters into WWTPs and then reaches the receiving environment. Its concentration in the effluent of WWTPs and freshwater was detected in the range from 0.008 to 9.7 μg L^{-1} [122], which can be attributed to the incomplete removal of GEM during wastewater treatment. GEM exhibits low volatility and biodegradability, and these characteristics favor their bioaccumulation and persistence in the environment, which contribute to the triggering of morphological, physiological, genotoxic and endocrine effects [44]. It shows high acute toxicity to fish, bacteria, rotifers and crustaceans, and also exhibits genotoxicity to *Escherichia coli* and *Salmonella typhimurium* [123]. Furthermore, its transformation products and the environmental behavior can rise more potential concerns to humans and ecosystems. GEM is not readily biodegradable, and several advanced treatment technologies including UV/Chlorine [123], photocatalysis [124] [126] and photo-Fenton process [127] have been conducted to remove GEM. These technologies require the addition of auxiliary oxidizing agents or catalysts, having the disadvantages of low removal efficiency or high energy consumption.

Bezafibrate

Bezafibrate (BZF) belongs to the group of fibrate drugs, which is an important class of pharmaceuticals largely used for the treatment of hyperlipidaemia, when high cholesterol levels are associated with increased levels of triglycerides [128]. This compound is extensively used throughout the world and consequently has been frequently detected in the environment [129]. The maximum concentrations of BZF found of in wastewater and surface water are 4.6 and 3.1 μg L^{-1}, respectively [130]. It has been detected in fish, sediments, suspended particulate matter and colloidal phase [131]. At the concentrations detected in the environment, BZF does not induce acute or chronic toxic effects in non-target organisms. Nevertheless, its harmfulness to the environment cannot be excluded due to the possible mixture of toxicity, synergistic and additives effects, bioaccumulation and biomagnification [128]. Ecotoxicological assays with BZF have shown EC_{50} values (half-maximum effective concentrations) for

Daphnia magna ranging from 30.3 to 240.4 mg L^{-1}, while for *Thamnocephalus platyurus* and *Anabaena sp.* EC_{50} was 39.69 and 7.62 mg L^{-1}, respectively [130]. Due to its persistence and low concentration in wastewater, current treatment techniques like biological degradation cannot efficiently remove BZF. The abatement of BZF from water has been studied by ozonation [128,132], photo-Fenton [133], UV/H_2O_2 [129], UV/TiO_2 [134] and membrane bioreactor [135]. All of these systems are still operated at lab-scale due to the high costs and energy consumption and it is worth to explore the abatement of BZF, spiked into wastewater, by EAOPs.

Besides the organic micropollutants mentioned above, bisphenol A (BPA) and naproxen (NPX) were also selected as the target pollutants. BPA, a phenolic compound that is widely used to produce polycarbonate plastics, has received great attention due to its endocrine disrupting activity and toxic effects to the environment and health [136]. NPX is one of the most common nonsteroidal anti-inflammatory drugs, which is widely used as painkiller and antipyretic. It does not have toxic effect by itself but potential long term toxic effects are caused because of its accumulation in water and soil [137]. Their removal by novel electrochemical processes will also be investigated.

All the target organic micropollutants studied in this Thesis are collected in Table 7.

Table 7. Organic micropollutants studied in this Thesis.

Micropollutant	CAS	Formula	MW (g mol^{-1})	Structure
BHA	25013-16-5	$C_{11}H_{16}O_2$	180.24	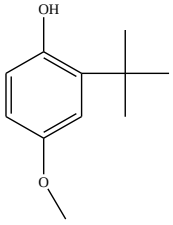
BP-3	131-57-7	$C_{14}H_{10}O_3$	228.25	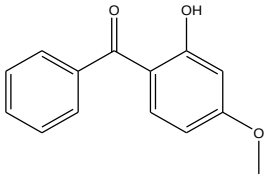
FLX	56296-78-7	$C_{17}H_{18}F_3NO$	309.33	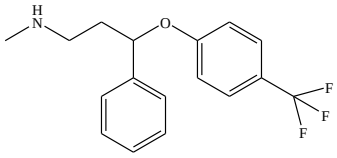
GEM	25812-30-0	$C_{15}H_{22}O_3$	250.33	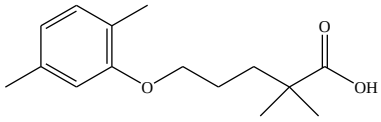
BZF	41859-67-0	$C_{19}H_{20}ClNO_4$	361.82	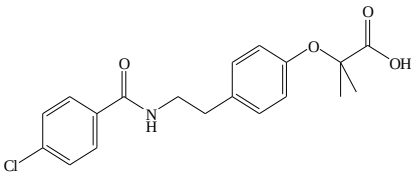
BPA	80-05-7	$C_{15}H_{16}O_2$	228.29	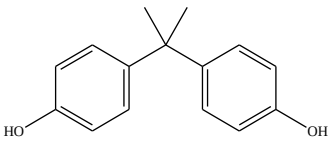
NPX	22204-53-1	$C_{14}H_{14}O_3$	230.26	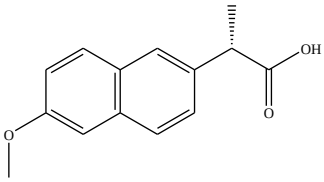

1.2. Electrocoagulation (EC)

EC process has been broadly performed for water and wastewater treatment to efficiently remove a variety of chemical pollutants, namely heavy metal ions, inorganic anions and organic dyes, pesticides, pharmaceuticals and personal care products [138].

During the last decades, this promising technology has been extensively studied to understand its principles, impact parameters, removal mechanisms and give evidence of its applicability. The fundamentals of EC technology are summarized hereby, distinguishing between classical and advanced systems.

1.2.1. Classical EC

As a coagulation technique, the fundamental mechanism behind EC performance is colloid destabilization [139]. This chemical step resulting in contaminant removal from solution occurs through charge balancing of colloidal particles, leading to particle aggregation and precipitation [140]. The key difference between chemical coagulation and EC is the mechanism of addition of ions to solution. In chemical coagulation this is carried out via the addition of soluble metal salts such as $FeCl_3$ or $Al_2(SO_4)_3$, whereas in EC the solubilization of the metal ions is achieved through corrosion of an electrode such as iron or aluminum [141].

In general, the specific steps taking place during the EC process are [142]:

(a) Production of metal ions from anode electrodissolution, along with H_2 gas evolution at the cathode;
(b) Destabilization of the pollutants and particulated suspension, and emulsion breaking;
(c) Formation of aggregates of the destabilized phases and their coagulation in the wastewater as flocs;
(d) Removal of coagulated pollutants by sedimentation or electroflotation; and
(e) Other electrochemical and chemical reactions promoting the transformation and removal of pollutants.

Specifically, when an iron, steel or stainless steel anode is employed in EC, Fe^{2+} is dissolved by Fe anode oxidation, as follows [143]:

$$Fe \rightarrow Fe^{2+} + 2e^- \quad (3)$$

Simultaneously, hydroxide ion and H_2 are generated at the cathode via water reduction reaction (4) [144]:

$$2H_2O + 2e^- \rightarrow 2OH^- + H_{2(g)} \quad (4)$$

The production of OH^- from reaction (4) causes an increase in pH during electrolysis leading to the formation of different iron hydroxocomplexes in solution. At pH > 5.5, $Fe(OH)_2$ precipitates and remains in equilibrium with Fe^{2+} up to pH 9.5 or with other monomeric species such as $Fe(OH)^+$ and $Fe(OH)_3^-$ at higher pH values [142]. The formation of insoluble $Fe(OH)_2$ can be written as follows:

$$Fe^{2+} + 2OH^- \rightarrow Fe(OH)_{2(s)} \quad (5)$$

Even though Fe(II) species generated can contribute to coagulation, the Fe(III) species present higher charge density favoring even more the coagulation-flocculation process [145]. Actually, Fe(II) species can be easily oxidized by reaction (6) to insoluble $Fe(OH)_3$ in the presence of O_2, which is commonly dissolved in water [146]:

$$4Fe^{2+} + 10H_2O + O_{2(g)} \rightarrow 4Fe(OH)_{3(s)} + 8H^+ \quad (6)$$

In turn, $Fe(OH)_3$ coagulates from pH > 1.0 and can be in equilibrium with soluble monomeric species like Fe^{3+}, $Fe(OH)^{2+}$, $Fe(OH)_2^+$ and $Fe(OH)_4^-$. At pH between 6.2 and 9.6, $Fe(OH)_3$ is the sole species present in solution, which is considered to be the preferred coagulant agent that is responsible for pollutant removal [142].

Moreover, the generated protons can be neutralized with the OH^- produced in reaction (4) or directly reduced to H_2 at the cathode by reaction (7):

$$2H^+ + 2e^- \rightarrow 2H_{2(g)} \quad (7)$$

The overall reactions for the generation of coagulants could be summarized as [146]:

$$Fe + 2H_2O \rightarrow Fe(OH)_{2(s)} + H_{2(g)} \quad (8)$$

$$4Fe + 10H_2O + O_2 \rightarrow 4Fe(OH)_{3(s)} + 4H_{2(g)} \quad (9)$$

In EC with Al anode, the generation of soluble Al^{3+} occurs by the oxidation of Al via anodic reaction (10), whereas the cathodic reaction (7) produces hydroxide ion and H_2.

$$Al \rightarrow Al^{3+} + 3e^- \quad (10)$$

Aluminum ions in the aqueous medium present complex equilibria with different monomeric species such as $Al(OH)^{2+}$, $Al(OH)_2^+$, $Al(OH)_3$ and $Al(OH)_4^-$ depending on the pH [142]. However, the main responsible for the formation of floccules and aggregates is $Al(OH)_3$, which is formed by complex precipitation mechanisms involving the overall reaction (11) in the solution:

$$Al + 3H_2O \rightarrow Al(OH)_{3(s)} + 3/2H_{2(g)} \quad (11)$$

Furthermore, some works have proposed the use of alternative anode materials such as Zn and Mg [147,148]. The reactivity is analogous to that described for Fe and Al anodes.

EC combines various electrochemical, chemical and physical mechanisms. These can be sequential and/or simultaneous. Considering Al anode as an example, a brief outline is given in Fig. 9 to highlight the complexity and the interplay between the mechanisms in the EC process [146].

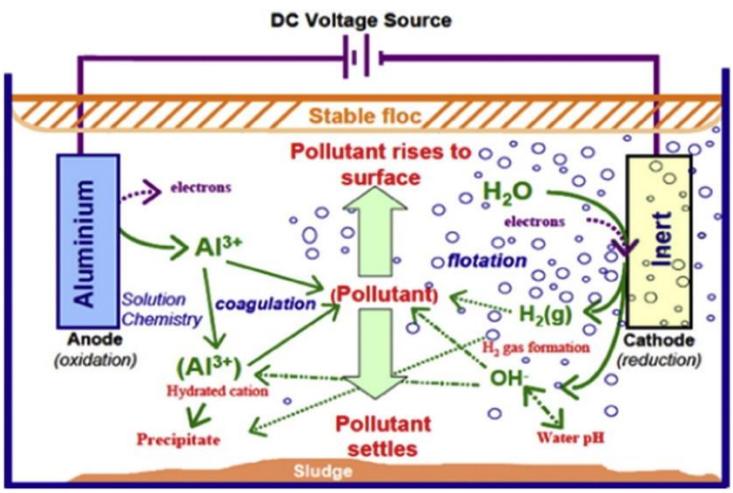

Figure 9. Schematic illustration of the removal of pollutants by EC process [146].

Note that, apart from the phase separation, degradation of organic pollutants is also feasible in EC system either by their reduction at the cathode or by the attack of oxidants like active chorine originated from the anodic oxidation of Cl^-, largely present in an actual wastewater (reaction (12), followed by reactions (1) and (2)) [149].

$$2Cl^- \rightarrow Cl_2 + 2e^- \quad (12)$$

The parameters affecting the EC effectiveness are related to the operation conditions such as current density and operation time, to wastewater features such as pH and conductivity, and to the geometry of the EC reactor and the electrode materials [146]. Current density determines the coagulant dosage at the anode and the H_2 evolution at the cathode governed by Faraday's law, as well as the energy consumption associated to the electrochemical process. The value of pH is another key factor influencing the performance of EC. First, pH governs the distribution of different hydrolyzed metal species in solution, thus determining the interaction mechanisms with pollutants in EC process [150]. Second, depending on the pK_a of many pollutants, their chemical structure changes with the variation of pH, which directly affects the pollutants net charges as well as their electrostatic interactions [142]. The selection of electrode material is also one of the control parameters that not only impacts the performance and efficiency of EC process but it is also associated to the cost.

The connection mode of the electrodes in the EC cell plays an important role in the removal efficiency, energy consumption and the cost [151]. The most typical arrangements are: monopolar electrodes in parallel connection (MP-P), monopolar electrodes in serial connection (MP-S), and bipolar electrodes in serial connection (BP-S), as schematized in Fig. 10 [142].

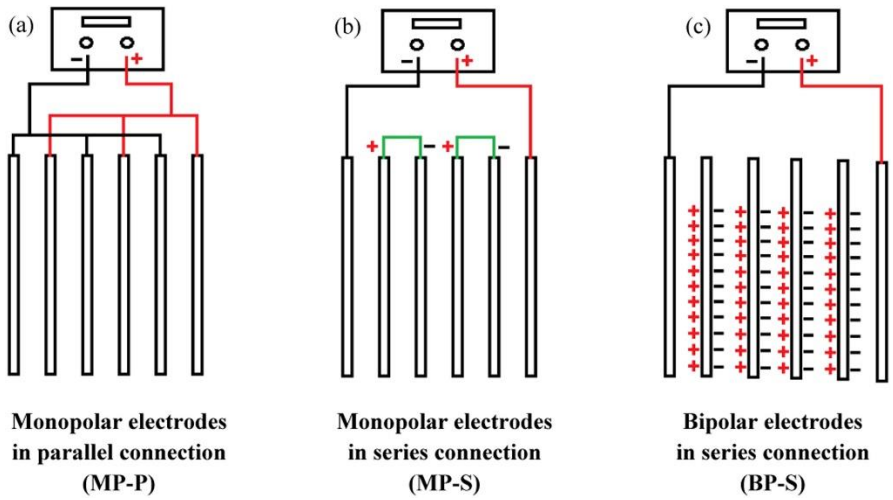

Figure 10. Different electrode arrangements in EC cells [142].

In monopolar electrodes arrangement, each electrode works as anode or cathode depending on its electrical polarity in the cell. In MP-P, each sacrificial anode is directly connected with another anode in the cell, using the same condition for cathodes. Meanwhile, in MP-S, each anode-cathode pair is internally connected but they are not connected with the outer electrodes. In the case of the bipolar electrodes, each electrode except the outer ones, present different polarity at each side depending on the charge of the electrode in front of it [144]. Actually, the relative efficiencies of different mode strongly depend on the operating parameters discussed previously as well as the water matrix and the nature of the pollutants [152]. The MP-P tends to present lower operational costs, whereas BP-S requires lower installation maintenance and sometimes it favors higher pollutant removal [142].

Overall, considering the features of EC approach, it presents many advantages as compared to the conventional physicochemical treatment of chemical coagulation. The main strengths as well as the specific drawbacks of the EC process are summarized in Table 8 [146,153].

Table 8. Advantages and drawbacks of EC process as compared to chemical coagulation [146,153].

Advantages	**Drawbacks**
More effective and rapid	Possible anode passivation and sludge deposition on the electrodes
pH control is not necessary, except for extreme values	Enough conductivity of the wastewater is required
Avoids the use of chemical coagulants	The sacrificial anodes are consumed and must be replaced periodically
Small sludge production	The use of electricity may be expensive
Simple equipment and reduced operation cost	An impermeable oxide film may be formed on the cathode, reducing the removal efficiency
Generated gas bubbles can enhance the mass transport	
Solar power can be used	

1.2.2. Advanced EC

The advanced EC processes are emergent technologies that use the simultaneous generation of in situ hydroxyl radicals ($^{\bullet}OH$) and other chemical oxidants by different mechanisms. These high oxidant species accelerate the anode dissolution by chemical oxidation and enhance the organic pollutants abatement via the oxidative action of radical species [142]. Several advanced EC technologies are presented below.

Photo-electrocoagulation (Photo-EC)

Ultraviolet (UV) irradiation is a well-known and extensively applied technology for water disinfection. Some organic pollutants can directly be photo-transformed by UVC irradiation to other compounds. Coupling EC with UV irradiation (usually $\lambda < 300$ nm) has been proposed as an alternative to achieve synergistic effect on the removal of organic pollutants by the generation of additional oxidants and radical species [142]. In the EC process, it is know that sacrificial anodes possess a low overpotential for O_2 evolution reaction, and hence, a poor $^{\bullet}OH$ production from H_2O oxidation is expected

[154]. However, it should be remembered that chloride ion is quasi-ubiquitous in water effluents. In the presence of Cl^-, hypochlorite could be formed from chloride oxidation according to reaction (12), followed by reactions (1) and (2). The electrogenerated active chlorine species can result in $^{\bullet}OH$ and $Cl^{\bullet}$ formation when the solution is irradiated with UVC light during the photo-EC process, as shown in reaction (13)-(15), which is not surprising according to the described UV/chlorine process [155,156].

$$HClO + hv \rightarrow {}^{\bullet}OH + Cl^{\bullet} \quad (13)$$

$$ClO^- + hv \rightarrow O^{\bullet-} + Cl^{\bullet} \quad (14)$$

$$O^{\bullet-} + H_2O \rightarrow {}^{\bullet}OH + OH^- \quad (15)$$

Furthermore, when iron anode is employed in EC process, a larger amount of $^{\bullet}OH$ is expected to be produced via reaction (16) and (17), especially at low pH [157,158].

$$Fe^{2+} + HClO \rightarrow Fe^{3+} + {}^{\bullet}OH + Cl^- \quad (16)$$

$$Fe(OH)^{2+} + hv \rightarrow Fe^{2+} + {}^{\bullet}OH \quad (17)$$

Then, the generation of these oxidants enhances the electrode dissolution by means of chemical oxidation reactions and favors the degradation of organic pollutants in water. Cotillas et al. [159] tested the effectiveness of photo-EC process, achieving a turbidity decay of 73% upon treatment of urban wastewater using a cylindrical flow cell with Fe anode at current density of 1.44 mA cm^{-2} with an inner 4 W UVC lamp, which proved the synergistic effect between UV irradiation and EC process.

Peroxi-electrocoagulation (Peroxi-EC)

Peroxi-EC consists in the simultaneous electrogeneration of hydrogen peroxide (H_2O_2) by the cathodic reduction of oxygen via reaction (18) and the anodic dissolution of iron as sacrificial anode [160,161]. In this case, H_2O_2 could be electrogenerated on a carbonaceous materials such as graphite, but with greater efficiency using gas-diffusion electrodes (GDE) with carbon-polytetrafluoroethylene (PTFE), graphene or carbon

nanotubes or nanofibers. Hydrated Fe^{3+} species are generated as coagulants that remove pollutants by their precipitation [142]. Additionally, homogeneous $^{\bullet}OH$ are generated in solution from Fenton's reaction (19), leading to the additional formation of Fe(III) species that enhance the coagulation process [162]. Thus, the electrogenerated radicals favor the sacrificial anode dissolution by direct chemical oxidation reaction (20) and (21), and organic pollutants are mineralized to CO_2, H_2O and inorganic ions. Nevertheless, competitive coagulation of by-products with $Fe(OH)_3$ can be also attained in concomitance with the organics oxidation [163,164].

$$O_{2(g)} + 2H^+ + 2e^- \rightarrow H_2O_2 \quad (18)$$

$$Fe^{2+} + H_2O_2 \rightarrow Fe^{3+} + {}^{\bullet}OH + OH^- \quad (19)$$

$$Fe + 2{}^{\bullet}OH \rightarrow Fe(OH)_2 \quad (20)$$

$$Fe + 3{}^{\bullet}OH \rightarrow Fe(OH)_3 \quad (21)$$

Apart from Fe, Cu could also be employed as sacrificial anode in the peroxi-EC process, with similar mechanisms [165]. Using this anodic material, the main coagulant species is the $Cu(OH)_2$ and $^{\bullet}OH$ is generated by the Fenton-like reaction using Cu^+ as catalyst instead of Fe^{2+}.

Additionally, peroxi-EC can be implemented with simultaneous UV irradiation, commonly called as photoperoxi-electrocoagulation [166]. The simultaneous irradiation with UV light promotes photochemical reactions that enhance and accelerate the Fenton's reaction, leading to the improvement of organic pollutants mineralization [142]. The implementation of these photochemical processes favors the oxidation of organic pollutants thanks to the combination of photo-Fenton process, suggesting novel alternatives for removing different organic pollutants in water [167].

Ozonation-assisted EC (Ozone-EC)

It is well established that ozone can oxidize various organic and inorganic compounds either by a direct ozone attack or indirect free radicals involving $^{\bullet}OH$, $O_2^{\bullet-}$ and $HO_2^{\bullet}$

generated upon the ozone decomposition in water via reactions (22)-(24) [168]:

$$O_3 + H_2O \rightarrow 2HO_2^{\bullet} \quad (22)$$

$$O_3 + HO_2^{\bullet} \rightarrow {}^{\bullet}OH + 2O_2 \quad (23)$$

$$O_3 + OH^- \rightarrow HO_2^{\bullet} + O_2^{\bullet-} \quad (24)$$

If ozone is bubbled into the Fe-based EC system, redox reactions (25)-(27) take place, in which ozone decomposes after its reaction with Fe^{2+} to yield the intermediate FeO^{2+}, a species that may evolve to $^{\bullet}OH$ [169]:

$$O_3 + Fe^{2+} \rightarrow FeO^{2+} + O_2 \quad (25)$$

$$FeO^{2+} + H_2O \rightarrow Fe^{3+} + {}^{\bullet}OH + OH^- \quad (26)$$

$$FeO^{2+} + Fe^{2+} + 2H^+ \rightarrow 2Fe^{3+} + H_2O \quad (27)$$

It is clear that there is a mutual activation between ozone and Fe^{2+}. The presence of Fe^{2+} enhances ozone decomposition to $^{\bullet}OH$, and the presence of ozone bubbles originates the O_3/Fe^{2+} catalytic system that yields the intermediate FeO^{2+} and finally produces $^{\bullet}OH$ and Fe^{3+}. These generated active species could accelerate the abatement of organic pollutants and, consequently, enhance the process efficiency [170]. Accordingly, the synergistic effect of ozone-EC has been investigated in many studies, especially for the treatment of organic pollutants. For instance, Asaithambi et al. [169] reported that the ozone-EC process was more effective than EC and ozonation alone, achieving 83% chemical oxygen demand (COD) removal as maximum.

Other advanced EC processes, including sono-electrocoagulation [171], coupling EC with membrane filtration [172], and simultaneous EC coupled with electro-oxidation [173], have also been widely studied aiming to achieve more efficient removal of organic pollutants. One of the most promising combination technologies is the sequential EC/EAOPs, where the electrogenerated dissolved iron species in EC process can be directly used as catalyst in the subsequent EAOPs [149]. The mechanisms and advantages of this system are discussed in subsection 1.4.1.

1.3. Electro-oxidation (EO)

In the past decades, great progress has been made in the field of EO technology for the treatment of refractory organic pollutants in water/wastewater. In fact, the electrochemical processes offer an alternative solution to many environmental problems due to numerous advantages as shown in subsection 1.1.4. The oxidation of organic pollutants in EO process can take place in two ways (Fig. 11) [87,174,175]:

a) Direct oxidation, where pollutants can be oxidized at the anode surface by direct electron transfer without participation of other substances;
b) Indirect oxidation, where pollutants are oxidized through the mediation of some electroactive species generated at the anode surface, which act as intermediates for electrons shuttling between the anode and the organic compounds.

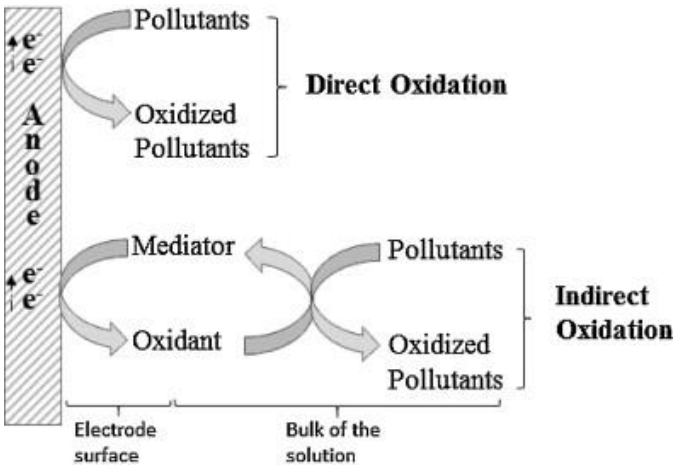

Figure 11. Schematic of direct and indirect oxidation in EO process [174].

The direct oxidation is usually not very effective in the degradation of organic pollutants mainly because of the electrode deactivation due to the formation of a polymeric layer on the anode surface, which is commonly called the poisoning effect. The indirect oxidation occurs on the electrode surface by mediation of the powerful physisorbed $^{\bullet}OH$ (i.e., $M(^{\bullet}OH)$) from reaction (28). The radical is formed from water oxidation via reaction (29) and or in the bulk of the solution by other powerful electrogenerated oxidants [87].

$$R + M(^{\bullet}OH) \rightarrow M + CO_2 + H_2O \quad (28)$$

$$M + H_2O \rightarrow M(^{\bullet}OH) + H^+ + e^- \quad (29)$$

where M is the metal surface and R is an organic molecule. Other electrogenerated oxidizing reagents, including ozone, chlorine, peroxide, hypochlorite and peroxodisulfate, also play important roles in the degradation of organic pollutants. Among these, active chlorine generated from the oxidation of chloride is probably the most commonly produced mediator, due to their effective activity and ubiquitous presence in wastewater at elevated concentration compared to other species [174]. Active chlorine is formed at the anode by reaction (12), followed by reaction (1) and (2). Under these conditions, dimensionally stable anodes (DSA®) such as those based on ruthenium dioxide (RuO_2) form large amounts of active chlorine to rapidly attack the organics, although only partial mineralization is usually achieved due to the accumulation of persistent chloroderivatives [176].

The efficiency of the EO process is highly dependent on the nature of the electrode material and the operation conditions. During the EO process, secondary reactions, like OER, take place inevitably at high potentials and decrease the current efficiency for the desired oxidation reactions [177]. Considering the competing reactions between anodic oxidation of organics and the simultaneous oxygen evolution at the anode, a comprehensive model has been proposed to divide the anodes into two classes: active and non-active ones. Active anodes present low oxygen evolution potential and the $M(^{\bullet}OH)$ is easily transformed into a higher state oxide or superoxide MO. Therefore, only partial oxidation of organics can be achieved by this chemisorbed species at the anode surface. In contrast, non-active anodes present high oxygen evolution potential, allowing the generation of larger amounts of active $M(^{\bullet}OH)$, which is so weakly physisorbed at the anode surface and can yield complete oxidation to the organic pollutants [87,174,177].

As a general rule, the larger potential for O_2 evolution of the anode material, the weaker

in the interaction of M(•OH) with the anode surface and the higher is the chemical reactivity toward organics oxidation [175]. Table 9 presents the oxygen evolution potential of several most commonly used anode materials in the EO process. As can be seen, RuO_2, iridium dioxide (IrO_2), platinum (Pt) and graphite electrodes are typical examples of active anodes, exhibiting potential for O_2 evolution lower than 1.8 V/SHE, whereas lead dioxide (PbO_2), tin dioxide (SnO_2), boron-doped diamond (BDD) and sub-stoichiometric Ti_4O_7 electrodes can be considered as non-active electrodes, presenting oxygen evolution potentials from 1.7 to 2.6 V/SHE [175,178].

Table 9. Oxygen evolution potential at various anode materials used in EO process [175,178].

Anode material	**Oxygen evolution potential (V/SHE)**	**Adsorption enthalpy of M-OH**	**Oxidation power of the anode**
RuO_2	1.4-1.7	Chemisorption of •OH	
IrO_2	1.5-1.8		
Pt	1.6-1.9		
Graphite	1.7		
Ebonex® (Ti_4O_7)	1.7-1.8		
PbO_2	1.8-2.0		
SnO_2	1.9-2.2		
BDD	2.2-2.6	Physisorption of •OH	

Although SnO_2 and PbO_2 anodes are attractive materials for the electrochemical oxidation of recalcitrant organics, their industrial application may be restricted by their specific features. For SnO_2, the main problem is their short service life, whereas for PbO_2, the main issue is the presence of toxic Pb^{n+} ions in the treated water [177]. Among the most widely used anodes in the EO process, BDD has been reported to yield the highest organic oxidation rates and the greatest current efficiencies [179]. This anode material presents extraordinary properties such as: [174]:

(a) Wide potential window in aqueous and non-aqueous solutions. The H_2 evolution is initiated at ~ -1.2 V vs SHE, and O_2 evolution begins at ~ +2.4 V vs SHE;

(b) Good stability and corrosion resistance in strongly acidic media, owing to the strong atomic connection and sp^3-hybridised orbital structure;
(c) Inert surface with low adsorption properties; and
(d) Low background current.

However, the efficient mineralization of organics by BDD anode is usually accompanied by a high energy consumption due to its moderate conductivity. The production of perchlorate ion (ClO_4^-) on BDD surface in the presence of Cl^- can cause an important environmental impact. Moreover, the BDD thin film usually possesses low mechanical stability. All these drawbacks, along with its high cost, restrict the large scale application of BDD anode.

Alternatively, DSA® anodes have been extensively employed in the EO process due to their mechanical resistance as well as a relatively low cost. As active anodes, the generated chemisorbed M(•OH) is easily transformed into other species, resulting in a partial oxidation of organics. The DSA®-O_2 electrode is based on IrO_2, which is a good catalysts for O_2 evolution reaction, reducing the overpotential for water dissociation. The DSA®-Cl_2 electrode is based on RuO_2, which favors the efficient transformation of Cl^- into active chlorine with insignificant production of ClO_4^-.

In general, the indirect oxidation of organic pollutants with simultaneous oxygen evolution occurs on the active or non-active anode surface as highlighted in Fig. 12 [180].

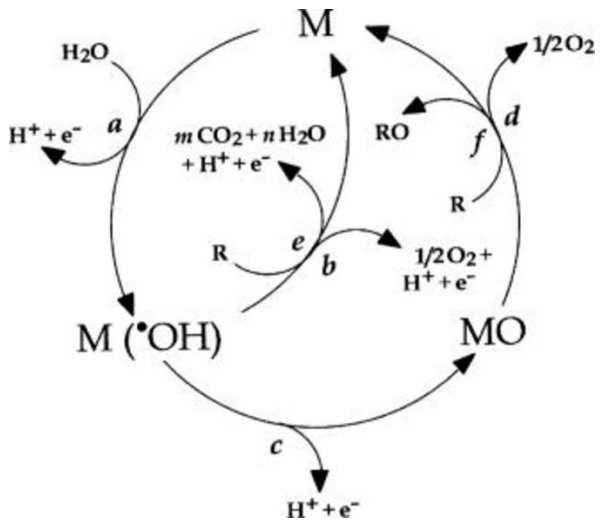

Figure 12. Scheme of the indirect oxidation with simultaneous oxygen evolution [180]: (a) water discharge to hydroxyl radicals, (b) O_2 evolution by recombination of radicals, (c) formation of superoxide MO, (d) O_2 evolution by decomposition of superoxide MO, (e) oxidation of the organic compound via radicals, and (f) oxidation of the organic compound via superoxide MO.

Among the various anodes, photoanodes synthesized with photosensitive materials such as TiO_2 allow the development of PEC systems, which have emerged in recent years as low cost EAOPs from the efficient destruction of organic pollutants [181]. This method combines photocatalysis and anodic oxidation, allowing a synergistic effect in the degradation of organics due to: (a) generation of electron-hole (h^+) pairs at the anode surface, (b) production of $^{\bullet}OH$ from the oxidation of water by h^+ and reduction of H_2O_2 by e^-, and (c) direct oxidation of organics by h^+ [182].

The utilization of mixed metal oxides (MMOs) as anodes in the EO process has been widely explored [183,184]. They are more stable and exhibit an upgraded elecrocatalytic activity as compared to their respective single-component metal oxides due to the increased surface area, active acidic or basic sites, or the change in the chemical states of the metal ions. MMO anodes are usually prepared by depositing the MMOs layer on inert substrates such as titanium, carbon and stainless steel, and they can be classified as bulk mixed metal oxide anodes and supported metal oxide anodes (shown in Fig. 13) [177].

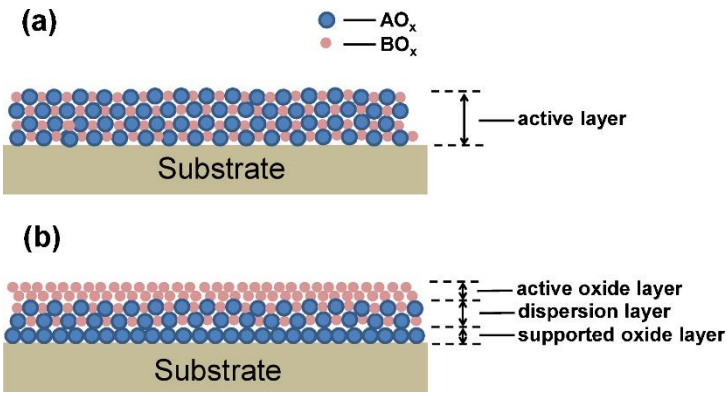

Figure 13. Diagram of the surface oxides structures of (a) binary bulk mixed metal oxide anode, and (b) supported metal oxide anode [177].

For the preparation of bulk mixed metal oxide anode, a mixture of metal precursors is employed to deposit different metal oxides on the substrate concurrently and homogenously, achieving a surface layer with completely mixed metal oxides. Various methods including thermochemical decomposition, electrodeposition, chemical vapor deposition and physical vapor deposition have been reported to produce the bulk mixed metal oxide layers [177,185,186]. Typical MMO anodes based on the bulk mixed metal oxide system include Ir-Ru binary MMO anodes, Sn-Sb binary MMO anodes, Ti-Ru binary MMO anodes and Ir-Ru-Sn ternary MMO anodes. Other well-known anodes are supported MMOs, which can be prepared by depositing an active metal oxide film on a metal oxide support [187]. These kinds of anodes can be prepared by the spontaneous dispersion of one crystalline metal oxide over another metal oxide. Although the supported oxide layer does not directly participate in the surface reactions, it can enhance the performance of the MMO anode by increasing the electrocatalytic activity, enhancing the stability, improving the electrode conductivity and increasing the surface area [188,189]. The metal oxide films of supported metal oxide anodes are prepared layer by layer by different synthesis techniques, including thermochemical degradation of the support layer and electrodeposition of the active layer [190]. Some supported metal oxides which are widely employed include TiO_2 nanotubes (TiO_2-NTs) and binary MMOs of Ir-Ru-O and Ir-Ta-O [177].

Besides the anode material, there are several operation variables that can affect the EO

process for the treatment of organic pollutants, including pH, current density, supporting electrolyte and temperature [177]. The effect of pH and temperature have been investigated in many articles, but the findings are diverse and sometimes even contradictory depending on the target pollutants, supporting electrolytes and employed anodes. In general, many studies reported that the removal efficiency of organic pollutants by EO tends to increase in the lower pH range and higher temperature [177,191]. The current density plays an important role in EO because it determines the extension of electron transfer and the generation of oxidizing agents [192]. Higher current density can enhance the removal efficiency of organic pollutants, but also upgrade the competing side reaction. Various types of electrolytes have been used to increase the solution conductivity in the EO process. Some of them are highly stable during the treatment, such as $NaClO_4$ and $NaNO_3$, whereas others participate in the anode surface reaction to generate active species like Cl_2.

1.4. Fenton-based electrochemical advanced oxidation processes (EAOPs)

Over the last two decades, EAOPs have attracted increasing attention as a promising class of AOPs for the degradation of organic micropollutants in wastewater. The simplest and most popular EAOP is EO, explained in subsection 1.3, where the organics can be directly oxidized at the anode surface and/or indirectly oxidized by physisorbed M($^{\bullet}$OH) and/or intermediate active species such as active chlorine. The technologies discussed in this section are based on the $^{\bullet}$OH generated in the bulk of the treated contaminated solutions, thus minimizing the limitations inherent to the $^{\bullet}$OH formed at the anode surface in the EO systems. The Fenton-based EAOPs mainly include electro-Fenton (EF), photoelectro-Fenton (PEF) and solar photoelectro-Fenton (SPEF) processes [175]. The Fenton's reagent, a mixture of H_2O_2 and Fe(II), constitutes the basis of the chemical generation of the strong oxidant $^{\bullet}$OH, which was firstly proposed by the pioneering work of Fenton in 1894, and its mechanism has been gradually established during the subsequent decades [193,194].

The electrochemical production of H_2O_2 with the addition of Fe^{2+} to the bulk originates the common and widely studied EF, and further combination with photoirradiation provided by artificial light or sunlight leads to PEF and SPEF processes. These Fenton-based EAOPs have been proven as efficient technologies for the destruction of recalcitrant and toxic organic pollutants [88].

1.4.1. Electro-Fenton (EF) and photoelectro-Fenton (PEF): homogenous catalysis

The EF process is among the most known and popular EAOPs and constitutes an indirect electrochemical manner to generate $^{\bullet}OH$ in aqueous solutions. It has been developed upon an extensive study over the last 25 years, with particularly remarkable contributions by Brillas' and Oturan's groups [193]. This process has been proposed to achieve the implementation of a new and powerful advanced oxidation method that overcome the drawbacks of the classical Fenton process. It allows the continuous in situ electrogeneration of H_2O_2 and/or regeneration of Fe(II) at the cathode, thus avoiding the use of high quantities of H_2O_2 and Fe(II) salt and increasing the effectiveness [158].

The H_2O_2 production rate is one of the key parameters that control the process efficiency. In EF, H_2O_2 can be continuously supplied to an acidic contaminated aqueous solution from the two-electron cathodic reduction of oxygen gas, directly injected as pure gas or bubbled air, as expressed in reaction (18).

The current efficiency of H_2O_2 production highly depends on some factors such as the cathode material and operation conditions (O_2 solubility, pH and temperature) [88]. The most frequently used carbonaceous cathodes are commercially available materials such as carbon-PTFE O_2 diffusion, graphite, graphite felt, carbon felt, activated carbon fiber, reticulated vitreous carbon, carbon sponge and carbon nanotubes [193,195].

GDEs have a thin and porous structure favoring the percolation of the injected gas across its pores to contact the solution at the carbon surface. These electrodes possess

a large number of active surface sites leading to a very fast O_2 reduction and large accumulation of H_2O_2. They usually incorporate PTFE that serves to bind the carbon particles into a cohesive layer and impart some hydrophobic character to the electrode [193]. Thus, the contact between the cathode and aqueous solution is quite limited, resulting in a poor cathodic reduction of Fe^{3+}, which is another important reaction in EF system that can reduce the initial addition of iron catalyst [175]:

$$Fe^{3+} + e^- \rightarrow Fe^{2+} \tag{30}$$

As a typical three-dimensional electrode, the carbon-felt (CF) cathode presents a high ratio of surface area to volume, yielding large values of mass transport coefficients of both, dissolved O_2 and Fe(III), due to the particular hydrodynamic conditions. It favors the fast generation of both components of Fenton's reagent (H_2O_2 and Fe(II)) in the bulk, but leading to much lower H_2O_2 accumulation compared to GDEs [193].

Recently, different carbonaceous materials such as carbon black, acetylene black and graphene, have been explored to improve the H_2O_2 production via the 2-electron O_2 electroreduction reaction. Carbon materials doped with various heteroatoms such as O, N, F, B and P have been widely studied and proven to efficiently improve the activity and selectivity for H_2O_2 production. In addition, the utilization of non-noble metal catalysts, including metal oxides and metal-doped conductive polymers either as such or supported, is considered another strategy to enhance the H_2O_2 production rate, which is very attractive for industrial and practical applications [195].

As mentioned above, Fe(II) is initially introduced in a catalytic amount and its electrocatalytic regeneration from the reduction of Fe(III) formed by Fenton's reaction is feasible depending on the cathode surface. In this scenario, Fenton's reagent can be continuously produced in the solution, forming $^{\bullet}OH$ via Fenton's reaction to ensure the destruction of organic pollutants in aqueous medium through their oxidation and mineralization, as follows [158]:

$$\text{Organic pollutants} + {}^{\bullet}OH \rightarrow \text{Intermediates} \quad (31)$$

$$\text{Intermediates} + {}^{\bullet}OH \rightarrow\rightarrow\rightarrow CO_2 + H_2O + \text{inorganic ions} \quad (32)$$

Compared with the classical Fenton process, the main advantages of the EF processes are: (a) in situ and controlled generation of Fenton's reagent, thus avoiding the risks related to transportation, storage and handling of H_2O_2, (b) minimization of parasitic reactions that waste $^{\bullet}OH$, thanks to the low Fenton's reagent concentration, and (c) smart modulation of the process by appropriate current or potential control [158].

The irradiation of a solution treated under EF conditions by means of artificial UV light or natural sunlight leads to the PEF and SPEF processes, respectively. These processes involve the treatment of the contaminated solution under EF conditions along with the simultaneous irradiation with UV or solar light to accelerate the mineralization rate of organics. Oxidizing $^{\bullet}OH$ are produced from Fenton's reaction, whereas the undesired accumulation of Fe(III) ions that decelerate the treatment is avoided by the reductive photolysis of $Fe(OH)^{2+}$, the predominant Fe(III) species in solution at pH 2.8-3.5, based on the photo-Fenton reaction (33), thereby regenerating Fe(II) and producing more radicals [88].

$$Fe(OH)^{2+} + h\nu \rightarrow Fe^{2+} + {}^{\bullet}OH \quad (33)$$

The direct photolysis by ligand-to-metal charge transfer excitation of complexes formed between Fe(III) and carboxylic acids also allows the regeneration of Fe(II) via reaction (34) [193]:

$$Fe(OOCR)^{2+} + h\nu \rightarrow Fe^{2+} + CO_2 + R^{\bullet} \quad (34)$$

Lamps providing UVA light (λ = 315-400 nm) are widely employed in PEF to achieve an efficient Fe(III) reduction by reactions (33) and (34). The degradation rates of organic pollutants are increased by higher irradiation intensity, up to a given value. UVC light is also used in PEF process by some researchers because $^{\bullet}OH$ can be

additionally generated through the homolytic cleavage of the hydrogen peroxide (-O–O-) bond via reaction (35), and direct photolysis of pollutants can take place when the light source emits radiation within the same wavelength range where the contaminants can absorb it.

$$H_2O_2 + h\nu \rightarrow 2^{\bullet}OH \quad (35)$$

However, the UVA lamps are the most widely employed [88], since UVC is relatively costly.

The use of commercial lamps in PEF is commonly responsible for high electrical costs, which can be minimized by the application of the SPEF process, where the solution is directly irradiated with free and renewable natural sunlight. When comparing SPEF with PEF using low energy power lamps, it is common to achieve higher degradation of pollutants in SPEF due to: (i) the higher UV intensity of natural sunlight, and (ii) the simultaneous presence of photons in the visible region ($\lambda > 400$ nm), which also allows the direct photolysis of Fe(III)-carboxylate complexes [175].

The degradation of organic pollutants in aqueous solution by all mentioned EAOPs depends on various operation parameters such as supporting electrolyte, current density, pH, stirring rate or liquid flow rate, and temperature [175]. The current density is a key parameter in EF and PEF processes since it regulates the amounts of oxidizing species produced. Within a certain range, the increase of current density can enhance the degradation of contaminants due to the greater production of M($^{\bullet}$OH) from reaction (28) and $^{\bullet}$OH from Fenton's reaction because of the faster generation of H_2O_2 via reaction (18). However, the current efficiency usually decreases with the increase in current density, which also results in the enhancement of cathodic competitive reactions, such as hydrogen evolution, H_2O_2 reduction by reaction (36), and the destruction of the generated $^{\bullet}$OH by non-oxidizing parasitic reactions according to reactions (37) to (39) [196].

$$H_2O_2 + 2H^+ + 2e^- \rightarrow 2H_2O \quad (36)$$

$$2M(^{\bullet}OH) \rightarrow 2M + O_2 + 2H^+ + 2e^- \quad (37)$$

$$H_2O_2 + {}^{\bullet}OH \rightarrow HO_2^{\bullet} + H_2O \quad (38)$$

$$Fe^{2+} + {}^{\bullet}OH \rightarrow Fe^{3+} + OH^- \quad (39)$$

The solution pH is another important factor that has influence on the performance of EF, PEF and SPEF processes. The optimum pH is in general close to 3.0 [197]. According to the literature, at high pH values (especially pH > 5.0) some events occur that inhibit the abatement of organics, such as: (a) deactivation of Fe(II) by formation of ferric hydroxides, (b) decrease of $^{\bullet}OH$ production by the absence of H^+, (c) presence of CO_3^{2-} and HCO_3^- with the consequent scavenging of $^{\bullet}OH$, and (d) decomposition of H_2O_2 to water and oxygen [174,198]. At extremely low pH values, organics oxidation is also inhibited since the electrogenerated H_2O_2 reacts with H^+ to form $H_3O_2^+$, therey decelerating the reaction rate between H_2O_2 and Fe(II) and, consequently, yielding a lower amount of $^{\bullet}OH$ [199].

The homogeneous EF and PEF processes are efficient for the degradation and mineralization of wastewater contaminated with different classes of organic micropollutants. However, their potential exploitation is still limited due to the relatively high operation costs that are inherent to the long treatment time required. As mentioned above, the use of EC as pre-treatment has been envisaged to overcome these limitations [149]. EC involves the in situ generation of coagulants from dissolution of an appropriate sacrificial anode (Fe or Al), forming flocs that precipitate and adsorb colloids and organics. Partial oxidation of the organic matter is also feasible (see above). When Fe anode is employed, the generated coagulants also act as a source of iron catalyst for subsequent EAOPs. Thus, the sequential EC/EAOPs have been proposed by our research group to achieve a more efficient removal of organic pollutants with low energy consumption and operation costs. In this Thesis, the application of sequential EC/EAOPs for the treatment of urban wastewater was tested for the first time. In addition, the performance of single EC and EAOPs was examined for comparison.

Another major challenge of EF and PEF is that they are only optimal at strong acidic pH conditions, which is negative and disadvantageous from the environmental point of view, since a final neutralization step may become necessary to obtain environmentally friendly effluents. Additionally, the non-recyclability of the catalysts and the production of high amount of iron sludge make the technique unsuitable for operation in continuous mode [200]. New advanced EAOPs are then needed to overcome these drawbacks.

1.4.2. Advanced EF and PEF (I): chelated catalysts

As mentioned above, the conventional EF and PEF processes have some intrinsic disadvantages, including the need to operate within a narrow pH range (2.8-3.5). A strict pH control is substantially required to ensure that ion species exert their catalytic role, avoiding any precipitation of inactive iron oxyhydroxides and maximizing the concentration of photoactive species. As shown in Fig. 14, by starting from a pH of about 1, free Fe(III) concentration gradually disappears to give rise to the formation of both, $FeOH^{2+}$ and $Fe(OH)_2^+$ aquo-complexes. At pH values 2.0-3.0, $Fe(OH)^{2+}$ is predominant, ensuring the maximum system reactivity. It is clear that the reactivity decreases with increasing pH above 3.0 due to a decrease in concentration of both, photoactive $FeOH^{2+}$ and dissolved iron. At pH higher than 4.0, dissolved iron precipitates as ferric hydroxide, dramatically affecting the efficiency [201].

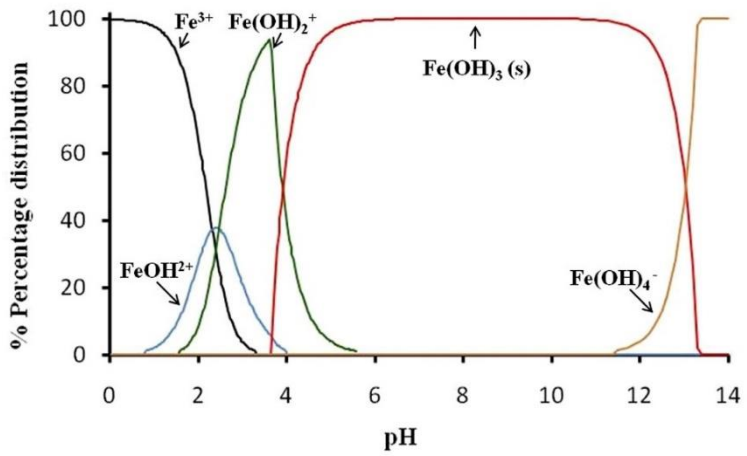

Figure 14. Speciation diagram of ferric hydroxyl-species as a function of pH for a solution containing 1.0×10^{-5} M of Fe(III) at 25 °C [201].

The possibility of working at neutral pH has driven most of the research in recent years. Some compounds, such as carboxylates and polycarboxylates, are able to form stable complexes with Fe(III), which can: (i) impede the iron precipitation at near-neutral pH, (ii) significantly absorb UV/Vis light, and (iii) undergo photoreduction through a ligand-to-metal charge transfer, generating Fe(II) ions [202].

$$[Fe^{III}L] + h\nu \rightarrow [Fe^{III}L]^* \rightarrow Fe^{2+} + L^{\bullet} \quad (40)$$

However, the concentrations of these complexing agents in industrial and urban wastewater are usually very poor and hence, their external addition to ensure efficient performance is required. In the last two decades, several articles demonstrated the enhanced activity within the field of photo-Fenton processes at near-neutral pH with the intentional addition of specific ligands [201]. However, none of the resulting Fe(III) complexes were tested in Fenton-based EAOPs. The most effective ligands that are used frequently in photo-Fenton process include: oxalate [203], citrate [204], ethylenediamine-*N,N'*-disuccinic acid (EDDS) [205], ethylenediaminetetraacetic acid (EDTA) [206], nitrilotriacetic acid (NTA) [207] and humic acid [208].

The ability of a single ligand to form strong complexes with Fe(III) is essential to prevent the precipitation of Fe(III) as iron hydroxide. As reported, when EDTA is adopted, the formation of soluble complexes allows to shift to basic pH values with no precipitation of Fe(III). The use of oxalate, citrate, NTA and EDDS may make Fe(III) soluble at near-neutral pH by forming stable complexes. In contrast, the addition of tartrate does not significantly shift the precipitation of Fe(III) to higher pH values, and the Fe(III)-tartrate complex is not present at pH higher than 5.0 [201]. Moreover, the stability and speciation of Fe(III) complexes highly depend on the iron:ligand molar ratio and the pH value.

The photolytic decomposition of Fe(III) complexes represented by reaction (40) is another key factor in photo-Fenton process to ensure an efficient degradation of organic pollutants. In the case of oxalate, the predominant iron complexes include $[FeHC_2O_4]^{2+}$,

$[Fe(C_2O_4)]^+$, $[Fe(C_2O_4)_2]^-$ and $[Fe(C_2O_4)_3]^{3-}$. Their proportion in solution highly depends on the iron: oxalate molar ratio and pH [209]. For instance, in the presence of 1:3 molar ratio, $[Fe(C_2O_4)_2]^-$ (43.1%) and $[Fe(C_2O_4)_3]^{3-}$ (56.0%) account for the largest proportion of Fe(III) species at pH 5.0 (Fig. 15) [203]. The Fe(III)-oxalate complexes absorb more strongly in the UVA-visible region (290-570 nm) and are photochemically more reactive than the $Fe(OH)^{2+}$ species. The quantum yield for Fe(II) formation at 436 nm and pH 4.0 is reported as 1.0 ± 0.25 for $[Fe(C_2O_4)_2]^-$ and 0.6 ± 0.46 for $[Fe(C_2O_4)_3]^{3-}$, but only as 0.14 ± 0.04 at 313 nm and pH 4.0 for $Fe(OH)^{2+}$ [209]. Other Fe(III) chelates are also proven to be able to absorb light more intensely than $Fe(OH)^{2+}$, with an extension of absorptions in the visible range [201]. These advanced properties of Fe(III)-ligand complexes allow the photo-Fenton system to more efficiently exploit the solar radiation and generate a higher amount of active radicals.

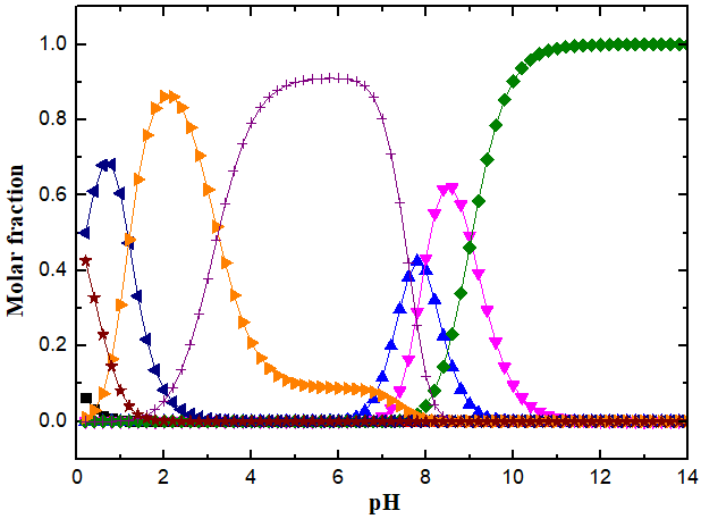

Figure 15. Speciation diagram for Fe(III) species, including hydroxyl and oxalate complexes, as a function of pH at a total iron concentration of 8.93×10^{-2} mM (i.e., 5 mg L^{-1}) and iron:oxalic acid molar ratio 1:3. Species: (■) Fe^{3+}, (●) $[FeOH]^{2+}$, (▲) $[Fe(OH)_2]^+$, (▼) $Fe(OH)_3$, (◆) $[Fe(OH)_4]^-$, (★) $[FeHC_2O_4]^{2+}$, (◀) $[Fe(C_2O_4)]^+$, (▶) $[Fe(C_2O_4)_2]^-$, (+) $[Fe(C_2O_4)_3]^{3-}$ [203].

Among all of these ligands, EDDS has attracted particular attention due to its reported biodegradability and lack of toxicity [210]. EDDS is a structural isomer of EDTA and it is reported to have metal-complexing properties similar to EDTA, being more easily degraded than EDTA upon irradiation with UV light at 315-400 nm. EDDS has two

chiral centers, existing in three stereoisomers denoted as [S,S]-EDDS, [R,S]-EDDS and [R,R]-EDDS as shown in Fig. 16 [211].

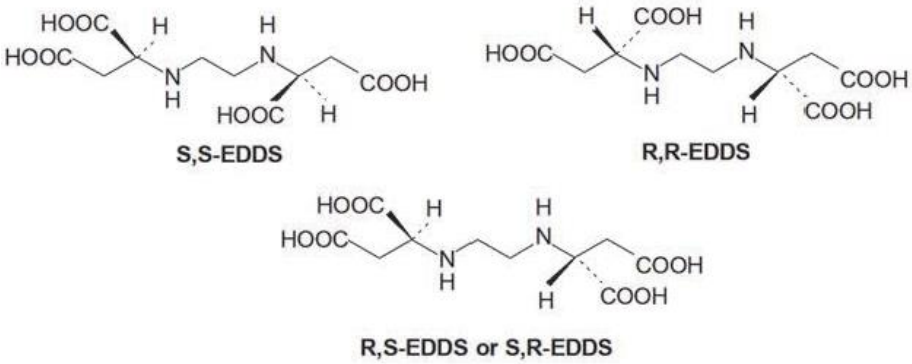

Figure 16. Chemical structures of EDDS stereoisomers [211].

The industrial manufacture of EDDS produces a mixture of isomers: 25% [S,S]-EDDS, 25% [R,R]-EDDS and 50% of the meso form [R,S]/[S,R]-EDDS. [S,S]-EDDS is readily biodegradable and [R,R]-EDDS is resistant, whereas [R,S]/[S,R]-EDDS is comparatively but not readily biodegradable [212]. EDDS has six coordinating sites (two N donors and four O donors), thus forming both, five- and six-membered chelate rings with metal ions at a ratio of EDDS to metal ion of 1:1 [213]. The iron chelation and the species distribution of Fe(III)–EDDS within the pH range 2.0-11.0 is presented in Fig. 17 [214].

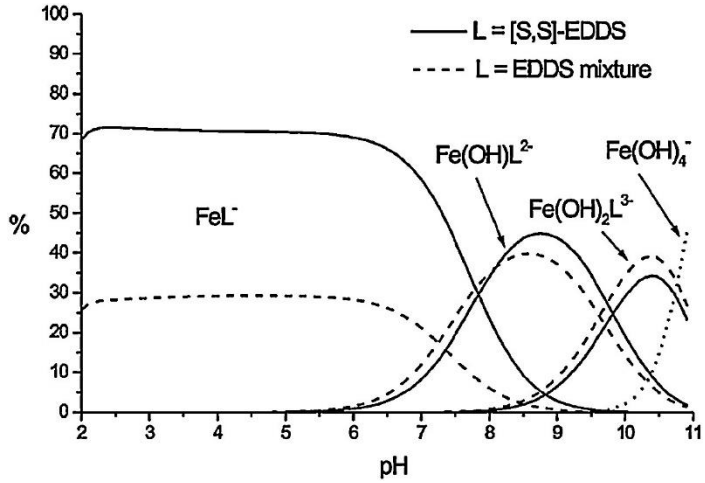

Figure 17. Species distribution of Fe(III)–EDDS over the pH range 2-11 (Note: EDDS mixture denotes the mixture of 25% [S,S]-EDDS, 50% [R,S]/[S,R]-EDDS, and 25% [R,R]-EDDS) [214].

EDDS, expressed as H_4L, as a weak tetraprotic acid has four consecutive pK_a values presented in reactions (41)-(44) [213]:

$$H_4L \rightarrow H^+ + H_3L^- \quad pK_1 = 2.4 \tag{41}$$

$$H_3L^- \rightarrow H^+ + H_2L^{2-} \quad pK_2 = 3.9 \tag{42}$$

$$H_2L^{2-} \rightarrow H^+ + HL^{3-} \quad pK_3 = 6.8 \tag{43}$$

$$HL^{3-} \rightarrow H^+ + L^{4-} \quad pK_4 = 9.8 \tag{44}$$

The addition of Fe(III) to the EDDS solution with a molar ratio 1:1 results in significant ionization of protons from the agent. As can be seen in Fig. 17, Fe(III)–EDDS exhibited four forms, FeL^-, $Fe(OH)L^{2-}$, $Fe(OH)_2L^{3-}$ and $Fe(OH)_4^-$ over the pH range 2.0-11.0. FeL^- is the dominant species at pH lower than approximately 7.8. $Fe(OH)L^{2-}$, $Fe(OH)_2L^{3-}$ and $Fe(OH)_4^-$ are gradually formed as the pH increases from 5.0 to 11.0. FeL^- has been shown to be highly photoactive, capable of producing $^{\bullet}OH$ efficiently at neutral pH [210] and Fe(III)–EDDS complex exhibits high stability even at pH values up to 9.0.

[S,S]-EDDS has been verified as a suitable alternative for EDTA for the wastewater remediation due to its strong chelating ability and biodegradability. It is very effective for increasing the efficiency of the Fenton and photo-Fenton processes at low ratio of EDDS to iron within a wide pH range of 3.0-9.0. The main reactions in Fe(III)–EDDS-modified photo-Fenton process are summarized as follows [205,212,215,216]:

$$\text{Fe(III)–EDDS} + h\nu \rightarrow Fe^{2+} + EDDS^{\bullet 3-} \tag{45}$$

$$\text{Fe(II)–EDDS} + H_2O_2 \rightarrow \text{Fe(III)–EDDS} + {}^{\bullet}OH + OH^- \tag{46}$$

$$\text{Fe(III)–EDDS} + H_2O_2 \rightarrow \text{Fe(II)–EDDS} + HO_2^{\bullet} + H^+ \tag{47}$$

$$\text{Fe(III)–EDDS/ Fe(II)–EDDS} + {}^{\bullet}OH \rightarrow \text{Oxidized products} \tag{48}$$

$$EDDS^{\bullet 3-} + O_2 \rightarrow EDDS^{\bullet} + O_2^{\bullet -} \tag{49}$$

$$EDDS^{\bullet} + O_2 \rightarrow EDDS_{OX} + H_2O_2 \tag{50}$$

The employment of Fe(III)–EDDS in conventional Fenton and photo-Fenton processes

has been studied in previous works. Huang et al. [217] found that the removal of BPA in Fe(III)–EDDS-driven Fenton process was much higher at pH between 8.0 and 9.0 than at pH < 5.0. Wu [218] reported that the 4-*tert*-butylphenol degradation in the UV-irradiated Fe(III)–EDDS/H_2O_2 system at pH 7.5 was much higher than that without UV. Li et al. [219] demonstrated that the quantum yield for $^{\bullet}OH$ formation upon photolysis of Fe(III)–EDDS increased with increasing pH from 3.0 to 9.0. Klamerth et al. [220] reported that the removal of 60 emerging contaminants was over 95% in Fe(III)–EDDS-modified photo-Fenton process at neutral pH.

EDDS is easily accessible and proved to be a promising agent for modifying the Fenton and photo-Fenton processes. However, the application of the conventional Fe(III)–EDDS-modified Fenton and photo-Fenton systems is still restricted by several drawbacks: (a) requirement of external addition of H_2O_2, (b) low Fe(II) regeneration rate in the absence of UV irradiation and (c) dramatically decreased mineralization and Fe(III) reduction efficiencies along with the decomposition of EDDS.

The introduction of Fe(III)–EDDS complex to modify Fenton-based EAOPs is proposed for the first time in this Thesis. The use of Fe(III)–EDDS was expected to enhance these processes owing to the following features: (a) it allows working at near-neutral pH values, (b) a higher quantum yield for Fe(II) can be achieved, and (c) additional active radicals such as $^{\bullet}OH$ and $O_2^{\bullet-}$ are produced. The advanced Fe(III)–EDDS-assisted EF and PEF might outperform the conventional Fe(III)–EDDS-modified Fenton and photo-Fenton processes due to: (a) in situ electrogeneration of H_2O_2 at the cathode, (b) a more efficient regeneration of Fe(II) because of the cathodic Fe(III) reduction, and (c) continuous mineralization by anodic oxidation even after the complete decomposition of EDDS.

Fe(III)–EDDS-modified EF and PEF processes are believed to be promising technologies for the abatement of recalcitrant and toxic micropollutants. However, the contribution to total organic carbon (TOC), the scavenging effect of EDDS on $^{\bullet}OH$ and

the production of iron sludge after the disappearance of EDDS are still the main concerns, preventing the occurrence of a larger mineralization.

1.4.3. Advanced EF and PEF (II): heterogeneous catalysts based on metal-organic frameworks (MOFs)

As mentioned above, the traditional homogeneous EF and PEF processes suffer from several drawbacks, such as the need for strict pH regulation, sludge production and the loss of the catalyst in the effluent [221]. To overcome these drawbacks, heterogeneous EF and PEF processes using solid catalysts have been developed as promising alternatives [222]. The advantages and disadvantages of homogeneous and heterogeneous EF and PEF are summarized in Table 10 [200].

Table 10. The advantages and disadvantages of homogeneous and heterogeneous EF and PEF [200].

EF and PEF	Advantages	Disadvantages
Homogeneous	Low quantity of catalyst needed and cheap catalyst source	Efficient only at narrow pH window
	Easier to operate compared to heterogeneous EF/PEF	Requires post-treatment
		Limited reusability and recyclability of the catalyst upon neutralization
Heterogeneous	Efficient over a wider pH working range	Possible additional cost due to solid catalysts production
	Easier post-treatment and separation of catalysts	Need of careful selection of catalysts to avoid negative environmental impacts
	Potentially high reusability and recyclability of the catalysts	
	Possible self-regulation of solution pH towards acidic values	
	Suitable for the treatment of actual wastewater	

Indeed, actual wastewater or effluents from WWTPs are not only multi-components but also have wide pH variation depending on the industrial setup or origin. The conventional homogeneous EF and PEF processes are not appropriate for the treatment of this kind of wastewater without prior pH adjustment. Conversely, heterogeneous EF and PEF treatments are suitable and efficient techniques for such effluents. This can be attributed to two main mechanisms: (a) the possible role of the heterogeneous catalyst as pH regulator in the presence of O_2, and (b) surface catalytic decomposition of H_2O_2 to $^{\bullet}OH$ [200]. Regarding the former, certain catalysts may undergo oxidation in the presence of O_2, with the consequent solution acidification, thus reaching the acidic values required for optimum efficient EF and PEF processes. The most common example of such catalysts is natural pyrite, which acts as both, iron source and pH regulator according to the following reactions [223]:

$$2FeS_2 + 7O_2 + 2H_2O \rightarrow 2Fe^{2+} + 4SO_4^{2-} + 4H^+ \quad (51)$$

$$2FeS_2 + 15H_2O_2 \rightarrow 2Fe^{3+} + 14H_2O + 4SO_4^{2-} + 2H^+ \quad (52)$$

$$FeS_2 + 14Fe^{3+} + 8H_2O \rightarrow 15Fe^{2+} + 2SO_4^{2-} + 16H^+ \quad (53)$$

Another advantage related to the application over a wide pH range is the elimination or inhibition of the formation of iron hydroxides during heterogeneous EF and PEF processes. The formation of sludge during conventional EF and PEF implies the loss of catalyst, which has adverse effect on the process efficiency and requires further appropriate disposal. The use of solid iron-based particles not only eliminates or inhibits the formation of sludge during the treatment, but it also allows simplifies the post-treatment separation and possible recycling of the catalyst [224].

In general, the degradation of organic pollutants during heterogeneous EF and PEF involves two mechanisms: (i) homogeneous catalyzed process upon the action of the Fe^{3+}/Fe^{2+} redox couple dissolved into the solution, and (ii) surface-catalyzed process at the solid catalyst-liquid interface, depending on the working pH and nature of the catalyst used [200]. As shown in Fig. 18, some solid catalysts undergo excessive

leaching of iron ions at acidic pH and hence, the H_2O_2 decomposition by homogeneous Fe^{3+}/Fe^{2+}-catalyzed mechanism plays a major role as compared to that by heterogeneous Fe(III)-OH/Fe(II)-OH at the surface of the solid catalyst. Some iron catalysts exhibit high stability even at acidic pH, undergoing very low iron leaching. Therefore, the predominant catalytic process not only depends on the working pH but also on the stability of the solid catalyst at low pH [200]. Although those solid catalysts experiencing high leaching of iron ions at acidic pH result in efficient production of •OH via homogeneous Fenton's reaction, they cannot be envisaged as ideal materials, owing to their weak recyclability and high production of iron sludge.

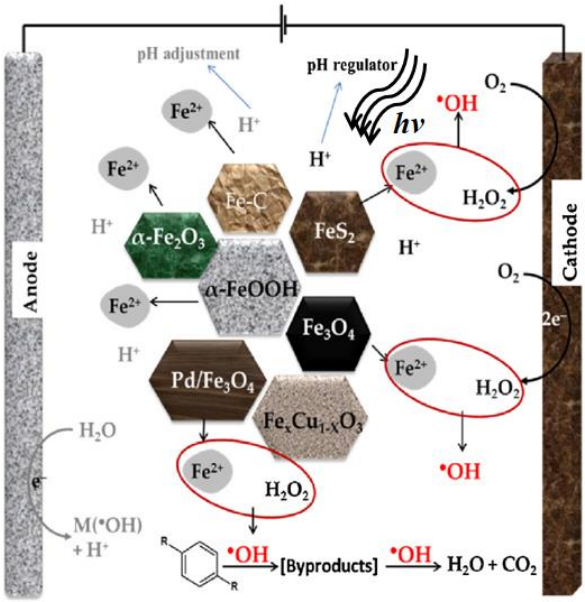

Figure 18. Mechanism of catalytic activation of H_2O_2 at acidic pH using supported or unsupported iron/iron-containing solid catalysts [200].

In contrast, at neutral and alkaline pH values, or for stable catalysts undergoing low iron leaching, the contribution of dissolved iron ions to the H_2O_2 activation is expected to be negligible. The electrogenerated H_2O_2 interacts strongly with the negatively charged catalyst surface and then, it can be directly decomposed by the ≡Fe(III)/Fe(II) surface redox pair to yield active radicals from reactions (54) and (55) [225].

$$\equiv Fe(III) + H_2O_2 \rightarrow \equiv Fe(II) + HO_2^{\bullet} + H^+ \quad (54)$$

$$\equiv Fe(II) + H_2O_2 \rightarrow \equiv Fe(III) + {}^{\bullet}OH + OH^- \quad (55)$$

On the other hand, some iron-based catalysts are also semiconductors, being possible to excite them to produce photogenerated electrons and holes upon irradiation with UV/Vis light, resulting in additional production of $^{\bullet}OH$, as follows [226]:

$$\text{Iron-based catalysts} + h\nu \rightarrow e^- + h^+ \quad (56)$$

$$h^+ + RH \rightarrow R^{\bullet} + H^+ \quad (57)$$

$$e^- + H_2O_2 \rightarrow {}^{\bullet}OH + OH^- \quad (58)$$

Many iron-based materials, such as iron minerals, iron/iron oxide, iron-loaded materials, zero-valent iron (ZVI) and metallic materials, have been reported as heterogeneous EF and PEF catalysts. Fig. 19 shows the scanning electron microscopy (SEM) images of several commonly used heterogeneous catalysts. They are expected to exhibit high activity, large surface area, high stability and low cost [224]. However, their characteristics, morphologies and catalytic activity usually vary significantly depending on the synthesis methods or nature.

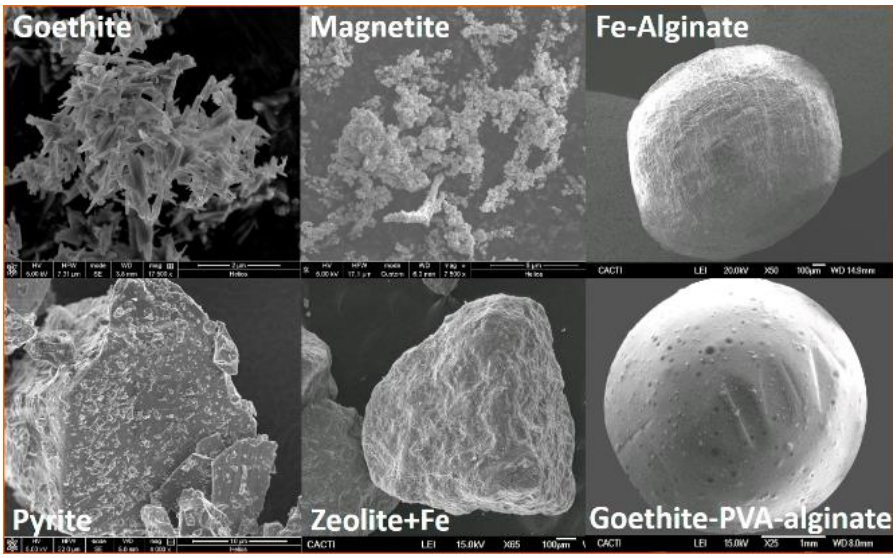

Figure 19. SEM images of several Fe-based catalysts [224].

Moreover, in most of these heterogeneous catalysts, iron mainly exists in the form of Fe(III). Therefore, the redox cycling of the Fe(III)/Fe(II) couple in the presence of H_2O_2 (reaction (54)) is critical to continuously ensure the occurrence of Fenton's reaction.

However, as compared to the reaction between Fe(II) and H_2O_2, the reduction of Fe(III) by H_2O_2 is always the rate-limiting step due to its low rate constant (0.001-0.01 $M^{-1}s^{-1}$) which determines the overall efficiency of the whole system [225]. Thus, finding ways to accelerate the Fe(III)/Fe(II) redox cycling in traditional heterogeneous EF and PEF is the core issue when developing more effective heterogeneous catalysts.

Additionally, the most important parameters are the catalytic activity and stability of the catalysts over wide experimental conditions. The materials should possess good catalytic activity regardless of the experimental conditions and high stability to ensure the reusability in several runs [227]. Closely related to the stability and reusability of catalysts, the minimization of iron leaching from solid phase is required, which is another key issue to evaluate the performance of heterogeneous EF and PEF. A very low concentration of iron species in aqueous phase could be acceptable because they can act as homogeneous catalyst. However, excessive iron leaching leads to the depletion of the active sites in the catalysts, even the loss of the solid catalytic activity, as well as the decrease of reusability [228]. Further, the toxicity and environmental compatibility of the catalysts are also important factors that should be considered for the material selection [200].

Although a wide range of materials have been used as catalysts or metal supports in heterogeneous EF and PEF or Fenton-like processes in the past decades [200,224,225], the development of new types of heterogeneous catalysts with low or moderate cost, high activity, good stability and environmental benignancy is a matter of paramount importance but still a great challenge.

Within this context, metal-organic frameworks (MOFs), also called porous coordination networks, or porous coordination polymers, are a group of very promising porous crystalline inorganic-organic hybrid materials that have become one of the fastest growing fields in both, materials science and chemistry in the last two decades [229]. In MOFs, organic ligands containing cyano and pyridyl, carboxylates,

phosphonates and crown ethers act as bridges to coordinate to metal ions [230]. Properties such as surface area, pore size and shape of MOFs are mainly determined by the nature of the metal ion and organic ligand. MOFs not only combine the respective beneficial characteristics of inorganic and organic components but they also exhibit unique properties that exceed the expectations for a simple mixture of the components [231]. Fig. 20 lists the structures of some typical MOFs [232]. Currently, more than 20,000 different structures with ultrahigh porosity, versatile functionality, changeable structure and large surface area have been synthesized and widely applied in diverse areas such as gas storage [233], sensing [234], separation [235] and catalysis [236].

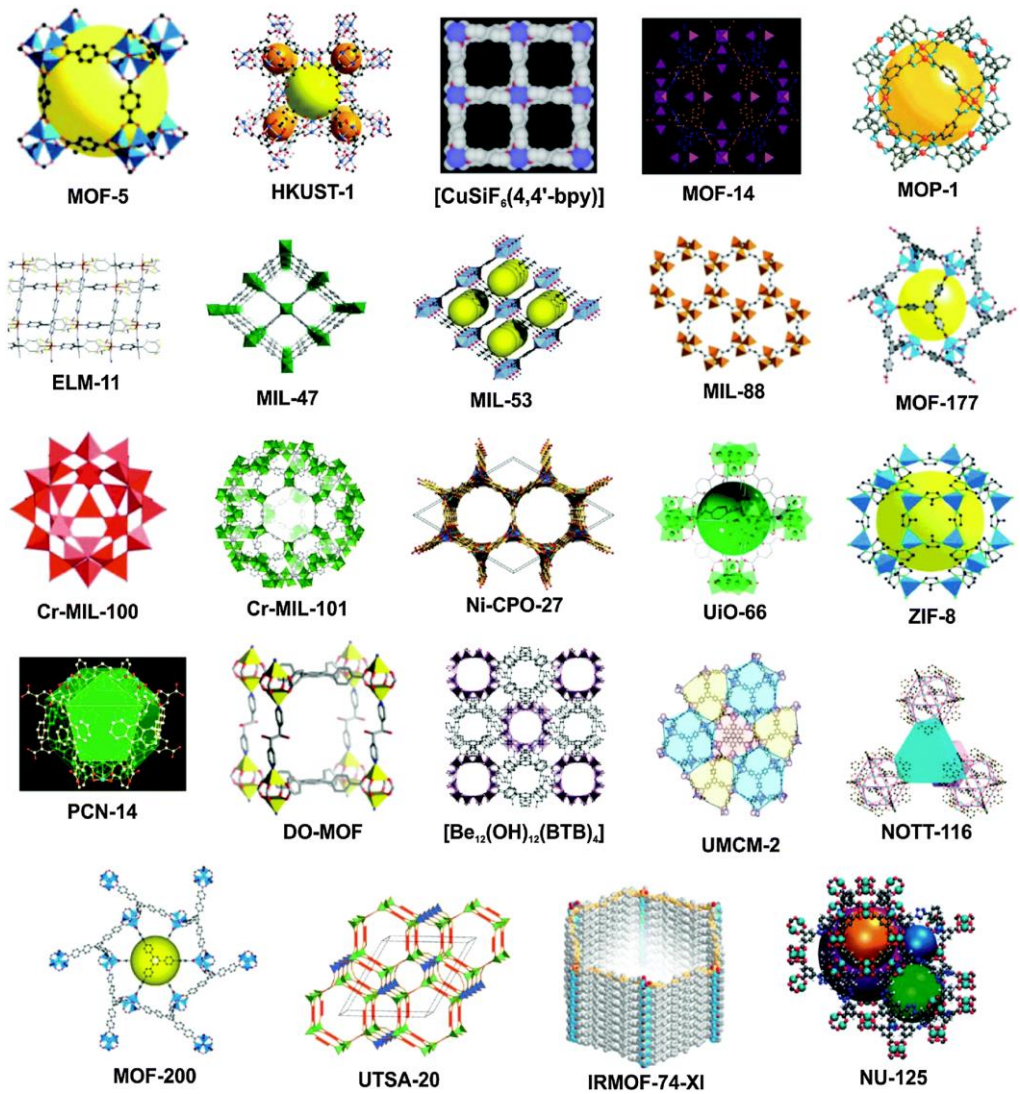

Figure 20. Scheme of some typical porous MOFs [232].

One of the most straightforward applications of MOFs appears in environmental remediation, since they can be employed for gas adsorption, selective ion trapping, reduction of metal toxicity and catalytic degradation of organic compounds [237,238]. Among the numerous environmental applications, iron-containing MOFs and their derivatives acting as Fenton-based AOPs catalysts have attracted extensive interest because of their excellent characteristics, such as chemical tenability, well-defined structure, large pore volume and high specific surface area [239].

The iron-based MOFs are regarded as promising potential heterogeneous Fenton-based AOPs catalysts because: (a) Fe is one of the basic catalysts for Fenton's reaction, (b) Fe is non-toxic and abundant in Earth crust minerals, and (c) Fe-based MOFs show an intense absorption in the visible light region due to the existence of iron-oxo (Fe-O) clusters [229]. The past few years have witnessed rapid progress in the development of Fe-based MOFs or their derivatives in catalyzed Fenton and photo-Fenton processes. To date, a vast number of Fe-based MOFs catalysts have been designed, employing multiple types of organic ligands (Fig. 21) to yield Fe-bpydc (where bpydc accounts for 2,2′-bipyridine-4,4′-dicarboxylic acid), MIL(Fe)-53, MIL(Fe)-88, MIL(Fe)-100, MIL(Fe)-101 and amino-modified Fe-based MOFs (NH_2-MILs) [237], where MIL accounts for Materials Institute Lavoisier.

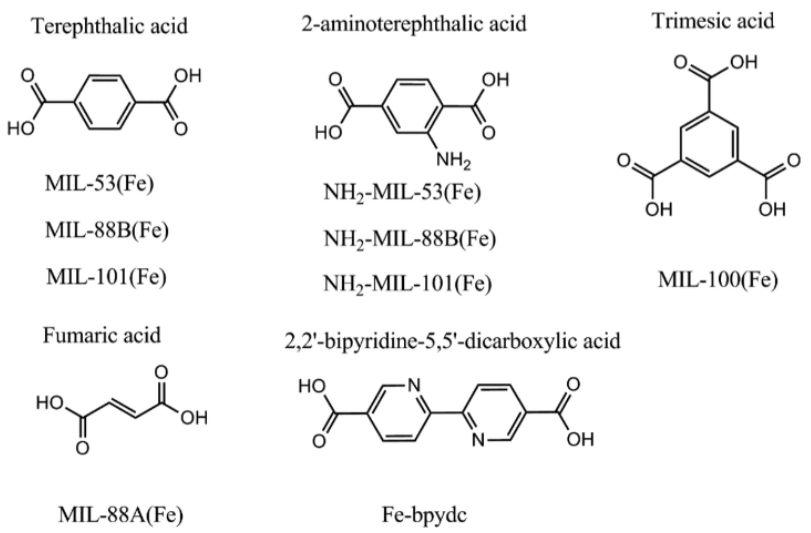

Figure 21. Schematic diagram of commonly used Fe-based MOFs and the corresponding organic ligand structures [237].

The synthesis procedures for MOF production include solvothermal, microwave-assisted heating and mechanochemical methods [240]. In the former, MOFs can be produced in a few hours to few days under different temperatures. Hydrothermal conditions of microwave-assisted synthesis usually allow obtaining MOFs rapidly. By the adjustment of synthesis methods and conditions such as the amount of solvent and the time of heating, controlling the morphology of MOFs with a narrow particle size distribution is possible [237]. However, for some MILs, it is nearly impossible to obtain crytals with high quality and purity, owing to multiple structures that can arise from the same initial metal and ligand precursor, as in the case of MIL(Fe)-88B, MIL(Fe)-53 and MIL(Fe)-101 [241]. Modification with nitrogen is feasible by introducing aminated organic ligands, leading to totally different morphologies as can be clearly distinguished in Fig. 22 in the case of MIL(Fe)-88B and NH_2-MIL(Fe)-88B [242].

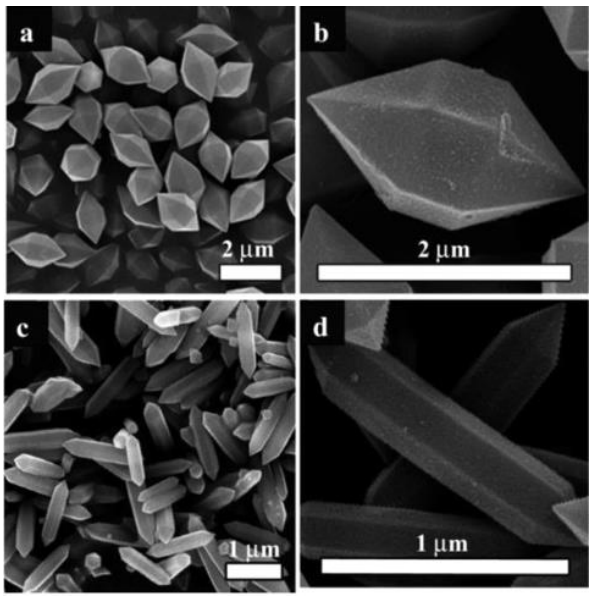

Figure 22. SEM images of (a, b) MIL(Fe) 88B and (c, d) NH_2-MIL(Fe) 88B [242].

Lately, direct employment of Fe-based MOFs as heterogeneous catalysts in Fenton and photo-Fenton has been reported. Sun et al. [243] evaluated and compared the catalytic Fenton oxidation of phenol by using MIL(Fe)-53, NH_2-MIL(Fe)-53 and Fe(BDC)(DMF,F) at mild pH, achieving the highest phenol removal (> 99%) and mineralization (78.7%) in the Fe(BDC)(DMF,F)-catalyzed Fenton process. Note that

BDC accounts for benzene-1,4-dicarboxylic acid (i.e., terephthalic acid). Li et al. [244] reported an Fe-based 2D MOF (Fe-bpydc)-catalyzed Fenton process, obtaining the total removal of phenol in 60 min with very low dosage of catalyst (0.01 g L^{-1}). Gao et al. [245] investigated the MIL(Fe)-88B-catalyzed Fenton process, achieving the total phenol removal in 30 min at pH 4.0. Additionally, these authors compared the performances of MIL(Fe)-53- and MIL(Fe)-101-catalyzed Fenton processes for phenol degradation, which were less efficient than that with MIL(Fe)-88B. Wang et al. [246] reported that MIL(Fe)-100 and MIL(Fe)-68 could achieve a highly selective catalysis by hydroxylating benzene to phenol during visible light-driven photo-Fenton treatment. Ai et al. [247] investigated the catalytic H_2O_2 oxidation by MIL(Fe)-53 under visible light irradiation for RhB removal, achieving its complete abatement in 50 min.

The reaction mechanisms of Fe-based MOFs-catalyzed Fenton and photo-Fenton processes are illustrated in Fig. 23 for MIL(Fe)-88B and MIL(Fe)-53 [245,247]. They involve: (i) Fenton's reaction initiated by the interaction of iron components on the surface of catalysts and H_2O_2, producing $^{\bullet}OH$, (ii) efficient reduction of Fe(III) to Fe(II) by H_2O_2 due to the enhanced electron charge transfer between H_2O_2 and MOFs, (c) the presence of photoinduced electrons in the photoexcited MOFs, which were captured by H_2O_2 to generate $^{\bullet}OH$ and (d) the direct oxidation of pollutnts by photogenerated holes.

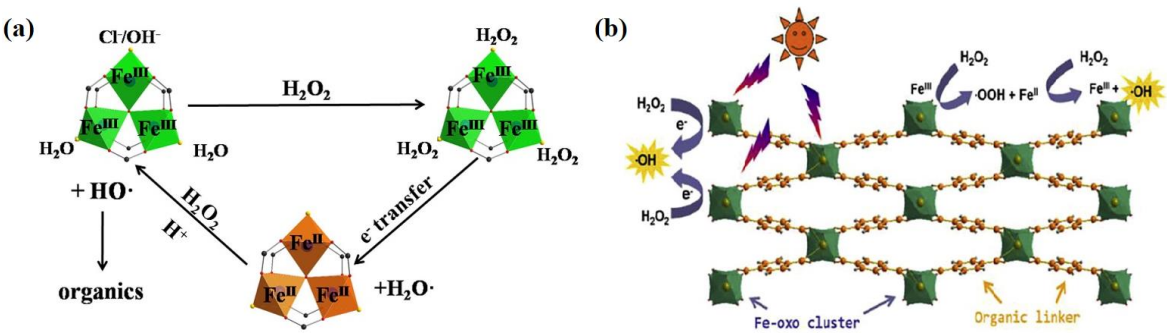

Figure 23. Proposed mechanisms for the activation of H_2O_2 by (a) MIL(Fe)-88B and (b) MIL(Fe)-53 under visible light irradiation [245,247].

Additionally, using MOFs as precursors to prepare carbonaceous materials as heterogeneous Fenton catalysts has also drawn enormous attention. Since MOFs can be designed to be three-dimensional structures, they offer great promise for utilization as

effective templates/precursors to construct various metal/metal oxide nanoparticles encapsulated inside a porous carbon matrix through direct pyrolysis/carbonization process [248]. Moreover, nitrogen-doped (N-doped) carbon has been deemed as a superior candidate for catalyst support since it can introduce electrocatalytic active sites and enhance the electrical conductivity [249]. Worth noting, the incorporation of N as heteroatom into the carbon framework is more feasible than in carbon nanotubes or graphene because it can be achieved by directly pyrolyzing N-containing MOFs. Several MOF-derived carbon hybrids have been successfully applied in Fenton-like degradation of organic contaminants. For instance, magnetic iron/carbon nanorods were fabricated by carbonization of MIL(Fe)-88A, achieving high catalytic activity for the decolorization of RhB solutions in the presence of H_2O_2 [250]. Magnetic γ-Fe_2O_3/C derived from MIL(Fe)-53 was employed to activate H_2O_2 for the degradation of Malachite Green under sunlight irradiation [251]. Fe-based magnetic nanoparticles embedded into mesoporous carbon hybrid (Fe@MesoC) derived from MIL(Fe)-100 were used as efficient Fenton catalyst for the degradation of sulfamethoxazole [248].

To our best knowledge, the use of Fe-based MOFs or their derivatives as heterogeneous EF and PEF catalysts has never been studied so far. Only one paper reported the introduction of bimetallic MOF(2Fe/Co) on the surface of carbon aerogel cathode, which was employed in SPEF system for efficient elimination of RhB and dimethyl phthalate [252]. Research in this field is still incipient. It is thus worthwhile to investigate the performance of Fe-based MOFs and their derivatives to catalyze EF and PEF processes, as well as to unravel the involved metal-ligand complexes-associated reaction mechanisms. Besides, the potential application of Fe-based MOFs in Fenton-like processes is still limited by several potential shortcomings such as aggregation, decomposition in water and iron leaching, which can also occur in EF and PEF processes [229]. There is room for the rational design of new excellent MOFs as EF and PEF catalysts and evaluate their performance under near-neutral conditions and even in actual wastewater.

CHAPTER 2
OBJECTIVES

2. Objectives

The conventional homogeneous EAOPs have been extensively studied for the treatment of recalcitrant organic pollutants in the environment and, more particularly, in water. These processes have been proven to be very efficient for the complete degradation and excellent mineralization of synthetic and actual wastewater contaminated with different classes of organic pollutants. However, their scale-up for industrial application is still limited by many inherent drawbacks, such as:

- ❖ The homogeneous EF/PEF treatments usually require a long time to achieve satisfactory removal percentages when dealing with large contents of organics, resulting in high energy consumption.
- ❖ The conventional EF/PEF processes are only viable under acidic pH conditions (pH 2.8-3.5). The need for a precise control of pH and a final neutralization step significantly hinders their practical application.
- ❖ Free ferrous ion is the most commonly used catalyst, which must be precipitated for disposal. The generation of undesirable iron sludge introduces the risk of secondary pollution and the need for additional sludge post-treatment.

The work carried out in this Thesis is focused on finding smart solutions to overcome the drawbacks mentioned above, with the following specific goals:

1. Use of single EC and sequential EC/EAOPs for the degradation of organic micropollutants:
   - ✧ Assessing the ability of single and sequential EC/EAOPs to remove selected micropollutants from synthetic and urban wastewater matrices;
   - ✧ Exploring the feasibility of sequential EC/EAOPs to remove micropollutants at neutral pH and in the absence of external iron addition;
   - ✧ Evaluating the energy consumption required to achieve complete TOC removal

by single EAOPs and sequential EC/EAOPs;

- ✧ Identifying the intermediates, especially toxic chlorinated byproducts, upon degradation of micropollutants, and proposing the degradation pathways.

2. Use of Fe(III)–EDDS-enhanced EF and PEF processes for the treatment of organic micropollutants at mild pH:
   - ✧ Investigating the feasibility of destruction of micropollutants from synthetic and urban wastewater within a wide pH range by Fe(III)–EDDS-enhanced EF/PEF processes employing either carbon-felt or air-diffusion cathodes;
   - ✧ Assessing the stability and photoactivity of the Fe(III)–EDDS complex and understanding the role and fate of EDDS and iron during all the treatments;
   - ✧ Finding out the optimum operation conditions, such as Fe(III):EDDS ratio, catalyst dosage and current density, for Fe(III)–EDDS-enhanced EF/PEF treatments to guide their practical application;
   - ✧ Elucidating the mechanisms for the generation of reactive oxygen species and degradation of micropollutants during the Fe(III)–EDDS-enhanced EF/PEF treatments;
   - ✧ Evaluating the potential ecotoxicological effects of transformation byproducts.

3. Use of raw and calcined Fe-based MOFs as efficient heterogeneous catalysts in Fenton-based EAOPs:
   - ✧ Designing and characterizing novel Fe-MOF-based materials, and then testing their catalytic activity as heterogeneous EF/PEF catalysts at near-neutral pH;
   - ✧ Assessing the stability and reusability of Fe-MOF-based catalysts during the treatment of both, synthetic and actual urban wastewater;
   - ✧ Distinguishing the homogeneous catalyzed mechanism for the Fe^{3+}/Fe^{2+} redox couple leached into the solution and surface-catalyzed mechanism at the catalyst-liquid interface during the EF/PEF treatments catalyzed with Fe-based MOFs;
   - ✧ Determining the reactive oxygen species involved in the degradation;

- ✧ Analyzing the band structure of photosensitive Fe-MOFs and investigating the synergistic effect in Fe-MOF-catalyzed PEF system;
- ✧ Clarifying the catalytic mechanism and the effects of structure on the catalytic activity of Fe-MOF-based catalysts.

CHAPTER 3
MATERIALS AND METHODS

3. Materials and methods

3.1. Pollutants under study and reagents

The properties, environmental concerns and degradation results reported in the literature for the model micropollutants investigated in this Thesis have been discussed in detail in subsection 1.1.5 (see also Table 7). All of them were of analytical grade provided by Sigma-Aldrich.

The rest of chemicals and reagents were: H_2SO_4 and NaOH solutions for pH adjustment, and Na_2SO_4, NaCl, KCl, Na_2CO_3 and $NaHCO_3$ used as electrolytes, were supplied by Merck. $FeSO_4$•$7H_2O$ from J.T. Baker and $FeCl_2$ and $Fe(ClO_4)_3$ from Sigma-Aldrich were used as commercial catalysts. EDDS (35% in H_2O) was purchased from Sigma-Aldrich. Ti(IV) oxysulfate for H_2O_2 determination was provided by Panreac, whereas 1,10-phenantroline monohydrate (99% purity) from Alfa-Aesar and ascorbic acid from Sigma-Aldrich were employed for soluble iron analysis. $FeCl_3$•$6H_2O$ from Panreac, $FeCl_2$•$4H_2O$ from Merck, $Fe(ClO_4)_2$, 2-methylimidazole, terephthalic acid, 2-aminoterephthalic acid, *N,N*-dimethyl formamide (DMF) from Sigma-Aldrich, and 2,2'-bipyridine-5,5'-dicarboxylic acid from T.C.I. were used for the synthesis of Fe-MOFs. Ethanol, acetone and HCl (37%) from Panreac were employed for cleaning the Fe-MOFs. Organic solvents of HPLC grade were purchased from Panreac and Merck. CH_2Cl_2 used for sample extraction in GC-MS analysis was supplied by Panreac. All reagents employed during toxicity bioassays were acquired from Modern Water. Unless otherwise specified, the above reagents were of analytical grade. All aqueous solutions were prepared with Millipore Milli-Q water (resistivity > 18.2 MΩ cm).

3.2. Water matrices

The trials in this Thesis were carried out in three different aqueous matrices:

(a) Urban wastewater

Urban wastewater effluents were obtained from a WWTP located in Gavà-Viladecans (Barcelona, Spain). Several sets of fresh samples were collected on different days from the primary treatment effluent (used in Appendix II) as well as from the secondary treatment effluent (used in other studies). After collection, all the samples were preserved in a refrigerator at 4 °C. The main characteristics of all the wastewater samples are summarized in Table 11. The pH of the actual wastewater varied between 7.0 and 8.0. The primary treatment effluent had higher total carbon (TC) and TOC (measured as NPOC) and relatively low contents of cations and anions compared to the secondary treatment effluent. In all the samples, the contents of Na^+, SO_4^{2-} and Cl^- prevailed over the other ions, and the total iron content was insignificant. Moreover, 18 organic compounds were detected for the primary treatment effluent by GC-MS, which included 17 cyclic molecules (3 of them aromatic and 5 with N as heteroatom) and 1 aliphatic compound (see details in Appendix II).

(b) Simulated matrices

The simulated matrices mimicked the main ionic content of urban wastewater, but without their natural organic matter components (primordially, soluble humic and fulvic acids). They were prepared in Milli-Q water by adding certain amount of salts, resulting in a solution with pH ~ 6.0 and slightly lower conductivity than the given wastewater.

Table 11. Main physicochemical characteristics of the collected primary or secondary treated urban wastewater once filtered under vacuum with a 0.45 μm membrane filter.

Parameter	Appendix I	Appendix II	Appendix IV	Appendix V	Appendix VI	Appendix VII
pH	7.9 ± 0.3	7.96	7.25	7.28	7.51	7.43
TC (mg L^{-1})	143.3	180.3	119.4	121.2	73.2	79.3
NPOC (mg L^{-1})	18.0 ± 0.9	37.7	9.3	9.7	13.7	10.8
Total nitrogen (mg L^{-1})	44.3	66.8	39.6	46.0	16.7	20.6
Conductivity (mS cm^{-1})	2.19 ± 0.11	2.13	1.36	2.13	2.05	2.08
Na^+ (mg L^{-1})	328	268.1	315.9	316.8	554.5	308.5
K^+ (mg L^{-1})	49	47.2	46.8	51.4	51.4	42.6
Mg^{2+} (mg L^{-1})	36	33.5	33.9	37.3	37.3	38.3
Ca^{2+} (mg L^{-1})	99	116.9	94.0	103.1	103.0	116.0
Total Fe (mg L^{-1})	0.19	0.22	0.11	0.19	0.09	< 0.04
SO_4^{2-} (mg L^{-1})	117	129.5	128.4	120.4	180.5	167.7
Cl^- (mg L^{-1})	480	375.9	569.8	595.0	534.6	504.0
NO_3^- (mg L^{-1})	0.85	-	16.9	18.7	61.4	50.6

-: not determined.

(c) Electrolyte solutions

The electrolyte solutions were prepared in Milli-Q water with the addition of different salts, including Na_2SO_4, NaCl and $NaHCO_3$.

3.3. Electrolytic cells

3.3.1. EC

The EC setup is depicted in Fig. 24. All trials were made in an undivided and open cylindrical glass cell of 150 mL capacity with a double jacket for circulation of thermostated water at 35 °C, under vigorous stirring with a magnetic follower. The anode was a pure Fe, pure Al or stainless steel (AISI 304 and 316L) plate with overall dimensions of 5.0 cm × 1.5 cm, 0.25 cm thickness, and immersed area of 10 cm^2. The same materials with analogous dimensions were used as cathode. One or two electrode pairs were placed alternately in parallel with an interelectrode gap of 1.0 cm. The electrodes were connected to a direct Amel 2053 current power supply providing a current up to 2 A, whereas the cell voltage was measured by a Demestres® DM 610 BR multimeter (Fig. 25). EC experiments were carried out under galvanostatic conditions in the range of 0-150 mA.

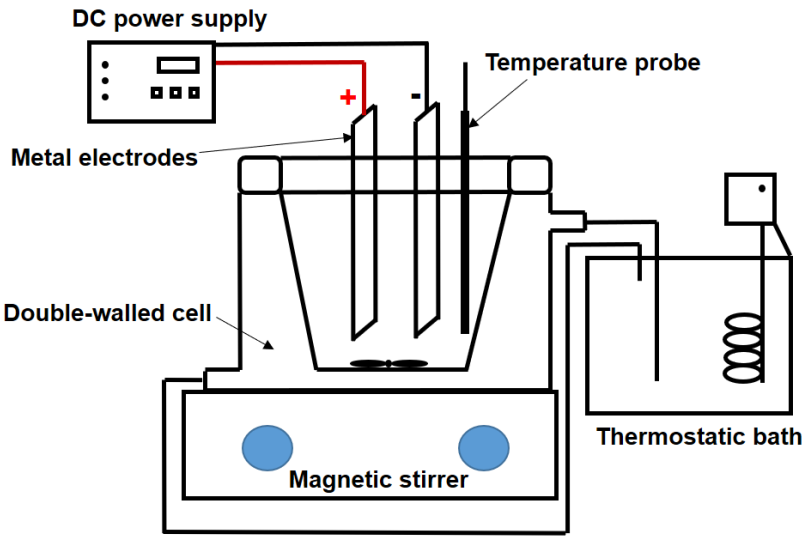

Figure 24. Schematic representation of the EC setup.

Figure 25. (a) AMEL 2053 DC power supply and (b) Demestres® DM610BR multimeter.

The electrodes used in EC trials are shown in Fig. 26. Apart from the common Fe and Al electrodes, the stainless steel (AISI 304 and AISI 316L), containing other metallic species like Cr, Ni, Mn and Mo, were also tested as sacrificial anodes, which may result in different EC performance. Before first use, all electrodes were mechanically abraded using SiC paper to remove surface oxides, followed by cleaning with 0.1 M NaOH or H_2SO_4 solution (20% in volume) and a final ultrasonic cleaning in ultra-pure water. Moreover, before each assay, the electrodes were cleaned and activated by immersion in H_2SO_4 solution (20% in volume) for 30 s, followed by washing with Milli-Q water and atmospheric drying.

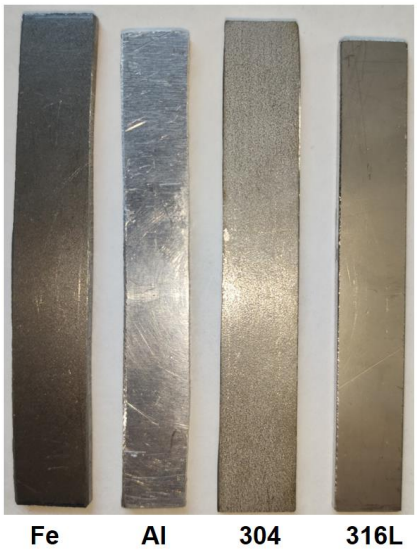

Figure 26. Electrodes employed in EC trials.

The connection mode employed in EC trials was a monopolar parallel electrical configuration (MP-P) with either one or two electrode pairs (Fig. 27). This mode was preferred because it avoids issues with bypass current and allows controlling the anode consumption and its periodic replacement [147].

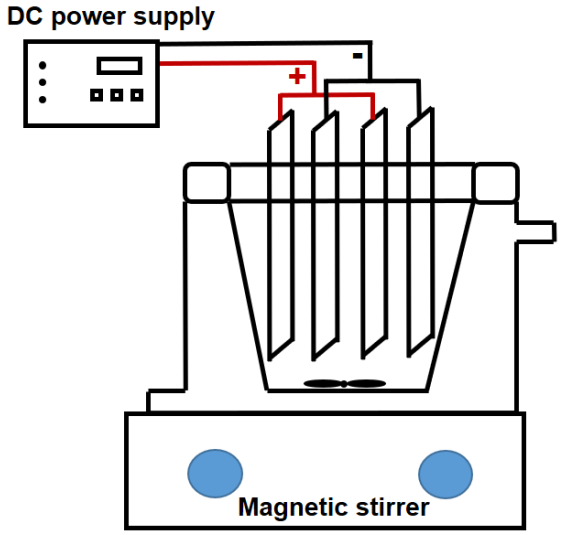

Figure 27. Electrodes arrangement in EC trials (MP-P).

3.3.2. EAOPs

The EAOPs experiments were performed with the same cell of EC but employing different electrodes (Fig. 28). The anode of 3 cm^2 geometric area was either a BDD thin-film electrode supplied by NeoCoat or a DSA®-O_2 (IrO_2-based anode) or DSA®-Cl_2 (RuO_2-based anode) plate from NMT Electrodes. The cathode was a 3 cm^2 carbon-PTFE air-diffusion electrode supplied by E-TEK or a carbon-felt piece (11.0 cm × 5.0 cm × 0.5 cm) purchased from Mersen. The interelectrode gap was about 1 cm. For the experiments with a carbon-felt cathode, compressed air was sparged through the solution at 0.35 L min^{-1} for 10 min prior to each electrolysis, which was maintained during the trials to ensure the saturation with O_2 for continuous H_2O_2 electrogeneration. The carbon-PTFE air-diffusion cathode fitted in a tubular gas chamber that was fed with compressed air at 1 L min^{-1}. All the trials were performed at constant current provided by the power source shown in Fig. 25, equipped with the multimeter of Fig. 26 for cell voltage measurement.

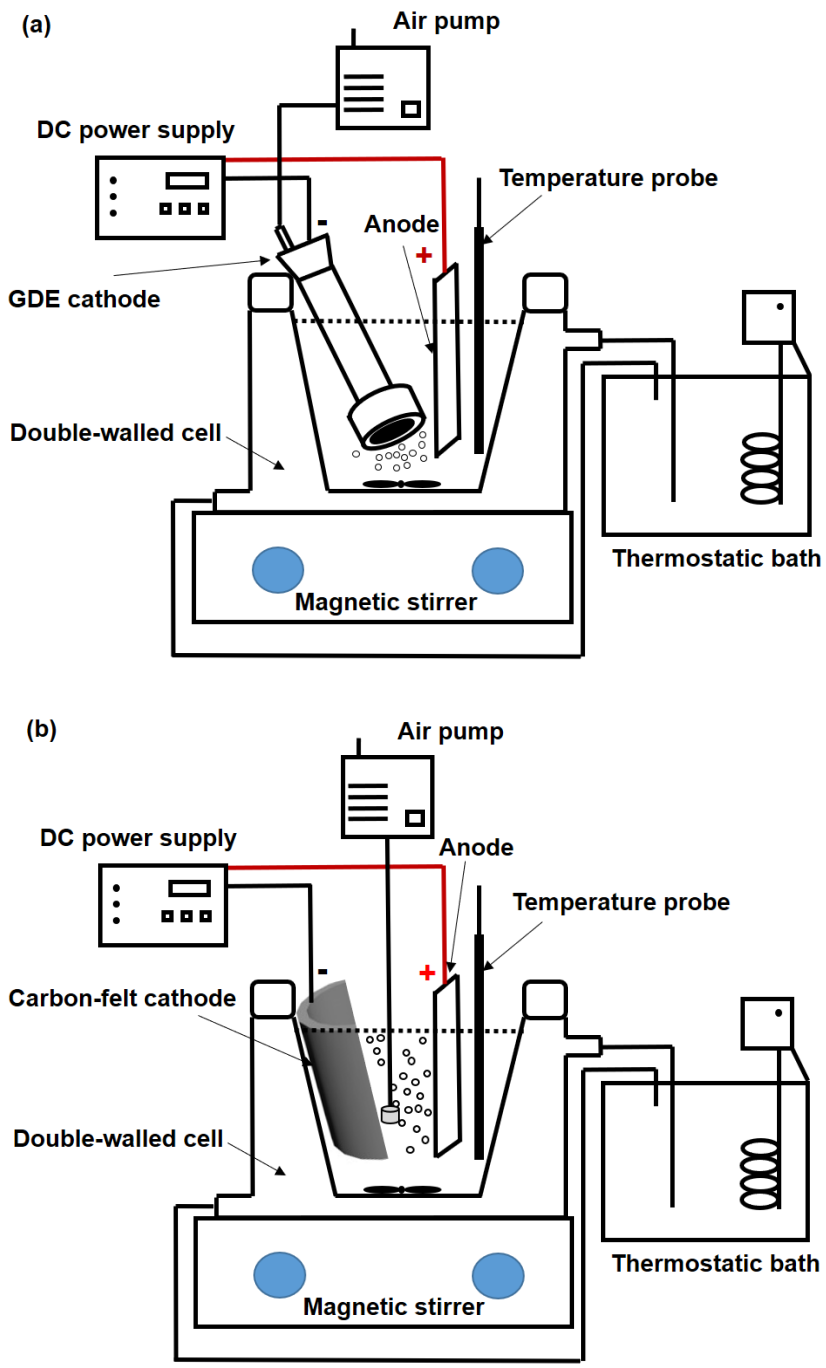

Figure 28. Sketch of a bench-scale EAOP reactor employing either (a) a carbon-PTFE GDE or (b) a carbon-felt cathode.

The anodes used in this Thesis, including a non-active anode (BDD) and two active anodes (DSA®-O_2 and DSA®-Cl_2), are shown in Fig. 29. They were employed as model anodes to describe the electrolyses of the micropollutants with two opposite behaviors. BDD behaves as a high efficiency electrode for the oxidation of organics, which is regarded as desirable electrode for the complete oxidation of organics to CO_2 during

wastewater treatment. On the contrary, DSA® electrodes usually favor the partial and selective oxidation of pollutants with a large amount of intermediates, like final carboxylic acids.

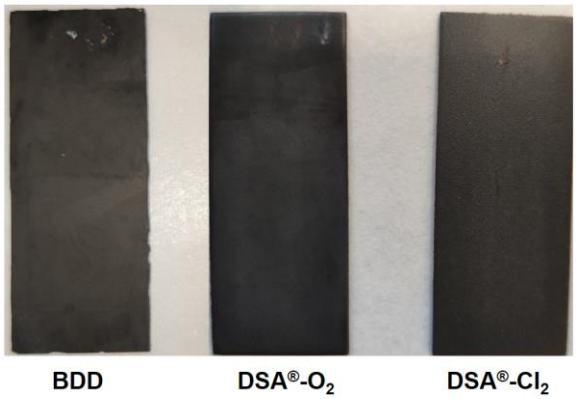

Figure 29. Anodes employed in EAOPs.

The SEM image of the BDD anode is presented in Fig. 30. It was a microcrystalline thin-film coated on polycrystalline p-silicon substrate by Hot Filament Chemical Vapor Deposition (HFCVD) technique. This method enables the activation of carbon-containing gas precursor consisting of methane (CH_4) and hydrogen gas (H_2) by energy/heat-assisted way, resulting in the deposition of diamond grains on certain substrates [253]. The BDD thin-film exhibits thickness of 2-3 μm, grain size of ~ 0.5 μm and boron dopant level of 700 ppm.

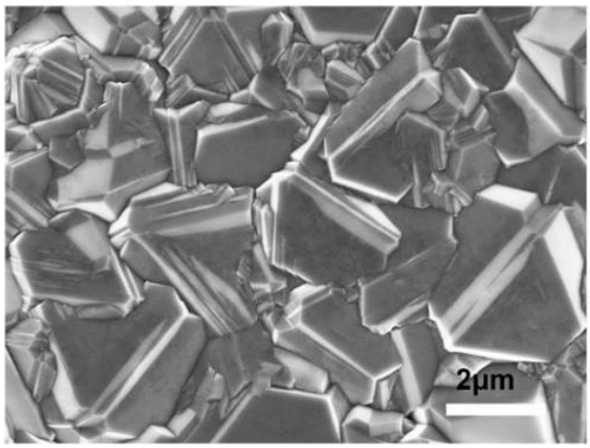

Figure 30. SEM image of the microcrystalline BDD thin film [253].

Fig. 31 depicts the setup of carbon-PTFE air-diffusion and carbon-felt cathodes used in

this Thesis. The GDE cathode consisted of a commercial carbon fiber-PTFE cloth with a diameter of 2 cm, which is placed on the bottom of a polypropylene gas chamber. The external surface contacted with the aqueous solution is the electroactive part of the carbon-PTFE cloth. A Ni-Cr mesh with the same dimension was arranged on the inner side of the carbon-PTFE sheet to improve and homogeneously distribute the electric current applied on the entire surface of cathode. The Ni-Cr mesh directly contacted with a Ni-Cr wire, together acting as electrical collectors for the charge transfer. The air was introduced through a glass tube, placed in the internal part of the polypropylene support, with a flow rate of 1 L min^{-1}. The three-dimensional carbon-felt cathode had a thickness of 0.5 cm. It is commonly used as electrode due to its excellent electrolytic efficiency, high surface area and porosity. The SEM image of carbon felt is presented Fig. 32, showing long smooth fibers dispersed randomly with homogeneous large void spaces between them. Each fiber had cylinder-like shape with shallow grooves along the long axis that was formed by the combination of thinner fibers, melted together.

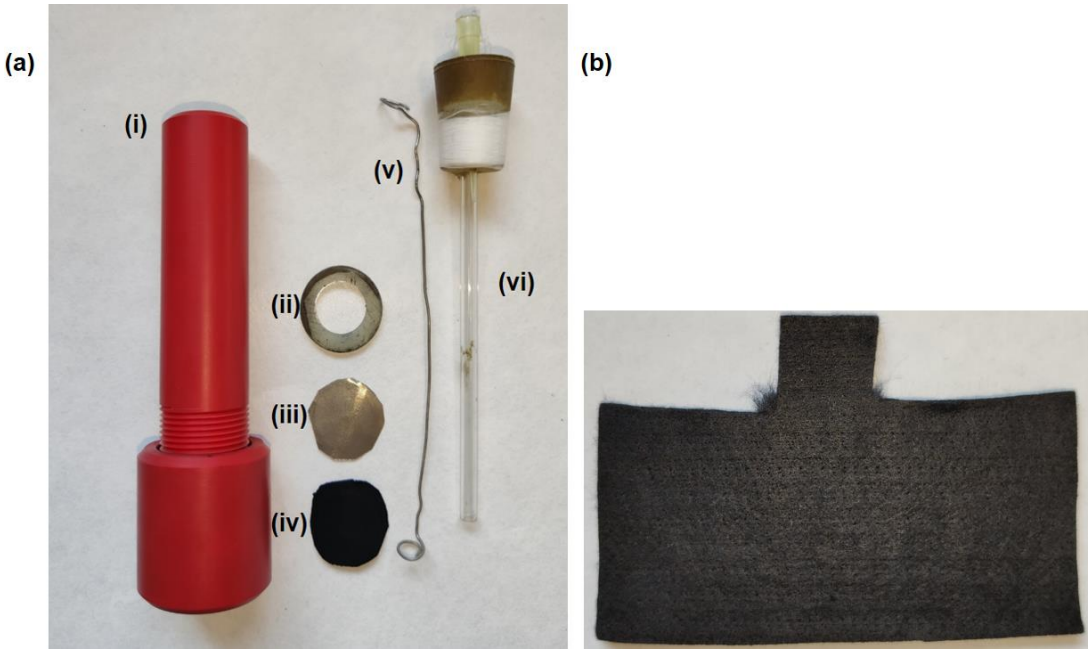

Figure 31. Setup of (a) carbon-PTFE air-diffusion electrode and (b) carbon-felt cathode. Parts depicted in (a) are: (i) Polypropylene holder, (ii) silicone gasket, (iii) Ni-Cr mesh, (iv) carbon-PTFE cathode, (v) Ni-Cr wire and (vi) glass tube for air feeding.

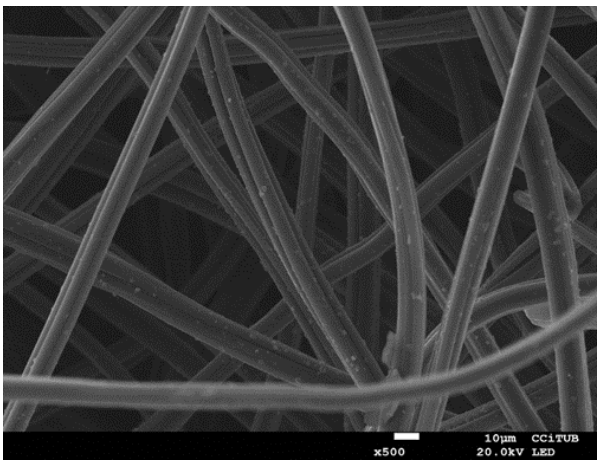

Figure 32. SEM image of carbon felt.

The mechanisms of H_2O_2 production at GDE and carbon-felt cathodes are shown in Fig. 33 [195]. The GDE exhibits the highest efficiency for the H_2O_2 production due to the advanced three-phase interface structure, enabling to overcome the limitations related to oxygen solubility and transport. The ability to generate H_2O_2 by GDE clearly outperforms the submerged carbon-felt electrode, which highly relies on the limited solubility and transport of O_2 in water.

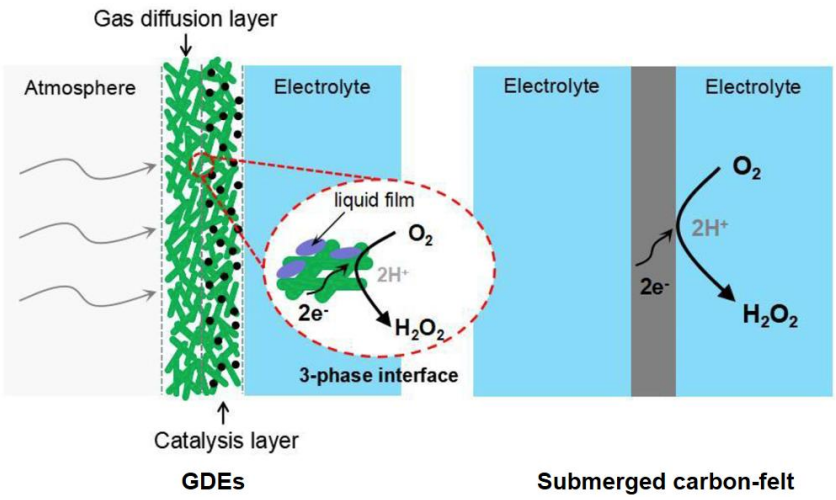

Figure 33. Different mechanisms of H_2O_2 production by GDE and submerged carbon-felt cathode [195].

On the contrary, the carbon-felt cathode exhibits excellent iron reduction ability due to the complete exposure to liquid phase, leading to an efficient iron mass transport. The highly efficient mass transport of O_2 to GDE surface favors the H_2O_2 production, but significantly inhibits the Fe(III) electroreduction. The ability of H_2O_2 generation and Fe(III) reduction on GDEs and carbon-felt cathodes is presented in Fig. 34.

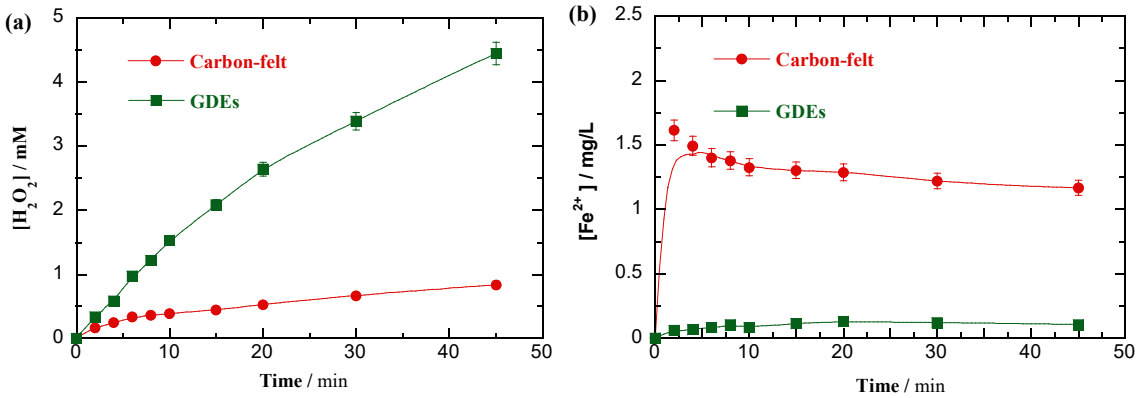

Figure 34. Time course of (a) H_2O_2 and (b) Fe^{2+} concentrations during the electrolysis of 150 mL of 50 mM Na_2SO_4 solution with 5.6 mg L^{-1} Fe^{3+} contents at pH 3.0 and 50 mA using a DSA®-O_2 anode. These data were obtained in our laboratory.

Before first use, a preliminary polarization of carbon-PTFE air-diffusion cathode and BDD and DSA® anodes was carried out in 100 mL of a 50 mM Na_2SO_4 solution at 300 mA for 180 min, allowing the surface cleaning and activation. The carbon-felt cathode was activated by immersion in a 4 M H_2SO_4 solution at 60 °C for 3 h. After each trial, the carbon-felt cathode was immersed in a 4 M H_2SO_4 solution for 10 min and then rinsed several times with Milli-Q water and dried in an oven at 90 °C.

For PEF experiments in Appendix I, II and IV, a Philips TL/6W/08 fluorescent black light blue tube of λ_{max} = 360 nm with average power density of 5 W m^{-2}, determined with a Kipp & Zonen CUV 5 UV radiometer, was placed at 7 cm above the solution surface. The PEF trials in Appendix VII were carried out under irradiation with a Xenon arc lamp (150 W and 300 W, $\lambda > 325$ nm, LOT Quantum Design), which was placed at 5 cm above the solution. The visible light catalyzed PEF process was performed by employing a UV filter (400FH90-50S) with a cut-off value of 400 nm.

3.4. Analysis of the processes performance

The performance of the different processes checked for the treatment of micropollutants in synthetic or urban wastewater was mainly assessed by the percentages of target pollutants and TOC decays, which were calculated according to the following equations:

$$\text{Target pollutants removal (\%)} = \frac{\Delta C}{C_0} \times 100 \quad (59)$$

$$\text{TOC removal (\%)} = \frac{\Delta TOC}{TOC_0} \times 100 \quad (60)$$

where ΔC and ΔTOC are the experimental target pollutants removal and TOC decay (mg L^{-1}), respectively, at electrolysis time *t*. C_0 and TOC_0 are the corresponding initial concentrations before electrolysis.

The mineralization current efficiency (MCE, in %) at each electrolysis time *t* (in h) was determined from ΔTOC at given current *I* (in A) by the following equation:

$$\text{MCE (\%)} = \frac{n\,F\,V\,\Delta TOC}{4.32\times10^{7}\,m\,I\,t} \times 100 \quad (61)$$

where *F* is the Faraday constant (96485 C mol^{-1}), *V* is the solution volume (in L), and 4.32×10^{7} is a conversion factor for the units homogenization (3600 s h^{-1} × 12000 mg C mol^{-1}), whereas *m* is the number of carbon atoms of the target pollutant and *n* is the number of electrons consumed per molecule of pollutant for overall mineralization.

The theoretical total mineralization reactions for the five main target micropollutants studied in this Thesis can be written as follows:

$$C_{11}H_{16}O_2 + 20H_2O \rightarrow 11CO_2 + 56H^+ + 56e^- \quad (62)$$

$$C_{14}H_{10}O_3 + 25H_2O \rightarrow 14CO_2 + 60H^+ + 60e^- \quad (63)$$

$$C_{17}H_{18}F_3NO + 36H_2O \rightarrow 17CO_2 + 3F^- + NO_3^- + 90H^+ + 86e^- \quad (64)$$

$$C_{15}H_{22}O_3 + 27H_2O \rightarrow 15CO_2 + 76H^+ + 76e^- \quad (65)$$

$$C_{19}H_{20}ClNO_4 + 37H_2O \rightarrow 19CO_2 + Cl^- + NO_3^- + 94H^+ + 92e^- \quad (66)$$

Moreover, the specific energy consumption per unit TOC mass (EC_{TOC}) at current I (in A) and time t (in h) was estimated as follows:

$$EC_{TOC}\ (\text{kWh (gTOC)}^{-1}) = \frac{E_{cell}\, I\, t}{V\, \Delta TOC} \tag{67}$$

where E_{cell} is the average cell voltage (in V), V is the solution volume (in L) and ΔTOC is the experimental TOC decay (in mg L^{-1}).

3.5. Homogeneous and heterogeneous catalysts

The catalysts used in advanced EF and PEF processes include one iron chelating reagent (Fe(III)–EDDS complex) and three solid materials based on Fe-MOFs (FeS_2/C, nano-ZVI@C-N and Fe-bpydc).

3.5.1. Preparation and synthesis

Fe(III)–EDDS complex

The Fe(III)–EDDS complexes with different ratios were formed by mixing appropriate amounts of $Fe(ClO_4)_3$ and EDDS solutions followed by vigorous stirring for 3 min. Stock solutions of 10 mM $Fe(ClO_4)_3$ and EDDS were stored in the dark and fresh complexes were prepared before each experiment. For example, the combination of both reagents with 0.1 mM gave rise to 0.1 mM Fe(III)–EDDS (1:1) complex. In contrast, to form the Fe(II)–EDDS complex, $FeCl_2$ was used as iron source.

FeS_2/C nanocomposites

The synthesis of Fe-MOF derived FeS_2/C nanocomposites is illustrated in Fig. 35. First, 0.04 mol of 2-methylimidazole was dissolved in 100 mL of ethanol, further adding 0.01 mol of $FeCl_2$•$4H_2O$ to obtain a homogeneous solution that was kept overnight. The slurry obtained upon centrifugation was washed repeatedly and then dried at 80 °C for 12 h. This Fe-MOF precursor was carefully mixed with sulfur (with mass ratio 1:2) and

transferred to an Al_2O_3 boat. The mixture was heated up to 400 ºC at 5 ºC min^{-1} in a purpose-made tubular furnace (Fig. 36) under N_2 stream, being kept at 400 °C for 2 h. The annealed sample was washed and dried in a vacuum oven at 80 ºC for 24 h. The final FeS_2/C black powder was stored hermetically under N_2 atmosphere.

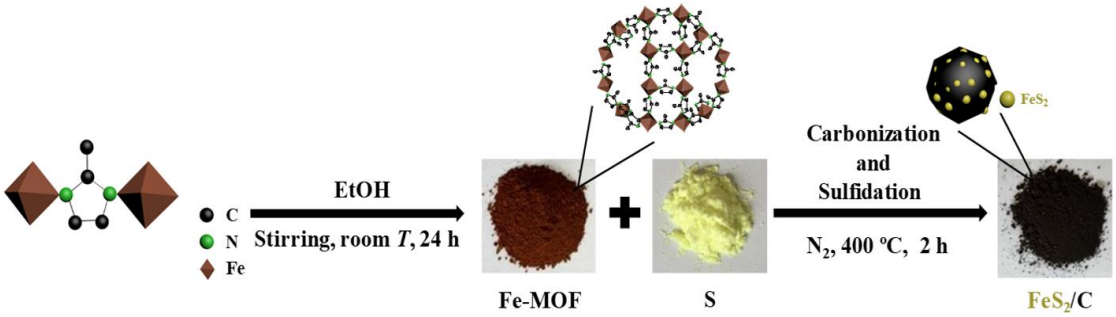

Figure 35. Schematic diagram for the fabrication of FeS_2/C nanocomposites.

Figure 36. Purpose-made tubular furnace used for the carbonization.

N-doped nano-ZVI@C rods

To synthesize the MIL(Fe)-type MOF, $FeCl_3$•$6H_2O$ and H_2BDC (5 mmol of each reactant) were mixed and dissolved in 25 mL DMF, and then stirred for 20 min to get a homogeneous solution. Subsequently, the mixture was poured into a 100 mL Teflon-lined stainless steel autoclave, which was placed in a fan oven preheated to 110 °C and kept for 24 h. The autoclave was then removed from the oven and cooled down naturally to room temperature, whereupon the powdery product was collected by filtration, sequentially washed with methanol and water, and finally dried overnight in an oven at 80 °C. The resulting powder was stored at room temperature in a covered glass container. The same procedure was followed to synthesize the NH_2-MIL(Fe)-type MOF,

but replacing H_2BDC by NH_2-BDC. Nano-ZVI@C and nano-ZVI@C-N (i.e., N-doped) were prepared by annealing the previous MOFs in a tube furnace at the required temperature for 4 h under N_2 atmosphere. The scheme of the preparation route of nano-ZVI@C-N with a pyrolysis temperature of 800 °C is illustrated in Fig. 37.

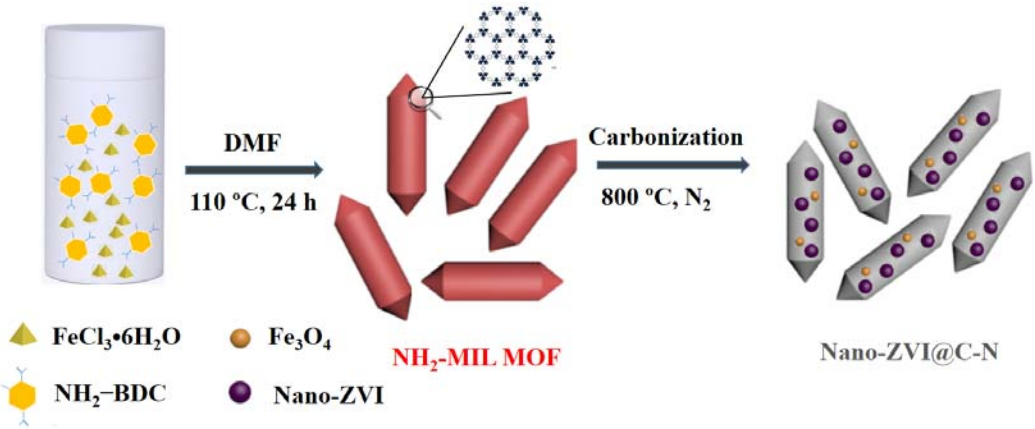

Figure 37. Scheme of the preparation route of nano-ZVI@C-N rods.

Fe-bpydc

The Fe-based 2D MOF, Fe-bpydc, was prepared via a hydrothermal method according to the previous report with slight modification [244]. Briefly, 0.5 mmol of 2,2'-bipyridine-5,5'-dicarboxylic acid was dissolved in 40 mL DMF, then added to 40 mL of $Fe(ClO_4)_2$ aqueous solution (1 mmol). The mixture was sonicated for 20 min to obtain a homogeneous solution. Subsequently, the mixture was heated in an oil bath at 120 ºC under vigorous stirring for 4 h. After cooling naturally, the red-brown solid product was separated by filtration, washed with ethanol several times, and dried in an oven at 60 °C overnight. The obtained sample was defined as Fe-bpydc. The synthesis and crystal growth of Fe-bpydc is presented in Fig. 38.

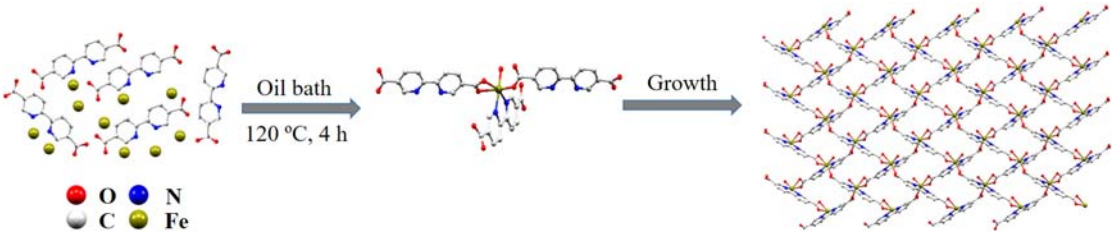

Figure 38. Schematic illustration of the synthesis and crystal growth of Fe-bpydc.

3.5.2. Characterization

Main catalyst characterization techniques involved in this Thesis are listed in Table 12.

Table 12. Characterization techniques used in this Thesis.

Techniques	**Carbon-felt loaded with Fe(III)**	**FeS_2/C**	**Nano-ZVI@C-N**	**Fe-bpydc**
Scanning electron microscopy (SEM)	√	√		√
Transmission electron microscopy (TEM)			√	
X-ray photoelectron spectroscopy (XPS)	√	√	√	√
X-ray powder diffraction (XRD)		√	√	√
Brunauer–Emmett–Teller (BET)		√	√	√
Dynamic light scattering (DSL)		√	√	√
Themogravimetric analysis (TGA)			√	√
Fourier transform infrared spectroscopy (FTIR)			√	√
Ultraviolet-visible diffuse reflectance (DR-UV/Vis)				√
Cyclic voltammetry	√			
Elemental analysis			√	
Zeta potential			√	
Magnetic properties			√	

SEM

The morphologies of the carbon felt and catalysts were observed by means of SEM with energy dispersive X-ray spectroscopy (EDS) using a JEOL JSM-7100 F field emission scanning electron microscope at 15 kV equipped with an INCA analyzer.

TEM

In some cases, the morphologies of the catalysts were also observed by TEM using a JEOL JEM-2100 LaB6 transmission electron microscope at 200 kV in STEM mode with a dark field detector. The beam size used in this mode was around 15 nm. The spectrometer is an Oxford Instruments INCA x-sight with Si (Li) detector. Map acquisition was made using the INCA Microanalysis Suite version 4.09 software.

XPS

XPS analysis in Appendix I-VI was performed with a Physical Electronics PHI 5500 Multitechnique System using an Al-Kα monochromatised X-ray source (1486.6 eV and 350 W) placed perpendicularly to the analyzer axis and calibrated using the $3d_{5/2}$ line of Ag (full width at half maximum of 0.8 eV). The analyzed area was a circle of 0.8 mm diameter. The selected resolution for the spectra was 187.85 eV of Pass Energy (PE) and 0.8 eV $step^{-1}$ for the general spectra, and 23.5 eV of PE and 0.1 eV $step^{-1}$ for the spectra of the different elements. A low energy electron gun (less than 10 eV) was used. All measurements were made under ultra-high vacuum at pressures between 5×10^{-9} and 2×10^{-8} Torr. The spectra were analyzed using the ULVAC-PHI MultiPakTM Software 8.2.

XPS measurements in Appendix VII for elemental analysis were performed in an ultrahigh vacuum spectrometer equipped with a VSW Class WA hemispherical electron analyzer. A dual anode of Al Kα X-ray source (1486.6 eV) was used as incident radiation and the constant pass energy mode (44 and 22 eV for survey and high resolution spectra respectively) was applied in all XPS measurements. The binding energies (BEs) of all peaks were referenced to the C 1s main peak at 285 eV. The CASA XPS program with a Shirley background subtraction and Gaussian -Lorentzian peak shape was used for the analysis of the peaks. High resolution XPS measurements for band alignment were performed on a Thermo Scientific K-Alpha spectrometer equipped with an Al Kα X-Ray source (1486.6 eV) and a 180° double focusing

hemispherical analyser with a 2D detector at an operating pressure of 1×10^{-8} mbar as well as a flood gun to minimise charging from photoemission. Powders were mounted onto conductive carbon tape adhered to a sample holder. To further correct for charging, all core lines were corrected a C 1s (C-C) core line, assumed to be at 284.8 eV. Data was further processed and analysed in the Avantage and CASA XPS software packages.

XRD

Most of the XRD analyses were performed using a PANalytical X'Pert Pro X-ray diffractometer in reflection–transmission mode with a spinning stage (2 revolutions per s). An anode voltage of 45 kV and an emission current of 40 mA were chosen as the operating conditions using a monochromatic Cu $K\alpha_1$ radiation source (λ = 1.5406 Å). A X'Celerator silicon strip detector was used in the diffractometer.

XRD analysis in Appendix VII was performed using the same equipment, but under the condition of an anode voltage of 40 kV, an emission current of 20 mA and a monochromatic Cu $K\alpha$ radiation source (λ = 1.54178 Å).

BET

Nitrogen adsorption and desorption isotherms were measured using a Micromeritics TriStar 3000 analyzer. The equivalent specific surface areas of the samples were determined using the BET method. Sample outgas was performed by applying vacuum to the sample for 4 h at 40 ºC. The total pore volume was ascertained from the volume of N_2 adsorbed at a relative pressure (P/P_0) of 0.97.

The measurement in Appendix VII was performed with a porosity and surface area analyzer (Micrometrics 3 Flex) under the same conditions described above.

DLS

Samples were analyzed using Laser Diffraction Particle Size Analyzer, LS 13 320 from Beckman Coulter. The dispersion media was acetone and samples were treated with

ultrasounds under the condition of 30 KHz and 200 W for 5 min before analysis.

TGA

TGA analyses were performed on a Mettler-Toledo TGA-851e thermobalance under nitrogen atmosphere with 50 mL min^{-1} flow rate, heating from 30 to 900 ºC at a heating rate of 10 ºC min^{-1}.

The TGA analysis in Appendix VII was performed upon nitrogen atmosphere at 100 mL min^{-1}, heating from 25 to 900 ºC at a heating rate of 10 ºC min^{-1} using a Netzsch TG 209 F1 Libra instrument.

FTIR

FTIR spectra in Appendix VII were recorded using an Agilent Technologies Cary 630 FTIR. The other samples were analyzed with a Thermo Scientific Nicolet 6700 FTIR. The spectra of each sample was collected 5 times, and corrected for the background noise. The experiments were made using powdered samples, without KBr addition.

DR-UV/Vis

DR-UV/Vis spectroscopy was measured using an Agilent Cary 500 UV–Vis-NIR spectrometer equipped with an integrating sphere. Spectral band width was set to 2 nm, with Spectralon as a standard. Spectra were analyzed using Kubelka-Munk function in order to eliminate any tailing contribution.

Cyclic voltammetry

The electrochemical characterization of Fe-loaded carbon-felt was carried out by cyclic voltammetry on an Autolab PGSTAT30 potentiostat. An undivided electrochemical cell containing 50 mL of a 50 mM Na_2SO_4 solution at natural pH and thermostatized at 25 °C was used. It was equipped with a carbon-felt piece (1.0 cm × 1.0 cm × 0.5 cm), in the absence or presence of pre-adsorbed Fe(III) species, a platinum spiral and an Ag|AgCl (KCl sat.) as the working, counter and reference electrode, respectively. The

voltammograms were recorded within a potential range from +0.700 V to -1.450 V at a scan rate of 0.100 V s^{-1}. Prior to each run, O_2 was purged out from solutions under a gentle N_2 stream.

Elemental analysis

The determination of C and N was performed using a Thermo Scientific Thermo EA 1108 elemental organic analyzer, working in standard conditions recommended by the supplier of the instrument corresponding to helium flow rate at 120 mL min^{-1}, combustion furnace at 1000 ºC, chromatografic column oven at 60 ºC and oxygen loop of 10 mL at 100 kPa.

Fe was analyzed by ICP-OES using a Perkin Elmer Optima 3200RL. Before analysis, digestion of 0.0159 g samples was carried out with a Milestone Ethos Plus microwave oven, using a high pressure closed PTFE reactor. A temperature program was followed to reach 180, 210, 220 and, finally, 230 ºC, employing HNO_3, HCl and H_2O_2 as oxidizing media.

Zeta potential

The zeta-potential of each sample as a function of pH was determined using a Malvern Zetasizer Nano ZS (Micromeritics AUTOCHEM 2920) at room temperature, using the Zetasizer version 7.11 software. Buffer solutions at pH values from 3.0 to 7.0 were prepared by mixing different volumes of 0.10 M acetic acid and 0.20 M sodium acetate solutions. The powdery catalyst was suspended in the different buffer solutions using an ultrasonic bath and then, the suspension was introduced in a disposable folded capillary cell (DTS 1070).

Magnetic property

The magnetic property of the catalyst was measured at 300 K under a varying magnetic field from -20000–20000 Oe on a Quantum Design SQUID MPMS-XL magnetometer.

Most of the analyses were carried out at the Scientific and Technological Centers of the UB (CCiTUB, http://www.ccit.ub.edu/EN/home.html) or the Analytical Lab of the ICL (Appendix VII). FTIR in Appendix VI and cyclic voltammetry were conducted at LEMMA. XPS, XRD, BET, DLS, TGA and elemental analysis at the CCiTUB were performed by technicians, but the results were analyzed by ourselves. The other analyses were completely made by the PhD candidate.

3.6. Analytical methods

3.6.1. Micropollutants and ethylenediamine-*N,N'*-disuccinic (EDDS) concentrations

All the micropollutants, except BZF, and EDDS studied in this Thesis were determined by reversed-phase High-Performance Liquid Chromatography (HPLC) using a Waters 600 liquid chromatograph fitted with a BDS Hypersil C18 5µm, 250mm×4.6mm, column at 35°C, coupled to a 996 photodiode array detector (PDA), but under different conditions. Samples were always diluted with the same organic solvents of mobile phase to stop the degradation processes.

BHA

The detection wavelength was set at 290 nm. The mobile phase was a 70:30 (v/v) acetonitrile (CH_3CN)/10mM KH_2PO_4 (pH 3.0) mixture eluted at 1.0 mL min^{-1}, and the peak of BHA was obtained at 5.1 min.

BP-3

BP-3 was analyzed with a mobile phase of CH_3CN and 10 mM KH_2PO_4 (50:50, v/v) mixture at 1 mL min^{-1}, and the injection volume was 10 µL. BP-3 was detected at retention time of 19.2 min. The detection wavelength was 277 nm.

FLX

The mobile phase for reversed-phase HPLC was a 50% (v/v) CH_3CN/10 mM KH_2PO_4 (pH 3.0) mixture at 1 mL min^{-1}. The detection wavelength was 227 nm and the chromatograms displayed a peak for fluoxetine at retention time of 13.2 min. The injection volume was 20 µL.

GEM

GEM was analyzed with a mobile phase of CH_3CN and 10 mM KH_2PO_4 (60:40, v/v; pH 3.0) at flow rate of 1 mL min^{-1}. The injection volume was 10 µL and the detection wavelength was set at 276 nm. The peaks of GEM appeared at the retention time of 11.4 min.

BZF

BZF was analyzed on a reversed-phase HPLC equipped with a Luna C18 3 µm, 100 mm × 4.6 mm and a SPD-20A detector. Acetonitrile, acetic acid in water (0.02%) and methanol (40:55:5, v/v) were used as the mobile phase at a flow rate of 1 mL min^{-1}. The column temperature was set at 30.0 °C and the injection volume was 10 µL. The peak of BZF was detected at wavelength of 210 nm, and appeared at a retention time of 6.8 min.

BPA and NPX were determined under the same conditions of FLX, with detection wavelengths of 228 and 231 nm, and retention times of 6.1 and 7.3 min, respectively.

Fe(III)-EDDS complex

The concentration of the Fe(III)–EDDS complex was determined with the PAD set at 240 nm. The mobile phase was a mixture of A and methanol (95:5, v/v), where A was Milli-Q water with 2 mM tetrabutylammonium hydrogensulfate and 15 mM sodium formate at pH 4.0, circulating at a flow rate of 0.8 mL min^{-1}. The Fe(III)–EDDS peak was displayed at 10.7 min.

3.6.2. Total organic carbon (TOC)

TOC of solutions was measured on a Shimadzu TOC VCSN analyzer upon injection of filtered 50 µL samples after immediate withdrawal from treated solutions. Reproducible values with ± 1% accuracy were always obtained. The direct incineration of the sample in a catalytic oven at 680 °C without acidification gave rise to the total carbon (TC), which was the sum of inorganic and organic carbon. The assessment of mineralization in this Thesis was performed by determining the non-purgeable organic carbon (NPOC) value, which was measured with a preliminary sample acidification to remove all the inorganic carbon. Since all the samples were filtered by 0.45 µm syringe filters before measurement, the obtained NPOC values were equal to dissolved organic carbon (DOC). In addition, this equipment was coupled to a TNM-1 (total nitrogen measurement) module, which was used to measure the total nitrogen (TN) in some samples by combusting all the nitrogen species to NO in the furnace at 680 °C.

3.6.3. Spectrophotometric determination of H_2O_2, active chlorine, ammonium ion and soluble iron species

H_2O_2

H_2O_2 concentration was determined by means of adding Ti(IV) oxysulfate to the samples to form a yellow complex in acid condition from reaction (68), which exhibits the maximum light adsorption at 408 nm [254].

$$Ti^{4+} + H_2O_2 + 2SO_4^{2-} \rightarrow (TiO_2(SO_4)_2)^{2-} + 2H^+ \quad (68)$$

The generation of this complex, proportional to H_2O_2 concentration, was then measured at 408 nm on a Shimadzu 1800 UV/Vis spectrophotometer. Specifically, a 20 mM Ti(IV) solution was firstly prepared by dissolving 3.2 g $TiO(SO_4)$ in 1 L of Milli-Q water with the assistance of 180 mL concentrated sulphuric acid addition. For analysis, 0.5 mL of

sample was mixed with 4 mL of Ti(IV) solution and 1.5 mL of 50 mM Na_2SO_4 solution, then 4 mL Milli-Q water was added to reach a total volume of 10 mL. The final solution was submitted for the measurement of absorbance.

Active chlorine

The active chlorine concentration was obtained by means of the *N,N*-diethyl-*p*-pheylenediamine (DPD) colorimetric method (4500-Cl. G) [255]. It is remarkable that when DPD reacts with small amounts of active chlorine at near-neutral pH, the dominant product had a pink colour proportional to the active chlorine concentration. However, the formation of colourless imine is favored at high concentration of active chlorine. The main interferences for the measurement come from other oxidants presented in the solution, such as manganese or copper, which can be eliminated by the addition of EDTA. The measurement was carried out by addition of 0.5 mL of buffer solution, 0.5 mL of DPD solution, 9 mL of Milli-Q water and 1 mL of sample sequentially to reach a total volume of 11 mL. The absorbance of the final solution was measured at the wavelength of 515 nm on a Shimadzu 1800 UV/Vis spectrophotometer. The calibration curve of active chlorine was prepared with $KMnO_4$. The dissolution of 0.891 g $KMnO_4$ in 1 L Milli-Q water is equal to 1,000 mg L^{-1} Cl_2.

Ammonium ion

Ammonium ion was determined by a sensitive photometric method [256]. Ammonia reacts with phenol and hypochlorite to give an indophenol, which is intensely blue in an alkaline medium. This method is called indophenol blue method or phenate method. Four stock reagents were prepared firstly: Phenol solution; nitroprusside solution; EDTA solution; and hypochlorite solution.

For analysis, 2 mL of sample, 1.5 mL of EDTA solution, 1 mL of phenol solution, 1 mL of nitroprusside solution and 1 mL of hypochlorite solution were mixed to reach the final solution, whose absorbance was measured at the wavelength of 630 nm on a Shimadzu 1800 UV/Vis spectrophotometer.

Soluble iron species

The spectrophotometric determination of soluble iron was performed using the 1,10-phenantroline method [257]. The soluble Fe^{2+} was determined by mixing 1 mL of sample, filtered with 0.45 µm cellulose syringe filters, with 1 mL of 0.2% (v/v) 1,10-phenanthroline and 1 mL of acetate/ acetic acid buffer (pH ~ 4), followed by dilution to 10 mL with Milli-Q water. The same steps were made to obtain the total dissolved iron ions, but adding ascorbic acid to transform all Fe^{3+} into Fe^{2+} before dilution to 10 mL. In each case, the Fe^{2+} concentration was measured from the absorbance of its complex with 1,10-phenantroline at $\lambda = 510$ nm using a Shimadzu 1800 UV/Vis spectrophotometer at 25 °C (method ASTM E394).

In some cases, quantitative analysis of Fe was also performed by inductively-coupled plasma with optical detection (ICP-OES) using a Perkin Elmer Optima 8300 spectrometer.

3.6.4. Anion and cation contents in initial and treated solutions

The concentrations of Cl^-, NO_3^- and F^- generated from the degradation of micropollutants were obtained by ion chromatographic (IC) upon injection of 25 µL aliquots into a Shimadzu 10 Avp LC equipped with a Shim-Pack IC-A1S, 100 mm × 4.6 mm, anion-exchange column at 40 °C and coupled with a Shimadzu CDD 10 Avp conductivity detector. A solution composed of 2.4 mM tris(hydroxymethyl)-aminomethane and 2.6 mM phthalic acid (pH 4.0) was eluted at 1.5 mL min^{-1} as the mobile phase.

The anion contents in wastewater were determined by IC upon injection of 20 µL aliquots into a Kontron 465LC fitted with a Waters IC-pack, 150 mm × 4.6 mm, anion column at 35 °C, coupled with a Waters 432 conductivity detector. The mobile phase for this analysis was a solution of boric acid, sodium gluconate, sodium tetraborate, acetonitrile, butanol and glycerine eluted at 2 mL min^{-1}.

The contents of metal ions in wastewater were obtained by ICP-OES using a Perkin Elmer Optima 8300 spectrometer.

3.6.5. Identification of the main radicals

In order to understand the role of different radicals during the EF and PEF processes, radical scavenging experiments were applied by employing *tert*-butanol (TBA) as $^{\bullet}OH$ radicals scavenger ($k_{\bullet OH}$ = 3.8-7.6×10^8 $M^{-1}s^{-1}$) and benzoquinone (BQ) as $O_2^{\bullet-}$ radicals scavenger ($k_{O2\bullet-}$ = 8.0×10^9 $M^{-1}s^{-1}$), respectively [258]. Moreover, the radicals were detected by spin trapping, analyzing the $^{\bullet}OH$-DMPO adduct by electron spin resonance (ESR). To do this, 70 mL of a 10 mM DMPO solution in 0.05 M Na_2SO_4 at natural pH were electrolyzed in an undivided cell with a DSA-O_2 anode and a PTFE cathode under vigorous stirring with a magnetic bar at room temperature. The treated solution was immediately frozen with dry ice for preservation to be further analyzed by ESR with a Bruker ESP300E spectrometer controlled by Win-EPR 2.3 SimFonia software.

3.6.6. GC-MS and LC-QToF-MS

The organic components of the raw urban wastewater and the micropollutants as well as their metabolites were identified by gas chromatography-mass spectrometry (GC-MS) and/or liquid chromatography–hybrid quadrupole time-of-flight mass spectrometry (LC-QToF-MS) analysis. Aiming to identify as many reaction intermediates as possible, 150 mL of synthetic solutions or actual wastewater containing different micropollutants were electrolyzed under different conditions. The final solutions were extracted with CH_2Cl_2 (3×25 mL). The resulting organic solutions were dried over anhydrous Na_2SO_4, filtered and concentrated for analysis.

GC-MS analysis was made with an Agilent Technologies system composed of a 6890 N gas chromatograph with a 7683B series injector and a 5975 mass spectrometer in electron impact mode at 70 eV. A nonpolar Agilent J&W DB-5 or a polar HP INNOWax column of 0.25 µm, 30 m × 0.25 mm, was employed. The temperature ramp was: 36 °C

for 1 min, 5 °C min^{-1} up to 300 °C and hold time 10 min. The inlet, source and transfer line operated at 250, 230 and 280 °C. The NIST05 MS library was used for interpretation.

LC-QToF-MS analysis was carried out using an Agilent 1200 Series system coupled to an AB Sciex Applied Biosystems mass spectrometer, operating in positive ion mode. A Zorbax Eclipse XDB C18 Solvent Saver Plus 3.5µm (100 mm × 3.0 mm) column at 30 ºC was utilized as stationary phase. The mobile phase was a mixture of two solutions, namely 0.1% formic acid in water (A) and 0.1% formic acid in methanol (B), in gradient mode. Solution A was injected at 95.0% during the first 10 min, 5.0% from 10 to 11 min, and 95.0% again until 15 min, at a flow rate of 0.6 mL min^{-1}.

3.6.7. EEM-PARAFAC

Excitation-emission matrix (EEM) fluorescence spectroscopy (i.e., FEEM) coupled with parallel factor analysis (PARAFAC) was used to characterize and assess the dissolved organic matter (DOM) changes in wastewater samples, which allowed the differentiation of different organic components [259]. EEM fluorescence analysis was performed with a 1 cm cuvette using an AMINCO-BOWMAN Series 2 fluorescence spectrometer by scanning 351 individual emission wavelengths (250-600 nm) with 5 nm increments of excitation wavelengths between 240 and 460 nm. For each sample analyzed, an EEM was generated with an intensity value in each coordinate point. The scan rate was set at 18 nm s^{-1} for all samples analyzed, the slit widths were adjusted to 5 and 2 nm for excitation and emission wavelengths, respectively, and the photomultiplier tube voltage was set to 750 V. Prior to the analysis, the samples were tempered at room temperature. The spectra were recorded in the ratio mode to ensure normalization of the signal and enable comparison within samples analyzed.

The resulting matrices containing 351×45 emission intensity readings for each sample were further analyzed with PARAFAC to decompose them into a set of trilinear terms and a residual array. This was done in order to estimate the number of organic fractions

present in our samples. The PARAFAC analysis was conducted in MATLAB, according to the N-way v. 3.00 Toolbox. The first and second order Rayleigh diagonals were trimmed and the samples were smoothed. The morphology of the contour plots obtained from the model, the explained variation, the split half validation and also the residual arrays were the parameters used to select the appropriate number of components in the model. The maximum fluorescence intensity (F_{max}) was used to track changes in NOM. The F_{max} value was determined by selecting the point of maximum intensity for each factor in each sample. The PARAFAC model can be written as:

$$X_{ijk} = \sum_{f=1} a_{if} b_{jf} c_{kf} + E_{ijk} \quad (69)$$

where X_{ijk} is the matrix used providing intensity values at specific coordinate points, a_{if}, b_{jf}, c_{kf} correspond to the scores, the estimated emission spectrum and estimated excitation spectrum at specific coordinates, respectively, the f value defines the number of components in the model and the E_{ijk} accounts for by the residual variation not explained in the model.

3.6.8. Acute toxicity

Acute ecotoxicity of micropollutants and their metabolic products was assessed by means of the Microtox® toxicity test, which employs bioluminescent bacteria *Vibrio fischeri*, a marine organism [260]. When exposed to a toxic substance, bacteria respiration is disrupted, inhibiting the metabolic pathway that converts chemical energy into visible light. Response to toxicity is therefore measured as a change in luminescence. The tests were conducted by following the protocol recommended by the manufacturer (Modern Water). After reconstitution of a freeze-dried culture of *Vibrio fischeri* (Microtox® Acute Reagent) in 1 mL of the Microtox® Reconstitution solution, 10 µL of this reagent were mixed with 0.5 mL of the Microtox® Diluent. After waiting 15 min for the stabilization of bacteria light emission, luminescence was obtained by means of a Microtox® M500 analyzer with a temperature-controlled

photometer. Then, bacteria dilutions and the sample (adjusted with the Microtox® Osmotic Adjustment Solution) were mixed to finally prepare 45%, 22.5%, 11.25% and 5.6% serial dilutions. After 15 min of contact, luminescence of all dilutions was recorded. Results were expressed as EC_{50}, which is the sample dilution causing a 50% reduction in light emission after 15 min of contact.

3.6.9. Other analyses

The electrical conductance and pH were measured with a Metrohm 644 conductometer and a Crison GLP 22 pH-meter, respectively.

CHAPTER 4
RESULTS AND DISCUSSION

4. Results and discussion

This chapter presents the most relevant findings of this Thesis. It is divided into three parts: (**1**) Single EC and sequential EC/EAOPs for the treatment of organic micropollutants spiked into urban wastewater (Appendices I and II); (**2**) Fe(III)–EDDS-enhanced EF and PEF processes for the treatment of organic micropollutants at mild pH (Appendices III and IV); and (**3**) Raw and calcined Fe-based MOFs as efficient heterogeneous catalysts in Fenton-based EAOPs (Appendices V, VI and VII).

4.1. Single EC and sequential EC/EAOPs for the degradation of organic micropollutants

4.1.1. Electrochemical treatment of butylated hydroxyanisole: Electrocoagulation versus advanced oxidation

This work was focused on a fundamental study to compare the removal of BHA from water either by EC or EAOPs before starting with the coupled EC/EAOPs. The results revealed that single EC with an Fe|Fe cell achieved a very poor abatement of BHA and dissolved organic carbon (DOC), reaching the adsorption/desorption equilibrium at about 25-30 min, whereas PEF process with a BDD anode could slowly but effectively remove BHA and DOC from urban wastewater, obtaining almost total mineralization after a long treatment period up to 660 min.

Specifically, 150 mL of 76 μM BHA, a synthetic phenolic antioxidant added to food, pharmaceuticals and cosmetics (detailed in subsection 1.1.5), was spiked into a simulated matrix or urban wastewater to be firstly treated by the classical EC process in an Fe|Fe cell. In the simulated matrix, the DOC profile was similar to BHA decay, with a final abatement of 10.2%, suggesting that BHA was the main organic adsorbed onto the hydroxides, whereas the retention of its possible byproducts was insignificant.

In contrast, in urban wastewater, a more relevant DOC decay of 24.1% was achieved, which differed from the BHA removal (3.6%), suggesting that the EC treatment mainly promoted the removal of NOM components in wastewater, inhibiting that of BHA.

Then, the effect of pH, number of Fe|Fe pairs and applied current on the performance of EC treatment was assessed. First, the effect of pH was examined using one Fe|Fe pair at 100 mA, finding a slight increase of BHA and DOC decays in the order: natural pH 5.9 < pH 11.0 < pH 3.0. The larger disappearance at pH 3.0 can be accounted for by the attack of active chlorine (Cl_2/HClO) formed by the anodic oxidation of Cl^-, which cause the destruction of BHA and NOM components in urban wastewater. The removal at pH 11.0 could be associated with its enhanced adsorption because of the large formation of such flocs in alkaline medium, along with a poor destruction by ClO^-, the weakest active chlorine species. Further, a system with two Fe|Fe pairs placed in monopolar parallel connection was tested at natural pH and 100 mA. The results evidenced larger BHA and DOC decays, achieving 10.5% and 30.2%, respectively. This was attributed to the smaller current density applied to each anode, which allowed a higher current efficiency and a more controlled release of Fe^{2+}. The influence of the applied current was investigated at natural pH using the two Fe|Fe pairs as well. The results highlighted the enhancement of BHA and DOC removals upon increasing current, as expected by the greater amounts of flocs formed with ability to cause a larger adsorption.

After the evaluation of a single EC treatment, the degradation of BHA in the synthetic solution was carried out by H_2O_2-based EAOPs. First, 150 mL of 76 μM BHA in 50 mM Na_2SO_4 solution and simulated matrix at natural pH 5.9 were treated by EO-H_2O_2 using a RuO_2-based or BDD anode, at 100 mA for 300 min. A very slow decay of BHA and DOC in 50 mM Na_2SO_4 solution using either RuO_2-based or BDD anode was obtained, due to the limited amount of adsorbed M($^{\bullet}$OH) formed on the anode surface, which was the only active species to attack the pollutants. The superiority of BDD agreed with the expected higher oxidation power of BDD($^{\bullet}$OH) as compared to

$RuO_2(^{\bullet}OH)$. However, the contaminant concentration fell very rapidly, practically independent of the anode nature, in the simulated matrix, ending below the limit of quantification at about 30 min. The great BHA decay can be accounted for by the attack of a low and constant active chlorine concentration, whose action was much quicker than the simultaneous attack of $M(^{\bullet}OH)$.

Once assessed the oxidation power of $M(^{\bullet}OH)$ and active chlorine with BHA and its byproducts, the performance of EF and PEF processes was analyzed in the presence of 0.5 mM Fe^{2+} as catalyst. A similar BHA decay with total removal in only 8 min was achieved in both cases, evidencing a very quick reaction of this pollutant with $^{\bullet}OH$ formed from Fenton's reaction, much faster than the concomitant attack of $M(^{\bullet}OH)$ and active chlorine. However, the mineralization of BHA, especially by EF process with the RuO_2-based anode in simulated matrix, was slow due to the generation of more refractory chlorinated byproducts, which were resistant to $RuO_2(^{\bullet}OH)$, active chlorine and $^{\bullet}OH$. In contrast, using BDD anode, a gradual drop of DOC in EF and PEF processes was obtained, confirming the very effective oxidation of byproducts by $BDD(^{\bullet}OH)$.

Finally, the study of BHA removal by EAOPs was extended to urban wastewater as matrix by spiking this compound at 76 μM. The occurrence of a rapid BHA concentration abatement was ascertained in all the EAOPs, with total removal at about 30 min, still much slower than that described in the simulated matrix. This slower decay in urban wastewater was accounted for by the parallel attack of generated oxidants on NOM components and low $^{\bullet}OH$ production at pH 7.9. In addition, the greater DOC decay with BDD anode confirmed its superiority, since the RuO_2-based anode was unable to mineralize BHA, NOM and all byproducts formed. Quicker trials were found in urban wastewater at pH 3.0, suggesting the important role of $^{\bullet}OH$ in the bulk to favor the formation of photoactive intermediates that were more rapidly photodecomposed by UVA photons in PEF.

4.1.2. Photoelectro-Fenton as post-treatment for electrocoagulated benzophenone-3-loaded synthetic and urban wastewater

After a fundamental investigation on the performance of isolated EC and EAOPs, this work was extended to the EC/EAOPs coupling system to verify their synergistic effect on the treatment of micropollutant-contaminated wastewater.

Prior to that, aiming to gain insights into the EC process, several comparative trials were made with 150 mL of 30 mg C L^{-1} BP-3 in simulated matrix at pH 11.0 using an Al or Fe anode. As explained in subsection 1.2, these are the most common materials to generate insoluble $Al(OH)_3$ and $Fe(OH)_3$ flocs. The Al|Al cell attained 67.2% BP-3 decay and 47.0% TOC removal with final pH of 9.5, clearly outperforming that in Fe|Fe cell with 28.9% BP-3 and 17.7% TOC abatements. However, the greater performance using the Al|Al cell could be plausibly ascribed to the substrate precipitation from the pH decrease at 9.5 (< pK_a = 9.65). Under such circumstance, the neutral form predominated, which was much more insoluble than its anionic counterpart present at pH 11.0. The BP-3 removal was always larger than the TOC abatement, meaning that BP-3 was rather transformed into byproducts by oxidation and reduction reactions, which were not so easily coagulated by the flocs and became accumulated in the bulk. Envisaging the combination between EC and EAOPs, the Fe|Fe cell was preferred when extending the treatment to an urban wastewater matrix (natural pH of 8.0) due to the fact that the dissolved iron species was capable to act as catalyst in the subsequent EAOPs. These tests were made with 4 mg C L^{-1} BP-3 at 15 mA cm^{-2}, and the results revealed quick removals of BP-3 (40% in 20 min) and TOC (35% in 15 min).

The ability of H_2O_2-based EAOPs for the degradation of BP-3 in urban wastewater was also investigated using a RuO_2-based or BDD anode and electrolyzing 100 mL samples of pH 8.0 at 33.3 mA cm^{-2} for 360 min. BP-3 was rapidly removed with complete disappearance in 45 min, and the oxidation ability rose as EO-H_2O_2 < EF < PEF regardless of the anode. The results of TOC abatement suggested that BDD($^{\bullet}$OH)

always yielded much larger mineralization than $RuO_2(^{\bullet}OH)$, which agreed with the higher oxidation power expected from BDD. The best mineralization with 62.6% TOC removal was attained by PEF, followed by 55.5% TOC decay by EF. The superiority of PEF is mainly due to the photolysis of some intermediates, including Fe(III) complexes of final carboxylic acids. The effect of Fe^{2+} concentration and initial pH on EF and PEF processes were also examined because they modulate the $^{\bullet}OH$ production from Fenton's reaction.

In order to thoroughly investigate the intermediates produced during the treatment of BP-3 spiked into wastewater, the concentration of carboxylic acids was determined by ion-exclusion HPLC, whereas the aromatic intermediates were identified by GC-MS analysis. After 20 min of EC, 6 cyclic compounds were identified by GC-MS, including new molecules coming from hydroxylation and cleavage of BP-3, which confirmed the proposed concomitant production of $^{\bullet}OH$ during EC. In the case of EO-H_2O_2, low contents of maleic and oxalic acids were identified by ion-exclusion HPLC using RuO_2-based and BDD anodes. The primary intermediates generated from BP-3 were identified in simulated water by GC-MS analysis of samples after 2 min PEF treatment with BDD anode. The results revealed 14 cyclic molecules, including several toxic chloroderivatives. Furthermore, according to these byproducts, a reaction sequence for the initial BP-3 degradation was tentatively proposed.

Finally, the sequential EC/EF and EC/PEF treatments were conducted by electrolyzing 150 mL of 4 mg C L^{-1} BP-3 spiked into urban wastewater using a Fe|Fe cell in EC as pre-treatment of EF and PEF. The sequential EC (Fe|Fe cell, 15 mA cm^{-2}, 20 min)/PEF (BDD/air-diffusion cell, 33.3 mA cm^{-2}, 360 min) of BP-3-loaded urban wastewater at natural pH was much more powerful than EC/EF. The time needed for total mineralization by EC/PEF was shorter than in single PEF, then being sequential electrochemical processes a very interesting alternative.

GROUP OF ARTICLES INCLUDED IN SECTION 4.1

Page 127: **Electrochemical treatment of butylated hydroxyanisole: Electrocoagulation versus advanced oxidation**

Zhihong Ye, Enric Brillas, Francesc Centellas, Pere Lluís Cabot, Ignasi Sirés.

Separation and Purification Technology 208 (**2019**) 19-26

Page 141: **Photoelectro-Fenton as post-treatment for electrocoagulated benzophenone-3-loaded synthetic and urban wastewater**

Zhihong Ye, Juliana R. Steter, Francesc Centellas, Pere Lluís Cabot, Enric Brillas, Ignasi Sirés.

Journal of Cleaner Production 208 (**2019**) 1393-1402

Appendix I

Electrochemical treatment of butylated hydroxyanisole: Electrocoagulation versus advanced oxidation

Separation and Purification Technology 208 (2019) 19–26

Contents lists available at ScienceDirect

Separation and Purification Technology

journal homepage: www.elsevier.com/locate/seppur

Electrochemical treatment of butylated hydroxyanisole: Electrocoagulation versus advanced oxidation

Zhihong Ye, Enric Brillas, Francesc Centellas, Pere Lluís Cabot, Ignasi Sirés*

Laboratori d'Electroquímica dels Materials i del Medi Ambient, Departament de Química Física, Facultat de Química, Universitat de Barcelona, Martí i Franquès 1-11, 08028 Barcelona, Spain

ARTICLE INFO

Keywords:
Butylated hydroxyanisole
Electrochemical advanced oxidation processes
Electrocoagulation
Industrial additives
Urban wastewater

ABSTRACT

This work compares the removal of butylated hydroxyanisole (BHA), a ubiquitous antioxidant in food and pharmaceuticals, from water either by electrocoagulation (EC) with an Fe|Fe cell or H_2O_2-based electrochemical advanced oxidation processes like electrochemical oxidation (EO-H_2O_2), electro-Fenton (EF) and photoelectro-Fenton (PEF) with an air-diffusion cathode. BHA degradation by EC was very poor, whereas the dissolved organic carbon (DOC) was more effectively abated in urban wastewater. The effect of pH, number of Fe|Fe pairs and current on the EC performance was examined. The additive was also slowly degraded by EO-H_2O_2 with a RuO_2-based or BDD anode in 50 mM Na_2SO_4 solution. In the simulated matrix, BHA decay by EO-H_2O_2 was substantially enhanced owing to active chlorine generation from anodic oxidation of Cl^-, whereas the $^{\cdot}OH$-mediated oxidation at the BDD surface accounted for DOC decay. In EF and PEF, the $^{\cdot}OH$ produced in the bulk upgraded the mineralization, primordially using BDD. In raw urban wastewater at natural pH 7.9, the time course of BHA and DOC contents was affected by NOM oxidation, being accelerated in the order: EO-H_2O_2 < EF < PEF. The quickest decontamination of urban wastewater occurred in PEF at pH 3.0, because of the higher amounts of $^{\cdot}OH$ in the bulk along with UVA photolysis.

1. Introduction

Butylated hydroxyanisole (BHA, $C_{11}H_{16}O_2$, $M = 180.2\ g\ mol^{-1}$) is a synthetic phenolic antioxidant added to food, pharmaceuticals and cosmetics. It is widely used as industrial preservative since it delays or prevents the onset of lipid oxidation in such products, thereby ensuring their quantitative uptake into the body. BHA consists of a mixture of two liposoluble isomers, i.e., 2(3)-tert-butyl-4-hydroxyanisole [1,2], which can cause harmful effects on human health because of the potential formation of complexes with nucleic acids leading to DNA damage [2]. The Joint FAO/WHO Expert Committee on Food Additives (JECFA) limits the acceptable daily intake to $0.5\ mg\ kg^{-1}$ [1,2]. In Europe, BHA is limited to $200\ mg\ kg^{-1}$ on the fat content of products such as dehydrated soups and meat, gravies and bouillons [2]. Due to its frequent usage, it has been detected in rivers, groundwater and wastewater from various European and American countries, reaching up to $2\ \mu g\ L^{-1}$ [1]. However, only some few works have reported the removal of BHA from water, focusing on UVC photoloysis [3] and its combination with ozone [3] or $S_2O_8^{2-}$ [4], ozonation [3,5] and chlorination [6]. These treatments yield stable by-products like 3-tert-butyl-4,5-dihydroxyanisole, tert-butyl-1,4-hydroquinone and hydroquinone [3,6], which should be completely destroyed because they are highly toxic. Investigation on other powerful advanced oxidation processes (AOPs), not tested for BHA so far, is thus needed. The oxidation ability of AOPs is based on the large production of reactive oxygen species (ROS) like hydroxyl radical ($^{\cdot}OH$), which reacts with most organics causing their mineralization [7–9].

Several electrochemical methods (EAOPs) have been recently developed as an alternative to remove organic pollutants from water [10–15]. The leading EAOP is electrochemical oxidation (EO), which involves the generation of adsorbed hydroxyl radical (M($^{\cdot}OH$)) at the surface of an anode M, as follows [10,14,16,17]:

$$M + H_2O \rightarrow M(^{\cdot}OH) + H^+ + e^- \quad (1)$$

The oxidation power of M($^{\cdot}OH$) directly depends on the anode nature. It has been found that non-active boron-doped diamond (BDD) thin-films give rise to the most powerful oxidant (BDD($^{\cdot}OH$)) in inert electrolytes, because of its large O_2-evolution overpotential and quasi-free interaction between $^{\cdot}OH$ and BDD surface [10,16,18]. In contrast, active electrodes like dimensionally stable anodes (DSA®) accumulate much smaller amounts of M($^{\cdot}OH$) since this is quickly oxidized to the weaker oxidant MO [19,20]. In the presence of chloride, other powerful

* Corresponding author.
E-mail address: i.sires@ub.edu (I. Sirés).

https://doi.org/10.1016/j.seppur.2018.05.067
Received 19 April 2018; Received in revised form 17 May 2018; Accepted 29 May 2018
Available online 30 May 2018
1383-5866/

oxidants such as active chlorine (Cl_2/HClO/ClO^-) are also formed from reactions (2)–(4), depending on pH, competing with M($^{\cdot}$OH) to react with organics [21,22].

$$2Cl^- \rightarrow Cl_2(aq) + 2e^- \quad (2)$$

$$Cl_2(aq) + H_2O \rightarrow HClO + Cl^- + H^+ \quad (3)$$

$$HClO \leftrightarrows ClO^- + H^+ \quad pK_a = 7.54 \quad (4)$$

Setups that include an undivided cell equipped with a cathode like carbon felt [23–25], graphite [26], carbon-polytetrafluoroethylene (PTFE) in gas-diffusion mode [22,27–29], reticulated vitreous carbon [30], carbon nanotubes [31], carbon fiber [30,32] or BDD [33] allow the co-generation of weaker ROS such as H_2O_2 from O_2 reduction by reaction (5):

$$O_2(g) + 2H^+ + 2e^- \rightarrow H_2O_2 \quad (5)$$

This EAOP is known as EO with electrogenerated H_2O_2 (EO-H_2O_2). Under these conditions, addition of Fe^{2+} to the solution gives rise to electro-Fenton (EF) process [11,12,34]. In EF, homogeneous $^{\cdot}$OH are formed by Fenton's reaction (6), whose optimum pH is ca. 3, and Fe^{2+} can be regenerated upon Fe^{3+} reduction at the cathode. Organic pollutants can then be simultaneously attacked by both, M($^{\cdot}$OH) at the anode surface and $^{\cdot}$OH in the bulk. The photoelectro-Fenton (PEF) process involves the additional exposure of the solution to UV light [11–13,27]. The incident photons can photoreduce $Fe(OH)^{2+}$, the predominant Fe(III) species in the bulk, via reaction (7), as well as photodecompose photoactive intermediates like Fe(III) complexes with generated carboxylic acids according to the general reaction (8).

$$H_2O_2 + Fe^{2+} \rightarrow Fe^{3+} + {}^{\cdot}OH + OH^- \quad (6)$$

$$Fe(OH)^{2+} + h\nu \rightarrow Fe^{2+} + {}^{\cdot}OH \quad (7)$$

$$Fe(OOCR)^{2+} + h\nu \rightarrow Fe^{2+} + CO_2 + R^{\cdot} \quad (8)$$

A more classical electrochemical technology for wastewater treatment, already implemented in some companies, is electrocoagulation (EC). Its most characteristic feature is the removal of colloidal and charged particles by adsorption onto the Fe(III) or Al(III) hydroxides originated from the dissolution of Fe or Al anodes [35,36]. In the case of Fe, the anode is oxidized to Fe^{2+} via reaction (9), which is further oxidized to insoluble $Fe(OH)_3$ by O_2 gas according to reaction (10).

$$Fe \rightarrow Fe^{2+} + 2e^- \quad (9)$$

$$4Fe^{2+} + 10H_2O + O_{2(g)} \rightarrow 4Fe(OH)_{3(s)} + 8H^+ \quad (10)$$

Although EC is considered a phase separation method, earlier work has shown that neutral organic molecules can be attacked by active chlorine generated in the presence of Cl^- from reactions (2)–(4) [37], eventually producing by-products that can also adsorb onto the flocs formed along the treatment.

In this work, the performance of EC and EAOPs like EO-H_2O_2, EF and PEF to remove BHA from different water matrices was compared. Main experiments were performed in urban wastewater using an Fe anode in EC and a BDD or RuO_2-based one in EAOPs. The role of the generated flocs, oxidizing agents and/or UVA irradiation was clarified by using a 50 mM Na_2SO_4 solution and a simulated matrix with similar ionic content to the urban wastewater. The effect of several experimental parameters on BHA and dissolved organic carbon (DOC) removals was examined for each treatment.

2. Materials and methods

2.1. Reagents

BHA (99% purity) was supplied by Sigma-Aldrich as a mixture of two isomers, 10% of 2-tert-butyl-4-hydroxyanisole and 90% of 3-tert-butyl-4-hydroxyanisole. The catalyst used for the EF and PEF runs was $FeSO_4{\cdot}7H_2O$ of analytical grade from J.T. Baker. Millipore Milli-Q water with resistivity > 18.2 MΩ cm was employed for the preparation of all synthetic solutions. The salts used as electrolytes and other chemicals used for analysis were of HPLC or analytical grade from Alfa Aesar, Panreac and Merck.

2.2. Aqueous matrices employed to perform the electrochemical treatments

The trials were carried out in three different aqueous matrices:

(i) Real wastewater, which corresponded to secondary clarifier effluent from a municipal wastewater treatment plant located in Gavà-Viladecans (Barcelona, Spain). The sample was preserved at 4 °C before use. Its main characteristics were: pH = 7.9 ± 0.3; specific conductivity = 2.19 ± 0.11 mS cm^{-1}; DOC = 18.0 ± 0.9 mg L^{-1}; cations: 328 mg L^{-1} Na^+, 49 mg L^{-1} K^+, 99 mg L^{-1} Ca^{2+}, 36 mg L^{-1} Mg^{2+}, 0.19 mg L^{-1} Fe^{2+} and 36.9 mg L^{-1} NH_4^+; and anions: 117 mg L^{-1} SO_4^{2-}, 480 mg L^{-1} Cl^-, 0.85 mg L^{-1} NO_3^- and 0.79 mg L^{-1} NO_2^-.

(ii) A simulated matrix that mimicked the main ionic content of the urban wastewater, but without its natural organic matter (NOM) components (primordially, soluble humic and fulvic acids). It was prepared in Milli-Q water by adding salts that accounted for 140 mg L^{-1} SO_4^{2-}, 405 mg L^{-1} Cl^-, 309 mg L^{-1} Na^+ and 52 mg L^{-1} K^+. The resulting pH was 5.9 and the specific conductivity was 1.79 mS cm^{-1}.

(iii) A 50 mM Na_2SO_4 solution in Milli-Q water at pH 5.9, with specific conductivity of 6.9 mS cm^{-1}, which was used for a more thorough comparison.

2.3. Electrolytic systems

The electrolytic experiments were carried out in an open, undivided glass cell containing 150 mL samples under vigorous stirring provided by a magnetic follower. The cell had a double jacket for circulation of thermostated water at 35 °C.

For the EC trials, the anode and cathode were iron plates of 2.75 cm × 1.5 cm, 0.25 cm thickness. One or two electrode pairs were placed alternately in parallel with 1.0 cm separation. Before each run, the electrodes were cleaned with a 20% (v/v) H_2SO_4/water mixture, rinsed with Milli-Q water and dried to constant weight.

For the EO-H_2O_2, EF and PEF treatments, the anode of 3 cm^2 area was either a RuO_2-based plate (DSA®-Cl_2) purchased from NMT Electrodes (Pinetown, South Africa) or a BDD thin-film on a Si wafer purchased from NeoCoat (La Chaux-de-Fonds, Switzerland). The cathode was a 3 cm^2 carbon-PTFE air-diffusion electrode supplied by E-TEK (Division of De Nora N.A., Inc.), mounted as reported before [20] and fed with air at 1 L min^{-1} to continuously produce H_2O_2 from reaction (5). The interelectrode gap was close to 1.0 cm. The electrodes were initially activated/cleaned under polarization in 50 mM Na_2SO_4 at 300 mA for 180 min. The EF and PEF trials were performed in the presence of 0.50 mM Fe^{2+}, which is the optimum content found for these treatments under the present conditions. The PEF assays were ran by irradiation of the whole solution with a Philips TL/6W/08 fluorescent black light blue tube, placed at 7 cm above its surface and emitting UVA light (320–400 nm, λ_{max} = 360 nm) with irradiance of 5 W m^{-2}, as detected with a Kipp & Zonen CUV 5 radiometer.

2.4. Analytical methods

Constant current electrolyses were made with an Amel 2053 potentiostat-galvanostat. The electrical conductance was measured with a Metrohm 644 conductometer. The solution pH was determined with a Crison GLP 22 pH-meter. The active chlorine concentration was obtained by means of the *N,N*-diethyl-*p*-phenylenediamine colorimetric

method using a Shimadzu 1800 UV/Vis spectrophotometer at λ = 515 nm [38]. The concentration of anions and cations in the urban wastewater was obtained as described elsewhere [39].

Samples withdrawn from the treated aqueous matrices were microfiltered with 0.45 μm PTFE filters from Whatman before analysis. The BHA concentration was measured by reversed-phase HPLC using a Waters system, as described elsewhere [39,40]. The photodiode array detector was set at λ = 290 nm. The injected aliquot was 10 μL and the mobile phase was a 70:30 (v/v) mixture of acetonitrile and 10 mM KH_2PO_4 (pH 3.0) eluted at 1 mL min^{-1}. BHA appeared in the chromatograms at a retention time of 5.1 min.

The solution DOC was determined on a Shimadzu TOC-VCNS analyzer using the non-purgeable organic carbon method. Considering the following theoretical total mineralization reaction for BHA with a number of carbon atoms (m) of 11 and a number of exchanged electrons (n) of 56:

$$C_{11}H_{16}O_2 + 20\ H_2O \rightarrow 11\ CO_2 + 56H^+ + 56\ e^- \quad (11)$$

the mineralization current efficiency (MCE, in %) at each electrolysis time t (in h) was calculated from DOC decay (Δ(DOC), in mg L^{-1}) at given current I (in mA) by Eq. (12) [41]:

$$\%MCE = \frac{n\,F\,V\,\Delta(DOC)}{4.32 \times 10^7 mIt} \times 100 \quad (12)$$

where F is the Faraday constant (96,485 C mol^{-1}), V is the solution volume (in L), and 4.32×10^7 is a conversion factor for units homogenization (3600 s h^{-1} × 12,000 mg C mol^{-1}).

Each experiment to determine BHA and DOC decays was made in triplicate and average values are given along with the corresponding error bars (95% confidence intervals).

3. Results and discussion

3.1. Electrocoagulation of BHA in different aqueous matrices

Once the stability of the target pollutant in the whole pH range was verified, first assays were performed by treating 150 mL of 76 μM BHA. They were made in the simulated matrix or urban wastewater at their characteristic pH, applying 100 mA in an Fe|Fe cell for 60 min. In both cases, it was observed that the pH rose with electrolysis time up to a final value of 9.7 due to the excess of OH^- ions produced from cathodic water reduction, which occurred in concomitance with the Fe anode dissolution to Fe^{2+} via reaction (9).

Fig. 1a shows the change of the normalized BHA concentration during these experiments. As can be seen, the BHA content was finally reduced by 10.5% in the simulated matrix and 3.6% in urban wastewater. It is noticeable the faster removal during the first 5 min of electrolysis, which can be related to the quick adsorption of BHA onto the $Fe(OH)_3$ flocs produced, being much more remarkable in real wastewater. After that time, the partial redissolution of adsorbed BHA explains the increasing soluble content until the adsorption/desorption equilibrium was attained at about 25–30 min. The initially greater removal in urban wastewater suggests a strong influence of NOM components. They contributed to the entrapment of BHA, resulting in a larger adsorption, but at longer time the progressive cleavage of such components promoted the adsorption of resulting by-products over BHA on the $Fe(OH)_3$ flocs. As a result, the percentage of pollutant removal in real wastewater was lower. This explanation agrees with the normalized DOC decay in both media, as depicted in Fig. 1b. In the simulated matrix, the DOC profile was similar to BHA decay, with a final abatement of 10.2%. This suggests that BHA was the main organic adsorbed onto the hydroxides, with insignificant retention of its possible by-products such as those formed upon reaction with generated active chlorine [21]. The stability of these intermediates against coagulation justifies the appearance of a plateau. In contrast, in urban wastewater, a more relevant DOC decay of 24.1% was achieved, which

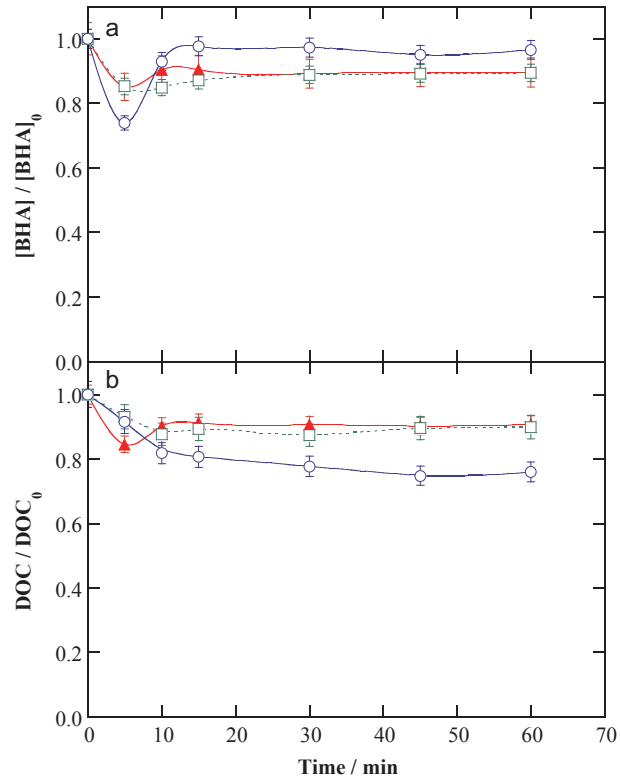

Fig. 1. Time course of the normalized (a) pollutant concentration and (b) dissolved organic carbon (DOC) for the electrocoagulation (EC) of 150 mL of (▲) 200 mg C L^{-1} (1.50 mM BHA) and (□,○) 10 mg C L^{-1} (76 μM BHA) in (▲,□) simulated matrix at natural pH 5.9 and (○) urban wastewater at natural pH 7.9, at 35 °C using an Fe|Fe pair at 100 mA.

differs from 3.6% of BHA removal shown in Fig. 1a. This means that in the latter matrix the EC treatment mainly promoted the removal of NOM components, inhibiting that of BHA.

The adsorption of BHA was checked with another assay carried out with much higher pollutant content (1.50 mM) in the simulated matrix under comparable conditions. Fig. 1a and b evidences quite similar profiles for BHA and DOC decays with electrolysis time, being also analogous to those discussed above for 76 μM BHA. As the only difference, the minimum DOC content at 5 min was more pronounced at higher BHA concentration, which suggests that the amount of pollutant adsorbed onto $Fe(OH)_3$ is regulated by its content in the matrix.

The effect of pH, number of Fe|Fe pairs and applied current on the performance of the EC treatment of 76 μM BHA spiked into urban wastewater was subsequently assessed. Fig. S1a shows a small substrate removal at all pH values tested using one Fe|Fe pair at 100 mA, slightly increasing in the order: natural pH 5.9 (3.6%) < pH 11.0 (8.8%) < pH 3.0 (11.2%). The larger disappearance at pH 3.0 can be accounted for by the attack of active chlorine (Cl_2/HClO) [37], which causes the destruction of BHA. The potential contribution of adsorption on flocs can be practically discarded at pH 3.0, confirming the low content of $Fe(OH)_3$ at pH < 3.5. The better removal at pH 11.0 could then be associated with its enhanced adsorption because of the larger formation of such flocs in alkaline medium, along with a poor destruction by ClO^-, the weakest active chlorine species [21,37]. In contrast, at pH 5.9 the initial removal by adsorption was predominant, followed by greater desorption as compared to the other pH values. The same tendency can be observed in Fig. S1b for the corresponding normalized DOC content, being reduced by 24.1%, 27.8% and 33.1% at pH 5.9, 11.0 and 3.0, respectively, owing to the increasing coagulation of NOM components. It can then be inferred that, despite the smaller formation of $Fe(OH)_3$, pH 3.0 resulted optimal for the EC treatment of BHA due to

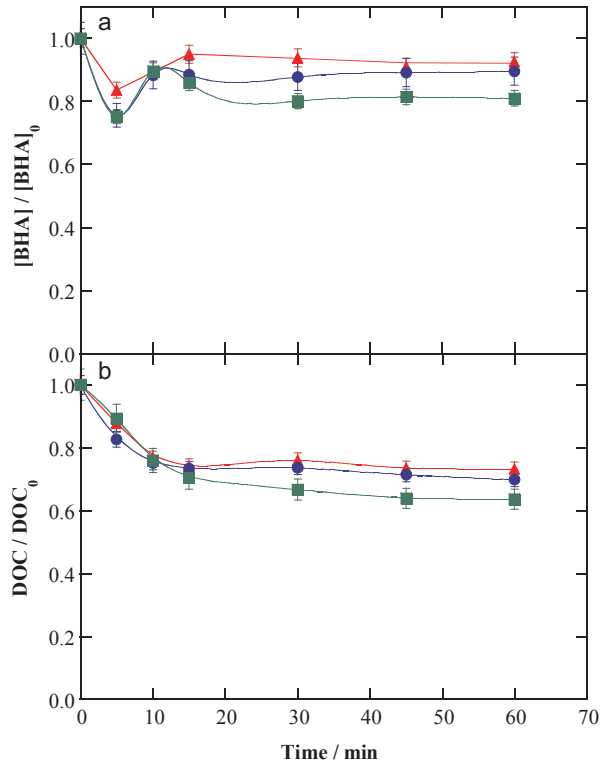

Fig. 2. Variation of normalized (a) pollutant concentration and (b) DOC with electrolysis time for the EC of 150 mL of solutions containing 10 mg C L^{-1} (76 μM BHA) in urban wastewater at natural pH 7.9 and 35 °C using two Fe|Fe pairs at a current of: (▲) 50 mA, (●) 100 mA and (■) 150 mA.

the positive contribution of generated active chlorine. However, all these results are indicative of a very poor BHA degradation during EC, since it can only be hardly destroyed by small amounts of active chlorine produced.

A system with two Fe|Fe pairs placed alternately in monopolar parallel connection was compared to the previous setup at natural pH 5.9 and 100 mA. Fig. S1a and b evidences larger BHA and DOC decays using four electrodes, achieving 10.5% and 30.2%, respectively. This can be related to the smaller current density applied to each anode since it: (i) increases the current efficiency by maximizing the Fe dissolution over the H_2O oxidation, and (ii) allows a more controlled release of Fe^{2+}, leading to a better formation and growth of hydroxides whose final size enhances the adsorption of BHA and NOM.

Based on this result, the influence of the applied current was examined between 50 and 150 mA at natural pH using the two Fe|Fe pairs. Fig. 2a highlights a large enhancement of the initial BHA removal during the first 5 min upon current increase, as expected by the greater amounts of Fe $(OH)_3$ flocs formed with ability to cause a larger adsorption. This was confirmed from the predominance of BHA adsorption over desorption at longer electrolysis time, finally yielding 7.4%, 10.5% and 19.2% removal at 50, 100 and 150 mA, respectively. The same tendency is shown in Fig. 2b, where DOC gradually disappears to attain removals of 26.8%, 30.2% and 36.4%. A smaller relative removal of NOM was then obtained as current was raised, due to the greater quantity of pollutants molecules adsorbed onto the more numerous flocs formed.

Since EC did not allow a significant decontamination of urban wastewater spiked with BHA, EAOPs were tested, as will be discussed in subsections below.

3.2. Generation of active chlorine in synthetic aqueous media by EO

Prior to the treatment of BHA in synthetic solutions, the ability of EO to accumulate active chlorine in the bulk of electrolyzed solutions was analyzed. To do this, 150 mL of a synthetic solution with 10 mM NaCl + 10 mM Na_2SO_4 at pH 5.9 were electrolyzed using a cell with a RuO_2-based or BDD anode and an Al cathode at 150 mA for 300 min. This arrangement prevents the consumption of HClO by reaction with H_2O_2, which typically occurs when an air-diffusion cathode is utilized [21,37,39]. As can be seen in Fig. S2, Cl^- ion abatement reached 88.5% with BDD and only 14.9% with the RuO_2-based anode, since the former material favors reaction (3). Conversely, with BDD the active chlorine was only accumulated up to 0.56 mM at 90 min and disappeared at 300 min, whereas all the active chlorine generated at the RuO_2-based anode remained stable, reaching a final concentration of about 1.5 mM that equated the Cl^- content lost. The total removal of active chlorine using BDD can be accounted for by its well known conversion into ClO_3^- and ClO_4^- ions [42,43]. These findings indicate that, in the EAOPs, the competitive oxidation with active chlorine will be more remarkable using a RuO_2-based anode.

3.3. Degradation of BHA in 50 mM Na_2SO_4 solution and simulated matrix by EO-H_2O_2

First, 150 mL of 76 μM BHA in both media at natural pH 5.9 were treated by EO-H_2O_2 using a RuO_2-based or BDD anode, at 100 mA for 300 min. During these tests, the solution pH decreased slightly, probably due to the formation of acidic by-products [11–13].

Fig. 3a depicts a very slow decay of the pollutant concentration in 50 mM Na_2SO_4 solution, being degraded by 63.8% and 70.7% at the end of the treatment using the RuO_2-based and BDD anode, respectively. Under these conditions, BHA reacts with adsorbed M(˙OH) originated from reaction (1) and thus, the superiority of BDD agrees with

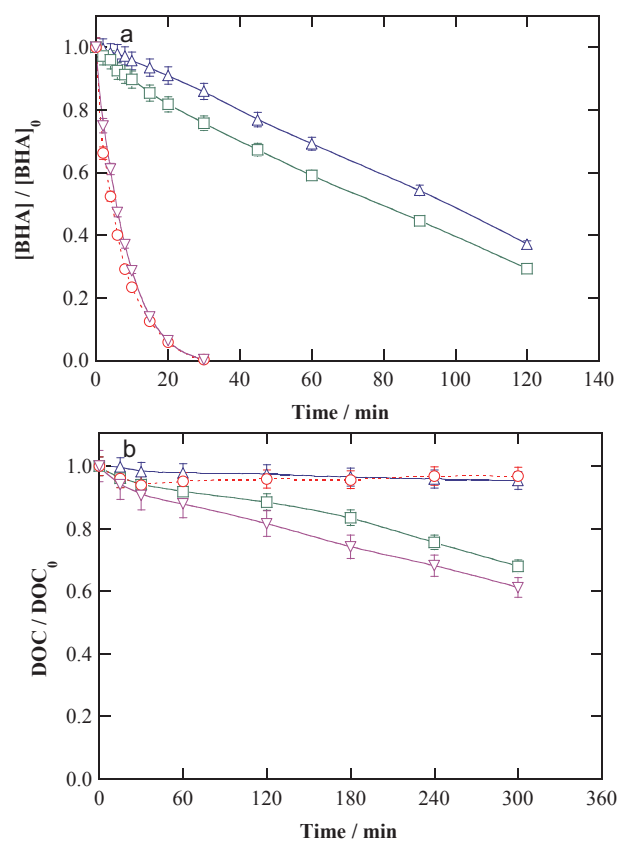

Fig. 3. Normalized (a) pollutant concentration and (b) DOC decays vs. electrolysis time for EO-H_2O_2 treatment of 150 mL of solutions containing 10 mg C L^{-1} (76 μM BHA) at pH 5.9 and 35 °C using a cell with a 3 cm^2 air-diffusion cathode. Aqueous matrix: (△,□) 50 mM Na_2SO_4 and (○,▽) simulated matrix. Anode: 3 cm^2 (△,○) RuO_2-based and (□,▽) BDD. Applied current: 100 mA.

Table 1
Pseudo-first-order rate constant for BHA degradation along with the corresponding *R*-squared and selected percentage of DOC removal, as determined for the degradation of 150 mL of 10 mg C L^{-1} (76 μM BHA) in different water matrices and pH values at 35 °C by various EAOPs using a cell with an air-diffusion cathode at 100 mA.

Method	Anode	pH	k_1 (min^{-1})	R^2	% DOC removal at 300 min
50 mM Na_2SO_4 solution					
EO-H_2O_2	RuO_2-based	5.9	7.6×10^{-3}	0.987	4.6
	BDD	5.9	9.6×10^{-3}	0.992	32.0
Simulated matrix					
EO-H_2O_2	RuO_2-based	5.9	0.14	0.997	3.3
	BDD	5.9	0.14	0.996	38.8
EF[a]	RuO_2-based	5.9	0.66	0.984	5.0
	BDD	5.9	0.57	0.985	66.5
PEF[a,b]	RuO_2-based	5.9	0.82	0.995	51.3
	BDD	5.9	0.87	0.986	81.2
Urban wastewater[c]					
EO-H_2O_2	RuO_2-based	7.9	7.2×10^{-2}	0.993	5.9
	BDD	7.9	8.5×10^{-2}	0.998	45.5
EF[a]	RuO_2-based	3.0	0.34[d]	–	13.8
	BDD	3.0	0.44[d]	–	57.1
	RuO_2-based	7.9	0.11	0.993	9.2
	BDD	7.9	0.13	0.995	47.8
PEF[a,b]	RuO_2-based	3.0	0.53[d]	–	23.7
	BDD	3.0	0.61[d]	–	65.8
	RuO_2-based	7.9	0.16	0.993	10.4
	BDD	7.9	0.19	0.994	51.0

[a] With 0.50 mM Fe^{2+} as catalyst.
[b] Under UVA irradiation.
[c] Total initial DOC: 28 mg C L^{-1}.
[d] Estimated as average value within the first 2 min of electrolysis.

the expected higher oxidation power of BDD(˙OH) as compared to RuO_2(˙OH) [10,16]. The concentration decays were analyzed using kinetic equations related to simple reaction orders, and excellent fits were obtained for a pseudo-first-order process, as shown in Fig. S3a. Alternatively, the very slow concentration decays in the EO-H_2O_2 processes could suggest the occurrence of a pseudo-zero-order kinetics. The apparent rate constants (k_1) along with the squared linear regression coefficients (R^2) are summarized in Table 1. This behavior can be interpreted considering that a constant but small M(˙OH) concentration attacks the pollutant once it arrives at the anode surface.

A very different trend can be observed in Fig. 3a in the simulated matrix, where the contaminant concentration fell very rapidly, practically independent of the anode nature, to be below the limit of quantification at about 30 min. From the good linear regressions (Fig. S3a), the k_1-values in the simulated matrix were 18.4-fold and 14.6-fold higher than those determined in 50 mM Na_2SO_4 solution using RuO_2-based and BDD anodes, respectively (see Table 1). The greater BHA decay in the simulated matrix can be accounted for by the attack of a low and constant active chlorine (HClO) concentration formed from reactions (3) and (4), whose action was much quicker than the simultaneous attack of M(˙OH).

The mineralization role of generated oxidants was analyzed from the DOC abatement in each medium under the aforementioned conditions. Fig. 3b reveals a very small DOC abatement (< 5%) using a RuO_2-based anode (see Table 1). This means that RuO_2(˙OH), alone in 50 mM Na_2SO_4 solution or in concomitance with active chlorine in the simulated matrix, is unable to destroy most of the intermediates (chlorinated and/or non-chlorinated) formed. In contrast, BDD(˙OH) was much more powerful and thus, the use of BDD yielded 32.0% and 38.8% DOC decay in such media, respectively. Consequently, this anode is preferable in EO-H_2O_2, although only a partial mineralization was achieved, being slightly superior in the presence of Cl^- ion because BDD(˙OH) is able to gradually mineralize chlorinated by-products. Accordingly, the MCE values determined for these experiments,

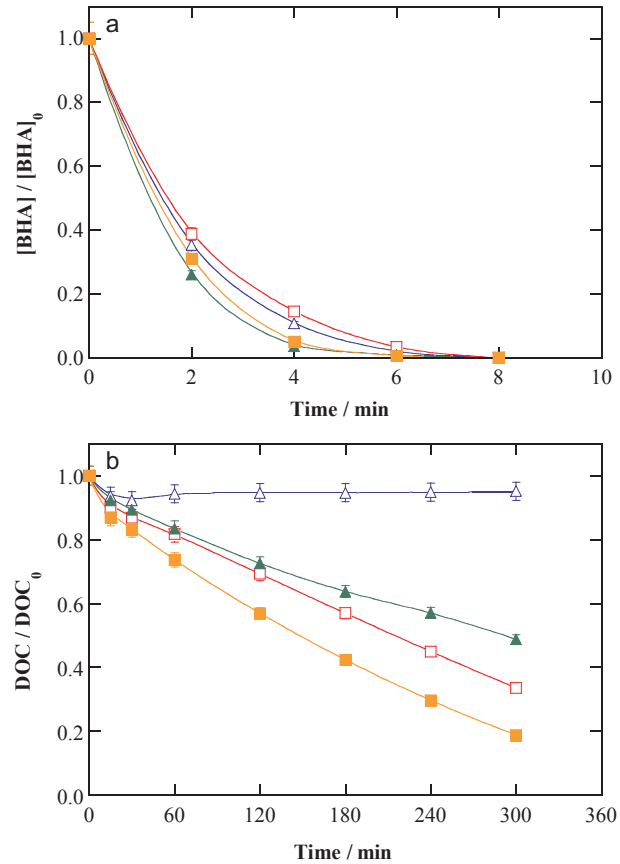

Fig. 4. Change of normalized (a) pollutant concentration and (b) DOC with electrolysis time for the treatment of 150 mL of 10 mg C L^{-1} (76 μM BHA) in a simulated matrix with 0.50 mM Fe^{2+} at pH 5.9 and 35 °C using a cell with an air-diffusion cathode. Method: (△,□) Electro-Fenton (EF) and (▲,■) photo-electro-Fenton (PEF) under UVA irradiation with a 6 W lamp. Anode: (△,▲) RuO_2-based and (□,■) BDD. Applied current: 100 mA.

illustrated in Fig. S4a, were below 0.15% using the RuO_2-based anode and between 1.1% and 1.3% with BDD, demonstrating the large recalcitrance of BHA by-products.

3.4. Degradation of BHA in synthetic aqueous solutions by EF and PEF

Once assessed the oxidation power of M(˙OH) and active chlorine with BHA and its by-products as target molecules, the performance of ˙OH formed in the bulk from Fenton's reaction (6) and UVA irradiation was analyzed under EF and PEF conditions in the presence of 0.50 mM Fe^{2+} as catalyst. Fig. 4a shows a similar BHA decay in all cases, with total removal in only 8 min. This is indicative of a very quick reaction of this pollutant with ˙OH, much faster than the concomitant attack of M(˙OH) and active chlorine (see Fig. 3a). The concentration decays of Fig. 4a obeyed to a pseudo-first-order reaction, as can be seen in Fig. S3b, which means that BHA is removed by small and constant amounts of mixed oxidants, i.e., RuO_2(˙OH) or BDD(˙OH), ˙OH as the prevalent one, and active chlorine when Cl^- is present. A look to Table 1 allows inferring that the k_1-values in EF and PEF were 4.1–4.7-fold and 5.9–6.2-fold higher than those found in EO-H_2O_2, respectively, regardless of the anode employed. The slightly faster BHA decay in PEF can be related to its oxidation by the additional ˙OH amount induced by photoreduction reaction (7).

A surprising result was obtained for the mineralization by EF process with the RuO_2-based anode in the simulated matrix, as can be observed in Fig. 4b. DOC was abated by less than 6%, meaning that most of the by-products cannot be transformed into CO_2 upon combined

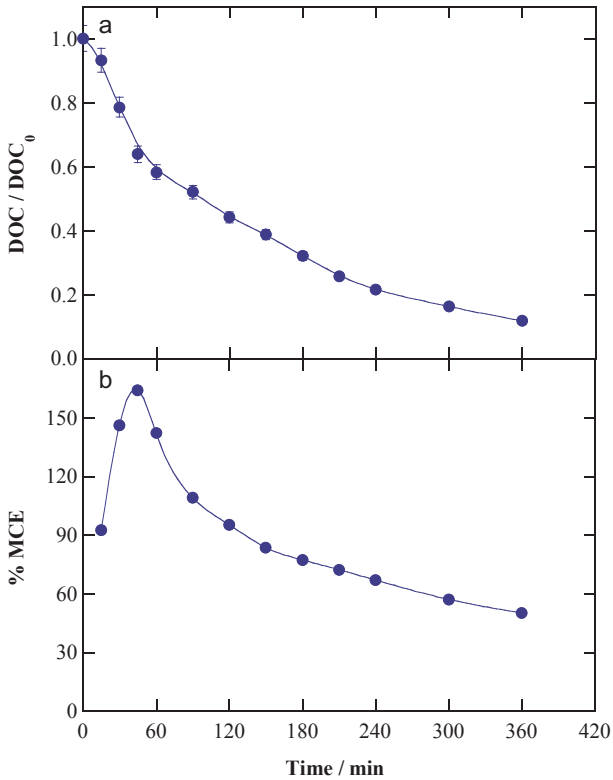

Fig. 5. Time course of the (a) normalized DOC and (b) mineralization current efficiency for the PEF degradation of 150 mL of 200 mg C L^{-1} (1.50 mM BHA) in a simulated matrix with 0.50 mM Fe^{2+} at pH 5.9 and 35 °C using a BDD/air-diffusion cell at 100 mA.

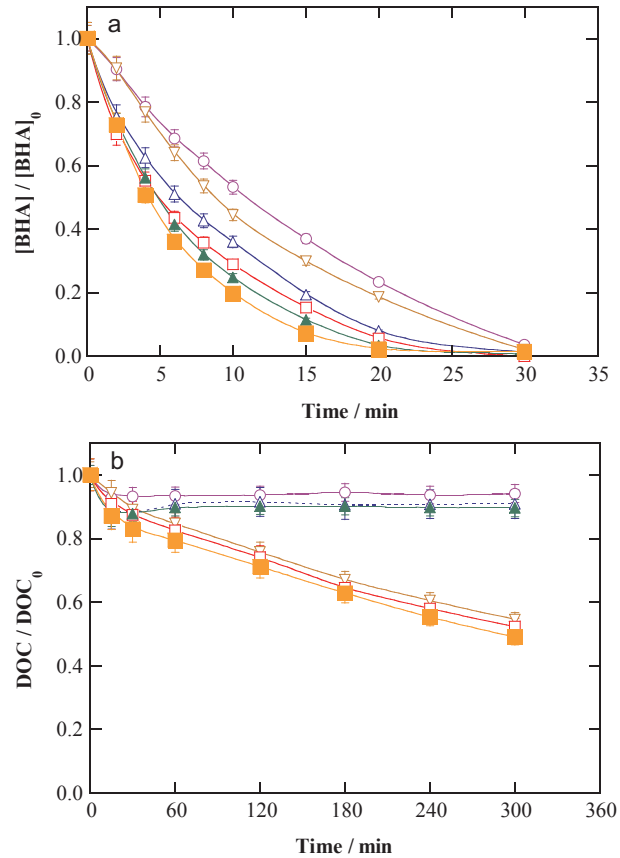

Fig. 6. Normalized (a) pollutant concentration and (b) DOC decays vs. electrolysis time for the treatment of 150 mL of 76 μM BHA, spiked into urban wastewater (total DOC of 28 mg L^{-1}) at natural pH 7.9 and 35 °C using a cell with an air-diffusion cathode. Method: (○,▽) EO-H_2O_2, (△,□) EF with 0.50 mM Fe^{2+} and (▲,■) PEF with 0.50 mM Fe^{2+} and 6-W UVA lamp. Anode: (○,△,▲) RuO_2-based and (▽,□,■) BDD. Applied current: 100 mA.

action of RuO_2(˙OH), active chlorine and ˙OH. In contrast, the analogous treatment under PEF conditions yielded 51.3% DOC removal at 300 min (see Fig. 4b and Table 1), as expected if a large quantity of photoactive by-products were generated and mineralized by UVA radiation. Using BDD anode, Fig. 4b shows a gradual drop of DOC in EF and PEF, achieving 66.5% and 81.2% removal (see Table 1). This confirms the very effective oxidation of by-products by BDD(˙OH) in EF. In turn, this yields photoactive by-products that can be more quickly photolyzed by UVA photons. Nevertheless, low MCE were determined in all these Fenton-based treatments (see Fig. S4b), with a final value of 2.8% for the most powerful treatment, i.e., PEF with BDD.

The final low MCE values in all the EAOPs are not surprising, because it is well known that their efficiency diminishes largely as the organic load becomes smaller [10–15]. To show this feature for BHA removal in the simulated matrix, an additional trial was performed by treating 150 mL of a highly concentrated solution (1.50 mM BHA) with 0.50 mM Fe^{2+} by PEF using a BDD/air-diffusion cell at 100 mA. A fast DOC abatement under these conditions can be seen in Fig. 5a, where 88.2% mineralization is reached at 360 min. Fig. 5b illustrates the MCE-time plot for this assay. An initial rise up to a 164.2% at 60 min can be observed, whereupon it dropped drastically down to 50.1%. This means that increasing contents of easy-to-mineralize by-products are formed at the beginning of PEF, whereas the generation of more recalcitrant molecules along with the reduction of the organic matter content cause the progressive MCE decay at long time [10]. Note that theoretical MCE values greater than 100% are feasible in this system, since oxidants are generated not only at the anode but also from H_2O_2 produced at the cathode.

3.5. Degradation of BHA in urban wastewater by EAOPs

The study of BHA removal by EAOPs was extended to urban wastewater as matrix by spiking this compound at 76 μM. First, 150 mL of the prepared solutions were treated at natural pH 7.9 at 100 mA for 300 min, with addition of Fe^{2+} as catalyst in EF and PEF. Fig. 6a illustrates the occurrence of a rapid BHA concentration abatement in all the EAOPs, with total removal at about 30 min. Hence, the disappearance in EO-H_2O_2 was somewhat slower than that described in the simulated matrix (see Fig. 3a), but much more difficult in the case of EF and PEF (see Fig. 4a). This slower decay in urban wastewater can be accounted for by the parallel attack of generated oxidants onto NOM components. The k_1-values for these trials are collected in Table 1, as determined from the kinetic analysis depicted in Fig. S3c. They highlight an increasing relative oxidation in the order: EO-H_2O_2 < EF < PEF, always being superior for the BDD anode. This trend is expected because BDD(˙OH) has higher oxidation power than RuO_2(˙OH). The attack of these species and active chlorine onto BHA in EO-H_2O_2 is reinforced by ˙OH formed from Fenton's reaction (6) in EF and, to a larger extent, by additional ˙OH produced from photolytic reaction (7) in PEF. Note that the k_1-values for EO-H_2O_2 in urban wastewater were halved as compared to the simulated matrix (see Table 1), as expected if some of the M(˙OH) and active chlorine react with NOM. In contrast, the data of Table 1 reveal a significant decrease of k_1 between 4.4-fold and 6.0-fold for the EF and PEF treatments in urban wastewater. This can be due to the smaller ˙OH production at its natural pH 7.9, if compared to the simulated matrix at pH 5.9 [11–13], along with the consumption of part of this radical by reaction with NOM.

Fig. 6b shows surprising profiles for DOC decays during the above experiments when a RuO_2-based anode was employed. As can be seen, the urban wastewater contaminated with BHA was very poorly

decontaminated, attaining 10.4% as maximal (PEF process, see Table 1). This differs from the PEF behavior found in the simulated matrix, where DOC was reduced by 51.3% under comparable conditions (see Fig. 4b and Table 1). This agrees with the low ˙OH production at pH 7.9, inhibiting to a large extent the generation of photoactive intermediates that could have been removed by UVA light. This fact was confirmed from the DOC abatement using the BDD anode. Fig. 6b depicts a quite similar mineralization rate using this anode in all processes, slightly increasing as EO-H_2O_2 < EF < PEF (see also Table 1). This means that the main oxidant of BHA by-products and NOM is BDD (˙OH) in all these treatments, with much smaller participation of ˙OH, active chlorine and UVA light. Comparison of Fig. 4b and 6b, as well as data of Table 1, allows inferring that the percentage of DOC decay was greater in urban wastewater for EO-H_2O_2, but superior in the simulated matrix for EF and PEF. However, since the initial DOC was much greater in urban wastewater (28 mg C L^{-1} vs. 10 mg C L^{-1}), a larger amount of organic carbon was always removed from the real matrix. This informs about the excellent ability of the EAOPs with a BDD anode to mineralize the NOM of urban wastewater at natural pH.

To better understand the oxidative role of ˙OH in EF and PEF, the comparative treatments of 76 μM BHA in urban wastewater with 0.50 mM Fe^{2+} were carried out at pH 3.0, where the rate of Fenton's reaction (6) becomes optimal [11–13]. Operating at 100 mA, Fig. 7a highlights a very fast removal of the pollutant, which disappeared in 4–6 min in all cases. These decays were much more rapid than in the analogous EF and PEF performed in the simulated matrix at pH 5.9 (see Fig. 4a), which corroborates the quick reaction of BHA with generated ˙OH in the bulk. When DOC removal was determined, a very poor

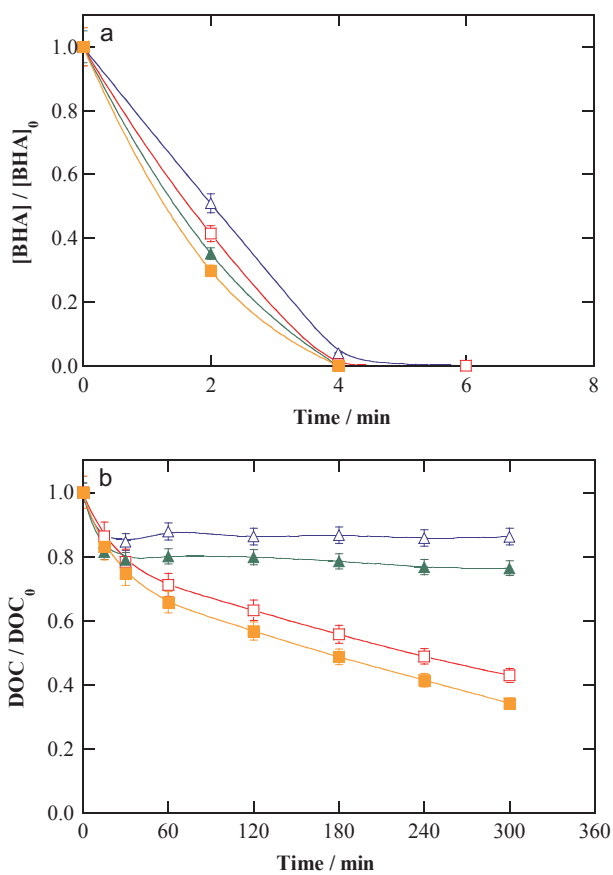

Fig. 7. Variation of normalized (a) pollutant concentration and (b) DOC with electrolysis time for the degradation of 150 mL of 76 μM BHA, spiked into urban wastewater (total DOC of 28 mg L^{-1}) with 0.50 mM Fe^{2+} at natural pH 3.0 and 35 °C using a cell with an air-diffusion cathode by applying 100 mA. Method: (△,□) EF and (▲,■) PEF. Anode: (△,▲) RuO_2-based and (□,■) BDD.

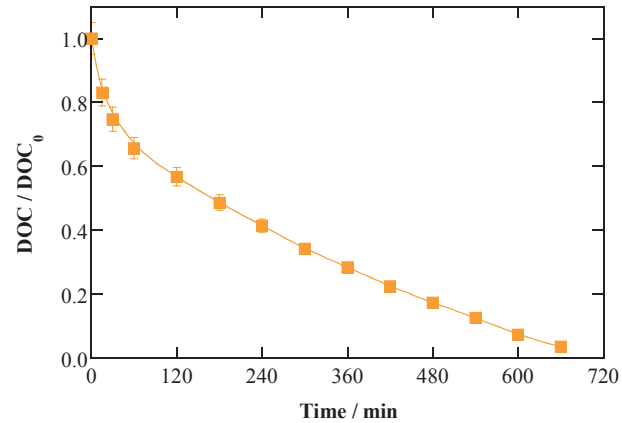

Fig. 8. Change of normalized DOC with electrolysis time for the PEF treatment of 150 mL of 10 mg C L^{-1} (76 μM BHA), spiked into urban wastewater with 0.50 mM Fe^{2+} at pH 3.0 and 35 °C using a BDD/air-diffusion cell at 100 mA.

mineralization was obtained again using the RuO_2-based anode (see Fig. 7b), although superior to that found at natural pH 7.9. Thus, for the powerful PEF, DOC was reduced by 23.7% at pH 3.0 vs. 10.4% at pH 7.9 (see Table 1). This suggests that the oxidation of BHA and NOM by ˙OH enhances the formation of photoactive intermediates that can be destroyed by UVA light. Fig. 7b also shows the beneficial use of BDD anode due to the pre-eminent attack of BDD(˙OH), since 47.8% and 65.8% DOC abatements were obtained after 300 min of EF and PEF, respectively. The latter photoassisted Fenton-based method with BDD is then the best EAOP for BHA and/or NOM mineralization in a simulated matrix and urban wastewater within all the range.

To end, the high oxidation power of the above PEF process with BDD at pH 3.0 was assessed by prolonging the electrolysis time until almost total mineralization was achieved. Fig. 8 evidences that 97.0% of DOC removal was attained after 660 min of this treatment at 100 mA, as expected if the simultaneous action of BDD(˙OH), active chlorine, ˙OH and UVA radiation can effectively destroy all the organic molecules contained in urban wastewater.

4. Conclusions

EC is not a convenient technology to remove BHA from water, as demonstrated with an Fe|Fe cell from the poor pollutant and DOC abatements in different aqueous media. The adsorption of BHA onto Fe$(OH)_3$ flocs was relatively high within the first minutes, but at longer time it underwent a progressive redissolution. The best results were obtained at pH 3.0 due to the simultaneous oxidation with generated active chlorine. The use of several Fe|Fe pairs and higher current promoted a larger coagulation. The treatment of BHA in a 50 mM Na_2SO_4 solution by EO-H_2O_2 revealed a slow pollutant abatement using RuO_2-based and BDD anodes, but with much greater mineralization rate using the latter anode due to the higher oxidation power of BDD(˙OH). In a simulated matrix, the oxidation of BHA by active chlorine enhanced its removal in EO-H_2O_2, but BDD(˙OH) had the pre-eminent role during DOC abatement. The same effect was found during EF and PEF treatments in the simulated matrix, where the production of ˙OH favored the BHA decay and, to a smaller extent, its mineralization, always being BDD the most suitable anode. The degradation profiles in urban wastewater at natural pH 7.9 spiked with BHA confirmed the superiority of PEF with BDD, since the RuO_2-based anode was unable to mineralize BHA, NOM and all by-products. The quicker removals in urban wastewater at pH 3.0 confirmed the important role of ˙OH in the bulk, favoring the formation of photoactive intermediates that were more rapidly photodecomposed by UVA photons. Almost total mineralization with 97.0% DOC removal was achieved at pH 3.0 in PEF with BDD after 660 min at 100 mA.

Acknowledgements

The authors thank financial support from project CTQ2016-78616-R (AEI/FEDER, EU) and PhD scholarship awarded to Z. Ye (State Scholarship Fund, CSC, China).

Appendix A. Supplementary material

Supplementary data associated with this article can be found, in the online version, at https://doi.org/10.1016/j.seppur.2018.05.067.

References

[1] K.H.G. Freitas, O. Fatibello-Filho, Simultaneous determination of butylated hydroxyanisole (BHA) and butylated hydroxytoluene (BHT) in food samples using a carbon composite electrode modified with $Cu_3(PO_4)_2$ immobilized in polyester resin, Talanta 81 (2010) 1102–1108.
[2] F. Shahidi, P. Ambigaipalan, Phenolics and polyphenolics in foods, beverages and spices: antioxidant activity and health effects – a review, J. Funct. Foods 18 (2015) 820–897.
[3] T.K. Lau, W. Chu, N. Graham, Reaction pathways and kinetics of butylated hydroxyanisole with UV, ozonation, and UV/O_3 processes, Water Res. 41 (2007) 765–774.
[4] T.K. Lau, W. Chu, N.J.D. Graham, The aqueous degradation of butylated hydroxyanisole by UV/$S_2O_8^{2-}$: study of reaction mechanisms via dimerization and mineralization, Environ. Sci. Technol. 41 (2007) 613–619.
[5] W. Chu, T.K. Lau, Ozonation of endocrine disrupting chemical BHA under the suppression effect by salt additive-with and without H_2O_2, J. Hazard. Mater. 144 (2007) 249–254.
[6] R. Rodil, J.B. Quintana, R. Cela, Oxidation of synthetic phenolic antioxidants during water chlorination, J. Hazard. Mater. 199–200 (2012) 73–81.
[7] M.A. Oturan, J.-J. Aaron, Advanced oxidation processes in water/wastewater treatment: principles and applications. A review, Crit. Rev. Env. Sci. Technol. 44 (2014) 2577–2641.
[8] M. Antonopoulou, E. Evgenidou, D. Lambropoulou, I. Konstantinou, A review on advanced oxidation processes for the removal of taste and odor compounds from aqueous media, Water Res. 53 (2015) 215–234.
[9] G. Lofrano, R. Pedrazzani, G. Libralato, M. Carotenuto, Advanced oxidation processes for antibiotics removal: a review, Curr. Org. Chem. 21 (2017) 1–14.
[10] M. Panizza, G. Cerisola, Direct and mediated anodic oxidation of organic pollutants, Chem. Rev. 109 (2009) 6541–6569.
[11] E. Brillas, I. Sirés, M.A. Oturan, Electro-Fenton process and related electrochemical technologies based on Fenton's reaction chemistry, Chem. Rev. 109 (2009) 6570–6631.
[12] I. Sirés, E. Brillas, M.A. Oturan, M.A. Rodrigo, M. Panizza, Electrochemical advanced oxidation processes: today and tomorrow, Environ. Sci. Pollut. Res. 21 (2014) 8336–8367.
[13] C.A. Martínez-Huitle, M.A. Rodrigo, I. Sirés, O. Scialdone, Single and coupled electrochemical processes and reactors for the abatement of organic water pollutants: a critical review, Chem. Rev. 115 (2015) 13362–13407.
[14] H. Särkkä, A. Bhatnagar, M. Sillanpää, Recent developments of electro-oxidation in water treatment – a review, J. Electroanal. Chem. 754 (2015) 46–56.
[15] F.C. Moreira, R.A.R. Boaventura, E. Brillas, V.J.P. Vilar, Electrochemical advanced oxidation processes: a review on their application to synthetic and urban wastewaters, Appl. Catal. B: Environ. 202 (2017) 217–261.
[16] F. Bonfatti, S. Ferro, F. Lavezzo, M. Malacarne, G. Lodi, A. De Battisti, Electrochemical incineration of glucose as a model organic substrate. I. Role of the electrode material, J. Electrochem. Soc. 146 (1999) 2175–2179.
[17] B. Boye, P.A. Michaud, B. Marselli, M.M. Dieng, E. Brillas, C. Comninellis, Anodic oxidation of 4-chlorophenoxyacetic acid on synthetic boron-doped diamond electrodes, New Diamond Front. Carbon Technol. 12 (2002) 63–72.
[18] P. Cañizares, R. Paz, C. Sáez, M.A. Rodrigo, Electrochemical oxidation of alcohols and carboxylic acids with diamond anodes. A comparison with other advanced oxidation processes, Electrochim. Acta 53 (2008) 2144–2153.
[19] O. Scialdone, A. Galia, S. Randazzo, Oxidation of carboxylic acids in water at IrO_2-Ta_2O_5 and boron doped diamond anodes, Chem. Eng. J. 174 (2011) 266–274.
[20] J.R. Steter, E. Brillas, I. Sirés, On the selection of the anode material for the electrochemical removal of methylparaben from different aqueous media, Electrochim. Acta 222 (2016) 1464–1474.
[21] A. Thiam, M. Zhou, E. Brillas, I. Sirés, Two-step mineralization of Tartrazine solutions: study of parameters and by-products during the coupling of electrocoagulation with electrochemical advanced oxidation processes, Appl. Catal. B: Environ. 150–151 (2014) 116–125.
[22] J.R. Steter, E. Brillas, I. Sirés, Solar photoelectro-Fenton treatment of a mixture of parabens spiked into secondary treated wastewater effluent at low input current, Appl. Catal. B: Environ. 224 (2018) 410–418.
[23] A. Dirany, I. Sirés, N. Oturan, A. Özcan, M.A. Oturan, Electrochemical treatment of the antibiotic sulfachloropyridazine: kinetics, reaction pathways, and toxicity evolution, Environ. Sci. Technol. 46 (2012) 4074–4082.
[24] A. El-Ghenymy, R.M. Rodríguez, E. Brillas, N. Oturan, M.A. Oturan, Electro-Fenton degradation of the antibiotic sulfanilamide with Pt/carbon-felt and BDD/carbon-felt cells. Kinetics, reaction intermediates, and toxicity assessment, Environ. Sci. Pollut. Res. 21 (2014) 8368–8378.
[25] M.S. Yahya, N. Oturan, K. El Kacemi, M. El Karbane, C.T. Aravindakumar, M.A. Oturan, Oxidative degradation study on antimicrobial agent ciprofloxacin by electro-Fenton process: kinetics and oxidation products, Chemosphere 117 (2014) 447–454.
[26] O. Scialdone, E. Corrado, A. Galia, I. Sirés, Electrochemical processes in macro and microfluidic cells for the abatement of chloroacetic acid from water, Electrochim. Acta 132 (2014) 15–24.
[27] A. Bedolla-Guzman, I. Sirés, A. Thiam, J.M. Peralta-Hernández, S. Gutiérrez-Granados, E. Brillas, Application of anodic oxidation, electro-Fenton and UVA photoelectro-Fenton to decolorize and mineralize acidic solutions of Reactive Yellow 160 azo dye, Electrochim. Acta 206 (2016) 307–316.
[28] A. Galia, S. Lanzalaco, M.A. Sabatino, C. Dispenza, O. Scialdone, I. Sirés, Crosslinking of poly(vinylpyrrolidone) activated by electrogenerated hydroxyl radicals: a first step towards a simple and cheap synthetic route of nanogel vectors, Electrochem. Commun. 62 (2016) 64–68.
[29] S. Lanzalaco, I. Sirés, M.A. Sabatino, C. Dispenza, O. Scialdone, A. Galia, Synthesis of polymer nanogels by electro-Fenton process: investigation of the effect of main operation parameters, Electrochim. Acta 246 (2017) 812–822.
[30] B. Ramírez-Pereda, A. Álvarez-Gallegos, J.G. Rangel-Peraza, Y.A. Bustos-Terrones, Kinetics of Acid Orange 7 oxidation by using carbon fiber and reticulated vitreous carbon in an electro-Fenton process, J. Environ. Manage. 213 (2018) 279–287.
[31] A. Khataee, A. Akbarpour, B. Vahi, Photoassisted electrochemical degradation of an azo dye using Ti/RuO_2 anode and carbon nanotubes containing gas-diffusion cathode, J. Taiwan Inst. Chem. Eng. 45 (2014) 930–936.
[32] A. Wang, J. Qu, H. Liu, J. Ru, Mineralization of an azo dye Acid Red 14 by photoelectro-Fenton process using an activated carbon fiber cathode, Appl. Catal. B: Environ. 84 (2008) 393–399.
[33] K. Cruz-González, O. Torres-López, A. García-León, E. Brillas, A. Hernández-Ramírez, J.M. Peralta-Hernández, Optimization of electro-Fenton/BDD process for decolorization of a model azo dye wastewater by means of response surface methodology, Desalination 286 (2012) 63–68.
[34] M. Panizza, M.A. Oturan, Degradation of Alizarin Red by electro-Fenton process using a graphite-felt cathode, Electrochim. Acta 56 (2011) 7084–7087.
[35] M.A. Sandoval, R. Fuentes, J.L. Nava, I. Rodríguez, Fluoride removal from drinking water by electrocoagulation in a continuous filter press reactor coupled to a flocculator and clarifier, Sep. Purif. Technol. 134 (2014) 163–170.
[36] H. Lin, Y. Wang, J. Niu, Z. Yue, Q. Huang, Efficient sorption and removal of perfluoroalkyl acids (PFAAs) from aqueous solution by metal hydroxides generated in situ by electrocoagulation, Environ. Sci. Technol. 49 (2015) 10562–10569.
[37] E. Bocos, E. Brillas, M.A. Sanromán, I. Sirés, Electrocoagulation: simply a phase separation technology? The case of bronopol compared to its treatment by EAOPs, Environ. Sci. Technol. 50 (2016) 7679–7686.
[38] APWA, AWWA, WEF, Standard Methods for the Examination of Water and Wastewater, 21st ed. Method Number 4500-Cl Chlorine (residual)–G. DPD Colorimetric Method, American Public Health Association, Washington D.C., 2005, pp. 4-67 and 4-68.
[39] C. Ridruejo, C. Salazar, P.L. Cabot, F. Centellas, E. Brillas, I. Sirés, Electrochemical oxidation of anesthetic tetracaine in aqueous medium. Influence of the anode and matrix composition, Chem. Eng. J. 326 (2017) 811–819.
[40] R. Salazar, E. Brillas, I. Sirés, Finding the best Fe^{2+}/Cu^{2+} combination for the solar photoelectro-Fenton treatment of simulated wastewater containing the industrial textile dye Disperse Blue 3, Appl. Catal. B: Environ. 115–116 (2012) 107–116.
[41] E.J. Ruiz, A. Hernández-Ramírez, J.M. Peralta-Hernández, C. Arias, E. Brillas, Application of solar photoelectro-Fenton technology to azo dyes mineralization: effect of current density, Fe^{2+} and dye concentration, Chem. Eng. J. 171 (2011) 385–392.
[42] D.K. Hubler, J.C. Baygents, B.P. Chaplin, J. Farrell, Understanding chlorite, chlorate and perchlorate formation when generating hypochlorite using boron doped diamond film electrodes, ECS Trans. 58 (2014) 21–32.
[43] H. Zöllig, A. Remmele, C. Fritzsche, E. Morgenroth, K.M. Udert, Formation of chlorination byproducts and their emission pathways in chlorine mediated electrooxidation of urine on active and nonactive type anodes, Environ. Sci. Technol. 49 (2015) 11062–11069.

SUPPLEMENTARY MATERIALS

Electrochemical treatment of butylated hydroxyanisole: Electrocoagulation versus advanced oxidation

Zhihong Ye, Enric Brillas, Francesc Centellas, Pere Lluís Cabot, Ignasi Sirés*

Laboratori d'Electroquímica dels Materials i del Medi Ambient, Departament de Química Física, Facultat de Química, Universitat de Barcelona, Martí i Franquès 1-11, 08028 Barcelona, Spain

Corresponding author: * i.sires@ub.edu (I. Sirés)

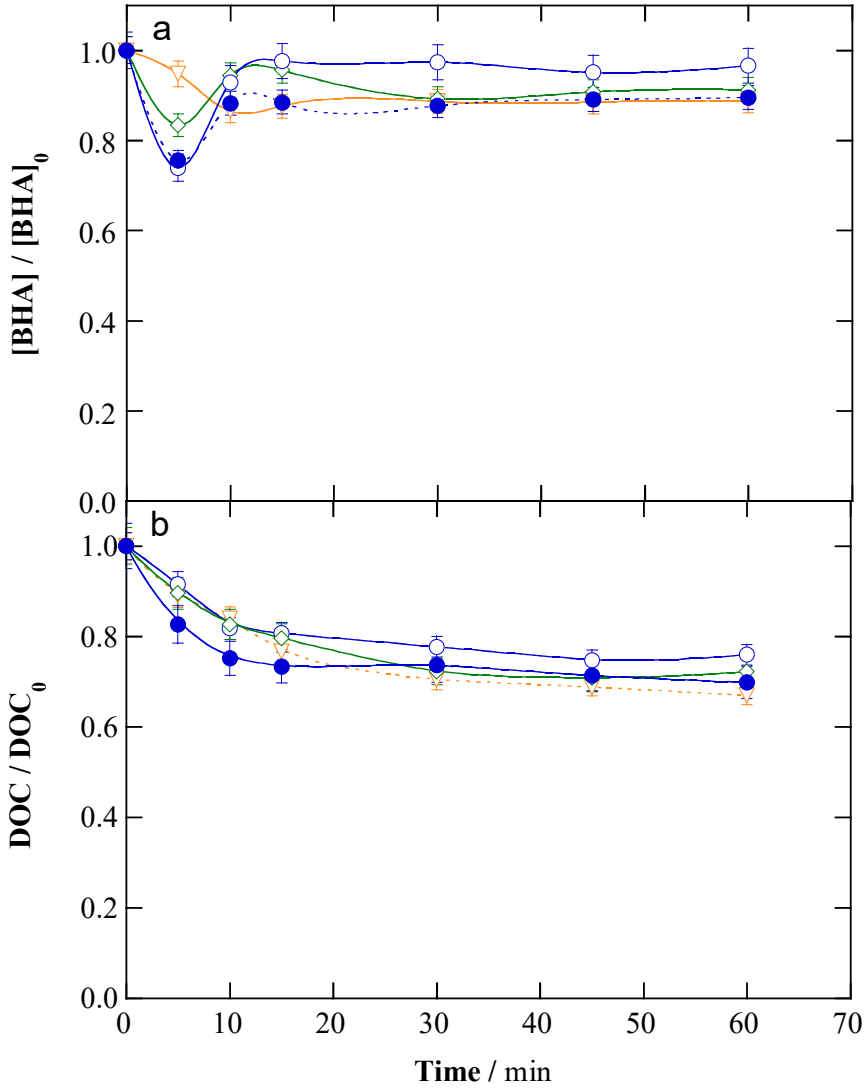

Fig. S1. Change of the normalized (a) pollutant concentration and (b) DOC with electrolysis time for the EC of 150 mL of 10 mg C L^{-1} (76 μM BHA), spiked into urban wastewater at 35 ºC. One Fe|Fe pair at pH: (▽) 3.0, (○) 7.9 (natural pH) and (◇) 11.0. (●) Two Fe|Fe pairs at natural pH. Applied current: 100 mA.

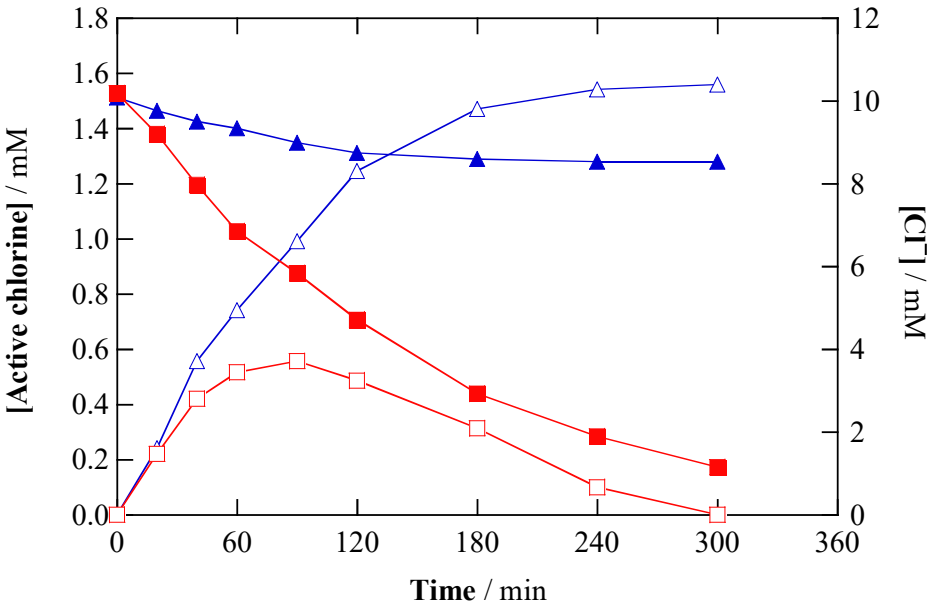

Fig. S2. Variation of (▲,■) Cl^- and (△,□) active chlorine during the EO of 150 mL of a 10 mM NaCl + 10 mM Na_2SO_4 mixture at pH 5.9 and 35 ºC using an electrolytic cell with (▲,△) RuO_2-based or (■,□) BDD anode and an Al cathode, at 150 mA.

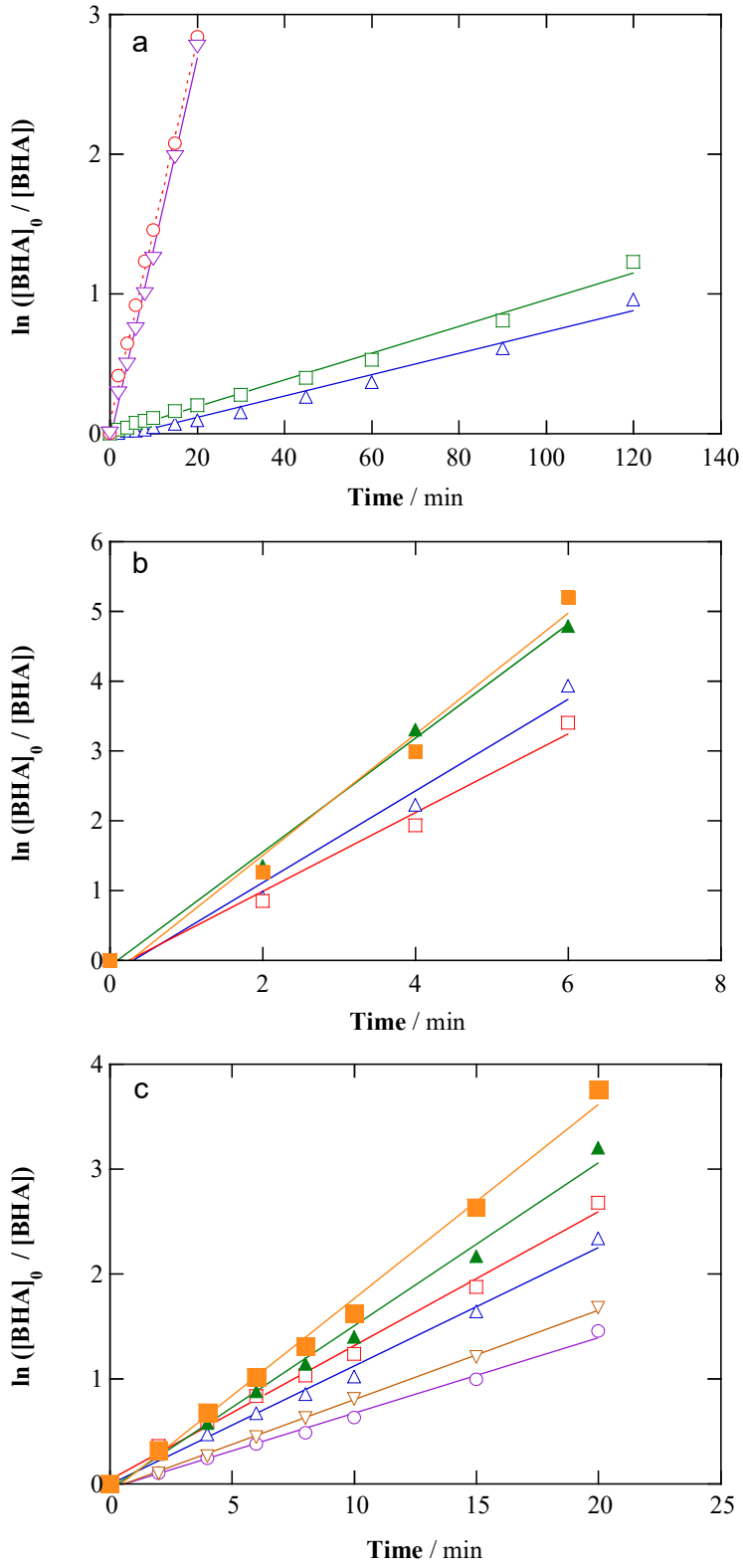

Fig. S3. Kinetic analysis for the BHA concentration decays of (a) Fig. 3a, (b) Fig. 4a and (c) Fig. 6a assuming a pseudo-first-order behavior.

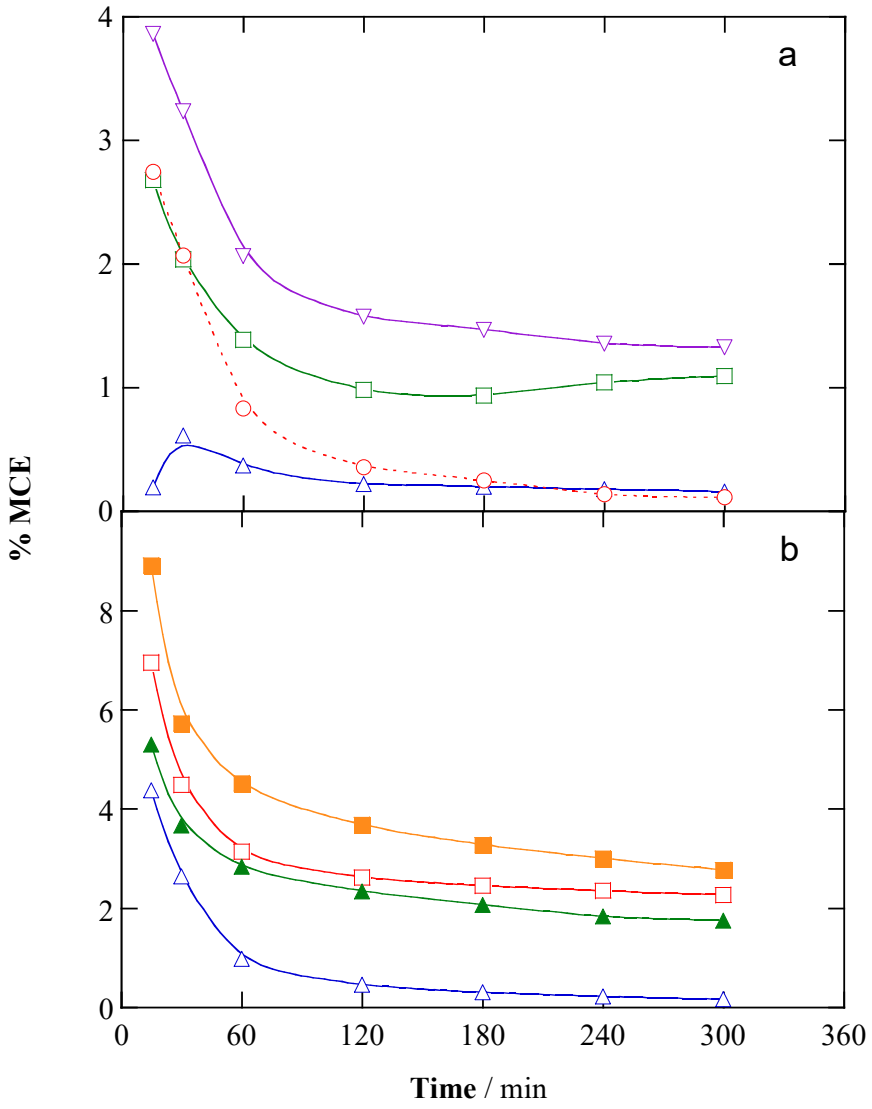

Fig. S4. Mineralization current efficiency vs. electrolysis time for the assays of (a) Fig. 3b and (b) Fig. 4b.

Appendix II

Photoelectro-Fenton as post-treatment for electrocoagulated benzophenone-3-loaded synthetic and urban wastewater

Journal of Cleaner Production 208 (2019) 1393–1402

Contents lists available at ScienceDirect

Journal of Cleaner Production

journal homepage: www.elsevier.com/locate/jclepro

Photoelectro-Fenton as post-treatment for electrocoagulated benzophenone-3-loaded synthetic and urban wastewater

Zhihong Ye, Juliana R. Steter, Francesc Centellas, Pere Lluís Cabot, Enric Brillas*, Ignasi Sirés**

Laboratori d'Electroquímica dels Materials i del Medi Ambient, Department de Química Física, Facultat de Química, Universitat de Barcelona, Martí I Franquès 1-11, 08028, Barcelona, Spain

ARTICLE INFO

Article history:
Received 16 June 2018
Received in revised form
20 September 2018
Accepted 15 October 2018
Available online 18 October 2018

Keywords:
Benzophenone-3
Electrocoagulation
Electro-Fenton
Oxidation products
Photoelectro-Fenton
Wastewater treatment

ABSTRACT

The removal of benzophenone-3 (BP-3), a ubiquitous pollutant in municipal wastewater treatment facilities, was optimal by means of a sequential electrocoagulation (EC)/UVA photoelectro-Fenton (PEF) treatment. Overall mineralization was attained upon combination of EC (Fe/Fe cell, 15 mA cm^{-2}, 20 min) with PEF (boron-doped diamond/air-diffusion cell, 33.3 mA cm^{-2}, 720 min), being superior to EC/electro-Fenton (EF) and requiring shorter time than single PEF. In EC, an Al/Al cell yielded the largest removal of BP-3 in a simulated matrix at pH 11.0 due to precipitation of its neutral form caused by a substantial pH drop, with optimum current density of 15 mA cm^{-2}. EC of BP-3-loaded urban wastewater at natural pH was quite effective also with a Fe/Fe cell, being preferred since it provided the required metal catalyst for subsequent treatment. Among the electrochemical advanced oxidation processes tested, PEF was superior to electrochemical oxidation with electrogenerated H_2O_2 (EO-H_2O_2) and EF, especially when using the boron-doped diamond instead of a RuO_2-based anode, due to the oxidation of generated active chlorine and hydroxyl radicals, along with the photolytic action of UVA irradiation. GC-MS revealed the formation of 14 cyclic products in PEF treatment, two of them being also formed during EC.

1. Introduction

Benzophenone-3 (BP-3, $C_{14}H_{10}O_3$, 2-hydroxy-4-methoxybenzophenone, $M = 228.25$ g mol^{-1}), also called oxybenzone, is widely employed as sunscreen agent due to its large ability to absorb UV light, limited photodecomposition and high lipophilicity (Abdallah et al., 2015). It is an active ingredient in lotions and personal care products including bath oils, soaps, mascaras and anti-aging creams (Downs et al., 2016). A release of 14,000 ton y^{-1} of BP-3 into the aquatic environment is estimated via wash-off from skin and clothes or indirectly via solid waste landfill leachate and wastewater treatment facilities (WWTFs), thereby being detected in natural water bodies, soil, fish and even in human milk (Gago-Ferrero et al., 2013; Downs et al., 2016). It has reached up to 7800 ng L^{-1} in untreated municipal wastewater, being reduced to 700 ng L^{-1} upon treatment (Liu et al., 2012). It has also been detected within the 10–20 ng g^{-1} range in sewage sludge and 3–21 ng g^{-1} in fish (Liu et al., 2012). Its potential toxicity arises from endocrine disruption, genotoxicant actuation, procarcinogenic activity, mutagenic ability of derivatives and skin penetration in humans (Downs et al., 2016).

The water solubility of BP-3 (p$K_a = 9.65$ (Gilberta et al., 2016; Li et al., 2016)) is very high at pH > 10 where its anionic form predominates, whereas its neutral form prevailing at pH ≤ 9 has very low solubility (<5 mg L^{-1}). Effective removal of BP-3 from synthetic aqueous matrices at pH 3–9 has been attained by biodegradation (Liu et al., 2012), ultrasound (Zúñiga-Benítez et al., 2016c), ozonation and peroxone oxidation (Gago-Ferrero et al., 2013), membrane catalytic ozonation (Guo et al., 2016), photo-Fenton (Zúñiga-Benítez et al., 2016b), TiO_2/photocatalysis (Zúñiga-Benítez et al., 2016a) and UV/H_2O_2 (Gong et al., 2015). Most of these works only determined the decay kinetics of BP-3 at concentrations ≤1 mg L^{-1}, but did not assess the formation of hydroxylated and/or chlorinated derivatives, potentially more toxic than BP-3 (Li et al., 2016).

Recently, electrochemical advanced oxidation processes (EAOPs) have received great attention for wastewater remediation because they cause large mineralization of aqueous solutions

* Corresponding author.
** Corresponding author.
E-mail addresses: brillas@ub.edu (E. Brillas), i.sires@ub.edu (I. Sirés).

https://doi.org/10.1016/j.jclepro.2018.10.181
0959-6526/

containing organic pollutants (Asghar et al., 2015; El-Ashtoukhy et al., 2017; Silva et al., 2018). The most typical EAOP is electrochemical oxidation (EO), which can be utilized with electrogenerated H_2O_2 (EO-H_2O_2) (Panizza and Cerisola, 2009; Sirés et al., 2014; Särkkä et al., 2015). Fenton-based EAOPs such as electro-Fenton (EF) (Brillas et al., 2009; Martínez-Huitle et al., 2015; Moreira et al., 2017) and photoelectro-Fenton (PEF) (Brillas et al., 2009; Brillas, 2014) are even more powerful. Their good performance results from the generation of the powerful oxidant hydroxyl radical (•OH). UVA light employed to irradiate the solution in PEF photolyzes photoactive intermediates, accelerating their conversion into CO_2 and making it the most efficient EAOP (Wang et al., 2008; Salazar et al., 2012; Urzúa et al., 2013). However, main drawbacks for PEF application include long time needed to destroy large contents of organic matter and poor light penetration when solutions contain colloidal particles. To overcome these limitations, the use of electrocoagulation (EC) as pre-treatment has been recently envisaged (Thiam et al., 2014; Bocos et al., 2016). EC involves the in situ generation of coagulants from dissolution of an appropriate sacrificial anode (Fe or Al), forming flocs that precipitate and adsorb colloids and organics. Partial oxidation of the organic matter with generated •OH and active chlorine (Cl_2/HClO/ClO^-) in the presence of Cl^- seems also feasible (Ghernaout et al., 2011; Ghernaout, 2013; Demirbas and Kobya, 2017). To date, sequential EC/EAOPs have only been examined by the dye Tartrazine (Thiam et al., 2014) and the antiseptic bronopol (Bocos et al., 2016) in synthetic solutions with ultrapure water. However, the viability of EC/EAOPs coupling has not been tested yet for urban wastewater, which contains natural organic water (NOM) that may exert some influence on the degradation of organic pollutants. Under these conditions, the treatment at natural pH can be performed, relying on the good performance of heterogeneous Fenton-like systems (Cheng et al., 2016, 2018a; 2018b).

The present article reports the first EC/EAOPs coupling for the removal of an organic pollutant spiked into an effluent from primary wastewater treatment. BP-3 was selected as model molecule, being determined its decay kinetics and total organic carbon (TOC) removal. First, the EC treatment of BP-3 in a simulated matrix with the same ionic composition as the urban wastewater, at pH 11.0, was tested with cells containing Al or Fe anode to elucidate the role of the BP-3 acid-base equilibrium. Analogous EC trials were made using the real effluent at natural pH, where the neutral form was predominant. Then, the single EO-H_2O_2, EF and PEF treatments of urban wastewater at natural pH spiked with BP-3 were studied using a RuO_2-based or boron-doped diamond (BDD) anode and an air-diffusion cathode. Intermediates of BP-3 formed by EC and PEF were identified by gas chromatography-mass spectrometry (GC-MS), leading to a route for BP-3 removal. Finally, sequential EC/EF and EC/PEF of BP-3-loaded urban wastewater were examined to compare their performance with that of single EAOPs.

2. Experimental

2.1. Chemicals

BP-3 (98% purity) was provided by Sigma-Aldrich. The salts used as supporting electrolytes were purchased from Panreac and Merck. Analytical grade $FeSO_4 \cdot 7H_2O$ used as catalyst was purchased from J.T. Baker. High-quality Millipore Milli-Q water (>18 MΩ cm) was used to prepare all synthetic solutions. Other chemicals were of HPLC or analytical grade from Panreac and Merck.

2.2. Urban wastewater

The real sample was collected from the primary clarifier of a WWTF located near Barcelona. This facility treated 50,000 $m^3\,d^{-1}$ of mixed urban and industrial wastewater. After collection, the urban wastewater was preserved in a refrigerator at 4 °C and was used in the next 15 d to prevent anaerobic degradation.

According to Table S1, the primary treated effluent had pH ~8.0 and low conductivity, total carbon (TC), TOC and TN. Na^+ prevailed over cations like K^+, Ca^{2+} and Mg^{2+}, with insignificant total iron content. Among anions, Cl^- predominated over SO_4^{2-}, both at relatively high contents. Table S2 summarizes the characteristics of 18 organic compounds detected for the raw wastewater by GC-MS, which included 17 cyclic (3 of them aromatic and 5 with N as heteroatom) and 1 aliphatic compounds. Worth mentioning, our target pollutant BP-3 was also contained in the real effluent.

2.3. Electrolytic systems

The electrolytic trials were made in an undivided, open glass cell with a double jacket for circulation of thermostated water at 35 °C, under vigorous stirring by a magnetic follower. This temperature was selected because it is the maximum value to operate without significant water evaporation from the solution, thus obtaining the best reactivities during the degradation trials with reproducible measurements. In EC, the anode was an iron or aluminum plate with immersed area of 10 cm^2. The same materials as well as stainless steel (AISI 304 or AISI 316L) plates of the same area were tested as cathode. The electrode pairs were placed alternately in parallel at distance of 1.0 cm. In EAOPs, the anode was a RuO_2-based plate from NMT Electrodes (Pinetown, South Africa) or a BDD thin film on Si supplied by NeoCoat (La Chaux-de-Fonds, Switzerland). The cathode was a carbon-PTFE air-diffusion electrode from E-TEK (Division of De Nora N.A., Inc.), mounted as described elsewhere (Steter et al., 2016) and fed with air pumped at 1 $L\,min^{-1}$ for continuous H_2O_2 generation. The area of all electrodes was 3 cm^2 and their distance was 1.0 cm, being prepared as described elsewhere prior to first use (Thiam et al., 2014). PEF was made under UVA irradiation ($\lambda_{max} = 360$ nm, 5 $W\,m^{-2}$) provided by a Philips fluorescent black light blue tube.

Fresh solutions of pollutant contained 30 mg C L^{-1} BP-3 (0.178 mM) in simulated matrix (pH 11.0, stirring for 2 h) or 4 mg C L^{-1} BP-3 (0.024 mM) in urban wastewater (natural pH, stirring for 12 h). In the sequential EC/EAOPs, the EC-treated solutions were centrifuged for 10 min at 4100 rpm to remove the sludge and easily collect the supernatant for post-treatment.

2.4. Analytical procedures

The electrical conductance and pH were measured on a Metrohm 644 conductometer and a Crison GLP 22 pH-meter. Trials were carried out at constant current density (j) using an Amel 2053 potentiostat-galvanostat. H_2O_2 concentration was determined using a Shimadzu 1800 UV/vis spectrophotometer at 25 °C following a standard methodology (Welcher, 1975). Samples withdrawn from treated solutions were microfiltered (0.45 μm) before analysis. TOC was determined on a Shimadzu TOC-VCNS analyzer. Total nitrogen and concentration of anions and cations, including total iron, were obtained as reported elsewhere (Ridruejo et al., 2017).

BP-3 content at $\lambda = 277$ nm and short-linear aliphatic carboxylic acids at $\lambda = 210$ nm were determined by reversed-phase and ion-exclusion HPLC using a Waters LC, as previously reported (Salazar

et al., 2012; Ridruejo et al., 2017). In the former case, an acetonitrile/10 mM KH_2PO_4 (50:50 v/v) mixture at 1 mL min^{-1} was used as mobile phase and BP-3 was detected at retention time (t_r) = 19.2 min, with limit of quantification = 0.15 mg L^{-1} and limit of detection = 0.05–0.10 mg L^{-1}.

Table S3 summarizes all the electrochemical characteristics of the single and sequential assays performed with simulated matrix, Na_2SO_4 and urban wastewater. All experiments were made in duplicate and average results are given, with the corresponding error bars in figures.

The organic components of the raw urban wastewater and electrolyzed solutions under EC and PEF conditions were extracted with CH_2Cl_2 (3 × 25 mL). The resulting organic solution was dried over anhydrous Na_2SO_4, filtered and concentrated to ca. 1 mL to be analyzed by GC-MS using optimized analytical conditions (Salazar et al., 2012) and a NIST05 MS library for interpretation. The analysis was made with an Agilent Technologies system composed of a 6890 N gas chromatograph with a 7683B series injector and a 5975 mass spectrometer in electron impact mode at 70 eV. A nonpolar Agilent J&W DB-5 or a polar HP INNOWax column of 0.25 μm, 30 m × 0.25 mm, was employed. The temperature ramp was: 36 °C for 1 min, 5 °C min^{-1} up to 300 °C and hold time 10 min. The inlet, source and transfer line operated at 250, 230 and 280 °C.

3. Results and discussion

3.1. EC treatment of BP-3 in a simulated matrix at pH 11.0

Comparative EC trials were made with 150 mL of 30 mg C L^{-1} BP-3 in simulated matrix at pH 11.0 using an Al or Fe anode. The composition of the simulated matrix mimicked the main ion content of urban wastewater (Table S1), with 1.8 mS cm^{-1} conductivity. Cathodes of the same materials as well as of AISI 304 or AISI 316L were employed to test the performance of each anode/cathode cell for 60 min at 10 mA cm^{-2}, without pH regulation. Fig. 1a and b shows a gradual decay of normalized TOC with time in all cases, but profiles depended on each material. For each anode, the best anode/cathode combinations were Al/Al and Fe/Fe, attaining 47.0% and 17.7% TOC removals with final pH of 9.5 and 10.8 and conductivities of 2.2–2.6 mS cm^{-1}. Moreover, BP-3 concentration decays reached 67.2% and 28.9% for these two cells.

Al^{3+} and Fe^{2+} are released to the bulk from sacrificial Al and Fe anodes via reactions (1) and (2) (Thiam et al., 2014; Bocos et al., 2016; Steter et al., 2016). At the cathode, H_2 gas and OH^- are produced from reaction (3), favoring the formation of insoluble metal hydroxides from reactions (4)–(6) (Ghernaout, 2013; Khandegar and Saroha, 2013; Brillas and Martínez-Huitle, 2015).

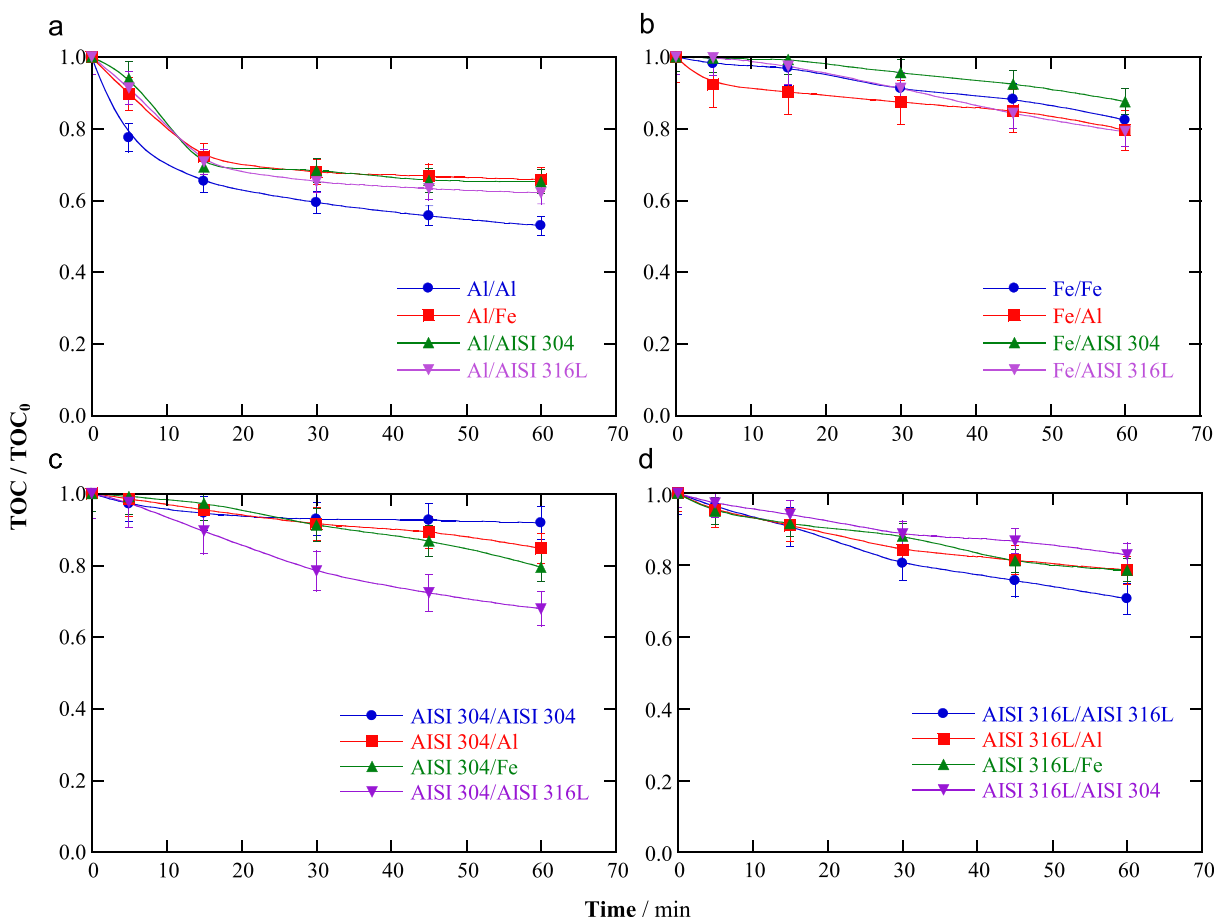

Fig. 1. Normalized TOC decay for the EC treatment of 150 mL of 30 mg C L^{-1} BP-3 in simulated matrix at pH 11.0 and 35 °C using anode/cathode cells (10 cm^2 electrode area) at 10 mA cm^{-2}. Anode: (a) Al and (b) Fe.

$$Al_{(s)} \rightarrow Al^{3+}{}_{(aq)} + 3e^- \quad (1)$$

$$Fe_{(s)} \rightarrow Fe^{2+}{}_{(aq)} + 2e^- \quad (2)$$

$$2H_2O + 2e^- \rightarrow H_{2(g)} + 2OH^- \quad (3)$$

$$Al^{3+}{}_{(aq)} + 3OH^- \rightarrow Al(OH)_{3(s)} \quad (4)$$

$$Fe^{2+}{}_{(aq)} + 2OH^- \rightarrow Fe(OH)_{2(s)} \quad (5)$$

$$4Fe^{2+}{}_{(aq)} + 10H_2O + O_{2(g)} \rightarrow 4Fe(OH)_{3(s)} + 8H^+{}_{(aq)} \quad (6)$$

The insoluble $Al(OH)_3$ and $Fe(OH)_n$ flocs with large surface area precipitate removing pollutants by surface complexation, electrostatic attraction or sweep coagulation in Al/Al and Fe/Fe cells (Ghernaout, 2013; Khandegar and Saroha, 2013). It is noticeable that higher BP-3 and TOC abatements were obtained using AISI 304/AISI 316L and AISI 316L/AISI 316L cells as compared to Fe/Fe cell (data not shown), due to the enhanced coagulation ability by the production of hydroxides from other metallic species contained in sacrificial stainless steel anodes, e.g., Cr-, Ni-, Mn- and Mo-based. However, the potential toxicity of these hydroxides prevent the large use of such anodes in EC. Fig. 1a and b also evidences the influence of the cathode material on TOC decay, suggesting the coexistence of reductive routes where BP-3 and its byproducts can be transformed at the cathode surface into compounds with different tendency to be coagulated.

The greater BP-3 and TOC abatements using the Al/Al cell could be plausibly ascribed to the substrate precipitation from the pH decrease at 9.5 ($<pK_a = 9.65$). Under such circumstances, the neutral form predominates, which is much more insoluble than its anionic counterpart present at pH 11.0. This was confirmed through an analogous EC trial upon pH regulated to 11.0. After 60 min, 27.1% BP-3 decay and 2.95% TOC reduction were found, values much lower than those obtained without pH regulation.

The effect of j on the performance of EC with Al/Al and Fe/Fe cells was further examined. It is expected that increasing j produces greater amounts of coagulants by acceleration of electrode reactions (1)–(3), enhancing the removal of BP-3 and its products. Fig. 2a–d reveals BP-3 removals of 67.6%–71.4% and 57.0%–60.1% using Al/Al and Fe/Fe cells at 15 and 20 mA cm^{-2}. TOC abatements reached 54.1% for Al/Al cell at 15 mA cm^{-2} and 44.3% for the Fe/Fe one at 20 mA cm^{-2}, slightly >41.3% found for 15 mA cm^{-2}. The fact that the Al/Al cell worked better at 15 mA cm^{-2} may be due to smaller BP-3 precipitation by the concomitant pH drop. The BP-3 removal was always larger than TOC abatement, meaning that BP-3 is rather transformed into byproducts by oxidation and reduction reactions, which are not so easily coagulated by $Al(OH)_3$ and $Fe(OH)_n$ flocs and become accumulated in the bulk.

To better clarify the superiority of the Al/Al cell to remove BP-3 at pH 11.0, the influence of the pollutant content was studied at 10–30 mg C L^{-1} at the optimum 15 mA cm^{-2}. Fig. S1a illustrates similar maximum BP-3 removal of 53.2%–58.3% starting at 10 and 20 mg C L^{-1}, raising substantially to 67.6% at 30 mg C L^{-1}. This agrees with the aforementioned precipitation of this molecule due to pH drop, occurring to larger extent at greater initial concentration. Similarly, Fig. S1b depicts a progressive increase of TOC decay

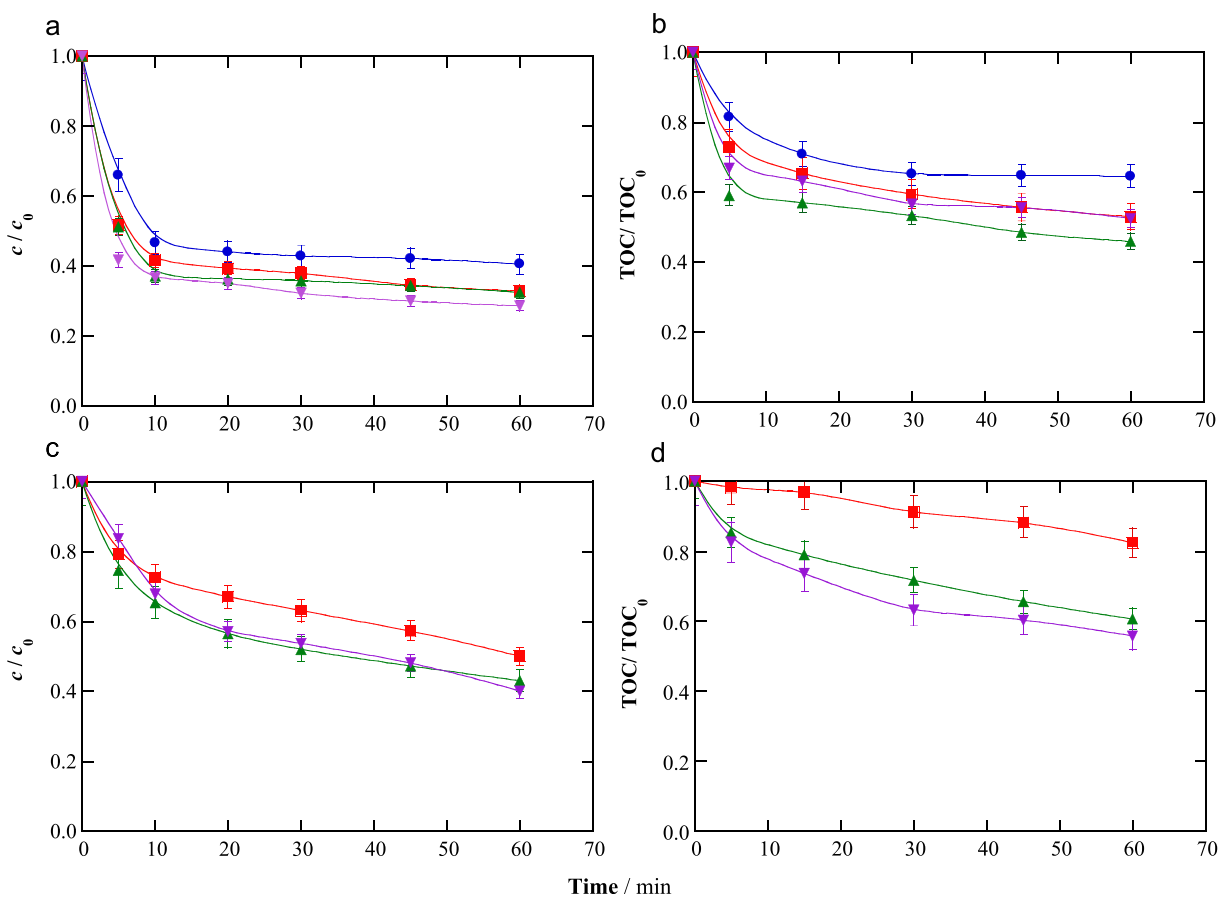

Fig. 2. Normalized (a,c) BP-3 concentration and (b,d) TOC abatements for the solution of Fig. 1 of pH 11.0, treated by EC with (a,b) Al/Al and (c,d) Fe/Fe cells. Current density: (●) 5 mA cm^{-2}, (■) 10 mA cm^{-2}, (▲) 15 mA cm^{-2} and (▼) 20 mA cm^{-2}.

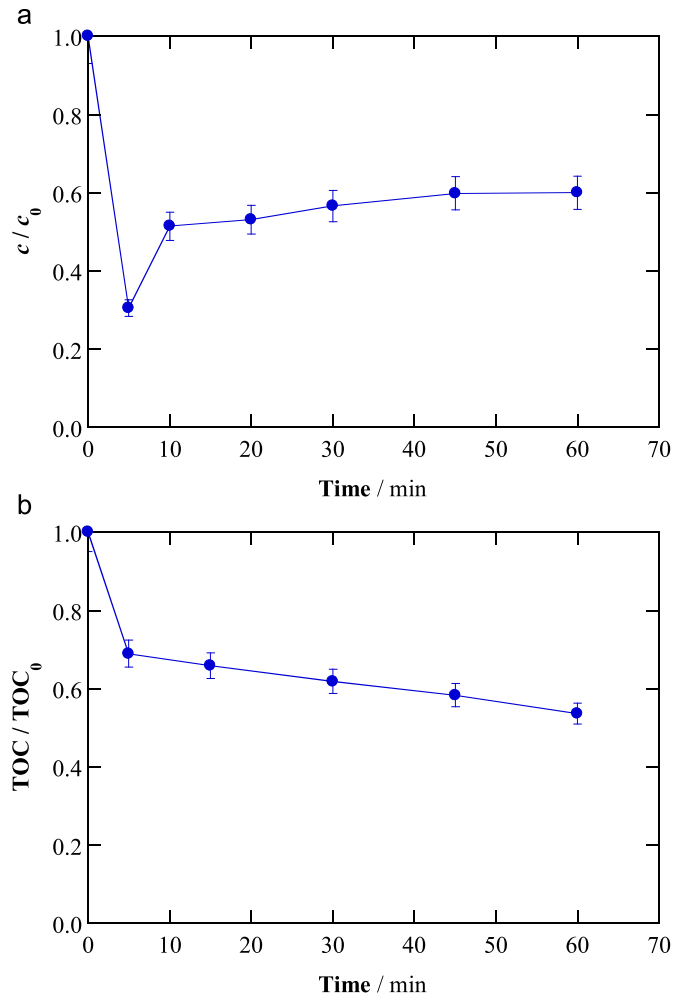

Fig. 3. Normalized (a) BP-3 concentration and (b) TOC removals for the EC treatment of 150 mL of 4 mg C L^{-1} BP-3 in urban wastewater at natural pH 8.0 and 35 °C using Fe/Fe cell at 15 mA cm^{-2}.

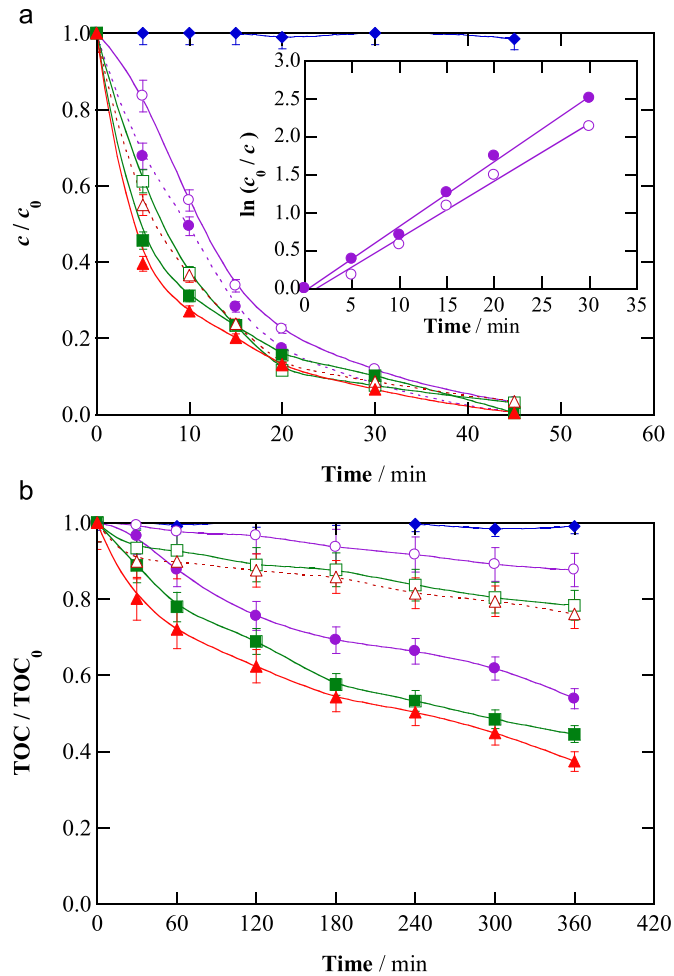

Fig. 4. Change of normalized (a) BP-3 concentration and (b) TOC for the treatment of 100 mL of 4 mg C L^{-1} BP-3 in urban wastewater at natural pH 8.0 and 35 °C using (○,□,△) RuO_2-based/air-diffusion and (●,■,▲) BDD/air-diffusion cells at 33.3 mA cm^{-2}. Method: (○,●) EO-H_2O_2, (□,■) EF with 10 mg L^{-1} Fe^{2+} and (△,▲) PEF with 10 mg L^{-1} Fe^{2+} and 6 W UVA irradiation. (◆) Only 6 W UVA irradiation.

from 39.7% to 54.1%, being again lower than BP-3 removal due to the formation of stable reduced and oxidized products.

Comparative EC trials using Na_2SO_4 were made to confirm the above behavior. With Fe/Fe cell, Fig. S2a and b reveals much larger BP-3 and TOC removals in simulated matrix as compared to EC in Na_2SO_4, since 57.0% and 39.4% were attained in the former medium, much larger than 41.3% and 20.1% in the latter one, which can be ascribed to additional oxidation with ClO^-. In Na_2SO_4, BP-3 also disappeared more quickly than TOC, as result of the simultaneous cathodic reduction and even by •OH-mediated oxidation of BP-3 (Thiam et al., 2014; Bocos et al., 2016). A smaller effect of the matrix was observed using Al/Al cell, where ca. 67% BP-3 was removed from both media due to its precipitation upon pH drop, whereas TOC was abated more largely in the simulated matrix (54.1% vs. 44.6%), indicating the coagulation of products oxidized by ClO^-.

3.2. EC treatment of BP-3 in urban wastewater

The EC treatment of BP-3 was extended to an urban wastewater matrix at natural pH 8.0 (Table S1) using the Fe/Fe cell, envisaging its further combination with EAOPs. These tests were made with 4 mg C L^{-1} BP-3 (saturated solution of the neutral form) at 15 mA cm^{-2}.

Fig. 3a shows a dramatic BP-3 decay of 69.6% during the first 5 min of EC process, which was followed by an increase of BP-3 concentration so that only 40% was effectively removed from 20 min of electrolysis. In the first stage, the formation of complexes of the neutral form of BP-3 with some components of urban wastewater stimulate the rapid coagulation with $Fe(OH)_n$. The subsequent unexpected behavior arises from the gradual degradation of such natural components, causing the release of BP-3 entrapped in $Fe(OH)_n$ flocs to the bulk. The same trend was found using several pairs of Fe electrodes in parallel at 15 mA cm^{-2} each (data not shown), reinforcing the idea of BP-3 complexation. Conversely, this effect was not observed with Al/Al cell. Fig. S3 shows continuous BP-3 reduction by 50% in simulated matrix and urban wastewater at 15 mA cm^{-2}, similarly to that obtained with Fe/Fe cell (Fig. 3a). This indicates that the suggested complexes of BP-3 do not coagulate on $Al(OH)_3$ flocs.

Fig. 3b depicts gradual TOC abatement with the Fe/Fe cell, reaching 46.5% at 60 min, although 35% was attained at 15 min. To assess the decontamination, 6 cyclic compounds as soluble organic components after 20 min of electrolysis were identified by GC-MS (Table S4). All the molecules present in the raw wastewater (Table S2), except 2,2,6,6-tetramethyl-4-piperidinone and BP-3, were completely removed by EC. New molecules like dioxybenzone and 2-hydroxy-4-methoxybenzaldehyde appeared in the

electrolyzed solution, coming from hydroxylation and cleavage of BP-3. This confirms the proposed concomitant production of •OH during EC.

3.3. Degradation of BP-3 in urban wastewater by EAOPs

First, the ability of the air-diffusion cathode to electrogenerate H_2O_2 from reaction (7) (Brillas et al., 2009; Sirés et al., 2014) by the different EAOPs in the atypical media employed was investigated using a BDD anode and electrolyzing 100 mL samples of pH 8.0 at 33.3 mA cm^{-2} for 360 min.

$$O_2(g) + 2H^+ + 2e^- \rightarrow H_2O_2 \quad (7)$$

Fig. S4 highlights a gradual H_2O_2 accumulation over time in all cases. In EO-H_2O_2, 41.1 and 36.1 mM were finally obtained in the simulated matrix and urban wastewater. Oxidation of water at BDD anode originated physisorbed BDD(•OH) by reaction (8) (Marselli et al., 2003; Özcan et al., 2008; Panizza and Cerisola, 2009), which reacted with H_2O_2 to form the weaker oxidant hydroperoxyl radical ($HO_2^{\bullet}$) via reaction (9) (Brillas et al., 2009; Sirés et al., 2014; Moreira et al., 2017). This caused its partial destruction, impeding higher accumulation. The smaller content obtained in urban wastewater suggests a slow H_2O_2 disappearance from reaction with some organic pollutants. When 10 mg L^{-1} Fe^{2+} was added to the urban wastewater (EF conditions), H_2O_2 was slowly accumulated up to 32.8 mM due to its additional removal from Fenton's reaction (10) (Dirany et al., 2011; El-Ghenymy et al., 2013; Olvera-Vargas et al., 2015). This content decreased to 24.9 mM under UVA irradiation in PEF mainly because Fenton's reaction (10) accelerated by Fe^{2+} regeneration from photolysis of soluble Fe(III) species by reaction (11) (Flox et al., 2007; Thiam et al., 2015; Zhang et al., 2016). These findings corroborate that sufficient H_2O_2 was produced in complex matrices for a large •OH generation in EAOPs.

$$BDD + H_2O \rightarrow BDD(\bullet OH) + H^+ + e^- \quad (8)$$

$$BDD(\bullet OH) + H_2O_2 \rightarrow BDD(HO_2\bullet) + H_2O \quad (9)$$

$$Fe^{2+} + H_2O_2 \rightarrow Fe^{3+} + \bullet OH + OH^- \quad (10)$$

$$Fe(OH)^{2+} + h\nu \rightarrow Fe^{2+} + \bullet OH \quad (11)$$

The degradation of 4 mg C L^{-1} BP-3 in urban wastewater at natural pH 8.0 by EAOPs was performed under the above conditions. Fig. 4a depicts the concentration decay using active RuO_2-based and non-active BDD anodes, as well as the lack of BP-3 was not photoactive upon UVA irradiation. At 33.3 mA cm^{-2}, this pollutant was more rapidly removed with BDD and, regardless of the anode, the oxidation ability rose as EO-H_2O_2 < EF < PEF, always disappearing in 45 min. These results indicate that in EO-H_2O_2, BP-3 was simultaneously degraded by ClO^- generated from Cl^- oxidation at each anode and by RuO_2(•OH) or, to a larger extent, by BDD(•OH). This agrees with the higher oxidation power expected for BDD (Brillas et al., 2009; Panizza and Cerisola, 2009; Sirés et al., 2014). The greater concentration decay in EF can be accounted for additional oxidation with •OH originated from Fenton's reaction (10), whereas the superiority of PEF is due to the larger production of •OH induced from reaction (11). However, good pseudo-first-order BP-3 kinetics were obtained in the case of EO-H_2O_2 (inset of Fig. 4a), with apparent rate constants of 0.075 min^{-1} ($R^2 = 0.989$) for RuO_2-based and 0.085 min^{-1} ($R^2 = 0.995$) for BDD. This behavior suggests a constant production of all oxidants, whereas the presence of Fe^{2+} in EF and PEF did not allow a clear kinetic analysis.

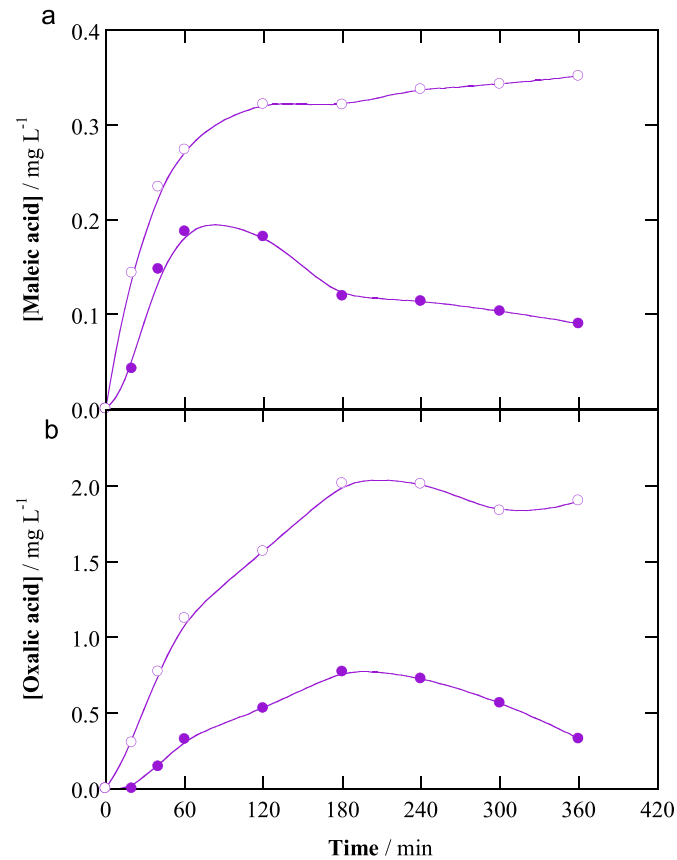

Fig. 5. Time course of (a) maleic and (b) oxalic acids concentration during the EO-H_2O_2 of the sample of Fig. 4 using (○) RuO_2-based/air-diffusion and (●) BDD/air-diffusion cells.

The action of oxidizing agents in each process was more evident from TOC profiles. Fig. 4b illustrates that BDD(•OH) always yielded much larger mineralization than RuO_2(•OH), then being BDD a better anode. The best mineralization with 62.6% TOC decrease was achieved by PEF, followed by 55.5% TOC removal by EF. The superiority of PEF is mainly due to the photolysis of some intermediates, including Fe(III) complexes of final carboxylic acids (Ruiz et al., 2011; Olvera-Vargas et al., 2015; Thiam et al., 2015). However, these products could only be confirmed in the case of EO-H_2O_2, where maleic and oxalic acids were identified by ion-exclusion HPLC. Fig. 5a and b shows the time course of these acids using RuO_2-based and BDD anodes. Their low content (<0.50 mg C L^{-1}) suggests that all treated solutions contained a mixture of recalcitrant molecules coming from the degradation of BP-3 and organic components of wastewater.

Fe^{2+} concentration and pH are two key parameters in Fenton-based EAOPs since they modulate •OH production from Fenton's reaction (10) (Brillas et al., 2009; Sirés et al., 2014; Martínez-Huitle et al., 2015). Fig. 6a and b shows a little effect of Fe^{2+} content on BP-3 degradation at natural pH in EF and PEF operating from 10 to 28 mg L^{-1}. A slightly better performance was achieved with 10 mg L^{-1} Fe^{2+}, suggesting lower •OH production at the highest Fe^{2+} content due to precipitation of the excess of iron ions at such high pH, which caused partial destruction of H_2O_2 by heterogeneous reaction (Brillas et al., 2009). Conversely, Fig. 6c and d reveal quicker degradation at pH 3.0 (optimum pH for Fenton's reaction (10)) (Brillas et al., 2009), for both treatments with 28 mg L^{-1} Fe^{2+}. BP-3 disappeared in 20 min, a time <45 min at pH 8.0 (Fig. 6a), and TOC was more largely reduced by 64.4% in EF and 72.5% in PEF. The

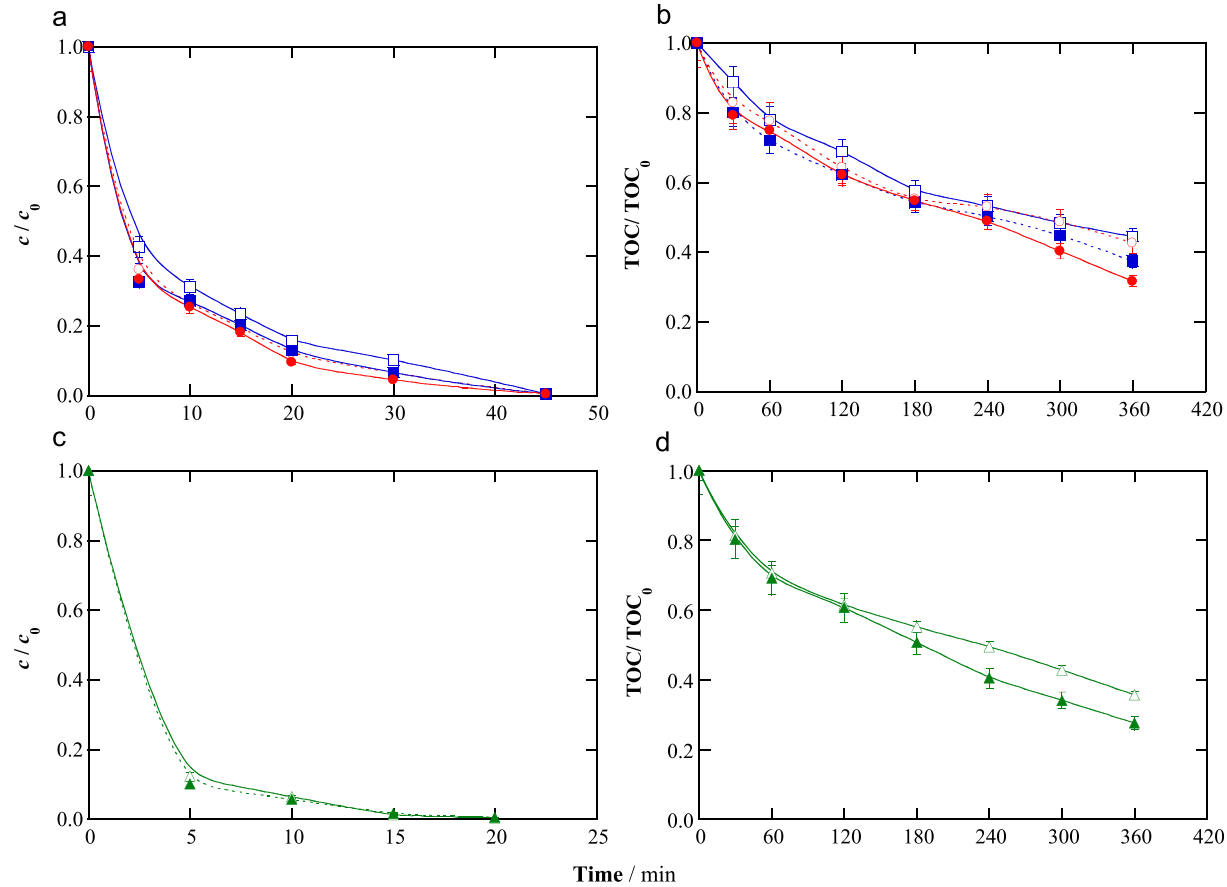

Fig. 6. Normalized (a,c) BP-3 concentration and (b,d) TOC decays for 100 mL of 4 mg C L^{-1} BP-3 in urban wastewater using BDD/air-diffusion cell at 33.3 mA cm^{-2} and 35 °C. (a,b) Natural pH 8.0: EF with (○) 10 and (□) 28 mg L^{-1} Fe^{2+}, and PEF with (●) 10 and (■) 28 mg L^{-1} Fe^{2+}. (c,d) pH 3.0: (△) EF and (▲) PEF, both with 28 mg L^{-1} Fe^{2+}.

superiority of BP-3 degradation at optimum pH 3.0 as compared to pH 8.0 is due to the faster degradation in the presence of larger amounts of •OH produced, either with BP-3, the organic components of urban wastewater or their products. Moreover, HClO was the dominant active chlorine species at pH 3.0, with much higher oxidation power than ClO^- formed at pH 8.0 (Sirés et al., 2014).

3.4. Detection of primary intermediates upon BP-3 degradation in a simulated water matrix

The primary intermediates generated from BP-3 (**1**) were identified in simulated water by GC-MS analysis of organic components produced after 2 min of PEF of 4 mg C L^{-1} BP-3 at pH 8.0 using BDD/air-diffusion cell at 33.3 mA cm^{-2}. Table S5 summarizes 14 cyclic molecules detected, including two direct hydroxylated derivatives of the parent molecule (**2** and **3**), three xanthene derivatives, non-chlorinated (**4**) or chloroderivatives (**6** and **7**), one dibenzenic intermediate (**14**), four monobenzenic intermediates (**5**, **11**, **12** and **13**) and four chlorobenzenic derivatives (**8**, **9**, **10** and **15**). Note that **2** and **5** were also formed during EC treatment of BP-3 (Table S4). The mass spectra of these products are given in Fig. S5.

From the above byproducts, a reaction sequence for the initial BP-3 degradation is proposed in Fig. 7. It can be valid for all EAOPs tested, since their main oxidants are hydroxyl radicals (BDD(•OH) and •OH), represented as •OH for the sake of simplicity, and active chlorine (HClO/ClO^-). The route is initiated by hydroxylation of **1** either at position C-2′ to yield **2** or at position C-4 to give **3** with loss of methoxy group. Further hydroxylation of **2** causes cyclization to form the xanthenone **4** or cleavage of the C(1')-CO bond to produce the benzaldehyde **5**. Chlorination of **4** yields consecutively the xanthenes derivatives **6** and **7**, which undergo hydroxylation with cleavage of the cyclic structure to yield the benzenic compound **8**. This byproduct is subsequently chlorinated to **9**, finally transformed into **10** via hydroxylation/chlorination with release of Cl^- and methoxy groups. On the other hand, hydroxylation of the aromatic rings of **3** causes its cleavage to yield **11** and **12**, whereas the attack of •OH onto the CO group of **3** promotes acid **13**. An esterification of **13** with an intermediate of **8** (possibly, 4-chlorophenol, resulting from the loss of methoxy group) yielded **14**. Alternatively, **13** may be converted into the chlorinated compound **15**.

3.5. Sequential EC/EF and EC/PEF treatments of BP-3 in urban wastewater

From the results for EC, $j = 15$ mA cm^{-2} and 20 min of electrolysis were chosen to electrolyze 150 mL of 4 mg C L^{-1} BP-3 spiked into urban wastewater at natural pH 8.0 using the Fe/Fe cell before treatment by EF and PEF. Fig. 8a and b depicts that 41% of BP-3 and 36% of TOC were removed by this pre-treatment, with total soluble iron of 7 mg L^{-1} and final pH 8.2. EAOPs were then performed with 100 mL of supernatant liquid using BDD/air-diffusion cell at 33.3 mA cm^{-2} for 360 min. Fig. 8a shows that BP-3 disappeared after 45 min of EF and PEF, as well as in PEF with 10 mg L^{-1} Fe^{2+}, all at natural pH. These results agree with the behavior of both single processes, meaning that BDD(•OH), ClO^- and •OH in the bulk are the main oxidants, without significant influence of Fe^{2+} addition since the catalyst supplied by EC is enough for an effective Fenton's reaction (10) to produce •OH at this pH. Fig. 8a also shows a notable

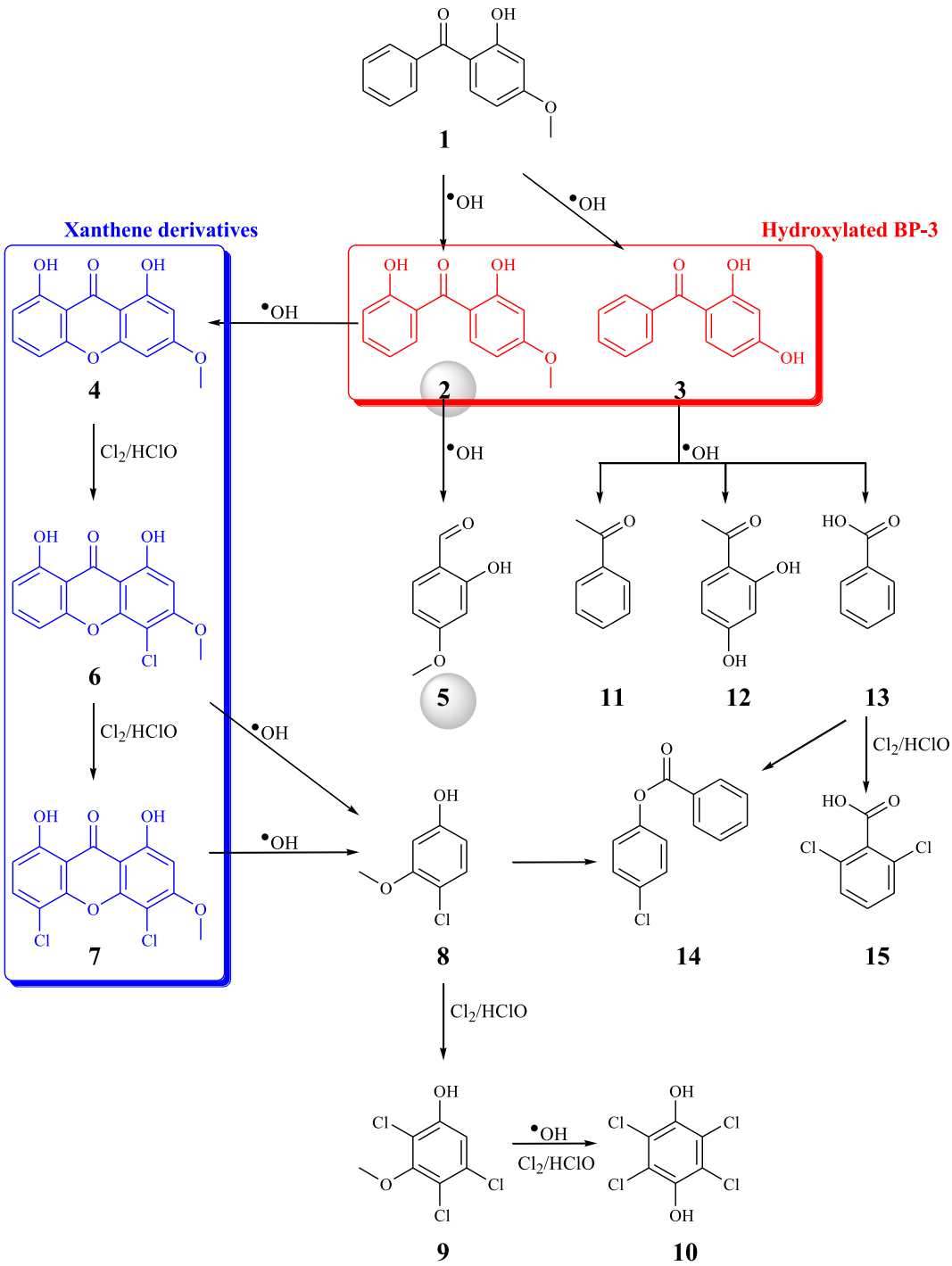

Fig. 7. Proposed reaction sequence for the initial degradation of BP-3 by EAOPs, tested in simulated water matrix.

influence of pH on BP-3 removal, disappearing at 10 min by PEF with 10 mg L^{-1} Fe^{2+} at pH 3.0 due to the greater production of •OH by enhancement of Fenton's reaction (10) and simultaneous oxidation by HClO. In the same assays, Fig. 8b illustrates final TOC abatements of 72.5% by EF, about 80% in both PEF at natural pH, and 87.3% in PEF at pH 3.0. The larger mineralization by PEF can be associated with the photolysis of some products upon UVA irradiation that enhances its transformation into CO_2, whereas the superiority of PEF at pH 3.0 can be related again to the larger •OH generation and the presence of HClO.

To confirm the benefits of sequential EC/PEF, additional experiments to reach total mineralization (>99% TOC reduction) were made. Fig. 9 reveals that urban wastewater was totally decontaminated in 820 min by PEF at natural pH by adding 10 mg L^{-1} Fe^{2+}. Shorter times of 720 and 680 min were required using EC/PEF, with PEF performed at natural pH or at pH 3.0. As expected, faster mineralization was achieved at pH 3.0 owing to the reasons exposed above. Sequential EC/PEF at natural pH is then more useful in practice than single PEF because lower electrical consumption is needed to mineralize all contaminants. On the other hand, the final sludge of the EC pre-treatment should be managed conveniently.

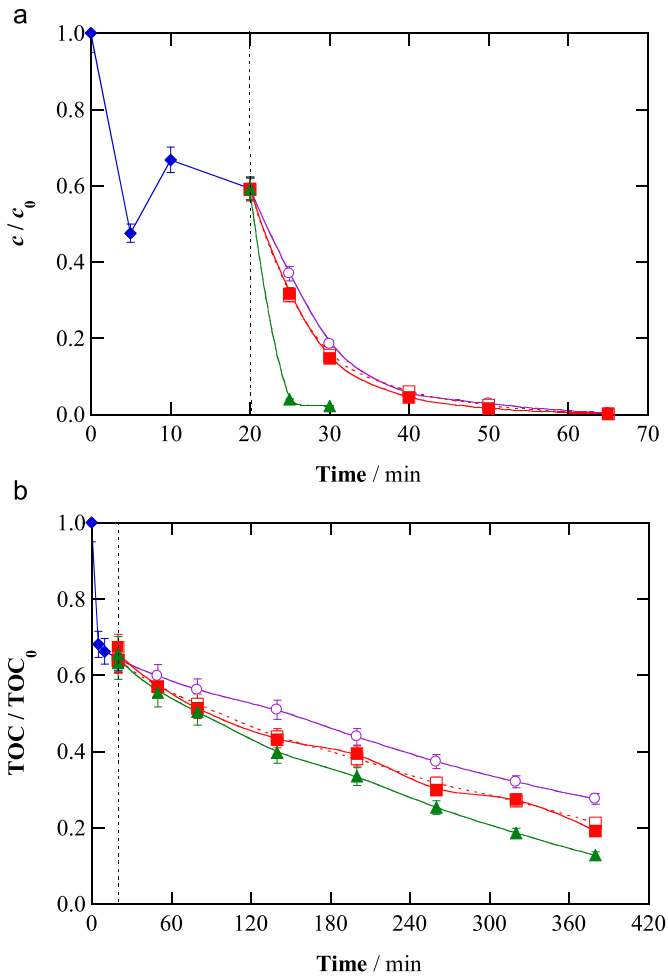

Fig. 8. Normalized (a) BP-3 concentration and (b) TOC decays for sequential EC/EAOPs treatment of 4 mg C L^{-1} BP-3 in urban wastewater at 35 °C. (◆) EC pre-treatment of 150 mL at natural pH 8.0 using Fe/Fe cell at 15 mA cm^{-2} for 20 min. Further degradation of 100 mL of supernatant liquid using BDD/air-diffusion cell at 33.3 mA cm^{-2} by: (○) EF and (□) PEF, both without addition of Fe^{2+}, (●) PEF with 10 mg L^{-1} Fe^{2+} and (■) PEF at pH 3.0 with 10 mg L^{-1} Fe^{2+}.

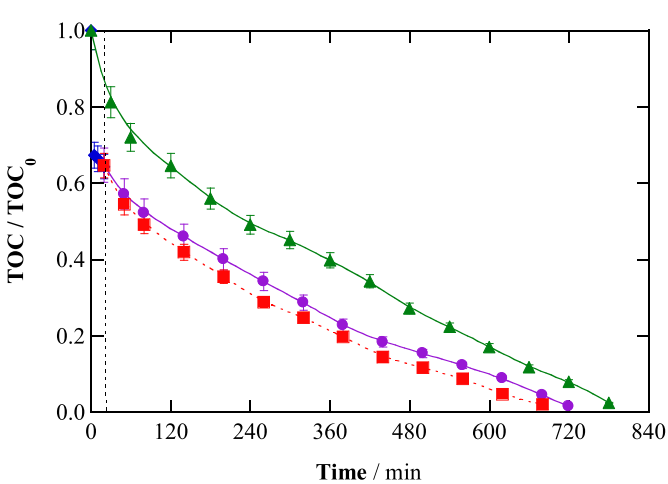

Fig. 9. Normalized TOC removal for 4 mg C L^{-1} BP-3 in urban wastewater at 35 °C. (▲) 100 mL at natural pH 8.0 with addition of 10 mg L^{-1} Fe^{2+}, treated by PEF with BDD/air-diffusion cell at 33.3 mA cm^{-2}. EC/PEF process: (◆) 150 mL of wastewater pre-treated by EC with Fe/Fe cell at 15 mA cm^{-2} for 20 min, followed by PEF treatment of 100 mL of supernatant liquid at (●) natural pH and (■) pH 3.0 with BDD/air-diffusion cell.

For the most powerful sequential EC/PEF treatment at natural pH, the average cell voltages (E_{cell}) listed in Table S3 allowed determining the energy consumption, as explained elsewhere (Thiam et al., 2015). A low value of 2.36 k Wh m^{-3} resulted in the EC pre-treatment, in contrast to much greater values of 172.8 and 345.6 k Wh m^{-3} for the subsequent PEF treatment at 360 and 720 min. These high consumptions could be reduced down to 136.8 and 273.6 k Wh m^{-3} upon replacement of the UVA lamp by sunlight, as proposed in earlier papers (Flox et al., 2007; Salazar et al., 2012; Brillas, 2014).

4. Conclusions

- The Al/Al cell was proven as optimal for EC treatment of BP-3 in simulated matrix at pH 11.0 due to: (i) precipitation of the neutral form of BP-3 from pH decrease, (ii) coagulation of the anionic form with hydroxide flocs, (iii) reductive transformation and (iv) oxidation of BP-3 and its byproducts by generated ClO^- and •OH. The three latter processes occurred in the Fe/Fe cell as well.
- BP-3 spiked into urban wastewater at natural pH 8.0 treated by EC with Fe/Fe cell at 15 mA cm^{-2} showed a dramatic content decay thanks to coagulation of its complexes with components of the wastewater, followed by partial BP-3 redissolution when they were oxidized by •OH and ClO^-.
- The oxidation power of EAOPs in this real sample rose as EO-H_2O_2 < EF < PEF, with larger effectiveness of the BDD/air-diffusion cell than using a RuO_2-based anode. The superiority of PEF was due to additional photolysis of intermediates.
- The organic molecules identified upon EC and EAOPs revealed a certain oxidation ability of EC process.
- The sequential EC (Fe/Fe cell, 15 mA cm^{-2}, 20 min)/PEF (BDD/air-diffusion cell, 33.3 mA cm^{-2}, 360 min) of BP-3-loaded urban wastewater at natural pH was much more powerful than EC/EF. The time needed for total mineralization by EC/PEF was shorter than in single PEF, then being sequential electrochemical processes a very interesting alternative.

Acknowledgements

The authors thank financial support from project CTQ2016-78616-R (AEI/FEDER, EU) and PhD scholarship awarded to Z. Ye (State Scholarship Fund, CSC, China). J.R. Steter thanks funding from process number 234142/2014-6 (CNPq, Brazil).

Appendix A. Supplementary data

Supplementary data to this article can be found online at https://doi.org/10.1016/j.jclepro.2018.10.181.

References

Abdallah, P., Deborde, M., Berne, F.D., Leitner, N.K.V., 2015. Kinetics of chlorination of benzophenone-3 in the presence of bromide and ammonia. Environ. Sci. Technol. 49 (24), 14359–14367.
Asghar, A., Raman, A.A.A., Daud, W.M.A.W., 2015. Advanced oxidation processes for in-situ production of hydrogen peroxide/hydroxyl radical for textile wastewater treatment: a review. J. Clean. Prod. 87, 826–838.
Bocos, E., Brillas, E., Sanromán, M.A., Sirés, I., 2016. Electrocoagulation: simply a phase separation technology? The case of bronopol compared to its treatment by EAOPs. Environ. Sci. Technol. 50 (14), 7679–7686.
Brillas, E., 2014. A review on the degradation of organic pollutants in waters by UV photoelectro-Fenton and solar photoelectro-Fenton. J. Braz. Chem. Soc. 25 (3), 393–417.
Brillas, E., Martínez-Huitle, C.A., 2015. Decontamination of wastewaters containing synthetic organic dyes by electrochemical methods. An updated review. Applied. Catal. B Environ. 166–167, 603–643.
Brillas, E., Sirés, I., Oturan, M.A., 2009. Electro-Fenton process and related electrochemical technologies based on Fenton's reaction chemistry. Chem. Rev. 109

(12), 6570–6631.
Cheng, M., Lai, C., Liu, Y., Zeng, G., Huang, D., Zhang, C., Qin, L., Hu, L., Zhou, C., Xiong, W., 2018a. Metal-organic frameworks for highly efficient heterogeneous Fenton-like catalysis. Coord. Chem. Rev. 368, 80–92.
Cheng, M., Zeng, G., Huang, D., Lai, C., Liu, Y., Zhang, C., Wan, J., Hu, L., Zhou, C., Xiong, W., 2018b. Efficient degradation of sulfamethazine in simulated and real wastewater at slightly basic pH values using Co-SAM-SCS/H_2O_2 Fenton-like system. Water Res. 138, 7–18.
Cheng, M., Zeng, G., Huang, D., Lai, C., Xu, P., Zhang, C., Liu, Y., Wan, J., Gong, X., Zhu, Y., 2016. Degradation of atrazine by a novel Fenton-like process and assessment the influence on the treated soil. J. Hazard. Mater. 312, 184–191.
Demirbas, E., Kobya, M., 2017. Operating cost and treatment of metalworking fluid wastewater by chemical coagulation and electrocoagulation processes. Process Saf. Environ. Protect. 105, 79–90.
Dirany, A., Efremova Aaron, S., Oturan, N., Sirés, I., Oturan, M.A., Aaron, J.J., 2011. Study of the toxicity of sulfamethoxazole and its degradation products in water by a bioluminescence method during application of the electro-Fenton treatment. Anal. Bioanal. Chem. 400 (2), 353–360.
Downs, C.A., Kramarsky-Winter, E., Segal, R., Fauth, J., Knutson, S., Bronstein, O., Ciner, F.R., Jeger, R., Lichtenfeld, Y., Woodley, C.M., Pennington, P., Cadenas, K., Kushmaro, A., Loya, Y., 2016. Toxicopathological effects of the sunscreen UV filter, oxybenzone (benzophenone-3), on coral planulae and cultured primary cells and its environmental contamination in Hawaii and the U.S. Virgin Islands. Arch. Environ. Contam. Toxicol. 70 (2), 265–288.
El-Ashtoukhy, E.-S.Z., Amin, N.K., Abd El-Latif, M.M., Bassyouni, D.G., Hamad, H.A., 2017. New insights into the anodic oxidation and electrocoagulation using a self-gas stirred reactor: a comparative study for synthetic C.I Reactive Violet 2 wastewater. J. Clean. Prod. 167, 432–446.
El-Ghenymy, A., Oturan, N., Oturan, M.A., Garrido, J.A., Cabot, P.L., Centellas, F., Rodríguez, R.M., Brillas, E., 2013. Comparative electro-Fenton and UVA photoelectro-Fenton degradation of the antibiotic sulfanilamide using a stirred BDD/air-diffusion tank reactor. Chem. Eng. J. 234, 115–123.
Flox, C., Garrido, J.A., Rodríguez, R.M., Cabot, P.L., Centellas, F., Arias, C., Brillas, E., 2007. Mineralization of herbicide mecoprop by photoelectro-Fenton with UVA and solar light. Catal. Today 129 (1–2), 29–36.
Gago-Ferrero, P., Demeestere, K., Díaz-Cruz, M.S., Barceló, D., 2013. Ozonation and peroxone oxidation of benzophenone-3 in water: effect of operational parameters and identification of intermediate products. Sci. Total Environ. 443, 209–217.
Ghernaout, D., 2013. Advanced oxidation phenomena in electrocoagulation process: a myth or a urbanity? Desalination Water Treat. 51 (40), 7536–7554.
Ghernaout, D., Naceur, M.W., Aouabed, A., 2011. On the dependence of chlorine by-products generated species formation of the electrode material and applied charge during electrochemical water treatment. Desalination 270 (1–3), 9–22.
Gilberta, E., Roussela, L., Serre, C., Sandouk, R., Salmon, D., Kirilov, P., Haftek, M., Falson, F., Pirot, F., 2016. Percutaneous absorption of benzophenone-3 loaded lipid nanoparticles and polymeric nanocapsules: a comparative study. Int. J. Pharm. 504 (1–2), 48–58.
Gong, P., Yuan, H., Zhai, P., Xue, Y., Li, H., Dong, W., Mailhot, G., 2015. Investigation on the degradation of benzophenone-3 by UV/H_2O_2 in aqueous solution. Chem. Eng. J. 277, 97–103.
Guo, Y., Xu, B., Qi, F., 2016. A novel ceramic membrane coated with MnO_2–Co_3O_4 nanoparticles catalytic ozonation for benzophenone-3 degradation in aqueous solution: fabrication, characterization and performance. Chem. Eng. J. 287, 381–389.
Khandegar, V., Saroha, A.K., 2013. Electrocoagulation for the treatment of textile industry effluent a review. J. Environ. Manag. 128, 949–963.
Li, Y.J., Qiao, X.L., Zhou, C.Z., Zhang, Y.N., Fu, Z.Q., Chen, J.W., 2016. Photochemical transformation of sunscreen agent benzophenone-3 and its metabolite in surface freshwater and seawater. Chemosphere 153, 494–499.
Liu, Y.S., Ying, G.G., Shareef, A., Kookana, R.S., 2012. Biodegradation of the ultraviolet filter benzophenone-3 under different redox conditions. Environ. Toxicol. Chem. 31 (2), 289–295.
Marselli, B., Garcia-Gomez, J., Michaud, P.A., Rodrigo, M.A., Comninellis, C., 2003. Electrogeneration of hydroxyl radicals on boron-doped diamond electrodes. J. Electrochem. Soc. 150 (3), D79–D83.
Martínez-Huitle, C.A., Rodrigo, M.A., Sirés, I., Scialdone, O., 2015. Single and coupled electrochemical processes and reactors for the abatement of organic water pollutants: a critical review. Chem. Rev. 115 (24), 13362–13407.
Moreira, F.C., Boaventura, R.A.R., Brillas, E., Vilar, V.J.P., 2017. Electrochemical advanced oxidation processes: a review on their application to synthetic and urban wastewaters. Applied. Catal. B Environ. 202, 217–261.
Olvera-Vargas, H., Oturan, N., Oturan, M.A., Brillas, E., 2015. Electro-Fenton and solar photoelectro-Fenton treatments of the pharmaceutical ranitidine in pre-pilot flow plant scale. Separ. Purif. Technol. 146, 127–135.
Özcan, A., Şahin, Y., Koparal, A.S., Oturan, M.A., 2008. Propham mineralization in aqueous medium by anodic oxidation using boron-doped diamond anode. Experimental parameters' influence on degradation kinetics and mineralization efficiency. Water Res. 42 (12), 2889–2898.
Panizza, M., Cerisola, G., 2009. Direct and mediated anodic oxidation of organic pollutants. Chem. Rev. 109 (12), 6541–6569.
Ridruejo, C., Salazar, C., Cabot, P.L., Centellas, F., Brillas, E., Sirés, I., 2017. Electrochemical oxidation of anesthetic tetracaine in aqueous medium. Influence of the anode and matrix composition. Chem. Eng. J. 326, 811–819.
Ruiz, E.J., Hernández-Ramírez, A., Peralta-Hernández, J.M., Arias, C., Brillas, E., 2011. Application of solar photoelectro-Fenton technology to azo dyes mineralization: effect of current density, Fe^{2+} and dye concentration. Chem. Eng. J. 171 (2), 385–392.
Salazar, R., Brillas, E., Sirés, I., 2012. Finding the best Fe^{2+}/Cu^{2+} combination for the solar photoelectro-Fenton treatment of simulated wastewater containing the industrial textile dye disperse blue 3. Applied. Catal. B Environ. 115–116, 107–116.
Särkkä, H., Bhatnagar, A., Sillanpää, M., 2015. Recent developments of electro-oxidation in water treatment - a review. J. Electroanal. Chem. 754, 46–56.
Silva, L.G.M., Moreira, F.C., Souza, A.A.U., Souza, S.M.A.G.U., Boaventura, R.A.R., Vilar, V.J.P., 2018. Chemical and electrochemical advanced oxidation processes as a polishing step for textile wastewater treatment: a study regarding the discharge into the environment and the reuse in the textile industry. J. Clean. Prod. 198, 430–442.
Sirés, I., Brillas, E., Oturan, M.A., Rodrigo, M.A., Panizza, M., 2014. Electrochemical advanced oxidation processes: today and tomorrow. Environ. Sci. Pollut. Res. 21 (14), 8336–8367.
Steter, J.R., Brillas, E., Sirés, I., 2016. On the selection of the anode material for the electrochemical removal of methylparaben from different aqueous media. Electrochim. Acta 222, 1464–1474.
Thiam, A., Sirés, I., Brillas, E., 2015. Treatment of a mixture of food color additives (E122, E124 and E129) in different water matrices by UVA and solar photo-electro-Fenton. Water Res. 81, 178–187.
Thiam, A., Zhou, M., Brillas, E., Sirés, I., 2014. Two-step mineralization of Tartrazine solutions: study of parameters and by-products during the coupling of electrocoagulation with electrochemical advanced oxidation processes. Applied. Catal. B Environ. 150–151, 116–125.
Urzúa, J., González-Vargas, C., Sepúlveda, F., Ureta-Zañartu, M.S., Salazar, R., 2013. Degradation of conazole fungicides in water by electrochemical oxidation. Chemosphere 93 (11), 2774–2781.
Wang, A., Qu, J., Liu, H., Ru, J., 2008. Mineralization of an azo dye Acid Red 14 by photoelectro-Fenton process using an activated carbon fiber cathode. Applied. Catal. B Environ. 84 (3–4), 393–399.
Welcher, F.J., 1975. In: Standard Methods of Chemical Analysis, Part B, sixth ed., vol. 2. R.E. Krieger Pub. Co., New York, p. 1827.
Zhang, Y., Wang, A., Tian, X., Wen, Z., Lv, H., Li, D., Li, J., 2016. Efficient mineralization of the antibiotic timethoprim by solar assisted photoelectro-Fenton process driven by a photovoltaic cell. J. Hazard. Mater. 318, 319–328.
Zúñiga-Benítez, H., Aristizábal-Ciro, C., Peñuela, G.A., 2016a. Heterogeneous photocatalytic degradation of the endocrine-disrupting chemical benzophenone-3: parameters optimization and by-products identification. J. Environ. Manag. 167, 246–258.
Zúñiga-Benítez, H., Aristizábal-Ciro, C., Peñuela, G.A., 2016b. Photodegradation of the endocrine-disrupting chemicals benzophenone-3 and methylparaben using Fenton reagent: optimization of factors and mineralization/biodegradability studies. J. Taiwan Inst. Chem. Eng. 59, 380–388.
Zúñiga-Benítez, H., Soltan, J., Peñuela, G.A., 2016c. Application of ultrasound for degradation of benzophenone-3 in aqueous solutions. Int. J. Environ. Sci. Technol. 13 (1), 77–86.

SUPPLEMENTARY MATERIAL

Photoelectro-Fenton as post-treatment for electrocoagulated benzophenone-3-loaded synthetic and urban wastewater

Zhihong Ye, Juliana R. Steter, Francesc Centellas, Pere Lluís Cabot, Enric Brillas*, Ignasi Sirés*

Laboratori d'Electroquímica dels Materials i del Medi Ambient, Departament de Química Física, Facultat de Química, Universitat de Barcelona, Martí i Franquès 1-11, 08028 Barcelona, Spain

* Corresponding author: *E-mail address*: brillas@ub.edu (E. Brillas)

E-mail address: i.sires@ub.edu (I. Sirés)

Table S1

Main physicochemical characteristics of the collected primary treated urban wastewater once filtered under vacuum with a 0.45 μm membrane filter.

Parameter (units)	Value
pH	7.96
Conductivity (mS cm^{-1})	2.13
TC (mg C L^{-1})	180.3
TOC (mg C L^{-1})	37.7
Total nitrogen (mg N L^{-1})	66.8
Na^+ (mg L^{-1})	268.1
K^+ (mg L^{-1})	47.2
Ca^{2+} (mg L^{-1})	116.9
Mg^{2+} (mg L^{-1})	33.5
Total iron (mg L^{-1})	0.22
Cl^- (mg L^{-1})	375.9
SO_4^{2-} (mg L^{-1})	129.5

Table S2.

Compounds detected in the raw urban wastewater by GC-MS using a non-polar (NP) or polar (P) column.

Chemical name	Molecular structure	Column	t_r (min)	Main fragmentation (*m/z*)
2,2,6,6-Tetramethyl-4-piperidinone	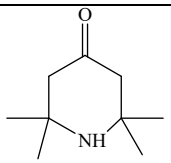	NP P	14.87 17.79	155,140,98,83
2-(1-Methyl-2-pyrrolidinyl)pyridine	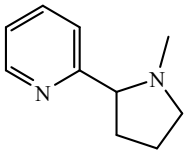	NP	21.50	161,133,119,84
(S)-3-(1-Methyl-2-pyrrolidinyl)pyridine or Nicotine	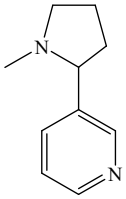	P	24.49	161,133,84
3,7-Dihydro-1,3,7-trimethyl-1H-purine-2,6-dione or Caffeine	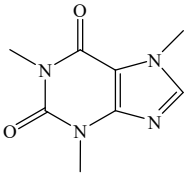	NP P	33.18 46.23	194,165,109,82
[1S-[1α(S*),4αβ,8aα]]-α-ethenyldecahydro-α,5,5,8a-tetramethyl-2-methylene-1-naphthalenepropanol or Manool	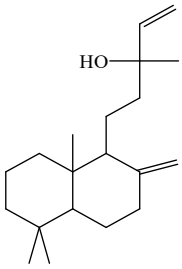	P	38.93	272,257,244,137
Octadecanoic acid	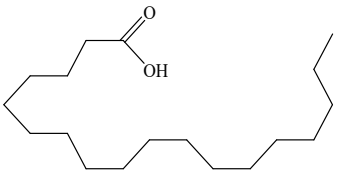	NP P	39.31 45.79	284,241,185,129

α-Methyl-4-(2-methylpropyl)-benzeneacetic acid or ((S)-(+)-Ibuprofen)	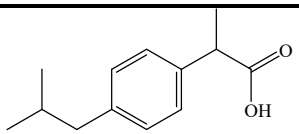	P	41.33	206,161,119,91
(S)-1-Methyl-5-(3-pyridinyl)-2-pyrrolidinone or Cotinine	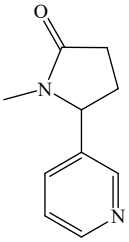	P	41.80	176,119,98
2-Methyl-3-[4-*t*-butyl]phenyl-propanoic acid	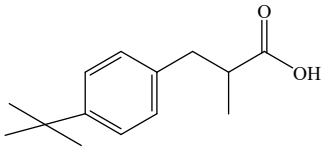	P	42.05	205,149,131
BP-3	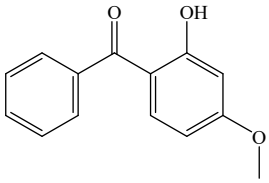	NP P	37.20 45.99	227,151,105,77
(3α,5β)-3-Hydroxy-androstane-11,17-dione or 11-Ketoetiocholanolone	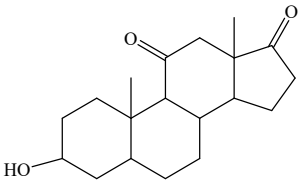	NP	46.62	304,286,271,232
(3β)-Cholesta-4,6-dien-3-ol	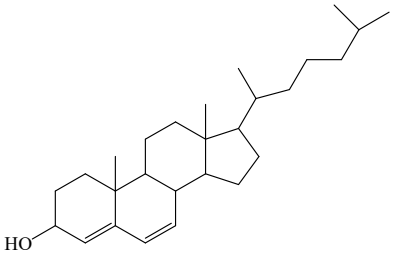	P	51.38	366,351,253,143
Cholestanol	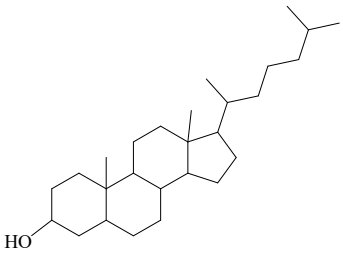	NP	53.26	388,373,355,233,216

(3β)-Cholest-5-en-3-ol	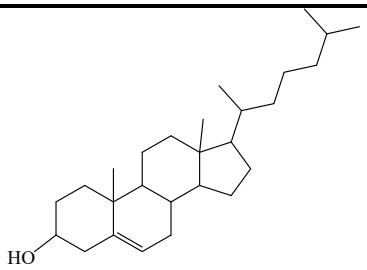	NP P	53.72 85.97	386,368,353,275,213
5α-Stigmast-8(14)-en-3β-ol	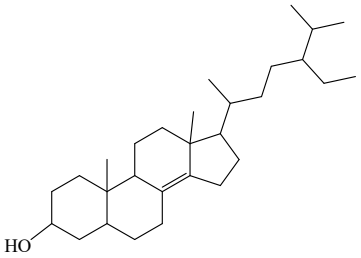	NP	56.16	414,396,381,303,255
(5β)- Cholestan-3-one	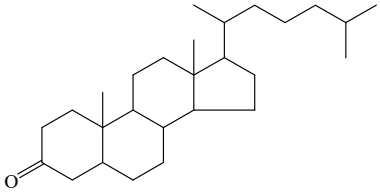	P	73.28	386,353,316,231
(3β,5β)-Cholestan-3-ol	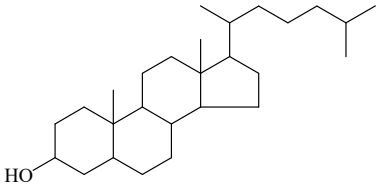	P	73.82	388,373,355,233
Stigmastanol	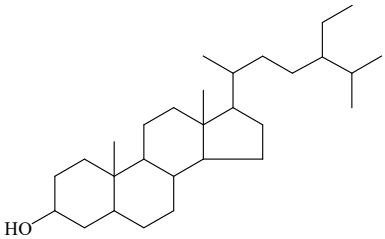	P	91.34	416,399,383,233,215

Table S3.

Characteristics of single and sequential EC and EAOPs trials made in this work.

Method	$[BP\text{-}3]_0$ (mg C L^{-1})	pH	Anode	Cathode	j (mA cm^{-2})	E_{cell} (V)	Electrolysis time[c] (min)
Simulated matrix							
EC	4	8.0	Al	Al	15	8.6	60
	10	11.0	Al	Al	15	7.9	60
	20	11.0	Al	Al	15	8.0	60
	30	11.0	Fe	Fe	10	5.1	60
	30	11.0	Fe	Fe	15	8.0	60
	30	11.0	Fe	Fe	20	9.8	60
	30	11.0	Fe	Al	10	5.1	60
	30	11.0	Fe	AISI 304	10	5.0	60
	30	11.0	Fe	AISI 316L	10	4.9	60
	30	11.0	Al	Fe	10	5.4	60
	30	11.0	Al	Al	10	5.5	60
	30	11.0	Al	Al	15	8.4	60
	30	11.0	Al	Al	20	10.0	60
	30	11.0	Al	AISI 304	10	5.3	60
	30	11.0	Al	AISI 316L	10	5.2	60
Na_2SO_4 medium							
EC	30	11.0	Fe	Fe	15	7.6	60
	30	11.0	Al	Al	15	8.3	60
Urban wastewater							
EC	4	8.0	Fe	Fe	15	7.1	20 and 60
EO-H_2O_2	4	3.0	RuO_2-based	Air-diffusion	33.3	16.7	360
	4	3.0	BDD	Air-diffusion	33.3	23.0	360
EF[a]	4	3.0	RuO_2-based	Air-diffusion	33.3	17.0	360
	4	3.0	BDD	Air-diffusion	33.3	22.6	360
	4	8.0	BDD	Air-diffusion	33.3	22.5	360
EF[b]	4	3.0	BDD	Air-diffusion	33.3	23.1	360
	4	8.0	BDD	Air-diffusion	33.3	23.2	360
EF post-treatment	-	8.2	BDD	Air-diffusion	33.3	22.5	360
PEF[a]	4	3.0	RuO_2-based	Air-diffusion	33.3	16.4	360
	4	3.0	BDD	Air-diffusion	33.3	23.2	360
	4	8.0	BDD	Air-diffusion	33.3	23.2	360 and 820
PEF[b]	4	3.0	BDD	Air-diffusion	33.3	22.9	360
	4	8.0	BDD	Air-diffusion	33.3	23.0	360
PEF post-treatment	-	8.2	BDD	Air-diffusion	33.3	22.8	360 and 720
	-	3.0	BDD	Air-diffusion	33.3	22.5	360 and 720
PEF[a] post-treatment	-	8.2	BDD	Air-diffusion	33.3	23.2	360

PEF[a] post-treatment	-	3.0	BDD	Air-diffusion	33.3	23.0	360

[a] With addition of 10 mg L^{-1} Fe^{2+}. [b] With addition of 28 mg L^{-1} Fe^{2+}. [c] Overall treatment time

Table S4.

Organic compounds identified by GC-MS with a non-polar column after 20 min of EC treatment of 150 mL of a solution containing 4 mg C L^{-1} BP-3 in urban wastewater at natural pH using a Fe/Fe cell at 15 mA cm^{-2}.

Chemical name	Molecular structure	t_r (min)	Main fragmentation (*m/z*)
2-Hydroxy-4-methoxybenzaldehyde	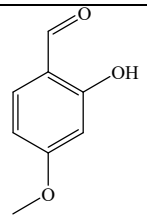	23.93	152,121,94
2-Phenoxyethanol	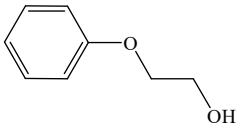	17.84	138,94,77
2,2,6,6-Tetramethyl-4-piperidinone	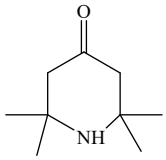	14.87	155,140,98,83
α-Hydroxy-benzeneacetic acid or Mandelic acid	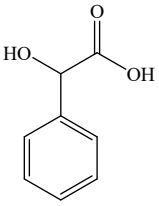	22.73	152,107,79
BP-3	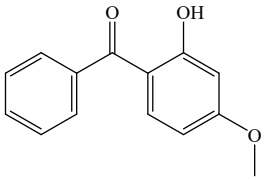	37.20	227,151,105,77

Dioxybenzone	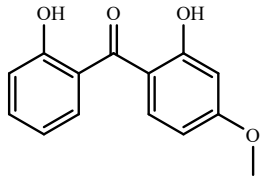	39.36	244,227,151,121

Table S5.

Aromatic intermediates identified by GC-MS with a non-polar o polar column after 2 min of PEF treatment of 100 mL of a solution containing 4 mg C L^{-1} BP-3 in a simulated water matrix at natural pH using a BDD/air-diffusion cell at 33.3 mA cm^{-2}.

Number	Chemical name	Molecular structure	Column	t_r (min)	Main fragmentation (*m/z*)
1	**BP-3**	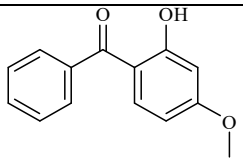	NP P	37.20 45.99	227,151,105,77
2	Dioxybenzone	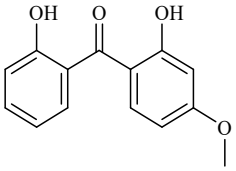	NP P	39.36 56.00	244,227,151, 121
3	2,4-Dihydroxybenzophenone	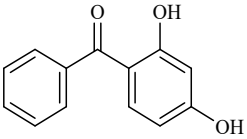	NP	38.54	214,133,97
4	1,8-Dihydroxy-3-methoxy-9H-xanthen-9-one	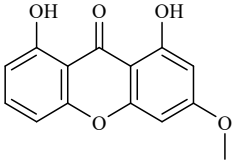	NP	45.25	258,243,215
5	2-Hydroxy-4-methoxybenzaldehyde	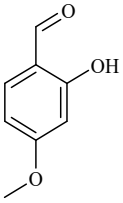	NP	23.93	152,121,94
6	4-Chloro-1,8-dihydroxy-3-methoxy-9H-xanthen-9-one	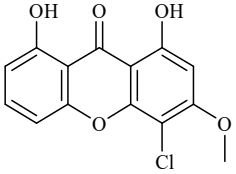	NP	47.26	292,277,221
7	4,5-Dichloro-1,8-dihydroxy-3-methoxy-9H-xanthen-9-one	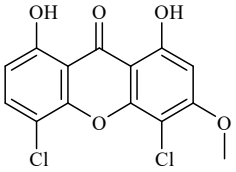	NP	47.69	326,295,268,167

8	4-Chloro-5-methoxyphenol	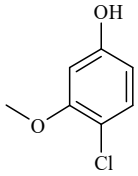	NP	24.20	158,129,115,93
9	3,4,6-Trichloro-5-methoxyphenol	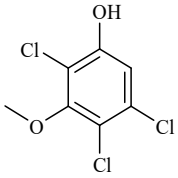	NP	26.40	228,215,185,122
10	Tetrachloro-hydroquinone	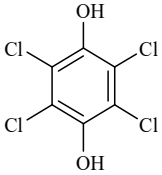	NP	38.34	248,210,171
11	Acetophenone	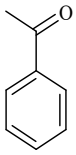	NP	13.31	120,105,77
12	2,4-Dihydroxyacetophenone	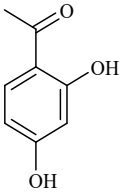	NP	17.69	153,135,105,78
13	Benzoic acid	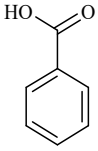	NP	16.49	122,105,77,51
14	4-Chlorophenyl benzoate	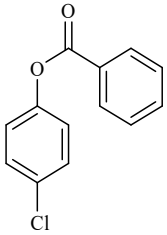	NP	19.67	232,105,77
15	2,6-Dichlorobenzoic acid	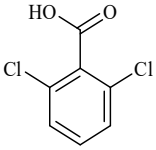	P	45.18	190,173,147,73

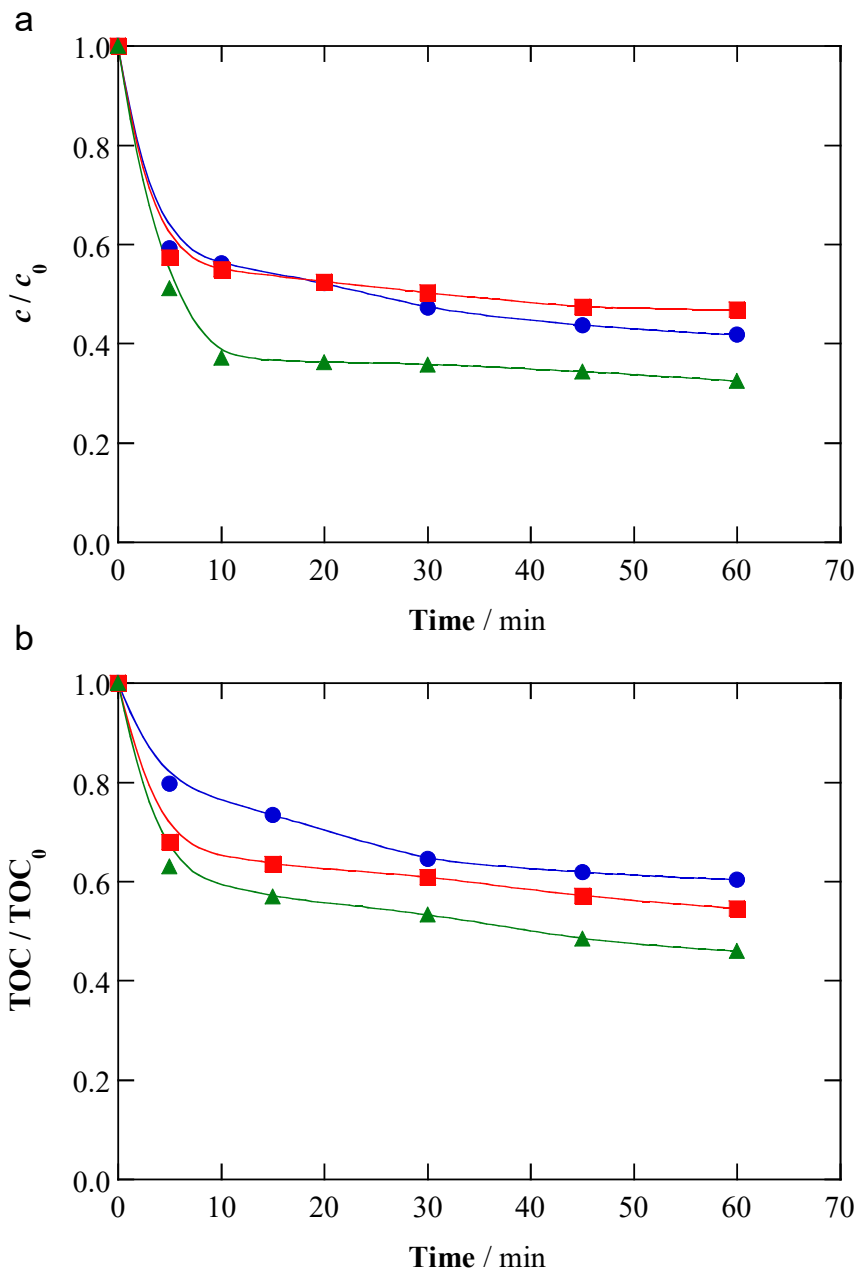

Fig. S1. Change of normalized (a) BP-3 concentration and (b) TOC decays with electrolysis time for the EC treatment of 150 mL of (●) 10, (■) 20 and (▲) 30 mg C L^{-1} BP-3 in a simulated matrix at pH 11.0 and 35 ºC using an Al/Al cell at 15 mA cm^{-2}.

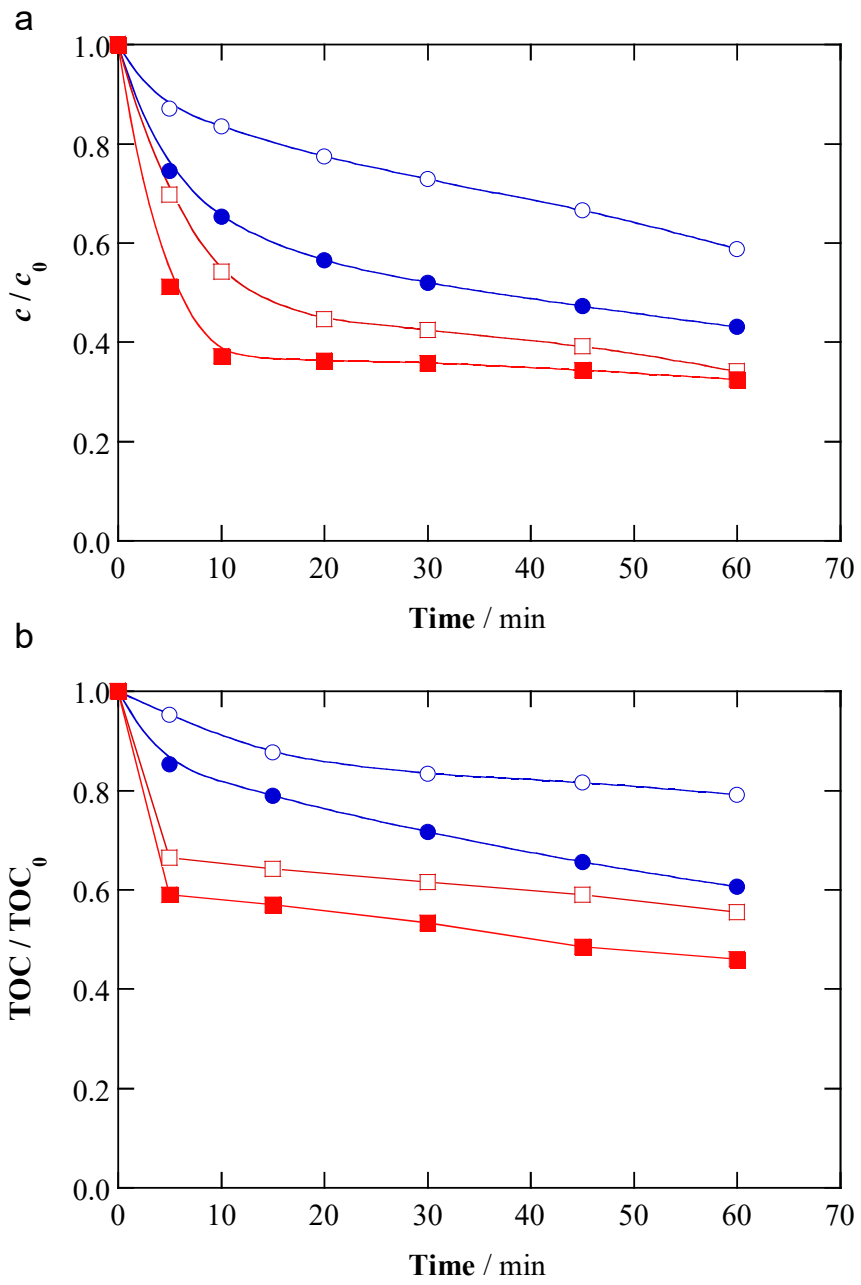

Fig. S2. Normalized (a) BP-3 concentration abatement and (b) TOC removal vs. electrolysis time for the EC treatment of 150 mL of 30 mg C L^{-1} BP-3 at pH 11.0 and 35 ºC. Experimental conditions: Na_2SO_4 using (○) Fe/Fe and (□) Al/Al cells, and simulated matrix using (●) Fe/Fe and (■) Al/Al cells. Both media had the same conductivity (1.8 mS cm^{-1}). Current density: 15 mA cm^{-2}.

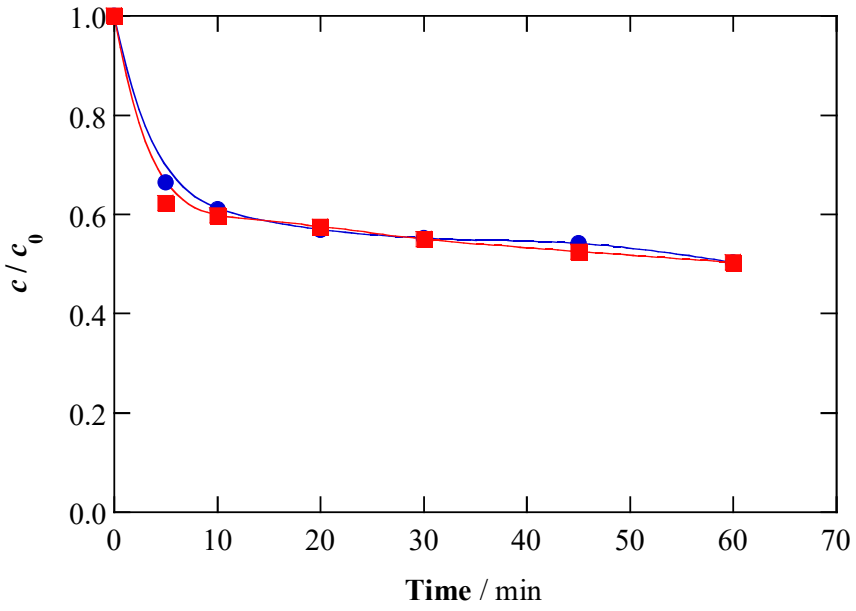

Fig. S3. Variation of normalized BP-3 concentration removal with electrolysis time for the EC treatment of 150 mL of 4 mg C L^{-1} BP-3 in (●) simulated matrix and (■) urban wastewater at pH 8.0 and 35 ºC using an Al/Al cell at 15 mA cm^{-2}.

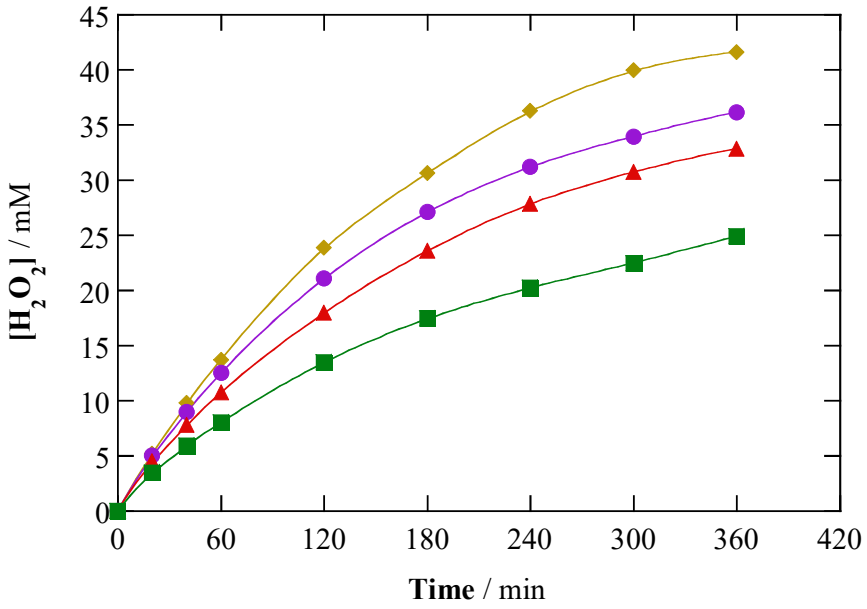

Fig. S4. Change of the concentration of accumulated H_2O_2 with electrolysis time during the electrolysis of 100 mL of: (◆) simulated matrix (EO-H_2O_2 conditions); urban wastewater with: (●) no catalyst in solution (EO-H_2O_2 conditions), (▲) addition of 10 mg L^{-1} Fe^{2+} (EF conditions) and (■) addition of 10 mg L^{-1} Fe^{2+} upon UVA irradiation (PEF conditions). Experiments were performed at natural pH using a BDD/air-diffusion cell at j = 33.3 mA cm^{-2} and 35 ºC.

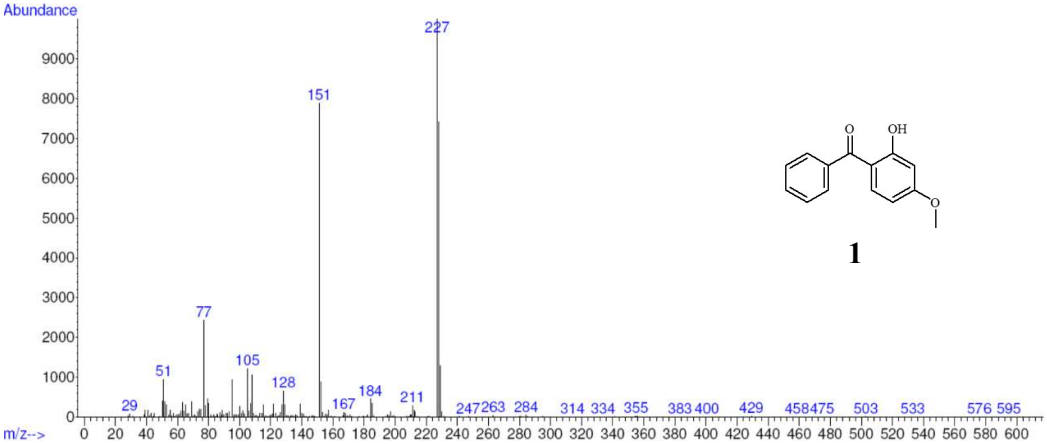
Abundance
m/z-->
227
151
77
105
51
128
29
167
184
211
247 263 284 314 334 355 383 400 429 458 475 503 533 576 595
O
OH
O
1

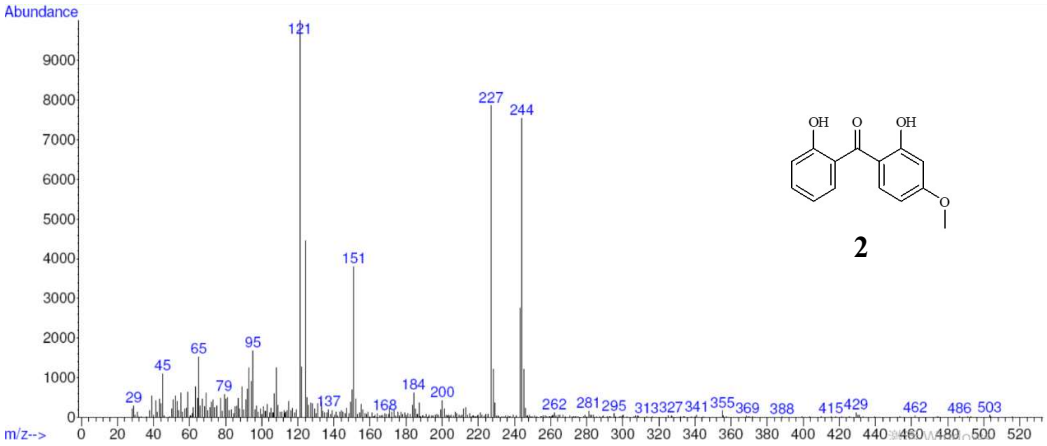
Abundance
m/z-->
121
227
244
151
65
95
45
79
29
137
168
184
200
262 281 295 313 327 341 355 369 388 415 429 462 486 503
OH
O
OH
O
2

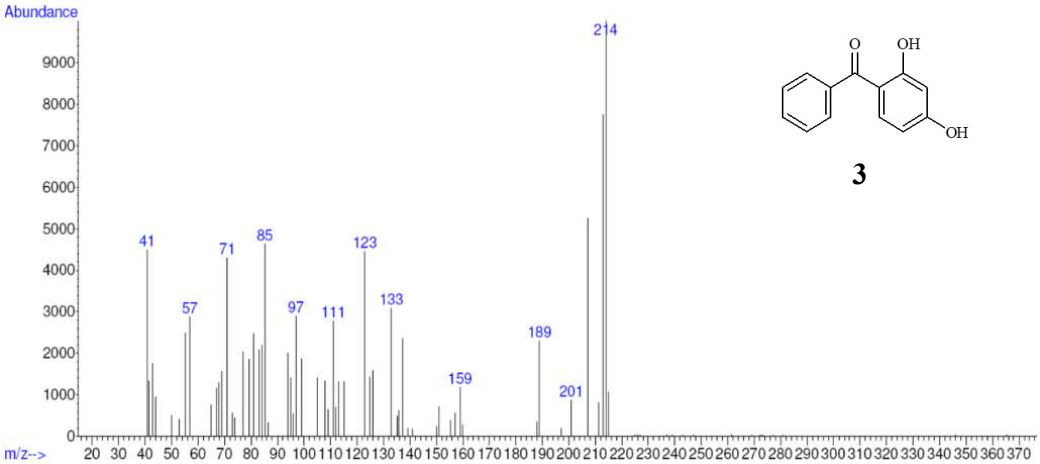
Abundance
m/z-->
214
41
71
85
123
57
97
111
133
189
159
201
O
OH
OH
3

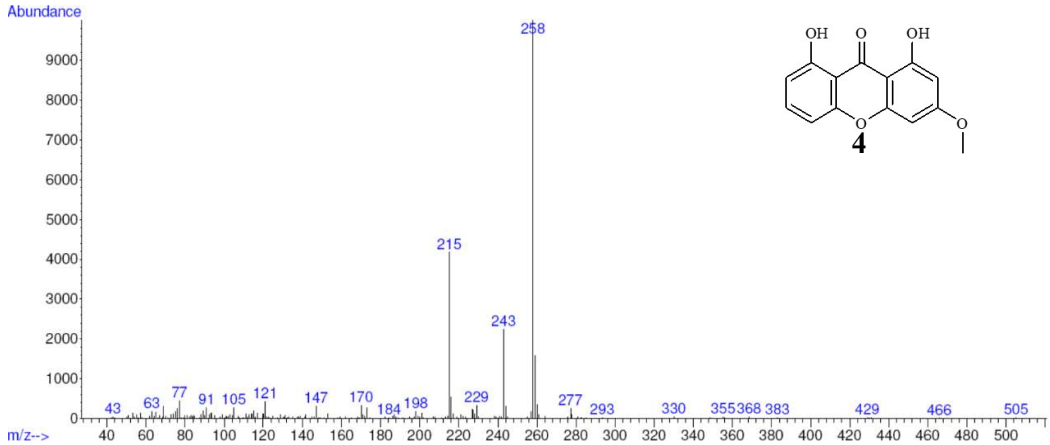
Abundance
m/z-->
258
215
243
OH
O
OH
O
O
4

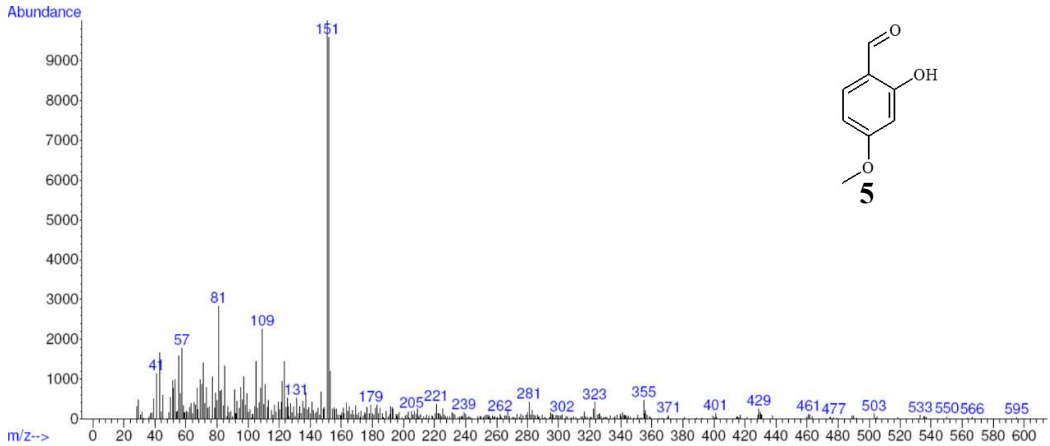
Abundance
m/z-->
151
81
109
57
41
O
OH
O
5

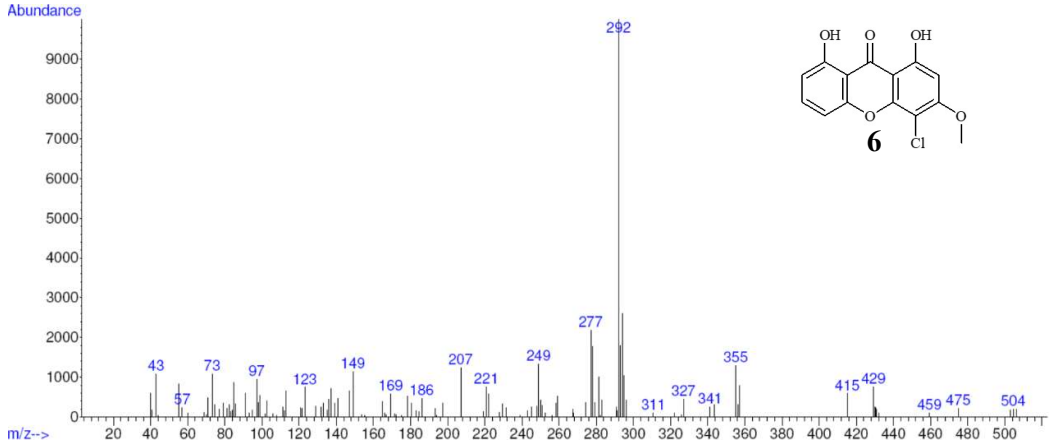
Abundance
m/z-->
292
277
OH
O
OH
O
O
Cl
6

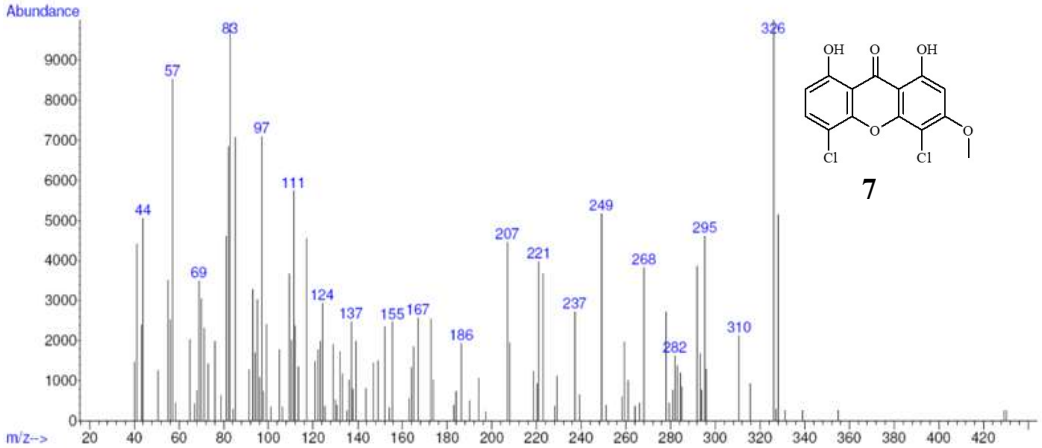
Abundance
m/z-->
326
83
57
97
111
44
69
124
137
155
167
186
207
221
237
249
268
282
295
310
OH
O
OH
O
Cl
Cl
O
7

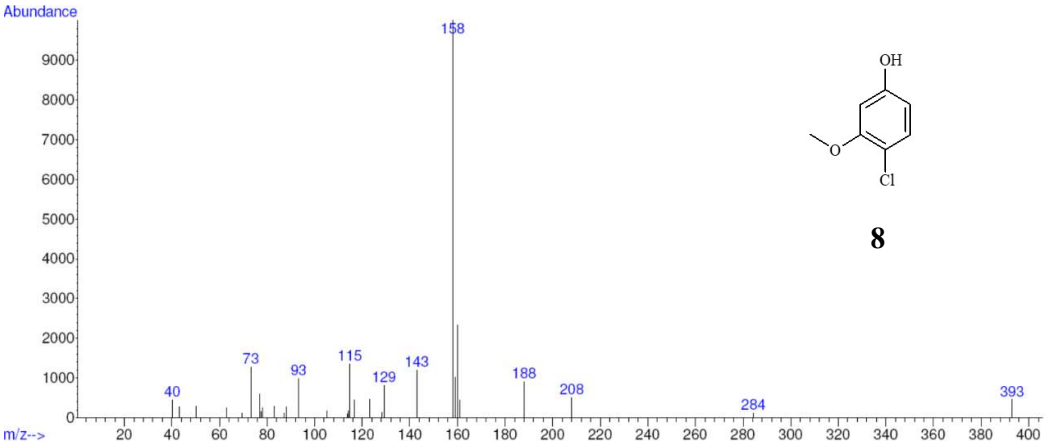
Abundance
m/z-->
158
40
73
93
115
129
143
188
208
284
393
OH
O
Cl
8

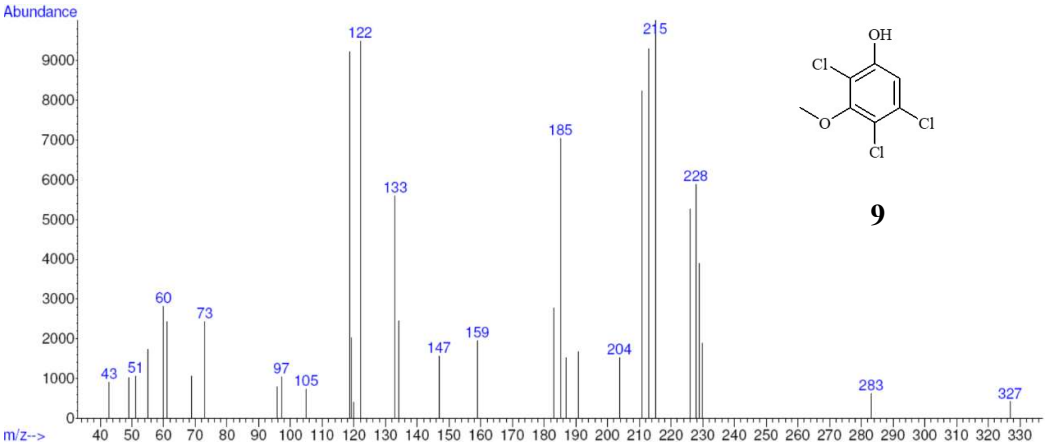
Abundance
m/z-->
122
215
133
185
228
60
73
43
51
97
105
147
159
204
283
327
OH
Cl
O
Cl
Cl
9

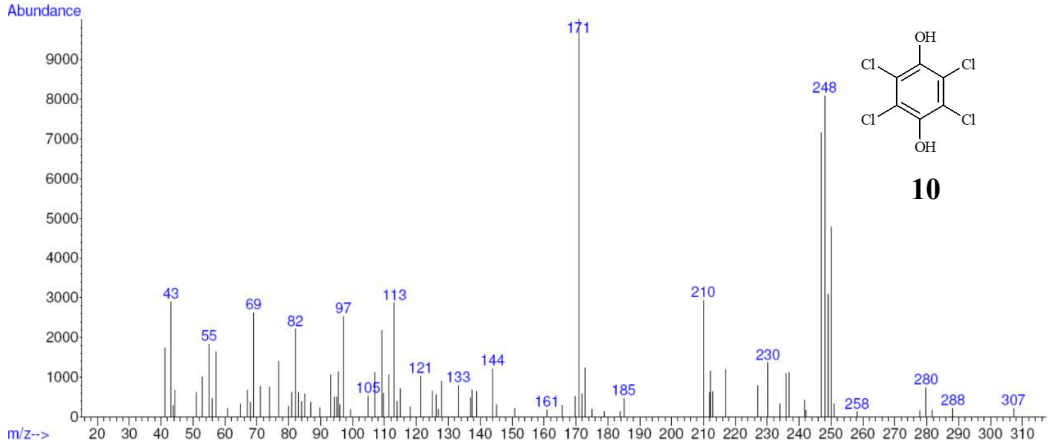
Abundance
m/z-->
171
248
43
69
55
82
97
113
105
121
133
144
161
185
210
230
258
280
288
307
OH
Cl
Cl
Cl
Cl
OH
10

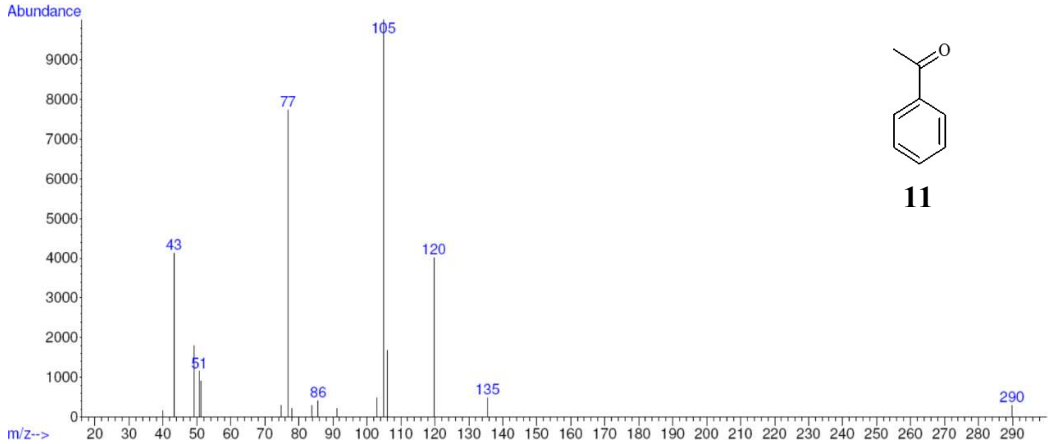
Abundance
m/z-->
105
77
43
120
51
86
135
290
O
11

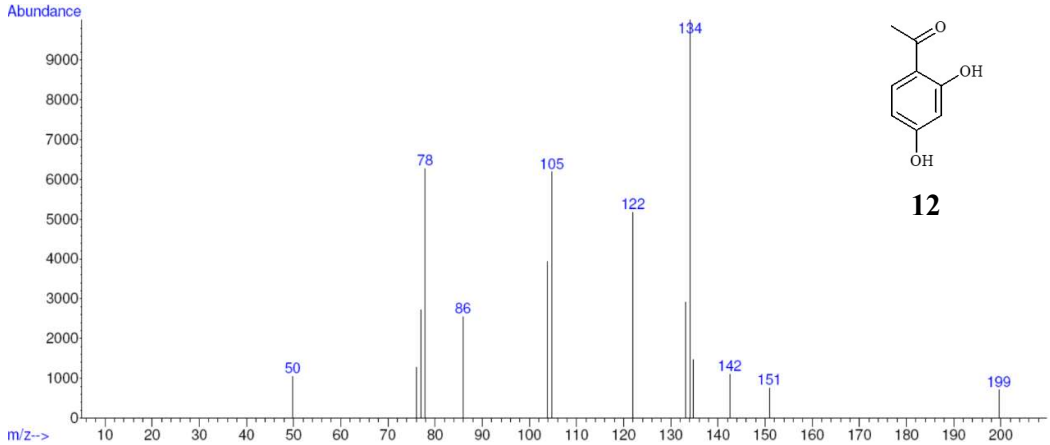
Abundance
m/z-->
134
78
105
122
86
50
142
151
199
O
OH
OH
12

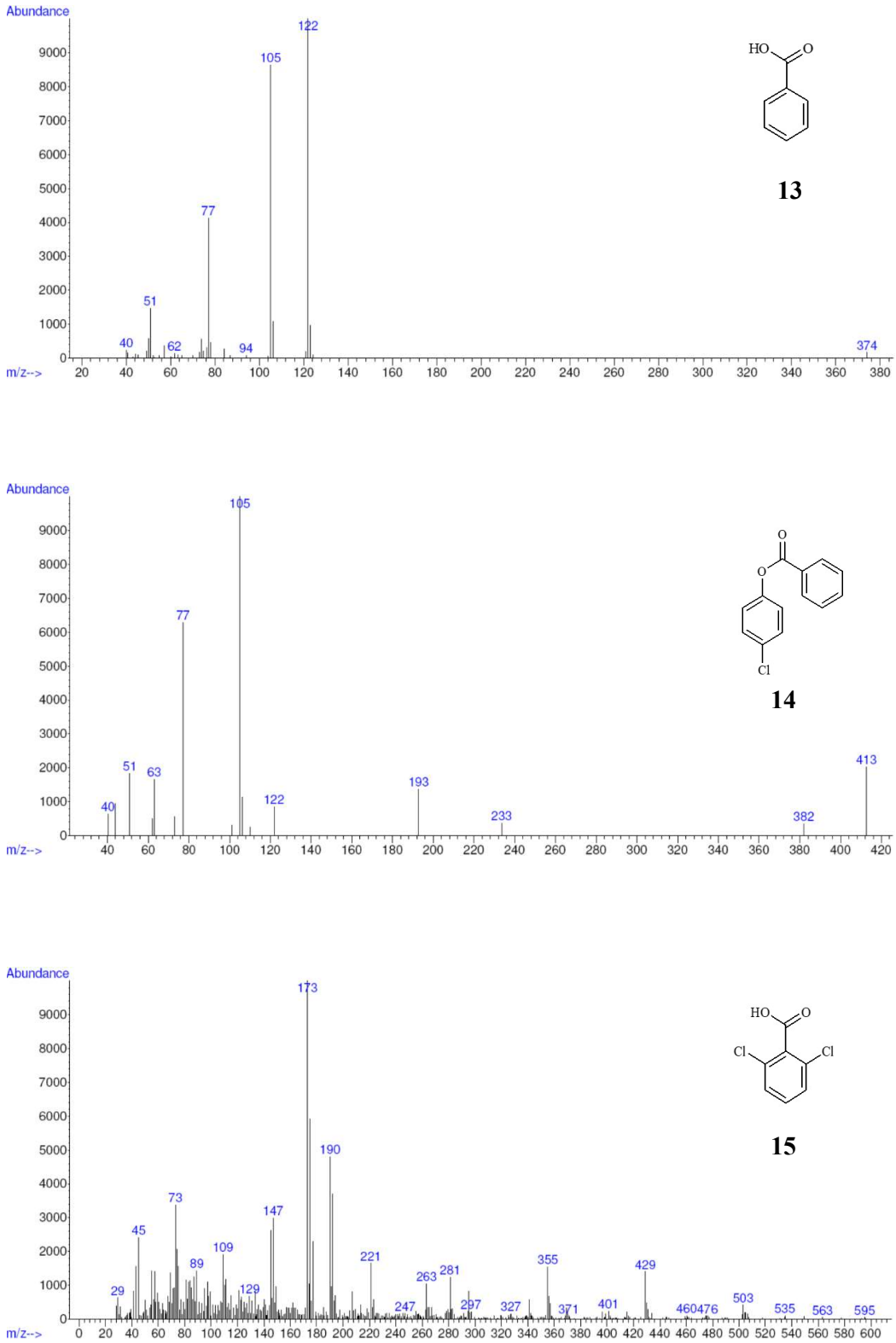

Fig. S5. Mass spectra obtained by GC-MS for the fifteen intermediates given in Table S5.

4.2. Fe(III)–EDDS-enhanced EF and PEF processes for the treatment of organic micropollutants at mild pH

4.2.1. Electro-Fenton process at mild pH using Fe(III)–EDDS as soluble catalyst and carbon felt as cathode

The EF systems equipped with a carbon-PTFE gas-diffusion cathode, in which the electrogenerated H_2O_2 reacts with externally added Fe^{2+} to form strong oxidizing $^{\bullet}OH$ under acidic conditions, have become excellent alternatives to treat refractory micropollutants. However, many industrial effluents and most natural sources of water possess circumneutral pH and the iron species is poorly recycled via cathodic reduction, which greatly impedes the use of conventional homogeneous EF. To overcome these handicaps, EF process catalyzed by Fe(III)–EDDS complex with a carbon-felt cathode was proposed for the first time in this work, and its performance was thoroughly evaluated by treating BHA-contaminated wastewater.

The degradation of 0.076 mM BHA using different iron species in 50 mM Na_2SO_4 medium at natural pH 5.7 with a carbon-felt or air-diffusion cathode was initially investigated. The largest BHA removal was achieved using the carbon-felt cathode with either Fe(II)–EDDS or Fe(III)–EDDS complex, reaching 95%-97% degradation at 45 min, whereas EF with $Fe(ClO_4)_3$ as catalyst attained a much lower BHA abatement of 60% due to partial precipitation of iron at high pH. The BHA decay obtained with an air-diffusion cathode was clearly much poorer than that with carbon felt, achieving only 21% removal at 45 min in Fe(III)–EDDS-assisted EF process. This behavior can be explained by the insignificant electroreduction of Fe(III)–EDDS on the air-diffusion cathode surface. Furthermore, the effect of Fe(III) and EDDS dosage and Fe(III):EDDS ratio on the performance of Fe(III)–EDDS-assisted EF process with carbon-felt cathode was investigated. The results revealed a slightly quicker BHA decay at higher Fe(III)–EDDS dosage and Fe(III):EDDS ratio, which can be justified by the increased amount

of Fe(II)–EDDS to foster the production $^{\bullet}OH$. However, an excess of EDDS contributed to the higher solution TOC and competed with BHA for $^{\bullet}OH$, decelerating the BHA degradation. Thus, 0.1 mM Fe(III)–EDDS (1:1) was selected as the optimum dosage to modify the EF process. The possibility of working within a wider pH range of 3.0-9.0 was also assessed. Similar BHA decay kinetics was found at alkaline pH up to 9.0 compared to that found at pH 5.7 and 7.0, attaining 95% removal at 45 min. Almost all the initial iron was kept soluble during the trial at pH 9.0, with only 6% precipitation thanks to the great stability of Fe(III)–EDDS at this pH.

The fate of iron, Fe(III)–EDDS and H_2O_2 was evaluated during the EF process using the carbon-felt or air-diffusion cathode in the absence or presence of BHA. In the absence of BHA, the former cathode allowed the generation of 2.71 mg L^{-1} Fe(II) (i.e., ~50% Fe(III) reduction) in 10 min, whereupon this content underwent an 8-fold decrease at 45 min due to the progressive abatement of EDDS, with 86% removal of Fe(III)–EDDS complex and the consequent precipitation of iron. In the presence of BHA, the decomposition of EDDS was somewhat inhibited, as BHA also consumed the $^{\bullet}OH$, ending in 76% Fe(III)–EDDS removal, which upgraded the Fe(III) electroreduction, with similar maximum Fe(II) regeneration but undergoing a much slower 2-fold decay thereafter. However, the air-diffusion cathode showed much lower ability for Fe(III) reduction with only 0.13 mg L^{-1} Fe(II) as maximal attained throughout all the treatments. Regarding the H_2O_2 production, up to 151 mg L^{-1} was attained at 45 min with the diffusion cathode, much higher than 10-13 mg L^{-1} as maximal achieved with carbon-felt cathode.

Additionally, the mineralization ability of the novel Fe(III)–EDDS-assisted EF process with carbon-felt cathode was assessed. In spite of the almost complete BHA removal achieved with IrO_2-based anode after 45 min at 50 mA, only 14% TOC abatement could be reached at 180 min, which means that some of the BHA and EDDS byproducts were refractory to oxidation. This occurred in concomitance with the progressive loss of Fe(III)–EDDS complex, which almost disappeared from solution in 60 min. Therefore,

the mineralization was pre-eminently caused by M(•OH) on the anode and may be a heterogeneous Fenton process. The use of a high oxidation power anode like BDD at pH 3.0 led to 71% TOC abatement, clearly outperforming the other systems.

The possibility of the additional contribution of heterogeneous Fenton reaction in this novel system was clarified by comparing the treatment of BHA solution using pre-prepared Fe(III)–EDDS complex at pH 9.0 with a sequential addition of iron species and EDDS. The former approach allowed working with the soluble complex, whereas precipitation of iron species on the cathode surface was presumed in the latter case. During the sequential addition, a very low iron content below 1 mg L^{-1} was detected in solution, but the degradation of BHA was very effective, with an analogous profile to that obtained following a simultaneous addition. The existence of iron precipitated on the cathode surface was verified via SEM-EDS analysis, and the XPS analysis of iron-loaded carbon felt after 10 min treatment confirmed the coexistence of ≡Fe(III) and ≡Fe(II). A further cyclic voltammetry study was conducted to verify the redox activity of the precipitated iron. The cyclic voltammograms showed a quasi-reversible adsorption signal related with ≡Fe(III) to ≡Fe(II) (reduction peak) and ≡Fe(II) to ≡Fe(III) (oxidation) transformations. The aforementioned results indicated that the heterogeneous reaction was a crucial mechanism especially in the absence of sufficient amount of soluble Fe(III)–EDDS.

Finally, eleven primary aromatic byproducts were identified by GC-MS analysis, and a plausible degradation pathway of BHA was proposed. These degradation routes included homogeneous Fenton's reaction in the bulk solution, heterogeneous Fenton at the cathode surface and electrocatalysis at the anode surface.

4.2.2. Expanding the application of photoelectro-Fenton treatment to urban wastewater using the Fe(III)–EDDS complex

After evaluating the performance of Fe(III)–EDDS-assisted EF process for the degradation of BHA in Na_2SO_4 solution, this work further reported the first investigation on the use of EDDS as chelating agent in the PEF treatment of fluoxetine spiked into wastewater at near-neutral pH. The use of Fe(III)–EDDS complex was expected to enhance the PEF process because: (i) this soluble complex can work at neutral pH, and (ii) the Fe(III)–EDDS photoreduction ensured a high quantum yield of Fe^{2+}, allowing the presence of sufficient iron catalyst for Fenton's reaction.

The application of different treatments was initially compared for the degradation of 0.049 mM fluoxetine in 0.050 M Na_2SO_4 medium at natural pH 5.7 using a carbon-PTFE air-diffusion cathode. A substantial fluoxetine removal of 34% was obtained in UVA/Fe(III)–EDDS trial, which was even higher than 24% achieved in EO process. The destruction of fluoxetine can be explained by the oxidative action of two types of radicals, $EDDS^{\bullet+}$ and superoxide radical ($O_2^{\bullet-}$), generated during the UVA irradiation of Fe(III)–EDDS complex (detailed in Appendix IV). The Fe(III)–EDDS-assisted EF process attained 69% fluoxetine removal in 60 min. This great performance was due to the production of a large amount of $HO_2^{\bullet}/O_2^{\bullet-}$. However, the catalytic complex in this EF process mainly existed as Fe(III)–EDDS, because the air-diffusion cathode had low ability for its electroreduction, explaining the null enhancement compared to the conventional EF process catalyzed by $FeSO_4$, which achieved slightly higher fluoxetine removal of 72%. The PEF treatments using $FeSO_4$ or $Fe(ClO_4)_3$ as catalyst yielded 88% and 83% fluoxetine removal, respectively, since UVA light allowed the continuous regeneration of Fe^{2+} from dissolved Fe^{3+} species. Finally, it was found that PEF with 0.1 mM Fe(III)–EDDS (1:1) was clearly superior to all the other treatments, being the only one that led to total drug removal in 60 min. The use of chelated Fe(III) was advantageous because: (i) it kept a higher amount of dissolved iron for longer time, in contrast to EF and PEF without EDDS, and (ii) the UVA radiation allowed that the main

form of such dissolved iron was Fe(II)–EDDS, in contrast to all the EF systems.

In order to better explain the trends of most of the aforementioned treatments, the fates of iron, H_2O_2 and Fe(III)–EDDS were investigated. In UVA photolysis with 0.1 mM Fe(III)–EDDS, 91% of Fe(III) was transformed into Fe^{2+} in 30 min, whereas the rest was soluble Fe(III), rather in uncomplexed form because the total disappearance of Fe(III)–EDDS complex occurred at 60 min. The results indicated a high quantum yield of Fe^{2+} upon Fe(III)–EDDS photoreduction. In Fe(III)–EDDS-catalyzed EF, the prevailing iron form of Fe(III) was confirmed, with only a minor production of Fe(II). Furthermore, the iron precipitation was particularly evident from 30 min, losing 42% of dissolved iron at the end of the treatment due to the continuous destruction of EDDS. In PEF with $Fe(ClO_4)_3$ as catalyst, the most relevant feature was the very low dissolved iron concentration at time zero (i.e., 1.5 mg L^{-1}), along with negligible production of Fe(II). In PEF with 0.1 mM Fe(III)–EDDS as catalyst, an accumulation as high as 1.7 mg L^{-1} Fe(II) (i.e., ~30% Fe(III) photoreduction) was achieved in 20 min, whereupon this content decayed progressively because of the gradual iron precipitation and the almost total disappearance of the very photoactive Fe(III)–EDDS complex. Hence, in the absence of enough EDDS, coagulation with $Fe(OH)_3$ probably played an important role in fluoxetine disappearance. Note that as a result of the greater presence of Fe(II) in this treatment, which stimulated Fenton's reaction, the accumulated H_2O_2 concentration (3.5 mM) was much lower than in the previous processes.

The degradation of 0.049 mM fluoxetine prepared in urban wastewater by Fe(III)–EDDS-catalyzed PEF was performed using the IrO_2/air-diffusion cell at 50 mA and natural pH 7.2. The drug removal at 60 min was as low as 53% instead of 100% attained in 0.050 M Na_2SO_4 solution. The slower decay in wastewater can be rather accounted for by its particular composition, since it contained: natural organic matter (NOM) that competitively consumed UVA photons and reacts with oxygen radicals, as well as with ions that act as radical scavengers. In order to eliminate the impact of CO_3^{2-} and HCO_3^- ions, CO_2 was stripped from the urban wastewater before the treatment, then a faster

and larger fluoxetine disappearance, reaching 78%, was obtained. In addition, the effect of solution pH, Fe(III)–EDDS dosage, Fe(III):EDDS ratio and applied current was assessed. As expected, a better performance was obtained at more acidic pH, since a lower pH value ensured that, as EDDS became destroyed, a larger amount of iron ions was dissolved rather than precipitated. For the other variables, the PEF treatment catalyzed with 0.20 mM Fe(III)–EDDS (1:1) using the IrO_2/air-diffusion cell at 50 mA was proven to be the most successful for the treatment of fluoxetine-contaminated wastewater.

Although the main goal of this work was to investigate the ability of the Fe(III)–EDDS-catalyzed PEF process to remove a target organic pollutant from urban wastewater, its mineralization ability was also tested. The PEF treatment catalyzed with 0.10 mM Fe(III)–EDDS (1:1) using the BDD anode at 100 mA achieved around 50% TOC removal at 300 min, which means that a higher residual TOC was still present in the final solution. This is not surprising because the decontamination occurred in two consecutive stages: (i) the first one, where the $^{\bullet}OH$ formed from Fenton's reaction had the leading role before the disappearance of EDDS, followed by (ii) a second one, where fluoxetine byproducts and organic components from the wastewater were destroyed by the adsorbed M($^{\bullet}OH$). In spite of yielding only a partial TOC abatement, the toxicity analysis revealed a high EC_{50} value after 180 min treatment, which was close to that of the raw urban wastewater (80-90 mg L^{-1}). These result means that the detoxification was still ensured during the Fe(III)–EDDS-catalyzed PEF.

Finally, the reaction byproducts of fluoxetine were detected by GC-MS analysis of the organic compounds extracted upon Fe(III)–EDDS-catalyzed PEF treatment of fluoxetine in either 0.050 M Na_2SO_4 or wastewater matrix. Based on the trends highlighted above, a very detailed mechanism for the Fe(III)–EDDS-catalyzed PEF treatment in urban wastewater at near-neutral pH was proposed.

GROUP OF ARTICLES INCLUDED IN SECTION 4.2

Page 178: **Electro-Fenton process at mild pH using Fe(III)–EDDS as soluble catalyst and carbon felt as cathode**

Zhihong Ye, Enric Brillas, Francesc Centellas, Pere Lluís Cabot, Ignasi Sirés.

Applied Catalysis B: Environmental 257 (**2019**) 117907

Page 200: **Expanding the application of photoelectro-Fenton treatment to urban wastewater using the Fe(III)–EDDS complex**

Zhihong Ye, Enric Brillas, Francesc Centellas, Pere Lluís Cabot, Ignasi Sirés.

Water Research DOI: 10.1016/j.watres.2019.115219

Appendix III

Electro-Fenton process at mild pH using Fe(III)–EDDS as soluble catalyst and carbon felt as cathode

Applied Catalysis B: Environmental 257 (2019) 117907

Contents lists available at ScienceDirect

Applied Catalysis B: Environmental

journal homepage: www.elsevier.com/locate/apcatb

Electro-Fenton process at mild pH using Fe(III)-EDDS as soluble catalyst and carbon felt as cathode

Zhihong Ye, Enric Brillas, Francesc Centellas, Pere Lluís Cabot, Ignasi Sirés*

Laboratori d'Electroquímica dels Materials i del Medi Ambient, Departament de Química Física, Facultat de Química, Universitat de Barcelona, Martí i Franquès 1-11, 08028 Barcelona, Spain

ARTICLE INFO

Keywords:
Butylated hydroxyanisole
Carbon-felt cathode
Electro-Fenton
Ethylenediamine-*N,N'*-disuccinic (EDDS) acid
Water treatment

ABSTRACT

The feasibility of destruction of organic pollutants in water at near-neutral pH by homogeneous electro-Fenton (EF) process employing a soluble Fe(III)–EDDS complex as catalyst is demonstrated for the first time. The performance of the Fe(III)–EDDS-assisted EF process with carbon-felt or air-diffusion cathodes was evaluated from the degradation of butylated hydroxyanisole (BHA) in sulfate medium. The influence of applied current, pH and Fe(III):EDDS ratio and dosage on BHA decay and mineralization was related to the evolution of H_2O_2 and iron concentrations. Using Fe(III)–EDDS, up to 50% Fe(II) regeneration was achieved in 10 min, whereas only 23% was transformed using hydrated Fe^{3+}. Almost total removal of BHA was achieved thanks to homogenous Fenton, heterogeneous Fenton with cathodically adsorbed Fe(III), and electrocatalysis. The mineralization partly corresponded to the gradual destruction of EDDS by hydroxyl radical ($k_{abs} = 5.22 \times 10^9\ M^{-1}\ s^{-1}$), and involved the formation of 5 oxidation and 6 dimerization or cyclization by-products.

1. Introduction

In recent years, the electrochemical advanced oxidation processes (EAOPs) based on Fenton's reaction (1) have been investigated in great detail owing to the great ability of the in-situ generated hydroxyl radical ($^{\bullet}OH$) to degrade aqueous organic micropollutants [1–3]. Among them, electro-Fenton (EF) is the most popular method due to its simplicity and easy scalability [4]. Homogeneous EF demands an acidic pH 2.5–3.5 to ensure the total solubilization of Fe(II) or Fe(III) salts, thereby yielding a very fast decontamination.

$$H_2O_2 + Fe(II) \rightarrow Fe(III) + {}^{\bullet}OH + OH^- \quad (1)$$

H_2O_2 is produced on site from the two-electron O_2 reduction reaction (2). Carbonaceous air-diffusion cathodes allow obtaining the highest H_2O_2 concentrations under ambient conditions, hampering any other reduction process [5–8]. Large surface area carbon-felt cathodes generate lower H_2O_2 contents even upon O_2-saturation of solutions [9–11], although they favor the simultaneous Fe(II) regeneration from reaction (3) that maintains the catalytic cycle, thus yielding complete removal of total organic carbon (TOC) [12–15].

$$O_2(g) + 2H^+ + 2e^- \rightarrow H_2O_2 \quad (2)$$

$$Fe(III) + e^- \rightarrow Fe(II) \quad (3)$$

The properties of carbon felt, including high porosity and specific surface area [16,17], make it an optimum choice as three-dimensional electrode. The latest advances on its application to EF treatment and many other electrochemical technologies have been recently reviewed [16,18].

Many industrial effluents and most natural sources of water are at circumneutral pH, which impedes the use of conventional homogeneous EF unless pH regulation and monitoring is carried out. In order to overcome such handicap, heterogeneous EF has been recently developed [19,20], mainly following two different strategies: (i) external addition of suspended iron-based catalysts [21,22], or (ii) use of iron-based particles supported on substrates like carbonaceous cathodes [23,24] or loaded on membranes and resins [25]. However, the loss of active sites and the lack of stability in consecutive degradation cycles due to iron leaching and gradual solubilization are potential drawbacks.

Lately, a novel alternative has been devised to carry out homogeneous catalytic water treatment operating at mild pH [26]. In particular, ethylenediamine-*N,N'*-disuccinic (EDDS) acid has been employed to form the Fe(III)–EDDS complex and catalyze the conventional Fenton-based processes. The performance of this aminopolycarboxylic acid (APCA) has only been tested in non-electrochemical Fenton-like systems, both in the dark [27] and under UV [28] or sunlight irradiation [29]. An electrochemical approach could enhance the continuous electroreduction of Fe(III)–EDDS complex from reaction (3), thus giving

* Corresponding author.
E-mail address: i.sires@ub.edu (I. Sirés).

https://doi.org/10.1016/j.apcatb.2019.117907
Received 1 April 2019; Received in revised form 30 May 2019; Accepted 26 June 2019
Available online 28 June 2019
0926-3373/

rise to a new kind of homogeneous EF process. Note that EDDS is a more suitable ligand than citrate, oxalate and the two most widely used APCAs, nitrilotriacetic (NTA) and ethylenediaminetetraacetic (EDTA) acids, due to its larger biodegradability [27].

Homogeneous catalysis with soluble Fe(III)–EDDS complex can be combined with electrocatalysis by equipping the electrochemical reactor with an anode that is able to produce M($^{\bullet}$OH) from water oxidation via reaction (4) [30,31]. Boron-doped diamond (BDD) thin films yield the most active type of M($^{\bullet}$OH) but, due to their high cost, dimensionally stable anodes based on RuO_2 or IrO_2 are more commonly employed.

$$M + H_2O \rightarrow M(^{\bullet}OH) + H^+ + e^- \quad (4)$$

In this work, the performance of EF process catalyzed with Fe (III)–EDDS complex to treat butylated hydroxyanisole (BHA) as a model contaminant of emerging concern was thoroughly evaluated. BHA is widely used as food antioxidant and preservative in the cosmetic industry [32], eventually ending in all kinds of water reservoirs. Lately, serious concerns have arisen due to evidences for carcinogenicity [32,33], adverse ecotoxicological effects [34] and its endocrine disrupting activity [35]. Several authors have studied its degradation by photoassisted methods [36,37], chemical treatments with O_3 [35,37] or chlorine [38], and electrochemical technologies like electrocoagulation as well as conventional EF and photoelectro-Fenton with air-diffusion cathodes and 0.5 mM $FeSO_4$ as catalyst source [39]. Considering the state of the art, the modification of the conventional homogeneous EF process based on EDDS is proposed for the first time. Aqueous solutions with a low BHA concentration and 50 mM Na_2SO_4 at natural pH have been treated in a cell with an IrO_2-based or BDD anode and a carbon-felt cathode, aiming to enhance the Fe(III)–EDDS reduction as a crucial step to produce $^{\bullet}$OH. The operation conditions were optimized from BHA and TOC decays. The contribution of heterogeneous Fenton reaction and the ability of the system for Fe(II) regeneration were assessed from scanning electron microscopy (SEM) with energy dispersive x-ray spectroscopy (EDS), x-ray photoelectron spectroscopy (XPS) and cyclic voltammetry, along with the analysis of the time course of uncomplexed iron species, H_2O_2 and Fe(III)–EDDS complex. A very low Fe (III) concentration was employed in all tests. The steady-state concentration of hydroxyl radicals in the novel system has also been determined. Comparative trials were also performed with a carbon-polytetrafluoroethylene (PTFE) air-diffusion cathode and hydrated Fe^{3+} as catalyst. Reaction by-products were identified by high-performance liquid chromatography (HPLC) and gas chromatography-mass spectrometry (GC-MS), and a degradation mechanism of Fe(III)–EDDS-assisted EF process was finally proposed.

2. Materials and methods

2.1. Chemicals

BHA (99% purity) and *p*-hydroxybenzoic acid (*p*HBA, ≥ 99%) were purchased from Sigma-Aldrich. Na_2SO_4, H_2SO_4, NaOH, $FeSO_4{\cdot}7H_2O$, $FeCl_2$ and $Fe(ClO_4)_3$ of analytical grade were supplied by Merck, J.T. Baker and Sigma-Aldrich. EDDS trisodium salt solution (~35% in H_2O) was supplied by Sigma-Aldrich. Ti(IV) oxysulfate for H_2O_2 determination was purchased from Panreac, whereas 1,10-phenantroline monohydrate (99% purity) from Alfa-Aesar and ascorbic acid from Sigma-Aldrich were employed for soluble iron analysis. Organic solvents of HPLC or analytical grade were purchased from Panreac and Merck. All aqueous solutions were prepared with Millipore Milli-Q water (resistivity > 18.2 MΩ cm).

The Fe(III)–EDDS complexes with different ratios were formed by mixing appropriate amounts of $Fe(ClO_4)_3$ and EDDS solutions [27] followed by vigorous stirring for 3 min. Stock solutions of 10 mM Fe $(ClO_4)_3$ and EDDS were stored in the dark, and fresh complexes were prepared before each experiment. For example, the combination of both reagents to reach 0.10 mM of each gave rise to 0.10 mM Fe(III)–EDDS (1:1) complex. To form the Fe(II)–EDDS complex, $FeCl_2$ was used as iron source. In some cases, a sequential addition of Fe(III) and EDDS was followed. Some comparative trials were also performed using $Fe_2(SO_4)_3$ or $FeCl_3$ instead of $Fe(ClO_4)_3$.

2.2. Electrolytic cells

Most of the experiments were carried out in an undivided glass cell thermostated at 25 °C under stirring with a PTFE follower at 700 rpm. A carbon-felt piece (11.0 cm × 5.0 cm × 0.5 cm) from Mersen was used as cathode. Before first use, it was activated by immersion in a 4 M H_2SO_4 solution at 60 °C for 3 h. The anode of 3 cm^2 geometric area was either an IrO_2-based coated Ti plate purchased from NMT Electrodes or a BDD thin film supplied by NeoCoat. The interelectrode gap was about 1.0 cm. Prior to each electrolysis, compressed air was sparged through the solution at 0.35 mL min^{-1} for 10 min, which was maintained during the trials to ensure the saturation with O_2 for H_2O_2 electrogeneration. After each trial, the cathode was immersed in a 4 M H_2SO_4 solution for 10 min and then rinsed several times with Milli-Q water and dried in an oven at 90 °C.

In some cases, the electrolytic trials were performed with the same cell but replacing the carbon felt by a 3 cm^2 carbon-PTFE air-diffusion electrode supplied by E-TEK, fitted in a tubular gas chamber that was fed with compressed air at 1 L min^{-1}. A preliminary polarization in 100 mL of a 50 mM Na_2SO_4 solution at 300 mA for 180 min ensured the surface cleaning and activation.

The electrolytic trials were made with 150 mL of 50 mM Na_2SO_4 solutions, without or with 0.076 mM BHA (10 mg L^{-1} TOC).

2.3. Carbon-felt cathode characterization

The morphological features of pristine and Fe(III)-loaded carbon felt were assessed by SEM-EDS employing a field emission scanning electron microscope (JEOL JSM-7100 F) at 15 kV equipped with an INCA analyzer.

XPS analysis was performed with a PHI 5500 Multitechnique System (Physical Electronics) using an Al-Kα monochromatised X-ray source (1486.6 eV and 350 W) placed perpendicularly to the analyzer axis and calibrated using the $3d_{5/2}$ line of Ag (full width at half maximum of 0.8 eV). The analyzed area was a circle of 0.8 mm diameter. The selected resolution for the spectra was 187.85 eV of Pass Energy (PE) and 0.8 eV/step for the general spectra, and 23.5 eV of PE and 0.1 eV/step for the spectra of the different elements. A low energy electron gun (less than 10 eV) was used. All measurements were made under ultra-high vacuum at pressures between 5×10^{-9} and 2×10^{-8} Torr. The spectra were analyzed using the ULVAC-PHI MultiPakTM Software 8.2.

The electrochemical characterization was carried out by cyclic voltammetry on an Autolab PGSTAT30 potentiostat. An undivided electrochemical cell containing 50 mL of a 50 mM Na_2SO_4 solution at natural pH and thermostatized at 25 °C was used. It was equipped with a carbon-felt piece (1.0 cm × 1.0 cm × 0.5 cm), in the absence or presence of pre-adsorbed Fe(III) species, a platinum spiral and Ag|AgCl (KCl sat.) as the working, counter and reference electrode, respectively. The voltammograms were recorded within a potential range from +0.700 V to -1.450 V at a scan rate of 0.100 V s^{-1}. Prior to each run, O_2 was purged out from solutions under a gentle N_2 stream. For comparison, voltammograms were also obtained with a pristine carbon-felt electrode in a 50 mL solution containing 0.10 mM $Fe(ClO_4)_3$ and 50 mM Na_2SO_4 solution at natural pH.

2.4. Other apparatus and analytical methods

Galvanostatic electrolyses were performed with an Amel 2053 potentiostat-galvanostat and the cell voltage (E_{cell}) was provided by a

Demestres 601BR digital multimeter. The electrical conductance and pH were measured with a Metrohm 644 conductometer and a Crison GLP 22 pH-meter, respectively. Once withdrawn from treated solutions, samples were microfiltered with 0.45 µm PTFE filters from Whatman. H_2O_2 concentration was determined from the light absorption of its yellow Ti(IV) complex, at λ = 408 nm, measured on a Shimadzu 1800 UV/Vis spectrophotometer at 25 °C. The dissolved Fe(II) content was obtained from the absorbance of their corresponding reddish complex formed with 1,10-phenantroline, at λ = 508 nm. Total dissolved Fe concentration was determined upon addition of ascorbic acid to the previous samples to transform all Fe(III) into Fe(II). Quantitative analysis of Fe was also performed by inductively-coupled plasma with optical detection (ICP-OES) using the Optima 3200 L spectrometer from Perkin Elmer. TOC of BHA solutions was determined on a Shimadzu TOC-VCNS analyzer, using the non-purgeable organic content procedure.

BHA concentration was analyzed by reversed-phase HPLC using a Waters 600 liquid chromatograph fitted with a BDS Hypersil C18 5 µm, 250 mm × 4.6 mm, column at 35 °C. It was coupled to a Waters 996 photodiode array detector (PAD) set at 290 nm. The mobile phase was a 70:30 (v/v) CH_3CN/10 mM KH_2PO_4 (pH 3.0) mixture eluted at 1.0 mL min^{-1}, and the peak of BHA was obtained at 5.1 min. Samples were always diluted with CH_3CN to stop the degradation of BHA. The concentration of the Fe(III)–EDDS complex was determined in the same HPLC system, with the PAD set at 240 nm. The mobile phase was a mixture of A and methanol (95:5, v/v), where A was Milli-Q water with 2 mM tetrabutylammonium hydrogensulfate and 15 mM sodium formate at pH = 4.0, circulating at a flow rate of 0.8 mL min^{-1}. The Fe (III)–EDDS peak was displayed at 10.7 min.

The competition kinetics method with *p*HBA as reference substrate allowed determining the absolute rate constant (k_{abs}) for the reaction between EDDS and hydroxyl radical, as well as the concentration of this radical. In these experiments, the Fe(III)–EDDS complex was monitored as explained above, whereas a 50:50 (v/v) CH_3CN/H_2O (2% acetic acid) mixture eluted at 1.0 mL min^{-1} was needed to obtain a well defined peak at 3.3 min for *p*HBA. Further details on the methodology can be found elsewhere [40].

Each experiment was performed at least in duplicate and average values are given. The corresponding error bars with 95% confidence interval are given in figures.

GC-MS analysis was performed in a 6890 N gas chromatograph (Agilent Technologies) coupled to a 5975C mass spectrometer operating in electron impact mode at 70 eV. A nonpolar Teknokroma Sapiens-X5 ms and a polar HP INNOWax column, both of 0.25 µm, 30 m × 0.25 mm, were used. The temperature ramp was: 36 °C for 1 min, 5 °C min^{-1} up to 320 °C, and hold time of 10 min. The temperature of the inlet, source and transfer line was 250, 230 and 300 °C. Liquid-liquid extractions with CH_2Cl_2 allowed obtaining an organic solution that was further dried over anhydrous Na_2SO_4, filtered and concentrated under reduced pressure. The mass spectra were identified with the NIST05 MS database.

3. Results and discussion

3.1. Comparison of BHA removal with carbon-felt and air-diffusion cathodes

Fig. S1 of Supplementary Material informs about the high stability of the 0.10 mM Fe(III)–EDDS (1:1) complex, regardless of the solution pH between 3.0 and 9.0 (Fig. S1a) or the exposure time to each pH (Fig. S1b-d). Speciation diagrams of ferric complexes as a function of pH determined with solutions containing EDDS showed that the use of this chelating agent may make Fe(III) soluble until near-neutral pH [41], but here we give an evidence on the stability of the complex even under more alkaline conditions (pH 9.0), which was unexpected.

In Fig. 1, the degradation of 0.076 mM BHA using different iron species at natural pH 5.7 with an IrO_2-based anode and a carbon-felt or air-diffusion cathode, at 50 mA, is depicted. The largest BHA removal was achieved using the carbon-felt cathode (Fig. 1a). In EF with 0.10 mM of either Fe(II)–EDDS (1:1) or Fe(III)–EDDS (1:1) complex, 95%–97% degradation was reached at 45 min. Using Fe(II)–EDDS, the faster BHA decay during the first 10 min can be accounted for by the presence of Fe(II) formed in its complexation equilibria, further yielding $^{\bullet}OH$ from homogeneous Fenton's reaction (1). Conversely, Fe (III)–EDDS is in equilibrium with Fe(III), which promotes the formation of the less powerful hydroperoxyl radical ($HO_2^{\bullet}$) from the following Fenton-like reaction:

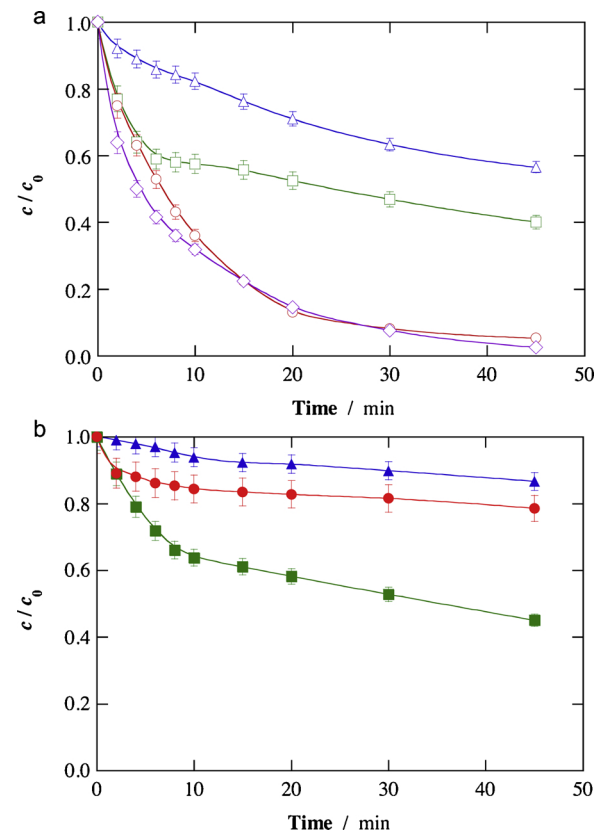

Fig. 1. Time course of the normalized BHA concentration decay during the treatment of 150 mL of 0.076 mM BHA solutions with 50 mM Na_2SO_4 at natural pH 5.7 and 50 mA by: (△,▲) EO-H_2O_2, (□,■) conventional homogeneous EF with 0.10 mM $Fe(ClO_4)_3$, and novel homogeneous EF with 0.10 mM (○,●) Fe (III)–EDDS (1:1) or (◇) Fe(II)–EDDS (1:1) complex, using a 3-cm^2 IrO_2-based anode and a (a) carbon-felt (11.0 cm × 5.0 cm × 0.5 cm) or (b) 3-cm^2 carbon-PTFE air-diffusion cathode.

$$H_2O_2 + Fe(III) \rightarrow Fe(II) + HO_2^{\bullet} + H^+ \quad (5)$$

Nonetheless, both profiles became very similar with electrolysis time because the interactions between complexed iron and H_2O_2, occurring via homogeneous reactions (6) and (7), are analogous to those from reactions (1) and (5), respectively [27]. Hence, in EF with Fe (II)–EDDS, the organics were mainly degraded by $^{\bullet}OH$ formed from reaction (6), especially during the first minutes. The resulting complex, Fe(III)–EDDS, can be at least partly reduced to Fe(II)–EDDS at the cathode (see below), which explains the quick BHA decay in EF with Fe (III)–EDDS. In addition, this latter complex can yield $HO_2^{\bullet}$ via reaction (7).

$$Fe(II)\text{–}EDDS + H_2O_2 \rightarrow Fe(III)\text{–}EDDS + {}^{\bullet}OH + OH^- \quad (6)$$

$$Fe(III)\text{–}EDDS + H_2O_2 \rightarrow Fe(II)\text{–}EDDS + HO_2^{\bullet} + H^+ \quad (7)$$

Typically, Fe(II) salts are unstable under oxygenated atmosphere

owing to gradual oxidation and, moreover, they are more expensive than Fe(III) ones. Since a similar degradation rate was obtained in both cases, all subsequent assays with EDDS were carried out with the Fe(III) salt.

The BHA decay was much slower in EF with $Fe(ClO_4)_3$ in the absence of EDDS, i.e., conventional homogeneous EF, attaining 60% at 45 min (Fig. 1a). The quick loss of oxidation power from about 10 min can be explained by the partial precipitation of iron as hydroxides/oxides at high pH. Once this occurred, BHA was slowly degraded thanks to: (i) the action of radicals formed from reaction (1) and (5) at a very small content of soluble catalyst, (ii) heterogeneous Fenton's reaction promoted by the solid hydroxides/oxides [19] and, possibly, (iii) adsorption onto solid iron. Note that, despite the iron precipitation, the EF process yielded a faster and larger removal than electro-oxidation with electrogenerated H_2O_2 (EO-H_2O_2). Since blank experiments in the absence of current did not show BHA adsorption on carbon felt, and the absence of ionizable atoms precluded a possible effect of electrosorption, the 44% BHA removal by EO-H_2O_2 at 45 min can be mainly related to the action of $IrO_2(^{\bullet}OH)$ formed via reaction (4). This informs about the much milder action of this radical as compared to homogeneous $^{\bullet}OH$.

Fig. 1b shows the trends obtained with an air-diffusion cathode, which clearly was much less effective than carbon felt to degrade BHA. A very slow disappearance of the pollutant under EO-H_2O_2 conditions can be seen, with a final removal of 13%. It is well known that this cathode possesses an extraordinary ability to generate H_2O_2 [5–8], much greater than carbon felt [9]. Since the H_2O_2 concentration is expected to be much higher than BHA one (= 0.076 mM), $IrO_2(^{\bullet}OH)$ is consumed to a large extent in H_2O_2 oxidation reaction, in contrast to that observed in Fig. 1a. On the other hand, the trend of BHA content in EF without EDDS looks like that commented for Fig. 1a, also attaining a similar decay of 55% at 45 min. As discussed above, in this system most of the iron precipitates and thus, the differences in the reduction power of both cathodes are of minor relevance as compared to heterogeneous reactions and adsorption on the oxides. Finally, it is worth highlighting the poor BHA degradation in Fe(III)–EDDS-assisted EF, with only 21% removal at 45 min. This behavior can be explained by the insignificant electroreduction of Fe(III)–EDDS on the air-diffusion cathode surface, as will be shown below. Since $^{\bullet}OH$ cannot be formed from reaction (6) and $IrO_2(^{\bullet}OH)$ cannot be accumulated, as shown in EO-H_2O_2, $HO_2^{\bullet}$ constituted the main oxidant. Apart from exhibiting a low oxidation power, the latter radical was greatly consumed in the degradation of EDDS, which competed with BHA.

The effect of the Fe(III) and EDDS dosage using the carbon-felt cathode can be seen in Fig. S2. A faster BHA removal was achieved with 0.20 mM Fe(III)–EDDS (1:1), as compared to 0.10 mM (Fig. 1a), in agreement with a higher amount of Fe(II)–EDDS formed upon cathodic reduction that eventually fostered the production of $^{\bullet}OH$ from reaction (6). Conversely, the decay at 0.40 mM Fe(III)–EDDS was analogous to that at 0.10 mM, which can be justified by the destruction of many $^{\bullet}OH$ during EDDS oxidation. Since all removals at 45 min were close to 95–97%, 0.10 mM was chosen as the optimum concentration in order to keep a low contribution of EDDS to solution TOC.

Some trials were also performed to assess the effect of the Fe(III):EDDS ratio, but 1:2 or higher ratios did not enhance sufficiently the EF performance (not shown). This means that the 1:1 ratio already ensured the total solubilization of 0.10 mM Fe(III) and hence, an excess of EDDS would become detrimental due to the parasitic reactions between $^{\bullet}OH$ and EDDS, decelerating the BHA degradation.

The different time course of key species during the EF process with 0.1 mM Fe(III)–EDDS (1:1) using the carbon-felt or air-diffusion cathode is depicted in Fig. 2. In the absence of BHA, the former cathode allowed the generation of 2.71 mg L^{-1} Fe(II) (i.e., ~50% Fe(III) reduction, Fig. 2a) in 10 min, whereupon this content underwent an 8-fold decrease at 45 min. As can be seen in Fig. 2b, this was due to the progressive abatement of EDDS, with 86% removal of Fe(III)–EDDS

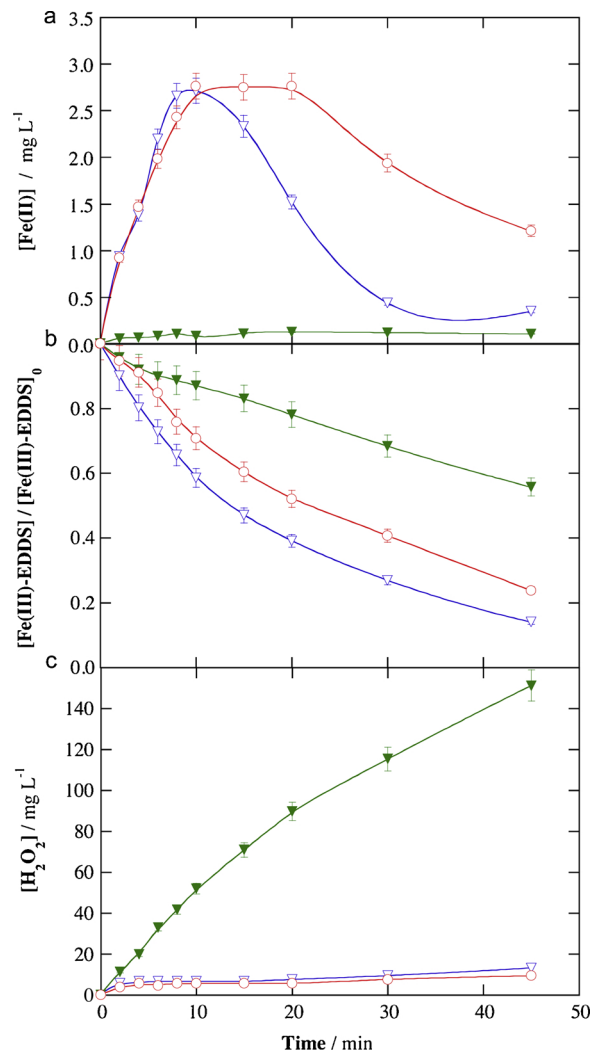

Fig. 2. Change of (a) Fe(II), (b) normalized Fe(III)–EDDS and (c) accumulated H_2O_2 concentrations with electrolysis time during the novel EF treatment of 150 mL of 50 mM Na_2SO_4 solutions (▽,▼) without and (○) with 0.076 mM BHA at natural pH 5.7 and 50 mA using an IrO_2-based anode and a (▽,○) carbon-felt or (▼) air-diffusion cathode, with 0.10 mM Fe(III)–EDDS (1:1) complex.

complex and the consequent precipitation of iron. In the presence of BHA, Fig. 2b shows that the decomposition of EDDS was somewhat inhibited, as BHA also consumed the $^{\bullet}OH$, ending in 76% of Fe(III)–EDDS removal. Consequently, the Fe(III) electroreduction was upgraded, with a similar maximum Fe(II) regeneration but undergoing a much slower 2-fold decay thereafter (Fig. 2a). This explains the successful BHA decay during the Fe(III)–EDDS-assisted EF treatment of Fig. 1a. Worth mentioning, suspended iron precipitates were not observed in none of the previous carbon-felt cells, as verified from the clear solutions, which means that the solid iron became rather adsorbed on the cathode surface (as will be explained in subsection 3.2).

The low ability of the air-diffusion cathode to reduce Fe(III) mentioned from Fig. 1b can be verified in Fig. 2a, where a very small concentration of 0.13 mg L^{-1} Fe(II) as maximal was attained throughout all the treatment. This agrees with the aforementioned poor BHA degradation (21%) in this system, which is also confirmed by the slow Fe(III)–EDDS disappearance with 44% removal at 45 min (Fig. 2b). On the other hand, Fig. 2c reveals the extremely low H_2O_2 production in the above cells with carbon felt, reaching 10–13 mg L^{-1} as maximal. This is much lower than 151 mg L^{-1} attained at 45 min with the diffusion cathode, resulting from the highly efficient mass transport of gaseous O_2 to the carbon-PTFE surface.

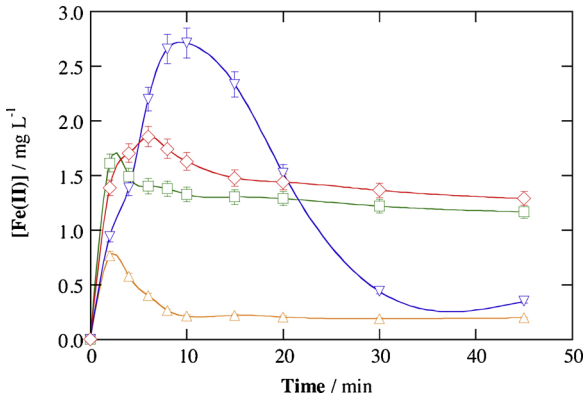

Fig. 3. Time course of Fe(II) concentration during the treatment of 150 mL of 50 mM Na_2SO_4 solutions at 50 mA by (△,□) conventional homogeneous EF with 0.10 mM $Fe(ClO_4)_3$ or (▽,◇) novel homogeneous EF with 0.10 mM Fe(III)–EDDS (1:1) complex, at (△,▽) natural pH and (□,◇) pH 3.0 using an IrO_2-based anode and a carbon-felt cathode.

An additional trial was performed in order to determine the steady-state concentration of hydroxyl radicals in the Fe(III)–EDDS-modified EF process. For this, the experiment shown in Fig. 2 with carbon felt in the absence of BHA was repeated in the presence of *p*HBA. Based on the apparent rate constants obtained for this latter compound and EDDS (Fig. S3), and considering the tabulated value k_{abs}($^{\bullet}$OH-*p*-HBA) = 2.19×10^9 M^{-1} s^{-1}, a k_{abs}-value of 5.22×10^9 M^{-1} s^{-1} was calculated for the reaction between EDDS and hydroxyl radicals. This value, along with the apparent rate constant for the disappearance of EDDS alone (determined from Fig. 2b), yielded a concentration of hydroxyl radicals of 9.5×10^{-12} M, which is close to the values typically reported in conventional homogeneous EF systems [40].

The evolution of Fe(II) concentration over time, using sulfate solutions without BHA, that results from the application of conventional (i.e., without EDDS) and novel (with 0.1 mM Fe(III)–EDDS) EF treatments with carbon-felt cathode at pH 3.0 and natural pH 5.7 is compared in Fig. 3. In the most widespread EF system with carbon felt, performed at the optimum pH 3.0 [9,13,15], 29% of hydrated Fe^{3+} could be reduced at the cathode as maximal, which occurred in only 2 min. An average Fe^{2+} concentration of 1.2 mg L^{-1} remained in solution during the whole electrolysis, ensuring the continuous degradation of BHA mainly by $^{\bullet}$OH formed from Fenton's reaction (1). Under the same conditions, the presence of EDDS slightly enhanced the Fe(II) regeneration, attaining 34% in 6 min, which can be related to a higher electroactivity of the Fe(III)–EDDS on carbon felt as compared to the hydrated Fe^{3+}. The average Fe^{2+} concentration was 1.3 mg L^{-1}, always higher than in the previous system despite the gradual destruction of EDDS. However, conventional EF seems preferable at pH 3.0, because it performs similarly to novel EF but without TOC increase from EDDS. On the other hand, based on Fig. 3, it is evident that the Fe(III)–EDDS-assisted EF is needed at natural pH. The absence of EDDS led to a poor generation of Fe(II) with a maximal of 0.76 mg L^{-1} in 2 min, which quickly decreased to 0.2 mg L^{-1}, due to immediate precipitation.

The accumulated concentrations of Fe(III) and total dissolved iron during the trials shown in Fig. 3 are depicted in Fig. S4. At pH 3.0, iron was always completely solubilized (i.e., 5.5 mg L^{-1}) along the electrolysis. In addition, a slightly lower amount of Fe(III) was present in solution when the Fe(III)–EDDS complex was used, in agreement with its easier electroreduction to Fe(II) discussed in Fig. 3. At pH 5.7, the absence of EDDS led to a fast decrease of Fe(III) concentration, as occurred with Fe(II), owing to the almost total removal of dissolved iron. On the other hand, at this pH, the larger stability of iron in the presence of EDDS is confirmed, with total solubilization at time zero, although it gradually disappeared because of EDDS destruction.

The previous experiments were carried out at 50 mA. Trying to enhance the Fe(II) regeneration rate, a higher current of 100 mA was employed. As can be observed in Fig. S5, only a minor enhancement was achieved at 0.1 mM Fe(III)–EDDS (1:1) complex, reaching 3.4 mg L^{-1} as maximal but following a very close profile to the one at 50 mA (Fig. 3). This suggests that the reduction of the Fe(III) complex was accelerated upon current increase, but also the EDDS destruction due to the faster production of $^{\bullet}$OH from reaction (6). On the other hand, a much greater enhancement of dissolved Fe(II) concentration (i.e., 5.6 mg L^{-1} at 10 min) was feasible operating with 0.2 mM Fe(III)–EDDS (1:1) complex at 100 mA. However, the regeneration efficiency, close to 55%, was only slightly higher than that found at 50 mA, as was discussed from Fig. 2. Furthermore, this was accompanied by the presence of a greater organic matter content in the form of EDDS, which then competed with BHA and its by-products to react with $^{\bullet}$OH.

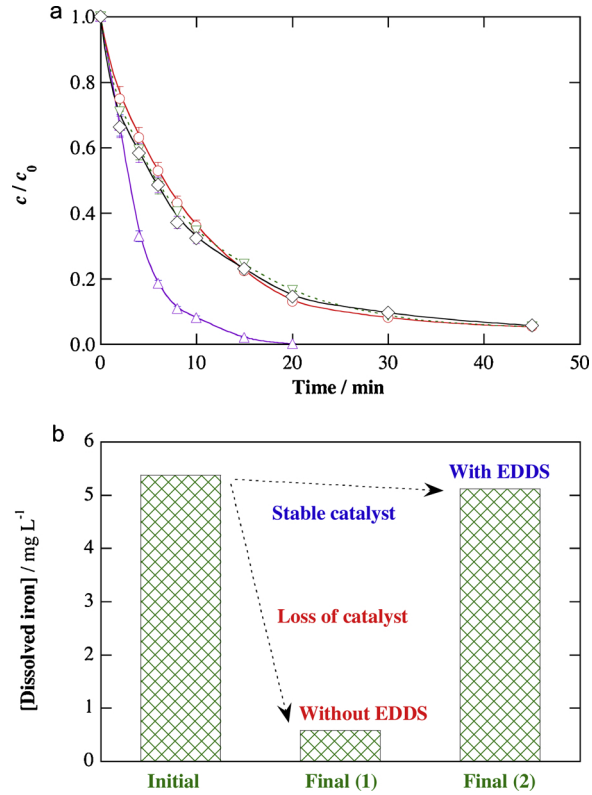

Fig. 4. (a) Normalized BHA concentration decay with electrolysis time during the treatment of 150 mL of 0.076 mM BHA solutions with 50 mM Na_2SO_4 at 50 mA by the novel homogeneous EF with 0.10 mM Fe(III)–EDDS (1:1) complex, using an IrO_2-based anode and a carbon-felt cathode. Initial pH: (△) 3.0, (○) 5.7 (natural), (▽) 7.0 and (◇) 9.0. (b) Change of dissolved iron concentration under the conditions of plot (a) at pH 9.0, as compared to that found in the absence of EDDS.

Once the high performance of the Fe(III)–EDDS-assisted EF process with carbon-felt cathode to degrade BHA in aqueous solutions at its natural pH 5.7 has been demonstrated (Fig. 1a), the possibility of working within a wider pH range of 3.0–9.0 at 50 mA was investigated. Solution pH was monitored during these electrolyses in order to adjust it when needed. As shown in Fig. 4a, it was certainly possible to operate at alkaline pH up to 9.0 since the same BHA decay kinetics as that found at pH 5.7 and 7.0 was maintained, attaining 95% removal at 45 min. Worth noticing in Fig. 4b, almost all the initial iron was kept soluble during the trial at pH 9.0, with only 6% precipitation. This was possible thanks to the greater stability of EDDS at this pH against oxidants as compared to more acid pH values. In contrast, in the absence of EDDS, the almost total (89%) disappearance of dissolved iron can be confirmed in Fig. 4b. Fig. 4a also evidences that the highest degradation rate was achieved at pH 3.0, reaching 100% BHA removal at 20 min.

This agrees with the characteristic optimum pH for Fenton's reaction in conventional EF with uncomplexed iron [1,4], which suggests that this value is also optimal for Fenton-like reaction (6).

The influence of the applied current on BHA degradation by EF with 0.1 mM Fe(III)–EDDS (1:1) complex at pH 5.7 using the carbon-felt cathode was also studied. Fig. S6 highlights the faster and larger pollutant removal as current was increased from 25 to 75 mA, corresponding to abatements from 87% to 100%. This trend cannot be related to the greater Fe(II)–EDDS generation, since it was demonstrated above that current has a minor effect on Fe(III)–EDDS reduction (Fig. S5). Therefore, current mainly determines the H_2O_2 concentration produced from reaction (2), which simultaneously affects the $^{\bullet}OH$ amount formed via reaction (6), as well as the $IrO_2(^{\bullet}OH)$ generation rate from reaction (4). Based on the small difference obtained, next trials were made at 50 mA.

3.2. TOC removal and fate of EDDS with carbon-felt cathode

The mineralization ability of the novel Fe(III)–EDDS-assisted process with carbon-felt cathode was assessed under different conditions, using solutions with 23 mg L^{-1} TOC corresponding to 0.076 mM BHA (10 mg L^{-1} TOC, i.e., 43% of total TOC) and 0.1 mM EDDS (13 mg L^{-1} TOC, i.e., 57% of total TOC). Fig. 5a shows that the treatment with the IrO_2-based anode was quite ineffective to mineralize the solution. In spite of the almost complete BHA removal achieved with this anode after 45 min (Fig. 1a), only 14% TOC abatement could be reached at 180 min. This means that some of the BHA and EDDS by-products were very refractory to oxidation. This occurred in concomitance with the progressive loss of oxidation power, as can be deduced from Fig. 5b. In

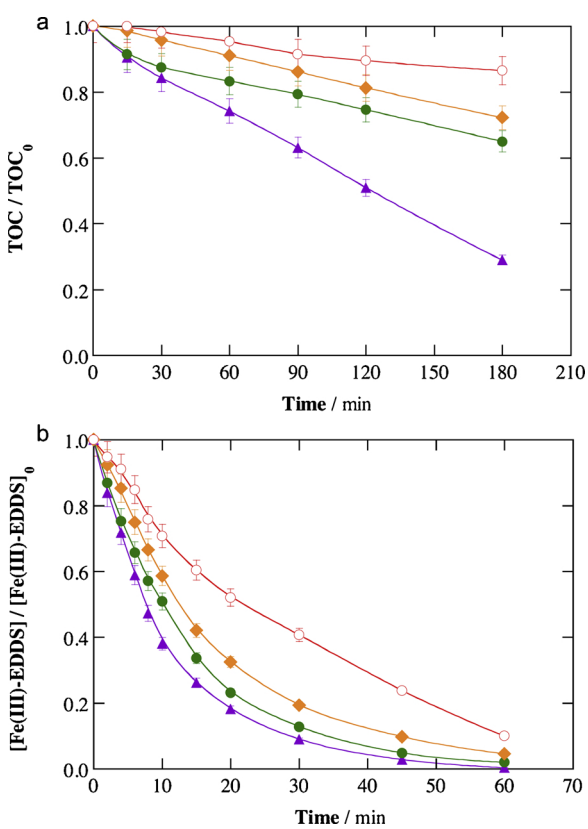

Fig. 5. Abatement of (a) normalized TOC and (b) Fe(III)–EDDS concentration with electrolysis time during the treatment of 150 mL of 0.076 mM BHA (10 mg L^{-1} TOC) solutions with 50 mM Na_2SO_4 at 50 mA by the novel homogeneous EF with 0.10 mM Fe(III)–EDDS (1:1) complex, using a (▲,●,◆) BDD or (○) IrO_2-based anode and a carbon-felt cathode. Initial pH: (▲) 3.0, (●,○) 5.7 (natural) and (◆) 9.0.

60 min, 90% of the Fe(III)–EDDS complex disappeared from solution, involving the precipitation of iron as explained above. Therefore, from 60 min, the mineralization was pre-eminently caused by $IrO_2(^{\bullet}OH)$ and, maybe, heterogeneous Fenton process (see subsection 3.3). A greater TOC abatement was feasible when the IrO_2-based anode was replaced by BDD. At pH 5.7, 35% mineralization was attained at 180 min, owing to the high oxidation power of BDD($^{\bullet}OH$) that could slowly destroy the very stable intermediates [1,31]. A similar but slightly slower TOC decay was found at pH 9.0, with a final removal of 28%. Nonetheless, the use of BDD at pH 3.0 clearly outperformed the other systems, reaching 71% mineralization, which confirms that this is the optimum pH for Fenton-like reaction (6) that produces $^{\bullet}OH$, as discussed from Fig. 4 with the IrO_2-base anode. As can be deduced from Fig. 5b, also in the BDD/carbon felt cells the degradation from 60 min was pre-eminently caused by $M(^{\bullet}OH)$, with the potential contribution of heterogeneous Fenton at the precipitated iron species.

E_{cell} values of 7.0 and 8.5 V were recorded during the trials with the IrO_2-based and BDD anodes, respectively. Based on the equation reported elsewhere [4], this gave rise to high energy consumptions of 7.0 and 8.5 kW h m^{-3} at 180 min, as expected from the use of non-optimized reactors operating in batch mode.

In the absence of BHA (i.e., initial TOC of 13 mg L^{-1}), Fig. S7 shows that EDDS could not be practically mineralized by $IrO_2(^{\bullet}OH)$, being reduced by 8% in 180 min. Hence, the 14% TOC abated in Fig. 5a almost exclusively corresponded to BHA transformation into CO_2, whereas the almost total disappearance of Fe(III)–EDDS in Fig. 5b was then accompanied by the transformation of EDDS into intermediates that were unable to complex and solubilize most of the released Fe(III). Conversely, TOC was reduced by 37% employing BDD, thereby generating small organics like carboxylic acids that are hard to become mineralized [4]. Note that the destruction of EDDS under the action of hydroxyl radicals has been reported above, showing a value close to that found by other authors at pH 8.0, i.e., $2.48 \pm 0.43 \times 10^9\ M^{-1}\ s^{-1}$ [42].

Trying to enhance the TOC removal, some trial was made with addition of EDDS at 30 min, once the Fe(III)–EDDS concentration was only around 0.04 mM. However, a positive effect was not observed, probably because precipitated iron became absorbed on the cathode and an insignificant amount was released to the solution. Blank experiments showed that carbon felt can adsorb around 80% of solid iron, especially under near-neutral and alkaline conditions.

3.3. Role of the heterogeneous process in Fe(III)–EDDS-assisted EF

Considering the Fe(III)–EDDS-assisted EF process at natural pH 5.7 using the IrO_2-based/carbon felt cell, discussed in previous subsections, BHA removal has been mainly accounted for by the action of $^{\bullet}OH$ formed from Fenton-like reaction (6), whereas TOC abatement was supposed to be caused by $IrO_2(^{\bullet}OH)$. However, it is still unclear if there might be an additional contribution of heterogeneous Fenton reaction in this novel system. To study this, the treatment of BHA solution as in Fig. 1a with 0.10 mM Fe(III)–EDDS (i.e., simultaneous addition of both reagents), but at pH 9.0, was compared with a sequential addition. The former approach allowed working with the soluble complex, whereas precipitation of iron species, either complexed (≡ Fe(III)–EDDS) or uncomplexed (≡ Fe) on the cathode surface (≡), was presumed in the latter case (Fig. S8a). As can be seen in Fig. S8b, a very low iron content below 1 mg L^{-1} was determined in solution during the sequential addition (see inset). Nevertheless, the degradation of BHA was very effective, with an analogous profile to that obtained following a simultaneous addition. Heterogeneous reaction was thus believed to be a crucial mechanism in the absence of sufficient amount of soluble Fe (III)–EDDS, which is exactly what occurs as EDDS becomes degraded, as stated above. On the other hand, the contribution of heterogeneous Fenton to TOC removal was insignificant (Fig. S8c).

The existence of such precipitates on the cathode surface was

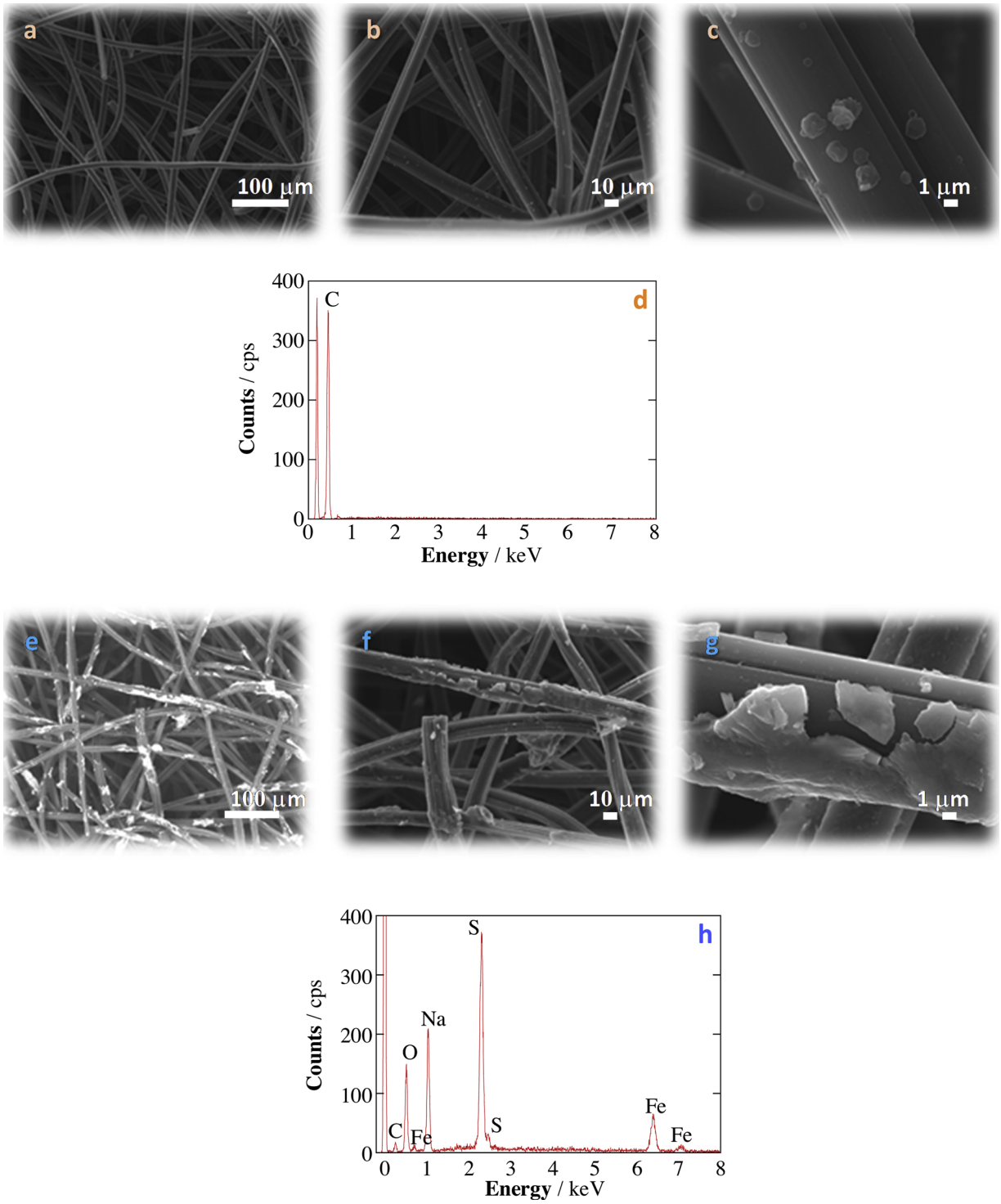

Fig. 6. Scanning electron micrographies at 200×, 500× and 5000× of: (a, b, c) pristine carbon felt (1.0 cm × 5.0 cm × 0.5 cm), and (e, f, g) carbon felt (1.0 cm × 5.0 cm × 0.5 cm) loaded with Fe(III) by following a sequential addition of 1 mM $Fe(ClO_4)_3$ and 1 mM EDDS in 150 mL of a 50 mM Na_2SO_4 solution at pH 9.0, maintaining a vigorous stirring for 15 min. (d, h) EDS analyses of the two samples.

verified via SEM-EDS analysis. The images in Fig. 6a-c depict the morphology of pristine carbon felt at different magnifications. Smooth carbon fibers with only random deffects arisen upon activation in acid medium can be observed. The EDS analysis of Fig. 6d confirms the high purity of this material before use. Then, the sequential procedure described above at pH 9.0 (Fig. S8a) was followed to load the fibers with solid iron and/or iron–EDDS, although using higher concentrations of $Fe(ClO_4)_3$ and EDDS aiming to enhance the formation of precipitates and facilitate the analysis. Fig. 6e-g perfectly illustrate the presence of iron precipitates on carbon fibers, dispersed throughout the whole volume of the sample and showing good attachment. Fig. 6h confirms the presence of iron and oxygen in those particles, alongside sodium and sulfur from the background electrolyte employed during the precipitation.

XPS analysis of iron-loaded carbon felt, once employed as cathode in the IrO_2-based/carbon felt cell at 50 mA for 10 min, was made in

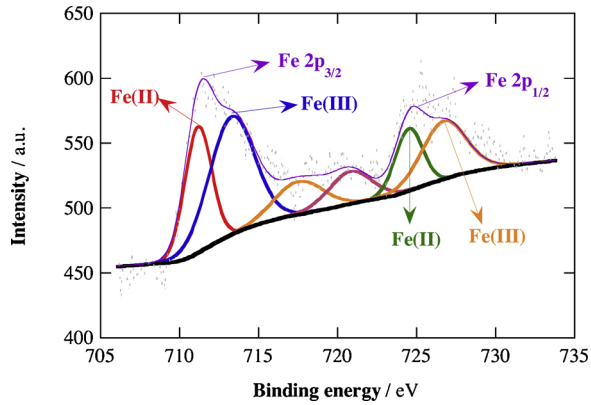

Fig. 7. XPS spectrum of Fe(III)-loaded carbon felt after 10 min of electrolysis at 50 mA using an IrO_2-based anode. The loading was made as described in Fig. 6.

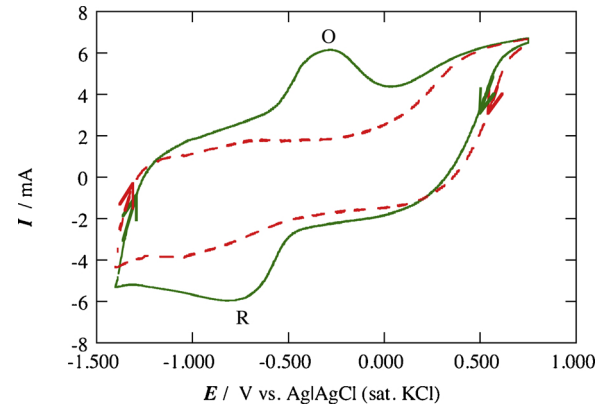

Fig. 8. Cyclic voltammograms recorded for a carbon-felt electrode (1.0 cm × 1.0 cm × 0.5 cm), in the (dashed line) absence and (solid line) presence of pre-adsorbed Fe(III) species, in 50 mL of 50 mM Na_2SO_4 solutions at natural pH and 25 °C. Initial and final potential: 0.700 V, reversal potential: -1.450 V. Scan rate: 0.100 V s^{-1}.

order to elucidate the nature of the iron particles. In the spectrum of Fig. 7, it is very interesting to notice the existence of ≡ Fe(II), which logically arouse during the short electrolyses made with the modified carbon-felt cathode, along with ≡ Fe(III). The existence of mixed oxide particles like Fe_3O_4 cannot be discarded either to explain the presence of ≡ Fe(II). Main peaks located at 711.2 and 713.4 eV for Fe(II) and Fe (III) in the Fe $2p_{3/2}$ region were detected, in addition to peaks at 724.6 and 726.8 eV for Fe(II) and Fe(III) in the Fe $2p_{1/2}$ region, respectively, consistent with previously reported spectra for iron-loaded carbonaceous materials [43,44]. In addition, two satellite peaks appeared at 717.6 and 720.9 eV. Two analogous experiments were performed employing either $FeCl_3$ or $Fe_2(SO_4)_3$ as Fe(III) source, instead of $Fe(ClO_4)_3$, aiming to assess any possible influence on the performance of the novel EF process. However, no substantial peak shifts were observed, as shown in Fig. S9. For $FeCl_3$ (Fig. S9a), the peaks appeared at 711.1 and 712.9 eV for Fe(II) and Fe(III) in the Fe $2p_{3/2}$ region, and 724.5 and 726.8 eV in the Fe $2p_{1/2}$ region. Using $Fe_2(SO_4)_3$ (Fig. S9b), the values were practically the same, with a difference of 0.1 eV as maximum.

Once confirmed the occurrence of heterogeneous Fenton process in the Fe(III)–EDDS-assisted treatment, resulting from the precipitation of iron-based particles on the carbon-felt cathode surface, the redox activity of this solid iron was assessed by cyclic voltammetry. A small piece of carbon felt was loaded with iron species as described in Fig. S8, but with each reagent at a final concentration of 0.10 mM to work in the same conditions employed for BHA degradation. A blank voltammogram was recorded on pristine carbon felt, immersed into 50 mL of a 50 mM Na_2SO_4 solution at natural pH. No peaks appeared over the potential range from +0.700 V to -1.450, as evidenced in Fig. 8. In contrast, with the modified working electrode, a quasi-reversible adsorption signal related with ≡Fe(III) to ≡Fe(II) (R, reduction peak) and ≡Fe(II) to ≡Fe(III) (O, oxidation peak) transformations was observed. The cathodic and anodic peak potential values appeared at E_p^c = -0.815 V vs. Ag|AgCl and E_p^a = -0.277 V vs. Ag|AgCl, respectively, yielding ΔE_p = 0.538 V. These peaks were very similar to those found in a voltammetric study with 0.10 mM $Fe(ClO_4)_3$ in a 50 mM Na_2SO_4 solution (Fig. S10), with E_p^c = -0.775 V vs. Ag|AgCl and E_p^a = -0.333 V vs. Ag|AgCl.

The aforementioned results allow concluding that the application of constant current in the novel EF treatment promotes at least the partial transformation of ≡ Fe(III) (and/or ≡ Fe(III)–EDDS) into ≡ Fe(II) (and/or ≡ Fe(II)–EDDS). From data obtained in Fig. 8, the half-wave potential ($E_{1/2}$) value of Fe(III)–EDDS/Fe(II)–EDDS was calculated as -0.316 V vs the standard hydrogen electrode (SHE). Other authors reported $E_{1/2}$ values of 0.186 V vs SHE at pH 7.0 [45] and 0.069 V vs SHE at pH 6.2 [27], in both cases on glassy carbon.

3.4. Reaction pathways and degradation mechanism

Based on the eleven primary aromatic by-products identified by GC-MS analysis, two different reaction pathways are proposed in Fig. 9 to explain the degradation of BHA (**1**) by the novel homogeneous EF process with Fe(III)–EDDS as catalyst and carbon felt as cathode.

Five by-products were formed through the oxidation route of **1** promoted by $^{\bullet}OH$ or M($^{\bullet}OH$). First, **1** was oxidized to either 3-*tert*-butyl-5-methoxybenzene-1,2-diol (**2**), also called 3-*tert*-butyl-4,5-dihydroxyanisole, or 2-*tert*-butylhydroquinone (**3**). The latter was then easily transformed into 2-*tert*-butyl-1,4-benzoquinone (**4**), since the oxidation of hydroquinones to benzoquinones is easily promoted in oxidizing media. Alternatively, the loss of the *tert*-butyl group of **3** yielded hydroquinone (**5**), which again was readily oxidized to *p*-benzoquinone (**6**). Note that compound **2** was also formed upon the action of O_3 and $S_2O_8^{2-}$ [36,37], whereas compound **3** is a typical metabolite in aqueous media and some authors has explained its formation by demethylation of the methoxy group of **1** [46]. Compound **3** has been reported during biological degradation, UV photolysis [47] and chlorination [38] of BHA. The conversion of **3** into **4** was also reported elsewhere [36–38,47].

The formation of the other six by-products involved dimerization and/or cyclization steps. Dimerization of **1** yielded 3,3′-di-*tert*-butyl-5,5′-dimethoxy-biphenyl-2,2′-diol (**7**), as also reported by Lau et al. [36,37]. This by-product could be transformed into bicyclohexyl-3,6,3′,6′-tetraene-2,5,2′,5′-tetraone (**8**) upon loss of both *tert*-butyl groups and complete oxidation of the four oxygenated groups. A similar product was found by some authors, but keeping the *tert*-butyl groups in the structure [36,37]. Alternatively, the dimer **7** could yield **9** thanks to cyclization and oxidation. This latter compound could also appear from reaction between **1** with **2**, followed by cyclization and oxidation. Subsequent loss of both methoxy groups of **9** alongside internal rearrangement justifies the formation of 2,6-di-*tert*-butyl-1H-dibenzofuran-4-one (**10**), which is similar to BHDQ in Lau et al. [36,37]. The formation of benzofuran derivative **11** is connected to the oxidation route describe above, since it can arise from internal cyclization of **3**. Finally, compound **12** can be explained by the loss of *tert*-butyl group of **1** and attack of the −OH group on another aromatic derivative of BHA.

Based on the large set of results summarized in this work, the degradation mechanism shown in Fig. 10 aims at explaining the performance of Fe(III)–EDDS-assisted EF process at circumneutral pH. For simplicity, hydrated Fe^{2+} and Fe^{3+} present in solution are also represented as Fe(II) and Fe(III). The carbon-felt surface allowed: (i) the two-electron reduction of O_2 to H_2O_2 via reaction (2), (ii) the reduction of dissolved Fe(III) and Fe(III)–EDDS, to yield uncomplexed and

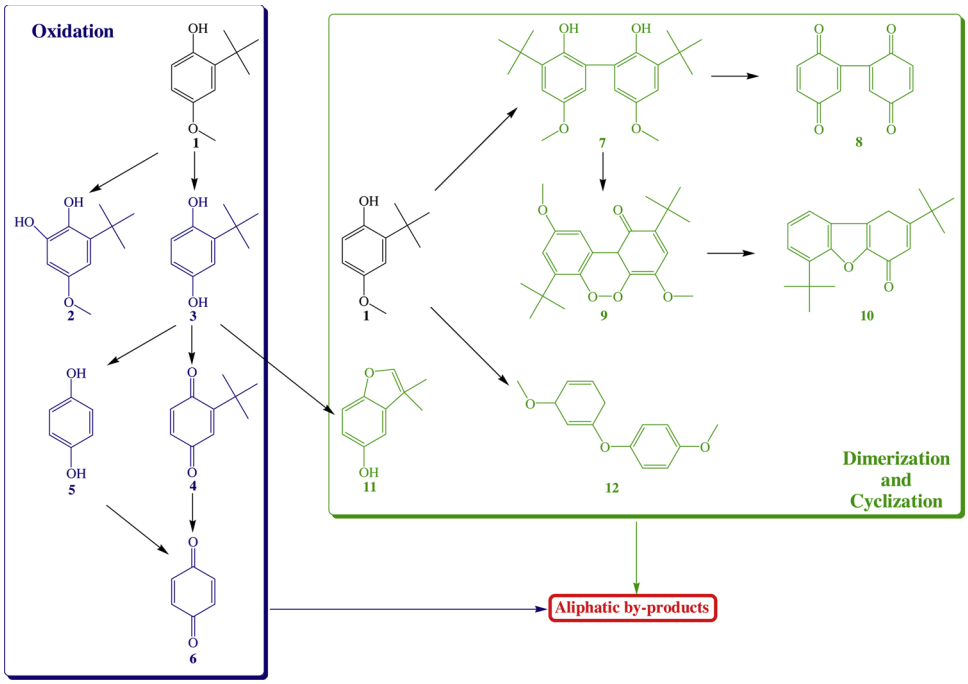

Fig. 9. Reaction pathways for BHA (**1**) degradation by the novel homogeneous EF process with 0.10 mM Fe(III)–EDDS (1:1) complex using an IrO_2-based anode and a carbon-felt cathode at circumneutral pH. The main oxidants are M(˙OH) formed at the anode surface from water oxidation and/or ˙OH in the bulk from Fenton's reaction (1) and Fenton-like reaction (6).

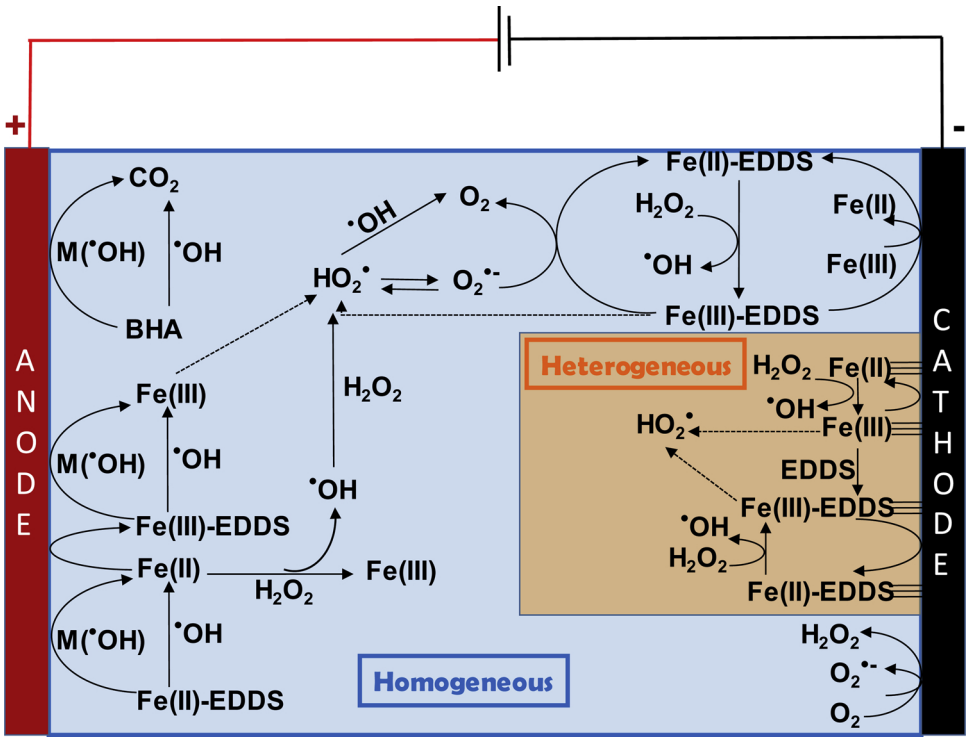

Fig. 10. Proposed mechanism for Fe(III)–EDDS-assisted EF treatment at circumneutral pH.

complexed Fe(II), respectively, which led to the formation of ˙OH from reaction (6) and (iii) the reduction of adsorbed ≡ Fe(III) and ≡ Fe (III)–EDDS to yield ≡ Fe(II) and ≡ Fe(II)–EDDS. These four species gave rise to heterogeneous Fenton and Fenton-like reactions, which yielded ˙OH and HO_2˙, respectively. Therefore, BHA was degraded by ˙OH formed from those reactions, in concomitance with M(˙OH) formed at the anode surface via reaction (4). In addition, it could undergo direct anodic oxidation, as depicted in Fig. 10. On the other hand, both kinds of radicals were responsible for the destruction of EDDS in the Fe (II)–EDDS and Fe(III)–EDDS complexes.

4. Conclusions

Fe(III)–EDDS-modified EF has been proven a very effective process for the removal of aromatic pollutants like BHA at mild pH. Carbon felt outperformed the air-diffusion cathode to run this process, despite the much lower H_2O_2 electrogeneration, because it allowed the regeneration of Fe(II). This species, either uncomplexed or complexed with EDDS, promoted the formation of ˙OH from classical Fenton's reaction and alternative Fenton-like reaction. A much higher Fe(III) reduction efficiency was observed in the novel Fe(III)–EDDS-assisted EF process as

compared to conventional EF with hydrated Fe^{3+}. The optimum pH for Fenton-like reaction between Fe(III)–EDDS and H_2O_2 was 3.0, which agrees with that of conventional Fenton's reaction. The contribution to total TOC and the scavenging effect of EDDS on $^{\bullet}OH$ are the main concerns, preventing the occurrence of a large mineralization. The use of a high oxidation power anode like BDD and solution acidification to pH 3.0 led to 71% TOC abatement after 180 min at 50 mA. Eleven aromatic by-products were identified during the mineralization of BHA. As revealed by SEM-EDS, XPS and voltammetric analyses, the degradation mechanism included homogeneous Fenton's reaction in the bulk solution, heterogeneous Fenton at the cathode surface and electrocatalysis at the anode surface. This new approach to EF treatment is environmental friendly, being very promising for management of water containing persistent organic pollutants.

Declaration of interests

The authors declare that they have no known competing financial interests or personal relationships that could have appeared to influence the work reported in this paper.

Acknowledgments

The authors thank financial support from project CTQ2016-78616-R (AEI/FEDER, EU) and PhD scholarship awarded to Z.H. Ye (State Scholarship Fund, CSC, China).

Appendix A. Supplementary data

Supplementary material related to this article can be found, in the online version, at doi:https://doi.org/10.1016/j.apcatb.2019.117907.

References

[1] I. Sirés, E. Brillas, M.A. Oturan, M.A. Rodrigo, M. Panizza, Environ. Sci. Pollut. Res. 21 (2014) 8336–8367.
[2] C.A. Martínez-Huitle, M.A. Rodrigo, I. Sirés, O. Scialdone, Chem. Rev. 115 (2015) 13362–13407.
[3] J. Radjenovic, D.L. Sedlak, Environ. Sci. Technol. 49 (2015) 11292–11302.
[4] E. Brillas, I. Sirés, M.A. Oturan, Chem. Rev. 109 (2009) 6570–6631.
[5] A. Galia, S. Lanzalaco, M.A. Sabatino, C. Dispenza, O. Scialdone, I. Sirés, Electrochem. Commun. 62 (2016) 64–68.
[6] S. Lanzalaco, I. Sirés, M.A. Sabatino, C. Dispenza, O. Scialdone, A. Galia, Electrochim. Acta 246 (2017) 812–822.
[7] G. Coria, T. Pérez, I. Sirés, E. Brillas, J.L. Nava, Chemosphere 198 (2018) 174–181.
[8] J.R. Steter, E. Brillas, I. Sirés, Appl. Catal. B: Environ. 224 (2018) 410–418.
[9] I. Sirés, J.A. Garrido, R.M. Rodríguez, E. Brillas, N. Oturan, M.A. Oturan, Appl. Catal. B: Environ. 72 (2007) 382–394.
[10] E. Isarain-Chávez, P.L. Cabot, F. Centellas, R.M. Rodríguez, C. Arias, J.A. Garrido, E. Brillas, J. Hazard. Mater. 185 (2011) 1228–1235.
[11] E. Isarain-Chávez, R.M. Rodríguez, P.L. Cabot, F. Centellas, C. Arias, J.A. Garrido, E. Brillas, Water Res. 45 (2011) 4119–4130.
[12] M. Zhou, Q. Tan, Q. Wang, Y. Jiao, N. Oturan, M.A. Oturan, J. Hazard. Mater. 215–216 (2012) 287–293.
[13] A. Dirany, I. Sirés, N. Oturan, A. Özcan, M.A. Oturan, Environ. Sci. Technol. 46 (2012) 4074–4082.
[14] F. Yu, M. Zhou, X. Yu, Electrochim. Acta 163 (2015) 182–189.
[15] O. Ganzenko, N. Oturan, I. Sirés, D. Huguenot, E.D. van Hullebusch, G. Esposito, M.A. Oturan, Environ. Chem. Lett. 16 (2018) 281–286.
[16] J. González-García, P. Bonete, E. Expósito, V. Montiel, A. Aldaz, R. Torregrosa-Macià, J. Mater. Chem. 9 (1999) 419–426.
[17] L.F. Castañeda, F.C. Walsh, J.L. Nava, C. Ponce de León, Electrochim. Acta 258 (2017) 1115–1139.
[18] T.X.H. Le, M. Bechelany, M. Cretin, Advances in carbon felt for electro-Fenton process, in: M. Zhou, M.A. Oturan, I. Sirés (Eds.), Electro-Fenton Process: New Trends and Scale-Up, Springer Nature, Singapore, 2018, pp. 145–173.
[19] S.O. Ganiyu, M. Zhou, C.A. Martínez-Huitle, Appl. Catal. B: Environ. 235 (2018) 103–129.
[20] P.V. Nidheesh, H. Olvera-Vargas, N. Oturan, M.A. Oturan, Heterogeneous electro-Fenton process: principles and applications, in: M. Zhou, M.A. Oturan, I. Sirés (Eds.), Electro-Fenton Process: New Trends and Scale-Up, Springer Nature, Singapore, 2018, pp. 85–110.
[21] C. Zhang, M. Zhou, G. Ren, X. Yu, L. Ma, J. Yang, F. Yu, Water Res. 70 (2015) 414–424.
[22] C. Zhang, M. Zhou, X. Yu, L. Ma, F. Yu, Electrochim. Acta 160 (2015) 254–262.
[23] Q. Peng, H. Zhao, L. Qian, Y. Wang, G. Zhao, Appl. Catal. B: Environ. 174–175 (2015) 157–166.
[24] Z. Ai, T. Mei, J. Liu, J. Li, F. Jia, L. Zhang, J. Qiu, J. Phys. Chem. C 111 (2017) 14799–14803.
[25] D. Fernández, I. Robles, F.J. Rodríguez-Valadez, L.A. Godínez, Chemosphere 199 (2018) 251–255.
[26] N. Wang, T. Zheng, G. Zhang, P. Wang, J. Environ. Chem. Eng. 4 (2016) 762–787.
[27] W. Huang, M. Brigante, F. Wu, C. Mousty, K. Hanna, G. Mailhot, Environ. Sci. Technol. 47 (2013) 1952–1959.
[28] J. Li, G. Mailhot, F. Wu, N. Deng, J. Photochem. Photobiol. A: Chem. 212 (2010) 1–7.
[29] P. Soriano-Molina, J.L. García-Sánchez, O.M. Alfano, L.O. Conte, S. Malato, J.A. Sánchez-Pérez, Appl. Catal. B: Environ. 233 (2018) 234–242.
[30] B. Marselli, J. García-Gomez, P.A. Michaud, M.A. Rodrigo, C. Comninellis, J. Electrochem. Soc. 150 (2003) D79–D83.
[31] M. Panizza, G. Cerisola, Chem. Rev. 109 (2009) 6541–6569.
[32] H. Verhagen, P.A.E.L. Schilderman, J.C.S. Kleinjans, Chemico-Biol. Interact. 80 (2) (1991) 109–134.
[33] F. Shahidi, P. Ambigaipalan, J. Funct. Foods 18B (2015) 820–897.
[34] A. Jos, G. Repetto, J.C. Ríos, A. del Peso, M. Salguero, M.J. Hazen, M.L. Molero, P. Hernández-Freire, J.M. Pérez-Martín, V. Labrador, A. Cameán, Aquat. Toxicol. 71 (2) (2005) 183–192.
[35] W. Chu, T.K. Lau, J. Hazard. Mater. 144 (2007) 249–254.
[36] T.K. Lau, W. Chu, N.J.D. Graham, Environ. Sci. Technol. 41 (2007) 613–619.
[37] T.K. Lau, W. Chu, N. Graham, Water Res. 41 (2007) 765–774.
[38] R. Rodil, J.B. Quintana, R. Cela, J. Hazard. Mater. 199–200 (2012) 73–81.
[39] Z. Ye, E. Brillas, F. Centellas, P.L. Cabot, I. Sirés, Sep. Purif. Technol. 208 (2019) 19–26.
[40] I. Sirés, E. Guivarch, N. Oturan, M.A. Oturan, Chemosphere 72 (2008) 592–600.
[41] L. Clarizia, D. Russo, I. Di Somma, R. Marotta, A. Andreozzi, Appl. Catal. B: Environ. 209 (2017) 358–371.
[42] Y. Zhang, N. Klamerth, P. Chelme-Ayala, M.G. El-Din, Environ. Sci. Technol. 50 (2016) 10535–10544.
[43] D. Zhou, L. Yang, L. Yu, J. Kong, X. Yao, W. Liu, Z. Xu, X. Lu, Nanoscale 7 (2015) 1501–1509.
[44] Y.-L. Liu, X.-Y. Xu, C.-X. Shi, X.-W. Ye, P.-C. Sun, T.-H. Chen, RSC Adv. 7 (2017) 8879–8885.
[45] Y. Zhang, N. Klamerth, S.A. Messele, P. Chelme-Ayala, M.G. El-Din, J. Hazard. Mater. 318 (2016) 371–378.
[46] R. Rodil, J.B. Quintana, G. Basaglia, M.C. Pietrogrande, R. Cela, J. Chromatogr. A 1217 (2010) 6428–6435.
[47] G. Alvarez-Rivera, M. Llompart, C. Garcia-Jares, M. Lores, J. Chromatogr. A 1390 (2015) 1–12.

SUPPLEMENTARY MATERIAL

Electro-Fenton process at mild pH using Fe(III)-EDDS as soluble catalyst and carbon felt as cathode

Zhihong Ye, Enric Brillas, Francesc Centellas, Pere Lluís Cabot, Ignasi Sirés*

Laboratori d'Electroquímica dels Materials i del Medi Ambient, Departament de Química Física, Facultat de Química, Universitat de Barcelona, Martí i Franquès 1-11, 08028 Barcelona, Spain

*Corresponding author: Tel.: +34 934039240; fax: +34 934021231.

E-mail address: i.sires@ub.edu (I. Sirés)

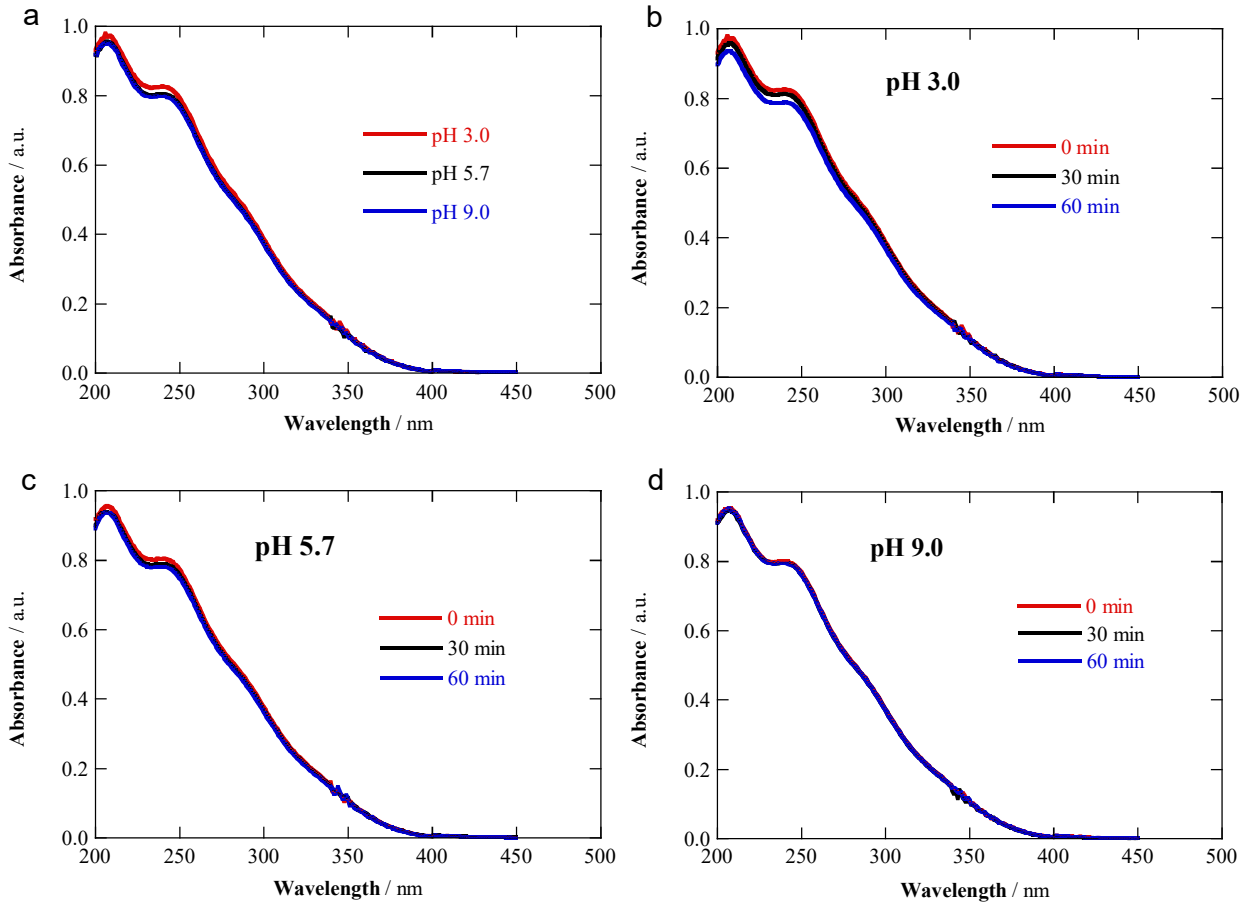

Fig. S1. Change of UV/Vis spectrum of 0.10 mM Fe(III)–EDDS (1:1) complex with (a) pH for a fresh solution and (b, c, d) time at different initial pH values.

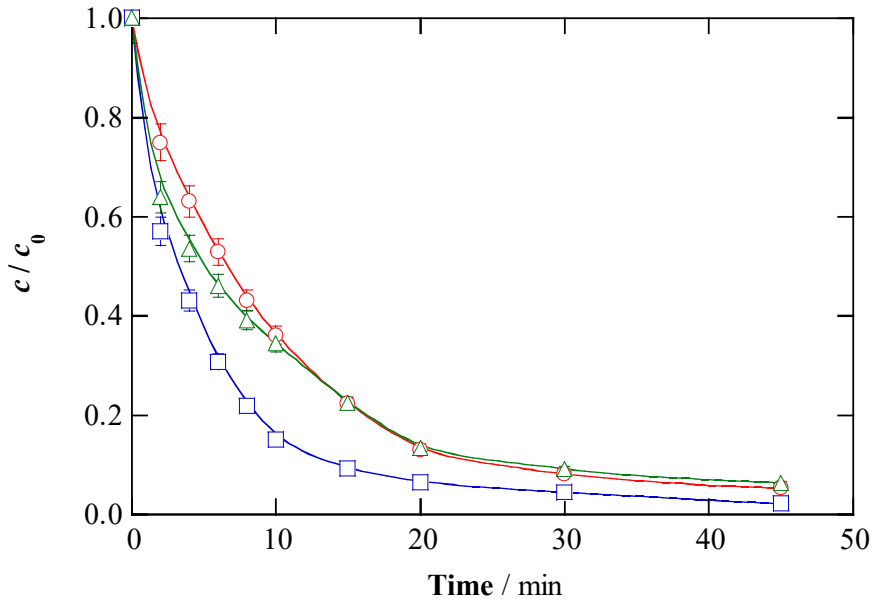

Fig. S2. Change of the normalized BHA concentration with electrolysis time during the treatment of 150 mL of 0.076 mM BHA solutions with 50 mM Na_2SO_4 at natural pH 5.7 by the novel homogeneous EF at 50 mA with: (○) 0.10 mM, (□) 0.20 mM and (△) 0.40 mM Fe(III)–EDDS (1:1) complex, using a 3-cm^2 IrO_2-based anode and a carbon-felt cathode (1.0 cm × 5.0 cm × 0.5 cm).

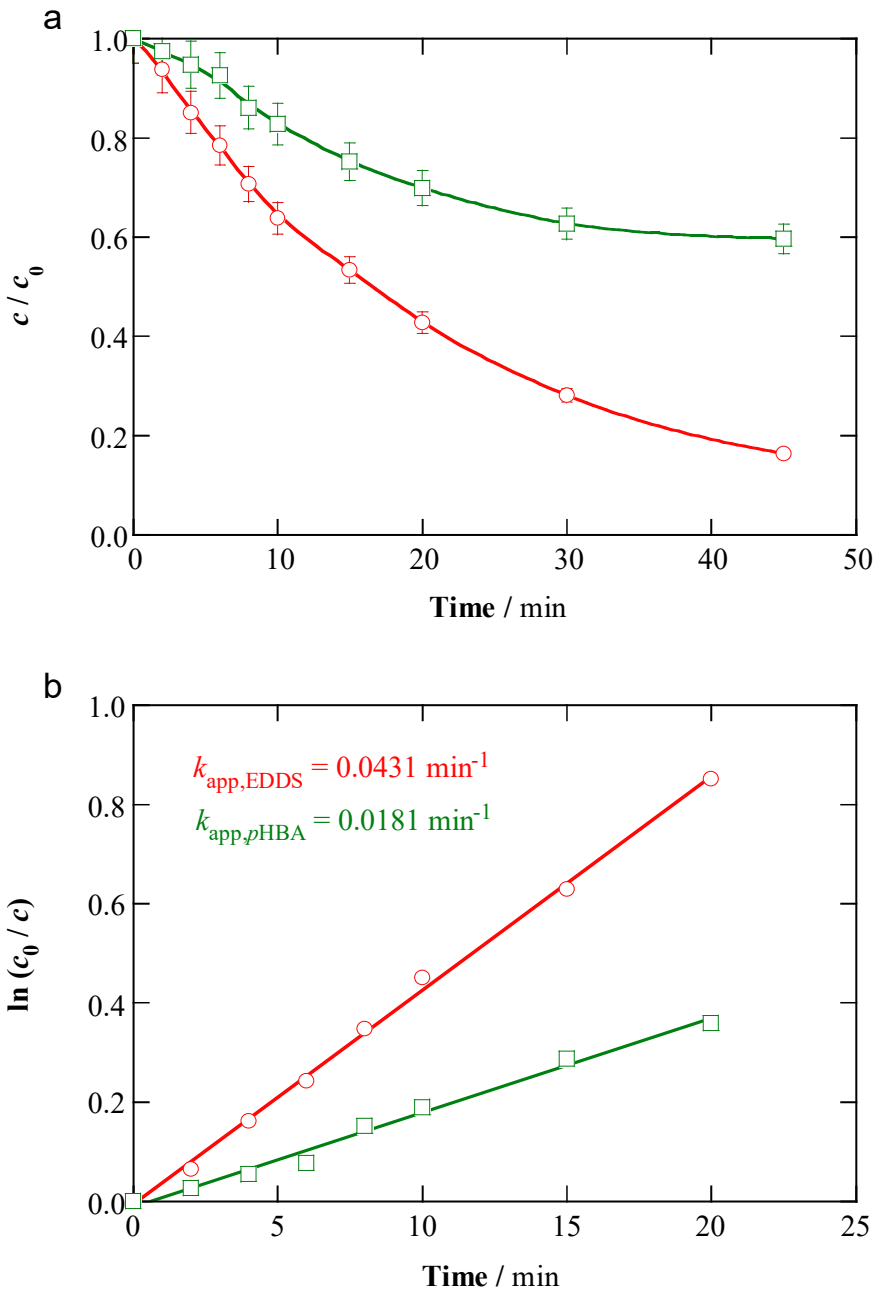

Fig. S3. (a) Decay of the normalized (○) EDDS and (□) *p*HBA concentrations during the novel EF treatment of 150 mL of 0.1 mM *p*HBA in 50 mM $NaSO_4$ at natural pH 5.7 and 50 mA using an IrO_2-based/carbon felt cell, with 0.10 mM Fe(III)–EDDS (1:1) complex. (b) Kinetic analysis considering a pseudo-first-order reaction between hydroxyl radicals and EDDS or *p*HBA.

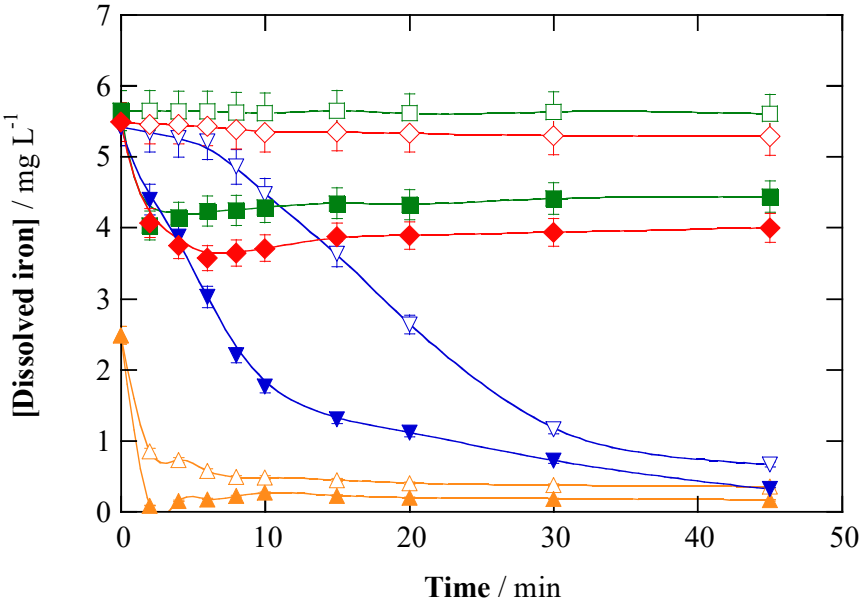

Fig. S4. Time course of (△,□,▽,◇) total dissolved iron and (▲,■,▼,◆) Fe(III) concentration for the same trials described in Fig. 3. The format of filled symbol for each Fe(III) curve matches with that used for total dissolved iron in the same experiment.

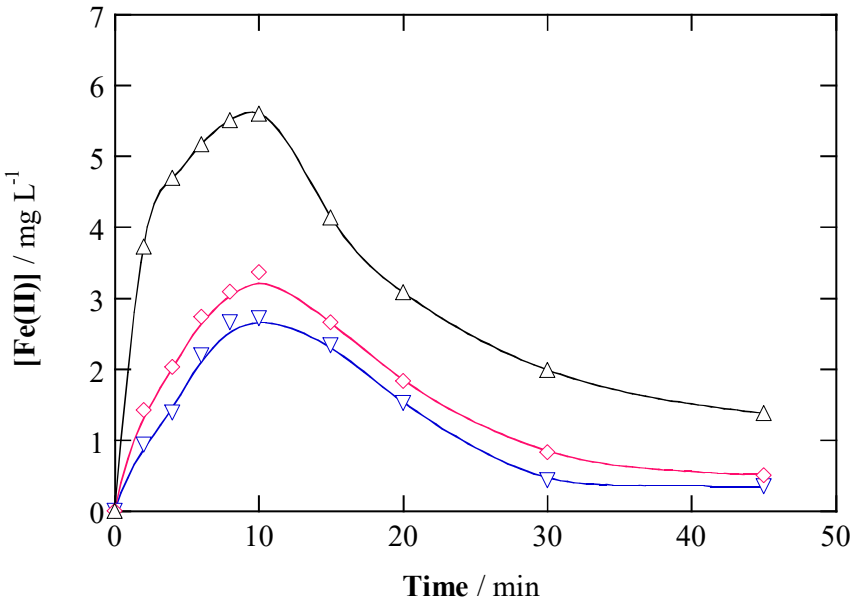

Fig. S5. Change of Fe(II) concentration with electrolysis time during the treatment of 150 mL of 0.076 mM BHA solutions with 50 mM Na_2SO_4 at natural pH 5.7 by the novel homogeneous EF using an IrO_2-based anode and a carbon-felt cathode, at: (▽) 50 mA with 0.10 mM Fe(III)–EDDS (1:1) complex, (◇) 100 mA with 0.10 mM Fe(III)–EDDS (1:1) complex, and (△) 100 mA with 0.20 mM Fe(III)–EDDS (1:1) complex.

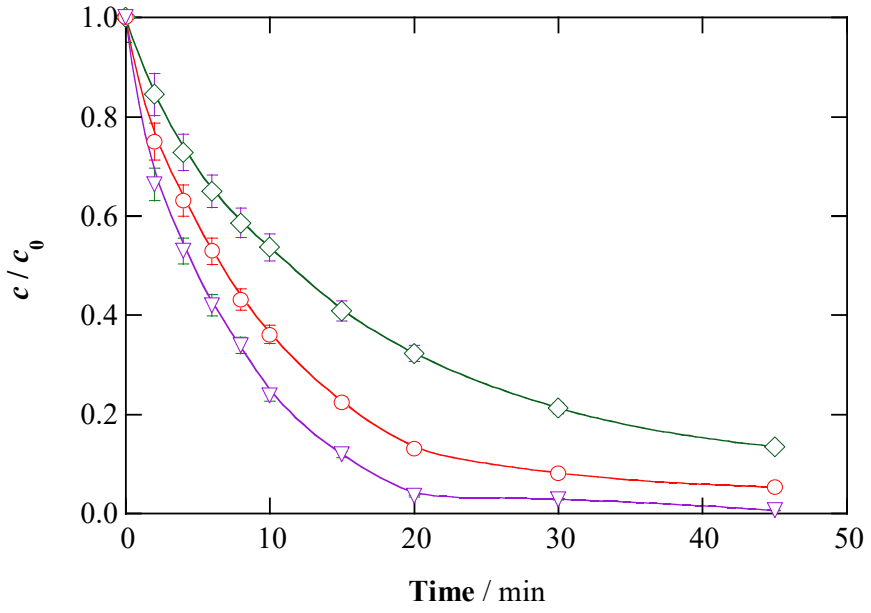

Fig. S6. Time course of the normalized BHA concentration decay during the treatment of 150 mL of 0.076 mM BHA solutions with 50 mM Na_2SO_4 at natural pH 5.7 by the novel homogeneous EF with 0.10 mM Fe(III)–EDDS (1:1) complex, using an IrO_2-based anode and a carbon-felt cathode. Current: (◇) 25 mA, (○) 50 mA and (▽) 75 mA.

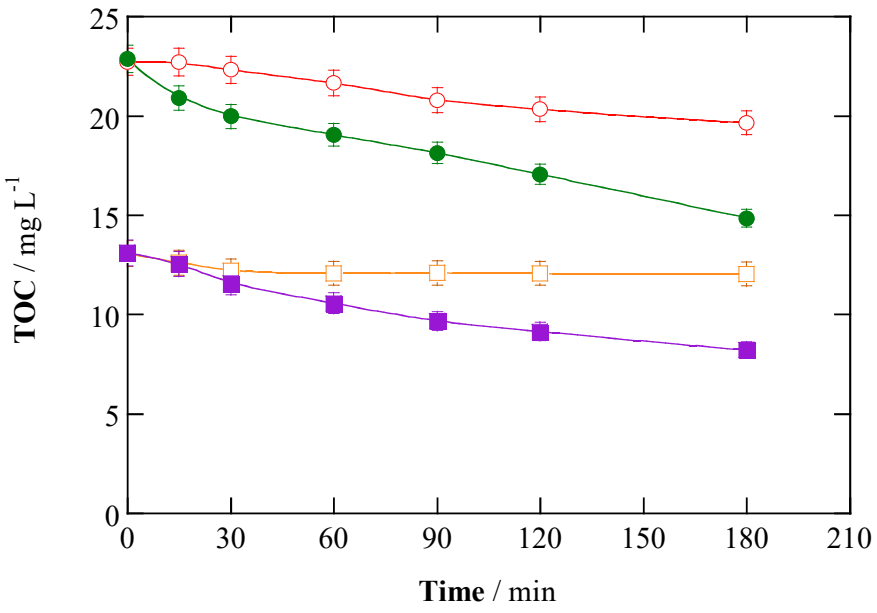

Fig. S7. TOC abatement with electrolysis time during the treatment of 150 mL of 50 mM Na_2SO_4 solutions (■,□) without and (●,○) with 0.076 mM BHA (10 mg L^{-1} TOC) at natural pH 5.7 and 50 mA by the novel homogeneous EF with 0.10 mM Fe(III)–EDDS (1:1) complex, using a (■,●) BDD or (□,○) IrO_2-based anode and a carbon-felt cathode.

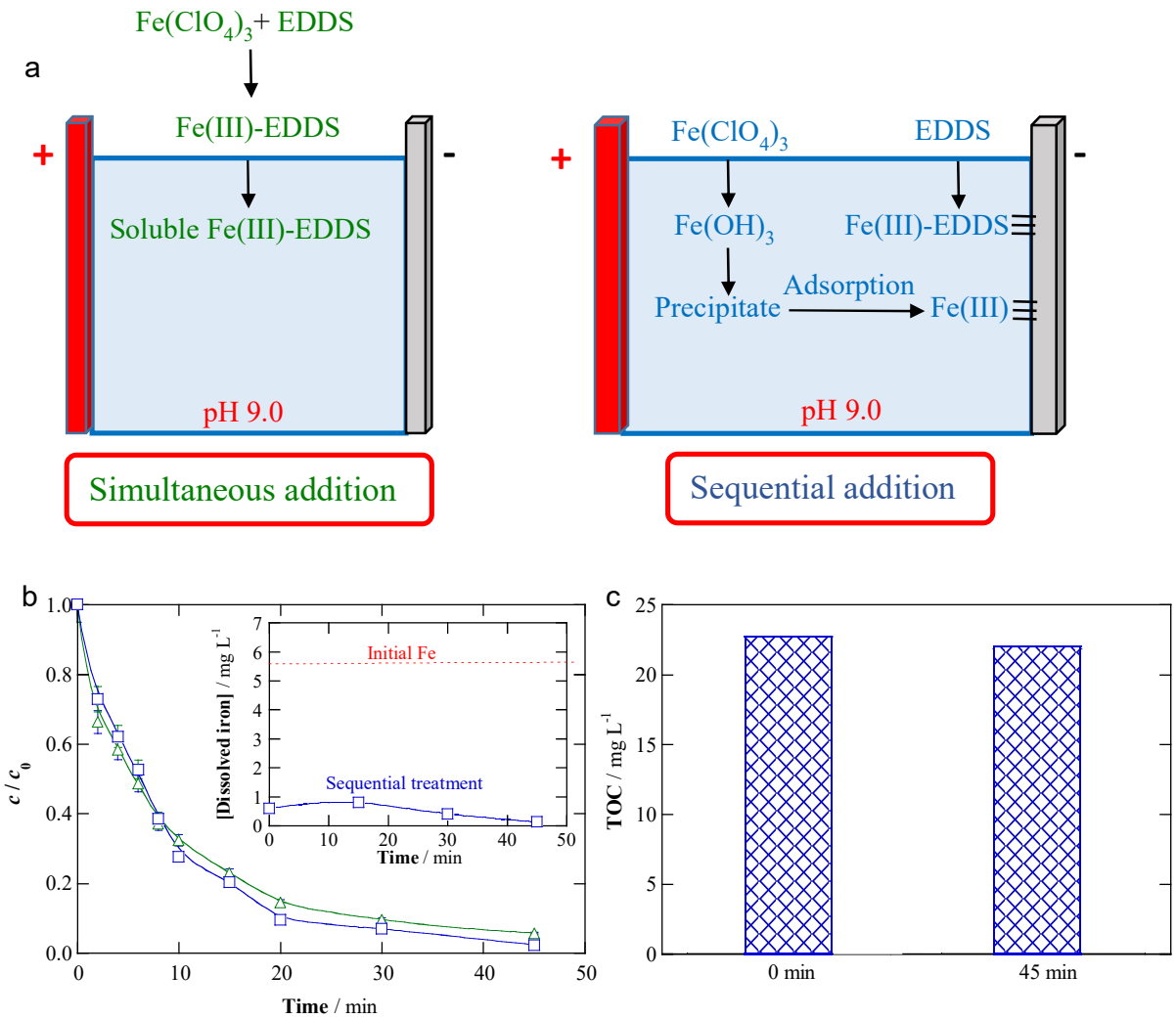

Fig. S8. Role of heterogeneous process in Fe(III)–EDDS-assisted EF process. (a) Comparison of simultaneous and sequential addition of reagents (0.10 mM each) to a cell containing 150 mL of 50 mM Na_2SO_4 solutions at pH 9.0 and equipped with a 3-cm^2 IrO_2-based anode and a carbon-felt cathode (1.0 cm × 5.0 cm × 0.5 cm). (b) Time course of the normalized BHA concentration decay during the treatment of 150 mL of solutions with 0.076 mM BHA and 50 mM Na_2SO_4 at pH 9.0 and 50 mA upon (△) simultaneous and (□) sequential addition. Inset: dissolved iron for the sequential trial. (c) TOC at 0 and 45 min for the sequential treatment.

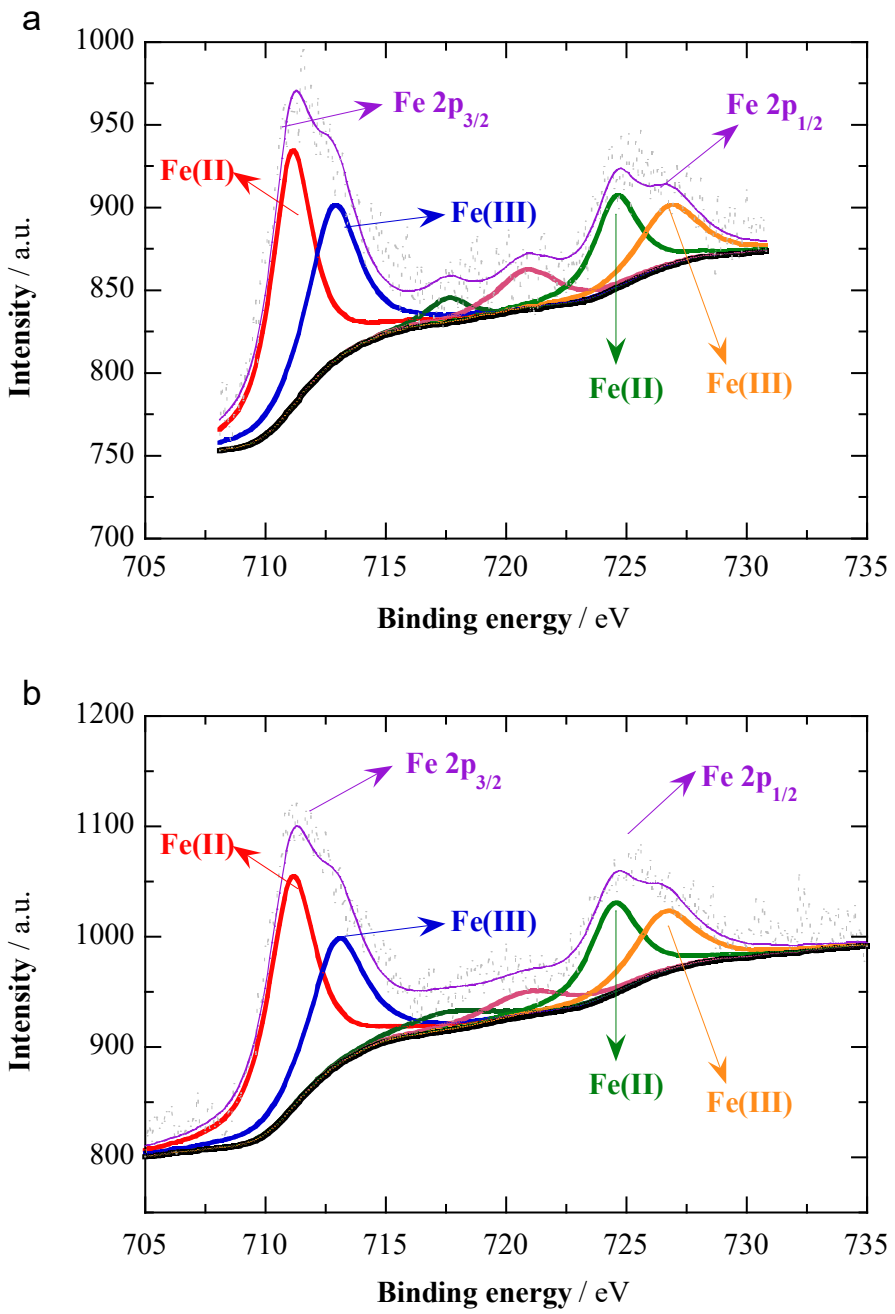

Fig. S9. XPS spectra of Fe(III)-loaded carbon felt after 10 min of electrolysis at 50 mA using an IrO_2-based anode. The loading was made as described in Fig. 6, but using (a) $FeCl_3$ and (b) $Fe_2(SO_4)_3$ instead of $Fe(ClO_4)_3$.

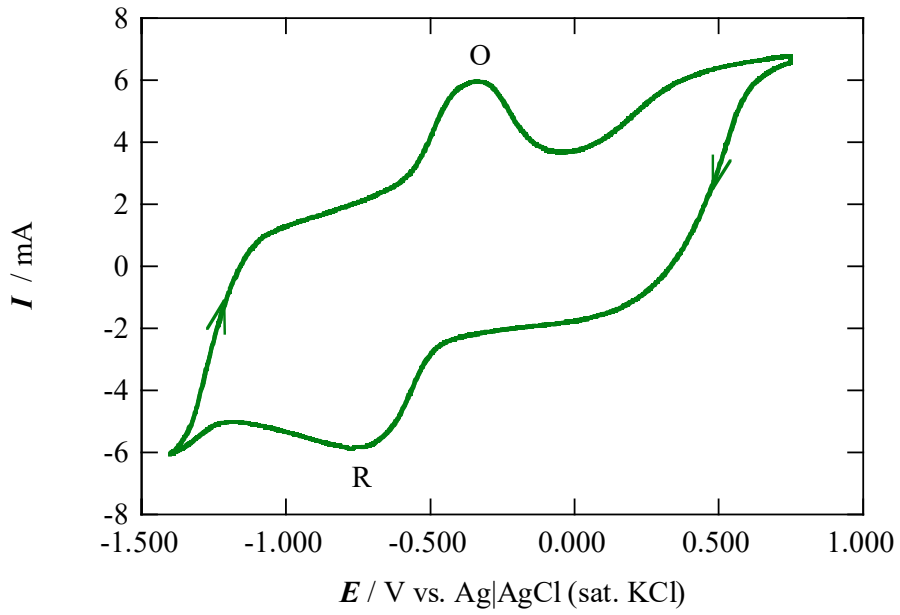

Fig. S10. Cyclic voltammogram recorded for a pristine carbon-felt electrode (1.0 cm × 1.0 cm × 0.5 cm) in 50 mL of 0.10 mM $Fe(ClO_4)_3$ with 50 mM Na_2SO_4 solution at natural pH and 25 ºC. Initial and final potential: 0.700 V, reversal potential: -1.450 V. Scan rate: 0.100 V s^{-1}.

Appendix IV

Expanding the application of photoelectro-Fenton treatment to urban wastewater using the Fe(III)–EDDS complex

Water Research xxx (xxxx) 115219

Contents lists available at ScienceDirect

Water Research

journal homepage: http://ees.elsevier.com

Expanding the application of photoelectro-Fenton treatment to urban wastewater using the Fe(III)-EDDS complex

Zhihong Ye, Enric Brillas, Francesc Centellas, Pere Lluís Cabot, Ignasi Sirés*

Laboratori d'Electroquímica dels Materials i del Medi Ambient, Departament de Química Física, Facultat de Química, Universitat de Barcelona, Martí i Franquès 1-11, 08028, Barcelona, Spain

ARTICLE INFO

Article history:
Received 14 August 2019
Received in revised form 17 October 2019
Accepted 18 October 2019
Available online xxx

Keywords
Ethylenediamine-*N,N'*-disuccinic (EDDS) acid
Fluoxetine
Gas-diffusion electrode
Hydrogen peroxide
Photoelectro-Fenton
Urban wastewater

ABSTRACT

This work reports the first investigation on the use of EDDS as chelating agent in photoelectro-Fenton (PEF) treatment of water at near-neutral pH. As a case study, the removal of the antidepressant fluoxetine was optimized, using an electrochemical cell composed of an IrO_2-based anode an air-diffusion cathode for in-situ H_2O_2 production. Electrolytic trials at constant current were made in ultrapure water with different electrolytes, as well as in urban wastewater (secondary effluent) at pH 7.2. PEF with Fe(III)–EDDS (1:1) complex as catalyst outperformed electro-Fenton and PEF processes with uncomplexed Fe(II) or Fe(III). This can be explained by: (i) the larger solubilization of iron ions during the trials, favoring the production of $^{\bullet}OH$ from Fenton-like reactions between H_2O_2 and Fe(II)–EDDS or Fe(III)–EDDS, and (ii) the occurrence of Fe(II) regeneration from Fe(III)–EDDS photoreduction, which was more efficient than conventional photo-Fenton reaction with uncomplexed Fe(III). The greatest drug concentration decays were achieved at low pH, using only 0.10 mM Fe(III)–EDDS in a 1:1 M ratio, although complete removal in wastewater was feasible only with 0.20 mM Fe(III)–EDDS due to the greater formation of $^{\bullet}OH$. The effect of the applied current and anode nature was rather insignificant. A progressive destruction of the catalytic complex was unveiled, whereupon the mineralization mainly progressed thanks to the action of $^{\bullet}OH$ adsorbed on the anode surface. Despite the incomplete mineralization using BDD as the anode, a remarkable toxicity decrease was determined. Fluoxetine degradation yielded F^- and NO_3^- ions, along with several aromatic intermediates. These included two chloro-organics, as a result of the anodic oxidation of Cl^- to active chlorine. A detailed mechanism for the Fe(III)–EDDS-catalyzed PEF treatment of fluoxetine in urban wastewater is finally proposed.

1. Introduction

Fenton's reaction (reaction (S1) in Table S1) has promoted the development of one of the most successful subtypes within the advanced oxidation processes (AOPs) for the degradation of organic pollutants in water (Brillas et al., 2009; Zhou et al., 2018). Indeed, Fenton process allows their fast removal thanks to the production of $^{\bullet}OH$ in the bulk solution, showing great potential to be integrated as a tertiary treatment in urban wastewater treatment facilities (WWTFs) (Zhang et al., 2019). Nevertheless, the risk, environmental impact and cost related to H_2O_2 synthesis, storage, transportation and handling is a major handicap. Fortunately, electrolyzers for in-situ H_2O_2 production from the two-electron reduction of gaseous O_2 (reaction (1)) have been devised in recent years (Brillas et al., 2009) and, among them, those equipped with a carbon-based air-diffusion cathode yield the largest accumulation of this oxidant upon facile modulation of input current (Sirés et al., 2007; Galia et al., 2016; Roth et al., 2016; Lanzalaco et al., 2017; Coria et al., 2018; Pérez et al., 2018).

$$O_2(g) + 2\,H^+ + 2\,e^- \rightarrow H_2O_2 \quad (1)$$

In the most simple configuration of electrochemical AOPs, a cathode with ability to electrogenerate H_2O_2 is combined with boron-doped diamond (BDD) (Panizza and Cerisola, 2009; Martínez-Huitle et al., 2015; Clematis et al., 2017) or a dimensionally stable anode (DSA®) based on IrO_2 (Scialdone et al., 2009; Lanzalaco et al., 2017, 2018) or RuO_2 (Ribeiro and De Andrade, 2004; Xu et al., 2017). Such high oxidation power anode materials (M) allow the production of adsorbed M($^{\bullet}OH$) via water oxidation, giving rise to the electro-oxidation (EO) process. If iron catalyst is present in the contaminated solution, the process is so-called electro-Fenton (EF). The Fe(II) regeneration is feasible from Fe(III) reduction when a large surface area cathode like carbon felt is employed (El-Ghenymy et al., 2014; Yahya et al., 2014; Yang et al., 2019). A more effective Fe(II) regeneration route, compatible with all kinds of cathode materials, arises from Fe(III) photoreduction. Classical photo-Fenton reaction (2) at optimum pH ~ 2.8 involves the continuous reduction of hydrated Fe^{3+} ion with concomitant $^{\bullet}OH$ production, thanks to ligand-to-metal charge

* Corresponding author.
E-mail address: i.sires@ub.edu (I. Sirés)

https://doi.org/10.1016/j.watres.2019.115219
0043-1354/

transfer (LMCT) occurring under UVA irradiation. Accordingly, photo-electro-Fenton (PEF) process has experienced an intense development with outstanding results (Flores et al., 2016; Steter et al., 2016; Komtchou et al., 2017; Alcocer et al., 2018; Aveiro et al., 2018; Vidal et al., 2018; Wang et al., 2018; Oriol et al., 2019).

$$[Fe(OH)]^{2+} + h\nu \rightarrow Fe^{2+} + {}^{\bullet}OH \quad (2)$$

EF and PEF have been proven very successful at acidic pH, which is mainly due to total solubilization of iron ions. Conversely, higher pH results in a considerable efficiency loss because of iron precipitation. For some time this has been an obstacle, impeding the application to urban wastewater treatment, but two smart solutions are currently available: (i) heterogeneous Fenton processes, employing iron catalyst in solid form (Zhou et al., 2018), and (ii) modified homogeneous Fenton processes, employing chelated iron as a soluble species (Clarizia et al., 2017). A priori, the latter option seems more appealing because it is expected to yield faster removals.

Only some few recent articles have assessed the performance of EF and PEF in urban wastewater, although chelated iron has never been used (Komtchou et al., 2015; Ridruejo et al., 2018; Guelfi et al., 2019a; Villanueva-Rodríguez et al., 2019; Ye et al., 2019a). Note that, in this kind of complex water matrix, the oxidation of Cl^- anion at the anode surface yields additional oxidants like active chlorine (Cl_2 and ClO^-) along with chlorine radicals (Table S1) (Panizza and Cerisola, 2009). Carboxylates like oxalate and citrate have been two widely used chelating agents in non-electrochemical Fenton treatments (Ye et al., 2019c). However, polydentate ligands like nitrilotriacetic (NTA), ethylenediaminetetraacetic (EDTA) and ethylenediamine-*N,N′*-disuccinic (EDDS) acids seem more interesting to ensure iron complexation (Clarizia et al., 2017). Furthermore, they enhance the LMCT because of their typically higher molar absorption coefficients in the near-UV and visible regions. Among polydentate ligands, EDDS is advantageous for photo-Fenton process. It forms soluble Fe(II)–EDDS and Fe(III)–EDDS complexes at a wide pH range, favoring the occurrence of reactions (3) and (4) at near-neutral pH that mimic Fenton's reaction (S1) and Fenton-like reaction (S2) (Zhang et al., 2016). Note that superoxide radical ($O_2^{\bullet-}$) originated in the latter reaction is transformed into $HO_2^{\bullet}$ at pH > 4.8–4.9 (reaction S9).

$$Fe(II)–EDDS + H_2O_2 \rightarrow Fe(III)–EDDS + {}^{\bullet}OH + OH^- \quad (3)$$

$$Fe(III)–EDDS + H_2O_2 \rightarrow Fe(II)–EDDS + O_2^{\bullet-} + 2H^+ \quad (4)$$

In spite of being a structural isomer of the persistent pollutant EDTA (Yuan and VanBriesen, 2006), it is considered a biodegradable substance. Mailhot and co-workers introduced for the first time EDDS in Fenton and photo-Fenton processes (Huang et al., 2012, 2013; Li et al., 2010; Wu et al., 2014). Since then, only some few works have explored the degradation of organic micropollutants by Fe(III)–EDDS-assisted photo-Fenton (Papoutsakis et al., 2015) and solar photo-Fenton (Soriano-Molina et al., 2018, 2019; Cuervo Lumbaque et al., 2019). It has been demonstrated that photo-Fenton-like reaction (5) exhibits a much higher quantum yield than conventional photo-Fenton reaction (2): 0.017 for the latter at 360 nm (Safarzadeh-Amiri et al., 1997) versus 0.10 for the former at 290–400 nm (Wu et al., 2014). In addition, the Fe(III)–EDDS complex is able to absorb in the visible region.

$$Fe(III)–EDDS + h\nu \rightarrow Fe^{2+} + EDDS^{\bullet+} \quad (5)$$

Based on these positive features, it is expected that Fe(III)–EDDS complex is also advantageous in PEF process. We have recently elucidated the mechanism of EF treatment with Fe(III)–EDDS (Ye et al., 2019b), but there is no article that discusses its particularities in PEF and the further application to the removal of pharmaceuticals in urban wastewater matrices. The occurrence of pharmaceutical residues and their transformation products in water, which mainly results from the absence or inefficiency of treatments at WWTFs (Bagnis et al., 2018; Kümmerer, 2019), has become a big obstacle to global water quality, posing serious threats to humans and ecosystems. Prozac® is one of the top-selling antidepressants worldwide, being the fluorinated molecule fluoxetine its active ingredient. This pollutant has been detected in effluents from WWTFs in the Baltic Sea (UNESCO, 2017). In Canada and China, fluoxetine has been detected in effluents from WWTFs and freshwater at ng L^{-1} level (Jennifer Ebele et al., 2017), being also detected in marine environment (Mezzelani et al., 2018). Fluoxetine has a proven ecotoxicological impact at environmental level (Desbiolles et al., 2018) and, as a result, it has been included in some list of priority substances (Jennifer Ebele et al., 2017). Several electrochemical technologies have been developed in recent years to enhance the removal of pharmaceuticals from water (Brillas and Sirés, 2015). In particular, fluoxetine was treated by EO with TiO_2 and PbO_2 (Wang et al., 2018). The great performance of EF and PEF has also been ascertained, using a BDD/air-diffusion cell, but only in a model aqueous matrix with 0.050 M Na_2SO_4 at pH 3.0 (Salazar et al., 2017).

To our knowledge, this is the first study dedicated to the Fe(III)–EDDS-catalyzed PEF process, which has been applied to the treatment of the pharmaceutical fluoxetine at circumneutral pH. The degradation performance was evaluated from high-performance liquid chromatography (HPLC) and total organic carbon (TOC) data. Most of the electrolyses have been carried out using an IrO_2/air-diffusion cell at constant current, both in urban wastewater and in model matrices to better assess the effect of key parameters like catalyst source, Fe(III)–EDDS dosage, Fe(III):EDDS ratio, pH or applied current on the concentrations of Fe(II) and Fe(III), Fe(III)–EDDS complex and H_2O_2. The main reaction by-products were identified by gas chromatography-mass spectrometry (GC-MS) and ion chromatography, whereas toxicity was assessed from Microtox® analysis.

2. Experimental

2.1. Chemicals

Fluoxetine hydrochloride (certified reference material) was purchased from Sigma-Aldrich. Sodium sulfate, heptahydrated iron(II) sulfate, sulfuric acid (96–98% solution) and sodium hydroxide pellets were of analytical grade from Merck, Panreac and J.T. Baker. $Fe(ClO_4)_3$ and EDDS trisodium salt solution (~35% aqueous solution) used to prepare the catalytic complex were purchased from Sigma-Aldrich. $TiOSO_4$ and 1,10-phenanthroline monohydrate employed for H_2O_2 and dissolved iron quantification, respectively, were from Sigma-Aldrich and Alfa Aesar. All the other chemicals were of analytical or HPLC grade supplied by Merck and Panreac.

2.2. Aqueous matrices employed to dissolve fluoxetine hydrochloride

The electrolytic trials were made with 150 mL of two different kinds of solutions:

(i) 0.050 M Na_2SO_4 in Millipore Milli-Q water (resistivity > 18 MΩ cm at 25 °C), whose natural pH was around 5.7;

(ii) Wastewater collected from the secondary effluent of a WWTF placed near Barcelona, at natural pH 7.2. Before use, the wastewater was preserved in a refrigerator at 4 °C, which allowed making all the experiments with water from the same batch. This urban wastewater had a specific conductivity of 1.35 mS cm^{-1}, total carbon content of 119.5 mg L^{-1} and TOC of 9.3 mg L^{-1}. The concentration of cations was: 0.11 mg L^{-1} Fe^{2+}, 33.9 mg L^{-1} Mg^{2+}, 94.0 mg L^{-1} Ca^{2+}, 46.8 mg L^{-1} K^+ and 315.9 mg L^{-1} Na^+. The content of anions was: 4.2 mg L^{-1}

NO_2^-, 16.9 mg L^{-1} NO_3^-, 569.8 mg L^{-1} Cl^- and 128.4 mg L^{-1} SO_4^{2-}. In most of the experiments, the wastewater was first conditioned: it was acidified to pH around 2.0 using H_2SO_4 solution; then, the volatile compounds where stripped under nitrogen stream, and pH was re-established with NaOH solution. Table S2 summarizes the seven organic compounds clearly identified in this aqueous sample.

When required, fluoxetine hydrochloride was spiked into the aqueous matrices at 0.049 mM (i.e., 10 mg L^{-1} TOC). For the preparation of the Fe(III)–EDDS (1:1) complex, 10 mM $Fe(ClO_4)_3$ and 10 mM EDDS solutions were prepared and stored in amber glass bottles. For each experiment, a fresh complex was prepared by mixing equal volumes in the dark. The mixture was stirred for 3 min, thereby withdrawing a small volume that was added to the fluoxetine solution. A similar procedure was followed to prepare complexes with other Fe(III):EDDS ratios. In some cases, $FeSO_4$ and $Fe(ClO_4)_3$ were used as uncomplexed catalysts for comparison.

2.3. Electrochemical systems

All the experiments were made in an undivided, jacketed glass cell. The cell contained 150 mL of contaminated solution, thermostated at 25 °C and stirred with a magnetic PTFE follower at 700 rpm, and a pair of electrodes (each of them with 3 cm^2 immersed geometric area) separated 1 cm from each other. A sketch of a similar setup can be seen elsewhere (Oriol et al., 2019). The air-diffusion cathode, made of carbon-PTFE on carbon cloth (Sainergy Fuel Cell), was continuously fed with air at 1 L min^{-1} to ensure the H_2O_2 electrogeneration. Three different anodes were employed in this study: Ti|IrO_2-based and Ti|RuO_2-based plates purchased from NMT Electrodes, and a Si|BDD plate from NeoCoat. Constant current was applied between the anode and cathode by means of an Amel 2049 potentiostat-galvanostat, whereas the voltage between both electrodes was continuously monitored on a Demestres 601BR digital multimeter. Prior to first use, all the electrodes were activated upon electrolysis in a 0.050 M Na_2SO_4 solution at 300 mA for 180 min. In all trials, except in UVA photolysis and EO, iron sources were added as catalyst. In UVA photolysis and PEF, the solution was irradiated with UVA light (λ_{max} = 360 nm, irradiance of 5 W m^{-2} as measured with a Kipp&Zonen CUV 5 UV radiometer) provided by a 6-W Philips TL/6W/08 black light blue fluorescent tube placed at 7 cm above the liquid surface.

2.4. Analytical methods

The electrical conductance of the raw wastewater was determined with a Metrohm 644 conductometer. The pH of all solutions, before and after the trials, was measured with a Crison GLP 22 pH-meter. All subsequent analyses were carried out after filtration of the samples with PTFE filters (0.45 μm) from Whatman. The concentration of H_2O_2 accumulated during the electrochemical assays was determined spectrophotometrically, since it formed a yellow complex with a Ti(IV) reagent that presented a maximum absorbance at λ = 408 nm (Welcher, 1975). A Unicam UV/Vis device thermostated at 25 °C was employed for these analyses, as well as for dissolved iron quantification. The total dissolved Fe(II) concentration was determined at λ = 510 nm upon direct reaction with 1,10-phenanthroline, whereas Fe(III) was determined in the same manner after mixing with ascorbic acid since this allows quantifying the total dissolved iron content upon complete conversion of Fe(III) into Fe(II). The TOC content of the samples was immediately measured after collection, using a Shimadzu TOC-VCSN analyzer that yielded values with ±1% accuracy. A Shimadzu TNM-1 unit coupled to the previous analyzer allowed the determination of total nitrogen (TN).

The decay of fluoxetine concentration was assessed by reversed-phase HPLC after preserving the withdrawn samples by dilution with acetonitrile. This analysis was made by injecting the diluted samples into a Waters 600 liquid chromatograph equipped with a BDS Hypersil C18 5 μm (250 mm × 4.6 mm) column at 25 °C and coupled to a Waters 996 photodiode array detector selected at λ = 227 nm. A 50:50 (v/v) CH_3CN/H_2O (0.010 M KH_2PO_4) mixture at pH 3.0 was eluted at 1.0 mL min^{-1} as mobile phase, allowing the detection of fluoxetine at retention time t_r = 13.2 min. The concentration of the Fe(III)–EDDS complex was determined with the same equipment but using a solution with 2 mM tetrabutylammonium hydrogensulfate and 15 mM sodium formate as the aqueous phase at pH 4.0, which was mixed with methanol (95:5, v/v) and eluted at 0.8 mL min^{-1} as mobile phase. The detector was set at 240 nm and the complex appeared at t_r = 10.7 min. All trials for HPLC analysis were made twice, and samples were injected at least in duplicate. Average values with the corresponding error bars are reported in the figures.

The concentration of accumulated inorganic ions was obtained by ion chromatography using a Shimadzu 10Avp liquid chromatograph fitted with a Shim-Pack IC-A1S (100 mm × 4.6 mm) anion column at 40 °C, coupled to a Shimadzu CDD 10Avp conductivity detector. Measurements were conducted with a solution composed of 2.4 mM tris(hydroxymethyl)aminomethane and 2.6 mM phthalic acid, at pH 4.0, eluted at 1.5 mL min^{-1} as mobile phase. Peaks appeared at t_r of 1.75 min (F^-), 2.5 min (Cl^-) and 4.0 min (NO_3^-). The NH_4^+ concentration was obtained as reported elsewhere (Guelfi et al., 2019b).

The concentration of metal cations in the real wastewater and total dissolved iron during the trials was analysed by inductively coupled plasma optical emission spectroscopy (ICP-OES) using an Optima 3200L spectrometer from Perkin Elmer.

To assess the toxicity of untreated and treated solutions, acute bioluminescence inhibition assays were performed using the marine bacteria *Vibrio fischeri*. First, all the collected samples were treated to adjust their pH to 7.0, being subsequently diluted. The acute ecotoxicity was measured after 15 min of incubation at 25 °C using an AFNOR T90-301 Microtox® system. The bioluminescent bacteria and other reagents were supplied by Modern Water and the analysis was conducted following the standard procedure recommended by the manufacturer. Results obtained are expressed as EC_{50} (in mg L^{-1}), which accounts for the concentration of solution at a given electrolysis time that causes the reduction of the 50% of bioluminescence intensity upon contact with the bacteria for 15 min.

Organic compounds contained in the real wastewater, as well as stable organic by-products accumulated during the electrochemical treatment of fluoxetine either in 0.050 M Na_2SO_4 or conditioned wastewater were identified by GC-MS, comparing with NIST05 database. The organic components were extracted with 75 mL of CH_2Cl_2 in three times, followed by thorough drying over anhydrous Na_2SO_4, filtration and concentration under reduced pressure. The analysis was carried out on a 6890N gas chromatograph coupled to a 5975C mass spectrometer, both from Agilent Technologies, in EI mode at 70 eV. Non-polar Teknokroma Sapiens-X5ms and polar HP INNOWax columns (0.25 μm, 30 m × 0.25 mm) were employed. The temperature was increased from 36 °C (1 min), up to 320 °C (hold time of 10 min) for the former and 250 °C for the latter, at 5 °C min^{-1}, with the inlet and source at 250 and 230 °C. The transfer line was at 280 °C or 250 °C, respectively.

3. Results and discussion

3.1. Fluoxetine degradation in 0.050 M Na_2SO_4 solutions at near-neutral pH

3.1.1. Comparative fluoxetine degradation by different methods

Since the main goal of this work was to employ the Fe(III)–EDDS complex as a photoactive catalyst in PEF process assisted with UVA light, its stability was first assessed in 0.050 M Na_2SO_4 medium at natural pH ~5.7, both in the dark and under UVA irradiation (Fig. S1). The 1:1 ratio was selected because it is presumed as the most photoactive (Wu et al., 2014). Fig. S1a highlights the high stability of the catalytic complex for 60 min in the dark at near-neutral pH. Conversely, in Fig. S1b, the great photoactivity of the Fe(III)–EDDS complex is evidenced, thus confirming the occurrence of photo-Fenton-like reaction (5).

In Fig. 1, the degradation of 0.049 mM fluoxetine in 0.050 M Na_2SO_4 medium at natural pH ~5.7 upon the application of different treatments is compared. Fig. 1a shows the null effect of UVA radiation alone, as expected from the absence of absorption of fluoxetine at such wavelength. In contrast, a substantial decay of 34% at 60 min was achieved in an analogous trial made in the presence of 0.1 M Fe(III)–EDDS (1:1) complex. The absence of cathodic H_2O_2 production could presumably discard the contribution of Fenton-based reactions (see Fig. S2 for a more detailed explanation). Therefore, the destruction of fluoxetine can be explained by the oxidative action of two types of radicals: (i) $EDDS^{\bullet+}$, which is formed along with Fe^{2+} via reaction (5), and pre-eminently (ii) $O_2^{\bullet-}$, whose presence has been confirmed from reaction (6) in aerated solutions at near-neutral pH (Hayyan et al., 2016).

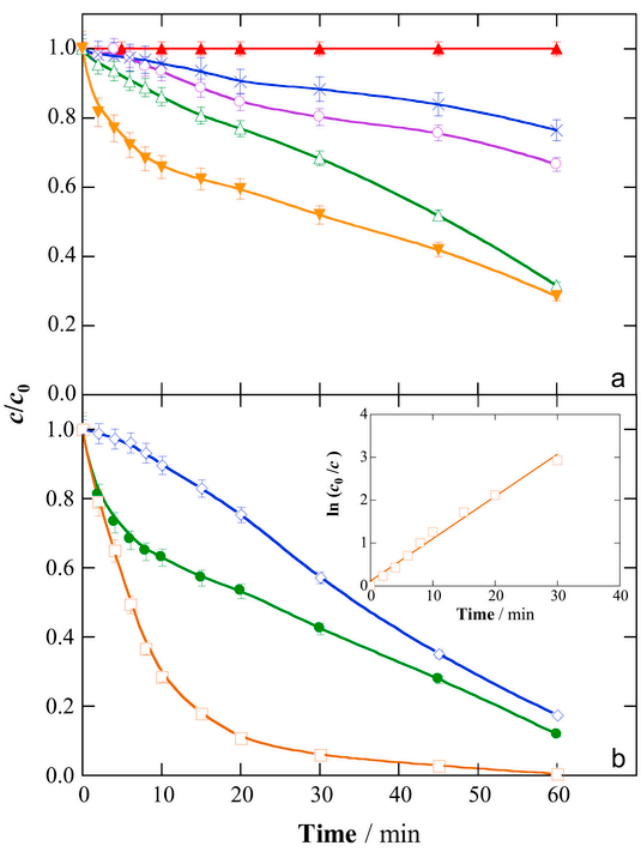

Fig. 1. Normalized fluoxetine concentration vs. electrolysis time during different treatments of 150 mL of 0.049 mM drug solutions with 0.050 M Na_2SO_4 at natural pH ~5.7. In the electrochemical assays, an IrO_2/air-diffusion cell was used at 50 mA and 25 °C. In (a), (▲) UVA photolysis, (◯) UVA photolysis with 0.10 mM Fe(III)–EDDS (1:1) complex, (×) EO, (△) EF with 0.10 mM Fe(III)–EDDS (1:1) complex and (▼) EF with 0.10 mM $FeSO_4$. In (b), (◇) PEF with 0.10 mM $Fe(ClO_4)_3$, (●) PEF with 0.10 mM $FeSO_4$ and (□) PEF with 0.10 mM Fe(III)–EDDS (1:1) complex. The inset panel presents the pseudo-first-order kinetic analysis for the latter assay.

$$Fe^{2+} + O_2 \rightarrow Fe^{3+} + O_2^{\bullet-} \quad (6)$$

All the other trials included in Fig. 1 were carried out using the IrO_2/air-diffusion cell at 50 mA. In the absence of catalyst (EO process), a poor drug disappearance of 24% was attained, as a result of the low oxidation power of $IrO_2(^{\bullet}OH)$ radicals and their confinement in the electrode vicinity. Moreover, $IrO_2(^{\bullet}OH)$ was consumed to a large extent in the oxidation of H_2O_2, whose concentration was high and greater than that from fluoxetine because of the use of the efficient air-diffusion cathode (see below). In contrast, a very small addition of Fe(III)–EDDS complex to the initial solution caused a great enhancement of fluoxetine concentration decay, reaching 69% at 60 min. This was due to the production of a large amount of $O_2^{\bullet-}$ from reaction (4), which is in equilibrium with its protonated form, $HO_2^{\bullet}$. In this EF process, the catalytic complex mainly existed as Fe(III)–EDDS, because the air-diffusion cathode has low ability for its electroreduction (Ye et al., 2019b). However, Fe(II)–EDDS formed as product in reaction (4) was able to react with H_2O_2 and generate $^{\bullet}OH$ via reaction (3). The final drug concentration decay in EF process when the chelated complex was replaced by $FeSO_4$ was also partial, although slightly higher (72%) and with a steeper profile, especially in the first minutes. Four factors could contribute to this behavior: (i) the presence of hydrated Fe^{2+} ions from the beginning promoted the production of $^{\bullet}OH$ from Fenton's reaction (S1); (ii) the oxidation of Fe^{2+} to Fe^{3+} from reaction (6) yielded $O_2^{\bullet-}$; (iii) the low solubility of Fe^{2+} and Fe^{3+} at near-neutral pH caused the precipitation of most of the iron as $Fe(OH)_3$, which could favor the fluoxetine disappearance by coagulation and heterogeneous Fenton's reaction (see subsection 3.2); and (iv) the absence of a competing target like EDDS allowed the action of all radicals and coagulants simply on fluoxetine (and its intermediates).

Fig. 1b reveals the greater performance of all PEF treatments. Up to 88% fluoxetine was removed at 60 min using $FeSO_4$ in the absence of EDDS, although the profile during the first 10 min was very similar to that obtained in EF with the same catalyst (Fig. 1a). This means that in that stage, the predominant degradation mechanism was the oxidation with the very oxidizing $^{\bullet}OH$ formed from conventional Fenton's reaction. After 10 min, UVA light in PEF allowed the continuous regeneration of Fe^{2+} from dissolved Fe^{3+} according to photo-Fenton reaction (2). Coagulation and heterogeneous Fenton's reaction with $Fe(OH)_3$ and oxidation by less powerful radicals mentioned above could also contribute to gradual drug disappearance. A similar fluoxetine concentration decay (83%) but with much lower conversion rate was observed using $Fe(ClO_4)_3$ as catalyst. This agrees with the previous treatment, since the mechanism was exactly the same but the absence of hydrated Fe^{2+} from the beginning impeded a faster initial fluoxetine disappearance. Finally, PEF with 0.1 mM Fe(III)–EDDS (1:1) complex was clearly superior to all the other treatments, being the only one that led to total drug abatement at 60 min. The used of chelated Fe(III) was advantageous because: (i) it kept a higher amount of dissolved iron for longer time, in contrast to EF and PEF without EDDS, and (ii) the UVA radiation allowed that the main form of such dissolved iron was Fe(II)–EDDS, in contrast to all the EF systems. This resulted in the largest production of $^{\bullet}OH$ via reaction (3), which degraded most of the fluoxetine molecules prior to significant degradation of EDDS (see Fig. S2). The contribution of additional routes like coagulation, heterogeneous Fenton's reaction and oxidation with other radicals cannot be discarded either, since they could justify that the degradation was almost as fast as

that previously achieved for 0.049 mM fluoxetine with 0.050 M Na_2SO_4 at pH 3.0 by PEF using a BDD/air-diffusion cell at a much higher current (300 mA) (Salazar et al., 2017). The inset panel in Fig. 1b shows the pseudo-first-order kinetics in PEF with Fe(III)–EDDS, yielding an apparent rate constant $k_1 = 0.0986\ min^{-1}$ ($R^2 = 0.987$).

3.1.2. Evolution of iron ions, dissolved iron and generated H_2O_2

In order to better explain the trends of most of the aforementioned treatments, the evolution of concentrations of Fe(II), Fe(III), dissolved iron and H_2O_2 is depicted in Figs. S2a–c, whereas the normalized Fe(III)–EDDS concentration can be seen in Fig. S2d. In UVA photolysis with 0.10 mM Fe(III)–EDDS, the almost complete photoreduction of chelated Fe(III) to Fe^{2+} can be deduced from Figs. S2a and b, thus confirming the occurrence of photo-Fenton-like reaction (5) as discussed in Fig. 1a. In 30 min, 91% of Fe(III) was transformed into Fe^{2+}. The rest was soluble Fe(III), rather in uncomplexed form because Fig. S2d highlights the total disappearance of the Fe(III)–EDDS complex at 60 min. Worth noting, Fig. S2c shows the accumulation of a low amount of H_2O_2 in this process. This phenomenon can be explained by reaction (S5), promoted by $O_2^{\bullet-}$, and suggests that fluoxetine decay in UVA photolysis (Fig. 1a) was also due to the action of $^{\bullet}OH$ formed from Fenton's reaction. Since $EDDS^{\bullet+}$ was also generated from reaction (5), the H_2O_2 accumulation could also be largely attributed to reaction (7) (Wu et al., 2014).

$$EDDS^{\bullet+} + O_2 \rightarrow EDDS_{OX} + H_2O_2 \quad (7)$$

In Fe(III)–EDDS-catalyzed EF, Figs. S2a and b confirm that the prevailing iron form was Fe(III), with only a minor production of Fe(II). In fact, from Fig. S2d, it is clear that such ion mainly existed as Fe(III)–EDDS. Furthermore, the iron precipitation was particularly evident from 30 min, losing 42% of dissolved iron at the end of the treatment. The presence of only a very low amount of $^{\bullet}OH$, formed as explained above, preserved the integrity of the Fe(III)–EDDS, but turned out to be detrimental for fluoxetine degradation (Fig. 1a). In PEF with $Fe(ClO_4)_3$ as catalyst, the most relevant feature was the very low dissolved iron concentration at time zero (i.e., $1.5\ mg\ L^{-1}$), which matched almost perfectly with Fe(III) concentration and decayed even more along the electrolysis. This suggests that fluoxetine concentration decay described for this process in Fig. 1b could be mainly due to coagulation with solid $Fe(OH)_3$. The H_2O_2 trends in Fig. S2c support this idea, because the profiles for EF with Fe(III)–EDDS, PEF with $Fe(ClO_4)_3$ and EO were almost coincident, which means that the reactions between H_2O_2 and complexed Fe(III)–EDDS (i.e., Fenton-like reaction) or precipitated $Fe(OH)_3$ (i.e., heterogeneous Fenton's reaction) were not so relevant. Finally, the aforementioned superiority of Fe(III)–EDDS-catalyzed PEF can be understood from Figs. S2a–d. This treatment allowed the accumulation of up to $1.7\ mg\ L^{-1}$ Fe(II) (i.e., ~30% Fe(III) photoreduction from reaction (5), Fig. S2a) in 20 min, whereupon this content decayed progressively because of the gradual iron precipitation (Fig. S2b) and the almost total disappearance of the very photoactive Fe(III)–EDDS complex (Fig. S2d). Hence, in the absence of enough EDDS, coagulation with $Fe(OH)_3$ probably contributed to fluoxetine disappearance (Fig. 1b). Note that as a result of the greater presence of Fe(II) in this treatment, which stimulated Fenton's reaction, the accumulated H_2O_2 concentration was lower than in the previous processes (3.5 mM vs ≥ 5.0 mM, Fig. S2c). It is interesting to observe that fluoxetine (and its reaction intermediates) played a protective role that enhanced the catalytic power of PEF process, as deduced when the latter treatment was carried out in the absence of the drug. In that trial, the Fe(III)–EDDS complex disappeared much more quickly (Fig. S2d), because the $^{\bullet}OH$ formed once the Fe^{2+} was photoregenerated mainly participated in the destruction of EDDS. This led to a much faster iron precipitation (Fig. S2b), with a consequently poor Fe(II) regeneration (Fig. S2a).

Aiming to clarify the role of oxidizing radicals during the fast degradation of fluoxetine by the Fe(III)–EDDS-catalyzed PEF treatment, the experiment discussed in Fig. 1b was performed in the presence of a radical scavenger. As can be seen in Fig. S3, the use of *p*-benzoquinone as a well-known $O_2^{\bullet-}$ scavenger ($k_2 \sim 1 \times 10^9\ M^{-1}\ s^{-1}$) caused a slow and evident deceleration of the drug degradation, only attaining 88% degradation at 60 min. This trend suggests the participation of $O_2^{\bullet-}$ as oxidant in this PEF process, being mainly produced upon Fe(III)–EDDS photolysis with UVA light as explained in Fig. 1a. However, Fig. S3 allows confirming that the prevalent radical was $^{\bullet}OH$ because an analogous trial in the presence of *tert*-butanol as single scavenger ($k_2 = 6.8 \times 10^9\ M^{-1}\ s^{-1}$) revealed the very slow fluoxetine concentration decay, with a disappearance of 17% as maximal at the end of the electrolysis.

3.1.3. Detection of inorganic ions and effect of experimental variables during PEF treatment

In order to have a first idea about the changes undergone by the fluoxetine structure during the PEF treatment with chelated iron, the inorganic ions accumulated in solution were analysed. A higher drug concentration as compared to all previous trials, i.e., 0.098 mM, was employed to allow a more accurate quantification. Considering that the pollutant was in the form of hydrochloride, this corresponded to a content of $1.4\ mg\ L^{-1}$ N, $3.5\ mg\ L^{-1}$ Cl and $5.6\ mg\ L^{-1}$ F. Fig. S4 confirms the presence of $3.4\ mg\ L^{-1}$ Cl^- in the initial solution, but this concentration decreased gradually along the electrolysis. At 60 min, 12% of Cl^- ion was converted to active chlorine ($Cl_2 + ClO^-$), with no traces of chlorine oxyanions (ClO_2^-, ClO_3^- and ClO_4^-) detected by ion chromatography. Transformation of fluoxetine by active chlorine was thus an additional degradation route, occurring in concomitance with oxidation by oxygen radicals, presumably coagulation with $Fe(OH)_3$, and UVA photolysis. The total amount of F^- ion at 60 min was $3.0\ mg\ L^{-1}$, which means that 46% of the initial F atoms where still contained in fluorinated by-products. The N atom of fluoxetine, as shown in Fig. S4, was very slowly converted into NO_3^- (only up to $0.12\ mg\ L^{-1}$). Neither NO_2^- nor NH_4^+ ions were detected and dissolved TN was constant. Hence, the solution at 60 min contained many *N*-rich derivatives. From this analysis, the following reaction can be proposed for total mineralization of fluoxetine:

$$C_{17}H_{19}F_3NO^+ + 36\ H_2O \rightarrow 17\ CO_2 + 3\ F^- + NO_3^- + 91\ H^+ + 86\ e^- \quad (8)$$

In order to assess the limits of PEF treatment with 0.1 mM Fe(III)–EDDS (1:1) complex to degrade fluoxetine using the IrO_2/air-diffusion cell at 50 mA, the effect of the initial drug concentration on the decay kinetics and the complex disappearance is presented in Fig. 2. Total disappearance within 60 min was obtained for fluoxetine concentrations up to 0.147 mM (i.e., $30\ mg\ L^{-1}$ TOC, Fig. 2a), whereas incomplete abatements resulted from more polluted solutions. This means that the oxidation (and coagulation) ability of the system gradually approached its maximal, as expected from the action of a quite constant amount of $^{\bullet}OH$, along with other oxygen radicals, active chlorine and $Fe(OH)_3$, on a larger number of fluoxetine molecules. Furthermore, the increase in drug concentration also entailed the accumulation of a greater amount of intermediates that consumed oxidants (and $Fe(OH)_3$). The slower degradation kinetics was reflected in the decreasing apparent rate constant, from $k_1 = 0.0986\ min^{-1}$ ($R^2 = 0.987$) at 0.049 mM fluoxetine to $0.0659\ min^{-1}$ ($R^2 = 0.998$) at 0.147 mM and $0.0226\ min^{-1}$ ($R^2 = 0.997$) at 0.490 mM. On the other hand, Fig. 2b informs about the slower degradation of the Fe(III)–EDDS complex as

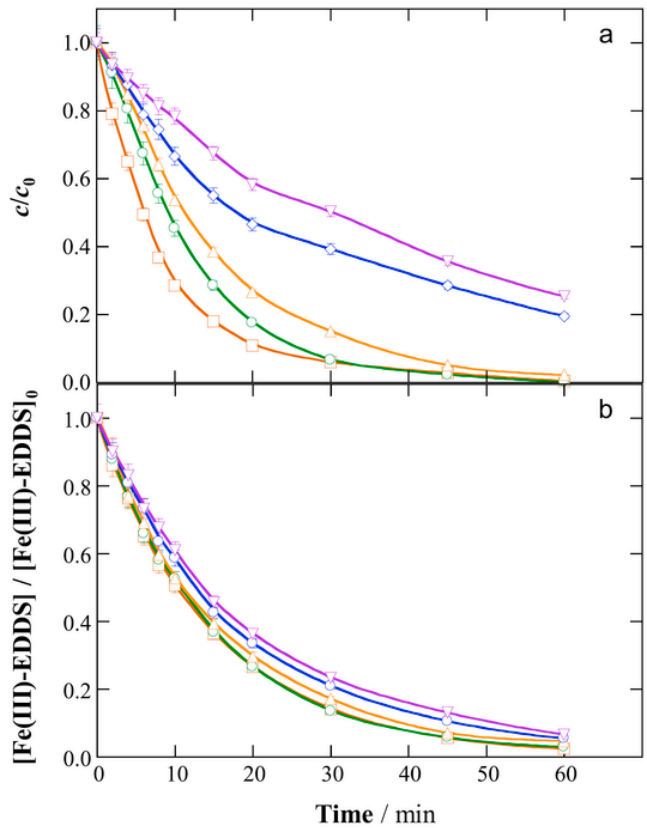

Fig. 2. Effect of fluoxetine concentration on the change of (a) normalized drug content and (b) normalized concentration of Fe(III)–EDDS (1:1) complex with electrolysis time during the PEF treatment of 150 mL of fluoxetine solutions with 0.10 mM Fe(III)–EDDS (1:1) complex and 0.050 M Na_2SO_4 at natural pH ~ 5.7 using an IrO_2/air-diffusion cell at 50 mA and 25 °C. Fluoxetine content: (□) 0.049 mM, (○) 0.098 mM, (△) 0.147 mM, (◇) 0.245 mM and (▽) 0.490 mM.

the initial fluoxetine content became higher, which confirms the protective role of the organic pollutants mentioned above. In fact, at the two highest fluoxetine concentrations, the complex was not completely destroyed at 60 min. Overall, these findings allow concluding that this PEF treatment was rather flexible, being feasible: (i) to quickly destroy micropollutants at low concentrations and (ii) to completely remove pollutants from more contaminated solutions, more slowly, thanks to the larger stability of the catalytic complex.

Trying to achieve a faster drug decay by the Fe(III)–EDDS-catalyzed PEF treatment, the effect of the applied current was investigated. As can be observed in Fig. 3, the value of 50 mA employed so far can be actually considered as the optimum one. The disappearance was much quicker than that at 10 mA (k_1 = 0.0559 min^{-1}, R^2 = 0.998), which additionally only attained a partial drug abatement, and slightly faster than that at 25 mA (0.0986 min^{-1} vs 0.0933 min^{-1}). At 75 mA, the profile was a bit better, but the incremental energy cost was not accompanied by a substantial enhancement of the decontamination rate. For this reason, no greater currents were tested. In any case, it is evident that the applied current did not have a preponderant influence on the process performance. This allows considering the UVA irradiation as the core of this modified PEF process, since the photoreduction of the complex via reaction (5) is the key step to provide Fe^{2+} needed for $^{\bullet}OH$ production. Since photoreduction has its own limited kinetics, a current increase mainly causes an excessive accumulation of H_2O_2 (reaction (1)) that cannot find enough Fe^{2+} ions. Therefore, the excess of H_2O_2 was partly used in parasitic reactions that consumed $^{\bullet}OH$ and $IrO_2(^{\bullet}OH)$, such as reaction (S4).

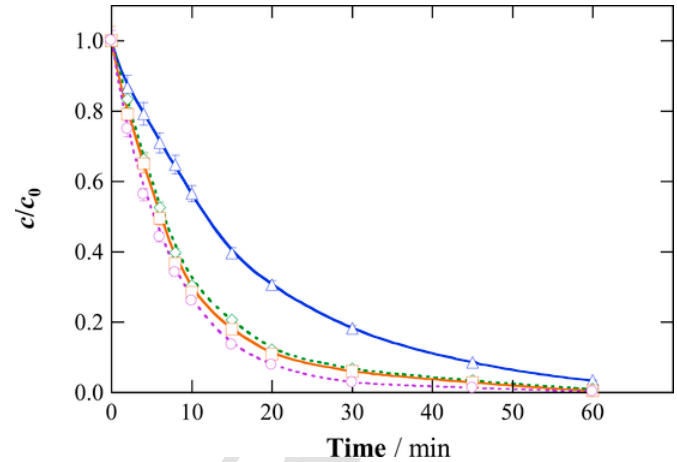

Fig. 3. Influence of applied current on the normalized fluoxetine concentration vs. electrolysis time during the PEF treatment of 150 mL of 0.049 mM drug solutions with 0.10 mM Fe(III)–EDDS (1:1) complex and 0.050 M Na_2SO_4 at natural pH ~ 5.7 and 25 °C using an IrO_2/air-diffusion cell. Current: (△) 10 mA, (◇) 25 mA, (□) 50 mA and (○) 75 mA.

As a preliminary study to further expand the use of Fe(III)–EDDS-catalyzed PEF process to urban wastewater treatment, some trials were carried out in model matrices with other electrolytes (always maintaining the same conductivity), trying to reveal the effect of anions typically found in such wastewater. In Fig. S5, the degradation profile in 0.043 M Na_2SO_4 + 0.013 M NaCl medium was exactly the same as that already commented in 0.050 M Na_2SO_4. Note that such concentration of Cl^- ion is typical in secondary effluents from WWTFs (see subsection 2.2). Hence, this similarity suggests that, although active chlorine could potentially contribute to fluoxetine degradation, Cl^- ion is also a hydroxyl radical scavenger that reduces the oxidation power of the PEF system. Chlorine radicals resulting from reactions (S15)-(S19) are less powerful and more selective than hydroxyl radical, which is detrimental for fluoxetine transformation. Similarly, CO_3^{2-} and HCO_3^- ions are known to scavenge the hydroxyl radicals via reactions (S22) and (S23) with fast kinetic constants. As a result, the decay of fluoxetine concentration in a 0.042 M Na_2SO_4 + 0.009 M $NaHCO_3$ mixture at natural pH ~8 was much slower, with only 77% disappearance at 60 min. In fact, such percentage was quite stable from ca. 30 min of electrolysis, which can be related to the presumed destruction of the catalytic complex around that time. Based on these results, it will be necessary to carry out some pre-treatment before addressing the PEF treatment of urban wastewater.

3.2. Fluoxetine degradation in urban wastewater

Fig. 4 highlights the normalized fluoxetine concentration decays during the PEF treatment of 0.049 mM drug solutions prepared in urban wastewater, using the IrO_2/air-diffusion cell at 50 mA. Considering the characteristics of the wastewater summarized in subsection 2.2, it is important to mention that the solutions with the spiked drug contained almost 20 mg L^{-1} TOC, which is twice the value of most of the solutions studied in subsection 3.1, and their natural pH was 7.2.

The PEF treatments of Fig. 4a were made with 0.1 mM Fe(III)–EDDS (1:1) complex at natural pH 7.2. Using the raw wastewater, the drug disappearance at 60 min was as low as 53% instead of 100% attained in 0.050 M Na_2SO_4 M (Fig. 1b). The higher TOC content may have a negative impact on the process performance, although probably of minor importance because Fig. 2a informed about the complete fluoxetine disappearance working up to 30 mg L^{-1} TOC. Therefore, the slower decay in wastewater can be rather accounted for by its particu-

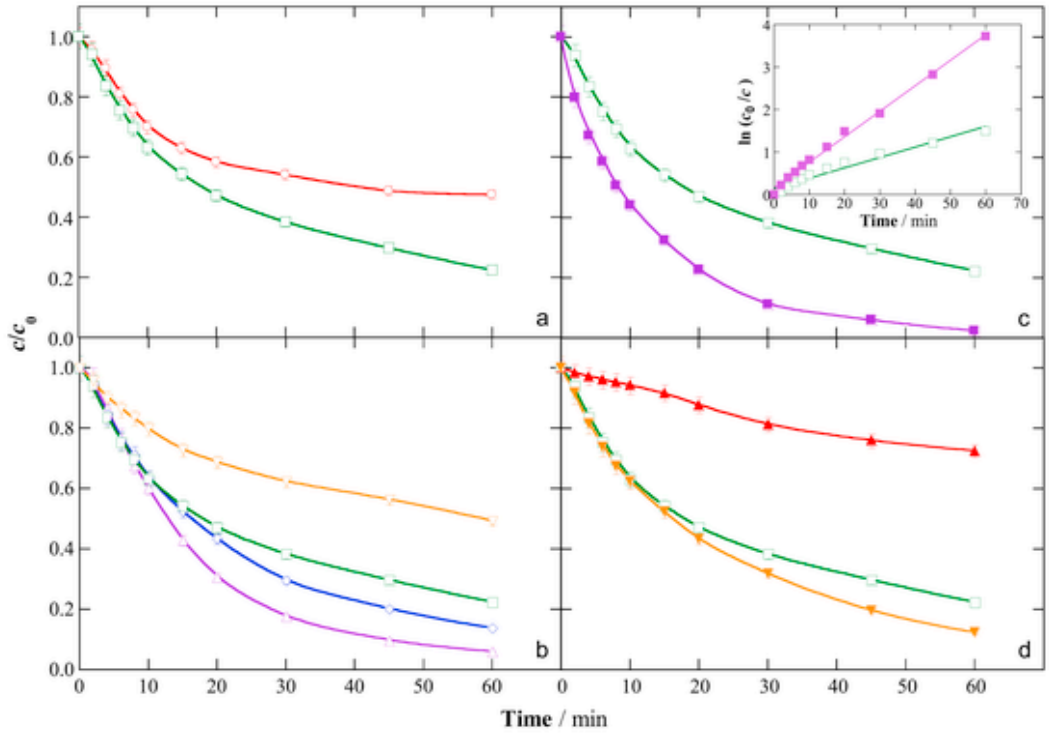

Fig. 4. Time course of normalized fluoxetine concentration during the PEF treatment of 150 mL of 0.049 mM drug solutions in urban wastewater using an IrO_2/air-diffusion cell at 50 mA and 25 °C. (a) (◯) Without and (□) with stripping, employing 0.10 mM Fe(III)–EDDS (1:1) complex at natural pH 7.2. (b) With stripping, employing 0.10 mM Fe(III)–EDDS (1:1) complex at pH: (△) 3.0, (◇) 5.0, (□) 7.2 and (▽) 9.0. (c) With stripping, employing (□) 0.10 mM or (■) 0.20 mM Fe(III)–EDDS (1:1) complex at natural pH 7.2. The pseudo-first-order kinetic analysis is shown in the inset panel. (d) With stripping, employing (▲) 0.10 mM $Fe(ClO_4)_3$, (□) 0.10 mM Fe(III)–EDDS (1:1) complex and (▼) 0.10 mM Fe(III) + 0.20 mM EDDS complex, all at natural pH 7.2.

lar composition, since it contained: natural organic matter (NOM) that competitively consumed UVA photons and reacts with oxygen radicals, and ions that act as radical scavengers, as shown from Fig. S5. The first feature was inherent from the matrix, but a proper conditioning could modify the second one. To this purpose, CO_2 was stripped from the urban wastewater following the procedure explained in subsection 2.2. In the absence of CO_3^{2-} and HCO_3^- ions, a faster and larger fluoxetine disappearance, reaching 78%, can be seen in Fig. 4. The lower transparency of the wastewater and its higher pH were two additional characteristics that affected negatively to fluoxetine removal, impeding that complete removal could be obtained, since they decreased the Fe^{2+} regeneration from reaction (5) and stimulated the precipitation of Fe(III) as $Fe(OH)_3$. Note that after 60 min of treatment in water without and with stripping, the initial pH decayed down to 6.2 and 4.6, respectively. Based on the positive influence of stripping, all subsequent trials were made with conditioned urban wastewater.

For the same PEF treatment, the effect of solution pH is shown in Fig. 4b. As expected, a better performance was obtained at more acidic pH, achieving 51%, 78%, 86% and 94% at pH 9.0, 7.2, 5.0 and 3.0. A lower pH value ensured that, as EDDS became destroyed, a larger amount of iron ions was dissolved rather than precipitated. This promoted a larger $^{\bullet}OH$ production from conventional Fenton's reaction (with uncomplexed Fe^{2+}) and Fenton-like reaction (with uncomplexed Fe^{3+}). At higher pH, coagulation with $Fe(OH)_3$ acquired more relevance for fluoxetine degradation.

The effect of the Fe(III)–EDDS dosage at pH 7.2, keeping the 1:1 ratio, can be seen in Fig. 4c. It is interesting to remark that almost complete fluoxetine abatement was achieved using 0.20 mM of the catalytic complex, exhibiting a much faster decay during the 60 min as compared to PEF with 0.10 mM of complex. The inset depicts the pseudo-first-order kinetics for both trials, yielding a greater $k_1 = 0.0246$ min^{-1} ($R^2 = 0.996$) at 0.20 mM. The upgraded abatement is in agreement with a higher amount of Fe^{2+} formed upon Fe(III)–EDDS photoreduction, which eventually fostered a much larger production of $^{\bullet}OH$ from Fenton's reaction. Nonetheless, despite the evident enhancement of drug disappearance upon increase of the Fe(III)–EDDS dosage, it was significantly slower than that in 0.050 M Na_2SO_4 with 0.10 mM of complex ($k_1 = 0.0986$ min^{-1}, Fig. 1b).

The influence of another key parameter like the Fe(III):EDDS ratio, at pH 7.2, is depicted in Fig. 4d. In general terms, the performance was better as the relative EDDS amount was increased, although the greatest difference really appeared when PEF without EDDS was compared to all other trials with EDDS. PEF with uncomplexed Fe(III) in the form of $Fe(ClO_4)_3$ yielded a very poor drug concentration decay (17% at 60 min), which was radically lower than that in Na_2SO_4 (83%, Fig. 1b). Such bad result can be related to a larger iron precipitation due to the higher pH, as well as to complexation with non-photoactive NOM components. In contrast, the use of the 1:2 complex yielded a final abatement of 88%, being slightly superior to that obtained with the 1:1 complex. Although the former complex has been reported to be less photoactive (Wu et al., 2014) and EDDS contributes to scavenge some of the oxygen radicals, in practice the larger amount of EDDS contributed to iron solubilization for longer time, ending in a faster fluoxetine degradation.

The PEF treatment catalyzed with 0.20 mM Fe(III)–EDDS (1:1), which has been the most successful in wastewater as discussed from Fig. 4c at 50 mA, was assessed in terms of the influence of the applied current using the IrO_2/air-diffusion cell. As evidenced in Fig. S6a, the behavior was globally similar to that found in Na_2SO_4. The lowest current (25 mA) was insufficient to yield the complete disappearance of fluoxetine, since the NOM components consumed most of the H_2O_2

produced at the cathode. A higher current like 50 mA was optimal to electrogenerate enough H_2O_2 that was able to react with photogenerated Fe^{2+} and then create $^{\bullet}OH$. A further increase in applied current was not efficient because the excess of H_2O_2 was wasted in parasitic reactions, as deduced from the analogous profile at 75 mA. Fig. S6b shows that when the IrO_2-based anode was replaced either by BDD or a RuO_2-based anode, at 50 mA, the decay profiles were exactly the same. This confirms that the dominant contribution to fluoxetine disappearance came from $^{\bullet}OH$ generated in the bulk via Fenton's reaction, rather than from M($^{\bullet}OH$) adsorbed on the anode surface.

To gain further insight into the effect of the $Fe(OH)_3$ precipitate on the performance of PEF process, an additional study was performed with solutions containing 0.049 mM drug and 0.050 M Na_2SO_4 at pH 7.2. Fig. S7 shows that, in the presence of 0.10 mM $Fe_2(SO_4)_3$, only 5.4% of fluoxetine was abated at 60 min, suggesting a low coagulation ability of the $Fe(OH)_3$ precipitate formed. This means that coagulation plays a minor role during the disappearance of fluoxetine. Several electrochemical treatments were carried out using the IrO_2/air-diffusion cell, at 50 mA. Fig. S7 evidences a higher drug decay (24%) in EO (i.e., without iron salt), which was upgraded in homogeneous PEF (36%) and even more in heterogeneous PEF (60%). In the case of homogeneous PEF, the solution containing fluoxetine, Na_2SO_4 and $Fe_2(SO_4)_3$ was previously filtered, yielding 0.13 mg L^{-1} of dissolved Fe^{3+}. These results corroborate the oxidation of fluoxetine by IrO_2($^{\bullet}OH$) at the anode as well as by homogeneous $^{\bullet}OH$ formed from the photo-Fenton (2) and Fenton's reaction (S1). Furthermore, the much greater drug decay found in heterogeneous PEF corroborates its oxidation via heterogeneous Fenton's reaction occurring at the $Fe(OH)_3$ surface.

Although the main goal of this work was to investigate the ability of the Fe(III)–EDDS-catalyzed PEF process to remove a target organic pollutant from urban wastewater, its mineralization ability was also tested. In previous assays, it has been demonstrated that the catalytic complex became gradually degraded, which means that the decontamination occurred in two consecutive stages: (i) the first one, where the $^{\bullet}OH$ formed from Fenton's reaction had the leading role, followed by (ii) a second one, where fluoxetine by-products and organic components from the wastewater were destroyed by the adsorbed M($^{\bullet}OH$). During all the treatment, coagulation with $Fe(OH)_3$ could also contribute to global mineralization, but with a minor role, as confirmed above. Aiming to enhance the oxidation power of the system, a BDD/air-diffusion cell and a higher current (100 mA) were employed to carry out these trials. Much lower TOC abatements were obtained using the IrO_2 and RuO_2 anodes due to their lower ability to produce oxidizing agents able to destroy the intermediates of fluoxetine and EDDS.

Fig. 5a shows the TOC decay trends for the PEF treatment of conditioned urban wastewater at pH 7.2 under three different conditions: with 0.10 mM Fe(III)–EDDS, either without or with 0.049 mM fluoxetine, and with 0.20 mM of complex in the presence of fluoxetine. A similar decay rate can be observed in all cases, achieving close TOC removal percentages around 50% at 300 min. This means that a higher residual TOC was present in the final solution as the initial content was increased. Hence, although the use of 0.20 mM Fe(III)–EDDS accelerated the decay of fluoxetine concentration (Fig. 4c), the TOC content at the end of the electrolysis was higher (20.8 mg L^{-1}), probably due to a slower removal of the products of EDDS. PEF process is known to yield great TOC abatements, usually higher than 90%. The incomplete TOC removal found in this study can then be mainly accounted for by the very poor contribution of photodecarboxylation by reaction (9). Since most of the iron was precipitated during the first degradation stage, the refractory oxidation by-products like carboxylic acids (Salazar et al., 2017) tended to become largely accumulated in the solution. In conventional PEF at acidic pH, such molecules form complexes with Fe(III) that are very photoactive, but in the Fe(III)–EDDS-catalyzed PEF their photodegradation only occurred before EDDS destruction. Afterwards, all these intermediates were only degraded by BDD($^{\bullet}OH$), probably with a minor contribution from coagulation with $Fe(OH)_3$.

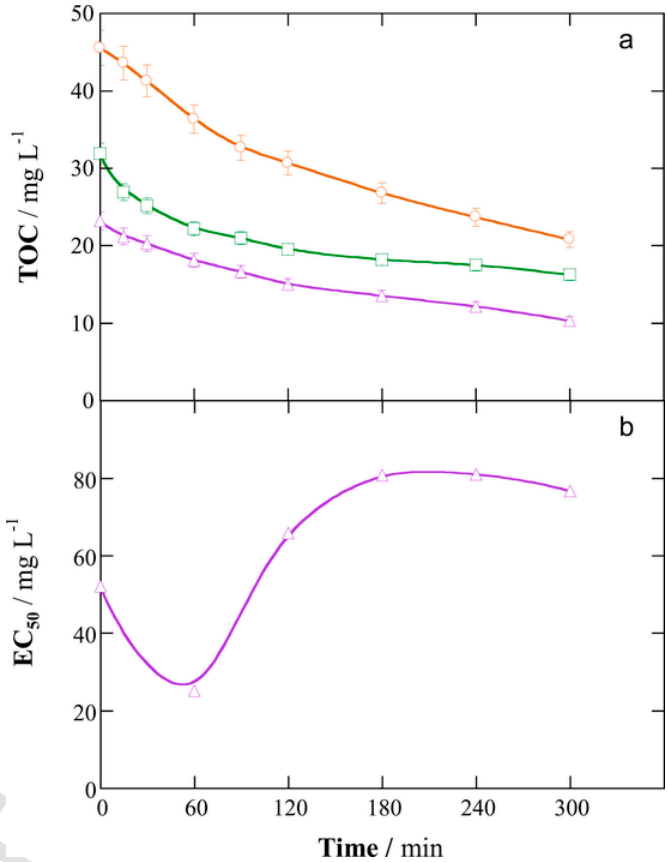

Fig. 5. (a) Change of TOC with electrolysis time during the PEF treatment of 150 mL of urban wastewater after stripping at natural pH 7.2 using a BDD/air-diffusion cell at 100 mA and 25 °C. The solution contained (△) 0.10 mM Fe(III)–EDDS (1:1) complex, without drug, (□) 0.049 mM fluoxetine + 0.10 mM Fe(III)–EDDS (1:1) complex and (○) 0.049 mM fluoxetine + 0.20 mM Fe(III)–EDDS (1:1) complex. (b) Time course of toxicity during the latter assay.

$$Fe(OOCR)^{2+} + h\nu \rightarrow Fe^{2+} + CO_2 + R^{\bullet} \quad (9)$$

In spite of yielding only a partial TOC abatement, it was more relevant to investigate the ability of the PEF process to reduce the overall toxicity. In Fig. 5b, the time course of toxicity (as EC_{50}) during the treatment of 0.049 mM fluoxetine in wastewater employing 0.10 mM Fe(III)–EDDS (1:1) complex (Fig. 5a) is depicted. The toxicity increased during the first 60 min, which can be explained by the generation of *N*- and *F*-rich toxic reaction by-products (see subsection 3.3), thereby showing a gradual decay. Higher EC_{50} values can be seen from 60 min, attaining a plateau from 180 min. The final EC_{50} value was close to that of the raw urban wastewater (80–90 mg L^{-1}). This result suggests that, although only 50% of TOC removal could be achieved at 300 min, detoxification was ensured. The absence of chlorine oxyanions (Fig. S4), the drug transformation into innocuous compounds and the generation of non-toxic products from EDDS justifies this trend.

3.3. Primary reaction by-products and mechanism for pollutant degradation

The GC-MS analysis of the organic compounds extracted upon different treatments revealed the generation of several by-products, which

confirms the presence of nitrogenated and fluorinated aromatic derivatives at short electrolysis time, as mentioned above.

Table 1 collects the intermediates detected after 20 min of Fe(III)–EDDS-catalyzed PEF treatment of fluoxetine in 0.050 M Na_2SO_4 (i.e., trial of Fig. 1a). *N*-demethylation of fluoxetine (**1**) yielded an aminoderivative (**2**). Alternatively, upon C–O bond cleavage, fluoxetine could be split into two halves: 4-trifluoromethyl-phenol (**3**), which has been reported by Salazar et al. (2017) as well, and the *N*-derivative 3-phenylpropenal (**5**). If the previous cleavage occurred upon hydroxylation with $^{\bullet}OH$ and $M(^{\bullet}OH)$, a similar transformation was observed but with the generation of a deaminated derivative (**4**). Some of the aromatic structures could be successively converted to styrene (**6**), benzaldehyde (**7**) and benzoic acid (**8**), whereas those that kept the lateral chain with the N atoms could experience internal cyclization to yield a quinolone (**9**). Finally, acetic acid, in the form of an ester (**10**), was formed as one of the aliphatic short-chain carboxylic acids that are persistent to oxidation, thus justifying the high final TOC commented above.

The by-products detected under analogous conditions but in the wastewater matrix (i.e., trial of Fig. 4c, but using 0.20 mM Fe(III)–EDDS) are summarized in Table S3. Fluoxetine (**1**) was converted to compound (**2**), but in this case the formation of the trifluorinated derivative (**3**) was accompanied by the accumulation of a different aromatic molecule (**11**). The sequential route yielding consecutive compounds (**6–8**), as well as the internal cyclization to yield the cyclic amine (**9**) were confirmed. Nevertheless, the main characteristic in urban wastewater was the production of two chloro-organic derivatives: compound **12** appeared upon chlorination of **3**, whereas compound **13** could be

Table 1
Products detected by GC-MS using a non-polar (NP) or polar (P) column after 20 min of PEF treatment of 150 mL of a 0.049 mM fluoxetine solution with 0.10 mM Fe(III)–EDDS (1:1) complex and 0.050 M Na_2SO_4 at natural pH ~ 5.7 using an IrO_2/air-diffusion cell at 50 mA and 25 °C.

Number	Chemical name	Molecular structure	Column	t_r (min)	Main fragments (m/z)
1	Fluoxetine	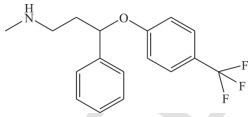	NP P	34.11 39.60	309, 44
2	*N*-[3-Phenyl-3-(4-trifluoromethylphenoxy)propyl]amine	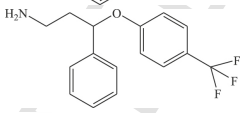	NP	41.28	295, 190, 117, 86
3	4-Trifluoromethyl-phenol	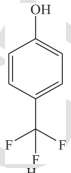	NP P	13.47 32.54	162, 143, 112
4	3-Methylamino-1-phenylpropan-1-one	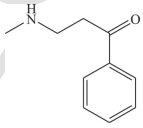	NP	18.44	162, 149, 107, 78
5	3-Phenylpropenal	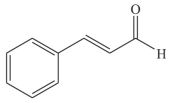	NP	16.63	131, 103, 77, 51
6	Styrene	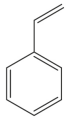	P	11.94	104, 78, 51
7	Benzaldehyde	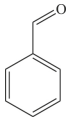	NP P	10.31 18.7	106, 77, 51
8	Benzoic acid	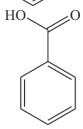	NP	20.52	122, 105, 77, 51
9	1-Methyl-1,2,3,4-tetrahydroquinoline	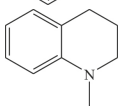	NP	21.16	147, 132, 118, 91
10	Acetic acid 2,3-dihydroxy propyl ester	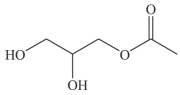	NP	18.34	143, 103, 43

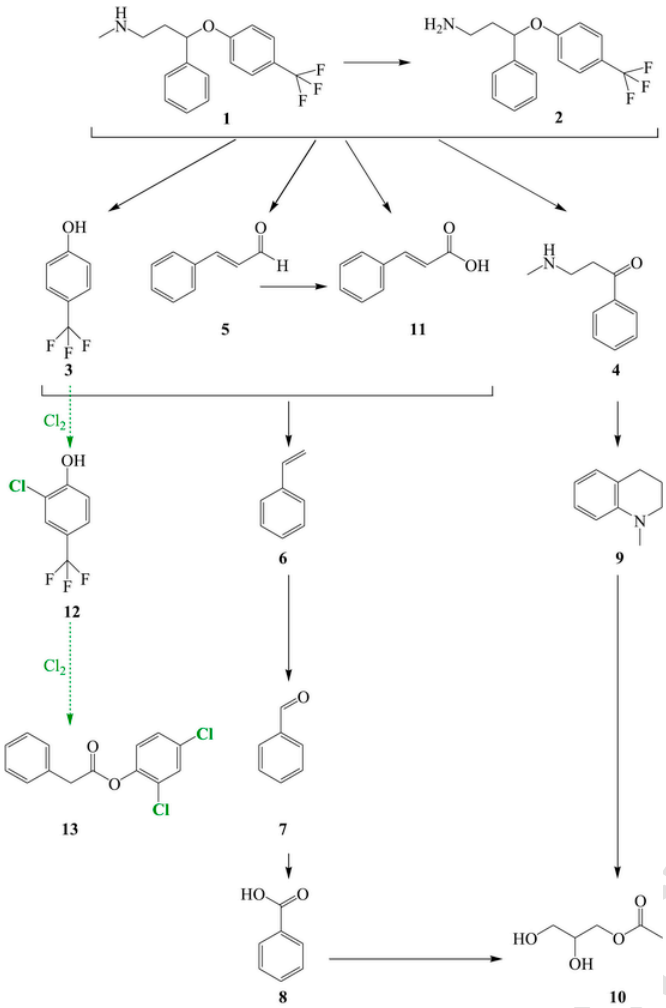

Fig. 6. Degradation route proposed for fluoxetine during the Fe(III)–EDDS-catalyzed PEF treatment at circumneutral pH. Chlorinated products detected in urban wastewater are highlighted in green. (For interpretation of the references to colour in this figure legend, the reader is referred to the Web version of this article.)

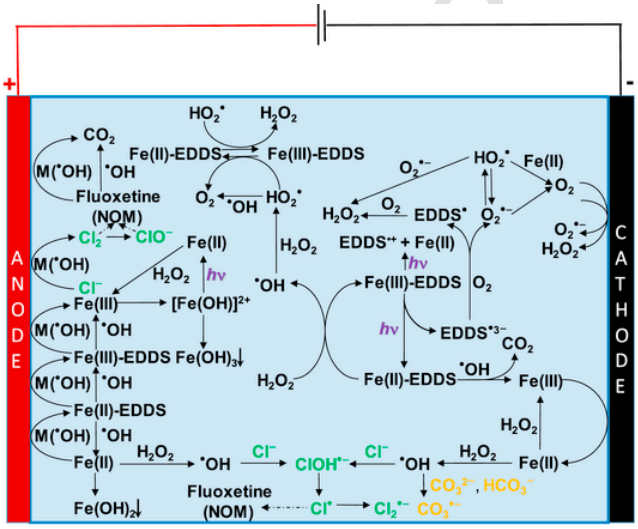

Fig. 7. Proposed mechanism for Fe(III)–EDDS-catalyzed PEF treatment at circumneutral pH.

formed from chlorination in $-CF_3$ position of **12**, followed by esterification with phenylacetic acid. These chloro-aromatic molecules contributed to the enhanced toxicity during the first 60 min (Fig. 5b). In addition, two organic components of wastewater namely **WW5** and **WW7** (Table S2) still remained as part of the TOC determined. Fig. 6 presents the proposed degradation route for fluoxetine.

Based on the trends highlighted above for fluoxetine, TOC and iron species, a very detailed mechanism for the Fe(III)–EDDS-catalyzed PEF treatment in urban wastewater at near-neutral pH is proposed in Fig. 7. To simplify, hydrated Fe^{2+} and Fe^{3+} have been written as Fe(II) and Fe(III). The main characteristic of the Fe(III)–EDDS complex is its great photoactivity, yielding Fe(II) either chelated with EDDS or in the uncomplexed form as written in reaction (5). The powerful oxidant $^{\bullet}OH$ is then generated upon participation of electrogenerated H_2O_2. In addition, the catalytic complex can react with H_2O_2 to produce $HO_2^{\bullet}$, or be gradually degraded by $^{\bullet}OH$ and M($^{\bullet}OH$). As a minor route, it can be electroreduced to Fe(II)–EDDS. The products of all these reactions, namely Fe(II), Fe(III) and Fe(II)–EDDS, then give rise to some crucial routes. At near-neutral pH and in the presence of O_2, free and complexed Fe(II) tend to be oxidized to free Fe(III), which is photoreduced via photo-Fenton reaction or precipitated as $Fe(OH)_3$ once the EDDS becomes degraded. As shown in Fig. 7 and Table S1, several radicals can be formed. Considering all this, fluoxetine and NOM components can be removed by: (i) direct anodic oxidation, (ii) indirect oxidation via adsorbed M($^{\bullet}OH$) and $^{\bullet}OH$ (and other oxygen radicals) in the bulk, as well as by active chlorine and chlorine radicals (see reactions in Table S1), (iii) coagulation with $Fe(OH)_2$ and $Fe(OH)_3$ (with a minor role) and (iv) direct phototransformation. Note that some iron precipitates might be photoactive, but this is not shown in the mechanism because the photoactivity of $Fe(OH)_3$ is expected to be insignificant (Pehkonen et al., 1993).

4. Conclusions

The total removal of organic pollutants like fluoxetine in urban wastewater at near-neutral pH is feasible by a novel PEF process with Fe(III)–EDDS as catalyst. In particular, the use of an IrO_2/air-diffusion cell at 50 mA with 0.20 mM of catalytic complex caused the disappearance of fluoxetine in 60 min. Fe(III)-EDDS showed a greater photoreduction ability than uncomplexed Fe(III). This, along with the larger solubility of iron ions, ended in a higher concentration of Fe(II) ions and hence, a greater $^{\bullet}OH$ production from Fenton's reaction. TOC abatement occurred in two consecutive stages. In the first one, $^{\bullet}OH$ had the leading role, accompanied by other oxygen radicals. In a second stage, once the EDDS was degraded and most of iron ions became precipitated, fluoxetine by-products and organic components from the wastewater were destroyed by the adsorbed M($^{\bullet}OH$). During all the treatment, coagulation with $Fe(OH)_3$ also contributed to global TOC decay, whereas active chlorine, chlorine radicals and heterogeneous Fenton's reaction had a minor importance. Stripping of wastewater with nitrogen had a positive effect, since it removed scavengers like CO_3^{2-} and HCO_3^-. A low current was enough to reach the best performance, since the $^{\bullet}OH$ production was limited by the Fe(III)-EDDS photodegradation kinetics. An excess of H_2O_2 electrogeneration at higher current was detrimental because it consumed hydroxyl radicals. TOC abatement was incomplete (50% at 300 min) due to poor contribution of photodecarboxylation of refractory aliphatic by-products like carboxylic acids, which only occurred before total EDDS destruction. However, total detoxification was ensured. In conclusion, this new PEF treatment was quite flexible since it allowed the treatment of low concentrations of pollutants, in a quicker manner, or high concentrations, more slowly, thanks to the larger stability of the catalytic complex. A thorough mechanism for the removal of the organic matter has been proposed.

Declaration of competing interest

The authors declare that they have no known competing financial interests or personal relationships that could have appeared to influence the work reported in this paper.

Acknowledgements

The authors thank financial support from project CTQ2016-78616-R (AEI/FEDER, EU) and PhD scholarship awarded to Z.H. Ye (State Scholarship Fund, CSC, China).

Appendix A. Supplementary data

Supplementary data to this article can be found online at https://doi.org/10.1016/j.watres.2019.115219.

References

Alcocer, S., Picos, A., Uribe, A.R., Pérez, T., Peralta-Hernández, J.M., 2018. Comparative study for degradation of industrial dyes by electrochemical advanced oxidation processes with BDD anode in a laboratory stirred tank reactor. Chemosphere 205, 682–689.

Aveiro, L.R., Da Silva, A.G.M., Candido, E.G., Antonin, V.S., Parreira, L.S., Papai, R., Gaubeur, I., Silva, F.L., Lanza, M.R.V., Camargo, P.H.C., Santos, M.C., 2018. Application and stability of cathodes with manganese dioxide nanoflowers supported on Vulcan by Fenton systems for the degradation of RB5 azo dye. Chemosphere 208, 131–138.

Bagnis, S., Fitzsimons, M.F., Snape, J., Tappin, A., Comber, S., 2018. Processes of distribution of pharmaceuticals in surface freshwaters: implications for risk assessment. Environ. Chem. Lett. 16, 1193–1216.

Brillas, E., Sirés, I., 2015. Electrochemical removal of pharmaceuticals from water streams: reactivity elucidation by mass spectrometry. Trac. Trends Anal. Chem. 70, 112–121.

Brillas, E., Sirés, I., Oturan, M.A., 2009. Electro-Fenton process and related electrochemical technologies based on Fenton's reaction chemistry. Chem. Rev. 109, 6570–6631.

Clarizia, L., Russo, D., Di Somma, I., Marotta, R., Andreozzi, R., 2017. Homogeneous photo-Fenton processes at near neutral pH: a review. Appl. Catal. B Environ. 209, 358–371.

Clematis, D., Cerisola, G., Panizza, M., 2017. Electrochemical oxidation of a synthetic dye using a BDD anode with a solid polymer electrolyte. Electrochem. Commun. 75, 21–24.

Coria, G., Pérez, T., Sirés, I., Brillas, E., Nava, J.L., 2018. Abatement of the antibiotic levofloxacin in a solar photoelectro-Fenton flow plant: modeling the dissolved organic carbon concentration-time relationship. Chemosphere 198, 174–181.

Cuervo Lumbaque, E., Salmoria Araújo, D., Moreira Klein, T., Lopes Tiburtius, E.R., Argüello, J., Sirtori, C., 2019. Solar photo-Fenton-like process at neutral pH: Fe(III)-EDDS complex formation and optimization of experimental conditions for degradation of pharmaceuticals. Catal. Today 328, 259–266.

Desbiolles, F., Malleret, L., Tiliacos, C., Wong-Wah-Chung, P., Laffont-Schwob, I., 2018. Occurrence and ecotoxicological assessment of pharmaceuticals: is there a risk for the Mediterranean aquatic environment? Sci. Total Environ. 639, 1334–1348.

El-Ghenymy, A., Rodríguez, R.M., Brillas, E., Oturan, N., Oturan, M.A., 2014. Electro-Fenton degradation of the antibiotic sulfanilamide with Pt/carbon-felt and BDD/carbon-felt cells. Kinetics, reaction intermediates, and toxicity assessment. Environ. Sci. Pollut. Res. 21 (14), 8368–8378.

Flores, N., Sirés, I., Garrido, J.A., Centellas, F., Rodríguez, R.M., Cabot, P.L., Brillas, E., 2016. Degradation of *trans*-ferulic acid in acidic aqueous medium by anodic oxidation, electro-Fenton and photoelectro-Fenton. J. Hazard Mater. 319, 3–12.

Galia, A., Lanzalaco, S., Sabatino, M.A., Dispenza, C., Scialdone, O., Sirés, I., 2016. Crosslinking of poly(vinylpyrrolidone) activated by electrogenerated hydroxyl radicals: a first step towards a simple and cheap synthetic route of nanogel vectors. Electrochem. Commun. 62, 64–68.

Guelfi, D.R.V., Brillas, E., Gozzi, F., Machulek, A., Jr., de Oliveira, S.C., Sirés, I., 2019. Influence of electrolysis conditions on the treatment of herbicide bentazon using artificial UVA radiation and sunlight. Identification of oxidation products. J. Environ. Manag. 231, 213–221.

Guelfi, D.R.V., Ye, Z., Gozzi, F., de Oliveira, S.C., Machulek, A., Jr., Brillas, E., Sirés, I., 2019. Ensuring the overall combustion of herbicide metribuzin by electrochemical advanced oxidation processes. Study of operation variables, kinetics and degradation routes. Separ. Purif. Technol. 211, 637–645.

Huang, W., Brigante, M., Wu, F., Hanna, K., Mailhot, G., 2012. Development of a new homogenous photo-Fenton process using Fe(III)-EDDS complexes. J. Photochem. Photobiol. A Chem. 239, 17–23.

Huang, W., Brigante, M., Wu, F., Mousty, C., Hanna, K., Mailhot, G., 2013. Assessment of the Fe(III)−EDDS complex in Fenton-like processes: from the radical formation to the degradation of bisphenol A. Environ. Sci. Technol. 47, 1952–1959.

Jennifer Ebele, A., Abou-Elwafa Abdallah, M., Harrad, S., 2017. Pharmaceuticals and personal care products (PPCPs) in the freshwater aquatic environment. Emerg. Contam. 3, 1–16.

Komtchou, S., Dirany, A., Drogui, P., Bermond, A., 2015. Removal of carbamazepine from spiked municipal wastewater using electro-Fenton process. Environ. Sci. Pollut. Res. 22, 11513–11525.

Komtchou, S., Dirany, A., Drogui, P., Robert, D., Lafrance, P., 2017. Removal of atrazine and its by-products from water using electrochemical advanced oxidation processes. Water Res. 125, 91–103.

Kümmerer, K., 2019. From a problem to a business opportunity-design of pharmaceuticals for environmental biodegradability. Sustain. Chem. Pharm. 12, 100136.

Lanzalaco, S., Sirés, I., Sabatino, M.A., Dispenza, C., Scialdone, O., Galia, A., 2017. Synthesis of polymer nanogels by electro-Fenton process: investigation of the effect of main operation parameters. Electrochim. Acta 246, 812–822.

Lanzalaco, S., Sirés, I., Galia, A., Sabatino, M.A., Dispenza, C., Scialdone, O., 2018. Facile crosslinking of poly(vinylpyrrolidone) by electro-oxidation with IrO_2-based anode under potentiostatic conditions. J. Appl. Electrochem. 48, 1343–1352.

Li, J., Mailhot, G., Wu, F., Deng, N., 2010. Photochemical efficiency of Fe(III)-EDDS complex: $^{\bullet}OH$ radical production and 17β-estradiol degradation. J. Photochem. Photobiol. A Chem. 212, 1–7.

Martínez-Huitle, C.A., Rodrigo, M.A., Sirés, I., Scialdone, O., 2015. Single and coupled electrochemical processes and reactors for the abatement of organic water pollutants: a critical review. Chem. Rev. 115 (24), 13362–13407.

Mezzelani, M., Gorbi, S., Regoli, F., 2018. Pharmaceuticals in the aquatic environments: evidence of emerged threat and future challenges for marine organisms. Mar. Environ. Res. 140, 41–60.

Oriol, R., Sirés, I., Brillas, E., De Andrade, A.R., 2019. A hybrid photoelectrocatalytic/photoelectro-Fenton treatment of Indigo Carmine in acidic aqueous solution using TiO_2 nanotube arrays as photoanode. J. Electroanal. Chem. 847, 113088.

Panizza, M., Cerisola, G., 2009. Direct and mediated anodic oxidation of organic pollutants. Chem. Rev. 109 (12), 6541–6569.

Papoutsakis, S., Brites-Nóbrega, F.F., Pulgarin, C., Malato, S., 2015. Benefits and limitations of using Fe(III)-EDDS for the treatment of highly contaminated water at near-neutral pH. J. Photochem. Photobiol. A Chem. 303–304, 1–7.

Pehkonen, S.O., Siefert, R., Erel, Y., Webb, S., Hoffmann, M.R., 1993. Photoreduction of iron oxyhydroxides in the presence of important atmospheric organic compounds. Environ. Sci. Technol. 27, 2056–2062.

Pérez, T., Coria, G., Sirés, I., Nava, J.L., Uribe, A.R., 2018. Electrosynthesis of hydrogen peroxide in a filter-press flow cell using graphite felt as air-diffusion cathode. J. Electroanal. Chem. 812, 54–58.

Ribeiro, J., De Andrade, A.R., 2004. Characterization of RuO_2-Ta_2O_5 coated titanium electrode -Microstructure, morphology, and electrochemical investigation. J. Electrochem. Soc. 151, D106–D112.

Ridruejo, C., Centellas, F., Cabot, P.L., Sirés, I., Brillas, E., 2018. Electrochemical Fenton-based treatment of tetracaine in synthetic and urban wastewater using active and non-active anodes. Water Res. 128, 71–81.

Roth, H., Gendel, Y., Buzatu, P., David, O., Wessling, M., 2016. Tubular carbon nanotube-based gas diffusion electrode removes persistent organic pollutants by a cyclic adsorption – electro-Fenton process. J. Hazard Mater. 307, 1–6.

Safarzadeh-Amiri, A., Bolton, J.R., Cater, S.R., 1997. Ferrioxalate-mediated photodegradation of organic pollutants in contaminated water. Water Res. 31 (4), 787–798.

Salazar, C., Ridruejo, C., Brillas, E., Yáñez, J., Mansilla, H.D., Sirés, I., 2017. Abatement of the fluorinated antidepressant fluoxetine (Prozac) and its reaction by-products by electrochemical advanced methods. Appl. Catal. B Environ. 203, 189–198.

Scialdone, O., Randazzo, R., Galia, A., Filardo, G., 2009. Electrochemical oxidation of organics at metal oxide electrode: the incineration of oxalic acid at IrO_2-Ta_2O_5 (DSA-O_2) anode. Electrochim. Acta 54 (4), 1210–1217.

Sirés, I., Garrido, J.A., Rodríguez, R.M., Brillas, E., Oturan, N., Oturan, M.A., 2007. Catalytic behavior of the Fe^{3+}/Fe^{2+} system in the electro-Fenton degradation of the antimicrobial chlorophene. Appl. Catal. B Environ. 72, 382–394.

Soriano-Molina, P., García-Sánchez, J.L., Alfano, O.M., Conte, L.O., Malato, S., Sánchez-Pérez, J.A., 2018. Mechanistic modeling of solar photo-Fenton process with Fe^{3+}-EDDS at neutral pH. Appl. Catal. B Environ. 233, 234–242.

Soriano-Molina, P., Plaza-Bolaños, P., Lorenzo, A., Agüera, A., García-Sánchez, J.L., Malato, S., Sánchez-Pérez, J.A., 2019. Assessment of solar raceway pond reactors for removal of contaminants of emerging concern by photo-Fenton at circumneutral pH from very different municipal wastewater effluents. Chem. Eng. J. 366, 141–149.

Steter, J., Brillas, E., Sirés, I., 2016. On the selection of the anode material for the electrochemical removal of methylparaben from different aqueous media. Electrochim. Acta 222, 1464–1474.

UNESCO, 2017. Emerging pollutants in water series. In: Pharmaceuticals in the Aquatic Environment of the Baltic Sea Region – A Status Report, 1.

Vidal, J., Huilñir, C., Santander, R., Silva-Agredo, J., Torres-Palma, R.A., Salazar, R., 2018. Effective removal of the antibiotic nafcillin from water by combining the photoelectro-Fenton process and anaerobic biological digestion. Sci. Total Environ. 624, 1095–1105.

Villanueva-Rodríguez, M., Bello-Mendoza, R., Hernández-Ramírez, A., Ruiz-Ruiz, E.J., 2019. Degradation of anti-inflammatory drugs in municipal wastewater by heterogeneous photocatalysis and electro-Fenton process. Environ. Int. 40, 2436–2445.

Wang, C., Niu, J., Yin, L., Huang, J., Hou, L.-A., 2018. Electrochemical degradation of fluoxetine on nanotube array intercalated anode with enhanced electronic transport and hydroxyl radical production. Chem. Eng. J. 346, 662–671.

Wang, A., Zhang, Y., Zhong, H., Chen, Y., Tian, X., Li, D., Li, J., 2018. Efficient mineralization of antibiotic ciprofloxacin in acid aqueous medium by a novel photoelectro-Fenton process using a microwave discharge electrodeless lamp irradiation. J. Hazard Mater. 342, 364–374.

Welcher, F.J., 1975. In: Standard Methods of Chemical Analysis, sixth ed. 2. R.E. Krieger Publishing Co, Huntington, New York, Part B.

Wu, Y., Passananti, M., Brigante, M., Dong, W., Mailhot, G., 2014. Fe(III)–EDDS complex in Fenton and photo-Fenton processes: from the radical formation to the degradation of a target compound. Environ. Sci. Pollut. Res. 21, 12154–12162.

Xu, A., Wei, K., Zhang, Y., Han, W., Li, J., Sun, X., Shen, J., Wang, L., 2017. A facile-operation tubular electro-Fenton system combined with oxygen evolution reaction for flutriafol degradation: modeling and Parameters optimizing. Electrochim. Acta 246, 1200–1209.

Yahya, M.S., Oturan, N., El Kacemi, K., El Karbane, M., Aravindakumar, C.T., Oturan, M.A., 2014. Oxidative degradation study on antimicrobial agent ciprofloxacin by electro-Fenton process: kinetics and oxidation products. Chemosphere 117, 447–454.

Yang, W., Zhou, M., Oturan, N., Li, Y., Oturan, M.A., 2019. Electrocatalytic destruction of pharmaceutical imatinib by electro-Fenton process with graphene-based cathode. Electrochim. Acta 305, 285–294.

Ye, Z., Brillas, E., Centellas, F., Cabot, P.L., Sirés, I., 2019. Electrochemical treatment of butylated hydroxyanisole: electrocoagulation versus advanced oxidation. Separ. Purif. Technol. 208, 19–26.

Ye, Z., Brillas, E., Centellas, F., Cabot, P.L., Sirés, I., 2019. Electro-Fenton process at mild pH using Fe(III)-EDDS as soluble catalyst and carbon felt as cathode. Appl. Catal. B Environ. 257, 117907.

Ye, Z., Sirés, I., Zhang, H., Huang, Y.-H., 2019. Mineralization of pentachlorophenol by ferrioxalate-assisted solar photo-Fenton process at mild pH. Chemosphere 217, 475–482.

Yuan, Z., VanBriesen, J.M., 2006. The formation of intermediates in EDTA and NTA biodegradation. Environ. Eng. Sci. 23, 533–544.

Zhang, M.-H., Dong, H., Zhao, L., Wang, D., Meng, D., 2019. A review on Fenton process for organic wastewater treatment based on optimization perspective. Sci. Total Environ. 670, 110–121.

Zhang, Y., Klamerth, N., Ashagre Messele, S., Chelme-Ayala, P., Gamal El-Din, M., 2016. Kinetics study on the degradation of a model naphthenic acid by ethylenediamine-*N,N'*-disuccinic acid-modified Fenton process. J. Hazard Mater. 318, 371–378.

Zhou, M., Oturan, M.A., Sirés, I. (Eds.), 2018. Electro-Fenton Process: New Trends and Scale-Up. Springer Nature, Singapore.

Expanding the application of photoelectro-Fenton treatment to urban wastewater using the Fe(III)-EDDS complex

Zhihong Ye, Enric Brillas, Francesc Centellas, Pere Lluís Cabot, Ignasi Sirés*

Laboratori d'Electroquímica dels Materials i del Medi Ambient, Departament de Química Física, Facultat de Química, Universitat de Barcelona, Martí i Franquès 1-11, 08028 Barcelona, Spain

* Corresponding author: i.sires@ub.edu (I. Sirés)

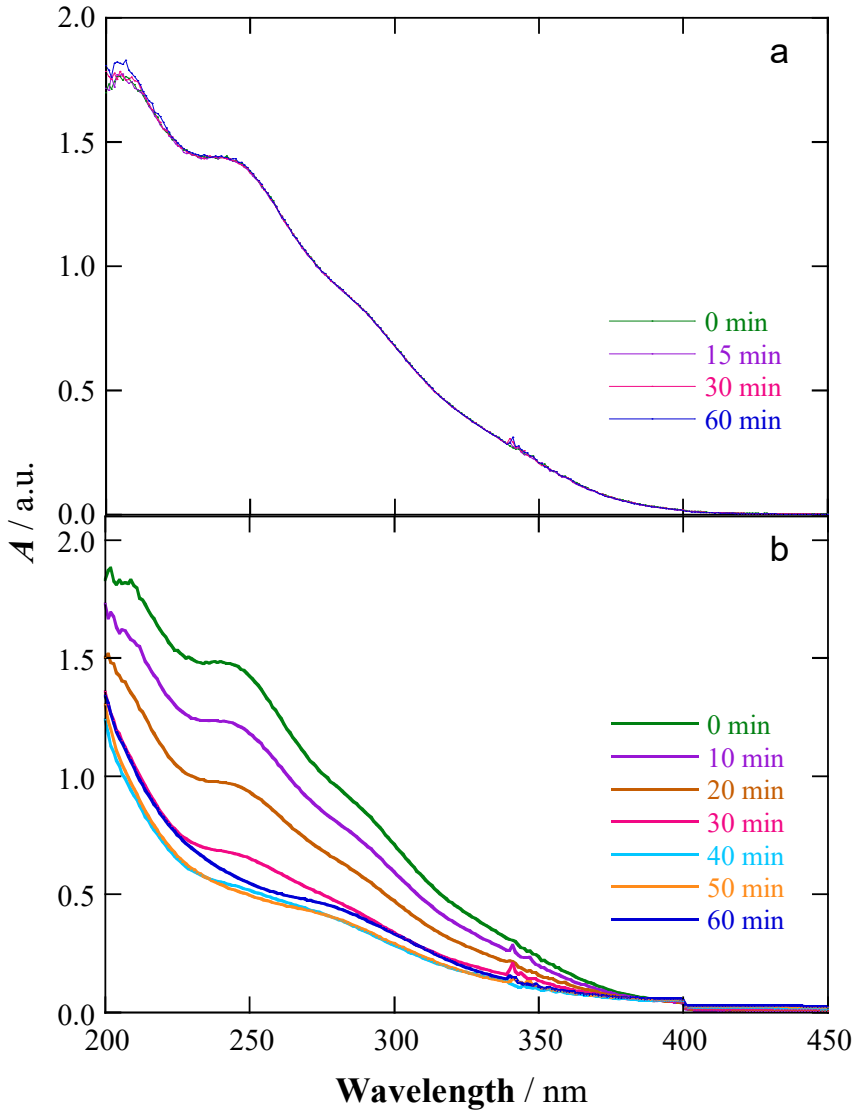

Fig. S1. Change of UV/Vis spectrum of 0.25 mM Fe(III)–EDDS (1:1) complex in a 0.050 M Na_2SO_4 solution at natural pH ~ 5.7 with time: (a) in the dark and (b) under UVA irradiation.

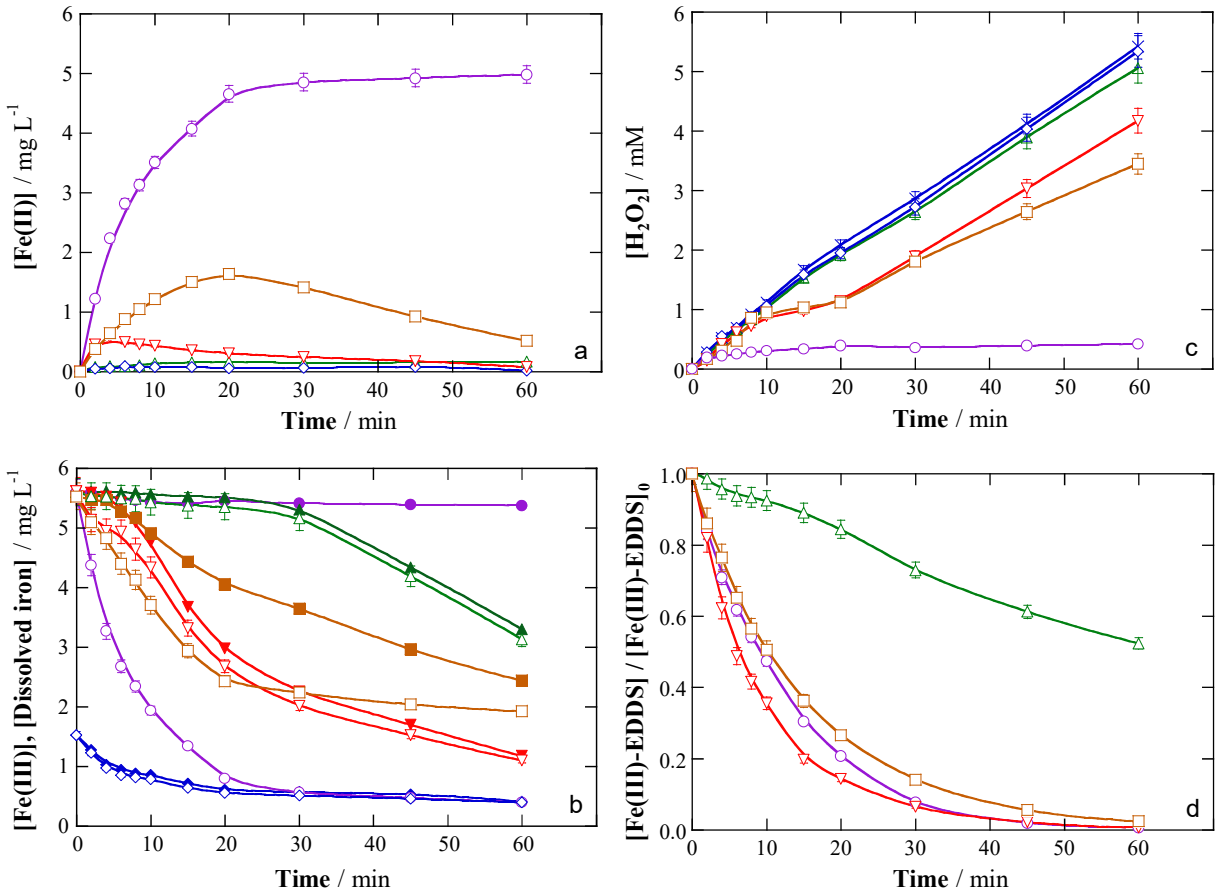

Fig. S2. (a) Dissolved Fe(II) concentration, (b) dissolved Fe(III) (hollow symbols) and total dissolved iron (filled symbols) concentrations, (c) accumulated H_2O_2 concentration and (d) normalized concentration of Fe(III)–EDDS (1:1) complex vs. time for different treatments of 150 mL of 0.049 mM fluoxetine solutions with 0.050 M Na_2SO_4 at natural pH ~ 5.7. In the electrochemical assays, an IrO_2/air-diffusion cell was used at 50 mA and 25 ºC. Process: (○,●) UVA photolysis with 0.10 mM Fe(III)–EDDS (1:1) complex, (×) EO, (△,▲) EF with 0.10 mM Fe(III)–EDDS (1:1) complex, (◇,◆) PEF with 0.10 mM $Fe(ClO_4)_3$, and PEF with 0.10 mM Fe(III)–EDDS (1:1) complex (□,■) with or (▽,▼) without fluoxetine.

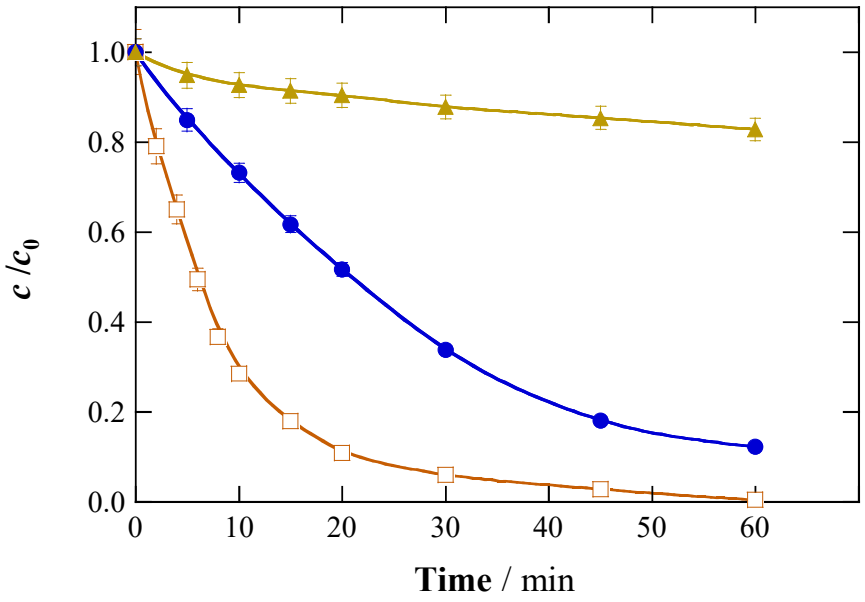

Fig. S3. (□) Normalized fluoxetine concentration with electrolysis time during the PEF treatment of 150 mL of 0.049 mM drug solutions with 0.10 mM Fe(III)–EDDS (1:1) complex and 0.050 M Na_2SO_4 at natural pH ~ 5.7 using an IrO_2/air-diffusion cell at 50 mA and 25 ºC, and same experiment but with addition of: (●) 2 mM *p*-benzoquinone or (▲) 20 mM *tert*-butanol.

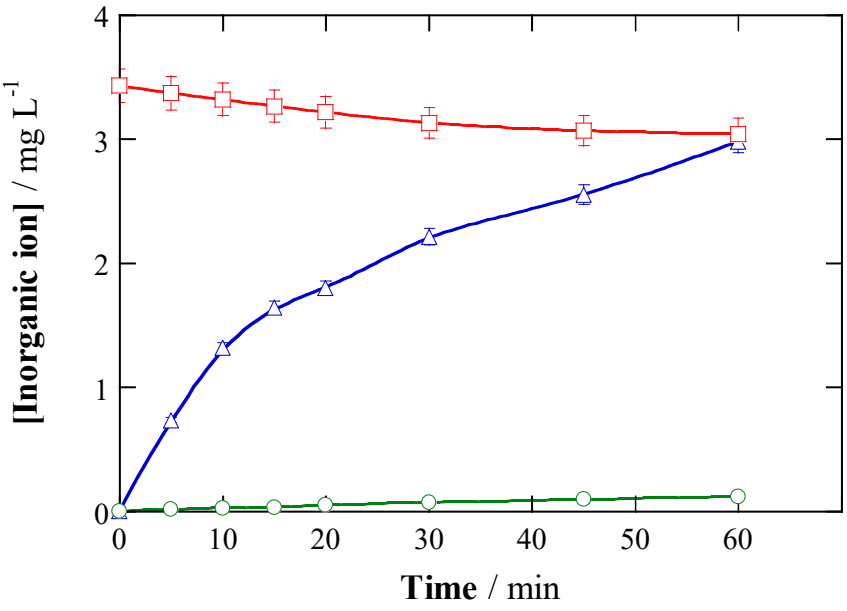

Fig. S4. Time course of the concentration of (□) Cl^-, (△) F^- and (○) NO_3^- detected during the PEF treatment of 150 mL of a 0.098 mM fluoxetine hydrochloride solution with 0.10 mM Fe(III)–EDDS (1:1) complex and 0.050 M Na_2SO_4 at natural pH ~ 5.7 using an IrO_2/air-diffusion cell at 50 mA and 25 ºC.

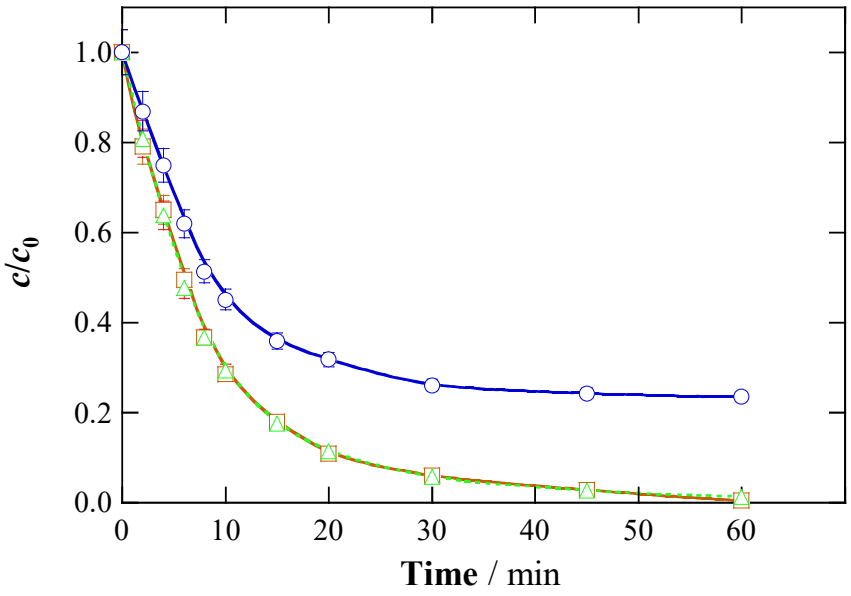

Fig. S5. Change of normalized fluoxetine concentration with electrolysis time during the PEF treatment of 150 mL of 0.049 mM fluoxetine solutions with 0.10 mM Fe(III)–EDDS (1:1) complex and (□) 0.050 M Na_2SO_4, (△) 0.043 M Na_2SO_4 + 0.013 M NaCl or (○) 0.042 M Na_2SO_4 + 0.009 M $NaHCO_3$, at natural pH using an IrO_2/air-diffusion cell at 50 mA and 25 ºC.

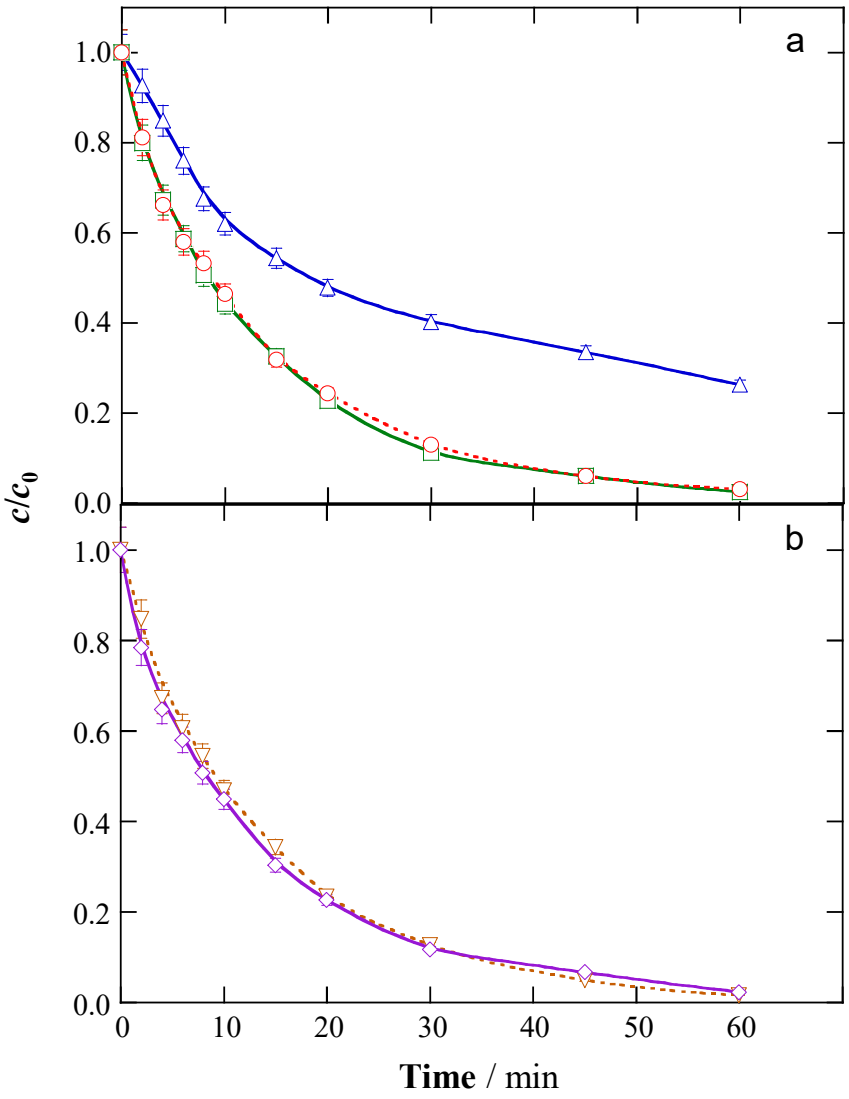

Fig. S6. Variation of normalized fluoxetine concentration with electrolysis time during the PEF treatment of 150 mL of urban wastewater after stripping, containing 0.049 mM fluoxetine with 0.20 mM Fe(III)–EDDS (1:1) complex at natural pH 7.2 using a cell with an air-diffusion cathode at 25 ºC. (a) IrO_2 anode and current: (△) 25 mA, (□) 50 mA and (○) 75 mA. (b) Anode: (▽) RuO_2 and (◇) BDD at 50 mA.

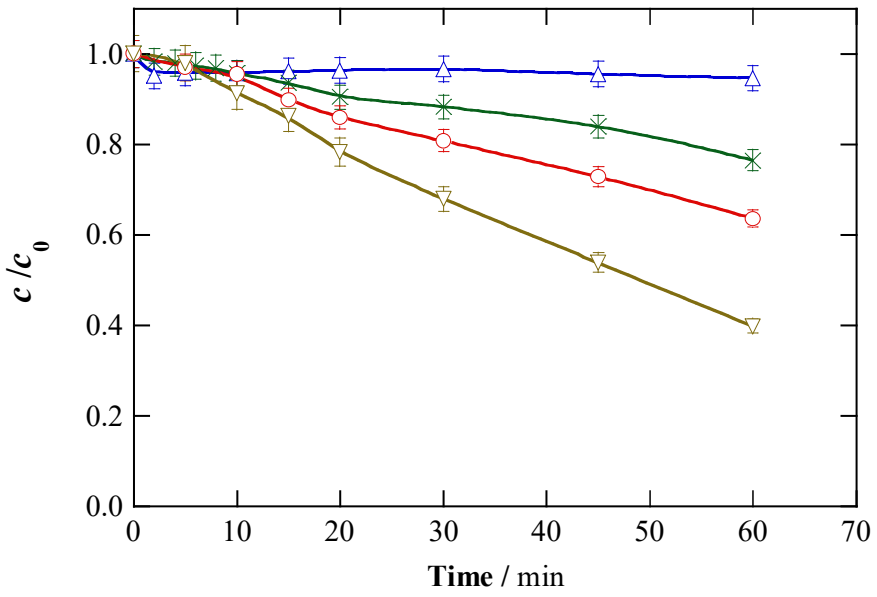

Fig. S7. Time course of normalized fluoxetine concentration during different treatments of 150 mL of 0.049 mM drug solutions with 0.050 M Na_2SO_4 at pH 7.2. In the electrochemical assays, an IrO_2/air-diffusion cell was used, at 50 mA and 25 ºC. (△) Coagulation with the precipitate formed in the presence of 0.10 mM $Fe_2(SO_4)_3$, (×) EO, (○) homogeneous PEF with 0.13 mg L^{-1} Fe^{3+} (which is the dissolved concentration determined in a 0.10 mM $Fe_2(SO_4)_3$ solution with 0.050 M Na_2SO_4 at pH 7.2), and (▽) heterogeneous PEF with the precipitate formed in the presence of 0.10 mM $Fe_2(SO_4)_3$.

Table S1.

Chemical reactions and equilibria involving hydrated Fe^{2+}, Fe^{3+} and/or radicals, and their constants. Analogous reactions are presumed for Fe(II)–EDDS and Fe(III)–EDDS.

Number	Reaction	Constant	Ref.
S1	$Fe^{2+} + H_2O_2 \rightarrow Fe^{3+} + {}^{\bullet}OH + OH^-$	63-76 $M^{-1}\ s^{-1}$	[1,2]
S2	$Fe^{3+} + H_2O_2 \rightarrow Fe^{2+} + O_2^{\bullet-} + 2H^+$		
	$Fe^{3+} + H_2O_2 \leftrightarrows [Fe^{III}(HO_2)]^{2+} + H^+$	$K = 3.1\times10^{-3}$	[1]
	$[Fe^{III}(HO_2)]^{2+} \rightarrow Fe^{2+} + O_2^{\bullet-} + H^+$	$2.7\times10^{-3}\ s^{-1}$	[1]
S3	$Fe^{2+} + {}^{\bullet}OH \rightarrow Fe^{3+} + OH^-$	$3.2\times10^{8}\ M^{-1}\ s^{-1}$	[1]
S4	$H_2O_2 + {}^{\bullet}OH \rightarrow H_2O + HO_2^{\bullet}$	$2.7\times10^{7}\ M^{-1}\ s^{-1}$	[1,2]
S5	$Fe^{2+} + O_2^{\bullet-} + 2H_2O \rightarrow Fe^{3+} + H_2O_2 + 2OH^-$	$1.0\times10^{7}\ M^{-1}\ s^{-1}$	[1,2]
S6	$Fe^{2+} + HO_2^{\bullet} + H_2O \rightarrow Fe^{3+} + H_2O_2 + OH^-$	$1.2\times10^{6}\ M^{-1}\ s^{-1}$	[1,2]
S7	$Fe^{3+} + O_2^{\bullet-} \rightarrow Fe^{2+} + O_2$	$5.0\times10^{7}\ M^{-1}\ s^{-1}$	[1,2]
S8	$Fe^{3+} + HO_2^{\bullet} \rightarrow Fe^{2+} + O_2 + H^+$	$(1.0\text{-}2.0)\times10^{3}\ M^{-1}\ s^{-1}$	[1,2]
S9	$HO_2^{\bullet} \leftrightarrows O_2^{\bullet-} + H^+$	$pK_a = 4.8\text{-}4.9$	[1,2]
S10	$HO_2^{\bullet} + {}^{\bullet}OH \rightarrow H_2O + O_2$	$7.1\times10^{9}\ M^{-1}\ s^{-1}$	[1]
S11	$HO_2^{\bullet} + O_2^{\bullet-} + H^+ \rightarrow H_2O_2 + O_2$	$9.7\times10^{7}\ M^{-1}\ s^{-1}$	[1,2]
S12	$2HO_2^{\bullet} \rightarrow H_2O_2 + O_2$	$8.3\times10^{5}\ M^{-1}\ s^{-1}$	[1,2]
S13	$O_2^{\bullet-} + {}^{\bullet}OH \rightarrow OH^- + O_2$	$1.01\times10^{10}\ M^{-1}\ s^{-1}$	[1]
S14	$2{}^{\bullet}OH \rightarrow H_2O_2$	$6.0\times10^{9}\ M^{-1}\ s^{-1}$	[1]
S15	$Cl^- + {}^{\bullet}OH \rightarrow ClOH^{\bullet-}$	$4.3\times10^{9}\ M^{-1}\ s^{-1}$	[3]
S16	$ClOH^{\bullet-} \rightarrow Cl^- + {}^{\bullet}OH$	$6.0\times10^{9}\ s^{-1}$	[3]
S17	$ClOH^{\bullet-} + H^+ \rightarrow Cl^{\bullet} + H_2O$	$2.1\times10^{10}\ M^{-1}\ s^{-1}$	[4]
S18	$Cl^{\bullet} + H_2O \rightarrow ClOH^{\bullet-} + H^+$	$2.5\times10^{5}\ M^{-1}\ s^{-1}$	[4]
S19	$Cl^{\bullet} + Cl^- \rightarrow Cl_2^{\bullet-}$	$8.5\times10^{9}\ M^{-1}\ s^{-1}$	[3]
S20	$Cl^{\bullet} + Fe^{2+} \rightarrow Fe^{3+} + Cl^-$	$1.3\times10^{10}\ M^{-1}\ s^{-1}$	[5]
S21	$Cl_2^{\bullet-} + Fe^{2+} \rightarrow Fe^{3+} + 2Cl^-$	$10^{7}\ M^{-1}\ s^{-1}$	[5]
S22	${}^{\bullet}OH + CO_3^{2-} \rightarrow CO_3^{\bullet-} + OH^-$	$4.0\times10^{8}\ M^{-1}\ s^{-1}$	[5]
S23	${}^{\bullet}OH + HCO_3^- \rightarrow CO_3^{\bullet-} + H_2O$	$8.5\times10^{6}\ M^{-1}\ s^{-1}$	[5]

[1] Brillas, E., Sirés, I., Oturan, M.A., 2009. Electro-Fenton process and related electrochemical technologies based on Fenton's reaction chemistry, Chem. Rev. 109, 6570-6631.

[2] Wu, Y., Passananti, M., Brigante, M., Dong, W., Mailhot, G., 2014. Fe(III)–EDDS complex in Fenton and photo-Fenton processes: from the radical formation to the degradation of a target compound. Environ. Sci. Pollut. Res. 21, 12154-12162.

[3] De Laat, J., Le, G.T., Legube, B., 2004. A comparative study of the effects of chloride, sulfate and nitrate ions on the rates of decomposition of H_2O_2 and organic compounds by Fe(II)/H_2O_2 and Fe(III)/H_2O_2, Chemosphere 55, 715-723.

[4] Grebel, J.E., Pignatello, J.J., Mitch, W.A., 2010. Effect of halide ions and carbonates on organic contaminant degradation by hydroxyl radical-based advanced oxidation processes in saline waters. Environ. Sci. Technol. 44, 6822-6828.

[5] Bianco, A., Polo-López, M.I., Fernández-Ibánez, P., Brigante, M., Mailhot, G., 2017. Disinfection of water inoculated with *Enterococcus faecalis* using solar/Fe(III)EDDS-H_2O_2 or $S_2O_8^{2-}$ process, Water Res. 118, 246-260.

Table S2.

Main compounds detected in the raw urban wastewater by GC-MS using a non-polar (NP) or polar (P) column.

Code	Chemical name	Molecular structure	Column	t_r (min)	Main fragments (*m/z*)
WW1	(S)-3-(1-Methyl-2-pyrrolidinyl) pyridine or Nicotine	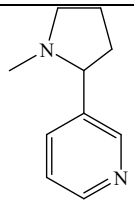	P	24.49	161, 133, 84
WW2	Cyclododecane	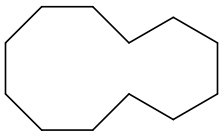	NP	29.48	168, 111, 97, 83
WW3	3,7-Dihydro-1,3,7-trimethyl-1H-purine-2,6-dione or Caffeine	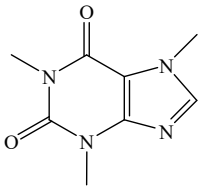	NP P	33.18 46.23	194, 165, 109, 82
WW4	7,9-Di-tert-butyl-1-oxa-spiro[4.5] deca-6,9-diene-2,8-dione	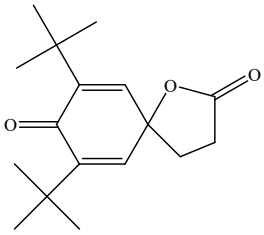	NP	34.31	276, 217, 205, 175
WW5	Octadecanoic acid	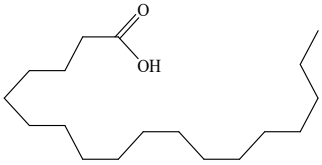	NP P	39.31 45.79	284, 241, 185, 129
WW6	Phthalic acid mono-(2-ethyl-hexyl) ester	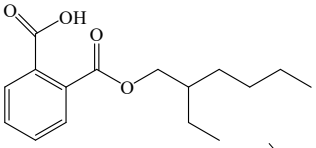	NP	45.3	279, 167, 149
WW7	(3β)-Cholest-5-en-3-ol	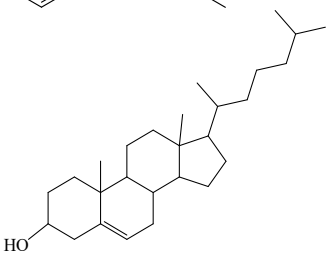	NP P	53.72 85.97	386, 368, 353, 275, 213

Table S3.

Products detected by GC-MS using a non-polar (NP) or polar (P) column after 20 min of PEF treatment of 150 mL of urban wastewater after stripping, containing 0.049 mM fluoxetine with 0.20 mM Fe(III)–EDDS (1:1) complex at natural pH 7.2 using an IrO_2/air-diffusion cell at 50 mA and 25 ºC.

Code	Chemical name	Molecular structure	Column	t_r (min)	Main fragments (*m/z*)
1	Fluoxetine	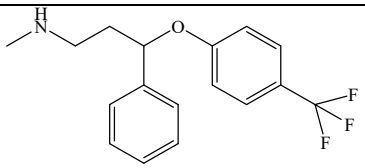	NP P	34.11 39.60	309, 44
2	*N*-[3-Phenyl-3-(4-trifluoromethyl phenoxy)propyl] amine	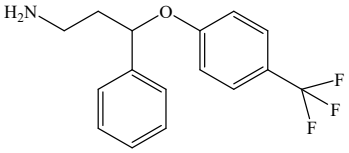	NP	41.28	295, 190, 117, 86
3	4-Trifluoromethyl-phenol	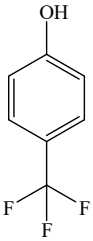	NP P	13.47 32.54	162, 143, 112
6	Styrene	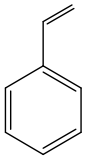	P	11.94	104, 78, 51
7	Benzaldehyde	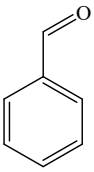	NP P	10.31 18.7	106, 77, 51
8	Benzoic acid	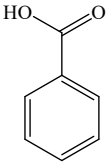	NP	20.52	122, 105, 77, 51

9	1-Methyl-1,2,3,4-tetrahydroquinoline	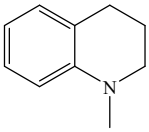	NP	21.16	147, 132, 118, 91
11	3-Phenylacrylic acid	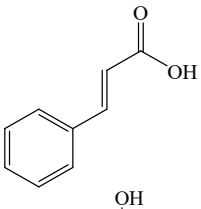	NP	26.26	147, 131, 103, 91
12	2-Chloro-4-trifluoromethylphenol	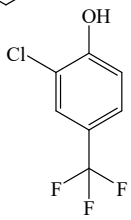	NP P	11.50 27.29	196, 177,132, 63
13	Phenylacetic acid 1,3-dichlorophenyl ester	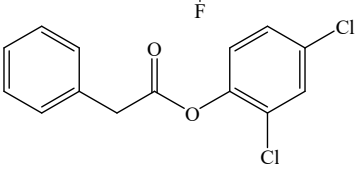	NP	44.90	280, 118, 91
WW5	Octadecanoic acid	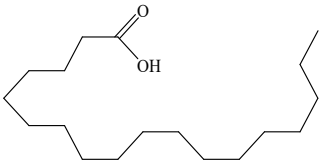	NP P	39.31 45.79	284, 241, 185, 129
WW7	(3β)-Cholest-5-en-3-ol	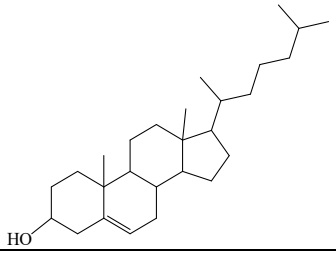	NP P	53.72 85.97	386, 368, 353, 275, 213

4.3. Raw and calcined Fe-based MOFs as efficient heterogeneous catalysts in Fenton-based EAOPs

4.3.1. A highly stable MOF-engineered FeS_2/C nanocatalyst for heterogeneous electro-Fenton treatment: Validation in wastewater at mild pH

The scientific fundamentals of EF are now quite well understood, but the lack of robustness and reliability of the catalysts involved is still a barrier for its viability at industrial scale. Homogeneous EF was proven viable to treat urban wastewater at near-neutral pH upon use of iron complexed with organic chelators. Nonetheless, heterogeneous catalysts seem a smarter choice, since they can simplify the post-treatment clean-up and minimize the dissolved iron content that eventually causes sludge production. Among various iron-based materials, mineral pyrite (FeS_2) has been confirmed as a very good candidate for EF treatment, but it suffers from excessive iron leaching, which limits the catalyst reusability and requires sludge management. This work addressed the synthesis and novel use of MOF-engineered FeS_2/C nanocomposite as EF catalyst for the first time, focusing on the treatment of fluoxetine spiked into urban wastewater at mild pH.

The characterization of the as-synthesized catalyst was first performed. SEM analysis showed a uniform distribution of particles with an average size of several hundreds of nanometers, whereas the largest magnifications revealed that these particles were aggregated framboids composed of small crystallites of about 100 nm. The XRD pattern confirmed the good agreement with the structure of pyrite FeS_2, with the presence of a small amount of Fe_2O_3 that probably appeared via surface oxidation occurring during the synthesis. A pyrite crystal of 28 nm × 35 nm could be clearly distinguished by high-resolution TEM, and the material surrounding the FeS_2 crystal was assigned to a carbon shell, eventually giving rise to a core-shell structure.

The removal of fluoxetine (0.049 mM) from urban wastewater by FeS_2/C catalyzed

heterogeneous EF process was then evaluated. As expected, the EO-H_2O_2 and homogeneous EF with 5 mg L^{-1} Fe^{2+} catalyst achieved only 41% and 47% fluoxetine decay at initial pH 3.0, respectively. The heterogeneous EF catalyzed with 0.5 g L^{-1} natural pyrite at initial pH 6.0 showed the lowest performance, attaining a fluoxetine decay as low as 19%. The FeS_2/C-catalyzed heterogeneous EF process at initial pH 6.0 clearly outperformed all the other treatments, reaching 91% drug removal. This outstanding result can be accounted for by the cooperation between homogeneous and heterogeneous Fenton's reactions as main mechanisms. The former was supported by the detection of 1.40 mg L^{-1} dissolved iron ion and the solution acidification ending at pH 3.0, eventually yielding $^{\bullet}OH$ via Fenton's reaction. An analogous experiment was made by replacing the wastewater by a phosphate buffer solution, which kept the pH constant, to estimate the percentage of contribution of heterogeneous catalysis. Under such conditions, the dissolved iron was almost negligible, and still 46% drug removal was obtained, which indicated the crucial role of heterogeneous reactions.

The presence of CO_3^{2-} and HCO_3^- in urban wastewater significantly negatively affected the fluoxetine abatement, since only 25% removal was achieved without preliminary stripping of the initial wastewater. This was due to the catalyst passivation by calcium and magnesium carbonates that impeded acidification and iron dissolution, as well as the well-known role of CO_3^{2-} and HCO_3^- as radical scavengers.

The effect of pH, catalyst dosage, applied current and anode on the normalized fluoxetine concentration decay upon heterogeneous EF treatment with FeS_2/C was assessed as well. The removal rate was enhanced at more acidic initial pH, in agreement with the gradually lower final pH and slightly higher dissolved iron concentration, which promoted the occurrence of Fenton's reaction. Overall disappearance was reached at pH 4.0, although it can be concluded that the treatment was valid within all the pH range (4.0-8.0). As expected, the use of a larger amount of catalyst progressively from 0.1 to 0.4 g L^{-1} allowed a faster removal, however, further increase to 0.5 g L^{-1} FeS_2/C did not improve the performance, probably because of the parasitic reaction

between $^{\bullet}OH$ and the excess of Fe(II). The positive contribution of greater current was evidenced, which resulted from a gradually greater iron release and H_2O_2 production. Finally, the replacement of the anode by RuO_2 or BDD had an important impact on the degradation rate, attaining the total disappearance at 60 and 50 min, respectively. This was feasible by the greater active chlorine concentration produced in the former case, and the more active $^{\bullet}OH$ in the latter one.

Then, the recyclability of the catalyst was investigated. A small but progressive performance decay was obtained and, after 5 cycles, fluoxetine removal at 60 min was 61% as maximal. However, proper cleaning with organic solvent and water allowed its complete regeneration. The adsorption of NOM and precipitates could probably explain the lower iron dissolution from cycle 1 to 5, further recovering upon surface conditioning.

Longer trials were performed to assess the mineralization ability of the heterogeneous EF treatment, using a BDD anode and a current of 100 mA. An impressive 90% TOC removal was found at 6 h, which outperformed even the conventional EF at pH 3.0, typically yielding TOC removals of 60% as maximal due to the accumulation of very refractory Fe(III) complexes with aliphatic organics. The solution became much less toxic, reaching an EC_{50} of 110 mg L^{-1} that was twice the initial.

FEEM analysis was made to obtain more specific information on the nature and time course of dissolved organic matter. The almost complete disappearance of the fluorescence signals after 120-180 min was observed and five kinds of components were identified upon PARAFAC analysis. The radical scavenging experiments and ESR analysis demonstrated the preponderant role of $^{\bullet}OH$ as main oxidant species. This work concluded with the proposal of a thorough mechanism for the FeS_2/C-catalyzed EF treatment of fluoxetine, as model organic pollutant, at mild pH.

4.3.2. Magnetic MIL(Fe)-type MOF-derived N-doped nano-ZVI@C rods as heterogeneous catalyst for the electro-Fenton degradation of gemfibrozil in a complex aqueous matrix

MOFs have attracted considerable attention in the field of environmental remediation. In particular, the application of iron-based MILs in Fenton process seems very promising. However, the direct use of most Fe-MOFs as catalysis is restricted due to their self-decomposition in water. Therefore, MOF-derived metal@carbon composite materials have been recently developed by pyrolysis of MOFs in inert atmosphere. Under such conditions, the carbonization of the organic polymers is induced and the resulting highly porous carbon is beneficial to minimize the mass transport limitations. Simultaneously, metal precursors are converted into metal nanoparticles.

This work addressed the synthesis of MIL(Fe)-type and NH_2-MIL(Fe)-type MOFs, along with the corresponding calcined magnetic materials. Their thorough characterization informed about their properties and, subsequently, they were employed as catalysts in heterogeneous EF treatment of gemfibrozil spiked into 0.050 M Na_2SO_4 solutions or into urban wastewater.

The XRD patterns of the as-synthesized MIL(Fe)-type and NH_2-MIL(Fe)-type showed a good agreement with the characteristic patterns of MIL-88B and NH_2-MIL-88B. The corresponding products upon calcination at 800 ºC consisted of nanoscale ZVI and iron oxides like Fe_3O_4, encapsulated by porous carbon. The presence of nitrogen enhanced all the peaks related to ZVI, meaning that N-doped carbon behaved as a better reducing agent. The elemental analysis of nano-ZVI@C-N rods obtained from the pyrolysis of NH_2-MIL-88B revealed a content of 51.5% Fe, 34.6% C, 11.8% O and 2.15% N. The morphological characterization by TEM analysis revealed that, after NH_2-MIL-88B was carbonized, its typical hexagonal rod-like shape was still preserved. Some of these structures appeared as truncated carbonaceous rods, although, in general, they showed a uniform size of 3-4 µm in length and 1.0-1.5 µm in width. In addition, iron atoms

from the MOF precursor aggregated into quite spherical nanoparticles embedded in the microporous carbon matrix. The magnetism of the synthesized material was assessed by recording the magnetization curve, which was strong enough for efficient post-treatment magnetic recovery of the catalyst particles using a permanent magnet or an external magnetic field.

Afterwards, comparative degradation of gemfibrozil (10 mg C L^{-1}) by different processes was performed. The direct use of NH_2-MIL(Fe)-88B as catalyst in heterogeneous EF at 50 mA yielded a 57% gemfibrozil concentration decay at 60 min, resulting from the production of $^{\bullet}OH$ via Fenton's reaction. The nano-ZVI@C powder exhibited a much larger adsorption capacity, accounting for a 45% drug removal, whereas the degradation percentage achieved in EF of 52% was close to the value obtained in the absence of current, indicating the poor catalytic performance. However, the drug removal by adsorption on the nano-ZVI@C-N catalyst surface was much lower, attaining only 10%. This was explained by the occurrence of two combined facts at pH 5.5: (i) the catalyst surface was negatively charged because its zeta-potential was 5.4; and (ii) the gemfibrozil molecules were predominantly deprotonated, since the drug pK_a is 4.7. The nano-ZVI@C-N-catalyzed EF process exhibited a clear superiority as compared to all the other treatments, yielding an abatement higher than 95% at 60 min. The results inform about the great catalytic activity of the ZVI and Fe_3O_4 nanoparticles distributed along the N-doped carbon rods, which are able to promote the formation of Fe(II) in solid state as well as Fe^{2+} in solution. This enhancement as compared to the nano-ZVI@C can be related to the presence of N, which was believed to increase the catalytic activity by decreasing the carbon bandgap energy.

Since the nano-ZVI@C-N catalyst was the best material to carry out the heterogeneous EF treatment, the effect of the pyrolysis temperature, pH, applied current and catalyst dosage on its performance was investigated. The drug destruction at 60 min employing the materials prepared by thermal treatment at 650, 700 and 900 ºC was only 58%, 69% and 44%, respectively, much lower than 95% found with the catalyst prepared at 800

ºC. To clarify this different performance, the four as-synthesized catalysts were characterized by XRD. The patterns indicated that the highest peak intensity of ZVI appered in the catalyst obtained at 800 ºC. As the pyrolysis temperature increased from 650 to 800 ºC, the in-situ reduction of iron by graphite carbon was enhanced, resulting in greater content of ZVI. In contrast, further increase to 900 ºC restricted the formation of ZVI because of the collapse of the framework with the condensation of polymers and release of gases, yielding an inadequate amount of reducing agent that ended in the excessive oxidation of the iron-based particles. The influence of pH was also assessed, revealing that the fastest decay was achieved at pH 3.0, reaching total removal at 30 min, due to the greater iron solubilization that could promote the production of $^{\bullet}OH$ from homogeneous Fenton's reaction. The other initial pH values also allowed efficient drug removal after 60 min, attaining decays of 95%, 84% and 69% at pH 5.5, 7.0 and 9.0, respectively. The final leached iron in these three trials was very low (0.1-0.2 mg L^{-1}), suggesting the relatively high stability of nano-ZVI@C-N at mild pH. The applied current did not play a crucial role in heterogeneous EF, because very similar final decay rates could be achieved. Since in all trials there was an excess of H_2O_2 concentration accumulated in the solution, Fenton's reaction could not occur more quickly as their rate was limited by the amount of catalyst and their own kinetics. The catalyst dosage had a more important role, since it is the source of Fe(II)/Fe(III) and their aqueous forms. The results showed gradual enhancement of gemfibrozil removal with the increase of catalyst dosage.

Furthermore, the successful treatment of urban wastewater contaminated by four organic micropollutants at pH 7.0 demonstrated the viability of this new system in practical application.The GC-MS analysis revealed the formation of 13 aromatic products from gemfibrozil oxidation. To conclude with this work, a thorough reaction mechanism for the nano-ZVI@C-N-catalyzed heterogeneous EF treatment was proposed, along with the gemfibrozil degradation routes.

4.3.3. The stability of an Fe-based 2D MOF during the photoelectro-Fenton treatment of organic micropollutants under UVA and visible light irradiation

The previous subsections have demonstrated the feasibility of Fe-MOF-derived nanomaterials as efficient heterogeneous EF catalysts. The above raw MOFs exhibited 3D bulk crystalline structures due to their coordinate forms and size of their coordination structure.The biggest obstacle, restricting their direct application as catalysts, is that they suffer from relatively low conductivity and poor mass transport. Recent studies revealed that 2D MOFs with short pathways for mass transport and compelling electronic properties create an opportunity for heterogeneous catalysis relative to their counterparts with other dimensionalities. In this subsection, for the first time, the novel employment of a 2D MOF, i.e., Fe-bpydc, as heterogeneous PEF catalyst under UV/Vis or visible light illumination was proposed, and its performance was thoroughly evaluated by treating bezafibrate in both, simulated matrix and urban wastewater.

Some characterization technologies were initially applied to investigate the physicochemical properties of the as-synthesized catalyst. The XRD pattern confirmed the well-crystal structure of the as-synthesized Fe-bpydc, in good agreement with the simulated one. The six-coordinate geometry of iron in Fe-bpydc is defined by the two oxygen donors of an η^2-carboxylate of a bpy-dicarb ligand, one oxygen of an η^1-carboxylate of a second bpy-dicarb ligand, two nitrogen donors of a third cheating bpy-dicarb ligand and one oxygen of the terminal H_2O ligand. The carboxylate groups and N atoms of the bpy-dicarb ligands bridge alternately the adjacent iron centers to form layered 2D metal-organic network. The H_2O ligands projected into the interlamellar region can be hydrogen-bonded to the pendant carboxylate groups, providing further extension of the 2D sheets. This explained perfectly the multilayered structures observed in FESEM images, which revealed a 2D irregular shaped plates with size up to dozens microns, along with thickness range from hundreds nanometers to few

micrometers.

Comparative degradation of bezafibrate (0.044 mM) by different processes was then conducted to evaluate the catalytic property of Fe-bpydc. Heterogeneous EF with 0.05 g L^{-1} Fe-bpydc achieved 42% bezafibrate removal in 90 min, which outperformed photocatalysis and EO. Heterogeneous PEF under visible light illumination was superior to EF, obtaining 55% bezafibrate decay. The enhanced performance proved that Fe-bpydc could be a promising visible light photocatalyst, but its catalytic activity was still limited due to the fast electron hole recombination. Further introduction of UV light to construct UV/Vis light assisted PEF system resulted in extraordinarily improved bezafibrate removal efficiency, reaching 92% in 90 min. This outstanding performance was explained on the basis that UV light irradiation offered powerful excitation energy to create more electron/hole pairs and enhanced the redox Fe(III)/Fe(II) cycling.

The effect of initial pH, applied current, catalyst dosage, anode and electrolyte on the normalized bezafibrate concentration decay upon heterogeneous PEF treatment with Fe-bpydc was investigated. Bezafibrate decay was enhanced at more acidic initial pH and decreased with rising initial pH, as a result of the higher $^{\bullet}OH$ oxidation potential and dissolved iron concentration at strong acidic pH. Although low pH led to higher iron leaching, which promoted the homogeneous Fenton's reaction to form $^{\bullet}OH$, it accelerated the decomposition of Fe-bpydc thus decreasing the reusability. As expected, the use of higher current and larger amount of catalyst gave rise to a remarkable increase in the degradation efficiency thanks to the fact that higher current resulted in greater H_2O_2 generation and higher dosage allowed greater accessibility of the active sites with H_2O_2 and organics. Worth noting, the catalyst dosage used in this study was 8-20 times lower than that reported in 3D MOF catalyzed Fenton system. This resulted from the unique 2D sheet structure of Fe-bpydc, which provided more active sites and allowed more efficient mass transport. The degradation profile in 0.041 M Na_2SO_4 + 0.009 M $NaHCO_3$ mixture with IrO_2 anode at natural pH ~ 8 was much slower, achieving only 39% disappearance at 90 min because of the well-known radical scavenging role of

CO_3^{2-} and HCO_3^-. The trial with RuO_2 anode in 0.025 M Na_2SO_4 + 0.035 M NaCl medium yielded the quickest bezafibrate decay due to the generation of active chlorine and $Cl^{\bullet}$.

The stability and reusability of Fe-bpydc was thoroughly evaluated as well. The cyclic usage of Fe-bpydc in bezafibrate degradation led to a gradual decrease in the removal efficiency, achieving 70% as maximal after three cycles. However, the comparison of XRD pattern and FTIR spectra of the fresh and used catalyst showed that the crystalline and chemical structure was extremely stable along the treatment. Thus, the catalyst deactivation was more likely related to the blockage of its active sites by byproducts. Further investigation on the stability of Fe-bpydc in water was performed by determining the iron and organic dissolution at different pH values. The results indicated a considerable decomposition of Fe-bpydc at acidic pH due to the interactions of iron with H^+, having much higher stability at near neutral pH.

In addition, the efficient destruction of four micropollutants in actual wastewater by Fe-bpydc catalyzed PEF proved the great potential of this new heterogeneous system for industrial application. The UV/Vis spectrum and XPS analysis confirmed that the valence and conduction band positions of Fe-bpydc were at 0.96 and -1.14 V, respectively. To end, a thorough mechanism of the boosting catalytic activity of Fe-bpydc in PEF system was proposed. Moreover, the LC-MS and GC-MS analyses identified 17 intermediates from bezafibrate decay and the possible degradation pathway of this drug was consequently elucidated.

GROUP OF ARTICLES INCLUDED IN SECTION 4.3

Page 238: **A highly stable MOF-engineered FeS_2/C nanocatalyst for heterogeneous electro-Fenton treatment: Validation in wastewater at mild pH**

Zhihong Ye, José A. Padilla, Elena Xuriguera, José L. Beltran, Francisco Alcaide, Enric Brillas, Ignasi Sirés.

Environmental Science & Technology (**Submitted**)

Page 293: **Magnetic MIL(Fe)-type MOF-derived N-doped nano-ZVI@C rods as heterogeneous catalyst for the electro-Fenton degradation of gemfibrozil in a complex aqueous matrix**

Zhihong Ye, José A. Padilla, Elena Xuriguera, Enric Brillas, Ignasi Sirés.

Applied Catalysis B: Environmental (**Submitted**)

Page 353: **The stability of an Fe-based 2D MOF during the photoelectro-Fenton treatment of organic micropollutants under UVA and visible light irradiation**

Zhihong Ye, Giulia E.M. Schukraft, Anouk L´Hermitte, Ying Xiong, Enric Brillas, Ignasi Sirés.

Water Research (**Submitted**)

Appendix V

A highly stable MOF-engineered FeS_2/C nanocatalyst for heterogeneous electro-Fenton treatment: Validation in wastewater at mild pH

A highly stable MOF-engineered FeS_2/C nanocatalyst for heterogeneous electro-Fenton treatment: Validation in wastewater at mild pH

Journal:	*Environmental Science & Technology*
Manuscript ID	Draft
Manuscript Type:	Article
Date Submitted by the Author:	n/a
Complete List of Authors:	Ye, Zhihong; University of Barcelona, Chemistry Padilla, José; Universitat de Barcelona, DIOPMA, Departament de Ciència de Materials i Química Física Xuriguera, Elena; Universitat de Barcelona, DIOPMA, Departament de Ciència de Materials i Química Física Beltran, Jose Luis; Universitat de Barcelona, Química Analítica Alcaide, Francisco; Centro de Tecnologias Electroquimicas, Energy Brillas, Enric; Universitat de Barcelona, Quimica Fisica Sirés, Ignasi; Universitat de Barcelona, Laboratori d'Electroquímica dels Materials i del Medi Ambient, Physical Chemistry Department

A highly stable MOF-engineered FeS_2/C nanocatalyst for heterogeneous electro-Fenton treatment: Validation in wastewater at mild pH

Zhihong Ye,[†] José A. Padilla,[‡] Elena Xuriguera,[‡] José L. Beltran,[§] Francisco Alcaide,[‖] Enric Brillas,[†] and Ignasi Sirés*,[†]

[†] Laboratori d'Electroquímica dels Materials i del Medi Ambient, Departament de Química Física, Facultat de Química, Universitat de Barcelona, Martí i Franquès 1-11, 08028 Barcelona, Spain

[‡] DIOPMA, Departament de Ciència de Materials i Química Física, Facultat de Química, Universitat de Barcelona, Martí i Franquès 1-11, 08028 Barcelona, Spain

[§] Secció de Química Analítica, Departament d'Enginyeria Química i Química Analítica. Universitat de Barcelona, Martí i Franquès 1-11, 08028 Barcelona, Spain

[‖] CIDETEC, Paseo Miramón 196, 20014 Donostia-San Sebastián, Spain

Paper submitted to be published in *Environmental Science and Technology*

*Corresponding author: Tel.: +34 934039240; Fax: +34 934021231.

E-mail address: i.sires@ub.edu (I. Sirés)

ABSTRACT

Herein, the novel application of FeS_2/C nanocomposite as a highly active, stable and recyclable catalyst for heterogeneous electro-Fenton (EF) treatment of organic water pollutants is discussed. The simultaneous carbonization and sulfidation of an iron-based metal organic framework (MOF) yielded well-dispersed pyrite FeS_2 nanoparticles of ~100 nm diameter linked to porous carbon. XPS analysis revealed the presence of doping N atoms. EF treatment with an IrO_2/air-diffusion cell ensured the complete removal of the antidepressant fluoxetine spiked into urban wastewater at near-neutral pH after 60 min at 50 mA with 0.4 g L^{-1} catalyst as optimum dose. The clear enhancement of catalytic activity and stability of the material as compared to natural pyrite was evidenced, as deduced from its characterization before and after use. The final solutions contained < 1.5 mg L^{-1} of dissolved iron and became progressively acidified. Fluorescence excitation−emission spectroscopy with PARAFAC analysis demonstrated the large mineralization of all wastewater components at 6 h, which was accompanied by a substantial decrease of toxicity. A mechanism with $^{\bullet}OH$ as dominant oxidant was proposed: the FeS_2 nanoparticles served as Fe^{2+} shuttles for homogeneous Fenton's reaction and provided active sites for heterogeneous Fenton process, whereas nanoporous carbon allowed minimizing the mass transport limitations.

TABLE OF CONTENTS (TOC) ART

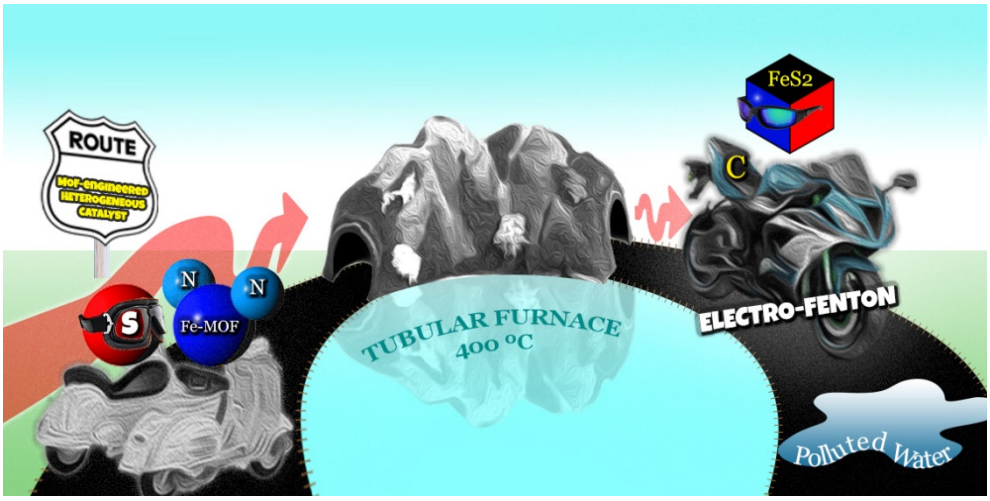

INTRODUCTION

Undoubtedly, Fenton process is currently one of the most attractive technologies to tackle the global water contamination by toxic, recalcitrant, non-biodegradable organic pollutants, owing to its great effectiveness combined with simplicity and low cost.[1] Aiming to overcome some inherent shortcomings,[2] gradual optimization led to the development of electro-Fenton (EF) process, which has become the most successful method among the so-called electrochemical advanced oxidation processes (EAOPs).[3,4] The scientific fundamentals of EF are now quite well understood, but the lack of robustness and reliability of some of the materials involved still hampers its final implementation at industrial scale.[2] On the one hand, much progress has been made on cathode development to enhance the H_2O_2 electrogeneration from the 2-electron O_2 reduction reaction (1).[5] The greatest H_2O_2 accumulation can be achieved using air-diffusion cathodes equipped with a gas chamber,[6-10] although high efficiencies for H_2O_2 production are also feasible with modified three-dimensional carbonaceous cathodes.[11-14] Substantial advances have also been made in the selection of electrocatalytic anodes (M) that promote the simultaneous generation of adsorbed M($^{\bullet}$OH) from water oxidation.[15-17]

$$O_{2(g)} + 2H^+ + 2e^- \rightarrow H_2O_2 \qquad (1)$$

Conversely, crucial concerns arise when the third cornerstone, i.e., the catalyst, is considered. Conventional EF treatment based on homogeneous catalytic decomposition of H_2O_2 in the presence of soluble Fe^{2+}, according to Fenton's reaction (2) at optimum pH ~ 3.0, is still the sole well-established application.[2]

$$Fe^{2+} + H_2O_2 \rightarrow Fe^{3+} + {}^{\bullet}OH + OH^- \qquad (2)$$

Lately, some approaches have been proposed to work at less acidic pH, thus trying to broaden the potential market of EF, which could embrace the treatment of urban

wastewater at near-neutral pH. For example, homogeneous EF is viable at high pH upon use of iron complexed with organic chelators.[18] Nonetheless, heterogeneous catalysts seem a smarter choice, since they can facilitate the post-treatment clean-up and minimize the dissolved iron content that eventually causes sludge production.[19] These catalysts include several types of synthetic iron-loaded structures, such as resins or zeolites,[20,21] as well as zero-valent ion,[2] iron-rich clays[22] and minerals like iron oxides[23-25] or pyrite (FeS_2).[24] In particular, mineral pyrite has been confirmed as a very good candidate for Fenton[26,27] or EF[28-30] treatments, since it is an excellent electron donor whose S_2^{2-} conversion to sulfate via reaction (3) and (4) is accompanied by Fe^{2+} and H^+ release. This allows the co-existence of two degradation routes: (i) conventional Fenton's reaction (2), whose occurrence is favored by the gradual acidification, and (ii) heterogeneous Fenton's reaction (5).[28] Although the pyrite-catalyzed EF has shown better performance than other heterogeneous EF treatments, it suffers from excessive iron leaching,[29] which limits the catalyst reusability and requires sludge management.

$$2FeS_2 + 7O_2 + 2H_2O \rightarrow 2Fe^{2+} + 4SO_4^{2-} + 4H^+ \quad (3)$$

$$2FeS_2 + 14Fe^{3+} + 8H_2O \rightarrow 15Fe^{2+} + 2SO_4^{2-} + 16H^+ \quad (4)$$

$$2FeS_2 + 15H_2O_2 \rightarrow 2Fe^{3+} + 14H_2O + 4SO_4^{2-} + 2H^+ \quad (5)$$

Technological development of heterogeneous EF demands the enhancement of catalyst stability. Within this context, synthetic FeS_2[31] and other iron sulfides[32] have revealed an extended life span and greater catalytic activity. In addition, immobilization in carbon-based substrates like graphene oxide may further improve the performance.[33] Lately, metal organic frameworks (MOFs) are being explored as a source for a new generation of highly porous heterogeneous catalysts for water treatment[34,35] Fe-based MOFs are particularly interesting because of their interconverting Fe(II) and Fe(III) active sites [36-38] These structures have been tested in Fenton, either as raw MOFs[39,40] or

as precursors of hybrids of Fe-based particles and porous carbon.[41,42] In contrast, the works on the application of MOFs in EF are much more scarce. To our knowledge, MOF-based suspended catalysts have never been employed, and only a small number of MOF-modified cathodes has been reported.[43-45]

This article addresses the synthesis and novel use of a MOF-engineered FeS_2/C nanocomposite, fabricated via simultaneous carbonization and sulfidation of an Fe-MOF precursor that was prepared at room temperature. For the first time, the nanomaterial has been introduced as heterogeneous EF catalyst, focusing on the treatment of fluoxetine spiked into urban wastewater at mild pH as case study because the pollution of freshwater[46,47] and seawater[48,49] by pharmaceuticals has become a serious menace for all living beings. Among them, waterborne antidepressants have proven effects on reproduction and development of vertebrates and invertebrates.[50] Fluoxetine is in the top five psychiatric drugs and, consequently, it has been detected in surface water[50] and wastewater treatment plant effluents.[51] EF could be an interesting alternative to remove fluoxetine from urban wastewater, but it has been validated uniquely for model solutions at pH 3.0.[52] The catalyst characterization before and after use, along with the determination of iron dissolution informed about the stability enhancement. Recyclability and mechanistic conclusions are also provided.

MATERIALS AND METHODS

Chemicals. Fluoxetine hydrochloride was acquired from Sigma-Aldrich. Analytical grade Na_2SO_4, H_2SO_4 (95% solution) and NaOH pellets were from Merck. $FeCl_2$•$4H_2O$, 2-methylimidazole and sulfur employed for the synthesis were purchased from Merck and Sigma-Aldrich. Natural pyrite (1.5-4.8 mm grains) was from Alfa Aesar. 1,10-Phenanthroline monohydrate (Alfa Aesar) and $TiOSO_4$ (Sigma-Aldrich) were used for

colorimetric analyses, whereas 5,5-dimethyl-1-pyrroline-N-oxide (DMPO, Sigma-Aldrich) was employed for electron spin resonance (ESR) analysis. Solvents and other reagents were supplied by Panreac and Merck. Unless stated otherwise, the assays were carried out in urban wastewater (Text S1).

Synthesis of the catalyst. The synthetic route followed to obtain the FeS_2/C catalyst, adapted from Pham et al.,[53] is schematized in Figure S1 (Supplementary Information). First, 0.04 mol of 2-methylimidazole was dissolved in 100 mL of ethanol, further adding 0.01 mol of $FeCl_2$•$4H_2O$ to obtain a homogeneous solution that was kept overnight. The slurry obtained upon centrifugation was washed repeatedly and then dried at 80 °C for 12 h. This iron–MOF precursor was carefully mixed with sulfur (with mass ratio 1:2) and transferred to an alumina oxide boat. The mixture was heated up to 400 ºC at 5 ºC min^{-1} in a tube furnace under N_2 stream, being kept at 400 °C for 2 h. The annealed sample was washed and dried in a vacuum oven at 80 ºC for 24 h. The final FeS_2/C black powder was stored hermetically under N_2 atmosphere.

The performance of the synthesized catalyst was compared with that of commercial pyrite, which was milled and washed with ethanol and nitric acid to obtain the dark shiny powder shown in Figure S1.[28]

Physicochemical characterization of fresh and used catalysts. The X-ray diffraction (XRD) analysis was made using a PANalytical X'Pert PRO MPD Alpha-1 powder diffractometer with Cu $K_{\alpha 1}$ radiation (λ = 1.5406 Å). The morphology was observed by field-emission scanning electron microscopy (FE-SEM) using a JEOL JSM7001F microscope operating at 15 kV and equipped with an Oxford Inca 300 analyzer for energy dispersive spectroscopy (EDS). Samples were also analyzed by high-resolution transmission electron microscopy (HRTEM) using a JEOL JEM-2100 LaB6 microscope operating at 200 kV and coupled to the same type of EDS detector for

mapping acquisition. X-ray photoelectron spectroscopy (XPS) was performed in a PHI 5500 Multitechnique System from Physical Electronics (Text S2). Dynamic light scattering (DLS) was carried out with an LS 13 320 laser diffraction particle size analyzer from Beckman Coulter. The dispersion medium was acetone and samples were sonicated before analysis. Electron spin resonance (ESR) spectra were obtained with a Bruker ESP300E spectrometer at room temperature, using DMPO as the $^{\bullet}OH$ spin trap (Text S3).

Electrochemical degradation and analytical procedures. The electrolytic trials were performed in an undivided glass cell containing 150 mL of fluoxetine solution thermostated at 30 ºC under vigorous magnetic stirring. The anode (3 cm^2) was either an IrO_2-based plate from NMT Electrodes or a boron-doped diamond (BDD) thin film supplied by NeoCoat. The cathode (3 cm^2) was a commercial carbon cloth coated with carbon-PTFE from BASF, mounted into a purpose-made gas-diffusion holder and fed with compressed air pumped at 1 L min^{-1} for continuous H_2O_2 electrogeneration. The interelectrode gap was about 1.0 cm. Before first use, a polarization in a 0.05 M Na_2SO_4 solution at 100 mA cm^{-2} for 180 min allowed the simultaneous activation of the anode and cathode. The EF treatments were performed after catalyst addition. Galvanostatic electrolyses were performed with an Amel 2053 potentiostat-galvanostat.

The electrical conductance and pH were measured with a Metrohm 644 conductometer and a Crison GLP 22 pH-meter, respectively. Prior all the analyses of samples with iron catalyst, the solids were removed with PTFE syringe filters from Whatman. The H_2O_2 concentration was determined colorimetrically,[8] using a Shimadzu 1800 UV/Vis spectrophotometer set at λ = 408 nm and 25 °C. The total dissolved iron concentration was determined by adding ascorbic acid to the sample, further measuring the light absorption of the colored complex (λ = 510 nm) formed between Fe^{2+} and 1,10-phenantroline. TOC was determined on a Shimadzu TOC-VCNS analyzer, which was

equipped with a Shimadzu TNM-1 unit for TN analysis. Fluoxetine concentration was determined by reversed-phase high performance liquid chromatography (HPLC), as previously reported,[52] obtaining a narrow peak at retention time of 13.2 min (λ = 227 nm). Duplicate trials were made to correctly assess the mineralization and fluoxetine disappearance, and average values have been plotted along with error bars accounting for 95% confidence level.

Fluorescence excitation−emission matrix (FEEM) spectroscopy was performed using a 1 cm cuvette and an Agilent Cary Eclipse fluorescence spectrophotometer by scanning 351 individual emission wavelengths (250–600 nm) with 5 nm increments of excitation wavelengths between 240 and 460 nm. For each sample, a FEEM was generated with an intensity value in each coordinate point (Text S4). The interpretation of the FEEM spectra was based on the classification suggested by Chen et al.,[54] who established four component families: aromatic proteins (phenols and indoles), fulvic and UV humic compounds, proteins from microorganisms and visible humic compounds and their hydrolysates. Details on the parallel factor analysis (PARAFAC) modeling can be found in our recent publication.[57] To evaluate the toxicity evolution during fluoxetine treatments, acute bioluminescence inhibition was monitored using *Vibrio fischeri* bacteria (Text S5).

RESULTS AND DISCUSSION

Characterization of the MOF-derived catalyst. The morphology of the as-synthesized catalyst was first evaluated by SEM. The micrographies at three lowest magnifications, gathered in Figure S2a, show a uniform distribution of particles with quite homogeneous dimensions. This presumably confirms the validity of the synthesis procedure to obtain a powder containing a large number of regular particles. As depicted

in Figure 1a, they had an average size of several hundreds of nanometers. Their particular morphological features can be clearly observed from the largest magnifications, at 33,000× (Figure 1a) and 100,000× (Figure S2a), which reveal that these particles were actually aggregated framboids composed of smaller crystallites of ca. 100 nm. From the corresponding EDS analysis in Figure S2b, the formation of nanosized Fe–S particles can be plausibly suggested. In addition, the presence of carbon confirms that the sulfidation process allowed the conversion of the organic skeleton of the MOF to carbon. Oxygen appeared in the spectrum as well and, in fact, some dark particles in the SEM contained a higher percentage of this element. Such particles could then be associated to the formation of a small amount of iron oxides. The particle size distribution determined by DLS is plotted in Figure S2c. The diameter of most of the particles was between 50 and 200 nm, yielding a unimodal distribution with a peak centered at 100 nm. This agrees with the abundance of primary small subparticles found in the SEM images, whose aggregation gave rise to larger secondary nanostructures. Based on this finding, the as-synthesized powder will be properly dispersed by means of ultrasounds prior to its use as catalyst in EF treatments described in next subsections. Worth noting, the size of MOF-derived FeS_2 particles synthesized by sulfidation using other protocols was also around 100 nm.[58] It is expected that nanometric size will have a very positive contribution to the catalytic activity.

The XRD pattern depicted in Figure 1b confirms the good agreement with the structure of pyrite FeS_2, as compared to JCPDS 65-1211 and to natural pyrite used in EF.[28] The main peaks could be associated to (200) plane at 33.1º, (210) at 37.1º, (211) at 40.8º, (220) at 47.4º, and (311) at 56.3º. The high crystallinity of the nanocatalyst can be deduced from the sharp diffraction peaks. Therefore, it can be now specified that the nanostructures observed by SEM were pyrite framboids, which were formed as a result

of Fe(III) reduction and combination with S during the pyrolysis. The presence of impurities like FeS and iron sulfate was completely discarded, whereas a small amount of Fe_2O_3 (JCPDS 89-0596) was detected, which agrees with the oxygen signal commented above from EDS data. This compound probably appeared via surface oxidation occurring during the synthesis, despite the nitrogen atmosphere, since the final material was stored hermetically before characterization and use. The oxide formation could proceed directly from FeS_2 or, more likely, via $Fe_2(SO_4)_3$ generation and further decomposition.[58]

Morphological characterization with more detailed data on composition was provided by TEM with EDS analysis. The high crystallinity of particles is corroborated from the high-resolution TEM image shown in Figure 1c. A pyrite crystal of 28 nm × 35 nm can be clearly distinguished, surrounded by a blurred area along the perimeter. In Figure 1d, several of these structures can be distinguished among the two large aggregates. By analyzing the composition of a few of the individual structures, in close contact with each other, the elements were distributed as highlighted in Figure 1e. The material surrounding the FeS_2 crystal nanoparticles can then be assigned to a carbon shell, eventually giving rise to a core-shell structure. In Figure 1f, another site analyzed by TEM is shown, along with the EDS elemental mapping, but the carbon shell was not so easy to identify. Note that the signal for oxygen was strong enough, as a result of residual Fe_2O_3, whereas that from nitrogen was very weak.

The surface composition was further analyzed by XPS. The general spectrum for the as-synthesized FeS_2/C nanocatalyst, depicted in Figure S2d, reveals the energy range of the five elements identified above, and the three most important were evaluated in detail. In the high resolution Fe 2p core level XPS spectrum, shown in Figure 2a, both the Fe $2p_{3/2}$ and Fe $2p_{1/2}$ bands consisted of two peaks. The first peak appeared at 707.2 eV,

which is very close to the expected value for Fe(II)–S, reported at 707.3 eV[56] and 706.8 eV.[27] This confirms the presence of pyrite FeS_2 as the only sulfide on the surface, since there was no peak at 708.9 eV that would correspond to Fe_2S_3.[27] FeS_2 was accompanied by residual Fe_2O_3, displaying a peak at 711.3 eV that matched perfectly with that expected for the Fe(III)–O bond.[56] The two peaks detected in the Fe $2p_{3/2}$ region were confirmed in the Fe $2p_{1/2}$ region. In particular, the Fe(II)–S peak appeared at 720.2 eV, which is closed either to 719.8 eV[55] or 720.0 eV.[56] In the high resolution S 2p of Figure 2b, the peak for S $2p_{3/2}$ appeared at 162.9 eV, in good agreement with that reported for S_2^{2-} at 162.7 eV[27] and 162.2 eV.[55] The presence of this sulfide was confirmed in the S $2p_{1/2}$ region, since the experimental peak at 163.9 eV matched very well with the expected signal at 164.0 eV.[56] No peaks were found within the region from 166 to 168 eV, which allows discarding the presence of stable SO_4^{2-} and SO_3^{2-}. Figure 2c shows the peaks that appeared after deconvolution of the N 1s band, which resulted from the presence of N atoms in the MOF. Upon sulfidation at high temperature, the iron–MOF collapsed with the formation of water vapor, CO_x and *N*-containing gases. However, some N remained as a dopant in the solid carbon, forming C–N bonds. In particular, two types of positions were occupied by N: (i) pyridinic, at 399.3 eV, which is close to that reported at 398.6 eV;[59] and (ii) graphitic, at 400. 7 eV, also close to 401.1 eV previously reported.[59] N-doping of carbon is another interesting feature of the synthesized FeS_2/C nanocatalyst, since it has been reported to enhance the catalytic activity.[13] Finally, the spectrum of carbon presented a sole peak, at 284.6 eV (not shown).[58]

Removal of fluoxetine from urban wastewater by heterogeneous EF process. In Figure 3a, fluoxetine removal during the treatment of solutions containing 0.049 mM drug (10 mg C L^{-1}) spiked into urban wastewater by various electrochemical processes using an IrO_2/air-diffusion cell at 50 mA is compared. As expected, a small removal of 41%

was attained after 60 min via electrochemical oxidation with electrogenerated H_2O_2 (EO-H_2O_2) at initial pH 3.0, since H_2O_2 produced from reaction (1) and $IrO_2(^{\bullet}OH)$ generated on the anode surface have a low oxidation ability.[3,4,6] In fact, the drug disappearance was mainly caused by active chlorine produced via Cl^- oxidation at IrO_2. Homogeneous EF at pH 3.0 is known to be much more effective thanks to the formation of $^{\bullet}OH$ from Fenton's reaction (2), but only a slight degradation enhancement was achieved, ending in 47% removal. This can be explained by the excessively low Fe^{2+} catalyst concentration, i.e., 5 mg L^{-1} (within the range of the amount of dissolved iron during heterogeneous EF, as explained below). It yielded the quickest drug disappearance until 15 min of electrolysis, whereupon the removal rate sharply decreased. The air-diffusion cathode exhibits a poor ability to regenerate Fe^{2+} via electrochemical Fe^{3+} reduction and hence,[2,3] the catalyst content from 15 min was rather low and accumulated in its less active form. In IrO_2/air-diffusion cells, the optimum Fe^{2+} catalyst concentration is in the range 27-55 mg L^{-1}.[8-10] Heterogeneous EF catalyzed with 0.5 g L^{-1} natural pyrite at initial pH 6.0 showed the lowest performance, attaining a fluoxetine concentration decay as low as 19%. Some authors have reported a fast pollutant removal by pyrite-EF,[28-30] but in those trials current was supplied once the spontaneous acidification and iron release had occurred. Conversely, poor performance of commercial pyrite at near-neutral pH was reported upon immediate Fenton treatment of alachlor.[31] On the other hand, the apparently surprising slow degradation as compared to EO-H_2O_2 can be justified by the substantial destruction of active chlorine on the catalyst surface. Figure 3a shows that the FeS_2/C-catalyzed heterogeneous EF process at initial pH 6.0 clearly outperformed all the other treatments, reaching 91% drug removal. This outstanding result can be accounted for by the cooperation between homogeneous and heterogeneous Fenton's reaction as main mechanisms. The former was supported by the detection of 1.40 mg L^{-1} of dissolved

iron ion and the solution acidification ending in pH 3.0, as show in Figure 3b, eventually yielding $^{\bullet}OH$ via reaction (2). Considering the low dissolved iron concentration, the second mechanism is expected to have a crucial role. In addition, the presence of Fe–S bonds maximized the contribution of heterogeneous catalysis,[32] which involved the H_2O_2 decomposition, pre-eminently at Fe(II) sites.[27] Several factors contribute to the superiority of the novel heterogeneous EF process over pyrite-EF. As can be seen in Figure 3b, only 0.28 mg L^{-1} iron were dissolved at 60 min and pH was not so acidic, which limited the participation of reaction (2). Regarding the surface-related Fenton's reaction: (i) the FeS_2/C catalyst was nanosized, thus offering a much larger area; (ii) molecular O_2 activation could be induced by a higher content of surface-bound Fe(II) on FeS_2, promoting the generation of superoxide radical ($O_2^{\bullet-}$);[31] and (iii) the presence of carbon enhanced both, the mass transport due to its porosity, and the catalytic activity, as also found for Fe_3O_4/C catalyst during octane degradation.[60] The reactivity was also favored by doping with N.

It is very remarkable that iron release with the new catalyst was much lower than that reported for pyrite-EF process with pre-dissolution (1.5 vs 8 mg L^{-1}).[28,29] The great stability of FeS_2/C was confirmed in all subsequent trials. Figure S3a informs about the need of preliminary stripping in order to remove CO_3^{2-} and HCO_3^- from the urban wastewater. Otherwise, fluoxetine removal was only 25%, owing to: (i) catalyst passivation by calcium and magnesium carbonates that impeded acidification (Figure S3b) and iron dissolution (Figure S3c) according to reactions (3)-(5), and (ii) the well-known role of CO_3^{2-} and HCO_3^- as radical scavengers.[3] Note that stirring of the catalyst suspension before current supply seems to cause adsorption to some extent. This can be better interpreted from Figure S4, which shows the trend of fluoxetine concentration when the treatment with FeS_2/C of Figure 3 and S3 was made without current supply. The

particles had an adsorption capacity around 30% during the first minutes (Figure S4a), mainly attributed to the carbon porosity, which occurred in concomitance with a poor pH decrease and iron release (Figure 4c and S4b). However, the interactions were weak and fluoxetine became completely desorbed again. This confirms that drug removal during EF treatment was caused by oxidative Fenton-based reactions. Another relevant conclusion is the preponderance of reaction (5) over (3) and (4) as the cause for Fe^{2+} and H^+ release.

Aiming to estimate the percentage of contribution of heterogeneous catalysis to the degradation reached by EF with FeS_2/C (91%, Figure 3a), an analogous experiment was made but replacing the wastewater by a phosphate buffer solution (Figure S5a), which kept the pH constant (Figure S5b). Under such conditions, the dissolved iron was almost negligible (< 0.25 mg L^{-1}, Figure S5c) and hence, the contribution of homogeneous Fenton's reaction to the final 46% drug removal could be presumed as insignificant. Since in EO-H_2O_2 the degradation at 60 min was 20% (Figure S5a), it could be inferred that the FeS_2/C catalyst was able to yield 26% degradation via pure heterogeneous catalysis. Now, going back to Figure 3a, one can conclude that the 91% drug removal was caused by homogeneous Fenton (~24%), heterogeneous Fenton (~26%) and EO-H_2O_2 (~41%).

The effect of pH, catalyst dosage, applied current and anode on the normalized fluoxetine concentration decay upon heterogeneous EF treatment with FeS_2/C is shown in Figure 4. As can be observed in Figure 4a, the removal rate was enhanced at more acidic initial pH, in agreement with the gradually lower final pH and slightly higher dissolved iron concentration (Figure S6), which promoted the occurrence of Fenton's reaction (2). Overall disappearance was reached at pH 4.0, although it can be concluded that the treatment was valid within all the pH range (4.0-8.0). As expected, the use of a larger amount of catalyst progressively from 0.1 to 0.4 g L^{-1} allowed a faster removal

(Figure 4b), which was due both to the greater contribution of heterogeneous catalysis and homogeneous Fenton's reaction thanks to more dissolved iron (see Figure S7). However, further increase to 0.5 g L^{-1} FeS_2/C did not improve the performance, probably because of the parasitic reaction between $^{\bullet}OH$ and the excess of Fe(III) or Fe(II). Figure 4c evidences the positive contribution of current increase, being more significant from 15 to 30 mA, which resulted from a gradually greater iron release (Figure S8a) and H_2O_2 electrogeneration (Figure S8b). The latter species had a prevailing role due to its higher concentration, which affected the availability of $^{\bullet}OH$ because of its parasitic consumption. Finally, the replacement of the anode by RuO_2 or BDD had an important impact on the degradation rate, attaining the total removal at 60 and 50 min, respectively. This was feasible by the greater active chlorine concentration produced in the former case, and the more active $^{\bullet}OH$ in the latter one.[3,4]

In all the trials, the preponderant role of $^{\bullet}OH$ as main oxidant species has been assumed. This was further confirmed by performing the EF treatment as in Figure 3a but in the presence of a radical scavenger, *p*-benzoquinone for $O_2^{\bullet-}$ and *tert*-butanol for $^{\bullet}OH$.[3,4,26] From Figure S9a it is clear that, although some authors highlighted the former radical produced by pyrite,[26] it played a minor role in the FeS_2/C-catalyzed EF. This agrees perfectly with Liu et al.,[31] who reported a 71-fold enhancement of the production rate constant of $^{\bullet}OH$ using non MOF-derived FeS_2 instead of pyrite. The presence of $^{\bullet}OH$ was corroborated via ESR analysis (Figure S9b).

Figure S10a shows the recyclability of the catalyst. A small but progressive performance decay was observed and, after 5 cycles, fluoxetine removal at 60 min was 61% as maximum. However, proper cleaning with organic solvent and water allowed its complete regeneration. As shown in Figure S10b, the adsorption of natural organic matter (NOM) and precipitates could probably explain the lower iron dissolution from cycle 1

to 5, further recovered upon surface conditioning. Note that most of published works report a higher recyclability, around 80-90%, but in model solutions without NOM. The catalyst was characterized after the 5th cycle in order to better elucidate the loss of performance. The SEM images in Figure S11a reveal a certain agglomeration of particles, forming larger framboids but still maintaining the nanometric subparticles. The EDS analysis (Figure S11b) evidences the presence of P, which confirms the precipitation of insoluble phosphates on the catalyst surface. Worth noting, the crystalline pyrite structure was stable along the treatment (Figure S11c), without any new alteration.

Mineralization and proposed mechanism. Longer trials were performed to assess the mineralization ability of the heterogeneous EF treatment, using the optimum FeS_2/C content shown in Figure 4b (i.e., 0.4 g L^{-1}). A BDD anode and a current of 100 mA were employed, looking for a more powerful system. It was a right choice since, as can be seen in Figure S12, an impressive 90% TOC removal was achieved at 6 h. This outperforms even the conventional EF process at pH 3.0, which typically yields TOC removals of 60% as maximal due to the accumulation of very refractory Fe(III) complexes with aliphatic organics.[2] In the present system, a very small amount of such complexes can be accumulated because the dissolved iron concentration was always low. Hence, the previously reported fluoxetine aromatic intermediates could be gradually degraded.[52] As illustrated, the toxicity increased during the first 120 min, as expected from the formation of chlorinated intermediates and oxychlorine anions.[52] Thereafter, the solution became much less toxic, reaching an EC_{50} of 110 mg L^{-1} that was twice the initial (i.e., toxicity was halved).

FEEM analysis was made during the same trial to obtain more specific information on the nature and time course of dissolved organic matter. In Figure 5a, the almost complete disappearance of the fluorescence signals after 120-180 min (samples 4-5) can

be observed. As revealed in Figure S13a, five kinds of components (C1-C5) were identified upon PARAFAC analysis of the spectra of the seven samples. The plots on the left correspond to the FEEM spectra of components, whereas on the right the emission and excitation signals for each one can be seen. Component C1, exhibiting the maxima at 260/296 nm (excitation/emission), was related to fluoxetine,[61] which was practically absent in urban wastewater (sample 1). C2 exhibited at 280/330 nm, was related to soluble microbial by-products. C3 comprised two pairs of peaks, at 280/485 and 400/485 nm, in agreement with those of humic-like substances. C4 was also characterized by two pairs of peaks, at 320/390 and 290/390 nm, associated to fulvic acids. Finally, C5 exhibited peaks at 250/440 and 345/440 nm and it was explained by the presence of humic-like substances.[57] Components C2-C5 accounted for the NOM mentioned in previous subsection. According to Figure 13b, five components was a good choice for PARAFAC model, since the standard deviation did not decrease significantly when a larger number of components was considered. The distribution of components C1-C5 in samples 1-7 of Figure 5a is depicted in Figure 5b, where it is confirmed that at 120 min (sample 4) there was no more fluoxetine and in sample 5 (180 min of electrolysis) all the fluorescent organic compounds had disappeared. Therefore, the residual TOC in Figure S12 corresponded to aliphatic products.

Taking into account the main homogeneous and heterogeneous reactions and species mentioned throughout the manuscript, a thorough mechanism is proposed in Figure 6 for the FeS_2/C-catalyzed EF treatment of fluoxetine, as model organic pollutant, at mild pH.

ASSOCIATED CONTENT

Supporting Information (SI) contains Text S1-S5, and Figures S1-S13. This information is available free of charge on the ACS Publications website.

ACKNOWLEDGMENT

The authors gratefully acknowledge financial support from project CTQ2016-78616-R (AEI/FEDER, EU). The PhD scholarship awarded to Z. Ye (State Scholarship Fund, CSC, China) is also acknowledged.

REFERENCES

(1) Zhang, M.; Dong, H.; Zhao, L.; Wang, D.; Meng, D. A review on Fenton process for organic wastewater treatment based on optimization perspective. *Sci. Total Environ.* **2019**, *670*, 110-121; DOI 10.1016/j.scitotenv.2019.03.180.

(2) Zhou, M.; Oturan, M. A.; Sirés, I. Electro-Fenton Process: New Trends and Scale-Up, *Springer Nature*, Singapore, **2018**.

(3) Sirés, I.; Brillas, E.; Oturan, M. A.; Rodrigo, M. A.; Panizza, M. Electrochemical advanced oxidation processes: today and tomorrow. a review. *Environ. Sci. Pollut. Res.* **2014**, *21*, 8336-8367; DOI 10.1007/s11356-014-2783-1.

(4) Martínez-Huitle, C. A.; Rodrigo, M. A.; Sirés, I.; Scialdone, O. Single and coupled electrochemical processes and reactors for the abatement of organic water pollutants: a critical review. *Chem. Rev.* **2015**, *115* (24), 13362-13407; DOI 10.1007/s11356-014-2783-1.

(5) Zhou, W.; Meng, X.; Gao, J.; Alshawabkeh, A. N. Hydrogen peroxide generation from O_2 electroreduction for environmental remediation: A state-of-the-art review. *Chemosphere* **2019**, *225*, 588-607; DOI 10.1016/j.chemosphere.2019.03.042.

(6) Galia, A.; Lanzalaco, S.; Sabatino, M. A.; Dispenza, C.; Scialdone, O.; Sirés, I. Crosslinking of poly(vinylpyrrolidone) activated by electrogenerated hydroxyl radicals: a first step towards a simple and cheap synthetic route of nanogel vectors. *Electrochem. Commun*. **2016**, *62*, 64-68; DOI 10.1016/j.elecom.2015.12.005.

(7) Roth, H.; Gendel, Y.; Buzatu P.; David, O.; Wessling, M. Tubular carbon nanotube-based gas diffusion electrode removes persistent organic pollutants by a cyclic adsorption – Electro-Fenton process. *J. Hazard. Mater.* **2016**, *307*, 1-6; DOI 10.1016/j.jhazmat.2015.12.066.

(8) Lanzalaco, S.; Sirés, I.; Sabatino, M. A.; Dispenza, C.; Scialdone, O.; Galia, A. Synthesis of polymer nanogels by electro-Fenton process: investigation of the effect of main operation parameters. *Electrochim. Acta*. **2017**, *246*, 812-822; DOI 10.1016/j.electacta.2017.06.097.

(9) Salmerón, I.; Plakas, K. V.; Sirés, I.; Oller, I.; Maldonado, M. I.; Karabelas, A. J.; Malato, S. Optimization of electrocatalytic H_2O_2 production at pilot plant scale for solar-assisted water treatment. *Appl. Catal. B: Environ.* **2019**, *242*, 327-336; DOI 10.1016/j.apcatb.2018.09.045.

(10) Ye, Z.; Guelfi, D. R. V.; Álvarez, G.; Alcaide, F.; Brillas, E.; Sirés, I. Enhanced electrocatalytic production of H_2O_2 at Co-based air-diffusion cathodes for the photoelectro-Fenton treatment of bronopol. *Appl. Catal. B: Environ.* **2019**, *247*, 191-199; DOI 10.1016/j.apcatb.2019.01.029.

(11) Pérez, T.; Coria, G.; Sirés, I.; Nava, J. L.; Uribe, A. R.; Electrosynthesis of hydrogen peroxide in a filter-press flow cell using graphite felt as air-diffusion cathode. *J. Electroanal. Chem.* **2018**, *812*, 54-58; DOI 10.1016/j.jelechem.2018.01.054.

(12) Su, P.; Zhou, M.; Lu, X.; Yang, W.; Ren, G.; Cai, J. Electrochemical catalytic mechanism of N-doped graphene for enhanced H_2O_2 yield and in-situ degradation of organic pollutant. *Appl. Catal. B: Environ.* **2019**, *245*, 583-595; DOI 10.1016/j.apcatb.2018.12.075.

(13) Yang, W.; Zhou, M.; Oturan, N.; Li, Y.; Su, P.; Oturan, M. A.; Enhanced activation of hydrogen peroxide using nitrogen doped graphene for effective removal of

herbicide 2,4-D from water by iron-free electrochemical advanced oxidation. *Electrochim. Acta* **2019**, *297*, 582-592; DOI 10.1016/j.electacta.2018.11.196.

(14) Yang, W.; Zhou, M.; Oturan, N.; Li, Y.; Oturan, M. A. Electrocatalytic destruction of pharmaceutical imatinib by electro-Fenton process with graphene-based cathode. *Electrochim. Acta* **2019**, *305*, 285-294; DOI 10.1016/j.electacta.2019.03.067.

(15) Sirés, I.; Low, C. T. J.; Ponce-de-León, C.; Walsh, F. C. The deposition of nanostructured β-PbO_2 coatings from aqueous methanesulfonic acid for the electrochemical oxidation of organic pollutants. *Electrochem. Commun.* **2010**, *12*, 70-74; DOI 10.1016/j.elecom.2009.10.038.

(16) Oturan, N.; Ganiyu, S. O.; Raffy, S.; Oturan, M. A. Sub-stoichiometric titanium oxide as a new anode material for electro-Fenton process: Application to electrocatalytic destruction of antibiotic amoxicillin. *Appl. Catal. B: Environ.* **2017**, *217*, 214-223; DOI 10.1016/j.apcatb.2017.05.062.

(17) Olvera-Rodríguez, I.; Hernández, R.; Medel, A.; Guzmán, C.; Escobar-Alarcón, L.; Brillas, E.; Sirés, I.; Esquivel, K. TiO_2/Au/TiO_2 multilayer thin-film photoanodes synthesized by pulsed laser deposition for photoelectrochemical degradation of organic pollutants. *Sep. Purif. Technol.* **2019**, *224*, 189-198; DOI 10.1016/j.seppur.2019.05.020.

(18) Ye, Z.; Brillas, E.; Centellas, F.; Cabot, P. L.; Sirés, I. Electro-Fenton process at mild pH using Fe(III)-EDDS as soluble catalyst and carbon felt as cathode. *Appl. Catal. B: Environ.* **2019**, *257*, 117907; DOI 10.1016/j.apcatb.2019.117907.

(19) Ganiyu, S. O.; Zhou, M.; Martínez-Huitle, C. A. Heterogeneous electro-Fenton and photoelectro-Fenton processes: a critical review of fundamental principles and application for water/wastewater treatment. *Appl. Catal. B: Environ.* **2018**, *235*, 103-129; DOI 10.1016/j.apcatb.2018.04.044.

(20) Fernandez, D.; Robles, I.; Rodriguez-Valadez, F. J.; Godinez, L. A. Novel arrangement for an electro-Fenton reactor that does not require addition of iron, acid and a final neutralization stage. Towards the development of a cost-effective technology for the treatment of wastewater. *Chemosphere* **2018**, *199*, 251-255; DOI 10.1016/j.chemosphere.2018.02.036.

(21) Rostamizadeh, M.; Jafarizad, A.; Gharibian, S. High efficient decolorization of Reactive Red 120 azo dye over reusable Fe-ZSM-5 nanocatalyst in electro-Fenton reaction. *Sep. Purif. Technol.* **2018**, *192*, 340-347; DOI 10.1016/j.seppur.2017.10.041.

(22) Özcan, A.; Özcan, A. A.; Demirci, Y.; Şener, E. Preparation of Fe_2O_3 modified kaolin and application in heterogeneous electro-catalytic oxidation of enoxacin. *Appl. Catal. B: Environ.* **2017**, *200*, 361-371; DOI 10.1016/j.apcatb.2016.07.018.

(23) Expósito, E.; Sánchez-Sánchez, C. M.; Montiel, V. Mineral Iron oxides as iron source in electro-Fenton and photoelectro-Fenton mineralization processes. *J. Electrochem. Soc.* **2007**, *154*, E116−E122; DOI 10.1149/1.2744134.

(24) Ltaïef, A. H.; Sabatino, S.; Proietto, F.; Ammar, S.; Gadri, A.; Galia, A.; Scialdone, O. Electrochemical treatment of aqueous solutions of organic pollutants by electro-Fenton with natural heterogeneous catalysts under pressure using Ti/IrO_2-Ta_2O_5 or BDD anodes. *Chemosphere* **2018**, *202*, 111-118; DOI 10.1016/j.chemosphere.2018.03.061.

(25) Meijide, J.; Pazos, M.; Sanromán, M. A. Heterogeneous electro-Fenton catalyst for 1-butylpyridinium chloride degradation. *Environ. Sci. Pollut. Res.* **2019**, *26*, 3145-3156; DOI 10.1007/s11356-017-0403-6.

(26) Zhang, Y.; Tran, H. P.; Hussain, I.; Zhong, Y.; Huang. S. Degradation of *p*-chloroaniline by pyrite in aqueous solutions. *Chem. Eng. J.* **2015**, *279*, 396-401; DOI 10.1016/j.cej.2015.03.016.

(27) Zhang, P.; Huang, W.; Ji, Z.; Zhou, C.; Yuan, S. Mechanisms of hydroxyl radicals production from pyrite oxidation by hydrogen peroxide: surface versus aqueous reactions. *Geochim. Cosmochim. Acta* **2018**, *238*, 394-410; DOI 10.1016/j.gca.2018.07.018.

(28) Labiadh, L.; Oturan, M. A.; Panizza, M.; Hamadi, N. B.; Ammar, S. Complete removal of AHPS synthetic dye from water using new electro-fenton oxidation catalyzed by natural pyrite as heterogeneous catalyst. *J. Hazard. Mater.* **2015**, *297*, 34-41; DOI 10.1016/j.jhazmat.2015.04.062.

(29) Barhoumi, N.; Labiadh, L.; Oturan, M. A.; Oturan, N.; Gadri, A.; Ammar, S.; Brillas, E. Electrochemical mineralization of the antibiotic levofloxacin by electro-Fenton-pyrite process. *Chemosphere* **2015**, *141*, 250-257; DOI 10.1016/j.chemosphere.2015.08.003.

(30) Barhoumi, N.; Oturan, N.; Olvera-Vargas, H.; Brillas, E.; Gadri, A.; Ammar, S.; Oturan, M. A. Pyrite as a sustainable catalyst in electro-Fenton process for improving oxidation of sulfamethazine. Kinetics, mechanism and toxicity assessment. *Water Res.* **2016**, *94*, 52-61; DOI 10.1016/j.watres.2016.02.042.

(31) Liu, W.; Wang, Y.; Ai, Z.; Zhang, L. Hydrothermal synthesis of FeS_2 as a high-efficiency Fenton reagent to degrade alachlor via superoxide-mediated Fe(II)/Fe(III) cycle. *ACS Appl. Mater. Interf.* **2015**, *7*, 28534-28544; DOI 10.1021/acsami.5b09919.

(32) Choe, Y. J.; Byun, J. Y.; Kim, S. H.; Kim, J. Fe_3S_4/Fe_7S_8-promoted degradation of phenol via heterogeneous, catalytic H_2O_2 scission mediated by S-modified surface Fe^{2+} species. *Appl. Catal. B: Environ.* **2018**, *233*, 272-280; DOI 10.1016/j.apcatb.2018.03.110.

(33) Liu, W.; Xu, L.; Li, X.; Shen, C.; Rashid, S.; Wen, Y.; Liu, W.; Wu, X. High-dispersive FeS_2 on graphene oxide for effective degradation of 4-chlorophenol. *RSC Adv.* **2015**, *5*, 2449-2456; DOI 10.1039/c4ra11354c.

(34) Dias, E. M.; Petit, C. Towards the use of metal–organic frameworks for water reuse: a review of the recent advances in the field of organic pollutants removal and degradation and the next steps in the field. *J. Mater. Chem. A* **2015**, *3*, 22484-22506; DOI 10.1039/c5ta05440k.

(35) Li, X.; Wang, B.; Cao, Y.; Zhao, S.; Wang, H.; Feng, X.; Zhou, J.; Ma, X. Water contaminant elimination based on metal–organic frameworks and perspective on their industrial applications. *ACS Sustain. Chem. Eng.* **2019**, *7*, 4548-4563; DOI 10.1021/acssuschemeng.8b05751.

(36) Liu, X.; Zhou, Y.; Zhang, J.; Tang, L.; Luo, L.; Zeng, G. Iron containing metal-organic frameworks: structure, synthesis, and applications in environmental remediation. *ACS Appl. Mater. Interf.* **2017**, *9*, 20255-20275; DOI 10.1021/acsami.7b02563.

(37) Cheng, M.; Lai, C.; Liu, Y.; Zeng, G.; Huang, D.; Zhang, C.; Qin, L.; Hu, L.; Zhou, C.; Xiong, W. Metal-organic frameworks for highly efficient heterogeneous Fenton-like catalysis. *Coord. Chem. Rev.* **2018**, *368*, 80-92; DOI 10.1016/j.ccr.2018.04.012.

(38) Sharma, V. K.; Feng, M. Water depollution using metal-organic frameworks-catalyzed advanced oxidation processes: a review. *J. Hazard. Mater.* **2019**, *372*, 3-16; DOI 10.1016/j.jhazmat.2017.09.043.

(39) Gao, C.; Chen, S.; Quan, X.; Yu, H.; Zhang, Y. Enhanced Fenton-like catalysis by iron-based metal organic frameworks for degradation of organic pollutants. *J. Catal.* **2017**, *356*, 125-132; DOI 10.1016/j.jcat.2017.09.015.

(40) Tang, J; Wang, J. Metal organic framework with coordinatively unsaturated sites as efficient Fenton-like catalyst for enhanced degradation of sulfamethazine. *Environ. Sci. Technol.* **2018**, *52*, 5367-5377; DOI 10.1021/acs.est.8b00092.

(41) Chen, D.; Chen, S.; Jiang, Y.; Xie, S.; Quan, H.; Hua, L.; Luo, X.; Guo, L. Heterogeneous Fenton-like catalysis of Fe-MOF derived magnetic carbon nanocomposites for degradation of 4-nitrophenol. *RSC Adv.* **2017**, *7*, 49024-49030; DOI 10.1039/c7ra09234b.

(42) Tang, J; Wang, J. Fenton-like degradation of sulfamethoxazole using Fe-based magnetic nanoparticles embedded into mesoporous carbon hybrid as an efficient catalyst. *Chem. Eng. J.* **2018**, *351*, 1085-1094; DOI 10.1016/j.cej.2018.06.169.

(43) Zhao, H., Chen, Y.; Peng, Q.; Wang, Q.; Zhao, G. Catalytic activity of MOF(2Fe/Co)/carbon aerogel for improving H_2O_2 and $^{\bullet}OH$ generation in solar photo–electro–Fenton process. *Appl. Catal. B: Environ.* **2017**, *203*, 127-137; DOI 10.1016/j.apcatb.2016.09.074.

(44) Le, T. X. H.; Cowan, M. G.; Drobek, M.; Bechelany M.; Julbe, A.; Cretin, M. Fe-Nanoporous carbon derived from MIL-53(Fe): a heterogeneous catalyst for mineralization of organic pollutants. *Nanomaterials* **2019**, *9*, 641; DOI 10.3390/nano9040641.

(45) Liu, K.; Yu, M.; Wang, H.; Wang, J.; Liu, W.; Hoffmann, M. R. Multiphase porous electrochemical catalysts derived from Iron-based metal−organic framework compounds. *Environ. Sci. Technol.* **2019**, *53*, 6474-6482; DOI 10.1021/acs.est.9b01143.

(46) Jennifer Ebele, A.; Abou-Elwafa Abdallah, M. Harrad, S. Pharmaceuticals and personal care products (PPCPs) in the freshwater aquatic environment. *Emerging Contam.* **2017**, *3*, 1-16; DOI 10.1016/j.emcon.2016.12.004.

(47) Bagnis, S.; Fitzsimons, M. F.; Snape, J.; Tappin, A.; Comber, S. Processes of distribution of pharmaceuticals in surface freshwaters: implications for risk assessment. *Environ. Chem. Lett.* **2018**, *16*, 1193-1216; DOI 10.1007/s10311-018-0742-7.

(48) Debiolles, F.; Malleret, L.; Tiliacos, C.; Wong-Wah-Chung, P.; Laffont-Schwob, I. Occurrence and ecotoxicological assessment of pharmaceuticals: is there a risk for the Mediterranean aquatic environment? *Sci. Total Environ.* **2018**, *639*, 1334-1348; DOI 10.1016/j.scitotenv.2018.04.351.

(49) Mezzelani, M.; Gorbi, S.; Regoli, F. Pharmaceuticals in the aquatic environments: Evidence of emerged threat and future challenges for marine organisms. *Marine Environ. Res.* **2018**, *140*, 41-60; DOI 10.1016/j.marenvres.2018.05.001.

(50) Sehonova, P.; Svobodova, Z.; Dolezelova, P.; Vosmerova, P.; Faggio, C. Effects of waterborne antidepressants on non-target animals living in the aquatic environment: a review. *Sci. Total Environ.* **2018**, *631-632*, 789-794; DOI 10.1016/j.scitotenv.2018.03.076.

(51) Vieno, N.; Hallgren, P.; Wallberg, P.; Phyhala, M.; Zandaryaa, S. Pharmaceuticals in the aquatic environment of the Baltic Sea region: a status report. *UNESCO Publishing* **2017**, 1-119.

(52) Salazar, C.; Ridruejo, C.; Brillas, E.; Yáñez, J.; Mansilla, H. D.; Sirés, I. Abatement of the fluorinated antidepressant fluoxetine (Prozac) and its reaction by-products by electrochemical advanced methods. *Appl. Catal. B: Environ.* **2017**, *203*, 189-198; DOI 10.1016/j.apcatb.2016.10.026.

(53) Pham, D. T.; Baboo, J. P.; Song, J.; Kim, S.; Jo, J.; Mathew, V.; Alfaruqi, M. H.; Sambandam, B.; Kim, J. Facile synthesis of pyrite (FeS_2/C) nanoparticles as an electrode material for non-aqueous hybrid electrochemical capacitors. *Nanoscale* **2018**, *10*, 5938-5949; DOI 10.1039/C7NR06352K.

(54) Chen, W.; Westerhoff, P.; Leenheer, J. A.; Booksh, K. Fluorescence excitation−emission matrix regional integration to quantify spectra for dissolved organic matter. *Environ. Sci. Technol.* **2003**, *37*, 5701-5710; DOI 10.1021/es034354c.

(55) Chen, J.; Zhou, X.; Mei, C.; Xu, J.; Zhou, S.; Wong, C. P. Pyrite FeS_2 nanobelts as high-performance anode material for aqueous pseudocapacitor. *Electrochim. Acta* **2016**, *222*, 172-176; DOI 10.1016/j.electacta.2016.10.181.

(56) Lu, Z.; Wang, N.; Zhang, Y.; Xue, P.; Guo, M.; Tang, B.; Bai, Z.; Dou, S. Pyrite FeS_2@C nanorods as smart cathode for sodium ion battery with ultra-long lifespan and notable rate performance from tunable pseudocapacitance. *Electrochim. Acta* **2018**, *260*, 755-761; DOI 10.1016/j.electacta.2017.12.031.

(57) Vera, M.; Martín-Alonso, J.; Mesa, J.; Granados, M.; Beltran, J L.; Casas, S.; Gibert, O.; Cortina, J. L. Monitoring UF membrane performance treating surface-groundwater blends: Limitations of FEEM-PARAFAC on the assessment of the organic matter role. *Chem. Eng. J.* **2017**, *317*, 961-971; DOI 10.1016/j.cej.2017.02.081.

(58) Lu, Z.; Wang, N.; Zhang, Y.; Xue, P.; Guo, M.; Tang, B.; Xu, X.; Wang, W.; Bai, Z.; Dou, S. Metal−organic framework-derived sea-cucumber-like FeS_2@C nanorods with outstanding pseudocapacitive Na-ion storage properties. *ACS Appl. Energy Mater.* **2018**, *1*, 6234-6241; DOI 10.1021/acsaem.8b01239.

(59) Liang, P.; Zhang, C.; Duan, X.; Sun, H.; Liu, S.; Tade, M. O.; Wang, S. An insight into metal organic framework derived N-doped graphene for the oxidative degradation of persistent contaminants: formation mechanism and generation of singlet oxygen from peroxymonosulfate. *Environ. Sci. Nano* **2017**, *4*, 315-324; DOI 10.1039/c6en00633g.

(60) Zhuang, Y.; Yuan, S.; Liu, J.; Zhang, Y.; Du, H.; Wu, C.; Zhao, P.; Chen, H.; Pei, Y. Synergistic effect and mechanism of mass transfer and catalytic oxidation of

octane degradation in yolk-shell Fe_3O_4@C/Fenton system. *Chem. Eng. J.* **2020**, *379*, 122262; DOI 10.1016/j.cej.2019.122262.

(61) Unceta, N.; Barrondo, S.; Ruiz de Azúa, I.; Gómez-Caballero, A.; Goicolea, M. A.; Sallés, J.; Barrio, R. J. Determination of fluoxetine, norfluoxetine and their enantiomers in rat plasma and brain samples by liquid chromatography with fluorescence detection. *J. Chromatogr. B* **2007**, *852*, 519-528; DOI 10.1016/j.jchromb.2007.02.008.

Figure captions

Figure 1. (a) SEM image at 33,000×, (b) XRD pattern, (c,d,e) TEM analysis and (f) site of interest along with EDS elemental mapping for the as-synthesized catalyst. In (b), the symbols account for the peaks related to (▼) FeS_2 pyrite (JCPDS 65-1211), and (◆) Fe_2O_3 (JCPDS 89-0597) references.

Figure 2. XPS spectrum of different elements present in the FeS_2 nanocatalyst: (a) Fe 2p, (b) S 2p, and (c) N 1s.

Figure 3. (a) Normalized fluoxetine concentration decay during the treatment of solutions containing 0.049 mM drug (10 mg C L^{-1}) spiked into 150 mL of urban wastewater by (×) EO-H_2O_2 at initial pH 3.0, (□) conventional EF with 5 mg L^{-1} Fe^{2+} at initial pH 3.0, and heterogeneous EF (▲) with 0.5 g L^{-1} natural pyrite at initial pH 6.0, and (◆) with 0.5 g L^{-1} FeS_2/C nanocatalyst at initial pH 6.0. All trials were carried out with an IrO_2/air-diffusion cell at 50 mA and 30 °C. (b) Final pH (filled bar) and iron concentration (dashed bar) after 60 min of the heterogeneous EF trials.

Figure 4. Time course of normalized fluoxetine concentration during the heterogeneous EF treatment of 150 mL of 0.049 mM drug (10 mg C L^{-1}) solutions, prepared with urban wastewater, using an IrO_2/air-diffusion cell (except in plot d) with the FeS_2/C nanocatalyst at 30 ºC. (a) Effect of pH, with 0.5 g L^{-1} nanocatalyst at 50 mA. Initial pH: (●) 8.0, (■) 7.0, (◆) 6.0, (▲) 5.0, and (▼) 4.0. (b) Effect of nanocatalyst dose, at pH 6.0 and 50 mA. Content: (○) 0.1, (□) 0.2, (△) 0.3, (▽) 0.4, and (◆) 0.5 g L^{-1} FeS_2/C. (c) Effect of applied current, at pH 6.0 with 0.5 g L^{-1} nanocatalyst. Current: (◣) 15, (◢) 30, and (◆) 50 mA. (d) Effect of anode, at pH 6.0 with 0.5 g L^{-1} nanocatalyst at 50 mA. Anode: (◆) IrO_2-based, (▷) RuO_2based, and (◁) BDD.

Figure 5. (a) FEEM spectra of: (1) urban wastewater at natural pH 6.0 after stripping, (2) same matrix with fluoxetine spiked at 0.098 mM, and samples withdrawn after (3) 1 h, (4) 2 h, (5) 3 h, (6) 4 h, and (7) 5 h of heterogeneous EF treatment of 150 mL of 0.098 mM drug solutions in urban wastewater with 0.4 g L^{-1} FeS_2/C nanocatalyst at pH 6.0 using a BDD/air-diffusion cell at 100 mA and 30 ºC. (b) Distribution of PARAFAC-derived components C1-C5 in samples 1-7 of plot (a).

Figure 6. Proposed mechanism for FeS_2/C-catalyzed heterogeneous EF treatment at mild pH.

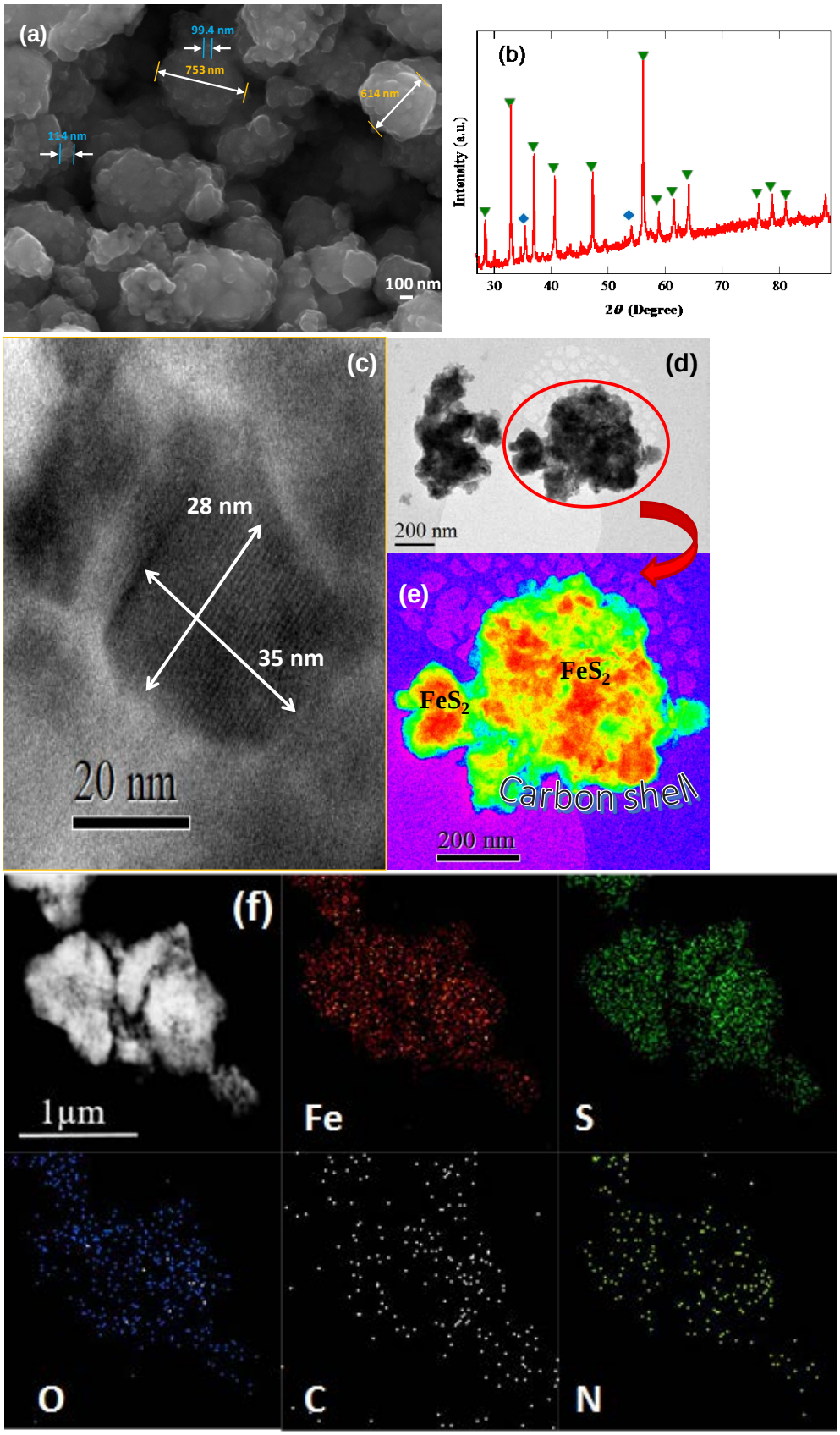
(a)
99.4 nm
753 nm
614 nm
114 nm
100 nm
(b)
Intensity (a.u.)
30
40
50
60
70
80
2θ (Degree)
(c)
28 nm
35 nm
20 nm
(d)
200 nm
(e)
FeS2
FeS2
Carbon shell
200 nm
(f)
1μm
Fe
S
O
C
N

Figure 1

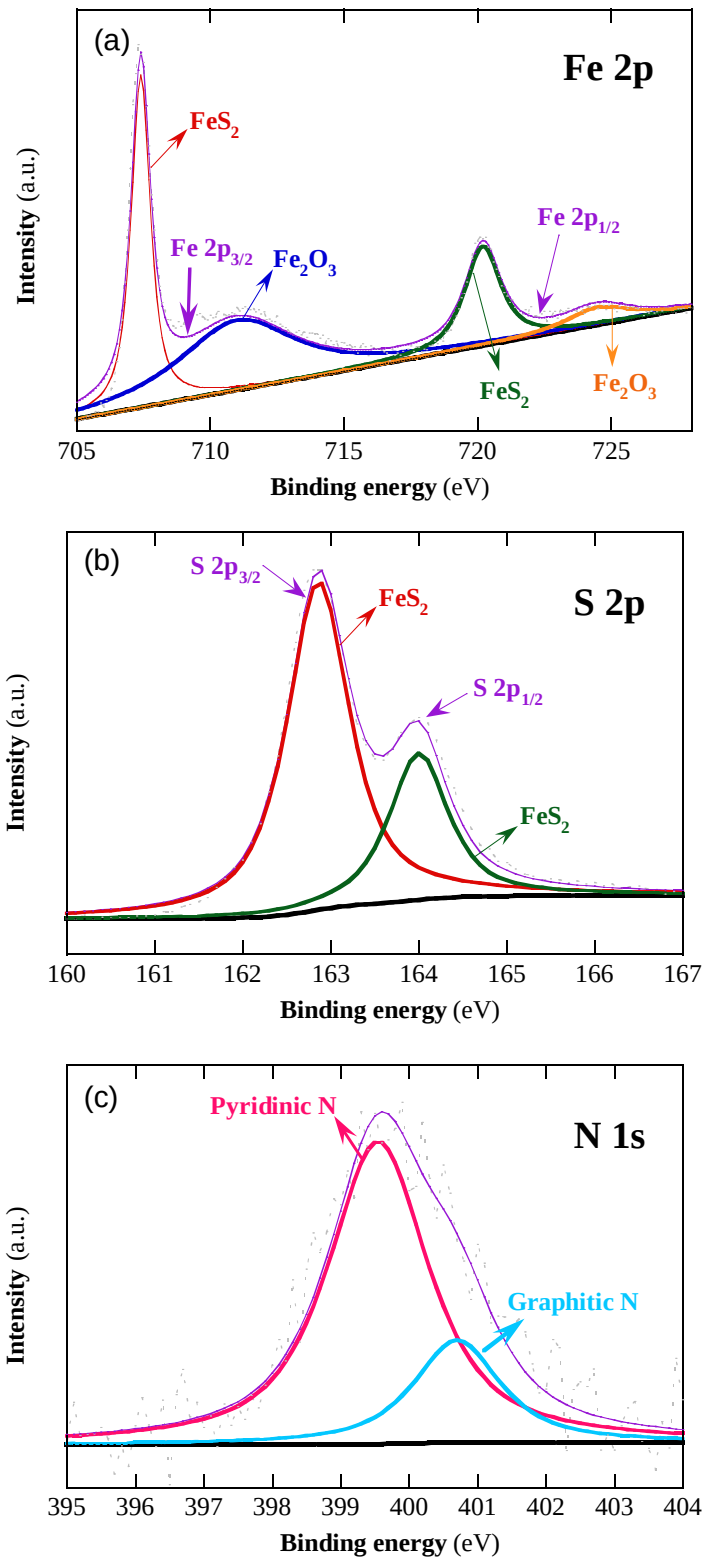
(a)
Fe 2p
FeS2
Fe 2p3/2
Fe2O3
Fe 2p1/2
FeS2
Fe2O3
Intensity (a.u.)
705
710
715
720
725
Binding energy (eV)
(b)
S 2p
S 2p3/2
FeS2
S 2p1/2
FeS2
Intensity (a.u.)
160
161
162
163
164
165
166
167
Binding energy (eV)
(c)
N 1s
Pyridinic N
Graphitic N
Intensity (a.u.)
395
396
397
398
399
400
401
402
403
404
Binding energy (eV)

Figure 2

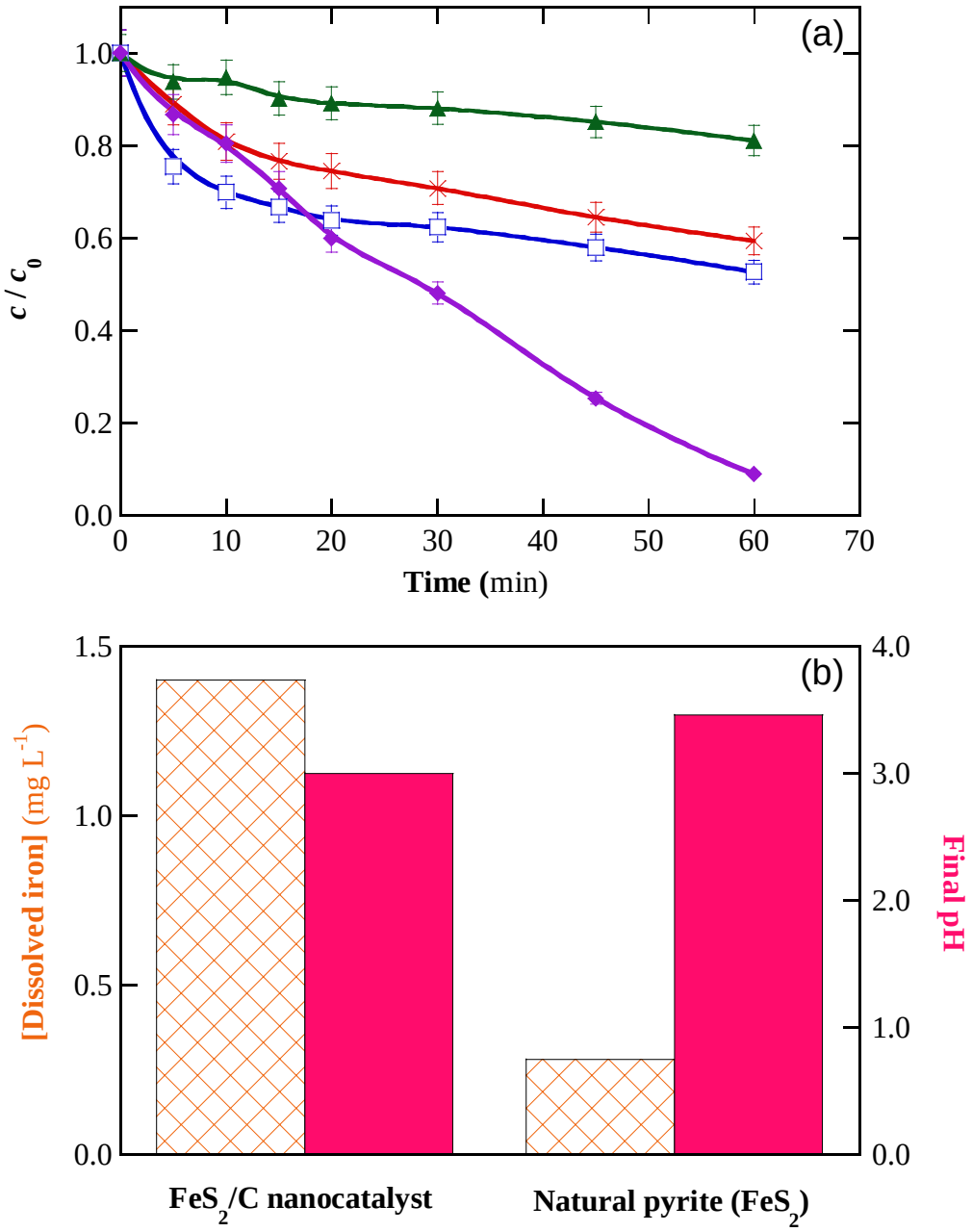
(a)
1.0
0.8
0.6
0.4
0.2
0.0
c / c0
0
10
20
30
40
50
60
70
Time (min)
(b)
1.5
1.0
0.5
0.0
[Dissolved iron] (mg L-1)
4.0
3.0
2.0
1.0
0.0
Final pH
FeS2/C nanocatalyst
Natural pyrite (FeS2)

Figure 3

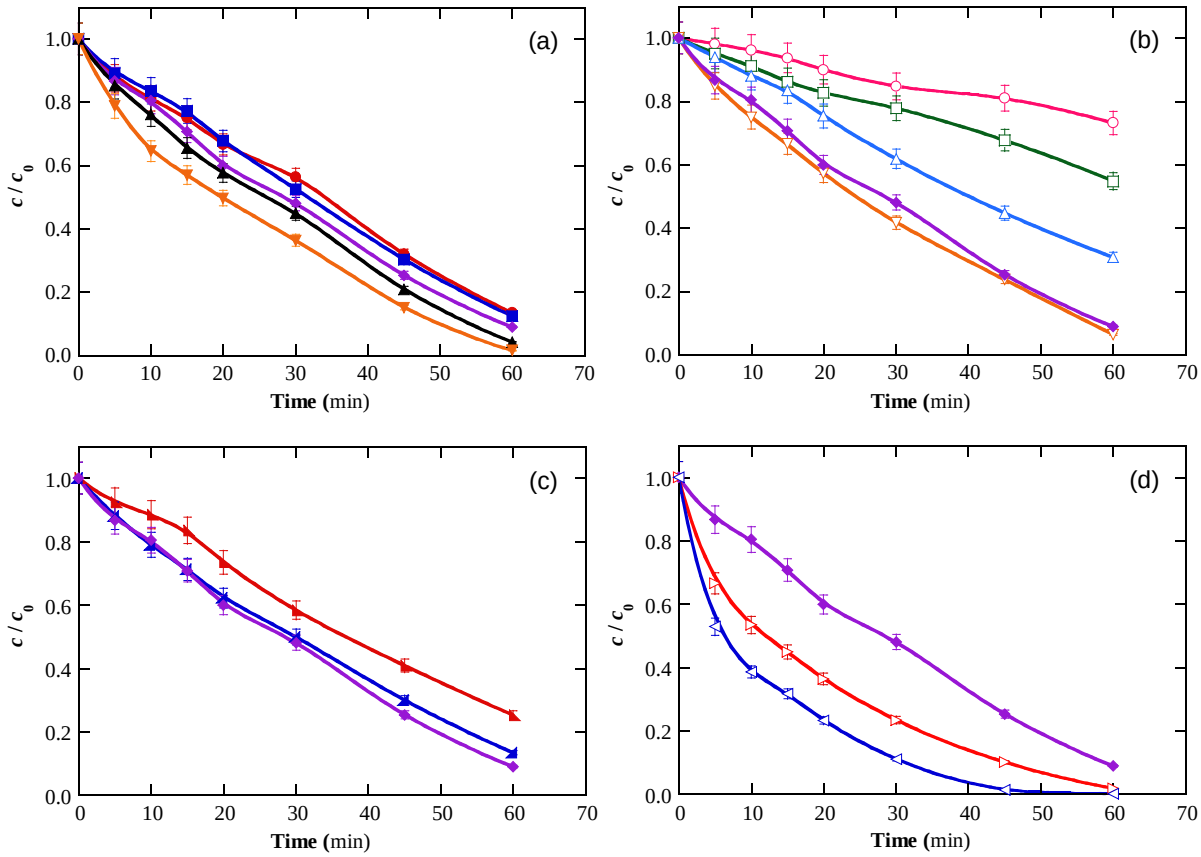

Figure 4

(a)

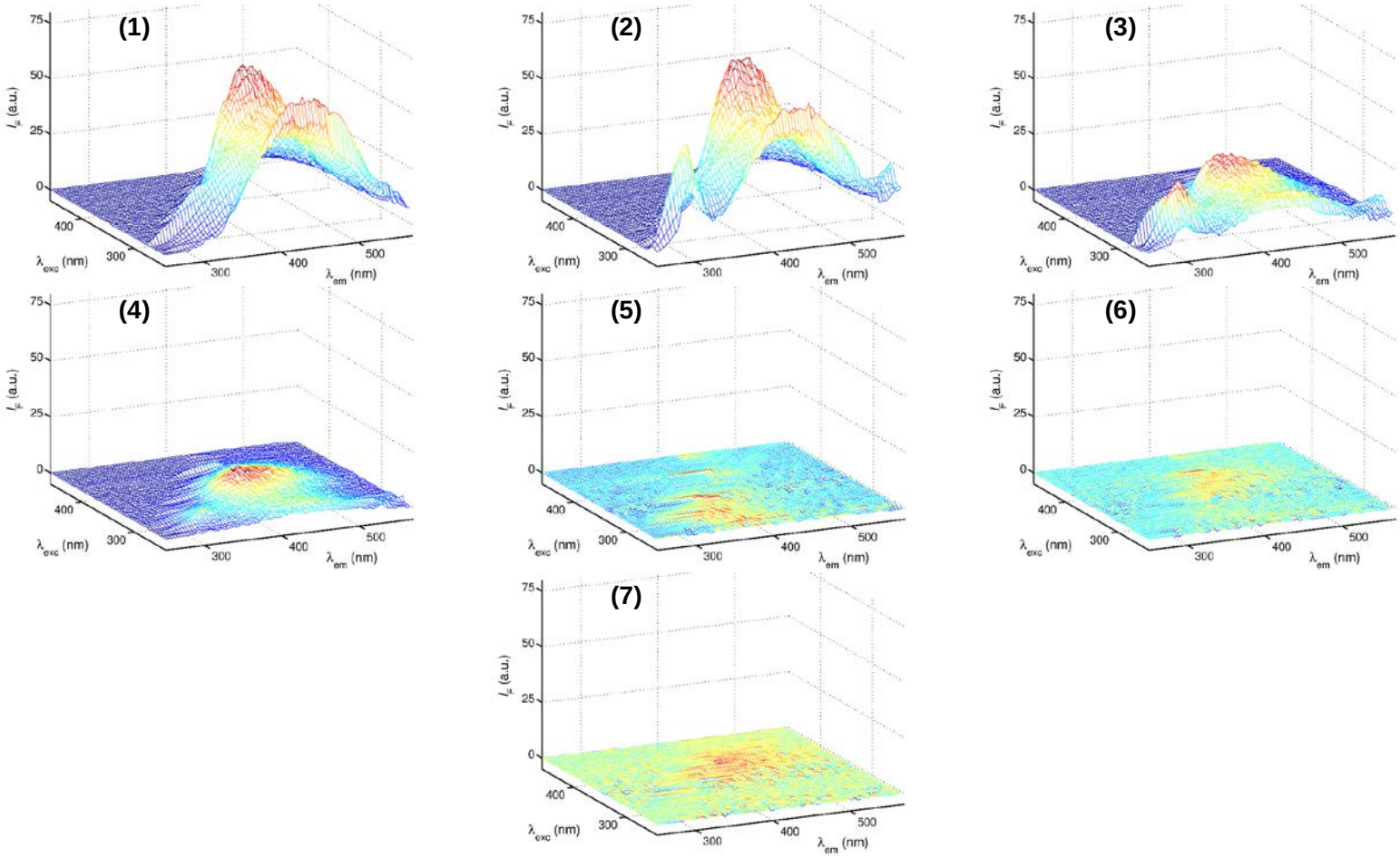
(1)
(2)
(3)
(4)
(5)
(6)
(7)
I_F (a.u.)
λ_{exc} (nm)
λ_{em} (nm)

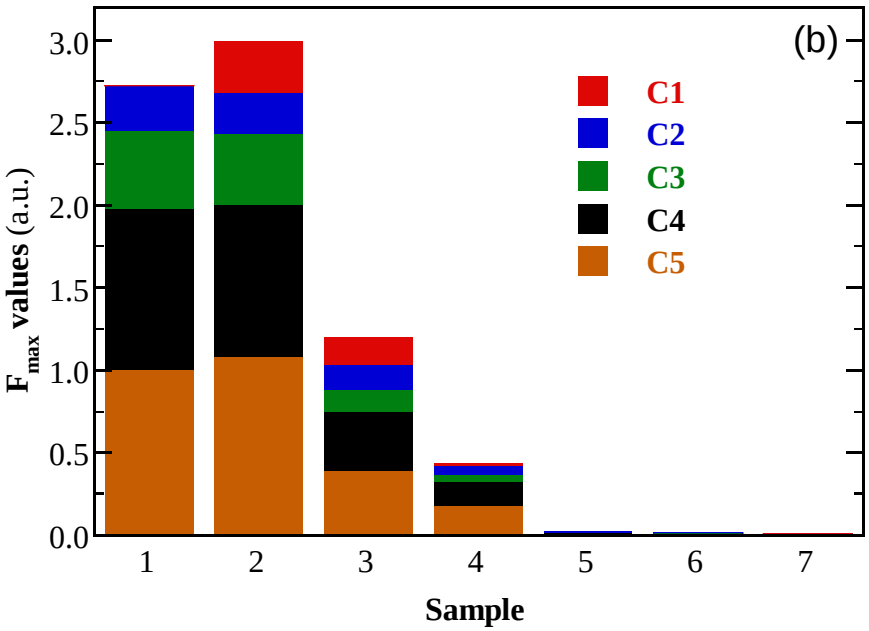
(b)
C1
C2
C3
C4
C5
F_{max} values (a.u.)
Sample

Figure 5

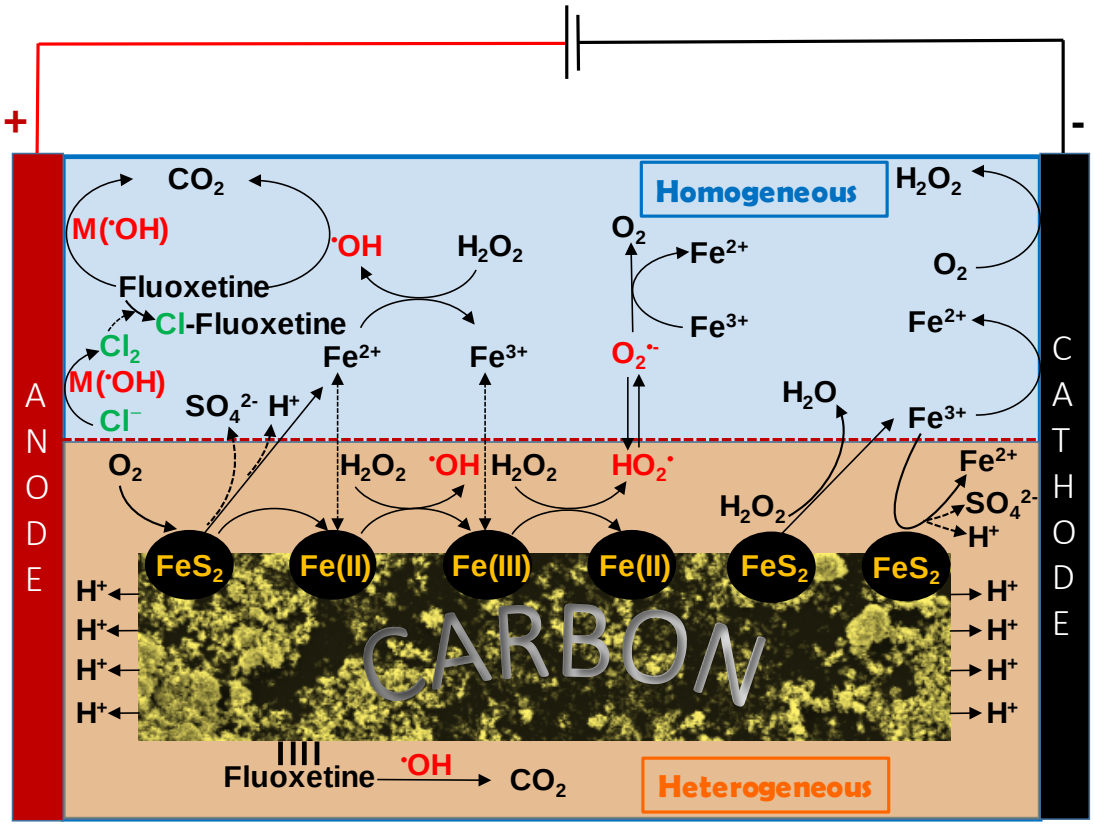
+
-
ANODE
CATHODE
Homogeneous
Heterogeneous
CO2
M(•OH)
Fluoxetine
Cl-Fluoxetine
Cl2
M(•OH)
Cl−
•OH
H2O2
Fe2+
Fe3+
SO4 2- H+
O2
Fe2+
Fe3+
O2•-
H2O2
O2
H2O
Fe3+
Fe2+
O2
H2O2
•OH
H2O2
HO2•
H2O2
Fe2+
SO4 2-
H+
FeS2
Fe(II)
Fe(III)
Fe(II)
FeS2
FeS2
H+
CARBON
Fluoxetine
•OH
CO2

Figure 6

SUPPORTING INFORMATION

A highly stable MOF-engineered FeS_2/C nanocatalyst for heterogeneous electro-Fenton treatment: Validation in wastewater at mild pH

Zhihong Ye,[†] José A. Padilla,[‡] Elena Xuriguera,[‡] José L. Beltran,[§] Francisco Alcaide,[‖] Enric Brillas,[†] and Ignasi Sirés*,[†]

[†] Laboratori d'Electroquímica dels Materials i del Medi Ambient, Departament de Química Física, Facultat de Química, Universitat de Barcelona, Martí i Franquès 1-11, 08028 Barcelona, Spain

[‡] DIOPMA, Departament de Ciència de Materials i Química Física, Facultat de Química, Universitat de Barcelona, Martí i Franquès 1-11, 08028 Barcelona, Spain

[§] Secció de Química Analítica, Departament d'Enginyeria Química i Química Analítica. Universitat de Barcelona, Martí i Franquès 1-11, 08028 Barcelona, Spain

[‖] CIDETEC, Paseo Miramón 196, 20014 Donostia-San Sebastián, Spain

*Corresponding author: Tel.: +34 934039240; Fax: +34 934021231.

E-mail address: i.sires@ub.edu (I. Sirés)

This document includes supplementary text and 13 figures, distributed as follows:

Text S1-S5	Pages S2-S3
Figures S1-S13	Pages S4-S17

Text S1

The most relevant parameters of the urban wastewater employed were: 9.7 mg L^{-1} total organic carbon (TOC), 46.0 mg L^{-1} total nitrogen (TN), pH 6.0, specific conductivity of 1.5 mS cm^{-1} and 595 mg L^{-1} Cl^{-}. The wastewater was usually acidified, followed by stripping with nitrogen to remove volatiles and final pH re-adjustment to 6.0.

Text S2

XPS analysis was made with a monochromatic X-ray source (Aluminum Kα line of 1486.6 eV energy, 350 W), placed perpendicular to the analyzer axis and calibrated using the $3d_{5/2}$ line of Ag with a full width at half maximum (FWHM) of 0.8 eV. The analyzed area was a circle of 0.8 mm diameter, and the selected resolution for the spectra was 187.85 eV of Pass Energy and 0.8 eV/step for the general spectra and 23.5 eV of Pass Energy and 0.1 eV/step for the spectra of the different elements. A low energy electron gun (less than 10 eV) was used in order to discharge the surface when necessary. All measurements were made in an ultrahigh vacuum (UHV) chamber pressure between 5×10^{-9} and 2×10^{-8} torr.

Text S3

For ESR analysis, 70 mL of a 10 mM DMPO solution in urban wastewater were electrolyzed and samples were withdrawn at different times. They were immediately frozen with dry ice for preservation, to be further analyzed with a Bruker ESP300E spectrometer, which was set up as follows: center magnetic field at 3495.00 G, sweep width of 100 G, microwave frequency of 9.79 GHz, microwave power of 2.00 mW, modulation amplitude of 2.00 G, time constant of 40.96 ms, conversion time of 200 ms and sweep time 204.8 s. Win-EPR and SimFonia 2.3 software were employed.

Text S4

The fluorescence spectrophotometer was controlled by Cary Eclipse Scan Application version 1.2. A Hellma QS cuvette (10 mm × 10 mm). The scan rate was set to 18 nm s^{-1}, the slit widths were adjusted to 5 and 2 nm for excitation and emission wavelengths, respectively, and the photomultiplier tube voltage was set to 750 V. Prior to the analysis, the samples were tempered at room temperature. The spectra were acquired in the ratio mode to ensure normalization of the signal and enable comparison within samples analyzed.

Text S5

For toxicity analysis, the pH of all samples was first adjusted to 7, followed by dilution. The acute ecotoxicity of the conditioned samples was measured after 15 min of incubation at 25 °C, employing an AFNOR T90-301 Microtox® system. The bioluminescent bacteria and needed reagents were supplied by Modern Water and the analysis was conducted following the standard procedure recommended by the manufacturer. The result have been expressed as EC_{50} (in mg L^{-1}), which informs about the concentration of solution at a given electrolysis time that causes a 2-fold reduction of bioluminescence intensity in 15 min.

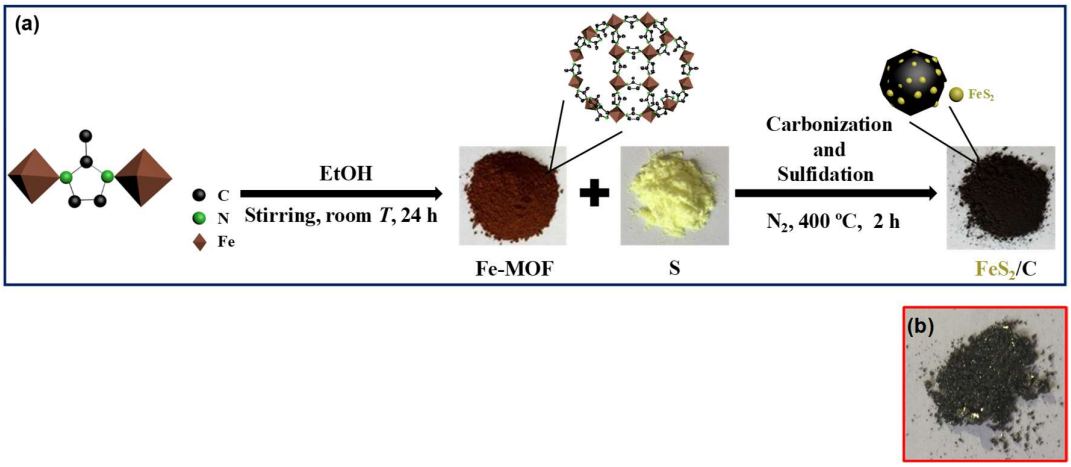

Figure S1. (a) Scheme of the synthetic route followed to obtain the FeS_2/C nanocatalyst. (b) Natural pyrite (FeS_2, commercial mineral).

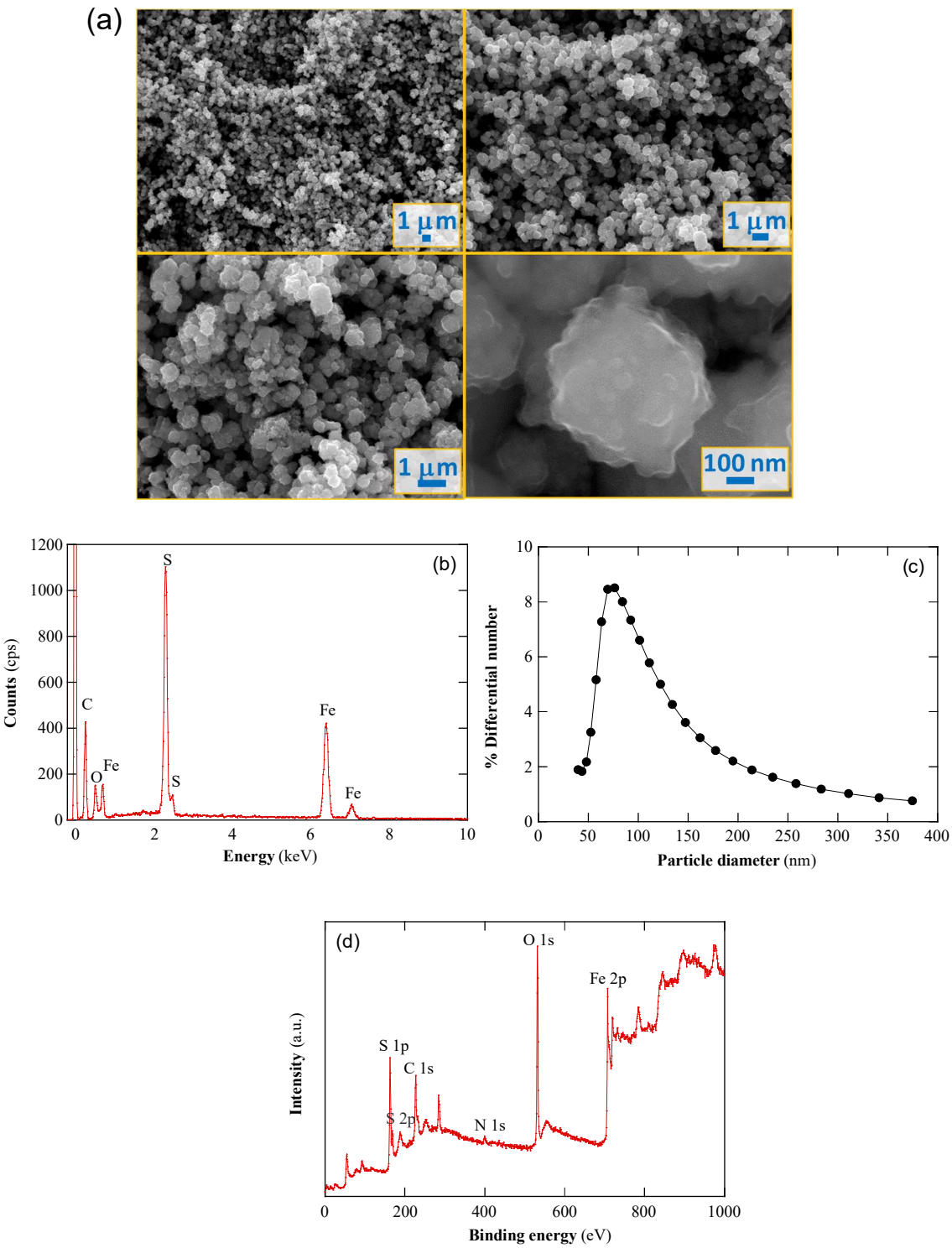

Figure S2. SEM images at 3,000×, 6,000×, 10,000×, and 100,000×. (b) EDS analysis, (c) DLS analysis, and (d) XPS general spectrum for the as-synthesized FeS_2/C nanocatalyst.

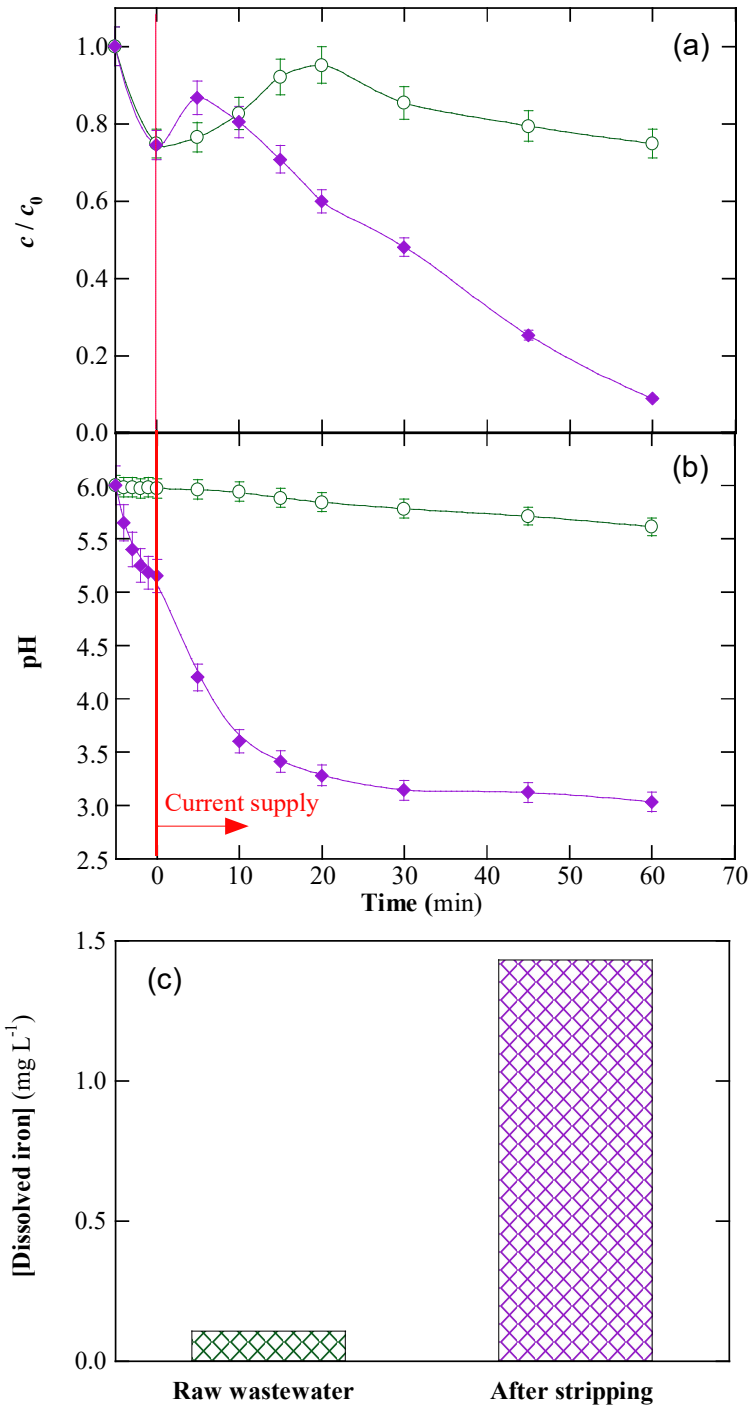

Figure S3. (a) Time course of normalized fluoxetine concentration during the heterogeneous EF treatment of 150 mL of 0.049 mM drug (10 mg C L^{-1}) in urban wastewater with 0.5 g L^{-1} FeS_2/C nanocatalyst at natural pH 6.0 using an IrO_2/air-diffusion cell at 50 mA and 30 ºC, (○) without and (◆) with preliminary stripping. (b) Change of pH in the above cases. As shown, current was supplied after some minutes under vigorous stirring. (c) Iron concentration after 60 min in both trials.

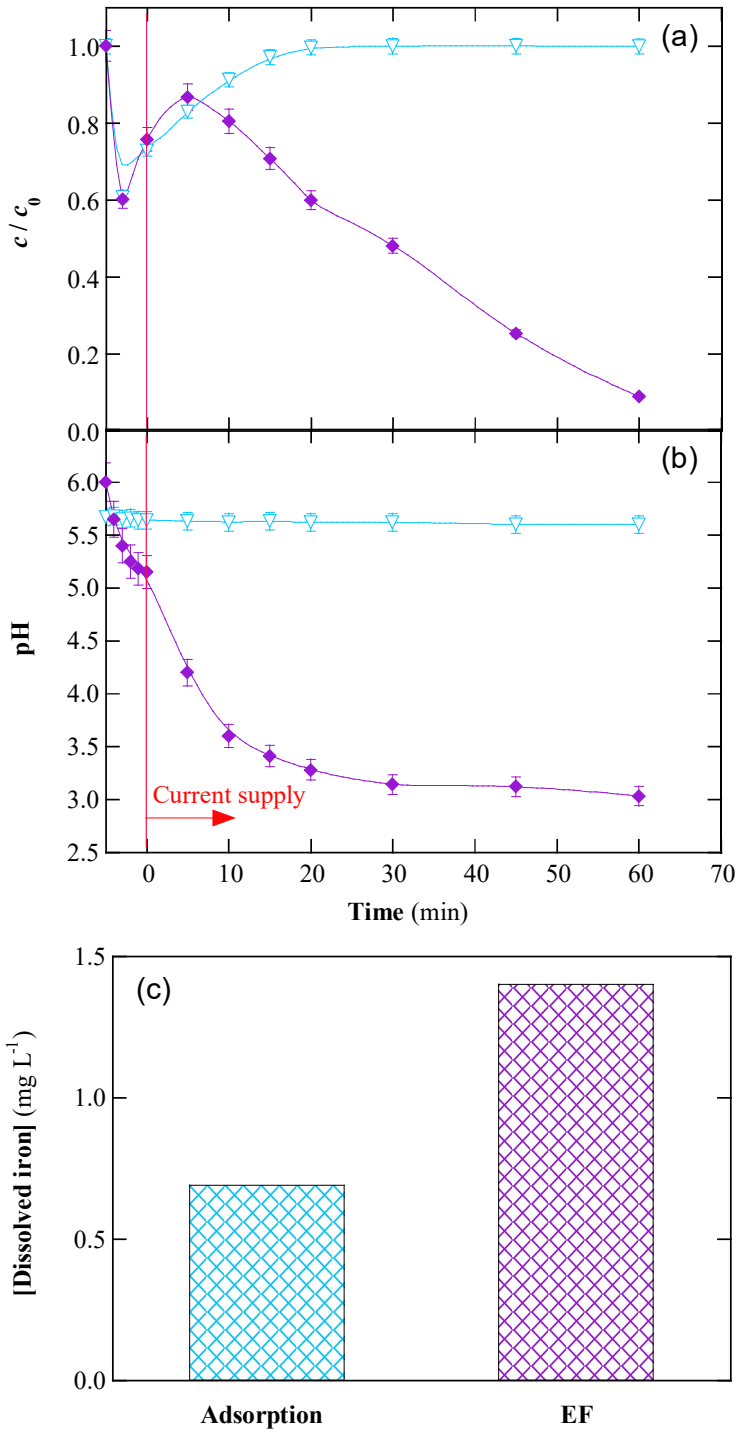

Figure S4. Comparison of fluoxetine removal by (◆) heterogeneous EF process using an IrO_2/air-diffusion cell at 50 mA (see Fig. 3a), and (▽) adsorption. Conditions: 0.049 mM fluoxetine (10 mg C L^{-1}) in urban wastewater with 0.5 g L^{-1} FeS_2/C nanocatalyst at natural pH 6.0 and 30 ºC. (b) Change of pH in both experiments. As shown, current was supplied after some minutes under vigorous stirring. (c) Iron concentration after 60 min of both trials.

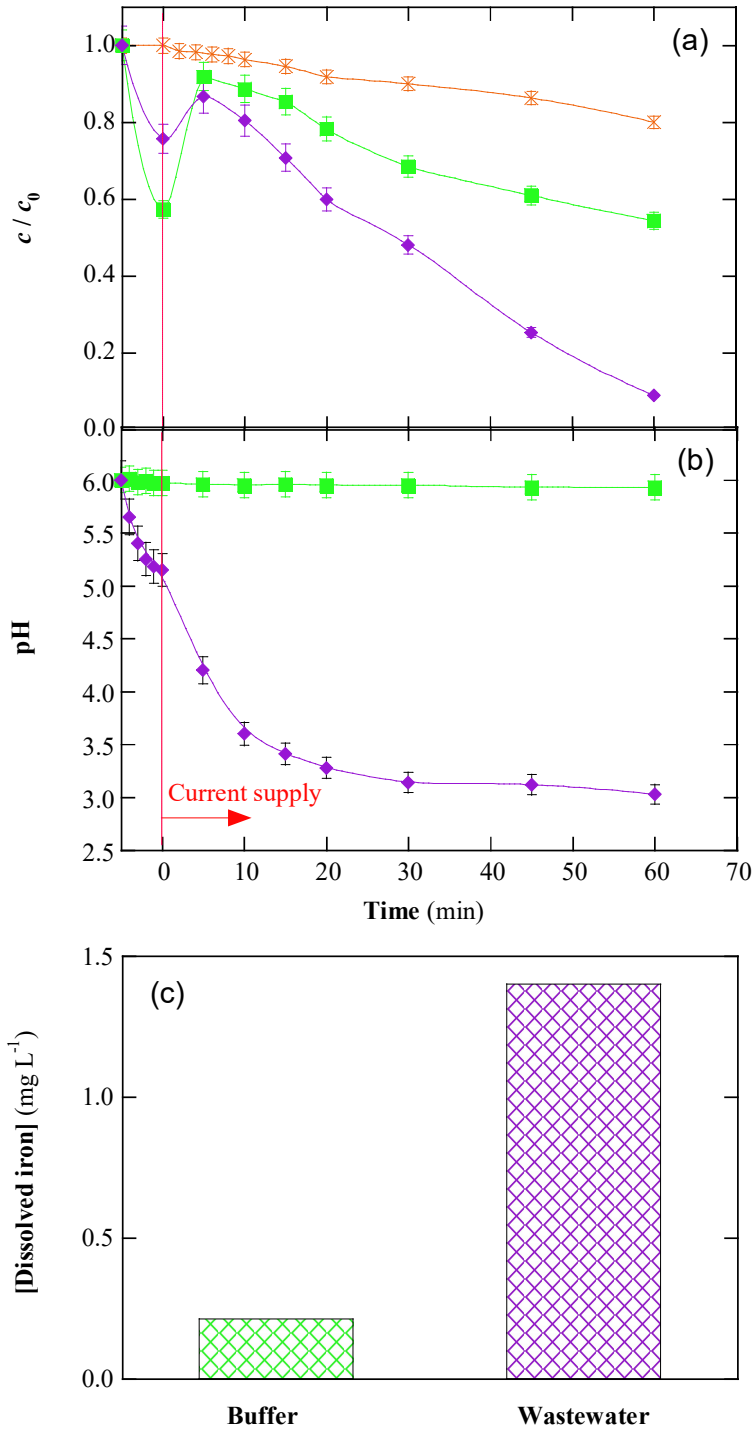

Figure S5. Change of (a) normalized fluoxetine concentration and (b) pH with electrolysis time during the heterogeneous EF treatment of 150 mL of 0.049 mM drug (10 mg C L^{-1}) solutions in (◆) urban wastewater and (■) phosphate buffer with 0.5 g L^{-1} FeS_2/C nanocatalyst at pH ~ 6.0.using an IrO_2/air-diffusion cell at 50 mA and 30 ºC. Current was supplied after some minutes under vigorous stirring. Comparison with (×) EO-H_2O_2 in phosphate buffer is shown. (c) Iron concentration after 60 min of EF.

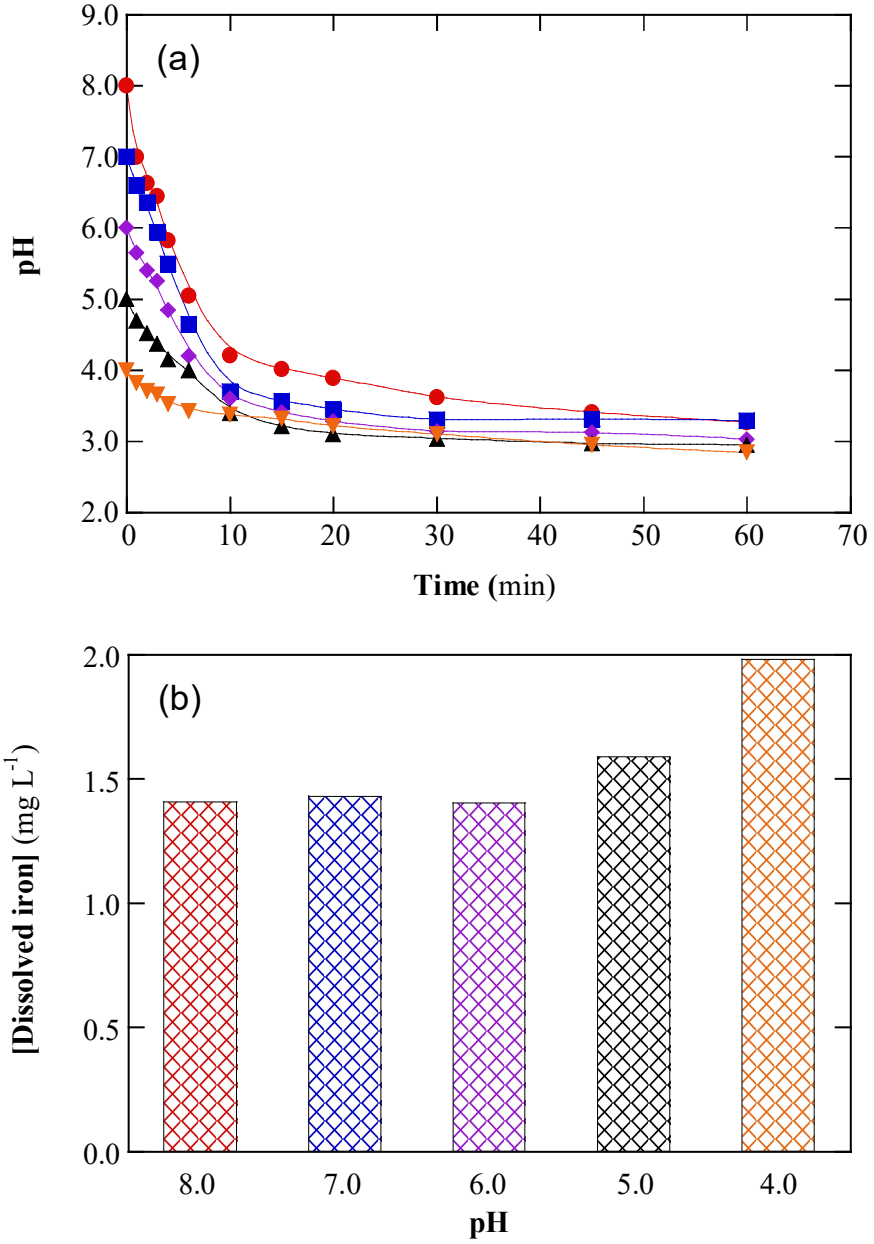

Figure S6. Evolution of (a) pH, and (b) iron concentration after 60 min of heterogeneous EF treatments shown in Fig. 4a.

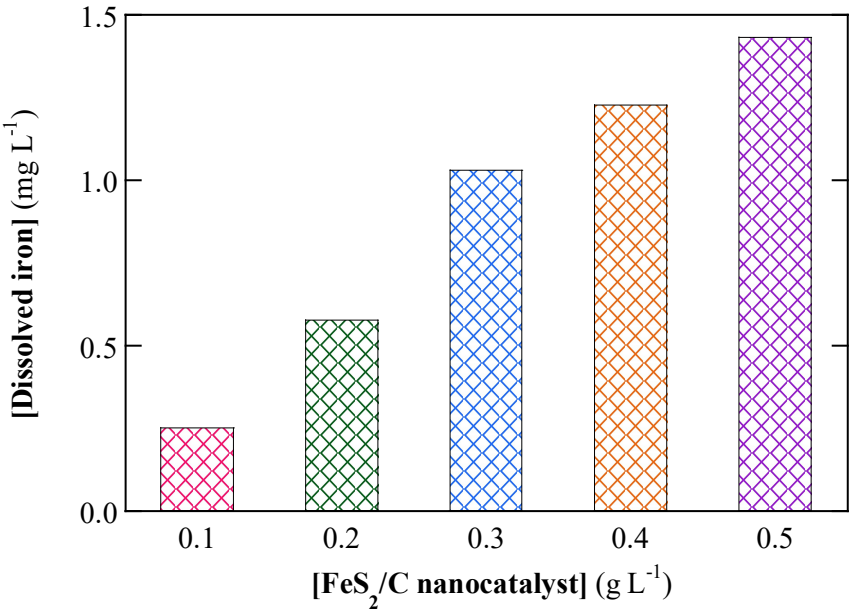

Figure S7. Iron concentration after 60 min of heterogeneous EF treatments shown in Fig. 4b.

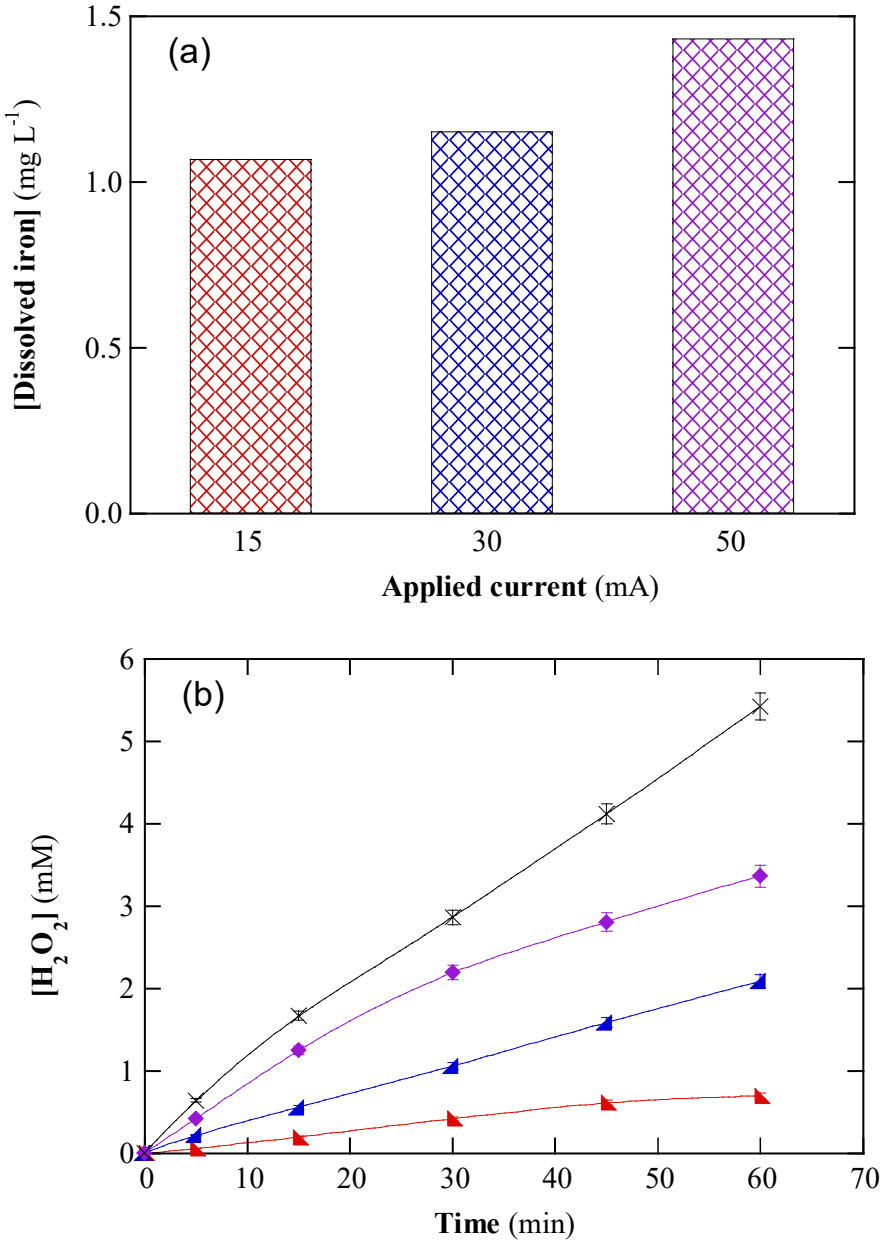

Figure S8. (a) Iron concentration after 60 min, and (b) variation of electrogenerated H_2O_2 concentration with electrolysis time for the heterogeneous EF treatments shown in Fig. 4c. Comparison with (×) EO-H_2O_2 is shown.

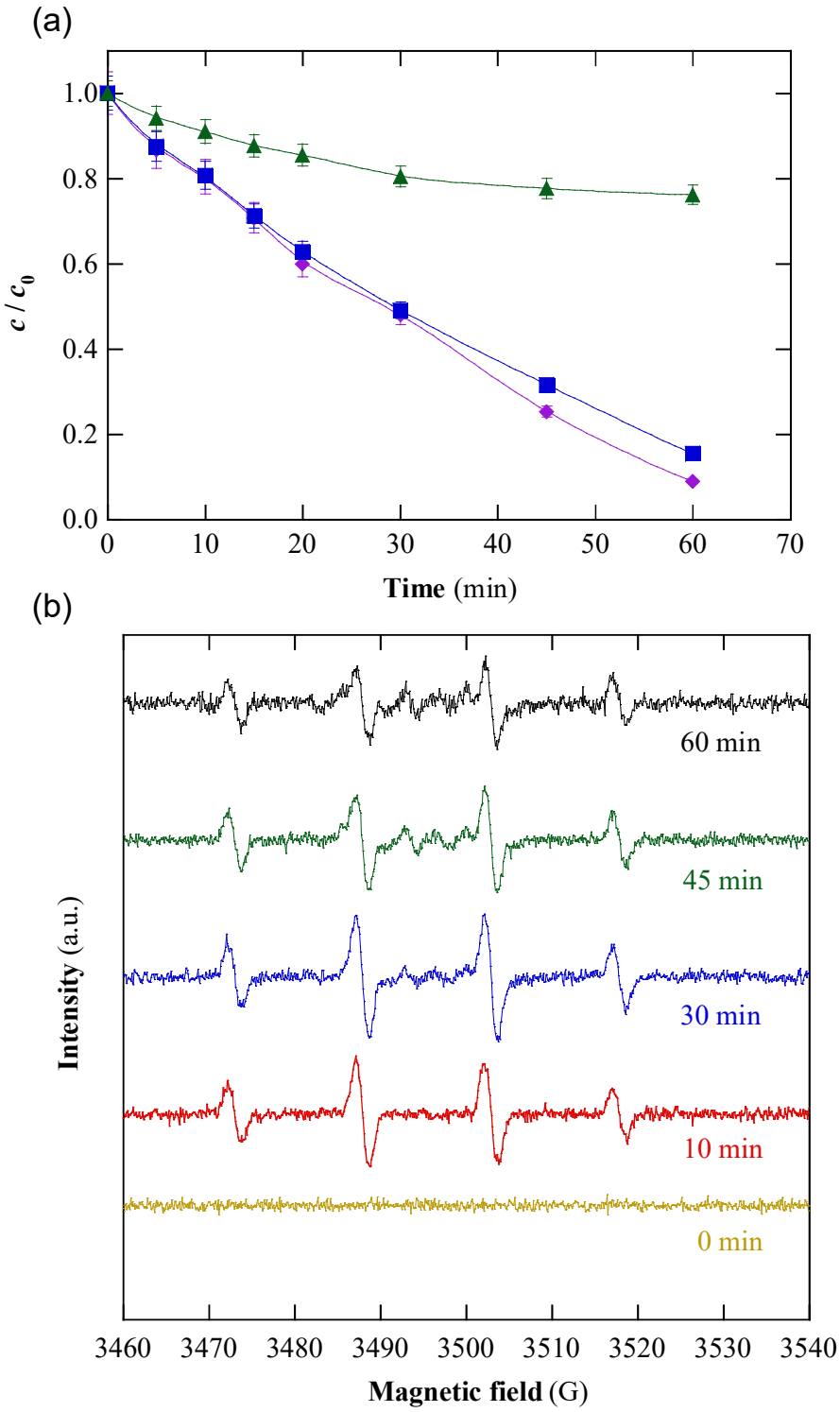

Figure S9. (a) Time course of (◆) normalized fluoxetine concentration during the heterogeneous EF treatment with 0.5 g L^{-1} FeS_2/C nanocatalyst shown in Fig. 3a. The same experiment in the presence of a radical scavenger: (■) 2 mM *p*-benzoquinone or (▲) 20 mM *tert*-butanol. (b) ESR spectra of the •OH-DMPO adduct at different electrolysis times for the EF trial without scavenger.

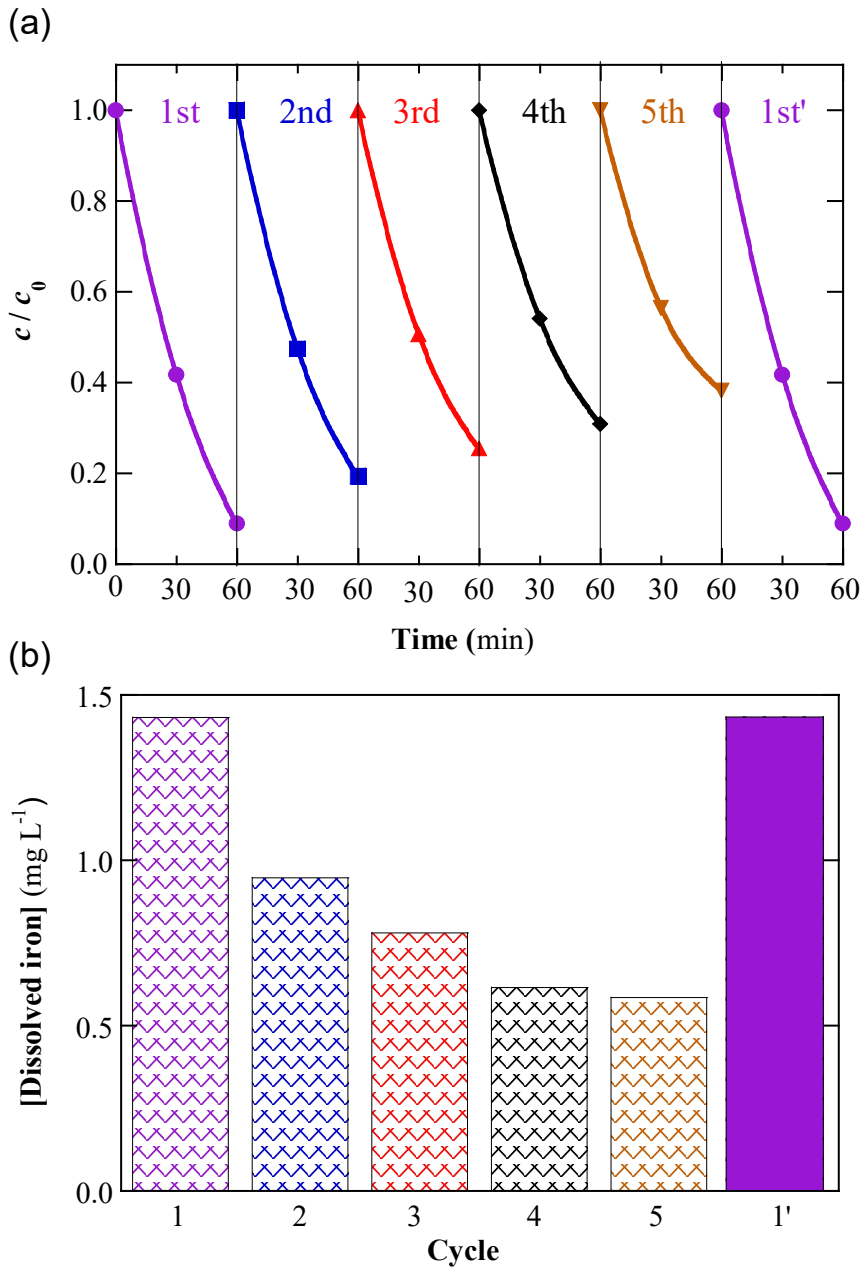

Figure S10. (a) Time course of normalized fluoxetine concentration during the heterogeneous EF treatment with 0.5 g L^{-1} FeS_2/C nanocatalyst shown in Fig. 3a, upon successive cycles 1st-5th. Cycle 1st' was made once the catalyst regeneration was performed after the 5th cycle. (b) Iron concentration after each 60-min cycle.

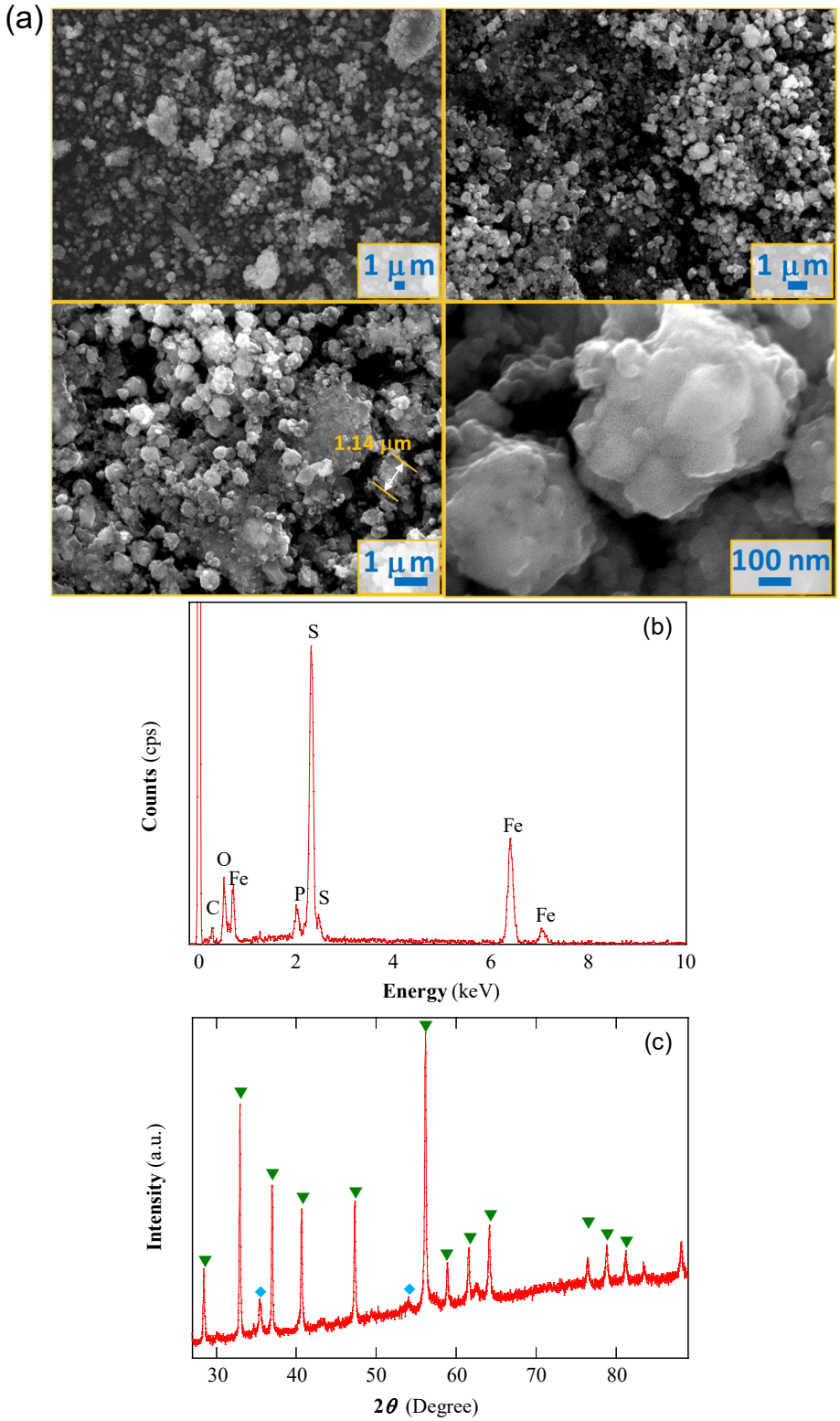

Figure S11. Characterization of the FeS_2/C nanocatalyst after the 5 cycles shown in Fig. S10. (a) SEM images at 3,000×, 6,000×, 10,000×, and 100,000×. (b) EDS analysis. (c) XRD pattern, where the symbols account for the peaks related to (▼) FeS_2 pyrite (JCPDS 65-1211), and (◆) Fe_2O_3 (JCPDS 89-0597) references.

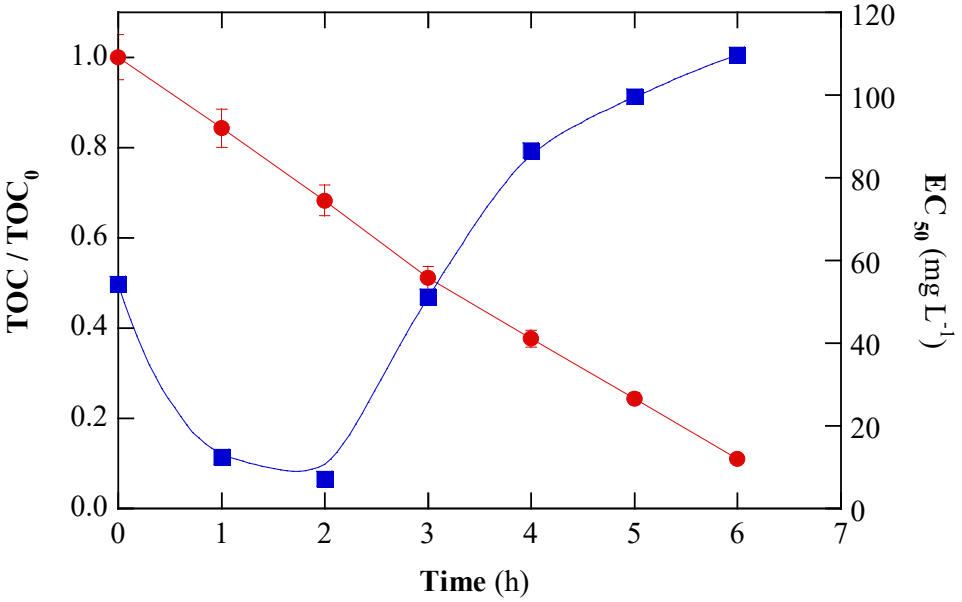

Figure S12. (●) Normalized TOC and (■) toxicity vs. electrolysis time during the heterogeneous EF treatment of 150 mL of a 0.098 mM fluoxetine (20 mg C L^{-1}) solution in urban wastewater with 0.4 g L^{-1} FeS_2/C nanocatalyst at natural pH 6.0 using an BDD/air-diffusion cell at 100 mA and 30 ºC.

(a)

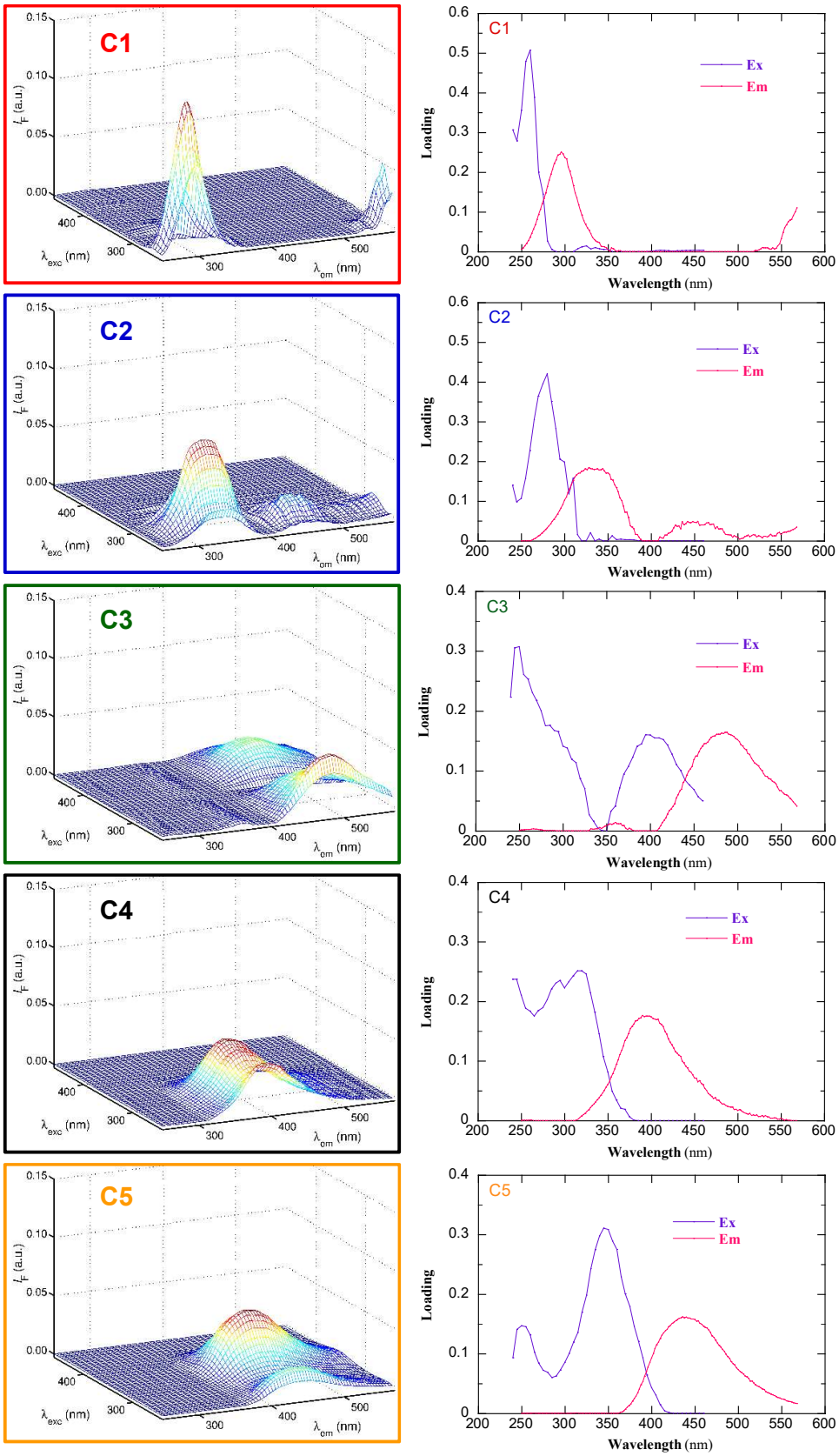
C1
C2
C3
C4
C5
I_F (a.u.)
λ_{exc} (nm)
λ_{em} (nm)
Loading
Wavelength (nm)
Ex
Em

(b)

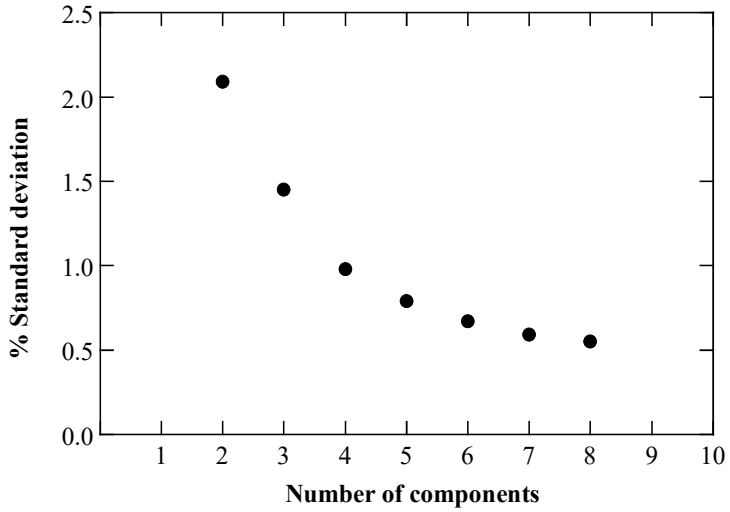

Figure S13. (a) Plots on the left: FEEM spectra of five different component families (C1-C5) identified upon the application of the PARAFAC model to the analysis of the seven samples. Plots on the right: emission and excitation signals for each component within 250-568 and 240-460 nm, respectively. (b) Variation of standard deviation, calculated from the PARAFAC model, as function of number of components in the aqueous solution to be treated by heterogeneous EF with FeS_2/C nanocatalyst.

Appendix VI

Magnetic MIL(Fe)-type MOF-derived N-doped nano-ZVI@C rods as heterogeneous catalyst for the electro-Fenton degradation of gemfibrozil in a complex aqueous matrix

Elsevier Editorial System(tm) for Applied Catalysis B: Environmental
Manuscript Draft

Manuscript Number:

Title: Magnetic MIL(Fe)-type MOF-derived N-doped nano-ZVI@C rods as heterogeneous catalyst for the electro-Fenton degradation of gemfibrozil in a complex aqueous matrix

Article Type: Research Paper

Keywords: Electro-Fenton; Gas-diffusion electrode; Metal-organic framework; Pharmaceutical; Water treatment

Corresponding Author: Dr. Ignasi Sires, Ph.D.

Corresponding Author's Institution: Universitat de Barcelona

First Author: Zhihong Ye, PhD

Order of Authors: Zhihong Ye, PhD; José A Padilla, PhD; Elena Xuriguera, PhD; Enric Brillas, PhD; Ignasi Sires, Ph.D.

Abstract: The application of metal-organic frameworks (MOFs) as heterogeneous catalysts in electro-Fenton (EF) process for water treatment is almost inexistent. Fe-MOFs synthesized from phthalic acid-based linkers were spindle-shaped MIL(Fe)-88B and NH2-MIL(Fe)-88B crystals, whereas their calcination yielded nano-ZVI@C and nano-ZVI@C-N. The lipid regulator gemfibrozil was spiked into 0.050 M Na2SO4 solutions or urban wastewater and treated in electrolytic cells with an air-diffusion cathode to generate H2O2. The nano-ZVI@C-N catalyst obtained at 800 °C showed the highest activity, with high stability as deduced from the low iron leaching and high recyclability. Almost total drug removal and significant mineralization was feasible in both matrices at near-neutral pH. The presence of core-shell nano-ZVI and Fe3O4 nanoparticles encapsulated in N-doped fusiform porous carbon rods was revealed, ensuring the Fe(III) conversion to Fe(II). Carbon doping with N contributed to the enhanced catalytic activity, and the strong magnetism facilitated the post-treatment catalyst recovery.

Magnetic MIL(Fe)-type MOF-derived N-doped nano-ZVI@C rods as heterogeneous catalyst for the electro-Fenton degradation of gemfibrozil in a complex aqueous matrix

Zhihong Ye [a], José A. Padilla [b], Elena Xuriguera [b], Enric Brillas [a], Ignasi Sirés [a,*]

[a] *Laboratori d'Electroquímica dels Materials i del Medi Ambient, Departament de Química Física, Facultat de Química, Universitat de Barcelona, Martí i Franquès 1-11, 08028 Barcelona, Spain*

[b] *DIOPMA, Departament de Ciència de Materials i Química Física, Facultat de Química, Universitat de Barcelona, Martí i Franquès 1-11, 08028 Barcelona, Spain*

Paper submitted to be published in *Applied Catalysis B: Environmental*

*Corresponding author: *E-mail address*: i.sires@ub.edu (I. Sirés)

Abstract

The application of metal-organic frameworks (MOFs) as heterogeneous catalysts in electro-Fenton (EF) process for water treatment is almost inexistent. Fe-MOFs synthesized from phthalic acid-based linkers were spindle-shaped MIL(Fe)-88B and NH_2-MIL(Fe)-88B crystals, whereas their calcination yielded nano-ZVI@C and nano-ZVI@C-N. The lipid regulator gemfibrozil was spiked into 0.050 M Na_2SO_4 solutions or urban wastewater and treated in electrolytic cells with an air-diffusion cathode to generate H_2O_2. The nano-ZVI@C-N catalyst obtained at 800 ºC showed the highest activity, with high stability as deduced from the low iron leaching and high recyclability. Almost total drug removal and significant mineralization was feasible in both matrices at near-neutral pH. The presence of core-shell nano-ZVI and Fe_3O_4 nanoparticles encapsulated in N-doped fusiform porous carbon rods was revealed, ensuring the Fe(III) conversion to Fe(II). Carbon doping with N contributed to the enhanced catalytic activity, and the strong magnetism facilitated the post-treatment catalyst recovery.

Keywords: Electro-Fenton; Gas-diffusion electrode; Metal-organic framework; Pharmaceutical; Water treatment

1. Introduction

Pharmaceutical residues have become one of the main targets among waterborne organic micropollutants, owing to their negative impact on the aquatic ecosystems [1]. They are present in all kinds of water streams, and their potentially deleterious effects on the fauna have been recognized [2]. Pharmaceuticals are ubiquitous in urban wastewater treatment plant (WWTP) influents, being discharged to surface water because of their poor biodegradation and sorption to sludge [3], as well as the low effectiveness of the current tertiary treatments to prevent their accumulation in the plant effluents [4-6]. Consequently, there exist a global consensus on the need for protection of humans and ecosystems from pharmaceutical pollution [7].

Much research is now focused on the development of more effective technologies that allow a proper management of urban wastewater, ensuring the complete degradation of such contaminants before discharge. The electrochemical advanced oxidation processes (i.e., electrochemical AOPs) offer a range of potentially viable technologies for this purpose [8-10]. Among them, the electro-Fenton (EF) process is particularly appropriate because it combines two key characteristics [11,12]: (i) it ensures the fast and complete destruction of the drug molecules, thanks to the massive production of a powerful oxidant like free hydroxyl radical ($^{\bullet}OH$) in the bulk solution via Fenton's reaction (1); and, (ii) unlike the conventional Fenton process [13], the H_2O_2 needed as reactant is produced on site from the cathodic O_2 reduction reaction (2) [14-18], thus becoming a safer, cheaper and more eco-friendly alternative.

$$Fe^{2+} + H_2O_2 \rightarrow Fe^{3+} + {}^{\bullet}OH + OH^- \quad (1)$$

$$O_2(g) + 2H^+ + 2e^- \rightarrow H_2O_2 \quad (2)$$

Furthermore, the anode (M) contributes to the generation of adsorbed hydroxyl radicals from reaction (3) and, in the presence of Cl^-, to chlorine production via reaction (4) [19-21]:

$$M + H_2O \rightarrow M(^{\bullet}OH) + H^+ + e^- \quad (3)$$

$$M + 2Cl^- \rightarrow M + Cl_2(aq) + 2e^- \quad (4)$$

Nonetheless, the main drawback for the deployment of homogeneous EF at larger scale is its restriction to acidic pH, in order to prevent the precipitation of the iron catalyst, with the consequent efficiency loss [11,12]. This is not compatible with urban wastewater effluents, whose pH is near neutral [22], which has fostered the recent development of heterogeneous EF although most of the investigation has been made with model solutions [23]. The performance of this process depends on the ability of the catalyst to generate $^{\bullet}OH$ from heterogeneous Fenton's reaction (5). Several materials have been employed as heterogeneous catalysts in EF, including: synthetic iron-loaded structures, such as carbon nanotubes [24], resins [25], zeolites or biosorbents [12]; waste materials like fly ash; zero-valent ion (ZVI) [23]; iron-rich soils (like clays) [26]; and minerals like iron oxides or pyrite [14,27]. However, it is unusual that these materials combine a high catalytic activity, stability and recyclability. In general, most of them lose some of their active sites during the treatment and suffer from excessive iron leaching. Excessive solubilization is highly detrimental because of the structural modification of the catalyst and the iron precipitation. This phenomenon requires sludge management after treatment, which would be costly and time consuming at industrial scale.

Within this context, metal-organic frameworks (MOFs) have appeared as potentially superior materials. MOFs are highly ordered and porous crystalline structures synthesized from metal ion/clusters and multidentate organic ligands. They might allow overcoming some current technical limitations, showing good perspectives for industrial applications [28], in particular for adsorption, filtration and degradation of organics in water [29]. Their appeal originates from the large porosity and chemical tunability, beneficial for adsorption, which adds to their particular catalytic nature as recently verified in MOF-catalyzed AOPs [30].

The use of iron-MOFs, either as ready-to-use materials or as precursors of Fe/C hybrids (i.e., MOF-derived materials), as catalysts for non-electrochemical Fenton-like process has received increasing attention due to their permanent porosity and tunable open metal centers. This favors the conversion of Fe(III) to Fe(II) active sites [31], which is crucial to maintain the continuous $^{\bullet}OH$ production from reaction (5) since, otherwise, the accumulation of Fe(III) causes the partial consumption of H_2O_2 through the competitive heterogeneous Fenton-like reaction (6) that yields the weaker oxidant hydrperoxyl radical ($HO_2^{\bullet}$).

$$Fe(II) + H_2O_2 \rightarrow Fe(III) + {}^{\bullet}OH + OH^- \quad (5)$$

$$Fe(III) + H_2O_2 \rightarrow Fe(II) + HO_2^{\bullet} + H^+ \quad (6)$$

In contrast, the application of MOFs to EF process is much more incipient. They have never been employed as suspended catalysts, and only a reduced number of articles have reported the use of MOF-modified cathodes [32-34]. The series of iron-based MILs (Materials from Lavoisier Institute, also called MIL(Fe)-type MOFs) prepared from Fe(III) and terephthalic acid, like MIL(Fe)-53, MIL(Fe)-88 and MIL(Fe)-101, seems particularly promising for the destruction of organic pollutants, as demonstrated in conventional Fenton process with MIL(Fe)-88B as catalyst [35]. However, the direct use of most Fe-MOFs as catalysts is restricted due to their self-decomposition in water. Therefore, MOF-derived metal@carbon composite materials, i.e., metal nanoparticles encapsulated in porous carbon, have been recently developed by pyrolysis of MOFs in inert atmosphere. Under such conditions, the carbonization of the organic polymers is induced and the resulting highly porous carbon is beneficial to minimize the mass transport limitations. Simultaneously, metal precursors are converted into metal nanoparticles [36]. The obtention of nanosized MOFs is interesting, aiming to increase the catalytic performance, but it complicates the post-treatment recovery. Hence, calcination may have an additional role as a method to produce magnetic materials [37-42]. Worth considering, nitrogen can be incorporated as heteroatom into the

framework when amine-containing linkers are employed, enhancing the activity and stability [43,44].

This work addresses the synthesis of MIL(Fe)-type and NH_2-MIL(Fe)-type MOFs, along with the corresponding calcined magnetic materials. Their thorough characterization informed about their properties and, subsequently, they were employed as catalysts in heterogeneous EF treatment of gemfibrozil spiked into 0.050 M Na_2SO_4 solutions or into urban wastewater. Gemfibrozil is one of the most frequently detected blood lipid regulators in water [45], being considered a high priority pharmaceutical by the Global Water Research Coalition [46]. Since its removal rate in WWTPs is only around 50% [47], it has been detected in groundwater [48] and rivers [46], showing a large persistence. It can affect negatively to aquatic organisms [48], acting as a peroxisome proliferator, and its high estrogenic activity has been shown [49,50]. Gemfibrozil solutions have been treated by conventional Fenton [51] and photo-Fenton [52] at pH 5.0, as well as by UVC and UVC/H_2O_2 [53]. Regarding the electrochemical AOPs, uniquely the performance of electro-peroxone [54] and electro-oxidation with electrogenerated H_2O_2 (EO- H_2O_2) with a BDD anode has been investigated [55], whereas EF treatment has not been attempted so far. In this study, the degradation products have been identified and the involved mechanism has been proposed. EF was also applied to the degradation of mixtures of gemfibrozil with other pharmaceuticals.

2. Materials and methods

2.1. Chemicals

Gemfibrozil ($C_{15}H_{22}O_3$, 250.33 g mol^{-1}) and 5,5-dimethyl-1-pyrroline-N-oxide (DMPO) were purchased from Sigma-Aldrich and used as received. Sodium sulfate, hydrochloric and sulfuric acids, and sodium hydroxide were acquired from Merck. The reagents for the synthesis of MOFs were $FeCl_3$•$6H_2O$ from Panreac, terephthalic acid (1,4-

benzenedicarboxylic acid, i.e., H_2-BDC) or 2-aminoterephthalic acid (NH_2-BDC) from Sigma-Aldrich, and N,N-dimethylformamide (DMF) from Sigma-Aldrich. Ethanol and methanol were from Panreac. $TiOSO_4$ and H_2O_2 (33% w/v) were from Sigma-Aldrich and Panreac, respectively. 1,10-Phenantroline monohydrate (Alfa-Aesar), $(NH_4)Fe(SO_4)\bullet 6H_2O$ (Panreac) and ascorbic acid (Sigma-Aldrich) were employed to determine the dissolved iron concentration. Organic solvents of HPLC or analytical grade were purchased from Panreac and Merck. All aqueous solutions for analyses, as well as synthetic gemfibrozil solutions, were prepared with Millipore Milli-Q water (ρ > 18.2 MΩ cm).

Some performance tests were made by spiking gemfibrozil into the secondary effluent from an urban wastewater treatment plant, whose general parameters were: 73.2 mg C L^{-1} of total carbon, 13.4 mg C L^{-1} of total organic carbon (TOC), 16.7 mg N L^{-1}, 2.1 mS cm^{-1}, pH 7.5; anions: 180.5 mg L^{-1} SO_4^{2-}, 534.6 mg L^{-1} Cl^- and 61.4 mg L^{-1} NO_3^-; cations: 554.5 mg L^{-1} Na^+, 51.4 mg L^{-1} K^+, 103.1 mg L^{-1} Ca^{2+}, 37.3 mg L^{-1} Mg^{2+} and 0.09 mg L^{-1} Fe^{3+}. Prior to storage at 4 ºC, the sample was acidified and the dissolved CO_2 was air-stripped. Before running the degradation trials, the solution pH was adjusted to 7.0 with a concentrated NaOH solution.

2.2. Synthesis procedure

To synthesize the MIL(Fe)-type MOF, $FeCl_3\bullet 6H_2O$ and H_2BDC (5 mmol of each reactant) were mixed and dissolved in 25 mL DMF, and then stirred for 20 min to get a homogeneous solution. Subsequently, the mixture was poured into a 100 mL Teflon-lined stainless steel autoclave, which was placed in a fan oven preheated to 110 °C and kept for 24 h. The autoclave was then removed from the oven and cooled down naturally to room temperature, whereupon the powdery product was collected by filtration, sequentially washed with methanol and water, and finally dried overnight in an oven at 80 °C. The resulting powder was stored at room temperature in a covered glass container. The same procedure was

followed to synthesize the NH_2-MIL(Fe)-type MOF, but replacing H_2BDC by NH_2-BDC. Nano-ZVI@C and nano-ZVI@C-N (i.e., N-doped) were prepared by annealing the previous MOFs in a tube furnace at the required temperature for 4 h under N_2 atmosphere. The two materials were collected via the application of an external magnet, and then washed and dried as described for the non-calcined materials.

2.3. Electrolytic trials

Most of the experiments were carried out under continuous stirring in a one-compartment glass cell, open to atmosphere and thermostated at 35 ºC. Electrolyses were performed at constant current employing an Amel 2053 potentiostat-galvanostat. The cathode was a 3-cm^2 carbon-Teflon air-diffusion electrode supplied by BASF, placed in a tubular gas chamber and fed with air pumped at 1 L min^{-1} for continuous H_2O_2 generation. The 3 cm^2-anode was either a Ti plate coated with IrO_2, purchased from NMT Electrodes, or a BDD thin film deposited on a Si wafer, supplied by NeoCoat. The interelectrode gap was 1.0 cm. Before first use of the electrodes, a polarization was run in 150 mL of a 0.05 M Na_2SO_4 solution at 300 mA for 180 min, allowing the conditioning of all their surfaces. All the degradation trials were made with 150 mL of 0.050 M Na_2SO_4 solutions or urban wastewater. The EF treatments were performed in the presence of one of the synthesized catalysts.

2.4. Catalyst characterization

Several techniques were used to analyze the morphological features, structure, composition, size and other relevant properties of the synthesized materials. The morphology was assessed by high resolution transmission electron microscopy (HRTEM), using a JEOL JEM-2100 LaB6 microscope operating at 200 kV in STEM mode with a dark-field detector, and coupled to an Oxford Inca energy-dispersive X-ray spectrometer (EDS). Mapping acquisition was accomplished with the Inca Microanalysis Suite version 4.09 software.

Powder X-ray diffraction (XRD) analysis was carried out using a PANalytical X'Pert PRO MPD Alpha-1 powder diffractometer in Bragg-Brentano $\theta/2\theta$ geometry with Cu $K_{\alpha 1}$ radiation (λ = 1.5406 Å). The 2θ-scans ranged from 4 to 100º, with a step size of 0.017º and measuring time of 150 s. Samples were prepared by pressing of the powdery materials with a glass plate to yield a flat surface.

The FTIR spectra were recorded on a Nicolet 6700 FTIR spectrometer (Thermo Scientific), equipped with a smart orbit to directly analyze the powders.

Thermogravimetric analysis (TGA) was performed on a Mettler-Toledo TGA-851e thermobalance. The powdery samples were placed in alumina crucibles of 70 µL volume. Dry N_2 was supplied at a flow rate of 50 mL min^{-1}, and the samples were heated from 30 ºC to 900 ºC at 10 ºC min^{-1}. A blank curve was previously obtained for signal correction.

The specific surface area was determined using the Brunauer–Emmett–Teller (BET) method, where N_2 was used as the adsorbate gas. The data where obtained using a TriStar 3000 surface area analyzer from Micromeritics within the range $0.05 \leq P/P_0 \leq 0.25$. Sample outgassing was performed under vacuum at 40 ºC for 4 h.

The particle size distribution was measured by dynamic light scattering (DLS), using an LS 13 320 laser diffraction particle size analyzer (Beckman Coulter). The dispersion medium was acetone and the samples were sonicated (30 kHz, 200 W) for 5 min) before analysis. The zeta-potential (ξ) of each sample as a function of pH was determined using a Malvern Zetasizer Nano ZS (Micromeritics AUTOCHEM 2920) at room temperature, using the Zetasizer version 7.11 software. Buffer solutions at pH values from 3.0 to 7.0 were prepared by mixing different volumes of 0.10 M acetic acid and 0.20 M sodium acetate solutions. The powdery catalyst was suspended in the different buffer solutions using an ultrasonic bath and then, the suspension was introduced in a disposable folded capillary cell (DTS 1070).

X-ray photoelectron spectroscopy (XPS) analysis was performed with a PHI 5500 Multitechnique System (Physical Electronics) using a monochromatic X-ray source (Al Kα line of 1486.6 eV energy, 350 W), placed perpendicular to the analyzer axis and calibrated using the $3d_{5/2}$ line of Ag with a full width at half maximum (FWHM) of 0.8 eV. The analyzed area was a circle of 0.8 mm diameter and the selected resolution for the spectra was 187.85 eV of Pass Energy (PE) and 0.8 eV/step for the general spectra, and 23.5 eV of PE and 0.1 eV/step for the different elements. The energy electron gun was lower than 10 eV. All measurements were made under ultra-high vacuum at pressures between 5×10^{-9} and 2×10^{-8} Torr. The spectra were analyzed using the ULVAC-PHI MultiPakTM software version 8.2.

Fe content of catalysts was analyzed by inductively-coupled plasma with optical detection (ICP-OES) using a Perkin Elmer Optima 3200RL. Digestion of samples (0.0159 g) was carried out in a Milestone Ethos Plus microwave oven, using a high pressure closed Teflon reactor. A temperature program was followed to reach 180 ºC, 210 ºC, 220 ºC and, finally, 230 ºC, employing HNO_3, HCl and H_2O_2 as oxidizing media. C and N were analyzed using a Thermo EA 1108 elemental organic analyzer (Thermo Scientific) operated under standard conditions: He flow rate of 120 mL min^{-1}, combustion furnace at 1000 ºC, chromatographic column oven at 60 ºC and oxygen loop of 10 mL at 100 kPa.

The magnetic characterization of the claimed catalysts was made on a Quantum Design SQUID MPMS-XL susceptometer. The hydroxyl radicals formed during the EF treatments were detected by spin trapping, analyzing the $^{\bullet}$OH-DMPO adduct by electron paramagnetic resonance (EPR). To do this, solutions of 75 mL of 10 mM DMPO with 0.050 M Na_2SO_4 at natural pH were electrolyzed at 25 mA. The samples were immediately frozen with dry ice upon withdrawal for preservation, to be further analyzed by EPR using a Bruker ESP300E spectrometer, which was set up as follows: center magnetic field at 3505.09 G, sweep width of 100 G, microwave frequency of 9.82 GHz, microwave power of 2.00 mW, modulation

amplitude of 1.5 G, time constant of 10.24 ms, conversion time of 81.92 ms and sweep time of 83.89 s. Win-EPR and SimFonia version 2.3 software were employed.

2.5. Other instruments and analytical methods

The specific conductivity of solutions was determined from measurements made with a Metrohm 644 conductometer, whereas their pH was measured on a Crison GLP 22 pH-meter. All the samples were microfiltered (0.45 μm, Whatman syringe filters) prior to any analysis. The time course of H_2O_2 concentration was assessed from the absorption (λ = 408 nm) of its yellow complex with Ti(IV), obtained on a Shimadzu 1800 UV/Vis spectrophotometer at room temperature. The dissolved Fe^{2+} concentration was obtained by measuring the absorption of the reddish solutions resulting upon its complexation with 1,10-phenantroline, whose maximum absorbance was at λ = 510 nm. Some samples were also measured by ICP-OES using an Optima 3200L spectrometer (Perkin Elmer).

Each degradation trial was carried out twice, and the averaged values are depicted in the corresponding figures, along with the error bars with 95% confidence interval. TOC from solutions was determined on a Shimadzu TOC-VCNS analyzer, using the non-purgeable organic carbon method. TN was determined on a Shimadzu TNM-1 unit coupled to the same analyzer. Gemfibrozil concentration was analyzed by reversed-phase high performance liquid chromatography (HPLC) using a Waters 600 chromatograph coupled to a Waters 996 photodiode array detector set at 276 nm. A BDS Hypersil C18 5 μm (250 mm × 4.6 mm) column at 35 ºC was fitted in the equipment. The mobile phase was a 60:40 (v/v) CH_3CN/10 mM KH_2PO_4 (pH 3.0) mixture eluted at 1.0 mL min^{-1}, and the peak of gemfibrozil was obtained at 11.4 min. Samples were always diluted with CH_3CN to stop the drug degradation.

Gas chromatography coupled to mass spectrometry (GC-MS) performed in a 6890N gas chromatograph (Agilent Technologies) coupled to a 5975C mass spectrometer operating in electron impact mode at 70 eV allowed the identification of reaction products. A nonpolar

Teknokroma Sapiens-X5ms and a polar HP INNOWax column, both of 0.25 μm (30 m × 0.25 mm), were used. The initial temperature was 36 ºC for 1 min, which was increased up to 320 ºC at 5 ºC min^{-1}. The temperature of the inlet, source and transfer line was 250, 230 and 300 ºC, respectively. CH_2Cl_2 allowed the extraction of the organics from the aqueous samples, yielding an organic solution that was dried over anhydrous Na_2SO_4. After filtration, it was concentrated under a gentle N_2 stream. The mass spectra were compared to those found in the NIST05 MS database.

3. Results and discussion

3.1. Characterization of the synthesized catalysts

Fig. 1 collects the powder XRD patterns of the four synthesized catalysts, namely two raw MOFs and two MOF-derived materials. In Fig. 1a, it can be observed that the diffractograms of the as-synthesized MIL(Fe)-type and NH_2-MIL(Fe)-type MOFs exhibit numerous diffraction peaks. Most of them are thin, revealing the high crystallinity of both materials. The main peaks (and the corresponding planes) for the former MOF appear at 9.3º (101), 9.5º (002), 12.5º (102), 13.9º (100), 16.1º (200), 16.4º (103), 16.5º (112), 18.8º (202) and 21.9º (211). The N-rich MOF presents a similar pattern, although those peaks tend to be shifted to slightly lower angles (when they are present) and some additional peaks can be seen. They appear at 7.5º (100), 8.2º (101), 9.4º (002), 12.2º (102), 18.0º (202) and 21.7º (212). In both cases, the values show a good agreement with the characteristic patterns of MIL(Fe)-88B and NH_2-MIL(Fe)-88B [56], rather than those expected for MIL(Fe)-53 (and NH_2-MIL(Fe)-53) [57] or MIL(Fe)-101 (and NH_2-MIL(Fe)-101) [58] that are also prepared from $FeCl_3$ and H_2BDC (or NH_2-BDC) mixtures.

Fig. 1b shows the diffractograms of the nano-ZVI@C and nano-ZVI@C-N catalysts obtained upon calcination of the corresponding MOFs at 800 ºC. The peaks at ~45º, ~65º and

~82º can be attributed to (110), (200) and (211) planes of nano-ZVI (JCPDS Ref. N. 87-0721). The cubic structure of Fe_3O_4 (JCPDS Ref. N. 65-3107) accounts for the peaks at 30.0º (220), 35.5º (311), 43.2º (400), 57.2º (511) and 62.6º (440). The presence of nanoscale ZVI (i.e., nano-ZVI, Fe^0) and iron oxide like Fe_3O_4 suggests that the porous frameworks of MIL(Fe)-88B and NH_2-MIL(Fe)-88B collapsed upon pyrolysis and yielded nanosized reduced and oxidized Fe-based nanoparticles encapsulated by porous carbon. The formation of nano-ZVI [42] or Fe_3O_4 [59] upon carbothermal reduction has also been reported considering other reactants.

Note that the presence of nitrogen enhanced all the peaks related to ZVI, which means that N-doped carbon behaved as a better reducing agent. This agrees with Liu et al. [44], who reported the increased encapsulation of Fe^0 in the porous carbon upon incorporation of NH_2-group to the organic precursor. In contrast, the peaks attributed to magnetite are analogous in both carbonized materials.

Based on the good perspectives of the nano-ZVI@C-N catalyst (800 ºC), resulting from the presence of porous carbon, N-doping and more abundant ZVI nanoparticles as compared to the nano-ZVI@C, its characterization was more extensive. The elemental analysis yielded a content of 51.5% Fe, 34.6% C, 11.8% O and 2.15%N. Its zeta-potential decreased as the pH of the tested solutions was higher, yielding an isoelectric point at pH 5.4, which suggests that its surface is negatively charged at a more alkaline pH.

Fig. S1 of Supplementary Material shows the FTIR spectra of the four materials, which inform about the surface functional groups. Sharp peaks for the MIL(Fe)-type and NH_2-MIL(Fe)-type MOFs within the region of 1600–1400 cm^{-1} can be associated to the asymmetrical and symmetrical stretching modes of the O–C–O framework, which is typical in Fe- MOFs [40]. In addition, the characteristic peak at 540 cm^{-1} can be related to the Fe–O stretching mode in both MOFs, as expected from the link between Fe atoms and the organic

ligand. The bands at 3456 cm^{-1} and 3373 cm^{-1} are ascribed to the asymmetrical and symmetrical stretching modes of the amine groups, respectively. The presence of N is also confirmed from the peaks at 1626 cm^{-1} and 1337 cm^{-1}, corresponding to N–H and C–N bonds, respectively.

After carbonization under N_2 atmosphere, all the peaks disappeared, which corroborates the complete decomposition of the organic ligands to yield porous carbon and the transformation of the iron species mainly into Fe^0, as observed in the XRD patterns.

Fig. S2a shows the XPS general spectrum for the nano-ZVI@C-N catalyst (800 ºC). The XPS spectrum of each element present in the catalyst (C 1s, Fe 2p, N 1s and O 1s) is shown in Fig. S2b-e. The C 1s band could be deconvoluted into four peaks centered at 284.5, 285.4, 286.6 and 289.4 eV, assigned to C–C, C=N, C–N and O–C=O functional groups, respectively [60]. The latter one is actually small, which can be related to the minor oxidation of the porous carbon at the high carbonization temperature. In the spectrum of Fe, the Fe $2p_{3/2}$ band contains peaks for Fe(II) and Fe(III) at 710.7 and 712.8 eV, respectively, whereas the Fe $2p_{1/2}$ band contains Fe(II) and Fe(III) at 724.2 and 726.8 eV [44,60]. These peaks confirm the presence of Fe_3O_4 in the calcined catalyst. In addition, the signal at 719.7 eV can be related to Fe^0 [61]. The N 1s spectrum could be deconvoluted into five peaks [60]: pyridinic N at 398.3 eV, FeN_x at 399.4 eV, graphitic N at 400.7 eV, quaternary N at 401.7 eV and oxidized N (i.e., N–O) at 404.2 eV. Alternatively, the peak at 399.4 eV can be associated to pyrrolic N [44]. This variety arises from cyclization reactions, which favor the incorporation of N atoms to carbon rings. The formation of quaternary N was promoted by iron at the high calcination temperature. Finally, Fig. S2e shows the peaks at 531.4 and 533.2 eV, which may be assigned to oxygen vacancies and C–O bonds on the carbon surface, respectively. The peak at 530.1 eV is typical of metal-oxygen bonds, in agreement with the presence of Fe_3O_4 [44].

TEM analysis was performed for the as-synthesized MOFs and the calcined catalysts, and the images and elemental mapping for the nano-ZVI@C-N catalyst (800 ºC) can be observed in Fig. 2. The morphological characterization reveals that, after NH_2-MIL(Fe)-88B was carbonized, its typical hexagonal rod-like shape was still preserved, as can be seen in Fig. 2a (highlighted in red). Some authors describe it as a needle-like morphology [35], although it is more convenient to consider it a spindle [36] or a fusiform rod. A shown in the magnified rod in Fig. 2b, some of these structures appeared as truncated carbonaceous rods although, in general, they showed a uniform size of 3-4 µm in length and 1.0-1.5 µm in width. In addition, iron atoms from the MOF precursor aggregated into quite spherical nanoparticles embedded in the microporous carbon matrix. Two types of particles can be distinguished: big ones (500-600 nm in diameter, in blue) and small ones (150 nm in diameter, in green). Such iron encapsulation is expected to contribute to the minimization of the erosion of nano-ZVI and magnetite, as well as to avoid the precipitation of iron ions on the nanoparticle surface. Fig. 2c evidences the core-shell structure of these particles, which according to the color image shown in Fig. 2d accounts for a carbon shell that surrounds a core composed of either nano-ZVI or Fe_3O_4 (in agreement with the XRD pattern). The elemental mapping of one of the rods, selected as the site of interest in Fig. 2e, confirmed the distribution of elements: Fe and O match quite perfectly with the particle sites, whereas C and N show a uniform distribution along the whole rod, thus confirming the N-doping of carbon mentioned in the XPS analysis. Note that the colors in Fig. 2e are not related to those in Fig. 2d.

The magnetic properties of the nano-ZVI@C-N catalyst synthesized at 800 ºC, which is a very relevant aspect for practical application, were also assessed. Fig. 3 shows the magnetization curve, showing the typical hysteresis loop that characterizes the ferromagnetic materials at room temperature. The saturation magnetization (M_s) was 66.7 emu g^{-1}, which is higher than those of Fe_3O_4 nanoparticles (44 emu g^{-1}) [62] and Fe_3O_4/carbon composites

derived from MIL(Fe)-101 (61.7 emu g^{-1}) [39], and it can be associated to the contribution of abundant nano-ZVI. The M_s of ZVI nanoparticles is 93 emu g^{-1} [63], greater than that of our material, as expected from the shielding effect of the porous carbon. Nonetheless, the magnetism of the synthesized material is strong enough for efficient post-treatment magnetic recovery of the catalyst particles using a permanent magnet or an external magnetic field. Worth mentioning, the hysteresis loop was small, exhibiting an almost perfect sigmoidal shape. Hence, the nano-ZVI@C-N catalyst showed a ferromagnetic behavior but approaching to superparamagnetic, since the coercive field is close to zero (i.e., only 200 Oe). The inherent magnetization of the material was possible due to the nanometric dimensions of the iron particles, since the large surface area exposed allow that the spin of the electrons of surface atoms aligns readily in response to even weak magnetic fields, thus simplifying its separation after use.

As can be seen from the N_2 adsorption/desorption isotherms depicted in Fig. S3a, the BET surface area of the nano-ZVI@C-N catalyst was much higher than that of its NH_2-MIL(Fe)-type MOF, yielding values of 216.9 and 56.4 m^2 g^{-1}, respectively. This confirms the large porosity conferred to the N-doped carbon rod upon pyrolysis at 800 ºC. The surface area of the calcined material is higher than that reported for MIL(Fe-88A-derived carbon rods (84 m^2 g^{-1}) [38] and within the range of that achieved for materials derived from NH_2-MIL(Fe)-88B (160 m^2 g^{-1}) [36], which is potentially beneficial to favor the exposure of active sites and the adsorption of the organic pollutants. On the other hand, the size reduction upon calcination is evident from DLS analysis of Fig. S3b, with mean values decreasing from 200 nm to 90 nm, in agreement with the collapse of the 3D framework. Furthermore, the size distribution became narrower, thus confirming the uniformity of the structural dimensions mentioned from Fig. 2.

In order to elucidate the transformation steps that occur during the pyrolytic process, the TGA curve of the as-synthesized NH_2-MIL(Fe)-type MOF was determined, along with that of the NH_2-BDC precursor, as shown in Fig. S4. The crystalline MOF presented an initial weight loss of 22% at 50-275 ºC, which can be related to the release of physisorbed solvent molecules (water, methanol and DMF) [37]. The subsequent weight loss, occurring within the temperature range from 275 ºC to 450 ºC, was larger (30.1%) and can be attributed to the partial decomposition of the organic ligands, as deduced from the trend of NH_2-BDC. In this stage, the residual NH_2-BDC reactant, the NH_2-BDC molecules encapsulated within the porous framework and the structural NH_2-BDC linker were gradually calcined. Above 475 ºC and up to about 800-850 ºC, the organic molecules completely decomposed, yielding a total weight loss of around 80%. Curve *a* shows the formation of Fe_3O_4 between 450-650 ºC, thereby being transformed into nano-ZVI from 650 ºC.

3.2. Performance of raw and calcined catalysts for gemfibrozil removal

Once confirmed the appealing properties of the raw and, especially, the calcined MOFs at 800 ºC, they were employed for the treatment of gemfibrozil solutions with 0.050 M Na_2SO_4 at natural pH 5.5, using an IrO_2/air-diffusion cell and 0.2 g L^{-1} of powdery material. Fig. 4 highlights that the use of NH_2-MIL(Fe)-type MOF as catalyst in heterogeneous EF at 50 mA yielded a 57% gemfibrozil concentration decay at 60 min, resulting from the production of $^{\bullet}OH$ via Fenton's reaction (5) and Fenton-like reaction (6) occurring at the catalyst surface. The nano-ZVI@C powder exhibited a large adsorption capacity (i.e., in the absence of current supply), accounting for a 45% drug removal, as could be expected from the porosity enhancement upon calcination. Worth noting, Fig. 4 shows the apparently poor catalytic performance of this material, since the degradation percentage achieved in EF (52%) was close to the value obtained in the absence of current. In both EF treatments, the drug disappearance was very fast during the first 10 min, reaching almost the maximal degradation,

whereupon the gemfibrozil concentration remained almost constant probably due to the insufficient generation of $^{\bullet}OH$ and the consequent accumulation of refractory organic products [9,11]. Surprisingly, the drug removal by adsorption on the nano-ZVI@C-N catalyst surface was much lower, attaining only 10% despite its significantly greater BET area mentioned above. This can be explained by the occurrence of two combined facts at pH 5.5: (i) the catalyst surface was negatively charged because its zeta-potential determined above was 5.4; and (ii) the gemfibrozil molecules were predominantly deprotonated, since the drug pK_a is 4.7 [46]. The nano-ZVI@C-N-catalyzed EF process exhibited a clear superiority as compared to all the other treatments, yielding an abatement higher than 95% at 60 min. The drug concentration decay agreed with a constant reaction rate that could be fitted well to a pseudo-first-order kinetics with k_1 = 0.0659 min^{-1} (Table 1), which informs about the great catalytic activity of the ZVI and Fe_3O_4 nanoparticles distributed along the N-doped carbon rods. Both typed of Fe-rich particles are able to promote the formation of Fe(II) in solid state as well as Fe^{2+} in solution. Furthermore, nano-ZVI fosters the conversion of Fe(III) to Fe(II) on the catalyst surface. The upgrading as compared to the nano-ZVI@C can be related to the presence of N, which is believed to increase the catalytic activity by decreasing the carbon bandgap energy [44]. It is thus necessary to emphasize that, under the latter EF conditions, gemfibrozil removal corresponded to drug destruction, not to a simple separation, based on the low adsorption described above, which corroborates the great interest in NH_2-MIL(Fe)-derived catalysts. Finally, the contribution of EO- H_2O_2 process to the whole degradation was evaluated in the absence of the powdery materials, revealing that 17% of the drug disappearance could be accounted for by the action of adsorbed $IrO_2(^{\bullet}OH)$ formed from water oxidation via reaction (3).

The EF trial with the nano-ZVI@C-N catalyst was repeated under the above conditions but in the presence of a given radical scavenger. Fig. S5a shows that the use of *p*-

benzoquinone had a very mild effect on the time course of the normalized gemfibrozil concentration. The profile and the final destruction percentage at 60 min (90%) were similar to those obtained in the absence of this scavenger, which is known to react quite selectively with superoxide radical ($O_2^{\bullet-}$). The generation of this oxidant should be feasible from Fenton-like reaction (6), as the conjugated base of $HO_2^{\bullet}$ with pK_a = 4.8-4.9 [11]. It can then be concluded that the Fe(III) conversion to Fe(II) on the calcined N-doped MOF-derived catalyst surface was very effective, thus minimizing the occurrence of reaction (6). In contrast, Fig. S5a also presents the gemfibrozil disappearance in the presence of *tert*-butanol as a selective $^{\bullet}$OH scavenger, achieving a final drug removal as low as 32%, which confirms the preponderant role of this radical, mainly formed from heterogeneous Fenton's reaction (5) thanks to the continuous Fe(II) regeneration. The production of $^{\bullet}$OH can be corroborated from the EPR signals detected in the absence of radical scavengers, as depicted in Fig. S5b. The use of the nano-ZVI@C-N catalyst provided more intense signals, especially at 30 min of electrolysis, as compared to those obtained in EF with nano-ZVI@C, which is in agreement with the greater catalytic activity described for the N-doped catalyst in Fig. 4.

For the best treatment among those summarized in Fig. 4, namely the EF process with nano-ZVI@C-N, Fig. S6 evidences that the solution pH did not change significantly along the electrolysis, only undergoing a slight acidification. This fact contributed to the very low iron leaching from the catalyst surface toward the solution (0.20 mg L^{-1} at 60 min), as illustrated in the same figure. This informs about the great stability of the calcined material, which is a crucial requirement for scale-up. In addition, Fig. S7 demonstrates the high recyclability of the nano-ZVI@C-N catalyst during the same EF treatment after reusing it in five consecutive trials. The reusability was assessed upon simple magnetic recovery of the catalyst from the reaction mixture under an external magnetic field due to their high M_s value. After the fifth trial, it was still possible to attain a 90% of gemfibrozil degradation at 60 min. The loss of

performance could be due to the gradual passivation of the nano-ZVI particles by iron oxides, thus causing the partial deactivation of some of the surface active sites.

Since the nano-ZVI@C-N catalyst was the best material to carry out the heterogeneous EF treatment, the effect of the pyrolysis temperature on its performance was investigated. The enhanced properties of the catalyst synthesized at 800 ºC are evident from Fig. 5a, since the drug destruction at 60 min employing the materials prepared by thermal treatment at 650, 700 and 900 ºC was only 58%, 69% and 44%, respectively. Fig. 5b shows the corresponding good pseudo-first-order kinetics exhibited by the fastest and slowest EF processes, i.e., those performed with powder prepared at 800 and 900 ºC, respectively. Aiming to clarify why the optimum temperature was 800 ºC, the four as-synthesized catalysts were characterized by XRD. The patterns of Fig. S8 reveal that the relationship between their performance and the nature and abundance of the iron-based structures present in the rods, especially with nano-ZVI, was quite straightforward. The presence of the latter particles, which are essential to ensure the Fe(III) reduction, was clearly greater when the pyrolysis temperature was increased from 650 to 800 ºC, as deduced from the higher intensity of the peaks, in particular that at ~45º. Worth noting, the accumulation of this iron form at 800 ºC, formed by in-situ reduction on graphitic carbon, can be explained by the gradual transformation of FeN_x (present only at 650 ºC) and Fe_3O_4 (present at 650 and 700 ºC). At 800 ºC, FeN_x disappeared and the amount of Fe_3O_4 had decreased. The synthesis at 900 ºC restricted the formation of nano-ZVI, with the concomitant promotion of Fe_3O_4. This phenomenon can be related to the collapse of the framework with the condensation of polymers and release of gases, yielding an inadequate amount of reducing agent that ended in the excessive oxidation of the iron-based particles [44]. This explanation is thus in good agreement with the pyrolysis mechanism elucidated from TGA data in Fig. S4.

3.3. Heterogeneous EF treatment of gemfibrozil solutions under different conditions

The effect of various experimental parameters, namely pH, applied current and catalyst dosage, on the performance of the heterogeneous EF treatment in 0.050 M Na_2SO_4 solutions was assessed using the nano-ZVI@C-N catalyst synthesized by pyrolysis at 800 ºC.

Fig. 6a shows the influence of pH, from 3.0 to 9.0, on gemfibrozil removal. The degradation percentage at any selected electrolysis time declined as the initial pH value became higher. The fastest decay was achieved at pH 3.0, reaching total removal at 30 min, which can be explained by the expected greater iron solubilization that could promote the production of $^{\bullet}OH$ from homogeneous Fenton's reaction (1) whose optimum pH is ~3.0. This is verified from Fig. S9a, which shows a large accumulation of dissolved iron (8.5 mg L^{-1} at 60 min). None of the other initial pH values allowed the complete disappearance of the drug after 60 min, attaining decays of 95%, 84% and 69% at pH 5.5, 7.0 and 9.0, respectively. The final leached iron in these three trials was very low (0.1-0.2 mg L^{-1}, Fig. S9a), suggesting the relatively high stability of nano-ZVI@C-N at mild pH. This does not preclude the occurrence of some additional iron leaching, not detected because of its precipitation on the catalyst surface, forming a thicker barrier at higher solution pH. Such precipitate could account for the gradually lower performance of the EF process. Note in Fig. S9a that in all cases, the solutions became slight acidified, which can be due to the production of acidic organic products like aliphatic carboxylic acids (see subsection 3.4). Worth highlighting, even the least effective heterogeneous EF treatment (i.e., at pH 9.0) could greatly outperform the EO-H_2O_2 process (Fig. 4).

In Fig. 6b, it can be seen that the applied current did not play a crucial role in heterogeneous EF, since very similar final decay rates could be achieved, especially at current values ≥ 50 mA. At 60 min, 86%, 95% and 100% gemfibrozil removal was found at 25, 50 and 75 mA, respectively. The total disappearance could be reached after only 45 min at 100 mA. As can be observed in Fig. S9b, in all trials there was an excess of H_2O_2 concentration

accumulated in the solution from reaction (2), which became higher as the applied current increased. This means that the current was partially wasted because homogeneous and heterogeneous Fenton's reaction (1) and (5) could not occur more quickly as their rate was limited by the amount of catalyst and their own kinetics. On the other hand, a current increase from 25 to 100 mA favored the larger production of $IrO_2(^{\bullet}OH)$, although its oxidation power is much lower than that of $^{\bullet}OH$, as deduced from Fig. 4.

The catalyst dosage had a more important role, since it is the source of Fe(II)/Fe(III) and their aqueous forms, which eventually determine the amount of $^{\bullet}OH$ produced. Fig. 6c shows a gradual enhancement of gemfibrozil removal, from 72% to 83%, 95% and 100% at 60 min as the catalysts concentration was increased from 0.05 to 0.10, 0.20 and 0.30 g L^{-1}. From Fig. 6b and c it can be inferred that, depending on the need, overall drug destruction is feasible either via current increase or via addition of a slightly greater amount of catalyst, thus providing certain flexibility to the technology.

All the decays of Fig. 6a-c agreed very well with a pseudo-first-order reaction kinetics, and the corresponding k_1-values are summarized in Table 1.

In Fig. 7, the trend obtained in EF at pH 5.5 and 50 mA using 0.2 g L^{-1} of catalyst (95% gemfibrozil degradation at 60 min) is compared with those resulting from EF trials performed with other anodes and electrolytes with the same specific conductivity. The use of an IrO_2/air-diffusion cell with 0.041 M Na_2SO_4 + 0.009 M $NaHCO_3$ led to a very poor drug removal, only attaining 31% at 60 min due to the inhibitory effect of HCO_3^- that act as very effective radical scavenger. This anion reacts with $^{\bullet}OH$ and $IrO_2(^{\bullet}OH)$ to form much weaker radicals like $CO_3^{\bullet-}$ [64]. The replacement of the IrO_2-based anode by BDD in sulfate medium was not particularly advantageous. Despite the well-known high oxidation power of this anode, the profile of the normalized gemfibrozil concentration was close to that obtained with IrO_2, being only slightly steeper and ending in 100% degradation at 60 min. This small contribution

of BDD($^{\bullet}$OH) to the drug disappearance can then be explained by the preponderant role of $^{\bullet}$OH formed from heterogeneous Fenton's reaction (5). In contrast, the use of a RuO_2/air-diffusion cell with 0.025 M Na_2SO_4 + 0.035 M NaCl was able to accelerate the gemfibrozil destruction, allowing the total removal at 45 min. The RuO_2-based anode is able to produce both, RuO_2($^{\bullet}$OH) via reaction (3) and, mainly, active chlorine from reaction (4). Therefore, chlorination acted in concomitance with $^{\bullet}$OH-mediated oxidation to significantly enhance the removal.

The ability of the heterogeneous EF process to remove not only the target pollutant but also its degradation products was assessed from TOC analysis in sulfate medium. The previous BDD/air-diffusion cell and a current of 100 mA were employed, since it was expected that quite refractory products could be formed along the electrolysis. As shown in Fig. S10, a substantial mineralization of 61% was achieved at 360 min, probably remaining in solution some small persistent organic molecules (see below).

3.4. Degradation products of gemfibrozil, performance in urban wastewater and mechanism

A sample withdrawn at 30 min from the solution treated by EF with 0.2 g L^{-1} nano-ZVI@C-N in the BDD/air-diffusion cell containing 0.050 M Na_2SO_4 at pH 5.5 was analyzed by GC-MS. Six aromatic (**1-7**) and six aliphatic (**8-13**) products were detected, some of them being previously reported during the sunlight-driven photocatalytic treatment of gemfibrozil solutions [65]. Based on the identified products, the degradation route of Fig. 8 is proposed. The initial hydroxylation of **1** with simultaneous decarboxylation yielded 5-(2,5-dimethyl-phenoxy)-2-methyl-pentan-2-ol (**2**), whose demethylation along with the oxidation of the alcohol group led to 5-(2,5-dimethyl-phenoxy)-pentan-2-one (**3**). Upon hydroxylation in their position C1, compounds **1**, **2** and **3** were split into benzenic and aliphatic products. Among the former, 2,5-dimethylphenol (**4**) initiated a sequence that successively produced 2-hydroxy-4-methyl-benzaldehyde (**5**), as well as its monohydroxylated and dihydroxylated derivatives (**6**

and **7**, respectively). On the other hand, the release of the side chain of **1** was identified as 2,2-dimethyl-pent-4-enal (**8**), which was transformed into 2,2-dimethyl-pent-4-enoic acid (**9**). This could then yield wither 2-methyl-penta-2,4-dien-1-ol (**10**) or 2-methylacrylic acid (**11**), whereas the side chain of **2** was clearly identified as 4-methyl-pentane-1,4-diol (**12**), which was converted to 4-methyl-pentan-1-ol (**13**). Note that the accumulation of the aliphatic products may explain the partial TOC abatement described in Fig. S10.

The results discussed so far allow envisaging good perspectives for heterogeneous EF catalyzed with calcined NH_2-MIL(Fe)-88B-type MOF, although the trials were made in model matrices. As a step forward to demonstrate the viability of the new system, a more complex aqueous matrix was considered. Four ubiquitous micropollutants, namely gemfibrozil, naproxen, fluoxetine and bisphenol A, were spiked into urban wastewater at pH 7.0 (each at 10 mg L^{-1} C). The RuO_2/air-diffusion cell was employed, in order to take advantage of it larger ability to remove gemfibrozil thanks to the production of active chlorine (Fig. 7). In Fig. 9, the 95% disappearance of gemfibrozil at 60 min, along with the total removal of the other three compounds is evidenced. The slower concentration decay of gemfibrozil as compared to the trial performed in sulfate/chloride medium described above can be accounted for by the presence of organic molecules that compete to react with $^{\bullet}OH$, $RuO_2(^{\bullet}OH)$ and ClO^{-}, i.e., the other three pollutants and, mainly, the natural organic matter (NOM).

Based on the complete set of results obtained in this work, the mechanism of Fig. 10 is proposed for the nano-ZVI@C-N-catalyzed heterogeneous EF treatment of gemfibrozil solutions at mild pH. The main oxidants are hydroxyl radicals, which can be formed via: (i) heterogeneous Fenton process through reaction between cathodically generated H_2O_2 and Fe(II) on the catalyst surface; (ii) homogeneous Fenton's reaction upon iron leaching; and (iii) H_2O_2 reduction on the N-doped carbon rods. In addition, active chlorine and $M(^{\bullet}OH)$

produced via anodic reactions can contribute to the degradation as well. The nano-ZVI and Fe_3O_4 nanoparticles present in the rods ensured the supply of Fe(II)/Fe(III), being nano-ZVI the main responsible for the continuous Fe(II) regeneration. The presence of N-doped porous carbon upgraded the electron transfer that promoted this kind of reaction, eventually enhancing the catalytic activity.

4. Conclusions

This investigation demonstrates that it is feasible to degrade gemfibrozil, as well as other typical organic micropollutants, in urban wastewater at mild pH by heterogeneous EF process using a calcined NH_2-MIL(Fe)-88B MOF as catalyst. At 60 min, 95% drug removal was achieved in a RuO_2/air-diffusion cell at 50 mA thanks to the action of $^{\bullet}OH$ formed from heterogeneous Fenton's reaction on the catalyst surface. Other oxidants like $RuO_2(^{\bullet}OH)$ and ClO^- also contributed to the decontamination, although with a less relevant role. The nano-ZVI@C-N catalyst was composed of core-shell nanoparticles of 150-600 nm distributed along N-doped carbon fusiform rods. It exhibited very good catalytic properties, along with: (i) environmental compatibility because of the low toxicity of iron; (ii) high stability that ensures its long service life, as deduced from the very low iron leaching at mild pH (0.20 mg L^{-1} at 50 mA); (iii) very efficient Fe(III)/Fe(II) redox cycling as a result of the abundance of nano-ZVI upon synthesis at 800 ºC, as revealed by the low performance loss (10%) after 5 cycles; and (iv) ferromagnetic properties, with high M_s and low coercive field that simplify its recovery after use by employing a weak magnetic field. The surface properties of the catalyst were analyzed by XRD and XPS and the effect of key parameters on its catalytic activity was assessed via electrolysis in 0.050 M Na_2SO_4 solutions at pH 5.5, which showed that its ability to degrade gemfibrozil was much greater than that of the raw MOF and NH_2-MOF, and that of the calcined ZVI@C catalyst. GC-MS analysis allowed the identification of twelve reaction

products, whereas the kinetic analysis of the drug concentration decays yielded the pseudo-first-order rate constants under different conditions.

Acknowledgments

The financial support from project CTQ2016-78616-R (AEI/FEDER, EU) and PhD scholarship awarded to Z.H. Ye (State Scholarship Fund, CSC, China) are gratefully acknowledged.

References

[1] T.H. Miller, N.R. Bury, S.F. Owen, J.I. MacRae, L.P. Barron, Environ. Pollut. 239 (2018) 129-146.

[2] A.J. Ebele, M.A.-E. Abdallah, S. Harrad, Emerg. Contam. 3 (2017) 1-16.

[3] K. Kümmerer, Sustain. Chem. Pharm. 12 (2019) 100136.

[4] S. Bagnis, M.F. Fitzsimons, J. Snape, A. Tappin, S. Comber, Environ. Chem. Lett. 16 (2018) 1193-1216.

[5] K. Kümmerer, D.D. Dionysiou, O. Olsson, D. Fatta-Kassinos, Science 361 (6399) (2018) 222-224.

[6] M. Mezzelani, S. Gorbi, F. Regoli, Mar. Environ. Res. 140 (2018) 41-60.

[7] Time to get clean, Nature 526 (7572) (2015) 164.

[8] L. Feng, E.D. van Hullebusch, M.A. Rodrigo, G. Esposito, M.A. Oturan, Chem. Eng. J. 228 (2013) 944-964.

[9] E. Brillas, I. Sirés, TrAC-Trend. Anal. Chem. 70 (2015) 112-121.

[10] C.A. Martínez-Huitle, M.A. Rodrigo, I. Sirés, O. Scialdone, Chem. Rev. 115 (2015) 13362-13407.

[11] E. Brillas, I. Sirés, M.A. Oturan, Chem. Rev. 109 (2009) 6570-6631.

[12] M. Zhou, M.A. Oturan, I. Sirés, Springer Nature, Singapore (2018).

[13] M.H. Zhang, H. Dong, L. Zhao, D.X. Wang, D. Meng, Sci. Total Environ. 670 (2019) 110-121.

[14] N. Barhoumi, L. Labiadh, M.A. Oturan, N. Oturan, A. Gadri, S. Ammar, E. Brillas, Chemosphere 141 (2015) 250-257.

[15] A. Galia, S. Lanzalaco, M.A. Sabatino, C. Dispenza, O. Scialdone, I. Sirés, Electrochem. Commun. 62 (2016) 64-68.

[16] S. Lanzalaco, I. Sirés, M.A. Sabatino, C. Dispenza, O. Scialdone, A. Galia, Electrochim. Acta 246 (2017) 812-822.

[17] T. Pérez, G. Coria, I. Sirés, J.L. Nava, A.R. Uribe, J. Electroanal. Chem. 812 (2018) 54-58.

[18] Z. Ye, D.R.V. Guelfi, G. Álvarez, F. Alcaide, E. Brillas, I. Sirés, Appl. Catal. B: Environ. 247 (2019) 191-199.

[19] G. Coria, I. Sirés, E. Brillas, J.L. Nava, Chem. Eng. J. 304 (2016) 817-825.

[20] J.R. Steter, E. Brillas, I. Sirés, Appl. Catal. B: Environ. 224 (2018) 410-418.

[21] R. Salazar, M.A. Ureta-Zañartu, C. González-Vargas, C.D.N. Brito, C.A. Martínez-Huitle, Chemosphere 198 (2018) 21-29.

[22] Z. Ye, J.R. Steter, F. Centellas, P.L. Cabot, E. Brillas, I. Sirés, J. Clean. Prod. 208 (2019) 1393-1402.

[23] S.O. Ganiyu, M. Zhou, C.A. Martínez-Huitle, Appl. Catal. B: Environ. 235 (2018) 103-129.

[24] P. Su, M. Zhou, G. Ren, X. Lu, X. Du, G. Song, J. Mater. Chem. A (2019), online.

[25] D. Fernández, I. Robles, F.J. Rodríguez-Valadez, L.A. Godínez, Chemosphere 199 (2018) 251-255.

[26] A.J. dos Santos, I. Sirés, A.P.M. Alves, C.A. Martínez-Huitle, E. Brillas, Chemosphere 240 (2020) 124838.

[27] A.H. Ltaïef, S. Sabatino, F. Proietto, S. Ammar, A. Gadri, A. Galia, O. Scialdone, Chemosphere 202 (2018) 111-118.

[28] X. Li, B. Wang, Y. Cao, S. Zhao, H. Wang, X. Feng, J. Zhou, X. Ma, ACS Sustainable Chem. Eng. 7 (2019) 4548-4563.

[29] E. Dias, C. Petit, J. Mater. Chem. A. 3 (2015) 22484-22506.

[30] V.K. Sharma, M. Feng, J. Hazard. Mater. 372 (2019) 3-16.

[31] M. Cheng, C. Lai, Y. Liu, G. Zeng, D. Huang, C. Zhang, L. Qin, L. Hu, C. Zhou, W. Xiong, Coord. Chem. Rev. 368 (2018) 80-92.

[32] H. Zhao, Y. Chen, Q. Peng, Q. Wang, G. Zhao, Appl. Catal. B: Environ. 203 (2017) 127-137.

[33] T.X.H. Le, M.G. Cowan, M. Drobek, M. Bechelany, A. Julbe, M. Cretin, Nanomaterials, 9 (2019) 641.

[34] K. Liu, M. Yu, H. Wang, J. Wang, W. Liu, M.R. Hoffmann, Environ. Sci. Technol. 53 (2019) 6474-6482.

[35] C. Gao, S. Chen, X. Quan, H. Yu, Y. Zhang, J. Catal. 356 (2017) 125-132.

[36] T. Zeng, M.D. Yu, H.Y. Zhang, Z.Q. He, J.M. Chen, S. Song, Catal. Sci. Technol. 7 (2017) 396-404.

[37] A. Banerjee, R. Gokhale, S. Bhatnagar, J. Jog, M. Bhardwaj, B. Lefez, B. Hannoyer, S. Ogale, J. Mater. Chem. 22 (2012) 19694-19699.

[38] K.Y. Andrew Lin, F.K. Hsu, RSC Adv. 5 (2015) 50790-50800.

[39] W. Li, X. Wu, S. Li, W. Tang, Y. Chen, Appl. Surf. Sci. 436 (2018) 252-262.

[40] J.T. Tang, J.L. Wang, Chem. Eng. J. 351 (2018) 1085-1094.

[41] Z. Wang, J. Yang, Y. Li, Q. Zhuang, J. Gu, Eur. J. Inorg. Chem. 2018 (2018) 23-30.

[42] Y. Wu, X. Chen, Y. Han, D. Yue, X. Cao, Y. Zhao, X. Qian, Environ. Sci. Technol. 53 (2019) 9081-9090.

[43] L. Shi, T. Wang, H. Zhang, K. Chang, X. Meng, H. Liu, J. Ye, Adv. Sci. 2 (2015) 1500006.

[44] C. Liu, Y. Wang, Y. Zhang, R. Li, W. Meng, Z. Song, F. Qi, B. Xu, W. Chu, D. Yuan, B. Yu, Chem. Eng. J. 354 (2018) 835-848.

[45] F. Desbiolles, L. Malleret, C. Tiliacos, P. Wong-Wah-Chung, I. Laffont-Schwob, Sci. Total Environ. 639 (2018) 1334-1348.

[46] P. Grenni, L. Patrolecco, N. Ademollo, M. Di Lenola, A.B. Caracciolo, Microchem. J. 136 (2018) 49-55.

[47] T. Deblonde, C. Cossu-Leguille, P. Hartemann, Int. J. Hyg. Environ. Health 214 (2011) 442-448.

[48] Y. Fang, A. Karnjanapiboonwong, D.A. Chase, J. Wang, A.N. Morse, T.A. Anderson, Environ. Toxicol. Chem. 31 (2012) 550-555.

[49] M. Isidori, M. Bellotta, M. Cangiano, A. Parrella, Environ. Int. 35 (2009) 826-829.

[50] G. Lee, S. Lee, N. Ha, Y. Kho, K. Parkd, P. Kimd, B. Ahne, S. Kima, K. Choi, Ecotoxicol. Environ. Saf. 173 (2019) 174-181.

[51] E. Cuervo Lumbaque, R.M. Cardoso, A. Dallegrave, L.O. dos Santos, M. Ibáñez, F. Hernández, C. Sirtori, J. Environ. Chem. Eng. 6 (2018) 3951-3961.

[52] V.A.B. Paiva, C.E.S. Paniagua, I.A. Ricardo, B.R. Gonçalves, S.P. Martins, D. Daniel, A.E.H. Machado, A.G. Trovó, J. Environ. Chem. Eng. 6 (2018) 1086-1092.

[53] C.E.S. Paniagua, I.A. Ricardo, E.O. Marson, B.R. Gonçalves, A.G. Trovó, J. Environ. Chem. Eng. 7 (2019) 103164.

[54] W. Yao, X. Wang, H. Yang, G. Yu, S. Deng, J. Huang, B. Wang, Y. Wang, Water Res. 88 (2016) 826-835.

[55] O. Rodríguez-Nava, H. Ramírez-Saad, O. Loera, I. González, Environ. Technol. 37 (2016) 2964-2974.

[56] M. Ma, H. Noei, B. Mienert, J. Niesel, E. Bill, M. Muhler, R.A. Fischer, Y. Wang, U. Schatzschneider, N. Metzler-Nolte, Chem. Eur. J. 19 (2013) 6785-6790.

[57] M. Pu, Y. Ma, J. Wan, Y. Wang, J. Wang, M.L. Brusseau, Catal. Sci. Technol. 7 (2017) 1129-1140.

[58] J. Wang, D. Chen, B. Li, J. He, D. Duan, D. Shao, M. Nie, Sci. Rep. 6 (2016) 26126.

[59] M. Angamuthu, G. Satishkumar, M.V. Landau, Micropor. Mesopor. Mater. 251 (2017) 58-68.

[60] P. Zhao, X. Hua, W. Xu, W. Luo, S. Chen, G. Cheng, Catal. Sci. Technol. 6 (2016) 6365-6371.

[61] S.-H. Zhang, M.-F. Wu, T.-T. Tang, Q.-J. Xing, C.-Q. Peng, F. Li, H. Liu, X.-B. Luo, J.-P. Zou, X.-B. Min, J.-M. Luo, Chem. Eng. J. 335 (2018) 945-953.

[62] E.M. Peña-Méndez, R.M. Mawale, J.E. Conde-González, B. Socas-Rodríguez, J. Havel, C. Ruiz-Pérez, Talanta 207 (2020) 120275.

[63] K. Rohith Vinod, P. Saravanan, M. Sakar, S. Balakumar, RSC Adv. 6 (2016) 45850.

[64] A. Bianco, M.I. Polo-López, P. Fernández-Ibánez, M. Brigante, G. Mailhot, Water Res. 118 (2017) 246-260.

[65] P. Chen, F. Wang, Z.-F. Chen, Q. Zhang, Y. Su, L. Shen, K. Yao, Y. Liu, Z. Cai, W. Lv, G. Liu, Appl. Catal. B: Environ. 204 (2017) 250-259.

Figure captions

Fig. 1. XRD patterns of (a) the as-synthesized MIL(Fe)-type (*a*) and NH_2-MIL(Fe)-type MOFs (*b*), and (b) the nano-ZVI@C (*a*') and nano-ZVI@C-N (*b*') catalysts obtained upon calcination at 800 ºC, respectively.

Fig. 2. (a,b,c,d) TEM analysis and (e) site of interest along with EDS elemental mapping showing the distribution of Fe, O, N and C for the nano-ZVI@C-N catalyst obtained upon calcination at 800 ºC.

Fig. 3. Magnetization curve recorded at 300 K for the nano-ZVI@C-N catalyst obtained upon calcination at 800 ºC. The inset shows a magnified view from -2000 to 2000 Oe.

Fig. 4. Normalized gemfibrozil concentration decay with electrolysis time during the (△,□) adsorption and (▲,■) EF treatments of 150 mL of drug solutions (10 mg C L^{-1}) with 0.050 M Na_2SO_4 at natural pH 5.5 and 35 ºC using 0.2 g L^{-1} of catalysts prepared by calcination at 800 ºC derived from: (△,▲) MIL(Fe)-type (thus called nano-ZVI@C) and (□,■) NH_2-MIL(Fe)-type (thus called nano-ZVI@C-N) MOFs. For comparison, the trends for (×) EO-H_2O_2 (no catalyst) and (●) EF with raw NH_2-MIL(Fe)-type catalyst are also shown. EO-H_2O_2 and EF trials were carried out with an IrO_2/air-diffusion cell at 50 mA.

Fig. 5. (a) Normalized gemfibrozil concentration vs. electrolysis time during the EF treatment of 150 mL of drug solutions (10 mg C L^{-1}) with 0.050 M Na_2SO_4 at natural pH 5.5 and 35 ºC in an IrO_2/air-diffusion cell at 50 mA, using 0.2 g L^{-1} of nano-ZVI@C-N catalyst prepared by pyrolysis at different temperatures: (●) 650 ºC, (▲) 700 ºC, (■) 800 ºC and (◆) 900 ºC. (b) Pseudo-first-order kinetic analysis of the drug decay concentration in the two latter trials.

Fig. 6. Normalized gemfibrozil concentration decay versus electrolysis time during the EF treatment of 150 mL of drug solutions (10 mg C L^{-1}) with 0.050 M Na_2SO_4 at 35 ºC in an

IrO_2/air-diffusion cell using the nano-ZVI@C-N catalyst synthesized by calcination at 800 ºC. (a) Effect of initial pH, using 0.2 g L^{-1} of catalyst at 50 mA. pH: (●) 3.0, (■) 5.5 (natural), (▲) 7.0 and (◆) 9.0. (b) Effect of applied current, using 0.2 g L^{-1} of catalyst at natural pH 5.5. *I*: (●) 25 mA, (■) 50 mA, (▲) 75 mA and (◆) 100 mA. (c) Effect of catalyst dosage, at natural pH 5.5 and 50 mA. Catalyst concentration: (●) 0.05 g L^{-1}, (▲) 0.1 g L^{-1}, (■) 0.2 g L^{-1} and (◆) 0.3 g L^{-1}.

Fig. 7. Normalized gemfibrozil concentration with electrolysis time during the EF treatment of 150 mL of drug solutions (10 mg C L^{-1}) at pH 5.5, 50 mA and 35 ºC using 0.2 g L^{-1} of the nano-ZVI@C-N catalyst prepared by calcination at 800 ºC. Different anodes (coupled to an air-diffusion cathode) and electrolytes (with the same total specific conductivity) were employed: (▼) IrO_2 anode with 0.041 M Na_2SO_4 + 0.009 M $NaHCO_3$, (■) IrO_2 anode with 0.050 M Na_2SO_4, (◣) BDD anode with 0.050 M Na_2SO_4 and (◢) RuO_2 anode with 0.025 M Na_2SO_4 + 0.035 M NaCl.

Fig. 8. Proposed degradation route of gemfibrozil solutions at mild pH by heterogeneous EF with the nano-ZVI@C-N catalyst using a BDD/air-diffusion cell.

Fig. 9. Normalized concentration decay vs electrolysis time during the EF process of 150 mL of a mixture of (■) gemfibrozil, (○) bisphenol A, (▽) naproxen and (▷) fluoxetine (each at 10 mg C L^{-1}), spiked into conditioned urban wastewater at pH 7.0 and 35 ºC in a RuO_2/air-diffusion cell, at 50 mA using 0.2 g L^{-1} of the nano-ZVI@C-N catalyst synthesized by calcination at 800 ºC.

Fig. 10. Proposed mechanism for the nano-ZVI@C-N-catalyzed heterogeneous EF treatment of gemfibrozil solutions at mild pH.

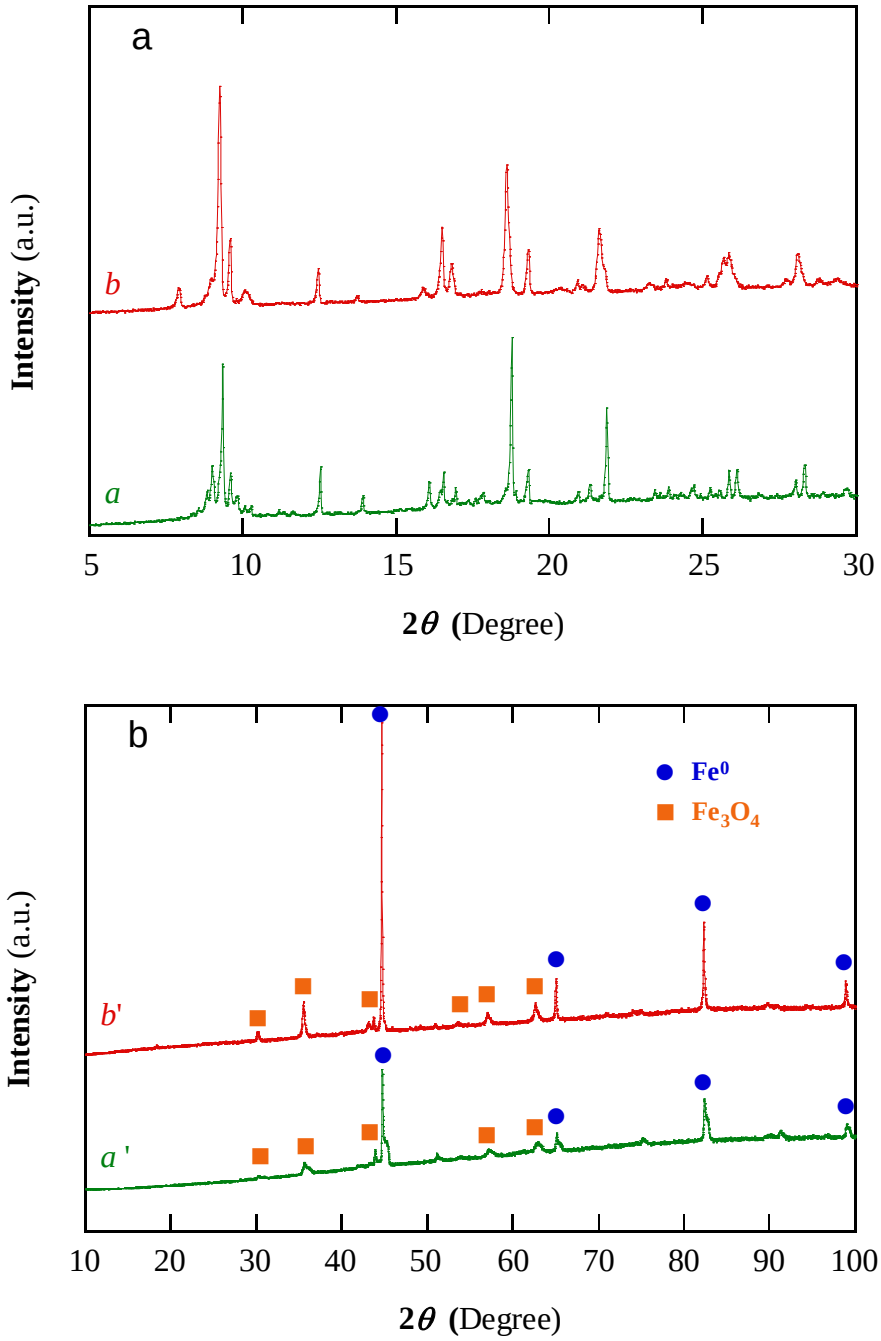
a
b
a
Intensity (a.u.)
5
10
15
20
25
30
2θ (Degree)
b
Fe0
Fe3O4
b'
a '
Intensity (a.u.)
10
20
30
40
50
60
70
80
90
100
2θ (Degree)

Fig. 1

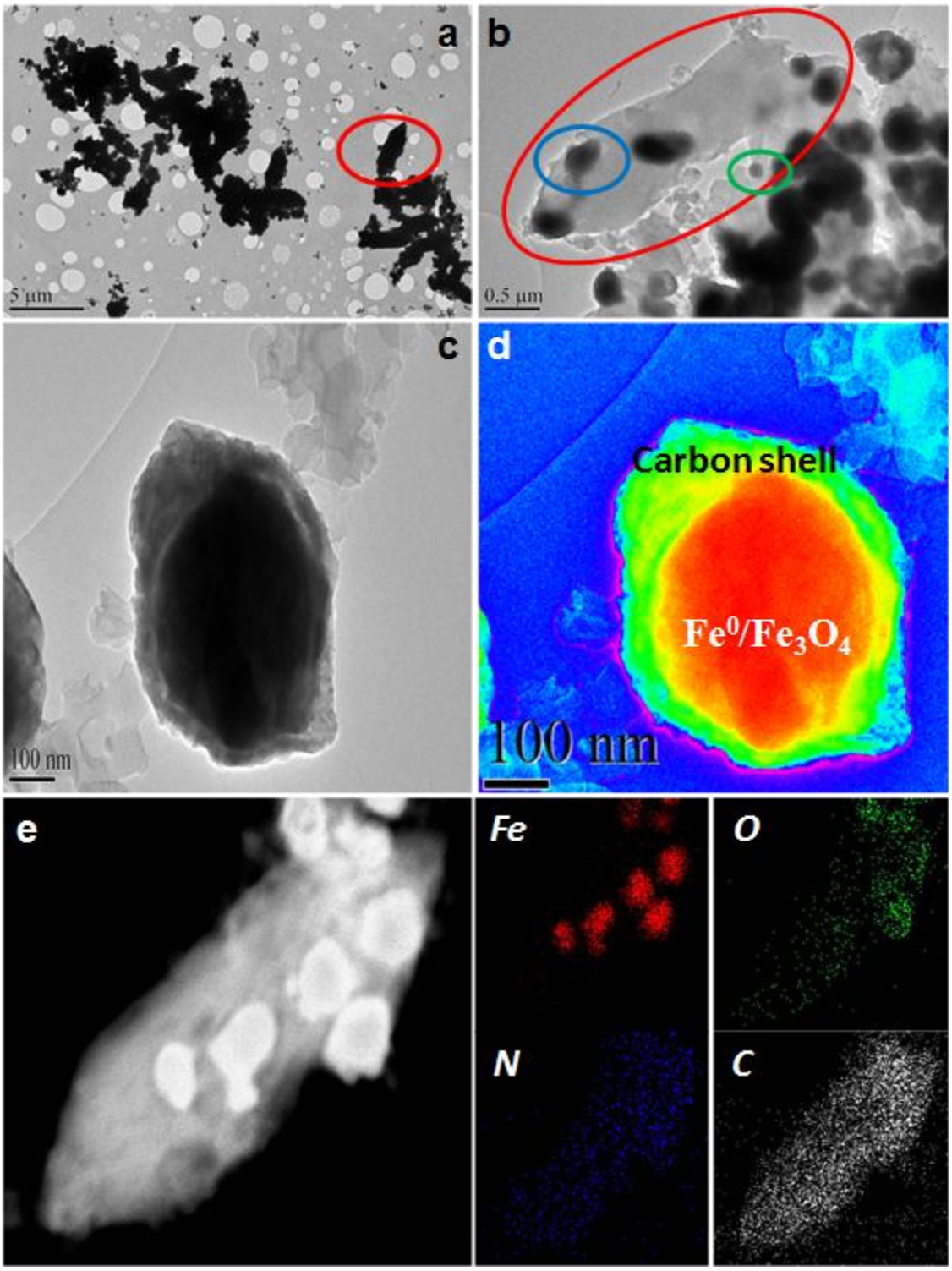

Fig. 2

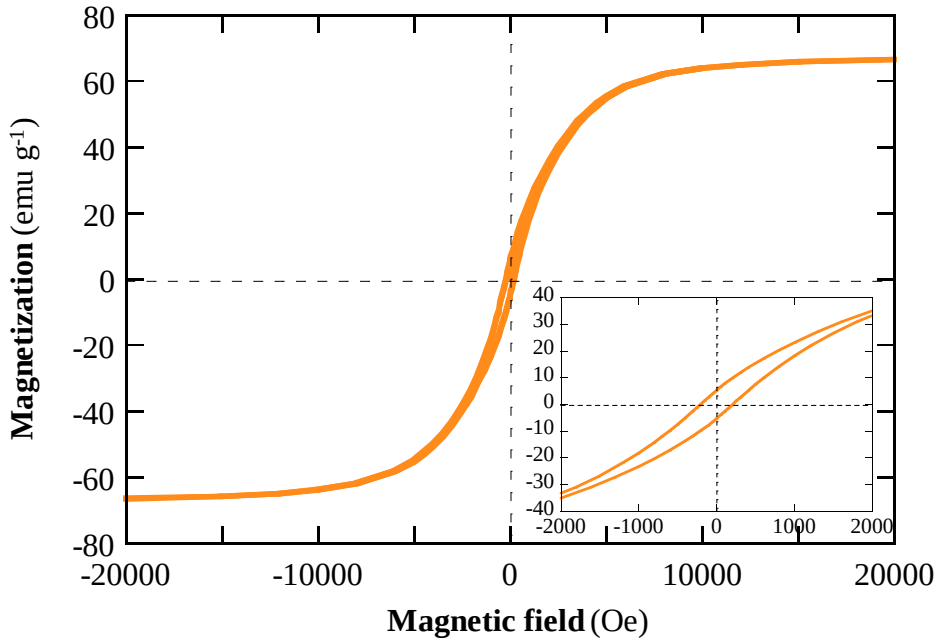
Magnetization (emu g-1)
Magnetic field (Oe)
80
60
40
20
0
-20
-40
-60
-80
-20000
-10000
0
10000
20000
40
30
20
10
0
-10
-20
-30
-40
-2000
-1000
0
1000
2000

Fig. 3

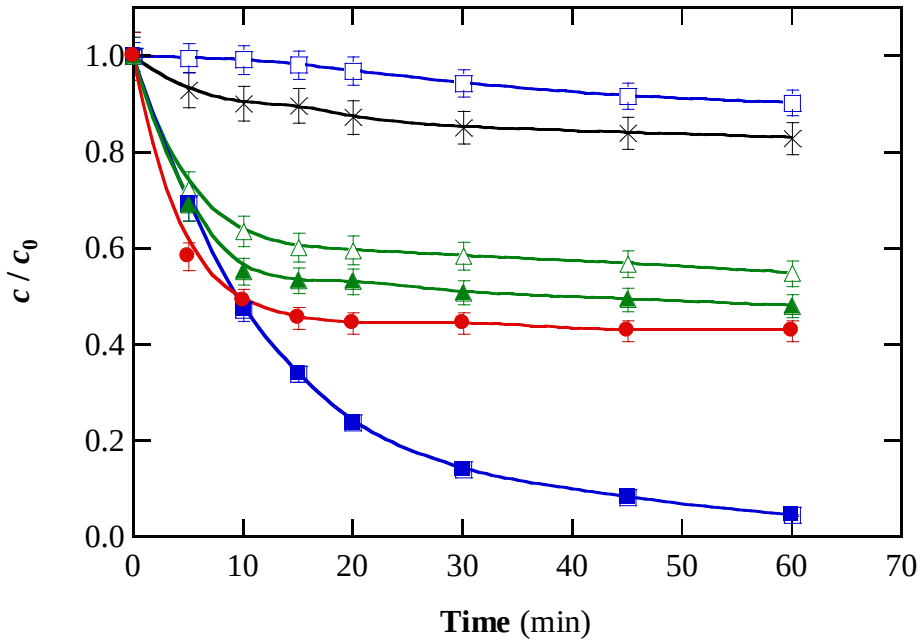

Fig. 4

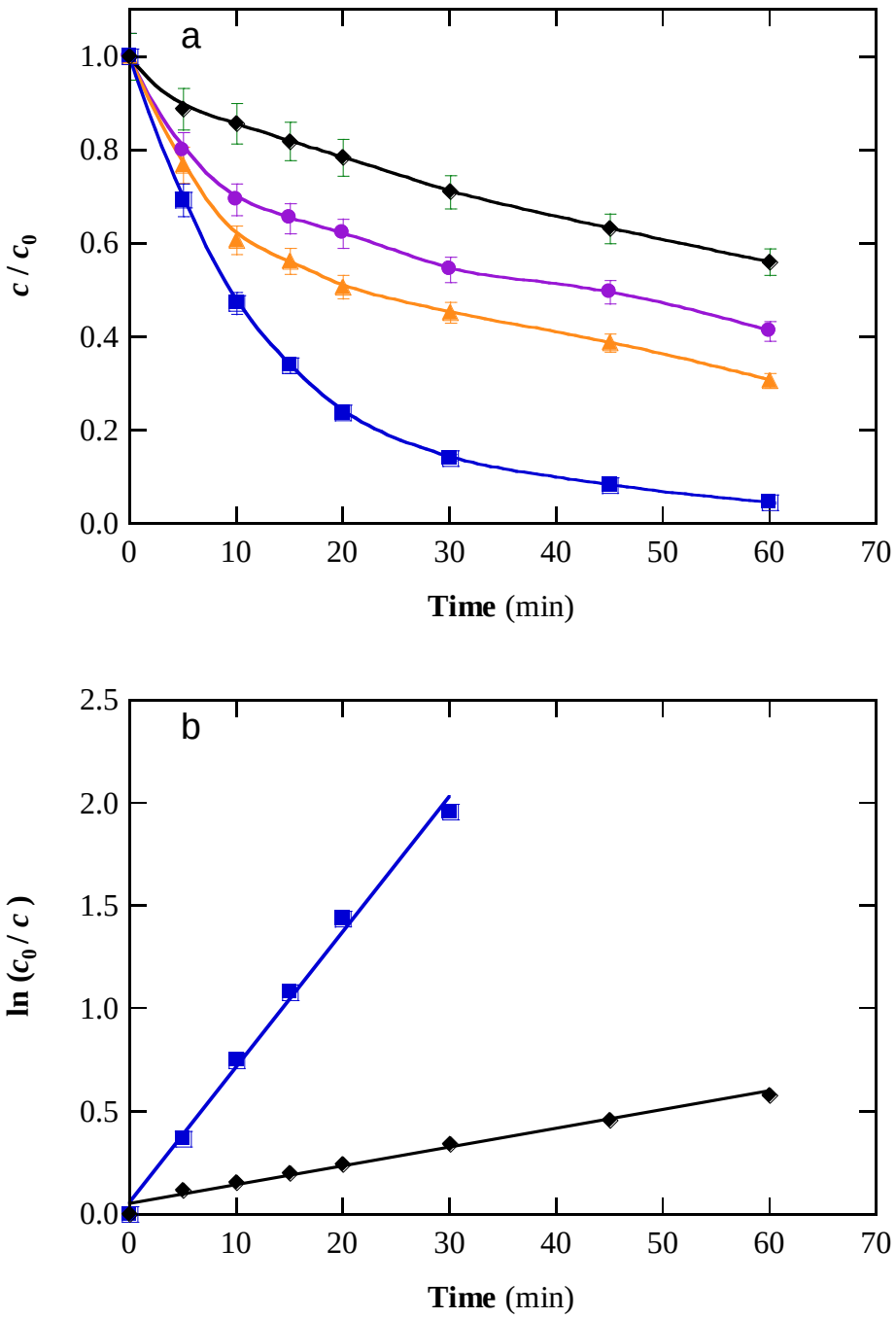
a
1.0
0.8
0.6
0.4
0.2
0.0
c / c0
0
10
20
30
40
50
60
70
Time (min)
b
2.5
2.0
1.5
1.0
0.5
0.0
ln (c0 / c)
0
10
20
30
40
50
60
70
Time (min)

Fig. 5

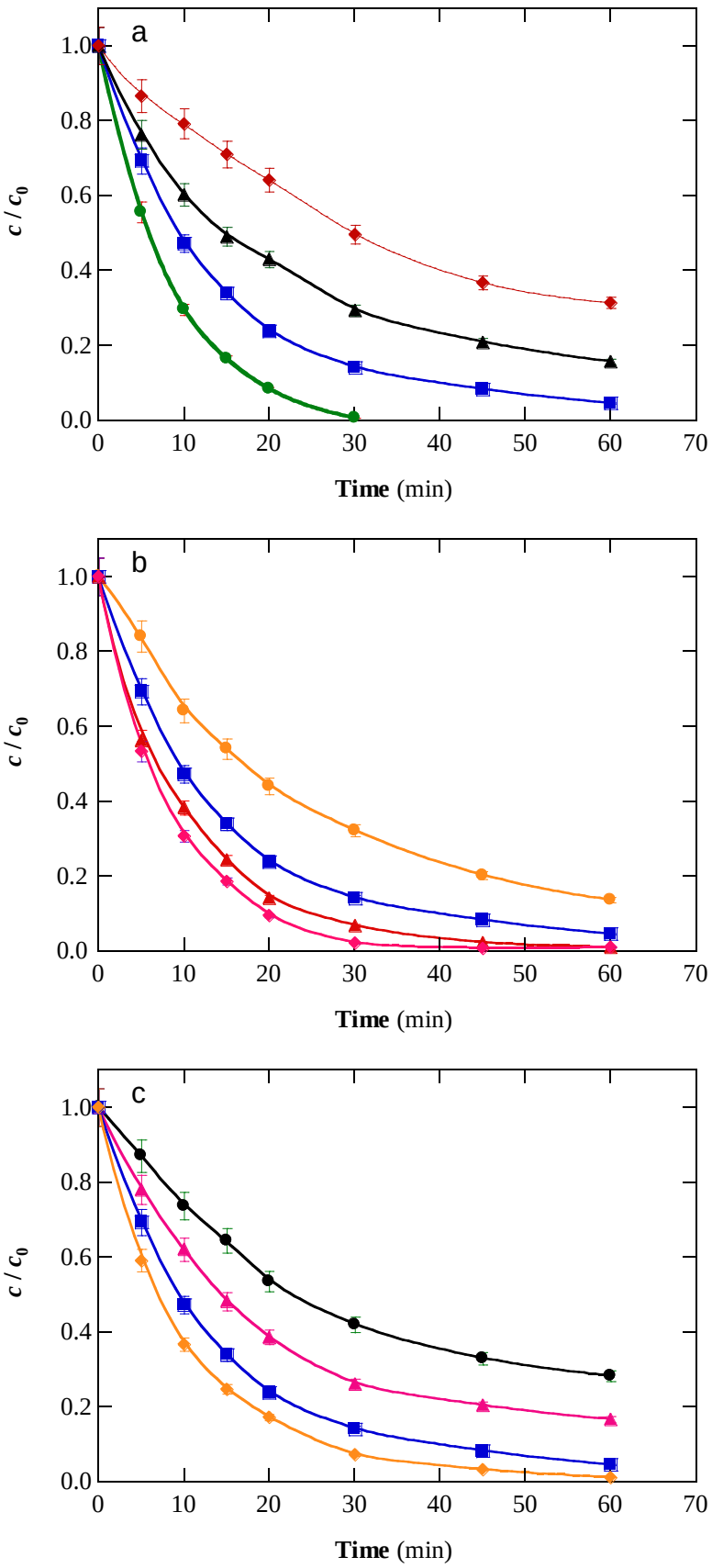

Fig. 6

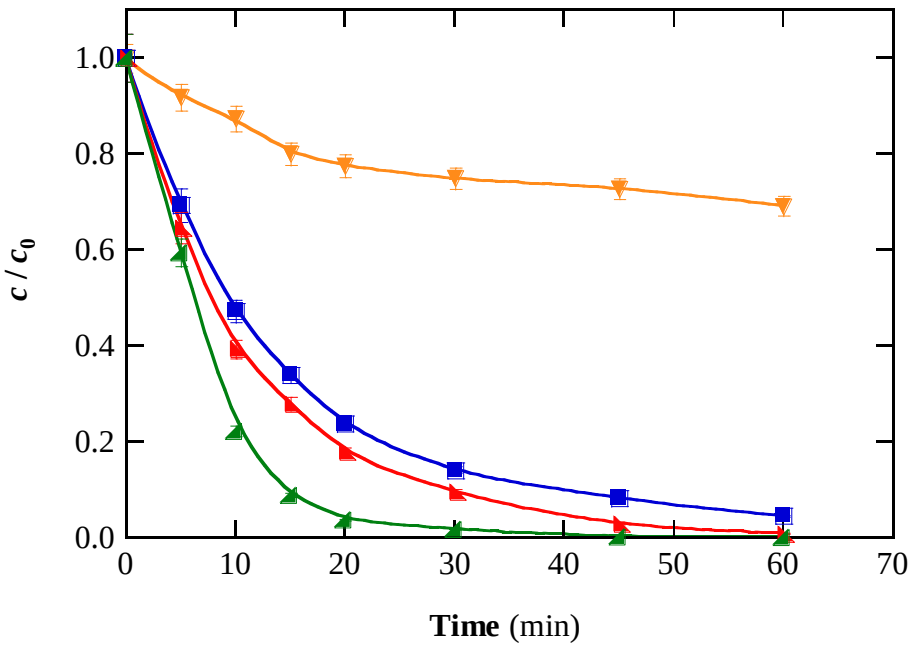

Fig. 7

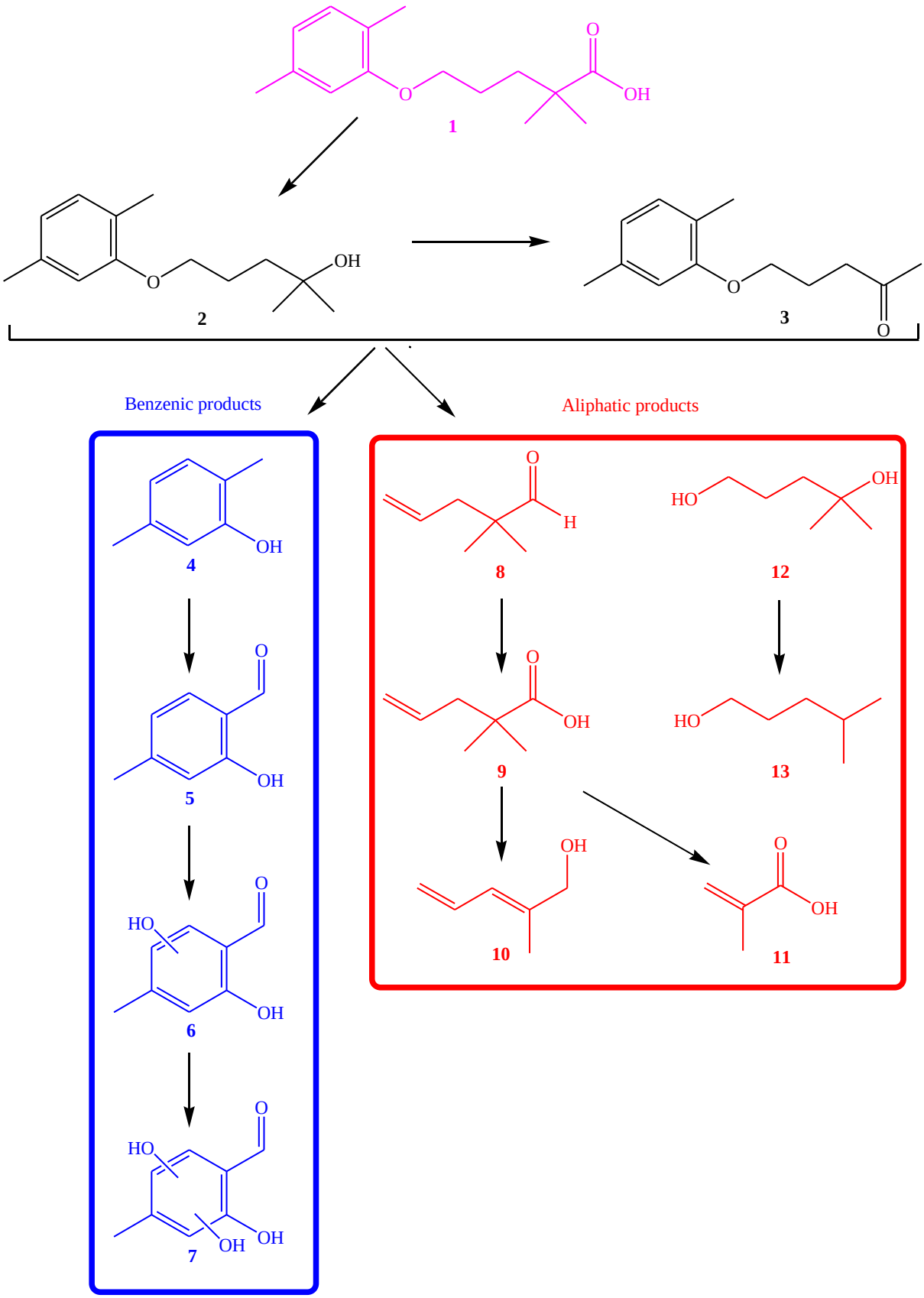
1
2
3
Benzenic products
Aliphatic products
4
5
6
7
8
9
10
11
12
13

Fig. 8

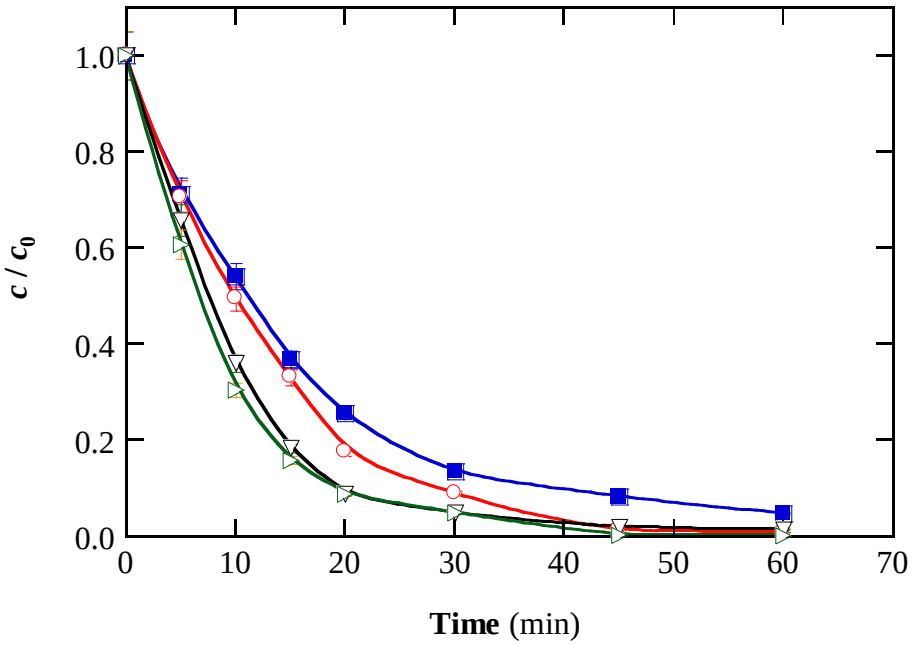

Fig. 9

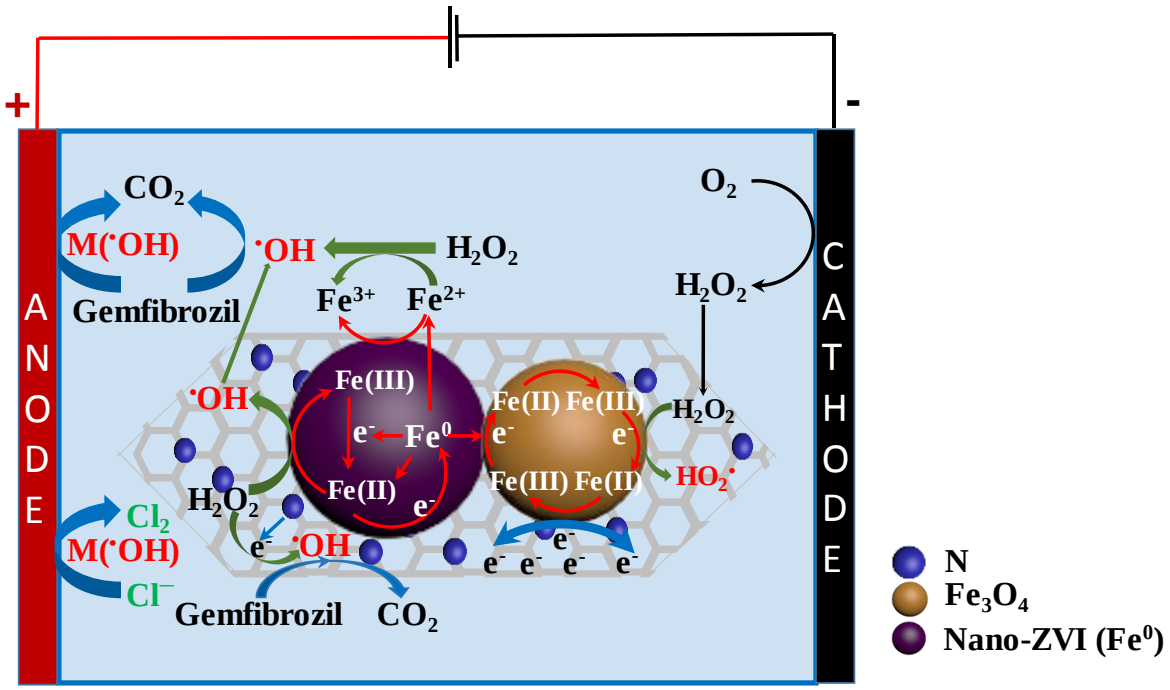
+
-
ANODE
CATHODE
CO2
M(•OH)
Gemfibrozil
•OH
H2O2
Fe3+
Fe2+
O2
H2O2
Fe(III)
Fe0
e-
Fe(II)
Fe(II) Fe(III)
Fe(III) Fe(II)
H2O2
HO2•
Cl2
M(•OH)
Cl−
Gemfibrozil
CO2
N
Fe3O4
Nano-ZVI (Fe0)

Fig. 10

Table 1.

Pseudo-first-order rate constants and *R*-squared values obtained for the gemfibrozil concentration decay during the EF treatment of 150 mL of drug solutions (10 mg C L^{-1}) in 0.050 M Na_2SO_4 at 35 ºC using an IrO_2/air-diffusion cell with a nano-ZVI@C-N catalyst synthesized by calcination at 800 ºC.

pH	*I* (mA)	[Catalyst] (g L^{-1})	k_1 (min^{-1})	R^2
3.0	50	0.2	0.1239	0.999
5.5 (natural)	25	0.2	0.0333	0.991
	50	0.05	0.0295	0.997
	50	0.1	0.0450	0.997
	50	0.2	0.0659	0.993
	50	0.3	0.0860	0.997
	75	0.2	0.0894	0.995
	100	0.2	0.1154	0.998
7.0	50	0.2	0.0400	0.989
9.0	50	0.2	0.0198	0.987

*Graphical Abstract

GRAPHICAL ABSTRACT

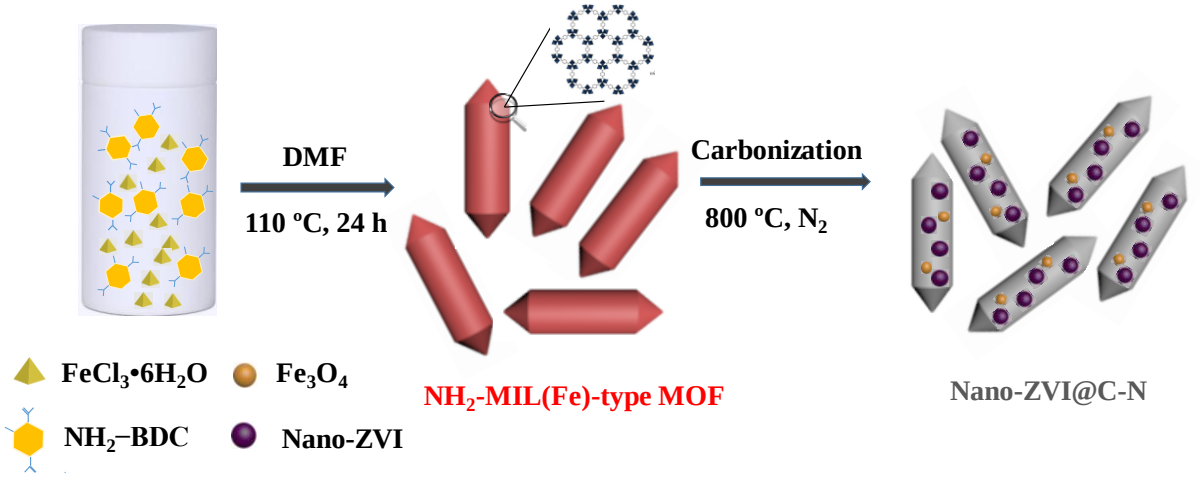

*Highlights (for review)

Research highlights

▶ Successful heterogeneous EF process at mild pH using MIL-88B-derived catalysts

▶ Magnetic N-doped nano-ZVI@C rods by pyrolysis: high activity, stability and recyclability

▶ Almost overall gemfibrozil degradation in raw urban wastewater with several pollutants

▶ Identification of 6 aromatic and 6 aliphatic products upon gemfibrozil degradation

▶ ZVI promoted continuous conversion of Fe(III) to Fe(II): heterogeneous Fenton's reaction

SUPPLEMENTARY MATERIAL

Magnetic MIL(Fe)-type MOF-derived N-doped nano-ZVI@C rods as heterogeneous catalyst for the electro-Fenton degradation of gemfibrozil in a complex aqueous matrix

Zhihong Ye [a], José A. Padilla [b], Elena Xuriguera [b], Enric Brillas [a], Ignasi Sirés [a,*]

[a] *Laboratori d'Electroquímica dels Materials i del Medi Ambient, Departament de Química Física, Facultat de Química, Universitat de Barcelona, Martí i Franquès 1-11, 08028 Barcelona, Spain*

[b] *DIOPMA, Departament de Ciència de Materials i Química Física, Facultat de Química, Universitat de Barcelona, Martí i Franquès 1-11, 08028 Barcelona, Spain*

*Corresponding author: *E-mail address*: i.sires@ub.edu (I. Sirés)

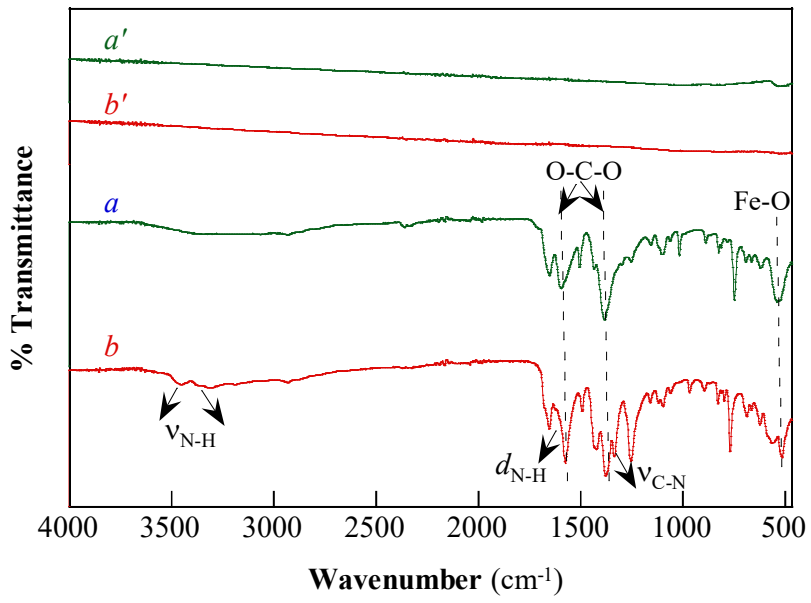

Fig. S1. FTIR spectra of the nano-ZVI@C (*a'*) and nano-ZVI@C-N (*b'*) catalysts obtained upon calcination at 800 ºC of the as-synthesized MIL(Fe)-type (*a*) and NH_2-MIL(Fe)-type MOFs (*b*), respectively.

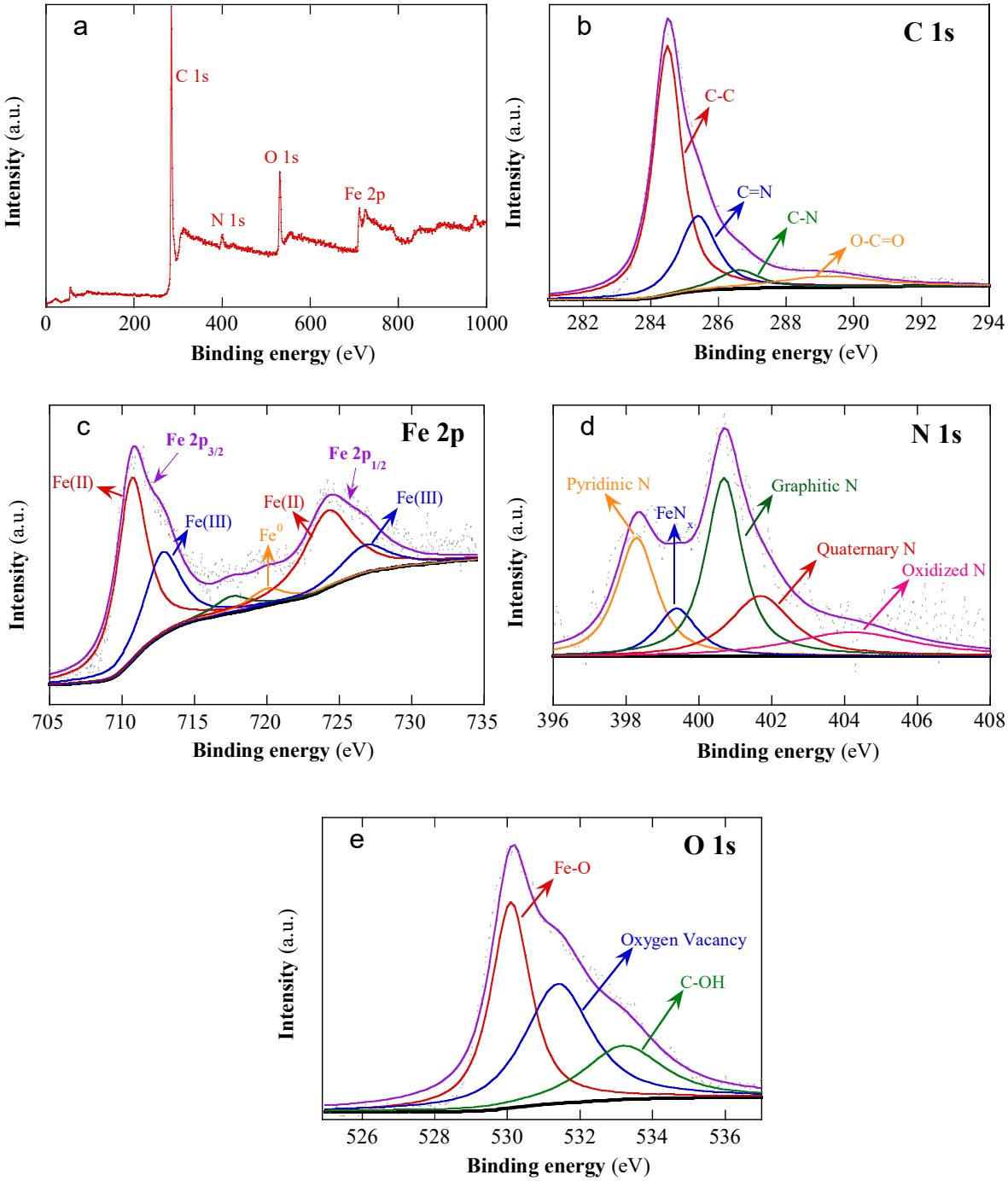

Fig. S2. (a) XPS general spectrum for the nano-ZVI@C-N catalyst obtained upon calcination at 800 ºC. The spectra of different elements present in the nanocatalyst are shown in: (b) C 1s, (c) Fe 2p, (d) N 1s and (e) O 1s.

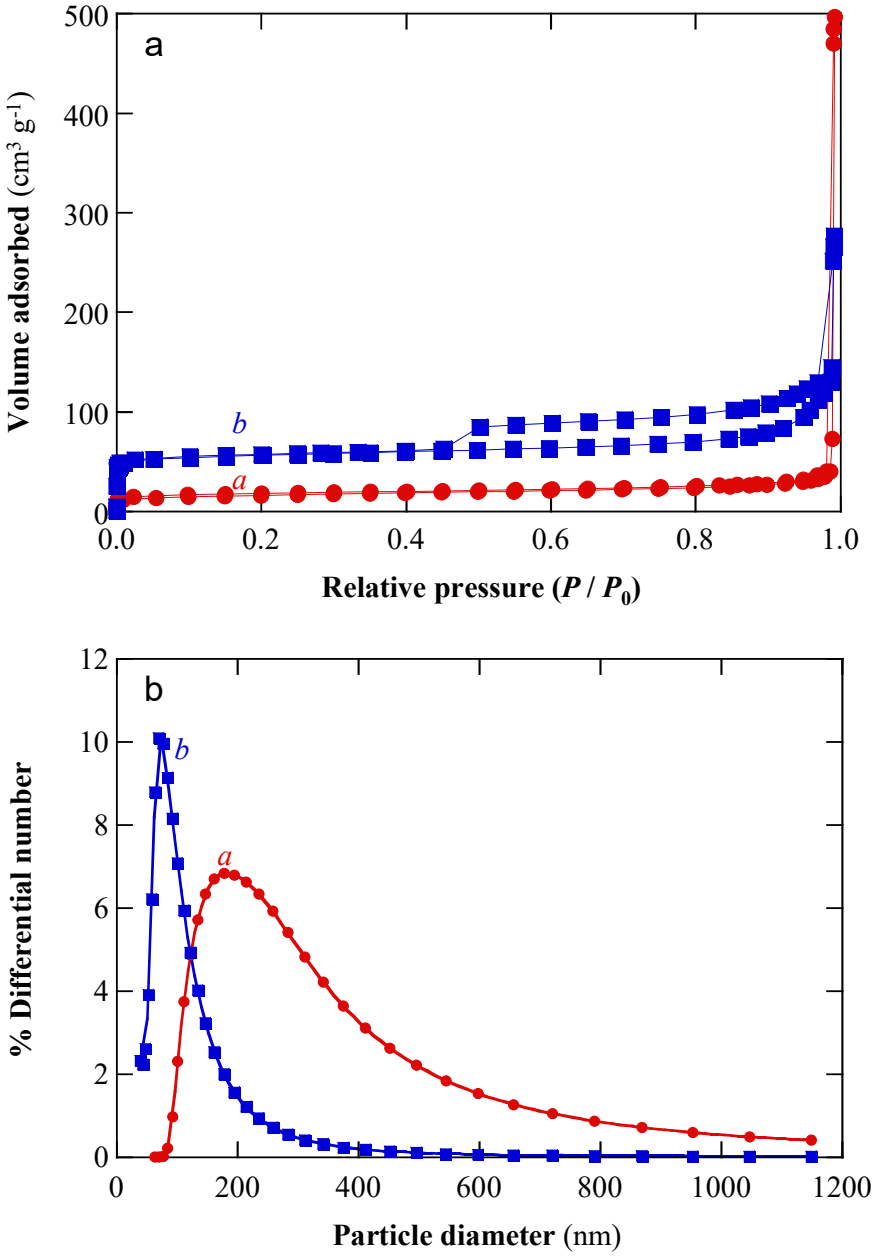

Fig. S3. (a) BET and (b) DLS analysis for the as-synthesized NH_2-MIL(Fe)-type MOF (*a*) and the nano-ZVI@C-N catalyst obtained upon calcination at 800 ºC (*b*).

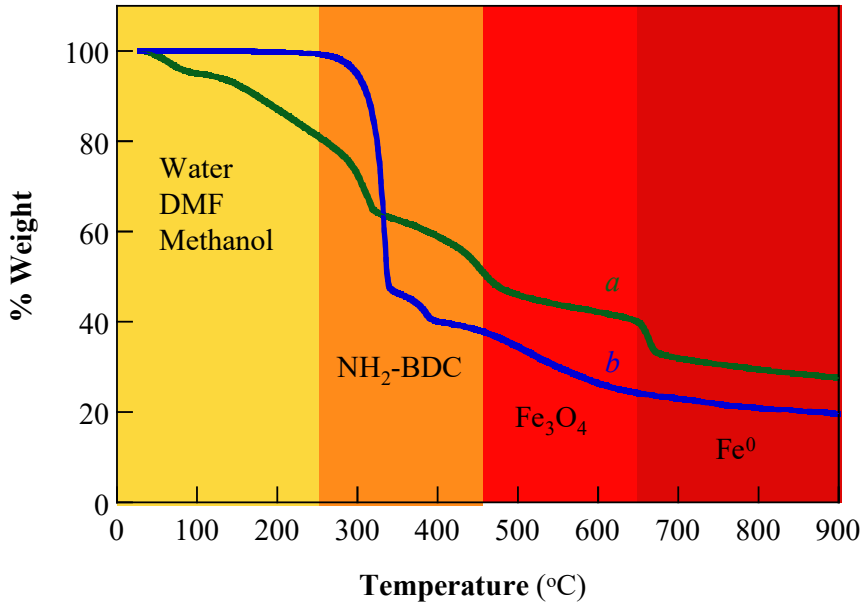

Fig. S4. TGA of the as-synthesized NH_2-MIL(Fe)-type MOF (*a*) and the NH_2-BDC precursor (*b*).

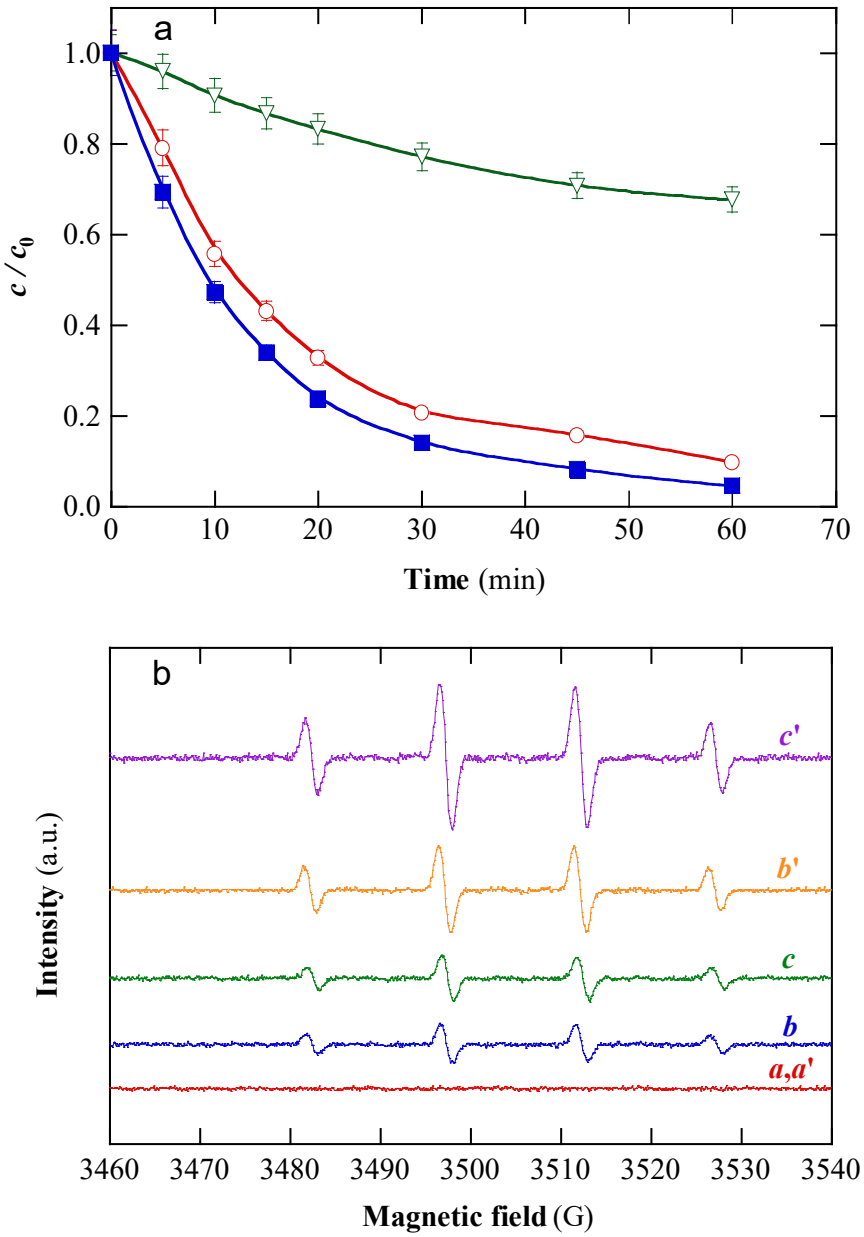

Fig. S5. (a) Time course of (■) normalized gemfibrozil concentration decay during the EF treatment with 0.2 g L^{-1} nano-ZVI@C-N catalyst shown in Fig. 4. The same experiment in the presence of a radical scavenger: (○) 2 mM *p*-benzoquinone ($O_2^{\bullet-}$ scavenger) or (▽) 20 mM *tert*-butanol ($^{\bullet}OH$ scavenger). (b) EPR spectra of the $^{\bullet}OH$-DMPO adduct at 0 min (*a*,*a*'), 10 min (*b*,*b*') and 30 min (*c*,*c*') of electrolysis for EF trials without scavenger using the nano-ZVI@C (*a*,*b*,*c*) or nano-ZVI@C-N catalyst (*a*',*b*',*c*').

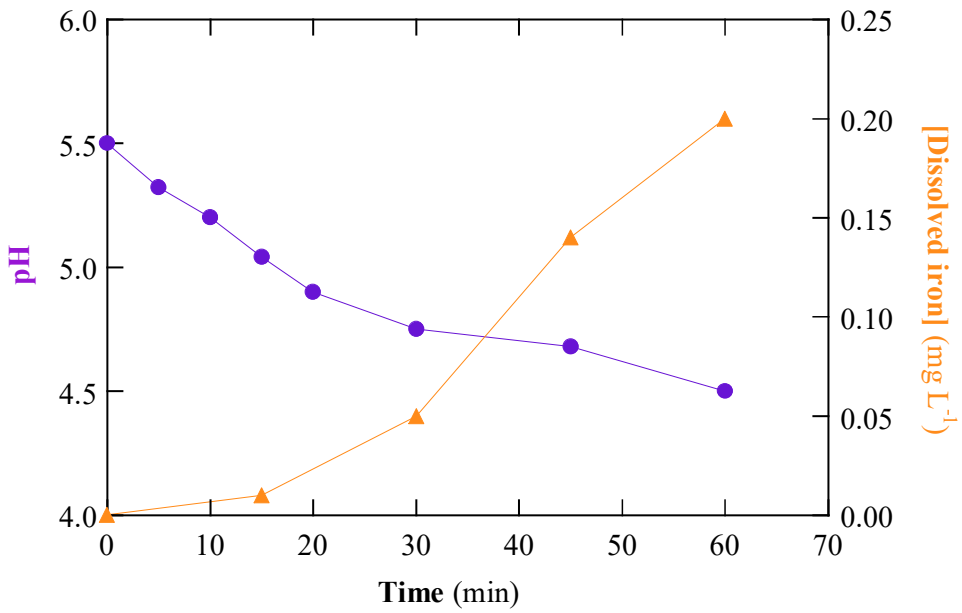

Fig. S6. Time course of (●) pH and (▲) iron concentration during the EF treatment with the nano-ZVI@C-N catalyst shown in Fig. 4.

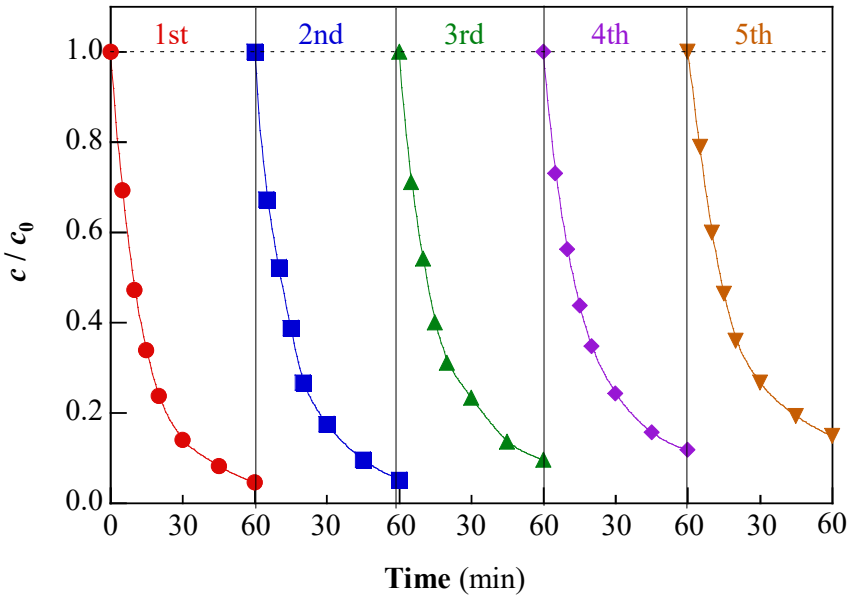

Fig. S7. Time course of normalized gemfibrozil concentration during the EF treatment with the nano-ZVI@C-N catalyst shown in Fig. 4 upon successive 60-min cycles (1st-5th).

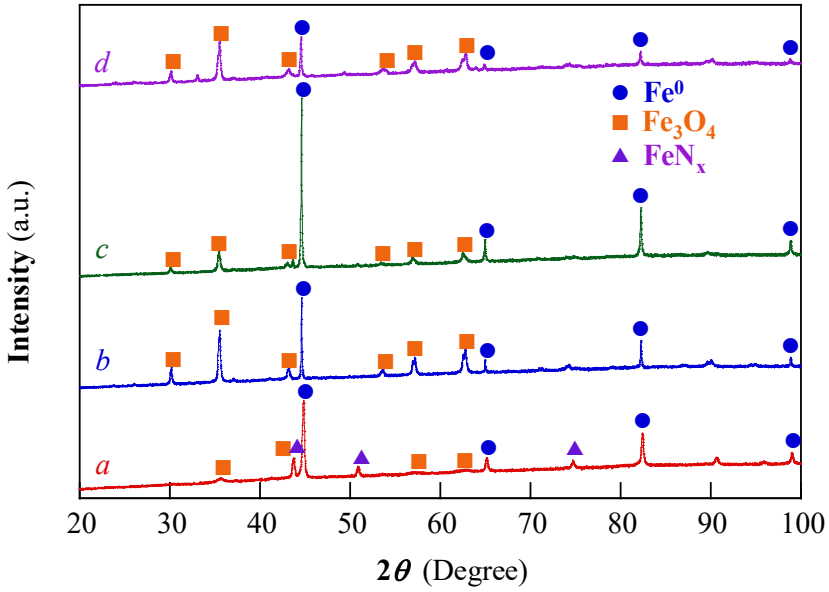

Fig. S8. XRD patterns of the nano-ZVI@C-N catalysts obtained upon calcination at 650 ºC (*a*), 700 ºC (*b*), 800 ºC (*c*) and 900 ºC (*d*).

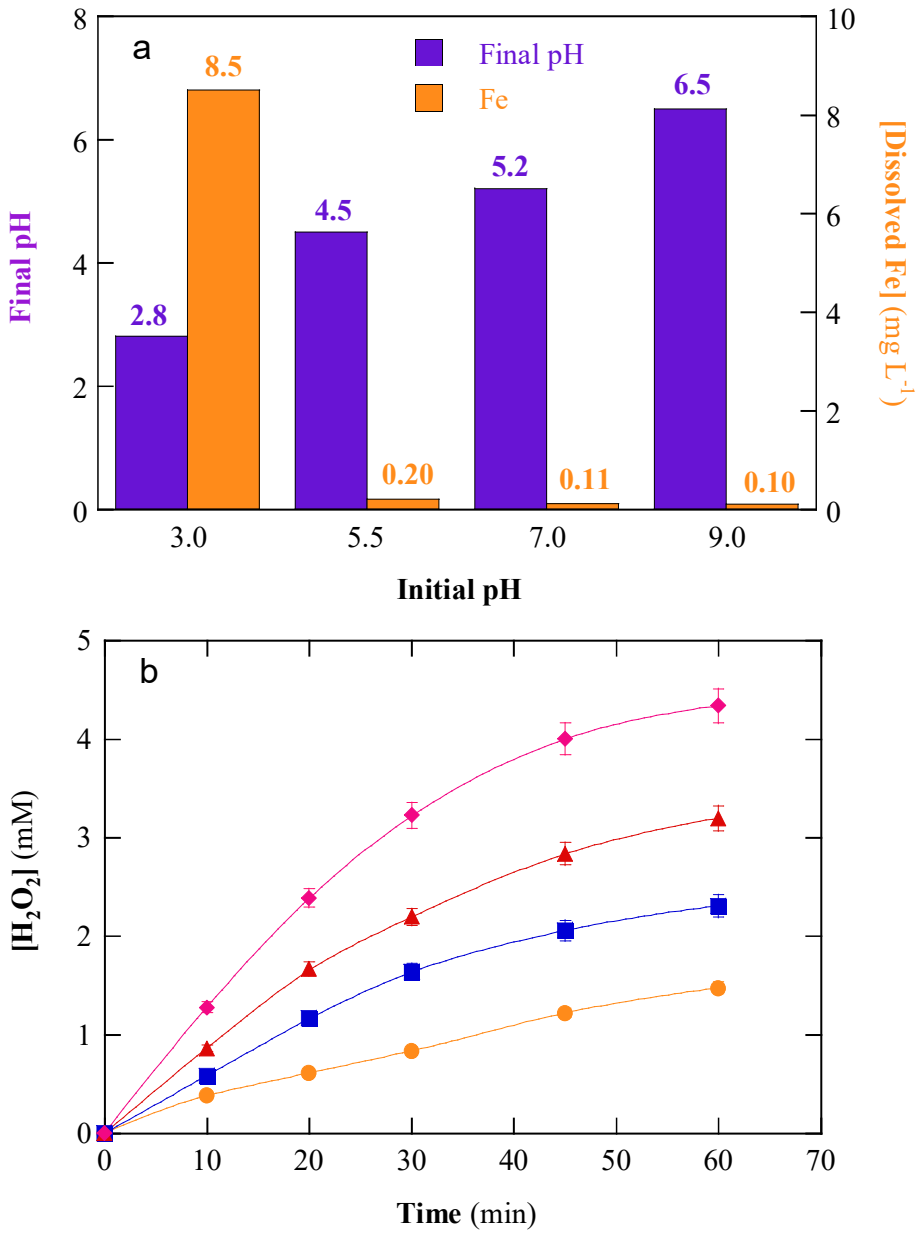

Fig. S9. (a) Solution pH and dissolved iron concentration after 60 min of the EF treatments shown in Fig. 6a. (b) Variation of electrogenerated H_2O_2 concentration with electrolysis time for the EF treatments shown in Fig. 6b, with applied current of: (●) 25 mA, (■) 50 mA, (▲) 75 mA and (◆) 100 mA.

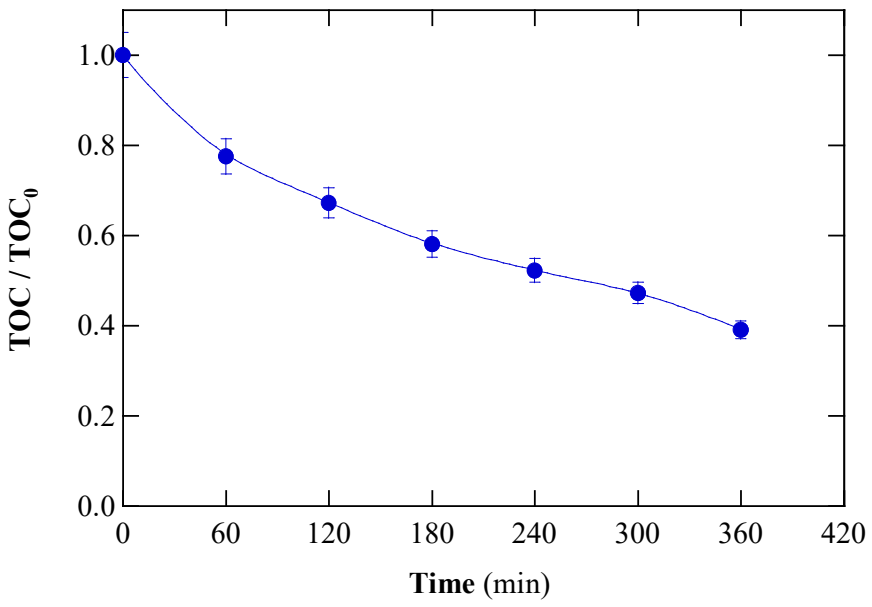

Fig. S10. Normalized TOC decay during the EF treatment with the BDD/air-diffusion cell shown in Fig. 7, but at I = 100 mA.

Table S1.

Main products detected by GC-MS after 30 min of EF treatment of gemfibrozil (10 mg C L^{-1}) in 0.050 M Na_2SO_4 at pH 5.5, 50 mA and 35 ºC using the BDD/air-diffusion cell and 0.2 g L^{-1} of the nano-ZVI@C-N catalyst synthesized by calcination at 800 ºC.

Number	Chemical name	Molecular structure	t_r (min)	Main fragment ions (*m/z*)
1	Gemfibrozil	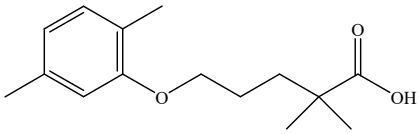	48.30	250,205,129, 122,107
2	5-(2,5-Dimethyl-phenoxy)-2-methyl-pentan-2-ol	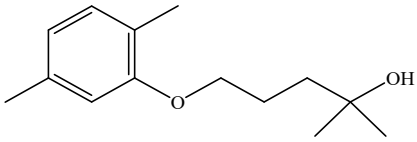	35.36	222,135,122, 107
3	5-(2,5-Dimethyl-phenoxy)-pentan-2-one	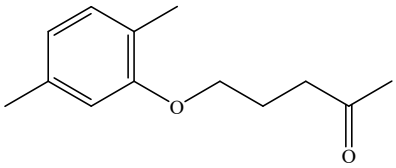	24.52	206,137,122,107
4	2,5-Dimethylphenol	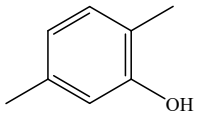	26.37	122,107,77
5	2-Hydroxy-4-methyl-benzaldehyde	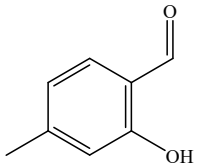	23.05	136,118,107,90,77
6	2-Hydroxy-4-methyl-benzaldehyde, monohydroxylated	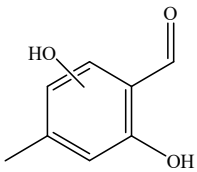	23.01	152,136,124, 107
7	2-Hydroxy-4-methyl-benzaldehyde, dihydroxylated	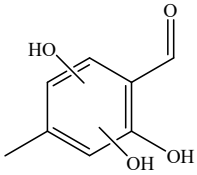	37.40	167,123,106

8	2,2-Dimethyl-pent-4-enal	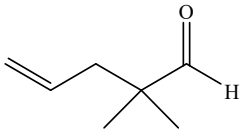	19.31	112,97,69,43
9	2,2-Dimethyl-pent-4-enoic acid	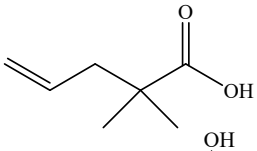	16.47	128,112,96,82
10	2-Methyl-penta-2,4-dien-1-ol	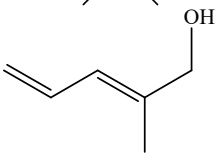	16.98	98,83,77,51
11	2-Methylacrylic acid	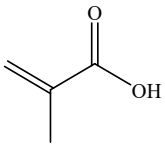	15.31	85,71,60,.43
12	4-Methyl-pentane-1,4-diol	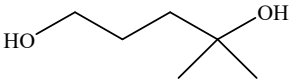	16.39	117,112,99,83, 70,57
13	4-Methyl-pentan-1-ol	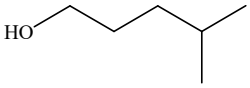	11.68	101,87,69,45

Appendix VII

The stability of an Fe-based 2D MOF during the photoelectro-Fenton treatment of organic micropollutants under UVA and visible light irradiation

Elsevier Editorial System(tm) for Water Research or its open access mirror
Manuscript Draft

Manuscript Number:

Title: The stability of an Fe-based 2D MOF during the photoelectro-Fenton treatment of organic micropollutants under UVA and visible light irradiation

Article Type: Research Paper

Keywords: Fe-bpydc; Heterogeneous photoelectro-Fenton; Metal-organic framework Pharmaceutical pollutants; Water treatment

Corresponding Author: Dr. Ignasi Sires, Ph.D.

Corresponding Author's Institution: Universitat de Barcelona

First Author: Zhihong Ye, PhD

Order of Authors: Zhihong Ye, PhD; Giulia E Schukraft, PhD; Anouk L´Hermitte, PhD; Ying Xiong, PhD; Enric Brillas, PhD; Camille Petit, PhD; Ignasi Sires, Ph.D.

Abstract: This work reports the novel application of an Fe-based 2D metal-organic framework (MOF), prepared with 2,2'-bipyridine-4,4'-dicarboxylate (bpydc) as organic linker, as highly active catalyst for heterogeneous photoelectro-Fenton (PEF) treatment of the lipid regulator bezafibrate in ultrapure water and urban wastewater. Well-dispersed 2D structures were successfully synthesized, thereby assessing their morphological, physicochemical and photocatalytic properties. UV/Vis-assisted PEF using an IrO2/air-diffusion cell with very low catalyst concentration (0.05 g L-1) outperformed electro-oxidation with electrogenerated H2O2, electro-Fenton and visible light-assisted PEF. Its excellent performance was due to: (i) the high tunability of the 2D structure, enhancing the mass transport and providing active sites for heterogeneous Fenton's reaction and in-situ conversion of Fe(III) into Fe(II); (ii) the role of photoinduced electrons to reduce H2O2 to *OH, and Fe(III) to Fe(II); (iii) and the enhanced charge transfer and excitation of Fe-O clusters, thus increasing the number of electron-hole pairs. The effective treatment of a mixture of four micropollutants spiked into urban wastewater revealed the great potential of (Fe-bpydc)-catalyzed PEF. LC-QToF-MS and GC-MS allowed the identification of 16 aromatic products and the elucidation of bezafibrate degradation route.

Suggested Reviewers: Abdoulaye Thiam Ph.D.
Professor, Universidad Tecnológica Metropolitana
layathiam@gmail.com
He is an expert in Fenton-based electrochemical processes

Francisco Alcaide Ph.D.
Senior researcher, CIDETEC Technological Center
falcaide@cidetec.es
He is an expert in electrochemical treatments with air-diffusion cathodes

Mehmet A Oturan Ph.D.

Professor, Université Paris-Est
mehmet.oturan@u-pem.fr
He is an expert in electro-Fenton process

José L Nava Ph.D.
Professor, Universidad de Guanajuato
jlnm@ugtomx.onmicrosoft.com
He is a specialist in the elecrochemical degradation of pharmaceuticals

Highlights

▶ Excellent catalytic activity of Fe-bpydc in PEF for organic micropollutants at mild pH

▶ Thorough investigation on the water stability and electronic structure of Fe-bpydc

▶ 16 Primary oxidation products detected by LC-QToF-MS and GC-MS

▶ Detailed mechanism for oxidizing radicals generation in (Fe-bpydc)-catalyzed PEF treatment

▶ Degradation routes for bezafibrate during the (Fe-bpydc)-catalyzed PEF process

Graphical Abstract

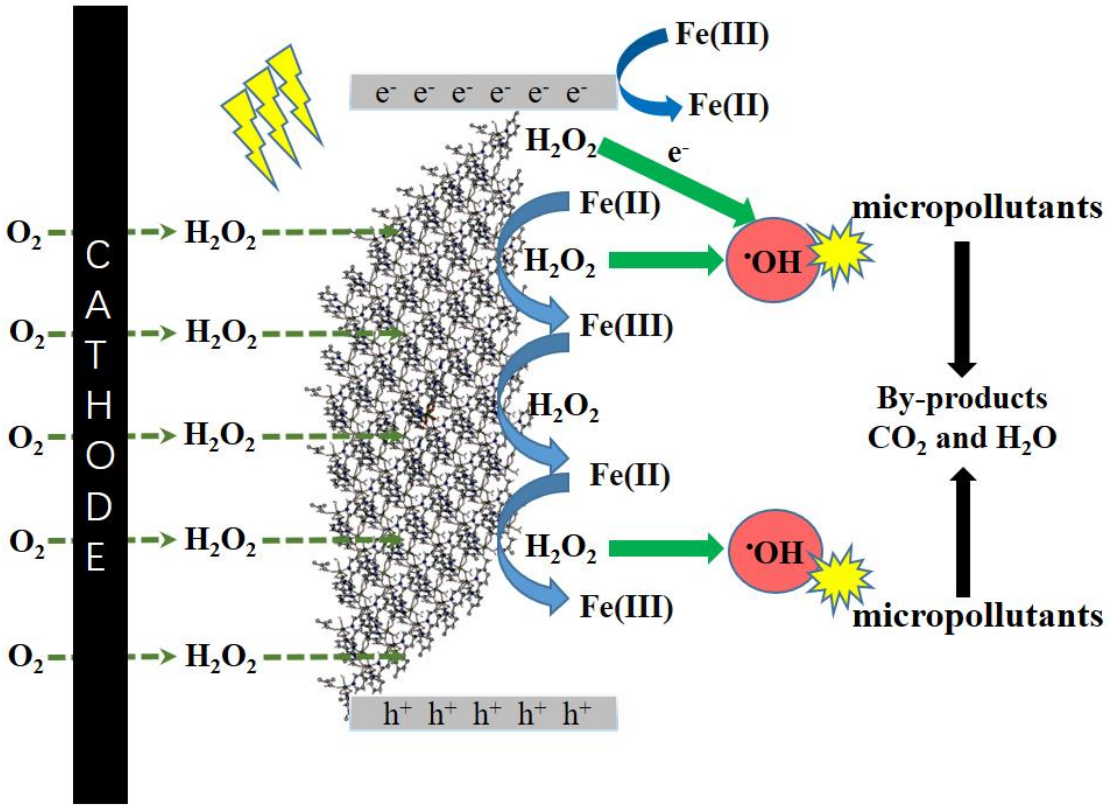

The stability of an Fe-based 2D MOF during the photoelectro-Fenton treatment of organic micropollutants under UVA and visible light irradiation

Zhihong Ye [1,2], Giulia E.M. Schukraft [2], Anouk L´Hermitte [2], Ying Xiong [2], Enric Brillas [1], Camille Petit [2,**], Ignasi Sirés [1,*]

[1] *Laboratori d'Electroquímica dels Materials i del Medi Ambient, Departament de Química Física, Facultat de Química, Universitat de Barcelona, Martí i Franquès 1-11, 08028 Spain*

[2] *Barrer Centre, Department of Chemical Engineering, Imperial College London, South Kensington Campus, London SW7 2AZ, UK*

* Corresponding author: i.sires@ub.edu (I. Sirés)

** Corresponding author: camille.petit@imperial.ac.uk (Camille Petit)

Abstract

This work reports the novel application of an Fe-based 2D metal-organic framework (MOF), prepared with 2,2'-bipyridine-4,4'-dicarboxylate (bpydc) as organic linker, as highly active catalyst for heterogeneous photoelectro-Fenton (PEF) treatment of the lipid regulator bezafibrate in ultrapure water and urban wastewater. Well-dispersed 2D structures were successfully synthesized, thereby assessing their morphological, physicochemical and photocatalytic properties. UV/Vis-assisted PEF using an IrO_2/air-diffusion cell with very low catalyst concentration (0.05 g L^{-1}) outperformed electro-oxidation with electrogenerated H_2O_2, electro-Fenton and visible light-assisted PEF. Its excellent performance was due to: (i) the high tunability of the 2D structure, enhancing the mass transport and providing active sites for heterogeneous Fenton's reaction and in-situ conversion of Fe(III) into Fe(II); (ii) the role of photoinduced electrons to reduce H_2O_2 to $^{\bullet}OH$, and Fe(III) to Fe(II); (iii) and the enhanced charge transfer and excitation of Fe-O clusters, thus increasing the number of electron-hole pairs. The effective treatment of a mixture of four micropollutants spiked into urban wastewater revealed the great potential of (Fe-bpydc)-catalyzed PEF. LC-QToF-MS and GC-MS allowed the identification of 16 aromatic products and the elucidation of bezafibrate degradation route.

Keywords: Fe-bpydc; Heterogeneous photoelectro-Fenton; Metal-organic framework Pharmaceutical pollutants; Water treatment

1. Introduction

The electrochemical advanced oxidation processes (EAOPs) constitute one the most attractive technologies for the treatment of persistent organic micropollutants in wastewater owing to their excellent efficiency, versatility and eco-friendliness (Brillas et al., 2009; Sirés et al., 2014; Zhou et al., 2018). Among them, electro-Fenton (EF) process is particularly prominent. The great effectiveness of EF arises from the production of hydroxyl radical ($^{\bullet}OH$) by Fenton's reaction (1), occurring between in-situ generated H_2O_2 from reaction (2) and added Fe^{2+} ions. In undivided cells, adsorbed hydroxyl radicals ($M(^{\bullet}OH)$) formed at the anode M from reaction (3) contribute to oxidation (Salmerón et al., 2019; Yang et al., 2019). Photoelectro-Fenton (PEF) process is a photo-assisted EF process induced by UV or sunlight illumination. UV photons can either photoexcite complexes of Fe(III) with organics like carboxylic acids by reaction (4), or photoreduce $[Fe(OH)]^{2+}$ species to regenerate Fe^{2+} with additional $^{\bullet}OH$ production by reaction (5) (Sirés and Brillas 2012; Brillas, 2014; Thiam et al., 2015; Ridruejo et al., 2017).

$$Fe^{2+} + H_2O_2 \rightarrow Fe^{3+} + {}^{\bullet}OH + OH^- \quad (1)$$

$$O_2(g) + 2\,H^+ + 2\,e^- \rightarrow H_2O_2 \quad (2)$$

$$M + H_2O \rightarrow M(^{\bullet}OH) + H^+ + e^- \quad (3)$$

$$Fe(OOCR)^{2+} + h\nu \rightarrow Fe^{2+} + CO_2 + R^{\bullet} \quad (4)$$

$$[Fe(OH)]^{2+} + h\nu \rightarrow Fe^{2+} + {}^{\bullet}OH \quad (5)$$

Although the fundamentals of homogeneous Fenton-based EAOPs have been extensively studied (Brillas et al., 2009; Martínez-Huitle et al., 2015; Moreira et al., 2017), major

challenges still hamper their implementation at industrial scale, such as: (i) the high effectiveness limited to pH ~3; (ii) the limited reusability of the catalyst; and (iii) the need of post-treatment iron sludge disposal and effluent neutralization (Ganiyu et al., 2018; Zhou et al., 2018). To overcome these handicaps, some approaches have been followed. For instance, homogeneous processes are feasible at higher pH upon use of soluble iron complexes like Fe(III)-EDDS as catalyst (Ye et al. 2019, 2020). However, heterogeneous EF and PEF seem a better choice and have gained wide acceptance owing to the feasible catalyst reusability and minimization of iron dissolution (Iglesias et al., 2015; Es'haghzade et al., 2017; Ganiyu et al., 2018; Poza-Nogueiras et al., 2018). Raw or synthetic iron-based materials are used as catalysts, including zero-valent iron (Zhou et al., 2018), minerals like iron oxides (Meijide et al., 2019), iron-rich clays (Özcan et al., 2017) and iron-loaded structures like zeolites or resins (Rostamizadeh et al., 2018). However, their morphological, physicochemical and catalytic properties usually vary significantly depending on the source or the synthesis procedure. Moreover, they show a limited Fe(III)/Fe(II) cycling, which decelerates Fenton's reaction (1) (Zhu et al., 2019). Thus, the technological development of heterogeneous EF and PEF demands the exploration of new types of catalysts.

Recently, metal-organic frameworks (MOFs) have attracted great attention due to their unique properties like porous crystallinity. These novel materials are composed of metal ions as nodes and organic linkers forming crystalline structures to build one-, two- and three-dimensional (1D, 2D and 3D) lattices (Silva et al., 2015; Liu et al., 2019). MOFs are superior to other porous materials because of their high tunable porosity, versatile functionality,

changeable structure and open metal sites (Li et al., 2019). These properties contribute to their wide applications in diverse areas such as gas storage (Cao et al., 2017), sensing (Feng et al., 2019), separation (Van de Voorde et al., 2014), drug delivery (Chen et al., 2018), catalysis (Zhang and Lin, 2014) and environmental remediation (Sharma and Feng, 2019). Fe-MOFs are of interest in AOPs due to the Fe(III)-Fe(II) interconversion and photosensitive iron-oxo (Fe-O) clusters (Sharma and Feng, 2019). Lately, several 3D Fe-based MOFs, mainly of the MIL (Metal Institute Lavoisier) family, have been developed as efficient catalysts in heterogeneous Fenton and photo-Fenton processes (Gao et al., 2017; Tang and Wang, 2018; Ahmad et al., 2019). However, the decomposition of MOFs within the field of water treatment has not been sufficiently considered yet, and their used in EF and PEF has been scarcely described.

2D MOFs usually exhibit remarkable properties such as numerous exposed active sites and small diffusion barrier for molecules, then favoring their potential application to catalysis (Bai et al., 2019). To our knowledge, the use of 2D Fe-MOFs as heterogeneous EF or PEF catalysts has never been reported, and only a small number of them or their derivatives have been tested in Fenton and photo-Fenton systems (Li et al., 2016, 2018; Hou et al., 2019). Using 2,2'-bipyridine-5,5'-dicarboxylate (bpydc) as linker, the resulting Fe-bpydc exhibits high catalytic activity for H_2O_2 activation at near-neutral pH (Li et al., 2016).

This article proposes, for the first time, the novel use of a very low amount of an Fe-bpydc 2D MOF as heterogeneous PEF catalyst under illumination with UV or visible light. The electronic structure of the catalyst and the performance of the heterogeneous PEF treatment of bezafibrate were thoroughly evaluated. This is a top-selling fibrate drug that lowers cholesterol

and triglycerides, with an extensive production and prescription in the entire world (Yin et al., 2020). Due to its hard removal by conventional wastewater treatment, it has been detected in wastewater, surface water, groundwater or even drinking water, at concentrations up to 4.6 μg L^{-1} (Sui et al., 2017; Shi et al., 2018). The chronic effects and ecological risk potential of bezafibrate pose serious threats to humans and ecosystems (Rivas et al., 2019; Solís et al., 2019; Ding et al., 2020), then being required its removal from the aquatic environment.

Bezafibrate solutions in ultrapure water and urban wastewater at natural pH has been treated with an (Fe-bpydc)-catalyzed PEF system using an IrO_2/air-diffusion cell. Initial pH, applied current (*I*) and catalyst dosage were optimized from bezafibrate content decay. Oxidation products were detected by gas chromatography-mass spectrometry (GC-MS) and liquid chromatography quadrupole time-of-flight mass spectrometry (LC-QToF-MS), allowing the proposal of a degradation pathway. The physicochemical properties and electronic structure of Fe-bpydc were studied by a variety of techniques. The stability of Fe-bpydc and its recyclability in PEF process were also investigated, and a thorough mechanism for (Fe-bpydc)-catalyzed PEF treatment of bezafibrate is proposed.

2. Experimental

2.1. Chemicals

Bezafibrate was purchased from Sigma-Aldrich. Sodium sulfate, sulfuric acid (96-98% solution) and sodium hydroxide pellets were of analytical grade from Merck. $Fe(ClO_4)_2$ and dimethylformamide (DMF) from Sigma-Aldrich, along with 2,2'-bipyridine-5,5'-dicarboxylate

(bpydc) from T.C.I., all of analytical grade, were employed for the Fe-bpydc synthesis. Analytical grade $TiOSO_4$ from Sigma-Aldrich was used for H_2O_2 determination. Analytical grade 5,5-dimethyl-1-pyrroline-N-oxide (DMPO) from Sigma-Aldrich was employed for electron spin resonance (ESR) analysis. All the other chemicals were of analytical or HPLC grade supplied by Merck and Panreac. All synthetic solutions were prepared with Millipore Milli-Q water (resistivity > 18.2 MΩ cm). The urban wastewater was collected from the secondary clarifier of a wastewater treatment facility located near Barcelona and its main characteristics are detailed in Text S1.

2.2. Synthesis of the catalyst

Fe-bpydc was prepared via a hydrothermal method according to a previous report slightly modified (Li et al., 2016). Briefly, 0.5 mmol of bpydc was dissolved in 40 mL DMF, then added to 40 mL of an aqueous solution with 1 mmol of $Fe(ClO_4)_2$. The mixture was sonicated for 20 min to obtain a homogeneous solution and subsequently heated in an oil bath at 120 ºC under vigorous stirring for 4 h. After cooling, the red-brown solid product was separated by filtration, washed with ethanol several times and dried overnight in an oven at 60 °C.

2.3. Catalyst characterization

The morphology of the synthesized Fe-bpydc was observed by field-emission scanning electron microscopy (FESEM) using a JEOL JSM7001F microscope. The X-ray diffraction (XRD) analysis was made with a PANalytical X'Pert PRO MPD Alpha-1 diffractometer, using Cu $K_{\alpha 1}$ radiation (λ = 1.54178 Å and operating at 40 kV and 20 mA in the range of 5-50°. X-ray photoelectron spectroscopy (XPS) for elemental analysis was performed in an ultrahigh

vacuum spectrometer (Text S2). Thermogravimetric analysis (TGA) was carried out with a Netzsch TG 209 F1 Libra instrument between 20 and 900 ºC at a heating rate of 10 ºC min^{-1} under N_2 atmosphere; meanwhile, the temperature was maintained at 120 ºC for 40 min. Nitrogen adsorption and desorption isotherms were measured using a Micrometrics 3Flex sorption analyzer at -196 ºC. DR-UV/Vis spectroscopy was measured using an Agilent Cary 500 UV–Vis-NIR spectrometer equipped with an integrating sphere. Attenuated total reflection Fourier transform-infrared (FT-IR) spectra were collected using an Agilent Technologies Cary 630 FTIR at room temperature. ESR spectra were obtained with a Bruker ESP300E spectrometer at room temperature, using DMPO as $^{\bullet}OH$ spin trap (Text S3).

2.4. Electrochemical systems

All the experiments were performed in an undivided glass cell containing 150 mL of contaminated solution, termostated at 25 ºC under vigorous magnetic stirring. The anode was either a 3 cm^2 IrO_2-based or Ru_2O-based plate purchased from NMT Electrodes or a 3 cm^2 boron-doped diamond (BDD) thin film supplied by NeoCoat. The cathode was a 3 cm^2 commercial carbon-PTFE from BASF, mounted as reported before (Steter et al., 2016) and fed with compressed air pumped at 1 L min^{-1} for continuous H_2O_2 electrogeneration. The interelectrode gap was close to 1.0 cm. Before first use, a polarization in a 0.05 M Na_2SO_4 solution at 100 mA cm^{-2} for 180 min allowed the simultaneous activation of the anode and cathode. In photocatalysis and PEF trials, the solution was irradiated with a Xe arc lamp (150 W or 300 W, $\lambda > 325$ nm,) purchased from LOT Quantum Design, placed at 5 cm above the liquid surface. A UV filter (400FH90-50S) with a cut-off value of 400 nm was equipped for visible light

catalytic reactions.

2.5. Analytical procedures

The electrical conductance of the raw urban wastewater was determined with a Metrohm 644 conductometer. The pH was measured with a Crison GLP 22 pH-meter. Prior all the analyses, samples were filtered with PTFE syringe filters from Whatman. The concentration of H_2O_2 accumulated during the electrochemical assays was determined by the colorimetric titanate method using a Shimadzu 1800 UV/Vis spectrophotometer set at $\lambda = 408$ nm and 25 °C (Welcher, 1975). The concentration of cations in the real wastewater and total dissolved iron during the trials was determined by inductively coupled plasma optical emission spectroscopy (ICP-OES) using an Optima 3200L spectrometer from Perkin Elmer. The TOC content of the samples was immediately measured after collection, using a Shimadzu TOC-VCSN analyzer with the non-purgeable organic content method, which yielded values with ±1% accuracy. A Shimadzu TNM-1 unit coupled to such analyzer allowed the determination of total nitrogen (TN).

Bezafibrate concentration was measured on a reversed-phase HPLC equipped with a Luna C18 3 μm, 100 mm×4.6 mm, column at 30 °C and a SPD-20A detector set at 210 nm. A 40:55:5 (v/v) acetonitrile, acetic acid in water (0.02%) and methanol mixture was used as the mobile phase eluted at 10 mL min^{-1}. The peak of bezafibrate appeared at 6.8 min. Before analysis, the samples were always diluted with acetonitrile to stop the degradation of bezafibrate.

Organic products accumulated during the electrochemical treatment of bezafibrate were identified by GC-MS and LC-QToF-MS, as stated in TexT S4.

3. Results and discussion

3.1. Characterization of Fe-bpydc catalyst

The morphology of the as-synthesized catalyst was first examined by FESEM. Fig. 1a and b display 2D irregular-shaped plates with size up to dozens of microns, whereas the thickness of the sheets ranged from hundreds nanometers to few micrometers, suggesting a co-existence of single and multiple layered structures. The lateral or vertical expansion of the 2D sheet structure concomitantly induces the formation of many open pores, which significantly enhance the mass transport (Kondo et al., 2006). The XRD pattern depicted in Fig. 1c confirms the highly crystalline structure of the as-synthesized Fe-bpydc, in good agreement with the simulated one (Finn and Zubieta, 2002; Li et al., 2016), suggesting the successful catalyst preparation. The poorly defined reflection observed at $2\theta \sim 35.7^{o}$ was related to the typical peak of iron oxide (JCPDS 89-0596), whose presence is probably due to the surface oxidation occurring during the synthesis. The simulated pattern calculated from CIF file using Mercury software also verified the structure of Fe-bpydc. As can be seen in Fig. 1d, the asymmetric unit of Fe-bpydc consists of one iron ion, one η^2-carboxylate, one η^1-carboxylate, two nitrogen donors, one coordinated and one lattice water molecules. The six-coordinate geometry of iron is defined by the two oxygen donors of an η^2-carboxylate of a bpy-dicarb ligand, one oxygen of an η^1-carboxylate of a second bpy-dicarb ligand, two nitrogen donors of a third cheating bpy-dicarb ligand and one oxygen of the terminal H_2O ligand (Finn and Zubieta, 2002). The carboxylate groups and N atoms of the bpy-dicarb ligands bridge alternately the adjacent iron centers to form layered 2D metal-organic network, and the H_2O ligands projected into the interlamellar region can be hydrogen-bonded to

the pendant carboxylate groups, providing further extension of the 2D plates (Finn and Zubieta, 2002; Zhang et al., 2016). This explains the multi-layered structures observed in FESEM images. The empirical formula of Fe-bpydc can then be proposed as $[Fe(C_{12}H_8N_2O_4)(H_2O)]\cdot H_2O$ with a molecular weight of 334 g mol^{-1}. The TGA curve of this material, shown in Fig. 1e, reveals a mass loss of ~10% during the constant heating at 120 °C, corresponding to the elimination of the coordinated and lattice water (10.7%, as calculated from the empirical formula) (Zhang et al., 2016). The dehydrated sample remained stable up to ~500 °C, whereupon it was decomposed. Moreover, the TGA curve of bpydc indicated that this organic linker was only stable up to ~300 °C.

The surface composition of Fe-bpydc was further analyzed by XPS. Fig. S1 highlights the presence of C, O, N and Fe elements. In the high resolution Fe 2p XPS spectrum of Fig. 2a, both the Fe $2p_{3/2}$ and Fe $2p_{1/2}$ bands consisted of two peaks. The fitting peaks located at 710.8 and 724.1 eV corresponded to Fe(II), whereas peaks appearing at 714.0 and 726.8 eV can be assigned to Fe(III) (Su et al., 2014). The existence of Fe(III) is due to the expected oxidation occurring during the synthesis, consistent with the XRD results. The high-resolution spectrum of N 1s of Fig. 2b clearly shows a single peak at 400.0 eV, corresponding to pyridinic N (Guo et al., 2013), in agreement with the structure of the as-synthesized Fe-bpydc (Fig. 1d). N-doping is another interesting feature of the synthesized catalyst, since it is expected to enhance the electron transfer and catalytic activity (Yang et al., 2019). The specific surface area and the pore structures of the Fe-bpydc samples were determined using N_2 adsorption−desorption measurements, which are depicted in Fig. S2. As can be seen, the Fe-bpydc particles exhibited

type I isotherm without a discernible hysteresis loop, which can be associated to the existence of uniform micropores in the structure (Tang and Wang, 2018). The specific BET surface area and total pore volume of the as-prepared Fe-bpydc were 14.53 m^2 g^{-1} and 0.036 cm^3 g^{-1}, respectively.

3.2. Catalytic properties of Fe-bpydc

Fig. 3a shows the degradation of 0.044 mM (10 mg C L^{-1}) bezafibrate in 0.050 M Na_2SO_4 at natural pH ~ 5.1 upon the application of different treatments. As can be seen, the presence of 0.05 g L^{-1} Fe-bpydc in the solution yielded negligible bezafibrate removal (5%) due to its poor adsorption capacity. A poor drug decay (7%) can also be observed by UV/Vis photocatalysis, which suggests that the photogenerated holes were not strong enough to directly oxidize bezafibrate, and the valence band (VB) position of Fe-bpydc cannot reach the oxidation potential of the $H_2O/^{\bullet}OH$ pair (see subsection 3.5), thus impeding the formation of $^{\bullet}OH$ from photoinduced water oxidation. In addition, this result informs about the stability of bezafibrate to direct photolysis under UV/Vis light irradiation. A small drug abatement of 27% was obtained after 90 min of electro-oxidation with electrogenerated H_2O_2 (EO-H_2O_2, without catalyst), as expected from the low oxidation ability of H_2O_2 and $IrO_2(^{\bullet}OH)$ produced from reactions (2) and (3), respectively (Sirés et al., 2014; Martínez-Huitle et al., 2015). In contrast, heterogeneous EF catalyzed with 0.05 g L^{-1} Fe-bpydc achieved substantial removal of 42% at 90 min thanks to the formation of $^{\bullet}OH$ from Fenton's reaction (1), confirming the hight catalytic activity of Fe-bpydc. The degradation in PEF under visible light illumination was clearly superior to that achieved in EF, attaining 55% removal in 90 min. This proves that Fe-bpydc can be a promising visible

light photocatalyst due to the direct excitation of the Fe-O cluster, since the photogenerated electrons may play an important role in the reduction of Fe(III) and the activation of H_2O_2 to form $^{\bullet}OH$ (Cheng et al., 2018). Unfortunately, the fast electron hole recombination rate on the photocatalyst still largely limited the bezafibrate removal efficiency. When the UV/Vis assisted PEF system was applied, the drug degradation was extraordinarily improved and clearly outperformed all the other treatments, showing a drug disappearance of 92% in 90 min. This outstanding result can be accounted for by: (i) the high absorbance of Fe-bpydc within the UV region; (ii) the enhanced generation of electron/hole pairs; and (iii) the UV photoreduction of the Fe(III) complex. In traditional homogeneous PEF, the photochemically active range is restricted to the UVA region, since these kinds of photons are able to promote reactions (4) and (5), thus regenerating Fe(II) and forming an additional amount of $^{\bullet}OH$ (Brillas, 2014; Brillas and Sirés 2015; Zhou et al., 2018). The introduction of Fe-bpydc as heterogeneous PEF catalyst allows the further utilization of visible light and the synergistic effect of photocatalysis and Fenton's reaction (1), accelerating the formation of $^{\bullet}OH$ to degrade bezafibrate.

Fig. S3 highlights a gradual H_2O_2 accumulation up to 14.8 mM in EO-H_2O_2, which decreases to 10.8 mM in Fe-bpydc catalyzed EF, due to its additional removal from Fenton's reaction (1). This content decreased largely up to 8.0 mM upon UV/Vis illumination in (Fe-bpydc)-catalyzed PEF mainly because the photogenerated electron/hole pairs accelerated the Fe(II) regeneration and H_2O_2 decomposition (Li et al., 2017).

The effect of light intensity was further investigated by employing 150 and 300 W Xe arc lamps. Fig. 3b shows that the visible light-assisted PEF under 300 W illumination yielded 87%

drug decay, which clearly outperformed that obtained with the 150 W lamp. This confirmed the promising visible light photocatalytic activity of Fe-bpydc. In addition, a very fast and complete drug degradation can be observed with the 300 W lamp under UV/Vis irradiation. This may be explained by the larger number of photons reaching the suspension per unit area, as the light intensity was increased, resulting in a faster degradation (Tokumura et al., 2008). The UV/Vis irradiation then showed a remarkable superiority as compared to visible light in the (Fe-bpydc)-catalyzed PEF, providing a greater photon energy that enhanced the charge transfer and promoted the Fe(III)/Fe(II) cycling (Zhao et al., 2017). However, the quick removal of bezafibrate at 300 W would entail a much higher operation cost. For this reason, subsequent studies were conducted under UV/Vis light irradiation with the 150 W lamp.

The effect of initial pH, applied current, catalyst dosage, anode and electrolyte on the normalized bezafibrate concentration decay upon heterogeneous PEF treatment with Fe-bpydc is shown in Fig. 4a-e. As can be observed in Fig. 4a, the degradation efficiency of bezafibrate was enhanced at more acidic initial pH, although the treatment was valid within all the pH range 3.0-9.0. Thus, overall disappearance was achieved in 90 min at initial pH 3.0, decreasing gradually down to 58% at pH 9.0. This loss of performance can be ascribed to the decrease of the oxidation potential of $^{\bullet}OH$, which changed from ~2.8 to 1.9 V when pH increased from 3.0 to 7.0 (Zhu et al., 2018). It should be stressed that 92% and 82% drug removal still can be achieved within 90 min at initial pH 5.1 and 7.0, respectively, implying the relatively high catalytic activity of Fe-bpydc at near-neutral pH.

Fig. 4b depicts the decrease of solution pH in all cases, owing to the generation of acidic

products like carboxylic acids (Borràs et al., 2011). Fig. 4b also reveals the slightly higher dissolved iron concentration at initial pH 3.0, which promoted the occurrence of homogeneous Fenton's reaction (1). However, the reusability may decrease because of the decomposition of Fe-bpyc under such conditions.

Fig. 4c evidences the positive contribution of increasing current, being more significant from 50 to 150 mA, giving rise to greater H_2O_2 electrogeneration that leads to a higher $^{\bullet}OH$ concentration. As expected, Fig. 4d corroborates that a larger amount of catalyst progressively from 0.0125 to 0.075 g L^{-1} allowed a substantial rise in the degradation efficiency (from 58% to 96%). This can be attributed to the larger amount of active sites available due to the larger number of Fe-bpydc plates, allowing more efficient collisions with the pollutant and H_2O_2 molecules (Soon and Hameed, 2013). However, no significant enhancement of bezafibrate decay can be observed in Fig. 4d after 90 min when comparing the trials with 0.05 and 0.075 g L^{-1} catalyst, probably because of the parasitic reaction between $^{\bullet}OH$ and the excess of Fe(III) or Fe(II). Note that the catalyst dosage used in this study was 8-20 times less than that reported in 3D MOF-catalyzed Fenton systems (Li et al., 2017; Tang and Wang, 2018). This means that the unique 2D structure of Fe-bpydc provided more active sites that ended in a more efficient mass transport (Bai et al., 2019). A low catalyst dosage is usually preferred for industrial application due to several advantages such as lower operation cost, easy recovery of catalyst and good light penetration through the suspension (Soon and Hameed, 2013).

Fig. 4e evidences that the degradation profile of the drug in a 0.041 M Na_2SO_4 + 0.009 M $NaHCO_3$ mixture with the IrO_2 anode at natural pH ~ 8.0 was much slower, achieving only 39%

abatement at 90 min. This can be attributed to the fact that CO_3^{2-} and HCO_3^- ions act as radical scavengers via reactions (6) and (7) (Bianco et al., 2017). When BDD with 0.050 M Na_2SO_4 was used, the decay profiles were exactly the same. This confirms that the dominant contribution to bezafibrate abatement came from $^{\bullet}OH$ generated in the bulk via Fenton's reaction (1), rather than from M($^{\bullet}OH$) at the anode surface. The trial with RuO_2 anode in 0.025 M Na_2SO_4 and 0.035 M NaCl medium gave the quickest bezafibrate decay, which could be due to its partial oxidation by active chlorine generated at the RuO_2 surface and $Cl^{\bullet}$ formed via reaction (8) (Ye et al., 2016; Steter et al., 2016).

$$^{\bullet}OH + CO_3^{2-} \rightarrow CO_3^{\bullet-} + OH^- \qquad k_2 = 4.0\times10^8\ M^{-1}\ s^{-1} \qquad (6)$$

$$^{\bullet}OH + HCO_3^- \rightarrow CO_3^{\bullet-} + H_2O \qquad k_2 = 8.5\times10^6\ M^{-1}\ s^{-1} \qquad (7)$$

$$HClO + h\nu \rightarrow {}^{\bullet}OH + Cl^{\bullet} \qquad (8)$$

3.3. Stability and reusability of Fe-bpydc

One critical issue in the practical application of MOFs is their lack of stability in water, which attacks the metal nodes displacing ligands and causing phase changes, loss in crystallinity and decomposition destroying the porosity of the materials (Taylor et al., 2012). Nevertheless, the decomposition of MOFs in water has been scarcely studied during wastewater remediation. The oxidative resistance of the pyridine ring to $^{\bullet}OH$ and its strong binding affinity with Fe(II) ion are key reasons for using bipyridine as ligand (Han et al., 2013). The introduction of carboxylic groups to the 2,2´-bipyridine ligand can stabilize the final products, because the carboxyl group could bind with Fe(III) ion in the catalytic cycle, thus avoiding its hydrolysis (Cheng et al., 2018). The reusability of catalytic Fe-bpydc was evaluated

from successive bezafibrate degradation trials. Fig. 5a shows a small but progressive performance loss of 30% as maximal after 3 cycles of 90 min. The turnover frequency (TOF) to evaluate the catalytic efficiency of active sites was calculated as follows (Li et al., 2019):

$$\mathrm{TOF} = \frac{n_p}{n_c\, t} \qquad (9)$$

where n_p is the mole of pollutants removed, n_c is the mole of catalyst and t is the reaction time (h). The TOF value after 3 cycles reached 0.161 h^{-1}, outperforming the value of MIL(Fe)-101 (Lv et al., 2015) but being lower than that of MIL(Fe)-88 A as Fenton catalysts (Liao et al., 2019). This proves the high catalytic activity of Fe-bpydc, but the considerable decrease in removal rate after three cycles (see Fig. 5a) suggests a slight deactivation of Fe-bpydc in water.

Further characterization of used catalyst was performed to assess the chemical and structure changes. The XRD patterns of Fig. 5b and FTIR spectra in Fig. S4 of fresh and used Fe-bpydc show a very stable crystalline and chemical structure along the treatment, without any evidence of alteration. The catalyst deactivation might be rather related to the blockage of its active sites by intermediates, as suggested elsewhere (Li et al., 2016). The significant exposure of active sites derived from the 2D structure also leads to greater blockage risk.

The assessment of the stability of Fe-bpydc in water was conducted by dosing 0.05 g L^{-1} of catalyst in Milli-Q water. The dissolved iron and TOC release vs. time at different initial pH values are displayed in Fig 5c and d. Quite fast decomposition of Fe-bpydc can be observed at initial pH 3.0, reaching 1.5 mg L^{-1} iron (~18 wt%) and 4.2 mg L^{-1} TOC leaching in 90 min. These results indicate the intolerance of Fe-bpydc to acidic condition because of the interactions of iron with H^+ (Laipan et al., 2016). Conversely, only ~0.8 mg L^{-1} iron (~9%) was leached when pH

increased to 5.1 and 7.0, revealing much higher stability of Fe-bpydc at near-neutral pH. Fortunately, the typical pH of urban wastewater and effluents from public facilities is usually higher than 6.0 (Ganiyu et al., 2018) and then, Fe-bpydc can be a promising heterogeneous PEF catalyst for wastewater treatment. Note that TOC detected from the dissolution of ligands may compete with bezafibrate and its products to react with $^{\bullet}$OH.

3.4. Mineralization and degradation of micropollutants in urban wastewater

A longer trial was performed to assess the mineralization ability of heterogeneous PEF treatment with 0.05 g L^{-1} catalyst using a BDD anode and applying I = 100 mA, in order to enhance the degradation ability of the system. As shows Fig. S5, 61% TOC was abated after 240 min of electrolysis, a value much higher than found for other MOFs in heterogeneous Fenton (Lv et al., 2015; Tang and Wang, 2017) as a result of the synergistic oxidation effect of bulk $^{\bullet}$OH formed from Fenton's reaction (1) and adsorbed BDD($^{\bullet}$OH) generated at the anode surface. Despite this, a relatively high residual TOC was still present in the final solution, which can be accounted for by the accumulation of refractory oxidation products, like carboxylic acids, as well as deactivation of Fe-bpydc catalyst. Moreover, the release of ligands also contributes to additional residual TOC since the pyridine ring and carboxylic groups from the ligands show high resistance to $^{\bullet}$OH.

The performance of the Fe-bpydc catalyzed PEF system was evaluated from the destruction of other micropollutants like bisphenol A, fluoxetine and naproxen, mixed in stripped urban wastewater at natural pH 7.2. The concentration decay of each compound is presented in Fig 6, where 93%, 85% and 78% degradation can be observed for naproxen,

fluoxetine and bisphenol A, respectively, in 90 min. The bezafibrate abatement of 61% was lower than 92% found in 0.050 M Na_2SO_4. This slower decay can be related to the presence of natural organic matter (NOM), in the wastewater that competitively consumed UV photons and reacted with $^{\bullet}OH$ (Ye et al., 2020). The lower transparency of the urban wastewater and its higher initial pH are two additional factors that affected negatively to bezafibrate decay. From these results, one can infer the validity of this new heterogeneous PEF system for real wastewater treatment.

3.5. Proposed reaction mechanism for heterogeneous PEF and bezafibrate degradation pathway

To ascertain the mechanism for (Fe-bpydc)-catalyzed heterogeneous PEF process, ESR analysis with DMPO as spin-trap was performed to detect the reactive oxygen radicals (ROS) generated. The ESR spectra depicted in Fig. S6 exhibit the four characteristic peaks of DMPO-$^{\bullet}OH$ adduct with an intensity ratio of 1:2:2:1, indicating the dominant role of $^{\bullet}OH$ in the PEF system.

The optical absorption and energy band gaps of Fe-bpydc were also ascertained to gain more insight into the reactions involved. Fig. S7a evidences that Fe-bpydc exhibited a broad adsorption in the UV/Vis region (200-800 nm). The Kubelka-Munk formula was used to convert the data into a Tauc plot (Fig. S7b) to estimate the band gap energy (E_g) of 2.1 eV, according to the procedure by Crake et al. (2019). Valence band XPS (VB-XPS) was recorded to determine the band position of Fe-bpydc. The spectrum of Fig. S7c shows an energy difference of 1.7 eV between the VB energy level (E_{VB}) and the Fermi energy level (E_f). The absolute value of the work function (E_Φ), corresponding to the energy difference between

Fermi and vacuum levels, was estimated as 3.7 eV from photoemission spectroscopy (photon energy of 33.2 eV, Fig. S7d) and excitation energy from XPS analysis (29.5 eV). Thus, the VB level (vs. vacuum level) was determined as -5.4 eV. Taking into account that 0 V vs. SHE is equivalent to -4.44 eV vs. vacuum, the latter value corresponded to a E_{VB} = 0.96 V as electrochemical energy potential. The conduction band energy E_{CB} (= $E_{VB} - E_g$) was then estimated as -1.14 V.

From the aforementioned findings, the mechanism of the boosting catalytic activity of Fe-bpydc in PEF system is proposed in Fig. 7. The photoinduced electrons (e^-) and holes (h^+) are generated upon the excitation of Fe-O clusters by UV/Vis illumination from reaction (10). In the absence of H_2O_2, the photogenerated holes (h^+) cannot oxidize H_2O to yield $^{\bullet}OH$ as the oxidation potential of $H_2O/^{\bullet}OH$ (2.8 V vs. SHE) is more positive than the VB value of Fe-bpydc (0.96 V vs. SHE) (Brillas et al., 2009), and cannot directly oxidize bezafibrate due to their poor oxidation capacity. As a result, the photoinduced carriers recombine very quickly. However, the CB position of Fe-bpydc (-1.14 V vs. SHE) is more negative than the standard reduction potentials of Fe(III)/Fe(II) (0.77 V vs. NHE) and $H_2O_2/^{\bullet}OH$ (0.87 V vs. NHE) (Silva et al., 2017; Guo et al., 2019); thus, in PEF system, the photoinduced electrons (e^-) are capable of participating in H_2O_2 and Fe(III) reduction to form $^{\bullet}OH$ and Fe(II) via reactions (11) and (12), which hinder the recombination of e^- and h^+ efficiently. On the other hand, Fe(II) at the catalyst surface (≡Fe(II)) reacts with H_2O_2 to form $^{\bullet}OH$ from reaction (13) and can be regenerated from ≡Fe(III) reduction via reaction (14), due to the enhanced electron/charge transfer in the unique 2D MOF structure (Gao et al., 2017).

$$\text{Fe-bpydc} + h\nu \rightarrow h^+ + e^- \quad (10)$$

$$e^- + H_2O_2 \rightarrow {}^{\bullet}OH + OH^- \quad (11)$$

$$e^- + \equiv\text{Fe(III)} \rightarrow \equiv\text{Fe(II)} \quad (12)$$

$$\equiv\text{Fe(II)} + H_2O_2 \rightarrow {}^{\bullet}OH + \equiv\text{Fe(III)} + OH^- \quad (13)$$

$$\equiv\text{Fe(III)} + H_2O_2 \rightarrow HO_2^{\bullet} + \equiv\text{Fe(II)} + H^+ \quad (14)$$

Fe-bpydc as heterogeneous PEF catalyst shows several advantages over other Fe-based materials such as: (i) the unique 2D sheet structure lead to easier mass transport; (ii) the greater accessibility of the active sites with H_2O_2 enhances reaction (13) and (14); (iii) the broad light absorption and low band gap energy facilitate the excitation of Fe-O clusters; and (iv) the photogenerated electrons (e^-) induced additional ${}^{\bullet}OH$ production and Fe(II) regeneration.

LC-QToF-MS and GC-MS analysis allowed the identification of 16 main products from bezafibrate degradation, summarized in Table S1 and S2, respectively. Fig. 8 envisages four possible routes proposed from the detected derivatives involving hydroxylation, decarboxylation, dechlorination and amino oxidation. The direct hydroxylation of the aromatic ring of bezafibrate **(1)** with ${}^{\bullet}OH$ and M(${}^{\bullet}OH$) yields the monohydroxylated intermediates **2** and **3**, which are subsequently hydroxylated to the polyhydroxylated compounds **4-7**. Hydroxylation has also been reported as the preferred reaction pathway for other AOPs (Rivas et al., 2019; Wu et al., 2019). The decarboxylation of the lateral group of **1** originates the product **9**, which is then hydroxylated to derivatives **10** and **11**. On the other hand, the hydroxylation on the chlorine position of **1** gives the product **12**, which is further hydroxylated again leading to compounds **13** and **14**. The decarboxylation of **12** or the dechlorination of **9**

yields the dihydroxylated product **15**. Finally, the attack on the –NH– group breaks down the molecule of **1** and the above derivatives to give the compounds **16** and **8** with a single benzenic ring. Further deamination of **16** generates **17**.

4. Conclusions

It has been demonstrated that the Fe-bpydc 2D MOF exhibited strong catalytic activity as heterogeneous PEF catalyst under UV/Vis irradiation. The use of a very low amount of catalyst (0.05 g L^{-1}) allowed the almost disappearance of bezafibrate in 90 min using an IrO_2 anode at 100 mA. The numerous active sites of the catalyst enhanced both, mass transport and charge transfer, allowing an efficient Fenton's reaction and redox Fe(III)/Fe(II) cycling on its surface. Moreover, the photoinduced electrons (e^-) also promoted the $^{\bullet}OH$ production and Fe(II) regeneration. However, the catalyst underwent a slight deactivation, leading to a performance loss (30%) after three cycles. The stability of Fe-bpydc at mild pH was moderate since the crystalline and chemical structure were extremely reproducible after three cycles, although iron and TOC leaching were observed. Fe-bpydc showed relatively low intolerance to acidic conditions. The great potential of (Fe-bpydc)-catalyzed PEF system for industrial application was confirmed from the fast degradation of bezafibrate, bisphenol A, fluoxetine and naproxen in urban wastewater. A thorough reaction mechanism for heterogeneous PEF and bezafibrate degradation routes based on the oxidation products detected is finally proposed.

Acknowledgements

The authors thank financial support from project CTQ2016-78616-R (AEI/FEDER, EU) and

PhD scholarship awarded to Z.H. Ye (State Scholarship Fund, CSC, China).

References

Ahmad, M., Chen, S., Ye, F., Quan, X., Afzal, S., Yu, H.T., Zhao, X.Y., 2019. Efficient photo-Fenton activity in mesoporous MIL-100(Fe) decorated with ZnO nanosphere for pollutants degradation. Appl. Catal. B: Environ. 245, 428-438.

Bai, W., Li, S., Ma, J., Cao, W., Zheng, J., 2019. Ultrathin 2D metal–organic framework (nanosheets and nanofilms)-based xD–2D hybrid nanostructures as biomimetic enzymes and supercapacitors. J. Mater. Chem. A 7, 9086-9098.

Bianco, A., Polo-López, M.I., Fernández-Ibánez, P., Brigante, M., Mailhot, G., 2017. Disinfection of water inoculated with *Enterococcus faecalis* using solar/Fe(III)EDDS-H_2O_2 or $S_2O_8^{2-}$ process. Water Res. 118, 246-260.

Borràs, N., Arias, C., Oliver, R., Brillas, E., 2011. Mineralization of desmetryne by electrochemical advanced oxidation processes using a boron-doped diamond anode and an oxygen-diffusion cathode. Chemosphere 85, 1167-1175.

Brillas, E., 2014. A review on the degradation of organic pollutants in waters by UV photoelectro-Fenton and solar photoelectro-Fenton. J. Braz. Chem. Soc. 25, 393-417.

Brillas, E., Sirés, I., 2015. Electrochemical removal of pharmaceuticals from water streams: Reactivity elucidation by mass spectrometry. TrAC-Trend. Anal. Chem. 70, 112-121.

Brillas, E., Sirés, I., Oturan, M.A., 2009. Electro-Fenton process and related electrochemical technologies based on Fenton's reaction chemistry. Chem. Rev. 109, 6570-6631.

Cao, C., Tan, C., Sindoro, M., Zhang, H., 2017. Hybrid micro-/nano-structures derived from metal-organic frameworks: preparation and applications in energy storage and conversion. Chem. Soc. Rev. 45, 2660-2677.

Chen, X., Tong, R., Shi, Z., Yang, B., Liu, H., Ding, S., Wang, X., Lei, Q., Wu, J., Fang, W., 2018. MOFs nanoparticles with encapsulated autophagy inhibitor in controlled drug delivery system for antitumor. ACS Appl. Mater. Inter. 10, 2328-2337.

Crake, A., Christoforidis, K.C., Godin, R., Moss, B., Kafizas, A., Zafeiratos, S., Durrant, J.R., Petit, C., 2019. Titanium dioxide/carbon nitride nanosheet nanocomposites for gas phase CO_2 photoreduction under UV-visible irradiation. Appl. Catal. B: Environ. 242, 369-378.

Ding, T., Wang, S., Yang, B., Li, J., 2020. Biological removal of pharmaceuticals by *Navicula* sp. and biotransformation of bezafibrate. Chemosphere 240, 124949.

Es'haghzade, Z., Pajootan, E., Bahrami, H., Arami, M., 2017. Facile synthesis of Fe_3O_4 nanoparticles via aqueous based electro chemical route for heterogeneous electro-Fenton removal of azo dyes. J. Taiwan Inst. Chem. Eng. 71, 91-105.

Feng, X., Yin, X., Bo, X., Guo, L., 2019. An ultrasensitive luteolin sensor based on MOFs derived CuCo coated nitrogen-doped porous carbon polyhedron. Sensors Actuators B Chem. 281, 730-738.

Finn, R.C., Zubieta, J., 2002. Hydrothermal synthesis and structural characterization of the two-dimensional networks $[M(H_2O)(bpy\text{-}dicarb)]\bullet H_2O$ (M=Fe, Co, Ni, Zn; bpy-dicarb=2,2´-bipyridyl-4,4´-dicarboxylic acid). Solid State Sci. 4, 83-86.

Ganiyu, S.O., Zhou, M., Martínez-Huitle, C.A., 2018. Heterogeneous electro-Fenton and

photoelectro-Fenton processes: a critical review of fundamental principles and application for water/wastewater treatment. Appl. Catal. B: Environ. 235, 103-129.

Gao, C., Chen, S., Quan, X., Yu, H., Zhang, Y., 2017. Enhanced Fenton-like catalysis by iron-based metal organic frameworks for degradation of organic pollutants. J. Catal. 356, 125-132.

Guo, P., Xiao, F., Liu, Q., Liu, H., Guo, Y., Gong, J.R., Wang, S., Liu, Y., 2013. One-pot microbial method to synthesize dual-doped graphene and its use as high-performance electrocatalyst. Sci. Rep. 3, 3499.

Guo, T., Wang, K., Zhang, G., Wu, X., 2019. A novel α-Fe_2O_3@g-C_3N_4 catalyst: synthesis derived from Fe-based MOF and its superior photo-Fenton performance. Appl. Surf. Sci. 469, 331-339.

Han, Z., Guo, J., Li, W., 2013. $Fe(bpy)_3^{2+}$ supported on amidoximated PAN fiber as effective catalyst for the photodegradation of organic dye under visible light irradiation. Chem. Eng. J. 228, 36-44.

Hou, X., Hu, K., Zhang, H., Zhang, T., Yang, M., Wang, G., 2019. Construction of 2D MOFs@reduced graphene oxide nanocomposites with enhanced visible light-induced fenton-like catalytic performance by seeded growth strategy. ChemCatChem 11, 4411-4419.

Iglesias, O., Meijide, J., Bocos, E., Sanromán, M.A., Pazos. M., 2015. New approaches on heterogeneous electro-Fenton treatment of winery wastewater. Electrochim. Acta, 169, 134-141.

Kondo, A., Noguchi, H., Ohnishi, S., Kajiro, H., Tohdoh, A., Hattori, Y., Xu, W.C., Tanaka, H., Kanoh, H., Kaneko, K., 2006. Novel expansion/shrinkage modulation of 2D layered MOF triggered by clathrate formation with CO_2 molecules. Nano Lett. 6, 2581-2584.

Laipan, M., Zhu, R., Zhu, J., He, H., 2016. Visible light assisted Fenton-like degradation of Orange II on Ni_3Fe/Fe_3O_4 magnetic catalyst prepared from spent FeNi layered double hydroxide. J. Mol. Catal. A Chem. 415, 9-16.

Li, X., Pi, Y., Wu, L.Q., Xia, Q., Wu, J.L., Li, Z., Xiao, J., 2017. Facilitation of the visible light-induced Fenton-like excitation of H_2O_2 via heterojunction of g-C_3N_4/NH_2-iron terephthalate metal-organic framework for MB degradation. Appl. Catal. B: Environ. 202, 653-663.

Li, X., Wang, B., Cao, Y., Zhao, S., Wang, H., Feng, X., Zhou, J., Ma, X., 2019. Water contaminant elimination based on metal–organic frameworks and perspective on their industrial applications. ACS Sustain. Chem. Eng. 7, 4548-4563.

Li, Y., Liu, H., Li, W.J., Zhao, F.Y., Ruan, W.J., 2016. A nanoscale Fe(II) metal-organic framework with a bipyridinedicarboxylate ligand as a high performance heterogeneous Fenton catalyst. RSC Adv. 6, 6756-6760.

Li, W.J., Li, Y., Ning, D., Liu, Q., Chang, L., Ruan, W., 2018. An Fe(II) metal-organic framework as a visible responsive photo-Fenton catalyst for the degradation of organophosphates. New J. Chem. 42, 29-33.

Liao, X., Wang, F., Wang, F., Cai, Y., Yao, Y., Teng, B., Hao, Q., Lu, S., 2019. Synthesis of (100) surface oriented MIL-88A-Fe with rod-like structure and its enhanced Fenton-like

performance for phenol removal. Appl. Catal. B: Environ. 259, 118064.

Liu, Y., Liu, Z., Huang, D., Cheng, M., Zeng, G., Lai, C., Zhang, C., Zhou, C., Wang, W., Jiang, D., Wang, H., Shao, B., 2019. Metal or metal-containing nanoparticle@MOF nanocomposites as a promising type of photocatalyst. Coord. Chem. Rev. 388, 63-78.

Lv, H., Zhao, H., Cao, T., Qian, L., Wang, Y., Zhao, G., 2015. Efficient degradation of high concentration azo-dye wastewater by heterogeneous Fenton process with iron-based metal-organic framework. J. Mol. Catal. A: Chem. 400, 81-89.

Martínez-Huitle, C.A., Rodrigo, M.A., Sirés, I., Scialdone, O., 2015. Single and coupled electrochemical processes and reactors for the abatement of organic water pollutants: a critical review. Chem. Rev. 115, 13362-13407.

Meijide, J., Pazos, M., Sanromán, M.A., 2019. Heterogeneous electro-Fenton catalyst for 1-butylpyridinium chloride degradation. Environ. Sci. Pollut. Res. 26, 3145-3156.

Moreira, F.C., Boaventura, R.A.R., Brillas, E., Vilar. V.J.P., 2017. Electrochemical advanced oxidation processes: a review on their application to synthetic and real wastewaters. Appl. Catal. B: Environ. 202, 217-261.

Özcan, A., Özcan, A.A., Demirci, Y., Şener, E., 2017. Preparation of Fe_2O_3 modified kaolin and application in heterogeneous electro-catalytic oxidation of enoxacin. Appl. Catal. B: Environ. 200, 361-371.

Ridruejo, C., Centellas, F., Cabot, P.L., Sirés, I., Brillas, E., 2017. Electrochemical Fenton-based treatment of tetracaine in synthetic and urban wastewater using active and non-active anodes. Water Res. 128, 71-81.

Rivas, F.J., Solís, R.R., Beltrán, F.J., Gimeno, O., 2019. Sunlight driven photolytic ozonation as an advanced oxidation process in the oxidation of bezafibrate, cotinine and iopamidol. Water Res. 151, 226-242.

Poza-Nogueiras, V., Rosales, E., Pazos, M., Sanroman. M.A., 2018. Current advances and trends in electro-Fenton process using heterogeneous catalysts – a review. Chemosphere 201, 399-416.

Rostamizadeh, M., Jafarizad, A., Gharibian, S., 2018. High efficient decolorization of Reactive Red 120 azo dye over reusable Fe-ZSM-5 nanocatalyst in electro-Fenton reaction. Separ. Purif. Technol. 192, 340-347.

Salmerón, I., Plakas, K.V., Sirés, I., Oller, I., Maldonado, M.I., Karabelas, A.J., Malato, S, 2019. Optimization of electrocatalytic H_2O_2 production at pilot plant scale for solar-assisted water treatment. Appl. Catal. B: Environ. 242, 327-336.

Sharma, V.K., Feng, M., 2019. Water depollution using metal-organic frameworks-catalyzed advanced oxidation processes: a review. J. Hazard. Mater. 372, 3-16.

Shi, X.T., Liu, Y.Z., Tang, Y.Q., 2018. Kinetics and pathways of bezafibrate degradation in UV/chlorine process. Environ. Sci. Pollut. Res. 25, 672-682.

Silva, A.C., Almeida, M.R., Rodriguez, M., Machado, A.R.T., Oliveira, L.C.A., Pereira, M.C., 2017. Improved photocatalytic activity of δ-FeOOH by using H_2O_2 as an electron acceptor. J. Photochem. Photobiol. A: Chem. 332, 54-59.

Silva, P., Vilela, S.M.F., Tome, J.P.C., Paz, F.A.A., 2015. Multifunctional metal–organic frameworks: from academia to industrial applications. Chem. Soc. Rev. 44, 6774-6803.

Sirés, I., Brillas, E., 2012. Remediation of water pollution caused by pharmaceutical residues based on electrochemical separation and degradation technologies: a review. Environ. Int. 40, 212-229.

Sirés, I., Brillas, E., Oturan, M.A., Rodrigo, M.A., Panizza, M., 2014. Electrochemical advanced oxidation processes: today and tomorrow. A review. Environ. Sci. Pollut. Res. 21, 8336-8367.

Solís, R.R., Rivas, F.J., Chávez, A.M., Dionysiou, D.D., 2019. Simulated solar photo-assisted decomposition of peroxymonosulfate. Radiation filtering and operational variables influence on the oxidation of aqueous bezafibrate. Water Res. 162, 383-393.

Soon, A.N., Hameed, B.H., 2013. Degradation of acid blue 29 in visible light radiation using iron modified mesoporous silica as heterogeneous photo-Fenton catalyst. Appl. Catal. A: Gen. 450, 96-105.

Steter, J.R., Brillas, E., Sirés, I., 2016. On the selection of the anode material for the electrochemical removal of methylparaben from different aqueous media. Electrochim. Acta 222, 1464-1474.

Steter, J.R., Brillas, E., Sirés, I., 2018. Solar photoelectro-Fenton treatment of a mixture of parabens spiked into secondary treated wastewater effluent at low input current. Appl. Catal. B: Environ. 224, 410-418.

Su, Y., Jiang, H., Zhu, Y., Yang, X., Shen, J., Zou, W., Chen, J., Li, C., 2014. Enriched graphitic N-doped carbon-supported Fe_3O_4 nanoparticles as efficient electrocatalysts for oxygen reduction reaction. J. Mater. Chem. A 2, 7281-7287.

Sui, Q., Gebhardt, W., Schroder, H.F., Zhao, W., Lu, S., Yu, G., 2017. Identification of new oxidation products of bezafibrate for better understanding of its toxicity evolution and oxidation mechanisms during ozonation. Environ. Sci. Technol. 51, 2262-2270.

Tang, J., Wang, J., 2017. Fe-based metal organic framework/graphene oxide composite as an efficient catalyst for Fenton-like degradation of methyl orange. RSC Adv. 7, 50829-50837.

Tang, J., Wang, J., 2018. Metal organic framework with coordinatively unsaturated sites as efficient Fenton-like catalyst for enhanced degradation of sulfamethazine. Environ. Sci. Technol. 52, 5367-5377.

Taylor, J.M., Vaidhyanathan, R., Iremonger, S.S., Shimizu, G.K.H., 2012. Enhancing water stability of metal-organic frameworks via phosphonate monoester linkers. J. Am. Chem. Soc. 134, 14338-14340.

Thiam, A., Sirés, I., Brillas, E., 2015. Treatment of a mixture of food color additives (E122, E124 and E129) in different water matrices by UVA and solar photoelectro-Fenton. Water Res. 81, 178-187.

Tokumura, M., Znad, H.T., Kawase, Y., 2008. Decolorization of dark brown colored coffee effluent by solar photo-Fenton reaction: effect of solar light dose on decolorization kinetics. Water Res. 42, 4665-4673.

Van de Voorde, B., Bueken, B., Denayer, J., De Vos, D., 2014. Adsorptive separation on metal–organic frameworks in the liquid phase. Chem. Soc. Rev. 43, 5766-5788.

Welcher, F.J., 1975. Standard Methods of Chemical Analysis, sixth ed, vol. 2, R.E. Krieger Publishing Co, Huntington, New York, Part B.

Wu, Y., Yang, Y., Liu, Y., Zhang, L., Feng, L., 2019. Modelling study on the effects of chloride on the degradation of bezafibrate and carbamazepine in sulfate radical-based advanced oxidation processes: conversion of reactive radicals. Chem. Eng. J. 358, 1332-1341.

Yang, W., Zhou, M., Oturan, N., Li, Y., Oturan, M.A, 2019. Electrocatalytic destruction of pharmaceutical imatinib by electro-Fenton process with graphene-based cathode. Electrochim. Acta 305, 285-294.

Ye, Z., Brillas, E., Centellas, F., Cabot, P.L., Sirés, I., 2019. Electro-Fenton process at mild pH using Fe(III)-EDDS as soluble catalyst and carbon felt as cathode. Appl. Catal. B: Environ. 257, 117907.

Ye, Z., Brillas, E., Centellas, F., Cabot, P.L., Sirés, I., 2020. Expanding the application of photoelectro-Fenton treatment to urban wastewater using the Fe(III)-EDDS complex. Water Res. in press. DOI: 10.1016/j.watres.2019.115219.

Ye, Z., Zhang, H., Zhang, X., Zhou, D., 2016. Treatment of landfill leachate using electrochemically assisted UV/chlorine process: effect of operating conditions, molecular weight distribution and fluorescence EEM-PARAFAC analysis. Chem. Eng. J. 286, 508-516.

Yin, Z., Tian, Y., Gao, P., Feng, L., Liu, Y., Du, Z., Zhang, L., 2020. Photodegradation mechanism and genetic toxicity of bezafibrate by Pd/g-C_3N_4 catalysts under simulated solar light irradiation: the role of active species. Chem. Eng. J. 379, 122294.

Zhang, G.M., Li, Y., Zou, X.Z., Zhang, J.A., Gu, J.Z., Kirillov, A.M., 2016. Nickel(II) and manganese(II) metal–organic networks driven by 2,2´-bipyridine-5,5´-dicarboxylate

blocks: synthesis, structural features, and magnetic properties. Transition Met. Chem. 41, 153-160.

Zhang, T., Lin, W., 2014. Metal–organic frameworks for artificial photosynthesis and photocatalysis. Chem. Soc. Rev. 43, 5982-5993.

Zhao, H., Chen, Y., Peng, Q., Wang, Q., Zhao, G., 2017. Catalytic activity of MOF(2Fe/Co)/carbon aerogel for improving H_2O_2 and •OH generation in solar photo–electro–Fenton process. Appl. Catal. B: Environ. 203, 127-137.

Zhou, M., Oturan, M.A., Sirés, I. (Eds.), 2018. Electro-Fenton Process: New Trends and Scale-Up. Springer Nature, Singapore.

Zhu, Y., Zhu, R., Xi, Y., Xu, T., Yan, L., Zhu, J., Zhu, G., He, H., 2018. Heterogeneous photo-Fenton degradation of bisphenol A over Ag/AgCl/ferrihydrite catalysts under visible light. Chem. Eng. J. 346, 567-577.

Zhu, Y., Zhu, R., Xi, Y., Zhu, J., Zhu, G., He, H., 2019. Strategies for enhancing the heterogeneous Fenton catalytic reactivity: a review. Appl. Catal. B: Environ. 255, 117739.

Figure

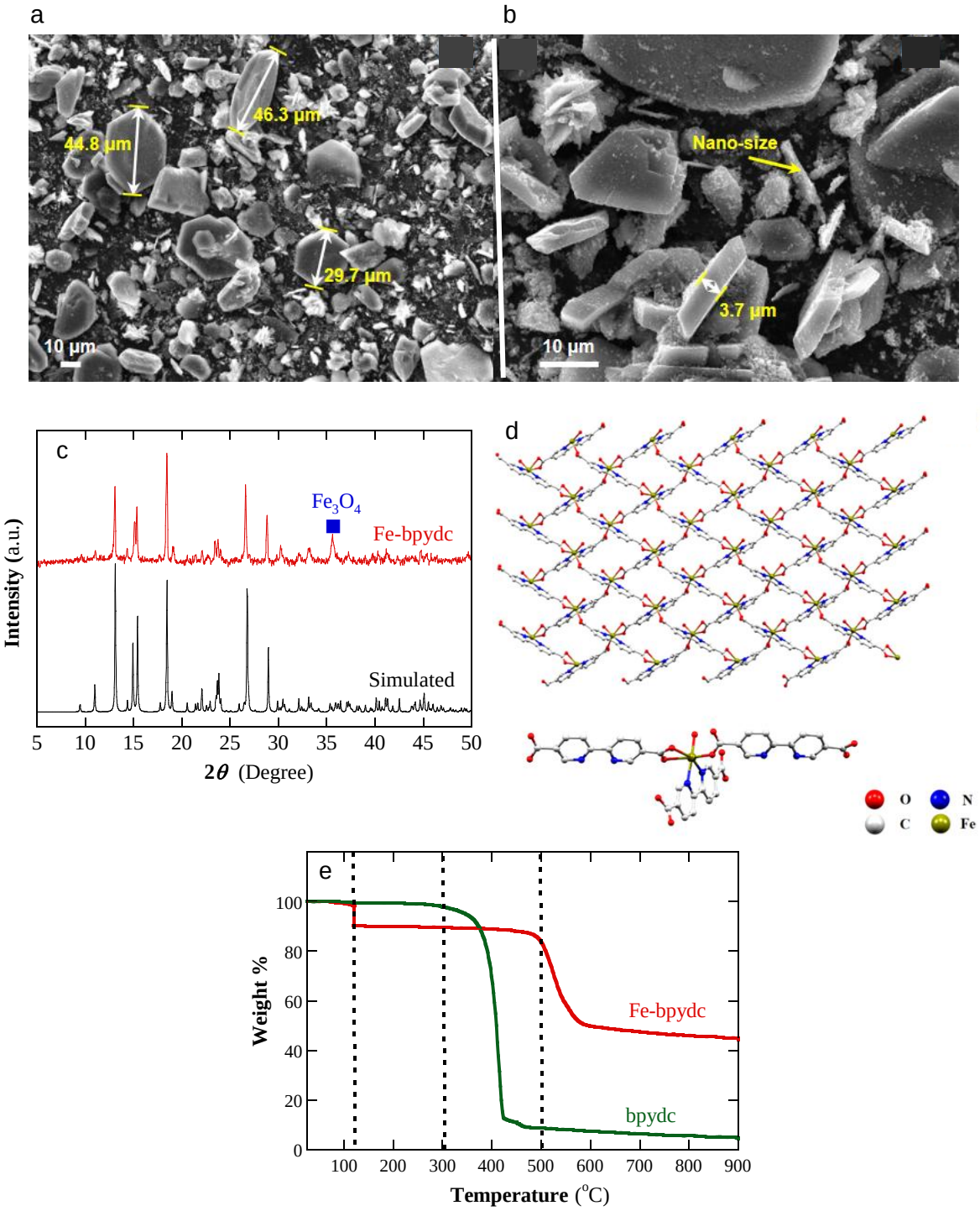

Fig. 1. FESEM images at (a) 500× and (b) 1,000×, (c) XRD pattern, (d) pictorial representation of the structure of the as-synthesized Fe-bpydc and (e) thermogravimetric curve.

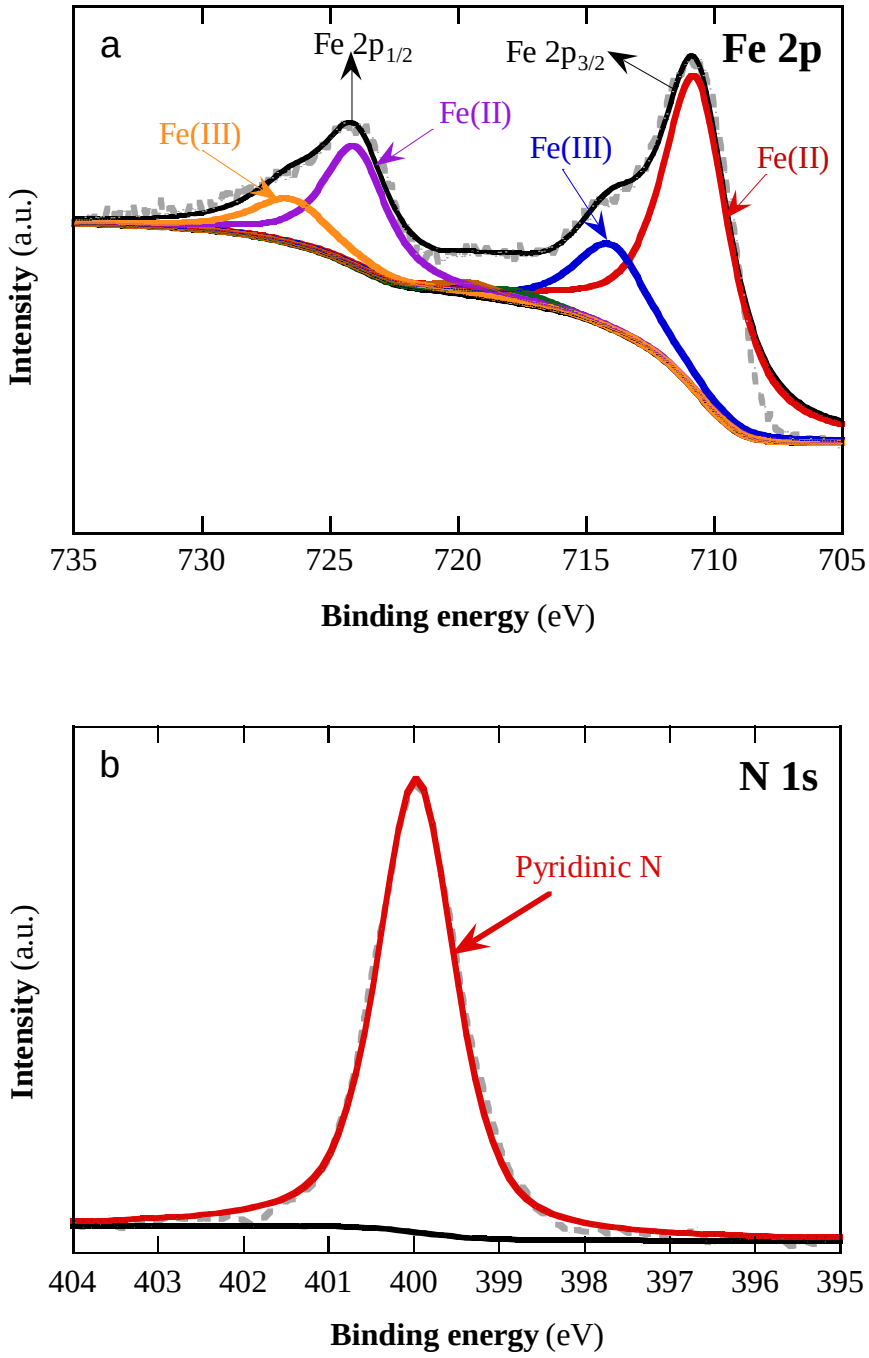

Fig. 2. XPS spectrum of (a) Fe 2p and (b) N 1s present in the Fe-bpydc catalyst.

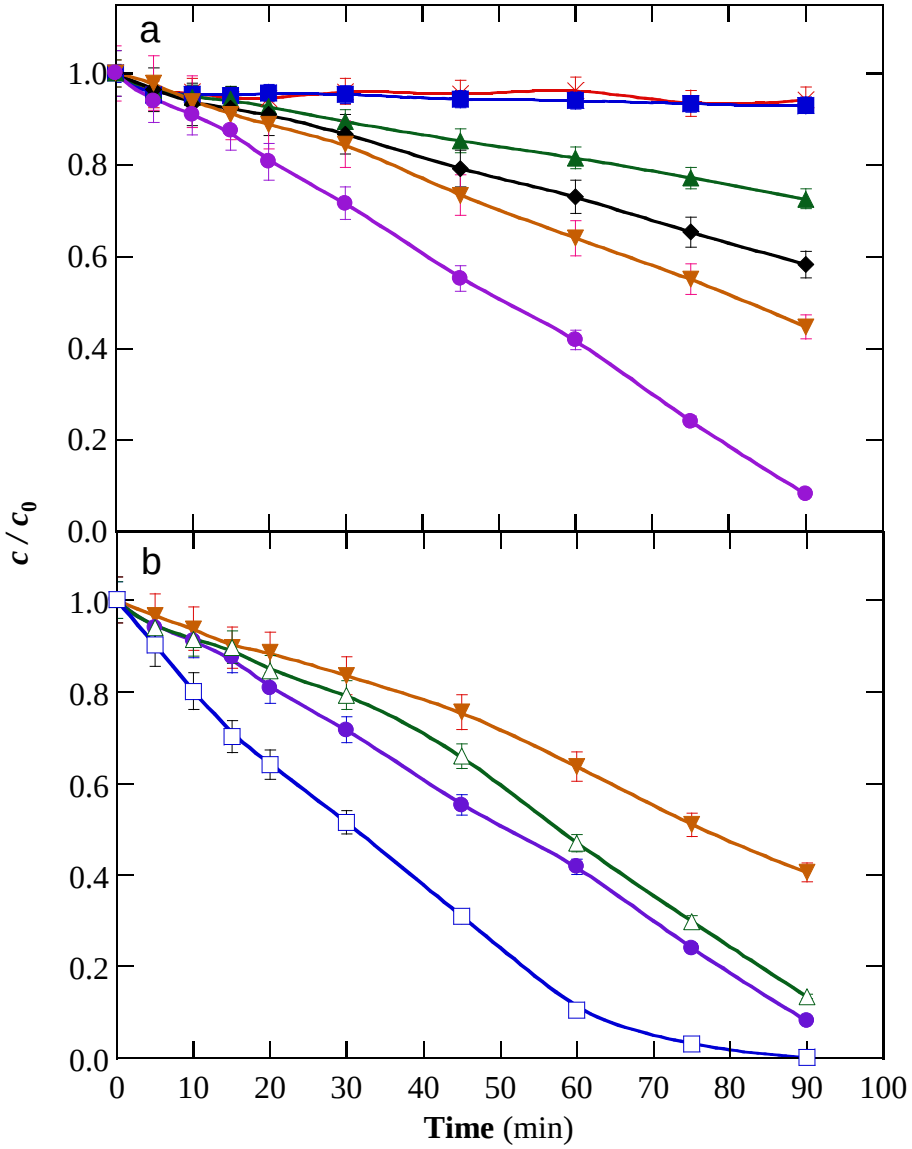

Fig. 3. Normalized bezafibrate concentration decay during different treatments of 150 mL of 0.044 mM (10 mg C L^{-1}) drug solution with 0.050 M Na_2SO_4 at natural pH ~ 5.1. In the electrochemical assays, an IrO_2/air-diffusion cell was used at 100 mA and 25 ºC. In (a), (×) adsorption with 0.05 g L^{-1} Fe-bpydc, (■) UV/Vis photocatalysis with 0.05 g L^{-1} Fe-bpydc catalyst, (▲) EO-H_2O_2, (◆) EF with 0.05 g L^{-1} Fe-bpydc catalyst, (▼) visible light PEF and (●) UV/Vis PEF with 0.05 g L^{-1} Fe-bpydc catalyst. In (b), (△) visible light PEF and (□) UV/Vis PEF with 0.05 g L^{-1} Fe-bpydc catalyst. A Xe lamp of 150 W and 300 W was employed in the photoassisted treatments of plot (a) and (b), respectively.

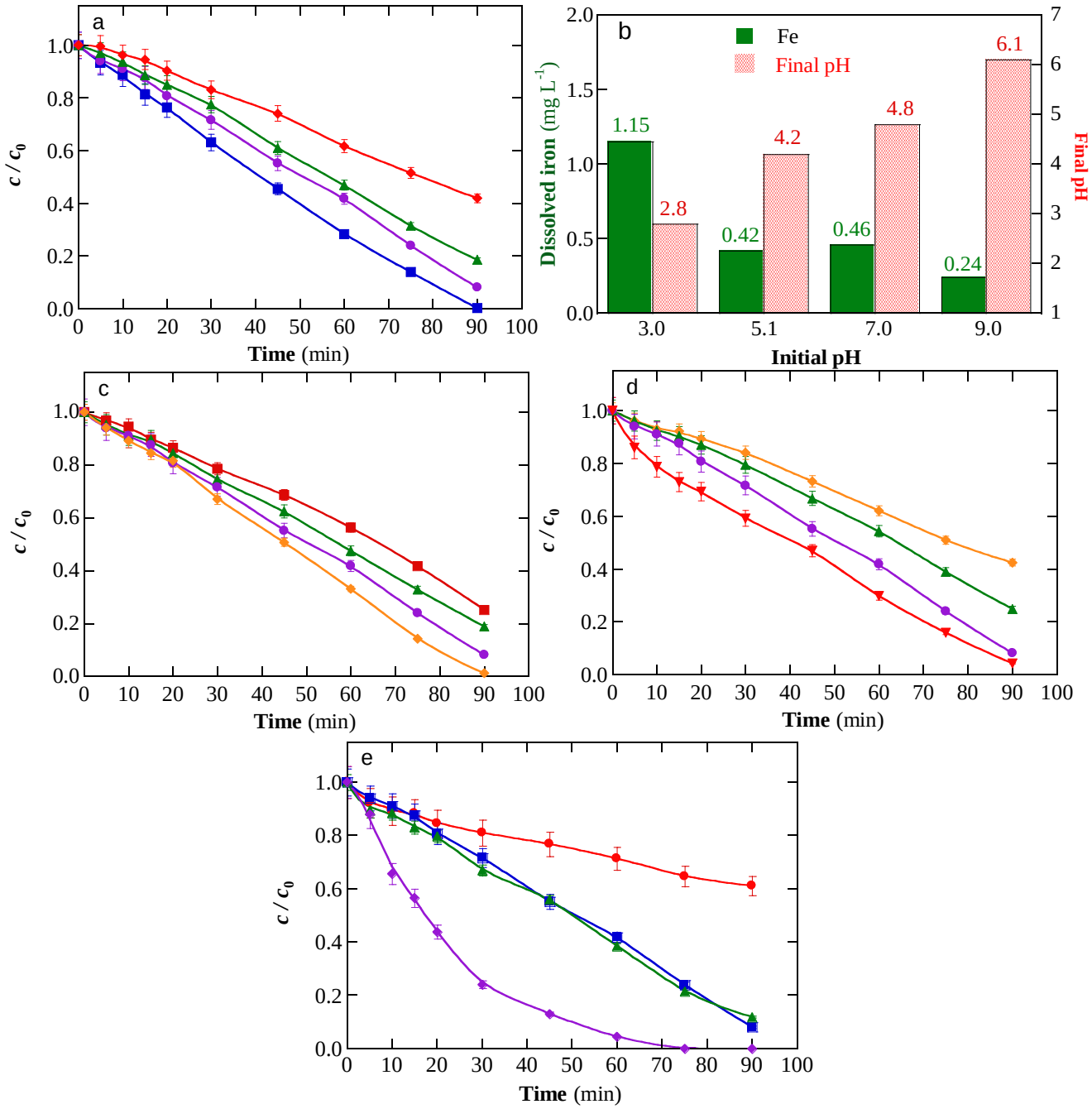

Fig. 4. (a,c,d,e) Time course of normalized bezafibrate concentration during the heterogeneous PEF treatments of 150 mL of 0.044 mM drug solutions with 0.050 M Na_2SO_4 using an IrO_2/air-diffusion cell (except in plot e) with Fe-bpydc catalyst at 25 ºC under irradiation with a 150 W Xe lamp. (b) Iron concentration (filled bar) and final pH (dashed bar) after 90 min of the trials of plot (a). In (a), 0.05 g L^{-1} catalyst at 100 mA and different initial pH: (■) 3.0, (●) 5.1, (▲) 7.0 and (◆) 9.0. In (c), pH 5.1 and 0.05 g L^{-1} catalyst, at different applied current values: (■) 50, (▲) 75, (●) 100 and (◆) 150 mA. In (d), pH 5.1 and 100 mA, at different catalyst doses: (◆) 0.0125, (▲) 0.025, (●) 0.05 and (▼) 0.075 g L^{-1} Fe-bpydc. In (e), effect of anode and electrolyte at natural pH with 0.05 g L^{-1} catalyst at 100 mA, using: (●) IrO_2-based anode in 0.041 M Na_2SO_4 + 0.009 M $NaHCO_3$ solution, (▲) BDD anode in 0.050 M Na_2SO_4 solution, (■) IrO_2-based anode in 0.050 M Na_2SO_4 solution and (◆) RuO_2-based anode in 0.025 M Na_2SO_4 + 0.035 M NaCl solution.

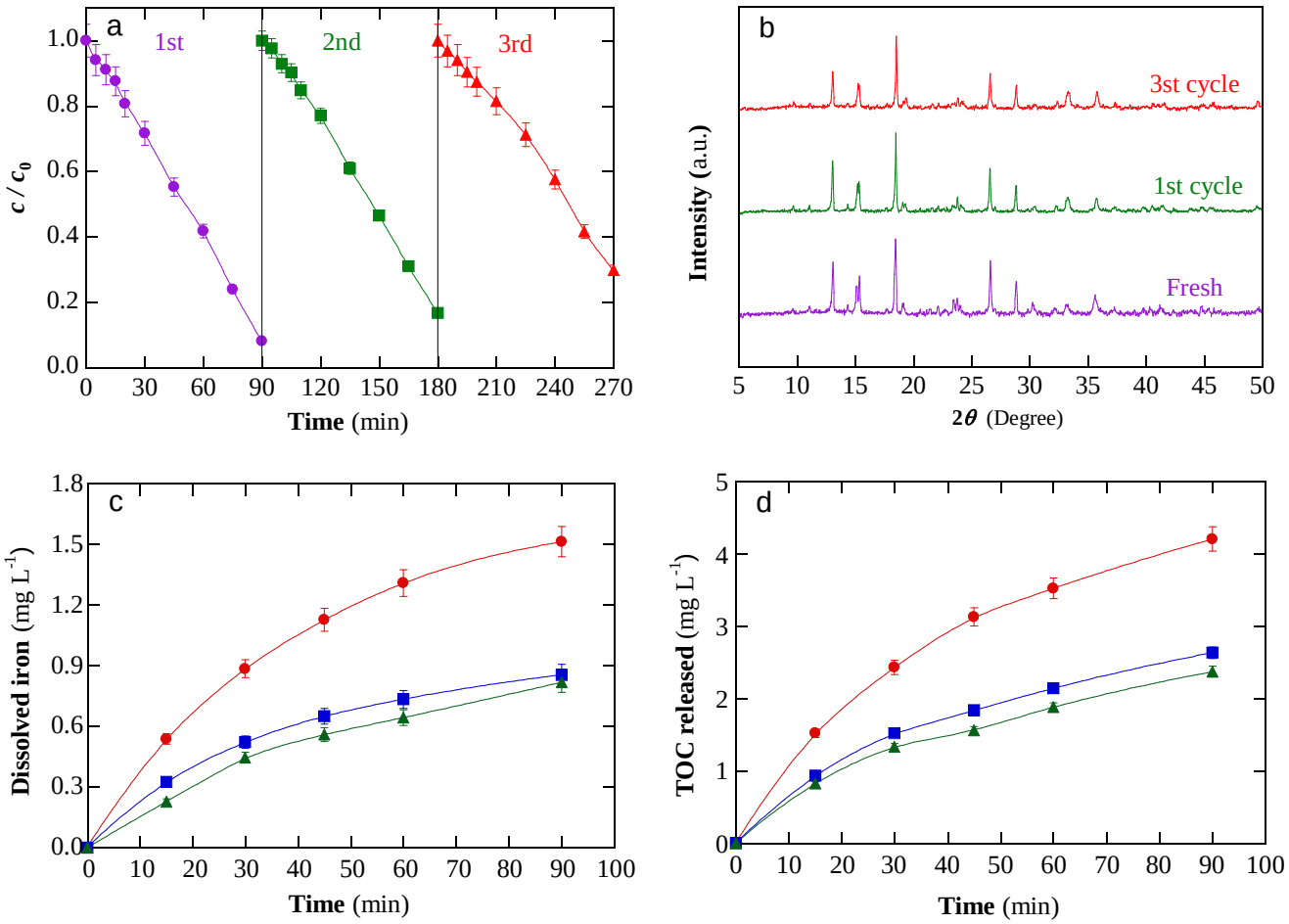

Fig. 5. (a) Reusability of Fe-bpydc in heterogeneous PEF treatment with 0.05 g L^{-1} catalyst for the trial shown in Fig. 3a**.** (b) XRD pattern of fresh and used Fe-bpydc. Time course of (c) dissolved iron concentration and (d) TOC released during constant stirring of 0.05 g L^{-1} Fe-bpydc in Milli-Q water with initial pH of: (●) 3.0, (■) 5.1 and (▲) 7.0.

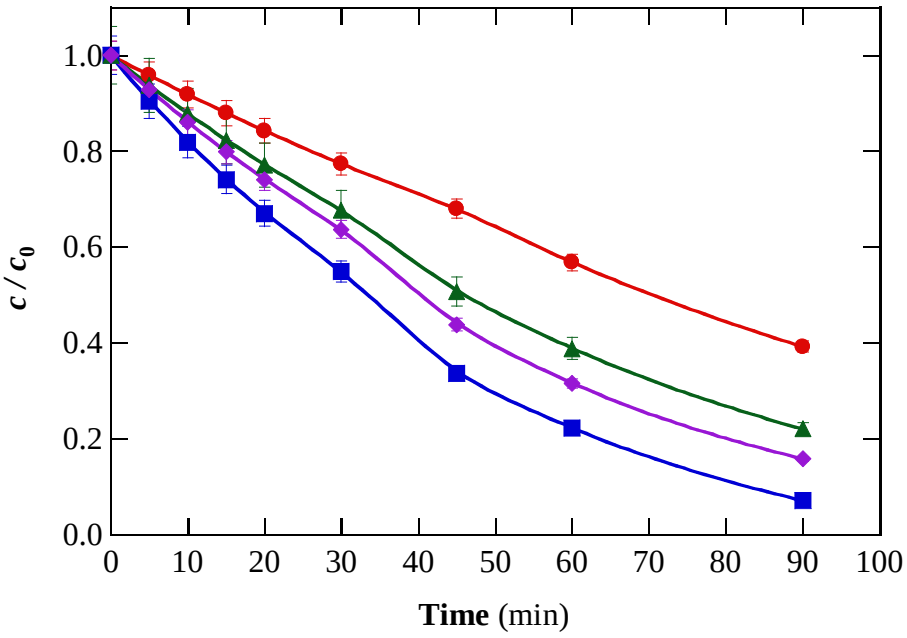

Fig. 6. Degradation of four selected micropollutants (10 mg C L^{-1} of each compound) spiked into 150 mL of urban wastewater by 0.05 g L^{-1} Fe-bpydc catalyzed heterogeneous PEF treatment at natural pH 7.4 using an IrO_2/air-diffusion cell at 100 mA and 25 ºC under irradiation with a 150 W Xe lamp. Micropollutants: (●) Bezafibrate, (▲) bisphenol A, (◆) fluoxetine and (■) naproxen.

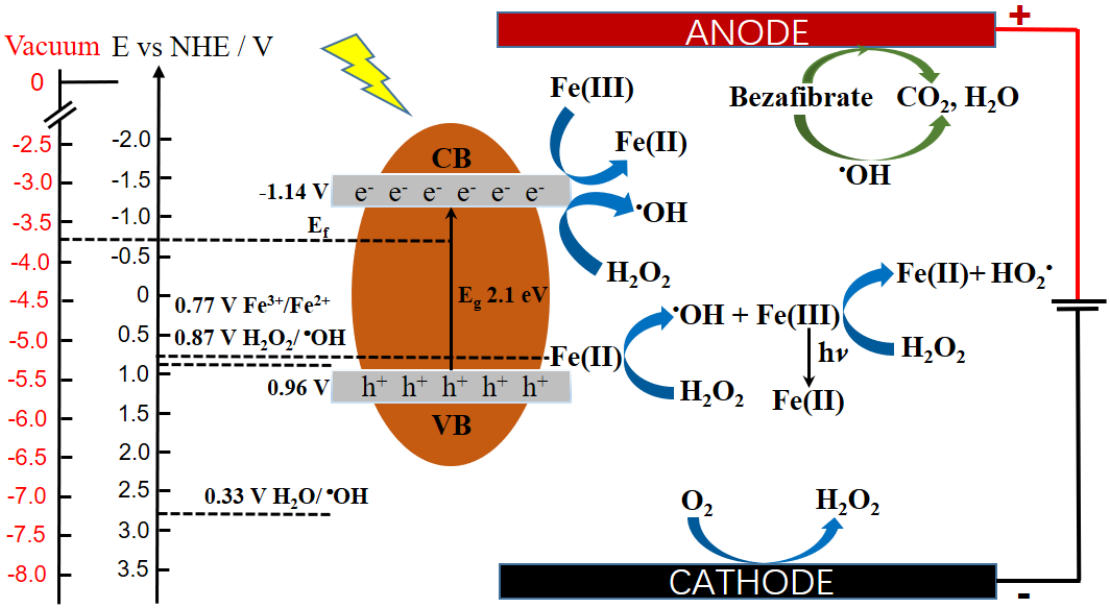

Fig. 7. Proposed mechanism for (Fe-bpydc)-catalyzed heterogeneous PEF treatment at mild pH.

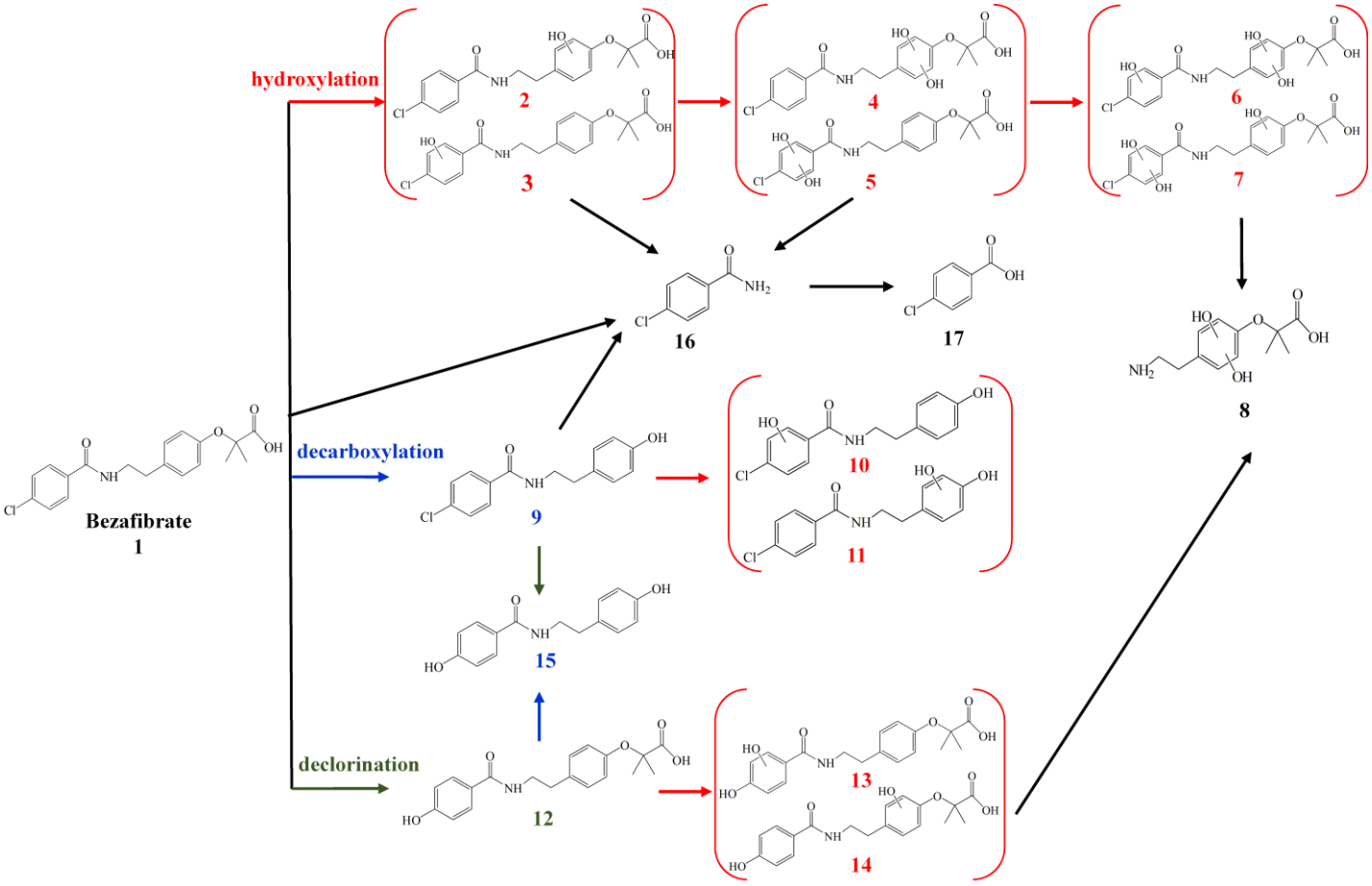

Fig. 8. Degradation routes proposed for bezafibrate during the (Fe-bpydc)-catalyzed PEF treatment at mild pH.

The stability of an Fe-based 2D MOF during the photoelectro-Fenton treatment of organic micropollutants under UVA and visible light irradiation

Zhihong Ye [1,2], Giulia E.M. Schukraft [2], Anouk L´Hermitte [2], Ying Xiong [2], Enric Brillas [1], Camille Petit [2,**], Ignasi Sirés [1,*]

[1] *Laboratori d'Electroquímica dels Materials i del Medi Ambient, Departament de Química Física, Facultat de Química, Universitat de Barcelona, Martí i Franquès 1-11, 08028 Barcelona, Spain*

[2] *Barrer Centre, Department of Chemical Engineering, Imperial College London, South Kensington Campus, London SW7 2AZ, UK*

* Corresponding author: i.sires@ub.edu (I. Sirés)

** Corresponding author: camille.petit@imperial.ac.uk (Camille Petit)

Text S1

An urban wastewater sample, whose natural pH was 7.2, was collected from the secondary effluent of a facility placed near Barcelona. It was preserved in a refrigerator at 4 ºC to maintain their characteristics. It had a conductivity of 2.08 mS cm^{-1}, total carbon content of 79.3 mg L^{-1} and TOC of 10.8 mg L^{-1}. The concentration of cations was: < 0.04 mg L^{-1} Fe^{2+}, 38.3 mg L^{-1} Mg^{2+}, 116.0 mg L^{-1} Ca^{2+}, 42.6 mg L^{-1} K^{+} and 308.5 mg L^{-1} Na^{+}. The content of anions was: 50.6 mg L^{-1} NO_3^{-}, 504.0 mg L^{-1} Cl^{-} and 167.7 mg L^{-1} SO_4^{2-}. Before the experiments, the wastewater was first conditioned, being acidified to pH around 2.0 with H_2SO_4 solution, nitrogen-stripped to remove the volatile compounds and then alkalinized with NaOH solution to re-establish the original pH.

Text S2

XPS analysis was made with an ultrahigh vacuum spectrometer equipped with a VSW Class WA hemispherical electron analyzer. An Al Kα X-ray dual anode source (1486.6 eV) was used as incident radiation and a constant pass energy mode (44 and 22 eV for survey and high resolution spectra, respectively) was applied. The CASA XPS program with a Shirley background subtraction and Gaussian-Lorentzian peak shape was used for peak analysis. High resolution measurements for band alignment were performed on a Thermo Scientific K-Alpha spectrometer equipped with an Al Kα X-ray source (1486.6 eV) and an 180° double focusing hemispherical analyzer with a 2D detector at an operating pressure of 1×10^{-8} mbar as well as a flood gun to minimize charging from photoemission. Powders were mounted onto conductive C tape adhered to a sample holder. To correct for charging, all core lines were corrected at C 1 s (C-C) core line, assumed as 284.8 eV. Data were processed with the Avantage and CASA XPS software.

Text S3

For ESR analysis, 150 mL of a 10 mM DMPO solution in 0.050 M Na_2SO_4 at pH 5.1 were electrolyzed using an IrO_2/air-diffusion cell at 100 mA with 0.05 g L^{-1} Fe-bpydc under UV/Vis light illumination and samples were withdrawn at different times. They were immediately frozen with dry ice for preservation. Further analysis was carried out with a Bruker ESP300E spectrometer using the following conditions: center magnetic field at 3495.00 G, sweep width of 100 G, microwave frequency of 9.79 GHz, microwave power of 2.00 mW, modulation amplitude of 2.00 G, time constant of 40.96 ms, conversion time of 200 ms and sweep time 204.8 s. Win-EPR and SimFonia 2.3 software were employed for analyzing the data obtained.

Text S4

The organic components withdrawn from treated bezafibrate solution were extracted with 75 mL of CH_2Cl_2 in three times, followed by thorough drying over anhydrous Na_2SO_4, filtration and concentration under reduced pressure. GC-MS analysis was performed in a 6890 N gas chromatograph (Agilent Technologies) coupled to a 5975C mass spectrometer operating in electron impact mode at 70 eV. A nonpolar Teknokroma Sapiens-X5 ms and a polar HP INNOWax column (0.25 µm, 30 m × 0.25 mm) were used. The temperature ramp was: 36 °C for 1 min, 5 °C min^{-1} up to 320 °C, and hold time of 10 min. The temperature of the inlet, source and transfer line was 250, 230 and 300 °C.

LC-QToF-MS analysis was carried out using an Agilent 1200 Series system coupled to an AB Sciex Applied Biosystems mass spectrometer, operating in positive ion mode. A Zorbax Eclipse XDB C18 Solvent Saver Plus 3.5µm (100 mm × 3.0 mm) column at 30 ºC was utilized as

stationary phase. The mobile phase was a mixture of two solutions, namely 0.1% formic acid in water (A) and 0.1% formic acid in methanol (B), in gradient mode. Solution A was injected at 95.0% during the first 10 min, 5.0% from 10 to 11 min, and 95.0% again until 15 min, at a flow rate of 0.6 mL min^{-1}.

Table S1

Products detected by LC-QToF-MS after 30 min of PEF treatment of 150 mL of a 0.044 mM bezafibrate solution with 0.05 g L^{-1} catalyst and 0.050 M Na_2SO_4 at natural pH ~ 5.1 using an IrO_2/air-diffusion cell at 100 mA and 25 ºC.

Number	Chemical formula	Molecular structure	t_r (min)	*m/z*
1	$C_{19}H_{20}O_4NCl$	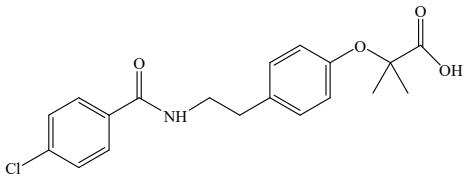	10.50	362.1111
2	$C_{19}H_{20}O_7NCl$	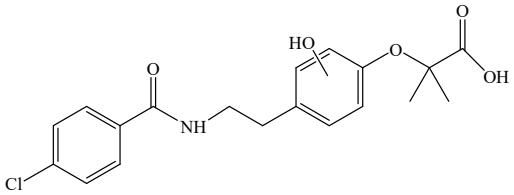	11.14	378.1147
		or		
3		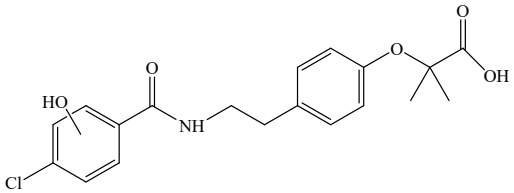		
4	$C_{19}H_{20}O_6NCl$	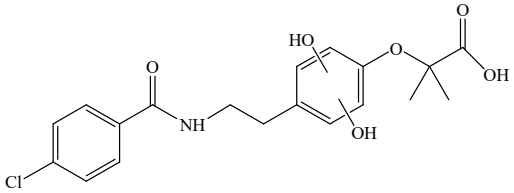	9.61	394.1069
		or		
5		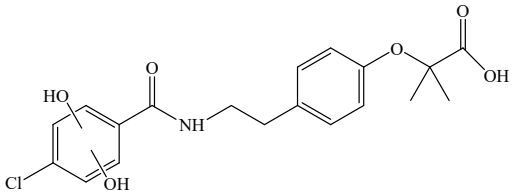		
6	$C_{19}H_{20}O_7NCl$	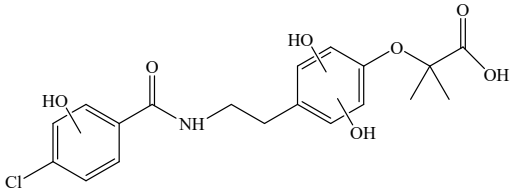	9.28	410.1038
		or		

7		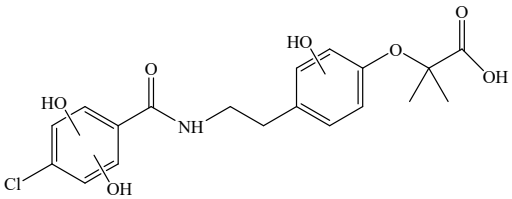		
8	$C_{12}H_{17}O_5N$	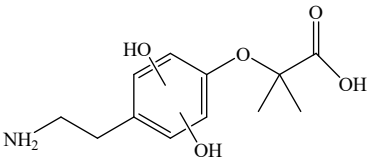	11.57	256.2648
9	$C_{15}H_{14}O_2NCl$	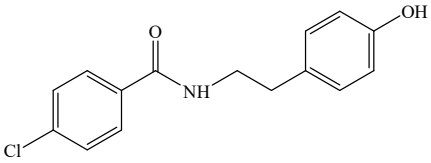	9.46	276.0836
10	$C_{15}H_{14}O_3NCl$	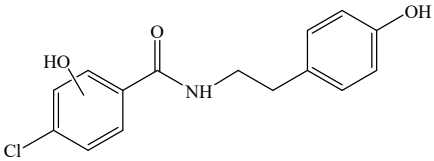	8.55	292.0770
		or		
11		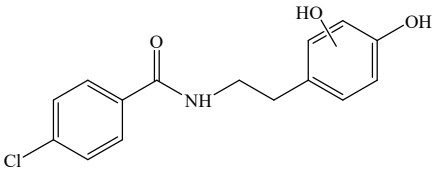		
12	$C_{19}H_{21}O_5N$	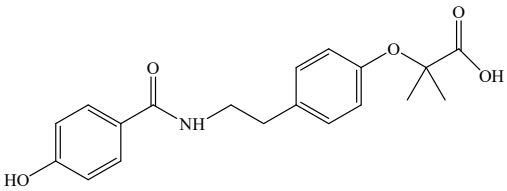	5.89	344.2306
13	$C_{19}H_{21}O_6N$	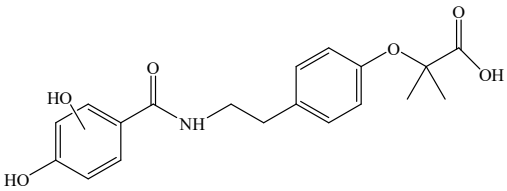	11.06	360.1039
		or		
14		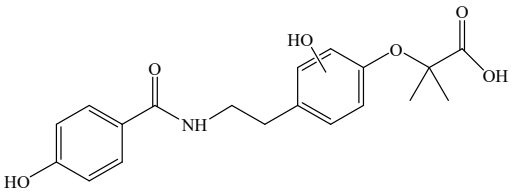		

Table S2

Products detected by GC-MS after 30 min of PEF treatment described in Table S1.

Number	Chemical formula	Molecular structure	t_r (min)	Fragmentation (*m/z*)
9	$C_{15}H_{14}O_2NCl$	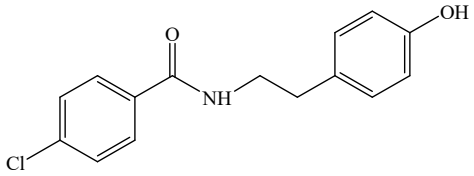	46.07	139, 120, 107
15	$C_{15}H_{15}O_3N$	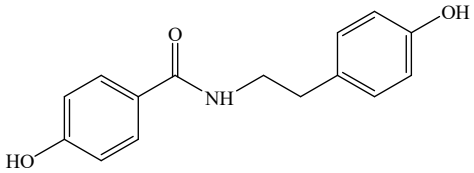	46.76	257, 120, 105
16	C_7H_6ONCl	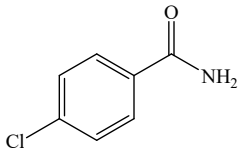	50.76	155, 139, 111
17	$C_7H_5O_2Cl$	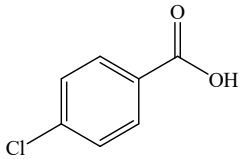	48.76	156, 139, 111

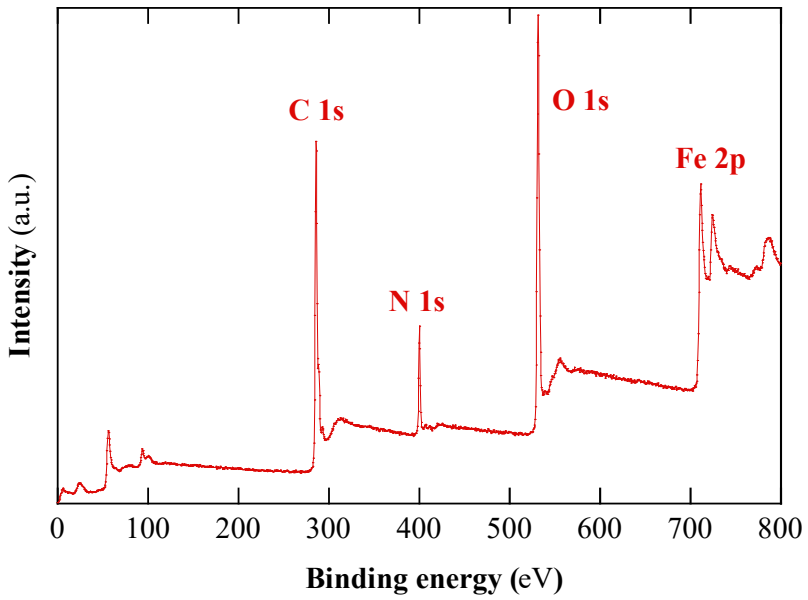

Fig. S1. XPS general spectrum for the as-synthesized Fe-bpydc catalyst.

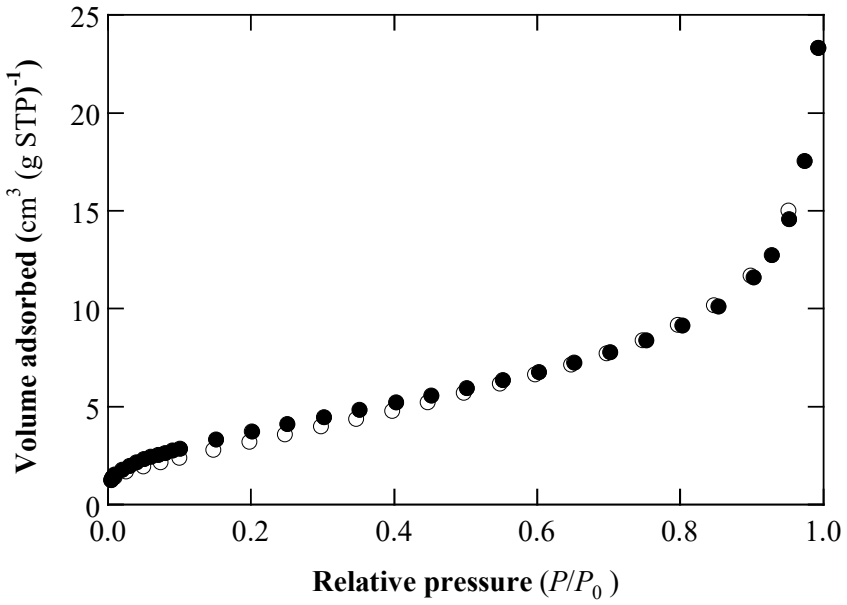

Fig. S2. N_2 adsorption-desorption isotherm at -196 °C.

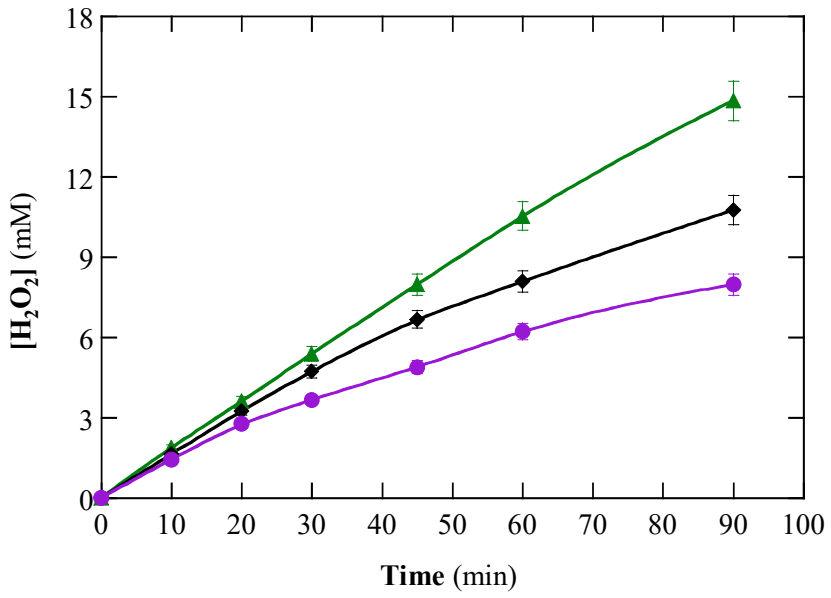

Fig. S3. Variation of accumulated H_2O_2 concentration with electrolysis time for the (▲) EO-H_2O_2, (◆) EF with 0.05 g L^{-1} Fe-bpydc catalyst and (●) PEF with 0.05 g L^{-1} Fe-bpydc catalyst under illumination with a 150 W Xe lamp for the trials shown in Fig. 3a.

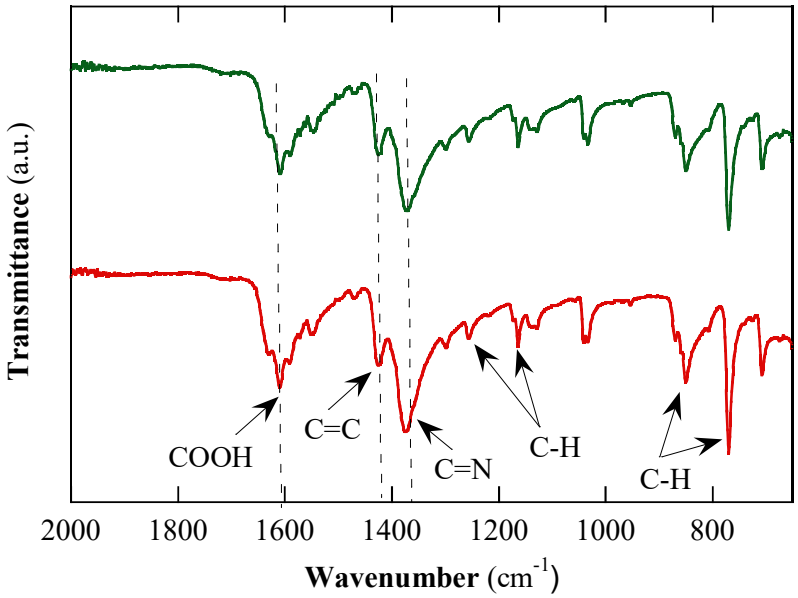

Fig. S4. FTIR spectra of fresh (red line) and used (green line) Fe-bpydc.

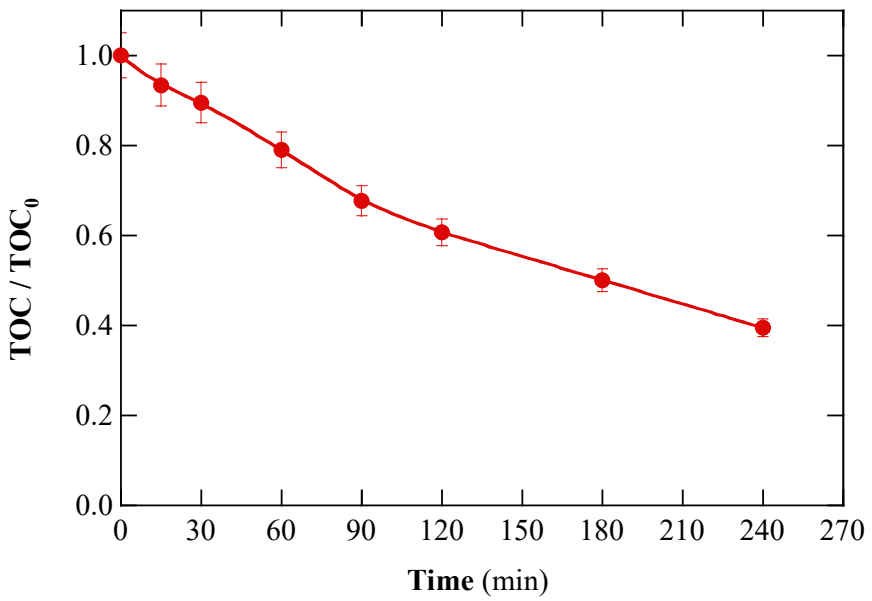

Fig. S5. Normalized TOC vs. electrolysis time during the heterogeneous PEF treatment of 150 mL of a 0.044 mM bezafibrate solution in 0.050 M Na_2SO_4 solution with 0.05 g L^{-1} catalyst at natural pH ~ 5.1 using a BDD/air-diffusion cell at 100 mA and 25 ºC under illumination with a 150 W Xe lamp.

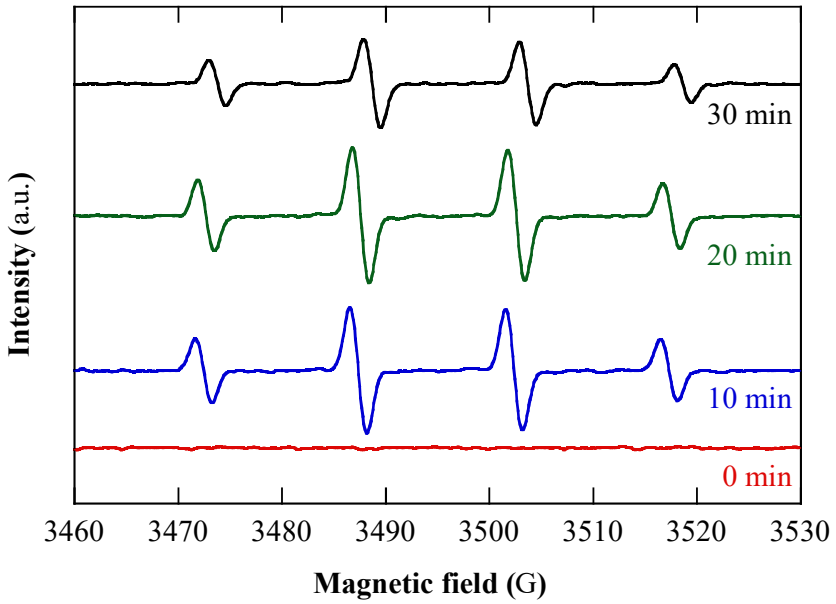

Fig. S6. ESR spectra of the •OH-DMPO adduct at different electrolysis times for the (Fe-bpydc)-catalyzed PEF trial.

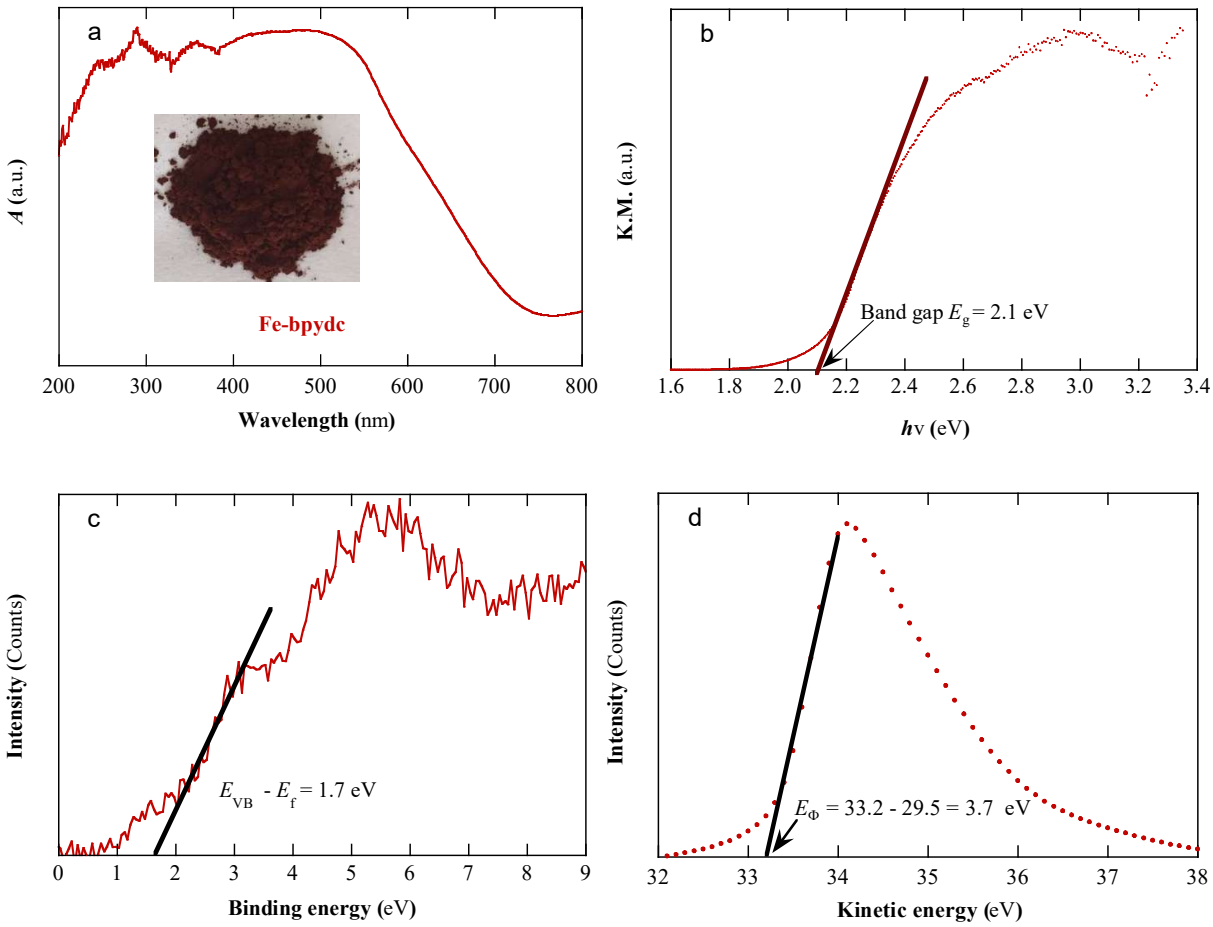

Fig. S7. (a) UV/Vis absorption spectrum of Fe-bpydc catalyst. Inset: Digital photograph of catalyst grains. (b) Kubelka-Munk UV/Vis light absorption plot of Fe-bpydc. (c) VB-XPS spectrum of Fe-bpydc. (d) Work function (E_ϕ) determination by photoemission spectroscopy (excitation energy of 29.5 eV).

CHAPTER 5
CONCLUSIONS AND PERSPECTIVES

5. Conclusions and perspectives

5.1. Conclusions

The main objective of this Thesis was to develop new processes and catalysts to overcome the main current drawbacks of conventional EAOPs: the long time required for TOC removal, the restriction to acidic pH (around 3.0), the excessive sludge production, and the poor recyclability. The enhancement has been evaluated by treating organic micropollutants in model solutions and urban wastewater at mild pH.

The conclusions for each specific goal proposed in Chapter 2 are:

Chapter 4.1 (Appendices I and II)

- ✧ EC is not a convenient technology to remove BHA from water, but it is quite efficient for the disappearance of BP-3, especially employing an Al|Al cell and working at pH 11.0, due to the precipitation of the neutral form of BP-3 upon spontaneous pH decrease. The other processes that occurred during the EC treatment for the removal of BHA and BP-3 include: (a) coagulation by hydroxide flocs, (b) reductive transformation and (c) oxidation by generated ClO^- and $^{\bullet}OH$.

- ✧ BP-3 spiked into urban wastewater at natural pH 8.0 treated by EC with an Fe|Fe cell at 15 mA cm^{-2} showed a dramatic content decay thanks to coagulation of its complexes with components of the wastewater, followed by partial BP-3 redissolution when they were oxidized by $^{\bullet}OH$ and ClO^-.

- ✧ The oxidation power of the EAOPs rose as EO-H_2O_2 < EF < PEF, with larger effectiveness of the BDD/air-diffusion cell as compared to a RuO_2-based cell. The superiority of PEF was due to photolysis of intermediates. The EAOPs clearly outperformed EC, but needing long time to destroy BHA, BP-3 and the byproducts.

- ✧ The organic byproducts of BP-3 identified upon EC and EAOPs revealed a certain oxidation ability of the EC process.

- ✧ The sequential EC/PEF treatment of BP-3-loaded urban wastewater at natural pH was much more powerful than EC/EF. The time needed for total removal by EC/PEF was shorter than in single PEF.

Chapter 4.2 (Appendices III and IV)

- ✧ The total removal of organic micropollutants at near-neutral pH is feasible by novel EF or PEF with Fe(III)–EDDS as catalyst.

- ✧ Carbon felt outperformed the air-diffusion cathode to run Fe(III)–EDDS-assisted EF process, despite the much lower H_2O_2 production, because it favored the regeneration of Fe(II). The air-diffusion cathode was preferred in PEF since Fe(III)–EDDS showed excellent photoreduction ability.

- ✧ Much higher Fe(III) reduction efficiency was found in Fe(III)–EDDS-enhanced EF/PEF processes as compared to conventional EF/PEF with Fe^{3+}.

- ✧ The reduction of absorbed ≡Fe(III) and ≡Fe(III)-EDDS to yield ≡Fe(II) and ≡Fe(II)-EDDS on carbon-felt in EF gave rise to heterogeneous Fenton and Fenton-like reactions.

- ✧ The contribution to total TOC and the scavenging effect of EDDS on $^{\bullet}OH$ are the main concerns in Fe(III)–EDDS-enhanced EF and PEF treatments, preventing the occurrence of a large mineralization. Once EDDS was decomposed, the residual TOC was mainly destroyed by the adsorbed M($^{\bullet}OH$).

Chapter 4.3 (Appendices V-VII)

- ✧ Fe-containing MOFs and their derivatives have great vitality for the elimination of micropollutants as high performance EF/PEF catalysts. FeS_2/C nanocomposite as EF catalyst outperformed natural pyrite and Fe^{2+} due to the cooperation of homogenous and heterogeneous Fenton's reaction; the pyrolysis of NH_2-MIL(Fe)-88B gave rise to N-doped nano-ZVI@C, which exhibited superior catalytic activity in EF; the direct use of av Fe-bpydc 2D MOF as PEF catalyst yielded an effective bezafibrate decay due to the synergy between photocatalysis and Fenton's reaction.

- ✧ The conversion of the organic skeleton of MOF to carbon during pyrolysis yielded a nano-sized core-shell FeS_2/C structure, which significantly enhanced the stability and activity of the catalyst, achieving remarkable FLX removal with very low iron leaching. The unique structure of FeS_2/C greatly improved the mass transport and electron transfer, leading to efficient surface reactions and limited homogeneous Fenton's reaction catalyzed by Fe^{2+}/Fe^{3+}, largely promoting the catalyst reusability.

- ✧ The nano-ZVI@C-N rods embedded in N-doped carbon matrix showed excellent catalytic activity and reusability towards micropollutants degradation owing to the abundant active sites and unique encapsulated nanostructures with a carbon shell. The incorporation of NH_2 group significantly improved the encapsulation of ZVI by porous carbon and led to N-doped sites in the catalyst, which greatly enhanced the stability and electron transfer, accelerating the Fenton's reaction and redox Fe(III)/Fe(II) cycling.

- ✧ The numerous active sites exposed in 2D Fe-bpydc favored the access of photons, H_2O_2 and organics, resulting in an enhanced excitation of Fe-O clusters and efficient Fenton's reaction and Fe(III) reduction, but it also increased the risk of catalyst deactivation. In the presence of H_2O_2, the photoinduced electrons could further participate in H_2O_2 and Fe(III) reduction to form additional $^{\bullet}OH$ and Fe(II), thus greatly hindering the recombination of electron-hole pairs.

5.2. Perspectives

This study has provided several strategies to unravel the difficulties for the future application of electrochemical advanced oxidation technologies at industrial scale. The drawbacks of traditional EAOPs can be largely diminished following the approaches that have been proposed in this Thesis. However, several issues are still pending in this field and more efforts should be made in order to introduce more innovative and competitive strategies or to further optimize and improve our proposal.

From my point of view, three main challenges for the scaling-up of EAOPs should be prioritized, including: (a) renewable energy sources should be employed to power the systems, thus reducing the energy consumption to get truly sustainable and eco-friendly technologies; (b) less expensive hardware and electrode materials should be developed, with particular focus on those for H_2O_2 electrogeneration; and (c) the reactor design should be addressed to overcome mass transport and photon transfer limitations.

Regarding the processes and catalysts proposed in this study, some improvements still can be made. Thus, the combination of EAOPs with other technologies, such as membrane filtration and adsorption, deserves to be explored since EC pre-treatment only allows negligible removal for some micropollutants. Although Fe(III)-EDDS is one of the commonly used iron complexes, the investigation of other iron chelates as EF/PEF catalyst is also recommended.

The application of Fe-MOFs and their derivatives as heterogeneous EF/PEF catalysts is still under an initial exploration and hence, further development is necessary. Herein, four aspects should be considered: (a) the synthesis of new Fe-MOFs and derivatives, as well as the control of the morphology and physicochemical properties are feasible by employing different organic linkers and synthetic methods; (b) the stability in water and recycle time are essential for the practical application and hence, the obtention of highly water-stable Fe-MOFs is still a great challenge; (c) the toxic effects on human

health and the environment caused by the disposal of these catalysts should be thoroughly evaluated; and (d) the cost of large-scale synthesis and application of Fe-MOFs should be estimated upon treatments at pilot scale. In conclusion, the development of low-cost and economically viable strategies that do not rely on expensive organic ligands is of great interest.

A final innovative approach could arise from the potential modification of carbonaceous cathodes (air-diffusion electrodes or others) with Fe-, Co- and/or Cu-based MOFs, since the transition metals in the carbon-based matrix electrodes can act as heterogeneous catalysts in the 2-electron oxygen reduction reaction, eventually enhancing the H_2O_2 production and/or the heterogenenous Fenton's reaction.

References

[1] C.J. Vörösmarty, P.B. McIntyre, M.O. Gessner, D. Dudgeon, A. Prusevich, P. Green, S. Glidden, S.E. Bunn, C.A. Sullivan, C.R. Liermann, P.M. Davies, Global threats to human water security and river biodiversity. *Nature* 467 (**2010**) 555–561.

[2] P. Steduto, J.M. Faurès, J. Hoogeveen, J. Winpenny, J. Burke, Coping With Water Scarcity: An Action Framework for Agriculture and Food Security. *Food and Agriculture Organization of the United Nations Rome* (**2012**).

[3] FAO-AQUASTAT, Food and Agriculture Organization of the United Nations (FAO). *AQUASTAT Database* (**2016**).

[4] N. Mancosu, R.L. Snyder, G. Kyriakakis, D. Spano, Water scarcity and future challenges for food production. *Water* 7 (**2015**) 975–992.

[5] S. Igor, World fresh water resources. In: Gleick PH (ed) Water in crisis: a guide to the world's. *Oxford University Press* (**1993**) 13–24.

[6] WWAP (UNESCO World Water Assessment Programme), The United Nations World Water Development Report 2019: Leaving No One Behind. *Paris, UNESCO* (**2019**).

[7] P. Burek, Y. Satoh, G. Fischer, M.T. Kahil, A. Scherzer, S. Tramberend, L. F. Nava, Y. Wada, S. Eisner, M. Flörke, N. Hanasaki, P. Magnuszewski, B. Cosgrove, D. Wiberg, Water Futures and Solution: Fast Track Initiative (Final Report) (**2016**).

[8] IEA (International Energy Agency), Water Energy Nexus: Excerpt from the World Energy Outlook 2016. *Paris, IEA Publications* (**2016**).

[9] FAO-AQUASTAT, Food and Agriculture Organization of the United Nations (FAO). *AQUASTAT Database* (**2012**).

[10] UN (United Nations), Sustainable Development Goal 6: Synthesis Report 2018 on Water and Sanitation. *New York, United Nations* (**2018**).

[11] J.X. Wang, R.Y. Li, J.K. Huang, T.T. Yan, T.H. Sun, Growing water scarcity,

food security and government responses in China. *Glob. Food Secur.* 14 (**2017**) 9–17.

[12] W. Xiong, Y. Li, W. Zhang, Q. Ye, S. Zhang, X. Hou, Integrated multi-objective optimization framework for urban water supply systems under alternative climates and future policy. *J. Clean. Prod.* 195 (**2018**) 640–650.

[13] B. Zutshi, S.G.R. Prasad, Impact of pollution on fresh and marine water resources – a review. *Poll Res.* 27 (**2008**) 461–466.

[14] Global Water Intelligence (GWI) Report (**2014**).

[15] S. Bolisetty, M. Peydayesh, R. Mezzenga, Sustainable technologies for water purification from heavy metals: review and analysis. *Chem. Soc. Rev.* 48 (**2019**) 463–487.

[16] V.K. Gupta, I. Ali, T.A. Saleh, A. Nayak, and S. Agarwal, Chemical treatment technologies for waste-water recycling—an overview. *RSC Adv.* 2 (**2012**) 6380–6388.

[17] M. Barlett, A.R.A. Lima, M.F. Costa, Distribution, sources and consequences of nutrients, persistent organic pollutants, metals and microplastics in South American estuaries. *Sci. Total Environ.* 651 (**2019**) 1199–1218.

[18] H. Wang, W. Zhang, L. Chen, J. Wang, T. Liu, The contamination and control of biological pollutants in mass cultivation of microalgae. *Bioresour. Technol.* 128 (**2013**) 745–750.

[19] L. Lahens, E. Strady, T. Kieu-Le, R. Dris, K. Boukerma, E. Rinnert, J. Gasperi, B. Tassin, Macroplastic and microplastic contamination assessment of a tropical river (Saigon River, Vietnam) transversed by a developing megacity. *Environ. Pollut.* 236 (**2018**) 661–671.

[20] O.M. Rodriguez-Narvaez, J.M. Peralta-Hernandez, A. Goonetilleke, E.R. Bandala, Treatment technologies for emerging contaminants in water: A review. *Chem. Eng. J.* 323 (**2017**) 361–380.

[21] S. Sauvé, M. Desrosiers, A review of what is an emerging contaminant. *Chem. Cent. J.* 8 (**2014**) 1–7.

[22] Y. Gruchlik, K. Linge, C. Joll, Removal of organic micropollutants in waste stabilisation ponds: A review. *J. Environ. Manag.* 206 (**2018**) 202–214.

[23] Y. Luo, W. Guo, H.H. Ngo, L.D. Nghiem, F. Hai, J. Zhang, S. Liang, X.C. Wang, A review on the occurrence of micropollutants in the aquatic environment and their fate and removal during wastewater treatment. *Sci. Total Environ.* 473–474 (**2014**) 619–641.

[24] J. Jiang, Z. Zhou, V.K. Sharma, Occurrence, transportation, monitoring and treatment of emerging micro-pollutants in waste water — A review from global views. *Microchem. J.* 110 (**2013**) 292–300.

[25] J. Diamond, K. Munkittrick, K.E. Kapo, J. Flippin, A framework for screening sites at risk from contaminants of emerging concern. *Environ. Toxicol. Chem.* 34 (**2015**) 2671–2681.

[26] F. Pomati, S. Castiglioni, E. Zuccato, R. Fanelli, D. Vigetti, C. Rossetti, D. Calamari, Effects of a complex mixture of therapeutic drugs at environmental levels on human embryonic cells. *Environ. Sci. Technol.* 40 (**2006**), 2442–2447.

[27] T. Rasheed, M. Bilal, F. Nabeel, M. Adeel, H.M.N. Iqbal, Environmentally-related contaminants of high concern: Potential sources and analytical modalities for detection, quantification, and treatment. *Environ. Int.* 122 (**2019**) 52–66.

[28] J.M. Brausch, G.M. Rand, A review of personal care products in the aquatic environment: Environmental concentrations and toxicity. *Chemosphere* 82 (**2011**) 1518–1532.

[29] M. Pedrouzo, F. Borrull, R.M. Marce, E. Pocurull, Analytical methods for personal-care products in environmental waters. *Trends Anal. Chem.* 30 (**2011**) 749–760.

[30] S. Varjani, G. Kumar, E.R. Rene, Developments in biochar application for pesticide remediation: Current knowledge and future research directions. *J. Environ. Manag.* 232 (**2019**) 505–513.

[31] R.T. Zoeller, T.R. Brown, L.L. Doan, A.C. Gore, N.E. Skakkebaek, A.M. Soto,

T.J. Woodruff, F.S. vom Saal, Endocrine-disrupting chemicals and public health protection: a statement of principles from the Endocrine Society. *Endocrinology* 153 (**2012**) 4097–4110.

[32] M. Giulivo, M. Lopez de Alda, E. Capri, D. Barcelo, Human exposure to endocrine disrupting compounds: their role in reproductive systems, metabolic syndrome and breast cancer. A review. *Environ. Res.* 151 (**2016**) 251–264.

[33] J.R. Shoaff, A.M. Calafat, S.L. Schantz, S.A.Korrick, Endocrine disrupting chemical exposure and maladaptive behavior during adolescence. *Environ. Res.* 172 (**2019**) 231–241.

[34] M.O. Barbos, N.F.F. Moreir, A.R. Ribeiro, M.F.R. Pereira, A.M.T. Silva, Occurrence and removal of organic micropollutants: An overview of the watch list of EU Decision 2015/495. *Water Res.* 94 (**2016**) 257–279.

[35] M. Bilal, M. Adeel, T. Rasheed, Y. Zhao, H.M.N. Iqbal, Emerging contaminants of high concern and their enzyme-assisted biodegradation – A review. *Environ. Int.* 124 (**2019**) 336–353.

[36] N.H. Tran, M. Reinhard, K. Y. Gin, Occurrence and fate of emerging contaminants in municipal wastewater treatment plants from different geographical regions-a review. *Water Res.* 133 (**2018**) 182–207.

[37] J. Wilkinson, P.S. Hooda, J. Barker, S. Barton, J. Swinden, Occurrence, fate and transformation of emerging contaminants in water: An overarching review of the field. *Environ. Pollut.* 231 (**2017**) 954–970.

[38] M. Patel, R. Kumar, K. Kishor, T. Mlsna, C.U.P. Jr., D. Mohan, Pharmaceuticals of emerging concern in aquatic systems: Chemistry, occurrence, effects, and removal methods. *Chem. Rev.* 119 (**2019**) 3510−3673.

[39] H.B. Quesada, A.T.A. Baptista, L.F. Cusioli, D. Seibert, C.O. Bezerra, R. Bergamasco, Surface water pollution by pharmaceuticals and an alternative of removal by low-cost adsorbents: A review. *Chemosphere* 222 (**2019**) 766−780.

[40] M. Köck-Schulmeyer, M. Villagrasa, M.L. Alda, R. Céspedes-Sánchez, F. Ventura, D. Barceló, Occurrence and behavior of pesticides in wastewater

treatment plants and their environmental impact. *Sci. Total Environ.* 458–460 (**2013**) 466–476.

[41] D. Montes-Grajales, M. Fennix-Agudelo, W. Miranda-Castro, Occurrence of personal care products as emerging chemicals of concern in water resources: A review. *Sci. Total Environ.* 595 (**2017**) 601–614.

[42] Y. Liu, S. Zhang, G. Ji, S. Wu, R. Guo, J. Cheng, Z. Yan, J. Chen, Occurrence, distribution and risk assessment of suspected endocrine-disrupting chemicals in surface water and suspended particulate matter of Yangtze River (Nanjing section). *Ecotoxicol. Environ. Saf.* 135 (**2017**) 90–97.

[43] C. Hurtado, C. Domínguez, L.P. Babace, N. Canameras, J. Comas, J.M. Bayona, Estimate of uptake and translocation of emerging organic contaminants from irrigation water concentration in lettuce grown under controlled conditions. *J. Hazard. Mater.* 305 (**2016**) 139–148.

[44] A. Gogoia, P. Mazumder, V.K. Tyagi, G.G.T. Chaminda, A.K. An, M. Kumar, Occurrence and fate of emerging contaminants in water environment: A review. *Groundw. Sustain. Dev.* 6 (**2018**) 169–180.

[45] B.W. Brooks, C.M. Foran, S.M. Richards, J. Weston, P.K. Turner, J.K. Stanley, K.R. Solomon, M. Slattery, T.W.L. Point, Aquatic ecotoxicology of fluoxetine. *Toxicol. Lett.* 142 (**2003**) 169–183.

[46] K. Fent, A.A. Weston, D. Caminada, Ecotoxicology of human pharmaceuticals. *Aquat. Toxicol.* 76 (**2006**) 122–159.

[47] J.C.G. Sousa, A.R. Ribeiro, M.O. Barbosa, C. Ribeiro, M.E. Tiritan, M.F.R. Pereira, A.M.T. Silva, Monitoring of the 17 EU Watch List contaminants of emerging concern in the Ave and the Sousa Rivers. *Sci. Total Environ.* 649 (**2019**) 1083–1095.

[48] European Commission, Screening Report Iceland: Chapter 27–Environment. *European Commission, Brussels* (**2011**).

[49] European Commission, Directive 2000/60/EC of the European Parliament and of the Council of 23 October 2000 establishing a framework for Community

action in the field of water policy. *Off. J. Eur. Communities.* 327 (**2000**) 1–72.

[50] European Commission, Decision 2001/2455/EC of the European Parliament and of the Council of November 2001 establishing the list of priority substances in the field of water policy and amending Directive 2000/60/EC. *Off. J. Eur. Communities.* 331 (**2001**) 1–5.

[51] European Commission, Directive 2008/105/EC of the European Parliament and of the Council of 16 December 2008 on environmental quality standards in the field of water policy. *Off. J. Eur. Union.* 348 (**2008**) 84–97.

[52] European Commission, Directive 2013/39/EU of the European Parliament and of the Council of 12 August 2013 amending Directives 2000/60/EC and 2008/105/EC as regards priority substances in the field of water policy. *Off. J. Eur. Union.* 226 (**2013**) 1–17.

[53] European Commission, Decision 2015/495/EU of 20 March 2015 establishing a watch list of substances for Union-wide monitoring in the field of water policy pursuant to Directive 2008/105/EC of the European Parliament and of the Council. *Off. J. Eur. Union.* 78 (**2015**) 40–42.

[54] European Commission, Decision 2018/840/EU of 5 June 2018 establishing a watch list of substances for Union-wide monitoring in the field of water policy pursuant to Directive 2008/105/EC of the European Parliament and of the Council and repealing Decision 2015/495/EU. *Off. J. Eur. Union.* 141 (**2018**) 9–12.

[55] S. Kim, K.H. Chu, Y.A.J. Al-Hamadani, C.M. Park, M. Jang, D. Kim, M. Yu, J. Heo, Y. Yoon, Removal of contaminants of emerging concern by membranes in water and wastewater: A review. *Chem. Eng. J.* 335 (**2018**) 896–914.

[56] C.Y. Teh, P.M. Budiman, K.P.Y. Shak, T.Y. Wu, Recent advancement of coagulation-flocculation and its application in wastewater treatment. *Ind. Eng. Chem. Res.* 55 (**2016**) 4363–4389.

[57] M. Sillanpää, M.C. Ncibi, A. Matilainen, M. Vepsäläinen, Removal of natural organic matter in drinking water treatment by coagulation: A comprehensive

review. *Chemosphere* 190 (**2018**) 54–71.

[58] A.I. Zouboulis, N.D. Tzoupanos, Polyaluminium silicate chloride - A Systematic study for the preparation and application of an efficient coagulant for water or wastewater treatment. *J. Hazard. Mater.* 162 (**2009**) 1379–1389.

[59] M. Huerta-Fontela, M.T. Galceran, F. Ventura, Occurrence and removal of pharmaceuticals and hormones through drinking water treatment. *Water Res.* 45 (**2011**) 1432–1442.

[60] S. Suarez, J.M. Lema, F. Omil, Pre-treatment of hospital wastewater by coagulation–flocculation and flotation. *Bioresour. Technol.* 100 (**2009**) 2138–2146.

[61] D.T. Moussa, M.H. El-Naas, M. Nasser, M.J. Al-Marri, A comprehensive review of electrocoagulation for water treatment: potentials and challenges. *J. Environ. Manag.* 186 (**2017**) 24–41.

[62] L. Shamaei, B. Khorshidi, B. Perdicakis, M. Sadrzadeh, Treatment of oil sands produced water using combined electrocoagulation and chemical coagulation techniques. *Sci. Total Environ.* 645 (**2018**) 560–572.

[63] M.B. Ahmed, J.L. Zhou, H.H. Ngo, W. Guo, N.S. Thomaidis, J. Xu, Progress in the biological and chemical treatment technologies for emerging contaminant removal from wastewater: A critical review. *J. Hazard. Mater.* 323 (**2017**) 274–298.

[64] J. Margot, L. Rossi, D.A. Barry, C. Holliger, A review of the fate of micropollutants in wastewater treatment plants. *Wiley Interdiscip. Rev. Water.* 2 (**2015**) 457–487.

[65] N.H. Tran, T. Urase, H.H. Ngo, J. Hu, S.L. Ong. Insight into metabolic and cometabolic activities of autotrophic and heterotrophic microorganisms in the biodegradation of emerging trace organic contaminants. *Bioresour. Technol.* 146 (**2013**) 721–731.

[66] K. Noguera-Oviedo, D.S. Aga, Lessons learned from more than two decades of research on emerging contaminants in the environment. *J. Hazard. Mater.* 316

(**2016**) 242–251.

[67] N. Pichel, M. Vivar, M. Fuentes, The problem of drinking water access: A review of disinfection technologies with an emphasis on solar treatment methods. *Chemosphere* 218 (**2019**) 1014–1030.

[68] J.L. Acero, F.J. Benitez, F.J. Real, G. Roldan, E. Rodriguez, Chlorination and bromination kinetics of emerging contaminants in aqueous systems. *Chem. Eng. J.* 219 (**2013**) 43–50.

[69] M. Deborde, U. Gunten, Reactions of chlorine with inorganic and organic compounds during water treatment-kinetics and mechanism: a critical review. *Water Res.* 42 (**2008**) 13–51.

[70] C.M.M. Bougeard, E.H. Goslan, B. Jefferson, S.A. Parsons, Comparison of the disinfection by-product formation potential of treated waters exposed to chlorine and monochloramine. *Water Res.* 44 (**2010**) 729–740.

[71] J.L. Acero, F.J. Benitez, F.J. Real, E. Rodriguez, Elimination of selected emerging contaminants by the combination of membrane filtration and chemical oxidation processes. *Water Air Soil Pollut.* 226 (**2015**) 1–14.

[72] EPA, 2011 EPA Water Treatment Manual: Disinfection. 978–184095–421–0 (**2011**).

[73] J. You, Y. Guo, R. Guo, X. Liu, A review of visible light-active photocatalysts for water disinfection: Features and prospects. *Chem. Eng. J.* 373 (**2019**) 624–641.

[74] S. Meng, L.F. Greenlee, Y.R. Shen, E. Wang, Basic science of water: challenges and current status towards a molecular picture. *Nano. Res.* 8 (**2015**) 3010–3085.

[75] L. Rizzo, S.Malato, D. Antakyali, V.G. Beretsou, M.B. Đolić, W. Gernjak, E. Heath, I. Tumbas, P. Karaolia, A.R.L. Ribeiro, G. Mascolo, C.S. McArdell, H. Schaar, A.M.T. Silva, D. Fatta-Kassinos, Consolidated vs new advanced treatment methods for the removal of contaminants of emerging concern from urban wastewater. *Sci. Total Environ.* 655 (**2019**) 986–1008.

[76] J.L. Acero, F.J. Benitez, F. Teva, A.I. Leal, Retention of emerging

micropollutants from UP water and a municipal secondary effluent by ultrafiltration and nanofiltration. *Chem. Eng. J.* 163 (**2010**) 264–272.

[77] A.R.D. Verliefde, Rejection of Organic Micropollutants by High Pressure Membranes (NF/RO) (PhD Thesis). *Water Management Academic Press, Netherlands* (**2008**).

[78] A.M. Urtiaga, G. Pérez, R. Ibáñez, I. Ortiz, Removal of pharmaceuticals from a WWTP secondary effluent by ultrafiltration/reverse osmosis followed by electrochemical oxidation of the RO concentrate. *Desalination* 331 (**2013**) 26–34.

[79] Á. Soriano, D. Gorri, A. Urtiaga, Membrane preconcentration as an efficient tool to reduce the energy consumption of perfluorohexanoic acid electrochemical treatment. *Sep. Purif. Technol.* 208 (**2019**) 160–168.

[80] G. Crini, E. Lichtfouse, L.D. Wilson, N. Morin-Crini, Adsorption-Oriented Processes Using Conventional and Non-Conventional Adsorbents for Wastewater Treatment. *Springer, Cham* (**2018**) 23–71.

[81] G. Crini, Recent developments in polysaccharide-based materials used as adsorbents in wastewater treatment. *Prog. Polym. Sci.* 30 (**2005**) 38–70.

[82] S. Karimi, M.T. Yaraki, R.R. Karri, A comprehensive review of the adsorption mechanisms and factors influencing the adsorption process from the perspective of bioethanol dehydration. *Renew. Sustain. Energy Rev.* 107 (**2019**) 535–553.

[83] D.B. Miklos, C. Remy, M. Jekel, K.G. Linden, J.E. Drewes, U. Hübner, Evaluation of advanced oxidation processes for water and wastewater treatment – A critical review. *Water Res.* 139 (**2018**) 118–131.

[84] A.R. Ribeiro, O.C. Nunes, M.F.R. Pereira, A.M.T. Silva, An overview on the advanced oxidation processes applied for the treatment of water pollutants defined in the recently launched Directive 2013/39/EU. *Environ. Int.* 75 (**2015**) 33–51.

[85] C. Teodosiu, A. Gilca, G. Barjoveanu, S. Fiore, Emerging pollutants removal through advanced drinking water treatment: A review on processes and

environmental performances assessment. *J. Clean. Prod.* 197 (**2018**) 1210–1221.

[86] M. Sillanpää, M.C. Ncibi, A. Matilainen, Advanced oxidation processes for the removal of natural organic matter from drinking water sources: A comprehensive review. *J. Environ. Manag.* 208 (**2018**) 56–76.

[87] C.A. Martínez-Huitle, M. Panizza, Electrochemical oxidation of organic pollutants for wastewater treatment. *Curr. Opin. Electrochem.* 11 (**2018**) 62–71.

[88] I. Sirés, E. Brillas, Remediation of water pollution caused by pharmaceutical residues based on electrochemical separation and degradation technologies: a review. *Environ. Int.* 40 (**2012**) 212–229.

[89] J. Radjenovic, D.L. Sedlak, Challenges and opportunities for electrochemical processes as next-generation technologies for the treatment of contaminated water. *Environ. Sci. Technol.* 49 (**2015**) 11292–11302.

[90] G. Chen, Electrochemical technologies in wastewater treatment. *Sep. Purif. Technol.* 38 (**2004**) 11–41.

[91] E.R. Coats, P.I. Wilson, Toward nucleating the concept of the water resource recovery facility (WRRF): perspective from the principal actors. *Environ. Sci. Technol.* 51 (**2017**) 4158–4164.

[92] A. Jos, G. Repetto, J.C. Ríos, A. del Peso, M. Salguero, M.J. Hazen, M.L. Molero, P. Fernández-Freire, J.M. Pérez-Martín, Ecotoxicological evaluation of the additive butylated hydroxyanisole using a battery with six model systems and eighteen endpoints. *Aquat. Toxicol.* 71 (**2005**) 183–192.

[93] V. Bhardwaj, P. Sharma, M.S. Chauhan, S. Chauhan, Micellization, interaction and thermodynamic study of butylated hydroxyanisole (synthetic antioxidant) and sodium dodecyl sulfate in aqueous-ethanol solution. *J. Saudi Chem. Soc.* 20 (**2016**) S109–S114.

[94] F. Shahidi, P. Ambigaipalan, Phenolics and polyphenolics in foods, beverages and spices: antioxidant activity and health effects – a review. *J. Funct. Foods* 18 (**2015**) 820–897.

[95] K.H.G. Freitas, O. Fatibello-Filho, Simultaneous determination of butylated

hydroxyanisole (BHA) and butylated hydroxytoluene (BHT) in food samples using a carbon composite electrode modified with $Cu_3(PO_4)_2$ immobilized in polyester resin. *Talanta* 81 (**2010**) 1102–1108.

[96] T.K. Lau, W. Chu, N. Graham, Reaction pathways and kinetics of butylated hydroxyanisole with UV, ozonation, and UV/O_3 processes. *Water Res.* 41 (**2007**) 765–774.

[97] T.K. Lau, W. Chu, N.J.D. Graham, The aqueous degradation of butylated hydroxyanisole by UV/$S_2O_8^{2-}$: study of reaction mechanisms via dimerization and mineralization. *Environ. Sci. Technol.* 41 (**2007**) 613–619.

[98] W. Chu, T.K. Lau, Ozonation of endocrine disrupting chemical BHA under the suppression effect by salt additive-with and without H_2O_2. *J. Hazard. Mater.* 144 (**2007**) 249–254.

[99] R. Rodil, J.B. Quintana, R. Cela, Oxidation of synthetic phenolic antioxidants during water chlorination. *J. Hazard. Mater.* 199–200 (**2012**) 73–81.

[100] P. Abdallah, M. Deborde, F.D. Berne, N.K.V. Leitner, Kinetics of chlorination of benzophenone-3 in the presence of bromide and ammonia. *Environ. Sci. Technol.* 49 (**2015**) 14359–14367.

[101] C.A. Downs, E. Kramarsky-Winter, R. Segal, J. Fauth, S. Knutson, O. Bronstein, F.R. Ciner, R. Jeger, Y. Lichtenfeld, C.M. Woodley, P. Pennington, K. Cadenas, A. Kushmaro, Y. Loya, Toxicopathological effects of the sunscreen UV filter, oxybenzone (benzophenone-3), on coral planulae and cultured primary cells and its environmental contamination in Hawaii and the U.S. Virgin Islands. *Arch. Environ. Contam. Toxicol.* 70 (**2016**) 265–288.

[102] P. Gago-Ferrero, K. Demeestere, M.S. Díaz-Cruz, D. Barceló, Ozonation and peroxone oxidation of benzophenone-3 in water: Effect of operational parameters and identification of intermediate products. *Sci. Total Environ.* 443 (**2013**) 209–217.

[103] Y.S. Liu, G.G. Ying, A. Shareef, R.S. Kookana, Biodegradation of the ultraviolet filter benzophenone-3 under different redox conditions. *Environ. Toxicol. Chem.*

31 (**2012**) 289–295.

[104] E. Gilberta, L. Roussela, C. Serre, R. Sandouk, D. Salmon, P. Kirilov, M. Haftek, F. Falson, F. Pirot, Percutaneous absorption of benzophenone-3 loaded lipid nanoparticles and polymeric nanocapsules: A comparative study. *Int. J. Pharm.* 504 (**2016**) 48–58.

[105] Y.J. Li, X.L. Qiao, C.Z. Zhou, Y.N. Zhang, Z.Q. Fu, J.W. Chen, Photochemical transformation of sunscreen agent benzophenone-3 and its metabolite in surface freshwater and seawater. *Chemosphere* 153 (**2016**) 494–499.

[106] H. Zúñiga-Benítez, J. Soltan, G.A. Peñuela, Application of ultrasound for degradation of benzophenone-3 in aqueous solutions. *Int. J. Environ. Sci. Technol.* 13 (**2016**) 77–86.

[107] Y. Guo, B. Xu, F. Qi, A novel ceramic membrane coated with MnO_2–Co_3O_4 nanoparticles catalytic ozonation for benzophenone-3 degradation in aqueous solution: Fabrication, characterization and performance. *Chem. Eng. J.* 287 (**2016**) 381–389.

[108] H. Zúñiga-Benítez, C. Aristizábal-Ciro, G.A.Peñuela, Photodegradation of the endocrine-disrupting chemicals benzophenone-3 and methylparaben using Fenton reagent: Optimization of factors and mineralization/biodegradability studies. *J. Taiwan Inst. Chem. Eng.* 59 (**2016**) 380–388.

[109] H. Zúñiga-Benítez, C. Aristizábal-Ciro, G.A.Peñuela, Heterogeneous photocatalytic degradation of the endocrine-disrupting chemical benzophenone-3: Parameters optimization and by-products identification. *J. Environ. Manage.* 167 (**2016**) 246–258.

[110] P. Gong, H. Yuan, P. Zhai, Y. Xue, H. Li, W. Dong, G. Mailhot, Investigation on the degradation of benzophenone-3 by UV/H_2O_2 in aqueous solution. *Chem. Eng. J.* 277 (**2015**) 97–103.

[111] C. Salazar, C. Ridruejo, E. Brillas, J. Yáñez, H.D. Mansilla, I. Sirés, Abatement of the fluorinated antidepressant fluoxetine (Prozac) and its reaction by-products by electrochemical advanced methods. *Appl. Catal. B: Environ.* 203

(**2017**) 189–198.

[112] C. Hiemke, S. Härtter, Pharmacokinetics of selective serotonin reuptake inhibitors. *Pharmacol. Ther.* 85 (**2000**) 11–28.

[113] C. Wang, J.F. Niu, L.F. Yin, J.X. Huang, L.A. Hou, Electrochemical degradation of fluoxetine on nanotube array intercalated anode with enhanced electronic transport and hydroxyl radical production. *Chem. Eng. J.* 346 (**2018**) 662–671.

[114] A. Izadyar, D. Ranawaka Arachchige, H. Cornwell, J.C. Hershberger, Ion transfer stripping voltammetry for the detection of nanomolarlevels of fluoxetine, citalopram, and sertraline in tap and river water samples. *Sens. Actuators B* 223 (**2016**) 226–233.

[115] J. Neuwoehner, K. Fenner, B.I. Escher, Physiological modes of action of fluoxetine and its human metabolites in algae. *Environ. Sci. Technol.* 43 (**2009**) 6830–6837.

[116] Y. Zhao, G. Yu, S. Chen, S. Zhang, B. Wang, J. Huang, S. Deng, Y. Wang, Ozonation of antidepressant fluoxetine and its metabolite product norfluoxetine: kinetics, intermediates and toxicity. *Chem. Eng. J.* 316 (**2017**) 951–963.

[117] F. Méndez-Arriaga, T. Otsu, T. Oyama, J. Gimenez, S. Esplugas, H. Hidaka, N. Serpone, Photooxidation of the antidepressant drug Fluoxetine (Prozac®) in aqueous media by hybrid catalytic/ozonation processes. *Water Res.* 45 (**2011**) 2782–2794.

[118] H.W. Yu, T. Anumol, M. Park, I. Pepper, J. Scheideler, S.A. Snyder, On-line sensor monitoring for chemical contaminant attenuation during UV/H_2O_2 advanced oxidation process. *Water Res.* 81 (**2015**) 250–260.

[119] A. Rossner, S. Snyder, D. Knappe, Removal of emerging contaminants of concern by alternative adsorbents. *Water Res.* 45 (**2009**) 3787–3796.

[120] J.L. Zurita, G. Repetto, Á. Jos, M. Salguero, M. López-Artíguez, A.M. Cameán, Toxicological effects of the lipid regulator gemfibrozil in four aquatic systems. *Aqua. Toxicol.* 81 (**2007**) 106–115.

[121] P. Zimetbaum, W.H. Frishman, S. Kahn, Effects of gemfibrozil and other fibric

acid derivates on blood lipids and lipoproteins. *J. Clin. Pharmacol.* 31 (**1991**) 25–37.

[122] C.E.S. Paniagua, I.A. Ricardo, E.O. Marson, B.R. Gonçalves, A.G. Trovó, Simultaneous degradation of the pharmaceuticals gemfibrozil, hydrochlorothiazide and naproxen and toxicity changes during UV-C and UV-C/H_2O_2 processes in different aqueous matrixes. *J. Environ. Chem. Eng.* 7 (**2019**) 103164.

[123] X. Kong, Z. Wu, Z. Ren, K. Guo, S. Hou, Z. Hua, X. Li, J. Fang, Degradation of lipid regulators by the UV/chlorine process: radical mechanisms, chlorine oxide radical ($ClO^{\bullet}$)-mediated transformation pathways and toxicity changes. *Water Res.* 137 (**2018**) 242–250.

[124] D. Fabbri, V. Maurino, M. Minella, C. Minero, D. Vione, Modelling the photochemical attenuation pathways of the fibrate drug gemfibrozil in surface waters. *Chemosphere* 170 (**2017**) 124–133.

[125] P. Chen, F. Wang, Z.F. Chen, Q. Zhang, Y. Su, L. Shen, K. Yao, Y. Liu, Z. Cai, W. Lv, G. Liu, Study on the photocatalytic mechanism and detoxicity of gemfibrozil by a sunlight-driven TiO_2/carbon dots photocatalyst: the significant roles of reactive oxygen species. *Appl. Catal. B: Environ.* 204 (**2017**) 250–259.

[126] J.S. Ma, W.Y. Lv, P. Chen, Y. Lu, F.L. Wang, F. Li, K. Yao, G.G. Liu, Photodegradation of gemfibrozil in aqueous solution under UV irradiation: kinetics, mechanism, toxicity, and degradation pathways. *Environ. Sci. Pollut. Res.* 23 (**2016**) 14294–14306.

[127] V.A.B. Paiva, C.E.S. Paniagua, I. Amildon Ricardo, B.R. Gonçalves, S. Pereira Martins, D. Daniel, A.E.H. Machado, A.G. Trovó, Simultaneous degradation of pharmaceuticals by classic and modified photo-Fenton process. *J. Environ. Chem. Eng.* 6 (**2018**) 1086–1092.

[128] R.F. Dantas, M. Canterino, R. Marotta, C. Sans, S. Esplugas, R. Andreozzi, Bezafibrate removal by means of ozonation: primary intermediates, kinetics, and toxicity assessment. *Water Res.* 41 (**2007**) 2525–2532.

[129] H. Yuan, Y.L. Zhang, X.F. Zhou, Degradation of bezafibrate with UV/H_2O_2 in surface water and wastewater treatment plant effluent. *Clean-Soil Air Water* 40 (**2012**) 239–245.

[130] B. Duarte, D. Prata, A.R. Matos, M.T. Cabrita, I. Cacador, J.C. Marques, H.N. Cabral, P. Reis-Santos, V.F. Fonseca, Ecotoxicity of the lipid-lowering drug bezafibrate on the bioenergetics and lipid metabolism of the diatom Phaeodactylum tricornutum. *Sci. Total Environ.* 650 (**2019**) 2085–2094.

[131] J. Liu, X. Dan, G. Lu, G. Shen, D. Wu, Z. Yan, Investigation of pharmaceutically active compounds in an urban receiving water: occurrence, fate and environmental risk assessment. *Ecotoxicol. Environ. Saf.* 154 (**2018**) 214–220.

[132] A.G. Gonçalves, J.J.M. Órfão, M.F.R. Pereira, Ozonation of bezafibrate promoted by carbon materials. *Appl. Catal. B: Environ.* 140–141 (**2013**) 82–92.

[133] A.G. Trovó, S.A.S. Melo, R.F.P. Nogueira, Photodegradation of the pharmaceuticals amoxicillin, bezafibrate and paracetamol by the photo-Fenton process – application to sewage treatment plant effluent. *J. Photochem. Photobiol. A* 198 (**2008**) 215–220.

[134] D.A. Lambropoulou, M.D. Hernando, I.K. Konstantinou, E.M. Thurman, I. Ferrer, T.A. Albanis, A.R. Fernández-Alba, Identification of photocatalytic degradation products of bezafibrate in TiO_2 aqueous suspensions by liquid and gas chromatography. *J. Chromatogr. A* 1183 (**2008**) 38–48.

[135] M. Clara, B. Strenn, O. Gans, E. Martinez, N. Kreuzinger, H. Kroiss, Removal of selected pharmaceuticals, fragrances and endocrine disrupting compounds in a membrane bioreactor and conventional wastewater treatment plants. *Water Res.* 39 (**2005**) 4797–4807.

[136] N. Liu, G. Liang, X. Dong, X. Qi, J. Kim, Y. Piao, Stabilized magnetic enzyme aggregates on graphene oxide for high performance phenol and bisphenol A removal. *Chem. Eng. J.* 306 (**2016**) 1026–1034.

[137] E. Kurtulbaş, M. Bilgin, S. Şahin, Ş.S. Bayazit, Comparison of different polymeric resins for naproxen removal from wastewater. *J. Mol. Liq.* 241 (**2017**)

633–637.

[138] K. Govindan, A. Angelin, M. Rangarajan, Critical evaluation of mechanism responsible for biomass abatement during electrochemical coagulation (EC) process: a critical review. *J. Environ. Manag.* 227 (**2018**) 335–353.

[139] P. Cañizares, F. Martínez, M. Carmona, J. Lobato, M.A. Rodrigo, Continuous electrocoagulation of synthetic colloid-polluted wastes. *Ind. Eng. Chem. Res.* 44 (22) (**2005**) 8171–8177.

[140] P.K. Holt, G.W. Barton, M. Wark, C.A. Mitchell, A quantitative comparison between chemical dosing and electrocoagulation. *Colloids Surf. A: Physicochem. Eng. Aspects* 211 (**2002**) 233–248.

[141] P. Krystynik, D.N. Tito, Key process parameters affecting performance of electro-coagulation. *Chem. Eng. Process. Process Intensif.* 117 (**2017**) 106–112.

[142] S. Garcia-Segura, M.M.S.G. Eiband, J.V. de Melo, C.A. Martínez-Huitle, Electrocoagulation and advanced electrocoagulation processes: a general review about the fundamentals, emerging applications and its association with other technologies. *J. Electroanal. Chem.* 801 (**2017**) 267–299.

[143] N. Daneshvar, H. Ashassi-Sorkhabi, A. Tizpar, Decolorization of organge II by electrocoagulation method. *Sep. Purif. Technol.* 31 (**2003**) 153–162.

[144] M.Y.A. Mollah, P. Morkovsky, J.A.G. Gomes, M. Kesmez, J. Parga, D.L. Cocke, Fundamentals, present and future perspectives of electrocoagulation. *J. Hazard. Mater.* 114 (**2004**) 199–210.

[145] A. Matilainen, M. Vepsäläinen, M. Sillanpää, Natural organic matter removal by coagulation during drinking water treatment: a review. *Adv. Colloid Interf. Sci.* 159 (**2010**) 189–197.

[146] J.N. Hakizimana, B. Gourich, M. Chafi, Y. Stiriba, C. Vial, P. Drogui, J. Naja, Electrocoagulation process in water treatment: a review of electrocoagulation modeling approaches. *Desalination* 404 (**2017**) 1–21.

[147] S. Vasudevan, J. Lakshmi, Effects of alternating and direct current in electrocoagulation process on the removal of cadmium from water – a novel

approach. *Sep. Purif. Technol.* 80 (**2011**) 643–651.

[148] A.S. Fajardo, R.F. Rodrigues, R.C. Martins, L.M. Castro, R.M. Quinta-Ferreira, Phenolic wastewaters treatment by electrocoagulation process using Zn anode. *Chem. Eng. J.* 275 (**2015**) 331–341.

[149] E. Bocos, E. Brillas, M.A. Sanromán, I. Sirés, Electrocoagulation: simply a phase separation technology? The case of bronopol compared to its treatment by EAOPs. *Environ. Sci. Technol.* 50 (**2016**) 7679–7686.

[150] C. Barrera-Díaz, F. Ureña-Nuñez, E. Campos, M. Palomar-Pardavé, M. Romero-Romo, A combined electrochemical-irradiation treatment of highly colored and polluted industrial wastewater. *Radiat. Phys. Chem.* 67 (**2003**) 657–663.

[151] M. Kobya, M. Bayramoglu, M. Eyvaz, Techno-economical evaluation of electrocoagulation for the textile wastewater using different electrode connections. *J. Hazard. Mater.* 148 (**2007**) 311–318.

[152] O. Sahu, B. Mazumdar, P.K. Chaudhari, Treatment of wastewater by electrocoagulation: a review. *Environ. Sci. Pollut. Res.* 21 (**2014**) 2397–2413.

[153] M.Y.A. Mollah, R. Schennach, J.P. Parga, D.L. Cocke, Electrocoagulation (EC)—science and applications. *J. Hazard. Mater.* 84 (**2001**) 29–41.

[154] A. Medel, J.A. Ramírez, J. Cárdenas, I. Sirés, Y. Meas, Evaluating the electrochemical and photoelectrochemical production of hydroxyl radical during electrocoagulation process. *Sep. Purif. Technol.* (**2018**) 59–67.

[155] D. Wang, J.R. Bolton, R. Hofmann, Medium pressure UV combined with chlorine advanced oxidation for trichloroethylene destruction in a model water. *Water Res.* 46 (**2012**) 4677–4686.

[156] P.Y. Chan, M.G. El-Din, J.R. Bolton, A solar-driven UV/Chlorine advanced oxidation process. *Water Res.* 46 (**2012**) 5672–5682.

[157] N. Kishimoto, Y. Nakamura, M. Kato, H. Otsu, Effect of oxidation–reduction potential on an electrochemical Fenton-type process. *Chem. Eng. J.* 260 (**2015**) 590–595.

[158] I. Sirés, E. Brillas, M.A. Oturan, M.A. Rodrigo, M. Panizza, Electrochemical advanced oxidation processes: Today and tomorrow. A review. *Environ. Sci. Pollut. Res.* 21 (**2014**) 8336–8367.

[159] S. Cotillas, J. Llanos, O.G. Miranda, G.C. Díaz-Trujillo, P. Cañizares, M.A. Rodrigo, Coupling UV irradiation and electrocoagulation for reclamation of urban wastewater. *Electrochim. Acta* 140 (**2014**) 396–403.

[160] E. Brillas, R. Sauleda, J. Casado, Peroxi-coagulation of aniline in acidic medium using and oxygen diffusion cathode. *J. Electrochem. Soc.* 144 (**1997**) 2374–2379.

[161] E. Brillas, B. Boye, M.A. Baños, J.C. Calpe, J.A. Garrido, Electrochemical degradation of chlorophenoxy and chlorobenzoic herbicides in acidic aqueous médium by the peroxi-coagulation method. *Chemosphere* 51 (**2003**) 227–235.

[162] S. Vasudevan, An efficient removal of phenol from water by peroxi-electrocoagulation processes. *J. Water Process Eng.* 2 (**2014**) 53–57.

[163] E. Brillas, J. Casado, Aniline degradation by electro-Fenton® and peroxi-coagulation processes using a flow reactor for wastewater treatment. *Chemosphere* 47 (**2002**) 241–248.

[164] M. Zarei, A. Niaei, D. Salari, A.R. Khataee, Removal of four dyes from aqueous medium by the peroxi-coagulation method using carbon nanotube-PTFE cathode and neural network modeling. *J. Electroanal. Chem.* 639 (**2010**) 167–174.

[165] C. Barrera-Díaz, B. Frontana-Uribe, B. Bilyeu, Removal of organic pollutants in industrial wastewater with na integrated system of copper electrocoagulation and electrogenerated H_2O_2. *Chemosphere* 105 (**2014**) 160–164.

[166] S. Farhadi, B. Aminzadeh, A. Torabian, V. Khatibikamal, M.A. Fard, Comparison of COD removal from pharmaceutical wastewater by electrocoagulation, photoelectrocoagulation, peroxi-electrocoagulation and peroxi-photoelectrocoagulation processes. *J. Hazard. Mater.* 219–220 (**2012**) 35–42.

[167] B. Boye, M.M. Dieng, E. Brillas, Electrochemical degradation of 2,4,5-trichlorophenoxyacetic acid in aqueous medium by peroxi-coagulation. Effect of pH and UV light. *Electrochim. Acta* 48 (**2003**) 781–790.

[168] Z. Al-Qodah, M. Al-Shannag, K. Bani-Melhem, E. Assirey, M.A. Yahya, A. Al-Shawabkeh, Free radical-assisted electrocoagulation processes for wastewater treatment. *Environ. Chem. Lett.* 16 (**2018**) 1–20.

[169] P. Asaithambi, M. Susree, R. Saravanathamizhan, M. Matheswaran, Ozone assisted electrocoagulation for the treatment of distillery effluent. *Desalination* 297 (**2012**) 1–7.

[170] R. Sauleda, E. Brillas, Mineralization of aniline and 4-chlorophenol in acidic solution by ozonation catalyzed with Fe^{2+} and UVA light. *Appl. Catal. B: Environ.* 29 (**2001**) 135–145.

[171] C.C. He, C.Y. Hu, S.L. Lo, Evaluation of sono-electrocoagulation for the removal of Reactive Blue 19 passive film removed by ultrasound. *Sep. Purif. Technol.* 165 (**2016**) 107–113.

[172] M. Ben-Sasson, Y.M. Lin, A. Adin, Electrocoagulation-membrane filtration hybrid system for colloidal fouling mitigation of secondary-effluent. *Sep. Purif. Technol.* 82 (**2011**) 63–70.

[173] X. Zhao, B. Zhang, H. Liu, J. Qu, Removal of arsenite by simultaneous electro-oxidation and electro-coagulation process. *J. Hazard. Mater.* 184 (**2010**) 472–476.

[174] A. Fernandes, M.J. Pacheco, L. Ciriaco, A. Lopes, Review on the electrochemical processes for the treatment of sanitary landfill leachates: Present and future. *Appl. Catal. B: Environ.* 176–177 (**2015**) 183–200.

[175] F.C. Moreira, A.R.B. Rui, E. Brillas, V.J.P. Vilar, Electrochemical advanced oxidation processes: a review on their application to synthetic and real wastewaters. *Appl. Catal. B: Environ.* 202 (**2016**) 217–261.

[176] C. Ridruejo, F. Centellas, P.L. Cabot, I. Sirés, E. Brillas, Electrochemical Fenton-based treatment of tetracaine in synthetic and urban wastewater using

active and non-active anodes. *Water Res.* 128 (**2017**) 71–81.

[177] W. Wu, Z.H. Huang, T.T. Lim, Recent development of mixed metal oxide anodes for electrochemical oxidation of organic pollutants in water. *Appl. Catal. A: Gen.* 480 (**2014**) 58–78.

[178] A. Kapalka, G. Fóti, C. Comninellis, Kinetic modelling of the electrochemical mineralization of organic pollutants for wastewater treatment. *J. Appl. Electrochem.* 38 (**2008**) 7–16.

[179] A. Anglada, A. Urtiaga, I. Ortiz, Contributions of electrochemical oxidation to waste-water treatment: fundamentals and review of applications. *J. Chem. Technol. Biotechnol.* 84 (**2009**) 1747–1755.

[180] B. Marselli, J. Garcia-Gomez, P.A. Michaud, M.A. Rodrigo, C. Comninellis, Electrogeneration of hydroxyl radicals on boron-doped diamond electrodes. *J. Electrochem. Soc.* 150 (**2003**) D79–D83.

[181] R. Oriol, I. Sirés, E. Brillas, A.R.D. Andrade, A hybrid photoelectrocatalytic/photoelectro-Fenton treatment of Indigo Carmine in acidic aqueous solution using TiO_2 nanotube arrays as photoanode. *J. Electroanal. Chem.* 847 (**2019**) 113088.

[182] I. Olvera-Rodríguez, R. Hernández, A. Medel, C. Guzmán, L. Escobar-Alarcón, E. Brillas, I. Sirés, K. Esquivel, TiO_2/Au/TiO_2 multilayer thin-film photoanodes synthesized by pulsed laser deposition for photoelectrochemical degradation of organic pollutants. *Separ. Purif. Technol.* 224 (**2019**) 189–198.

[183] O. Scialdone, Electrochemical oxidation of organic pollutants in water at metal oxide electrodes: a simple theoretical model including direct and indirect oxidation processes at the anodic surface. *Electrochim. Acta* 54 (**2009**) 6140–6147.

[184] O. Scialdone, S. Randazzo, A. Galia, G. Filardo, Electrochemical oxidation of organics at metal oxide electrodes: The incineration of oxalic acid at IrO_2–Ta_2O_5 (DSA-O_2) anode. *Electrochim. Acta* 54 (**2009**) 1210–1217.

[185] Y. Feng, Y.H. Cui, J. Liu, B.E. Logan, Factors affecting the electro-catalytic

characteristics of Eu doped SnO_2/Sb electrode. *J. Hazard. Mater.* 178 (**2010**) 29–34.

[186] N. Gelfond, N.B. Morozova, I.K. Igumenov, E.S. Filatov, S.A. Gromilov, Y.V. Shubin, R.I. Kvon, V.S. Danilovich, Structure of Ir and Ir-Al_2O_3 coatings obtained by chemical vapor deposition in the presence of oxygen. *J. Struct. Chem.* 51 (**2010**) 82–91.

[187] Y.Q. Wang, B. Gu, W.L. Xu, L.D. Lu, Electrochemical oxidation of phenol on Ti-based PbO_2 electrodes. *Rare Metal Mater. Eng.* 36 (**2007**) 874–878.

[188] H. An, H. Cui, W.Y. Zhang, J.P. Zhai, Y. Qian, X.C. Xie, Q. Li, Fabrication and electrochemical treatment application of a microstructured TiO_2-NTs/Sb-SnO_2/PbO_2 anode in the degradation of CI Reactive Blue 194 (RB 194). *Chem. Eng. J.* 209 (**2012**) 86–93.

[189] G.H. Zhao, X. Cui, M.C. Liu, P.Q. Li, Y.G. Zhang, T.C. Cao, H.X. Li, Y.Z. Lei, L. Liu, D.M. Li, Electrochemical degradation of refractory pollutant using a novel microstructured TiO_2 nanotubes/Sb-doped SnO_2 electrode. *Environ. Sci. Technol.* 43 (**2009**) 1480–1486.

[190] J. Niu, H. Lin, J. Xu, H. Wu, Y. Li, Electrochemical mineralization of perfluorocarboxylic acids (PFCAs) by Ce-doped modified porous nanocrystalline PbO_2 film electrode. *Environ. Sci. Technol.* 46 (**2012**) 10191–10198.

[191] D. Rajkumar, J.G. Kim, K. Palanivelu, Indirect Electrochemical oxidation of phenol in the presence of chloride for wastewater treatment. *Chem. Eng. Technol.* 28 (**2005**) 98–105.

[192] J.F. Niu, Y.P. Bao, Y. Li, Z. Chai, Electrochemical mineralization of pentachlorophenol (PCP) by Ti/SnO_2-Sb electrodes. *Chemosphere* 92 (**2013**) 1571–1577.

[193] E. Brillas, I. Sirés, M.A. Oturan, Electro-Fenton process and related electrochemical technologies based on Fenton's reaction chemistry. *Chem. Rev.* 109 (**2009**) 6570–6631.

[194] H.J.H. Fenton, Oxidation of tartaric acid in presence of iron. *J. Chem. Soc. Trans.* 65 (**1894**) 899–910.

[195] W. Zhou, X. Meng, J. Gao, A.N. Alshawabkeh, Hydrogen peroxide generation from O_2 electroreduction for environmental remediation: A state-of-the-art review. *Chemosphere* 225 (**2019**) 588–607.

[196] F.C. Moreira, S. Garcia-Segura, R.A.R. Boaventura, E. Brillas, V.J.P. Vilar, Degradation of the antibiotic trimethoprim by electrochemical advanced oxidation processes using a carbon-PTFE air-diffusion cathode and a boron-doped diamond or platinum anode. *Appl. Catal. B: Environ.* 160–161 (**2014**) 492–505.

[197] H. Zhang, X. Ran, X. Wu, Electro-Fenton treatment of mature landfill leachate in a continuous flow reactor. *J. Hazard. Mater.* 241–242 (**2012**) 259–266.

[198] M. Umar, H.A. Aziz, M.S. Yusoff, Trends in the use of Fenton, electro-Fenton and photo-Fenton for the treatment of landfill leachate. *Waste Manage.* 30 (**2010**) 2113–2121.

[199] Y. Wang, X. Li, L. Zhen, H. Zhang, Y. Zhang, C. Wang, Electro-Fenton treatment of concentrates generated in nanofiltration of biologically pretreated landfill leachate. *J. Hazard. Mater.* 229–230 (**2012**) 115–121.

[200] S.O. Ganiyu, M. Zhou, C.A. Martínez-Huitle, Heterogeneous electro-Fenton and photoelectro-Fenton processes: A critical review of fundamental principles and application for water/wastewater treatment. *Appl. Catal. B: Environ.* 235 (**2018**) 103–129.

[201] L. Clarizia, D. Russo, I. Di Somma, R. Marotta, R. Andreozzi, Homogeneous photo-Fenton processes at near neutral pH: a review. *Appl. Catal. B: Environ.* 209 (**2017**) 358–371.

[202] N. Klamerth, S. Malato, A. Agüera, A. Fernández-Alba, G. Mailhot, Treatment of municipal wastewater treatment plant effluents with modified photo-Fenton as a tertiary treatment for the degradation of micro pollutants and disinfection. *Environ. Sci. Technol.* 46 (**2012**) 2885–2892.

[203] Z. Ye, I. I. Sirés, H. Zhang, Y.H. Huang, Mineralization of pentachlorophenol by ferrioxalate-assisted solar photo-Fenton process at mild pH. *Chemosphere* 217 (**2019**) 475–482.

[204] C. Ruales-Lonfat, J.F. Barona, A. Sienkiewicz, J. Vélez, L.N. Benítez, C. Pulgarín, Bacterial inactivation with iron citrate complex: a new source of dissolved iron in solar photo-Fenton process at near-neutral and alkaline pH. *Appl. Catal. B: Environ.* 180 (**2016**) 379–390.

[205] P. Soriano-Molina, J.L. García Sánchez, S. Malato, L.A. Pérez-Estrada, J.A. Sánchez Pérez, Effect of volumetric rate of photon absorption on the kinetics of micropollutant removal by solar photo-Fenton with Fe^{3+}-EDDS at neutral pH. *Chem. Eng. J.* 331 (**2018**) 84–92.

[206] M.D. Engelmann, R.T. Bobier, T. Hiatt, I.F. Cheng, Variability of the Fenton reaction characteristics of the EDTA, DTPA, and citrate complexes of iron. *Biometals* 16 (**2003**) 519–527.

[207] J. De Laat, Y.H. Dao, N.H. El Najjar, C. Daou, Effect of some parameters on the rate of the catalysed decomposition of hydrogen peroxide by iron (III)-nitrilotriacetate in water. *Water Res.* 45 (**2011**) 5654–5664.

[208] M. Fukushima, K. Tatsumi, S. Nagao, Degradation characteristics of humic acid during photo-Fenton processes. *Environ. Sci. Technol.* 35 (**2001**) 3683–3690.

[209] B.M. Souza, M.W.C. Dezotti, R.A.R. Boaventura, V.J.P. Vilar, Intensification of a solar photo-Fenton reaction at near neutral pH with ferrioxalate complexes: a case study on diclofenac removal from aqueous solutions. *Chem. Eng. J.* 256 (**2014**) 448–457.

[210] S. Papoutsakis, F.F. Brites-Nóbrega, C. Pulgarin, S. Malato, Benefits and limitations of using Fe(III)-EDDS for the treatment of highly contaminated water at near-neutral pH. *J. Photochem. Photobiol. A: Chem.* 303–304 (**2015**) 1–7.

[211] D. Schowanek, T.C.J. Feijtel, C.M. Perkins, F.A. Hartman, T.W. Federle, R.J. Larson, Biodegradation of [S,S], [R,R] and mixed stereoisomers of Ethylene

Diamine Disuccinic Acid (EDDS), a transition metal chelator. *Chemosphere* 34 (**1997**) 2375–2391.

[212] Y. Zhang, N. Klamerth, S.A. Messele, P. Chelme-Ayala, M.G. El-Din, Kinetics study on the degradation of a model naphthenic acid by ethylenediamine-N, N′-Disuccinic acid-modified Fenton process. *J. Hazard. Mater.* 318 (**2016**) 371–378.

[213] Y. Zhang, M. Zhou, A critical review of the application of chelating agents to enable Fenton and Fenton-like reactions at high pH values. *J. Hazard. Mater.* 362 (**2019**) 436–450.

[214] M. Orama, H. Hyvönen, H. Saarinen, R. Aksela, Complexation of [S,S] and mixed stereoisomers of N, N′-ethylenediaminedisuccinic acid (EDDS) with Fe (III), Cu (II), Zn (II) and Mn (II) ions in aqueous solution. *J. Chem. Soc. Dalton Trans.* (**2002**) 4644–4648.

[215] A. Bianco, M.I. Polo-Lopez, P. Fernandez-Ibanez, M. Brigante, G. Mailhot, Disinfection of water inoculated with Enterococcus faecalis using solar/ Fe(III)EDDS-H_2O_2 or $S_2O_8^{2-}$ process. *Water Res.* 118 (**2017**) 246–260.

[216] Y. Wu, M. Passananti, M. Brigante, W. Dong, G. Mailhot, Fe(III)-EDDS complex in Fenton and photo-Fenton processes: from the radical formation to the degradation of a target compound. *Environ. Sci. Pollut. Res.* 21 (**2014**) 12154–12162.

[217] W. Huang, M. Brigante, F. Wu, C. Mousty, K. Hanna, G. Mailhot, Assessment of the Fe (III)-EDDS complex in Fenton-like processes: from the radical formation to the degradation of bisphenol A. *Environ. Sci. Technol.* 47 (**2013**) 1952–1959.

[218] Y. Wu, Application of Fe(III)-EDDS Complex in Advanced Oxidation Processes: 4-Ter-Butylphenol Degradation. *Université Blaise Pascal-Clermont-Ferrand II* (**2014**).

[219] J. Li, G. Mailhot, F. Wu, N.S. Deng, Photochemical efficiency of Fe(III)-EDDS complex: OH radical production and 17β-estradiol degradation. *J. Photochem.*

Photobiol. A: Chem. 212 (**2010**) 1–7.

[220] N. Klamerth, S. Malato, A. Aguera, A. Fernandez-Alba, Photo-Fenton and modified photo-Fenton at neutral pH for the treatment of emerging contaminants in wastewater treatment plant effluents: a comparison. *Water Res.* 47 (**2013**) 833–840.

[221] J. Casado, Towards industrial implementation of Electro-Fenton and derived technologies for wastewater treatment: a review. *J. Environ. Chem. Eng.* 7 (**2019**) 102823–102838.

[222] P.V. Nidheesh, H. Olvera-Vargas, N. Oturan, M.A. Oturan, Heterogeneous Electro-Fenton Process: Principles and Applications. *Springer Berlin Heidelberg, Berlin, Heidelberg* (**2017**).

[223] L. Labiadh, M.A. Oturan, M. Panizza, N.B. Hamadi, S. Ammar, Complete removal of AHPS synthetic dye from water using new electro-fenton oxidation catalyzed by natural pyrite as heterogeneous catalyst. *J. Hazard. Mater.* 297 (**2015**) 34–41.

[224] V. Poza-Nogueiras, E. Rosales, M. Pazos, M.Á. Sanromán, Current advances and trends in electro-Fenton process using heterogeneous catalysts–a review. *Chemosphere* 201 (**2018**) 399–416.

[225] Y. Zhu, R. Zhu, Y. Xi, J. Zhu, G. Zhu, H. He, Strategies for enhancing the heterogeneous Fenton catalytic reactivity: A review. *Appl. Catal. B: Environ.* 255 (**2019**) 117739.

[226] S. Giannakis, M.I.P. López, D. Spuhler, J.A.S. Pérez, P.F. Ibáñez, C. Pulgarin, Solar disinfection is an augmentable, in situ -generated photo-Fenton reaction—Part 1: a review of the mechanisms and the fundamental aspects of the process. *Appl. Catal. B: Environ.* 199 (**2016**) 199–223.

[227] J. Herney-Ramirez, M.A. Vicente, L.M. Madeira, Heterogeneous photo-Fenton oxidation with pillared clay-based catalysts for wastewater treatment: a review. *Appl. Catal. B: Environ.* 98 (**2010**) 10–26.

[228] Q. Wang, S. Tian, J. Long, P. Ning, Use of Fe(II)Fe(III)-LDHs prepared by co-

precipitation method in a heterogeneous-Fenton process for degradation of methylene blue. *Catal. Today* 224 (**2014**) 41–48.

[229] M. Cheng, C. Lai, Y. Liu, G. Zeng, D. Huang, C. Zhang, L. Qin, L. Hu, C. Zhou, W. Xiong, Metal-organic frameworks for highly efficient heterogeneous Fenton-like catalysis. *Coord. Chem. Rev.* 368 (**2018**) 80–92.

[230] V.K. Sharma, M. Feng, Water depollution using metal-organic frameworks-catalyzed advanced oxidation processes: a review. *J. Hazard. Mater.* 372 (**2019**) 3–16.

[231] Y. Liu, Z. Liu, D. Huang, M. Cheng, G. Zeng, C. Lai, C. Zhang, C. Zhou, W. Wang, D. Jiang, H. Wang, B. Shao, Metal or metal-containing nanoparticle@MOF nanocomposites as a promising type of photocatalyst. Coord. *Chem. Rev.* 388 (**2019**) 63–78.

[232] P. Silva, S.M.F. Vilela, J.P.C. Tome, F.A.A. Paz, Multifunctional metal–organic frameworks: from academia to industrial applications. *Chem. Soc. Rev.* 44 (**2015**) 6774–6803.

[233] C. Cao, C. Tan, M. Sindoro, H. Zhang, Hybrid micro-/nano-structures derived from metal-organic frameworks: preparation and applications in energy storage and conversion. *Chem. Soc. Rev.* 45 (**2017**) 2660–2677.

[234] M.F. de Lange, K.J. Verouden, T.J. Vlugt, J. Gascon, F. Kapteijn, Adsorption-driven heat pumps: the potential of metal–organic frameworks. *Chem. Rev.* 115 (**2015**) 12205–12250.

[235] B. Van de Voorde, B. Bueken, J. Denayer, D. De Vos, Adsorptive separation on metal–organic frameworks in the liquid phase. *Chem. Soc. Rev.* 43 (**2014**) 5766–5788.

[236] T. Zhang, W. Lin, Metal–organic frameworks for artificial photosynthesis and photocatalysis. *Chem. Soc. Rev.* 43 (**2014**) 5982–5993.

[237] X. Liu, Y. Zhou, J. Zhang, L. Tang, L. Luo, G. Zeng, Iron containing metal-organic frameworks: structure, synthesis, and applications in environmental remediation. *ACS Appl. Mater. Interfaces* 9 (**2017**) 20255–20275.

[238] E. Dias, C. Petit, Towards the use of metal-organic frameworks for water reuse: a review of the recent advances in the field of organic pollutants removal and degradation and the next steps in the field. *J. Mater. Chem. A.* 3 (**2015**) 22484–22506.

[239] R.R. Salunkhe, Y.V. Kaneti, Y. Yamauchi, Metal–organic framework-derived nanoporous metal oxides toward supercapacitor applications: Progress and prospects. *ACS Nano* 11 (**2017**) 529–5308.

[240] I. Cota, F. Fernandez Martinez, Recent advances in the synthesis and applications of metal organic frameworks doped with ionic liquids for CO_2 adsorption. *Coord. Chem. Rev.* 351 (**2017**) 189–204.

[241] M. Ma, A. Bétard, I. Weber, N.S. Al-Hokbany, R.A. Fischer, N. Metzler-Nolte, Iron-based metal–organic frameworks MIL-88B and NH_2-MIL-88B: high quality microwave synthesis and solvent-induced lattice "breathing". *Cryst. Growth Des.* 13 (**2013**) 2286–2291.

[242] M. Ma, H. Noei, B. Mienert, J. Niesel, E. Bill, M. Muhler, R.A. Fischer, Y. Wang, U. Schatzschneider, N. Metzler-Nolte, Iron metal–organic frameworks MIL-88B and NH_2-MIL-88B for the loading and delivery of the gasotransmitter carbon monoxide. *Chem. Eur. J.* 19 (**2013**) 6785–6790.

[243] Q. Sun, M. Liu, K. Li, Y. Zuo, Y. Han, J. Wang, C. Song, G. Zhang, X. Guo, Facile synthesis of Fe-containing metal-organic frameworks as highly efficient catalysts for degradation of phenol at neutral pH and ambient temperature. *Crystengcomm* 17 (**2015**) 7160–7168.

[244] Y. Li, H. Liu, W.J. Li, F.Y. Zhao, W.J. Ruan, A nanoscale Fe(II) metal-organic framework with a bipyridinedicarboxylate ligand as a high performance heterogeneous Fenton catalyst. *RSC Adv.* 6 (**2016**) 6756–6760.

[245] C. Gao, S. Chen, X. Quan, H.T. Yu, Y.B. Zhang, Enhanced Fenton-like catalysis by iron-based metal organic frameworks for degradation of organic pollutants. *J. Catal.* 356 (**2017**) 125–132.

[246] D. Wang, M. Wang, Z. Li, Fe-based metal-organic frameworks for highly

selective photocatalytic benzene hydroxylation to phenol. *ACS Catal.* 5 (**2015**) 6852–6857.

[247] L. Ai, C. Zhang, L. Li, J. Jiang, Iron terephthalate metal-organic framework: revealing the effective activation of hydrogen peroxide for the degradation of organic dye under visible light irradiation. *Appl. Catal. B: Environ.* 148–149 (**2014**) 191–200.

[248] J.T. Tang, J.L. Wang, Fenton-like degradation of sulfamethoxazole using Fe-based magnetic nanoparticles embedded into mesoporous carbon hybrid as an efficient catalyst. *Chem. Eng. J.* 351 (**2018**) 1085–1094.

[249] T. Zeng, M. Yu, H. Zhang, Z. He, J. Chen, S. Song, Fe/Fe_3C@N-doped porous carbon hybrids derived from nano-scale MOFs: robust and enhanced heterogeneous catalyst for PMS activation. *Catal. Sci. Technol.* 7 (**2017**) 396–404.

[250] K.Y.A. Lin, F.K. Hsu, Magnetic iron/carbon nanorods derived from a metal organic framework as an efficient heterogeneous catalyst for the chemical oxidation process in water. *RSC Adv.* 5 (**2015**) 50790–50800.

[251] C. Zhang, F.G. Ye, S.F. Shen, Y.H. Xiong, L.J. Su, S.L. Zhao, From metal-organic frameworks to magnetic nanostructured porous carbon composites: towards highly efficient dye removal and degradation. *RSC Adv.* 5 (**2015**) 8228–8235.

[252] H. Zhao, Y. Chen, Q. Peng, Q. Wang, G. Zhao, Catalytic activity of MOF(2Fe/Co)/carbon aerogel for improving H_2O_2 and $^{\bullet}OH$ generation in solar photo-electro-Fenton process. *Appl. Catal. B: Environ.* 203 (**2017**) 127–137.

[253] Y. He, H. Lin, Z. Guo, W. Zhang, H. Li, W. Huang, Recent developments and advances in boron-doped diamond electrodes for electrochemical oxidation of organic pollutants. *Sep. Purif. Technol.* 212 (**2019**) 802–821.

[254] F.J. Welcher (Ed.), 6th ed., Standard Methods of Chemical Analysis, Part B, vol. 2, *R.E. Krieger Pub. Co., New York* (**1975**) 1827.

[255] APWA, AWWA, WEF, Standard methods for the examination of water and

wastewater. Method Number 4500-Cl Chlorine (Residual)–G. DPD Colorimetric Method (twenty-first ed.). *American Public Health Association, Washington D.C.* (**2005**) 4–67 and 4–68.

[256] D.B. Horn, C.R. Squire, The estimation of ammonia using the indophenol blue reaction. *Clin. Chim. Acta* 14 (**1966**) 185–194.

[257] H. Tamura, K. Goto, T. Yotsuyanagi, M. Nagayama, Spectrophotometric determination of iron(III) with 1,10-phenanthroline in the presence of large amounts of iron(III). *Talanta* 21 (**1974**) 314–318.

[258] M. Cai, Y. Zhu, Z. Wei, J. Hu, S. Pan, R. Xiao, C. Dong, M. Jin, Rapid decolorization of dye Orange G by microwave enhanced Fenton-like reaction with delafossite-type $CuFeO_2$. *Sci. Total Environ.* 580 (**2017**) 966–973.

[259] M. Vera, J. Martín-Alonso, J. Mesa, M. Granados, J.L. Beltran, S. Casas, O. Gibert, J.L. Cortina, Monitoring UF membrane performance treating surface-groundwater blends: limitations of FEEM-PARAFAC on the assessment of the organic matter role. *Chem. Eng. J.* 317 (**2017**) 961–971.

[260] A. Cruz-Alcalde, C. Sans, S. Esplugas, Exploring ozonation as treatment alternative for methiocarb and formed transformation products abatement. *Chemosphere* 186 (**2017**) 725–732.

Publications and Meetings

Publications in Scientific Indexed Journals

[1] **Z. Ye**, E. Brillas, F. Centellas, P.L. Cabot, I. Sirés, Electrochemical treatment of butylated hydroxyanisole: Electrocoagulation versus advanced oxidation. *Sep. Purif. Technol.* 208 (**2019**) 19–26.

[2] **Z. Ye**, J.R. Steter, F. Centellas, P.L. Cabot, E. Brillas, I. Sirés, Photoelectro-Fenton as post-treatment for electrocoagulated benzophenone-3-loaded synthetic and urban wastewater. *J. Clean. Prod.* 208 (**2019**) 1393–1402.

[3] **Z. Ye**, E. Brillas, F. Centellas, P.L. Cabot, I. Sirés, Electro-Fenton process at mild pH using Fe(III)–EDDS as soluble catalyst and carbon felt as cathode. *Appl. Catal. B: Environ.* 257 (**2019**) 117907.

[4] **Z. Ye**, E. Brillas, F. Centellas, P.L. Cabot, I. Sirés, Expanding the application of photoelectro-Fenton treatment to urban wastewater using the Fe(III)-EDDS complex. *Water Res.* DOI: 10.1016/j.watres.2019.115219.

[5] **Z. Ye**, J.A. Padilla, E. Xuriguera, J.L. Beltran, F. Alcaide, E. Brillas, I. Sirés, A highly stable MOF-engineered FeS_2/C nanocatalyst for heterogeneous electro-Fenton treatment: Validation in wastewater at mild pH. *Environ. Sci. Technol.* (**Submitted**).

[6] **Z. Ye**, J.A. Padilla, E. Xuriguera, E. Brillas, I. Sirés, Magnetic MIL(Fe)-type MOF-derived N-doped nano-ZVI@C rods as heterogeneous catalyst for the electro-Fenton degradation of gemfibrozil in a complex aqueous matrix. *Appl. Catal. B: Environ.* (**Submitted**).

[7] **Z. Ye**, G.E.M. Schukraft, A. L´Hermitte, Y. Xiong, E. Brillas, I. Sirés, The stability of an Fe-based 2D MOF during the photoelectro-Fenton treatment of organic micropollutants under UVA and visible light irradiation. *Water Res.* (**Submitted**).

[8] **Z. Ye**, D.R.V. Guelfi, G. Alvarez, F. Alcaide, E. Brillas, I. Sirés, Enhanced

electrocatalytic production of H_2O_2 at Co-based air-diffusion cathodes for the photoelectro-Fenton treatment of bronopol. *Appl. Catal. B: Environ.* 247 (**2019**) 191–199.

[9] **Z. Ye**, I. Sirés, H. Zhang, Y.H. Huang, Mineralization of pentachlorophenol by ferrioxalate-assisted solar photo-Fenton process at mild pH. *Chemosphere* 217 (**2019**) 475–482.

[10] D.R.V. Guelfi, **Z. Ye**, F. Gozzi, S.C. Oliveira, A.M. Junior, E. Brillas, I. Sirés, Ensuring the overall combustion of herbicide metribuzin by electrochemical advanced oxidation processes. Study of operation variables, kinetics and degradation routes. *Sep. Purif. Technol.* 211 (**2019**) 627–645.

Oral presentations in Meetings

[1] **Z. Ye**, E. Brillas, F. Centellas, P.L. Cabot, I. Sirés, Fe-based MOFs as efficient catalysts for the degradation of emerging contaminants in urban wastewater. *4th Workshop 'Advanced Materials'*, **2019**, Varna (Bulgaria).

[2] **Z. Ye**, J.A. Padilla, E. Xuriguera, E. Brillas, I. Sirés, NH_2-MIL 88B derived magnetic Fe@C-N nanocomposite as heterogeneous electro-Fenton catalyst for the degradation of micropollutants. *XL Reunión del Grupo Especializado de Electroquímica de la RSEQ (XX Iberian Meeting of Electrochemistry)*, **2019**, Huelva (Spain). Keynote

[3] **Z. Ye**, J.A. Padilla, E. Xuriguera, J.L. Beltran, F. Alcaide, E. Brillas, I. Sirés, Fe-MOF-derived FeS_2/C nanocomposite as an efficient catalyst for electro-Fenton treatment in urban wastewater. *25th Topical Meeting of the International Society of Electrochemistry*, **2019**, Toledo (Spain).

[4] **Z. Ye**, E. Brillas, F. Centellas, P.L. Cabot, I. Sirés, Degradation of butylated hydroxyanisole by Fe(III)-EDDS-assisted electro-Fenton process at neutral pH using a carbon-felt cathode. *12th Environmental Conference for Doctoral Students (Tsinghua University)*, **2018**, Beijing (China).

[5] **Z. Ye**, E. Brillas, F. Centellas, P.L. Cabot, I. Sirés, Enhancement of photoelectro-

Fenton process with Fe(III)-EDDS: A case study on the fast degradation of a fluorinated antidepressant at near-neutral pH. *69th Annual Meeting of the International Society of Electrochemistry (69th ISE Meeting)*, **2018**, Bologna (Italy).

[6] **Z. Ye**, E. Brillas, F. Centellas, P.L. Cabot, I. Sirés, Electro-Fenton process at neutral pH using a carbon-felt cathode. *XXXIX Reunión del Grupo Especializado de Electroquímica de la RSEQ (3rd E3 Mediterranean Symposium: Electrochemistry for Environment and Energy)*, **2018**, Madrid (Spain).

[7] **Z. Ye**, J.R. Steter, F. Centellas, P.L. Cabot, E. Brillas, I. Sirés, Coupling electrocoagulation with electrochemical advanced oxidation processes for the removal of organic micropollutants from wastewater treatment plant effluents. *10th World Congress of Chemical Engineering: Joint Event 'Electrochemical Engineering'*, **2017**, Barcelona (Spain).

Poster presentations in Meetings

[1] **Z. Ye**, E. Brillas, F. Centellas, P.L. Cabot, I. Sirés, Degradation of butylated hydroxyanisole by Fe(III)-EDDS-assisted electro-Fenton process at neutral pH using a carbon-felt cathode. *69th Annual Meeting of the International Society of Electrochemistry (69th ISE Meeting)*, **2018**, Bolonia (Italy).

[2] **Z. Ye**, J.R. Steter, F. Centellas, P.L. Cabot, E. Brillas, I. Sirés, Coupling of electrocoagulation with electrochemical advanced oxidation processes for the removal of benzophenone-3. *XXXVIII Reunión del Grupo Especializado de Electroquímica de la RSEQ (XIX Encontro Ibérico de Electroquímica)*, **2017**, Vitoria (Spain).